

DOT/FAA/AR-02/117

Office of Aviation Research
Washington, D.C. 20591

Crack Growth-Based Predictive Methodologies for the Maintenance of Structural Integrity of Repaired and Nonrepaired Aging Engine Stationary Components

DISTRIBUTION STATEMENT A
Approved for Public Release
Distribution Unlimited

January 2003

Final Report

This document is available to the U.S. public
through the National Technical Information
Service (NTIS), Springfield, Virginia 22161.



U.S. Department of Transportation
Federal Aviation Administration

20030508 168

NOTICE

This document is disseminated under the sponsorship of the U.S. Department of Transportation in the interest of information exchange. The United States Government assumes no liability for the contents or use thereof. The United States Government does not endorse products or manufacturers. Trade or manufacturer's names appear herein solely because they are considered essential to the objective of this report. This document does not constitute FAA certification policy. Consult your local FAA aircraft certification office as to its use.

This report is available at the Federal Aviation Administration William J. Hughes Technical Center's Full-Text Technical Reports page: actlibrary.tc.faa.gov in Adobe Acrobat portable document format (PDF).

Technical Report Documentation Page

1. Report No. DOT/FAA/AR-02/117		2. Government Accession No.		3. Recipient's Catalog No.	
4. Title and Subtitle CRACK GROWTH-BASED PREDICTIVE METHODOLOGIES FOR THE MAINTENANCE OF STRUCTURAL INTEGRITY OF REPAIRED AND NONREPAIRED AGING ENGINE STATIONARY COMPONENTS				5. Report Date January 2003	
				6. Performing Organization Code	
7. Author(s) George S. Hirko, Robert W. Hatala, and Robert A. Mattern				8. Performing Organization Report No.	
9. Performing Organization Name and Address Pratt & Whitney 400 Main Street East Hartford, CT 06108				10. Work Unit No. (TRAIS)	
				11. Contract or Grant No. DTFA03-94-C-0067	
12. Sponsoring Agency Name and Address U.S. Department of Transportation Federal Aviation Administration Office of Aviation Research Washington, DC 20591				13. Type of Report and Period Covered Final Report	
				14. Sponsoring Agency Code ANE-110	
15. Supplementary Notes The FAA William J. Hughes Technical Center Technical COTR was Richard Micklos.					
16. Abstract This report contains the results of work conducted by Pratt & Whitney between October 1994 and January 2001 under the Federal Aviation Administration contract to study the effect of aging on stationary engine components. The goal was to determine if long-term operation and multiple repairs affect the crack growth in engine-critical static structures and to provide a generic case management methodology to ensure continued airworthiness of these cases. The contract covers the evaluation of material crack growth properties in typically used case alloys, the ability to accurately predict crack growth in these components, a description of the risk assessment process, and provides a case management methodology for industry usage.					
17. Key Words Aging engine, Crack growth, Static structure, Inspection interval, Material properties, Diffuser case, Repair risk, Combustion chamber				18. Distribution Statement This document is available to the public through the National Technical Information Service (NTIS) Springfield, Virginia 22161.	
19. Security Classif. (of this report) Unclassified		20. Security Classif. (of this page) Unclassified		21. No. of Pages 322	
22. Price					

ACKNOWLEDGEMENTS

The success of this program could not have been possible without the support and input from many different people.

The support of the Federal Aviation Authority is greatly appreciated. In particular, Tim Mouzakis of the New England Regional Center, Rick Micklos and Dr. Cathy Bigelow of the William J. Hughes Technical Center are thanked for their encouragement, advice, and help with the project.

Special thanks goes out to all the assistance received from the many Pratt & Whitney individuals that contributed, especially to Robert Hatala and Carl Kelly, the main investigators for task 1; Rahif Khodary, Beatriz Suarez-Crosse, and Rick Tucker, the prime investigators for task 2; and Robert Mattern and Lou Uliano, the prime contributors for task 3. This project couldn't have been completed without their help.

Many other people contributed to the completion of this task through their review, contributions, and advice, and to all of these nameless people goes a heartfelt thank you.

TABLE OF CONTENTS

	Page
EXECUTIVE SUMMARY	xxi
1. INTRODUCTION	1
2. RESULTS AND DISCUSSION	5
2.1 Task 1: Material Data Acquisition	5
2.1.1 Establishment of Database Needs and Identification of a Source of Program Materials	5
2.1.1.1 Introduction	5
2.1.1.2 Data Required to Refine the Material Database	7
2.1.2 Effects of Multiple Repair Cycles on Non-FM Materials Mechanical Properties	12
2.1.2.1 Effect of Multiple Tempers and High-Temperature Exposure on the Non-FM Properties of AMS 5613—Plans and Preparation	12
2.1.2.2 Effect of Multiple Tempers and High-Temperature Exposure on the Non-FM Properties of AMS 5613—Results	16
2.1.2.3 Effect of Multiple Tempers and High-Temperature Exposure on the Non-FM Properties of AMS 5613—Discussion	18
2.1.2.4 Effect of Multiple Tempers and High-Temperature Exposure on the Non-FM Properties of AMS 5616—Plans and Preparation	19
2.1.2.5 Effect of Multiple Tempers and High-Temperature Exposure on the Non-FM Properties of AMS 5616—Results	22
2.1.2.6 Effect of Multiple Tempers and High-Temperature Exposure on the Non-FM Properties of AMS 5616—Discussion	26
2.1.3 Materials FM Database Refinement	28
2.1.3.1 Testing Procedures	28
2.1.3.2 AMS 5613 FM Test Plan	29
2.1.3.3 AMS 5613 FM Test Results	29
2.1.3.4 AMS 5616 Base FM Test Plan	34

2.1.3.5	AMS 5616 Base FM Test Results	35
2.1.3.6	AMS 5663 FM Test Plan	40
2.1.3.7	AMS 5663 FM Test Results	43
2.1.3.8	PWA 1469 Base FM Test Plan	50
2.1.3.9	PWA 1469 FM Test Results	53
2.1.3.10	FM Data Summary	57
2.1.4	Metallurgical Evaluation of Long-Time Service Cases	60
2.1.4.1	JT8D Combustor Cases (AMS 5613)	60
2.1.4.2	JT9D TEC (Turbine Exhaust Cases) (AMS 5616)	60
2.1.4.3	JT9D TEC Metallographic Examination	60
2.1.4.4	JT9D TEC Metallurgical Evaluation Results	60
2.1.4.5	JT9D D/C (Diffuser Case) (AMS 5663)	62
2.1.4.6	JT9D Diffuser Metallographic Analysis—Plan	62
2.1.4.7	JT9D Diffuser Case Analysis—Results	63
2.1.4.8	JT9D Diffuser Case Properties Evaluation	65
2.1.4.9	JT9D Diffuser Analysis—Discussion	75
2.1.5	Cast Nickel Case Rig Test Evaluation	75
2.1.5.1	Test Case	76
2.1.5.2	Test History	80
2.1.5.3	Initial Crack Analysis—684 Cycles	83
2.1.5.4	Second Crack Analysis—2442 Cycles	85
2.1.5.5	Rupture Fracture Analysis—5589 Cycles	87
2.1.5.6	EDM Slot Analysis—5589 Cycles	92
2.1.6	Task 1 Summary	95
2.2	Task 2: Crack Growth Prediction Methodology	97
2.2.1	Guidelines for Critical Area Determination	98
2.2.2	Define Level of Analysis for Critical Areas	99
2.2.3	Crack Growth Prediction Methods	101
2.2.3.1	Linear Elastic Fracture Mechanics	101
2.2.3.2	Explicit Fracture Code Evaluation	104
2.2.3.3	SAFE-3D Evaluation	104
2.2.3.4	BEASY Evaluation	106
2.2.3.5	FRANC-3D Evaluation	106
2.2.3.6	Fracture Code Preliminary Evaluation Summary	107
2.2.3.7	FRANC-3D Validation	108
2.2.4	Prediction of Case Stress and Crack Growth	110

2.2.4.1	Aged Steel Alloy Case Analysis	110
2.2.4.2	Wrought Nickel Alloy Case Analysis	127
2.2.4.3	Aged Cast Nickel Alloy Case Analysis	158
2.2.5	Task 2 Conclusions	171
2.3	Task 3: Risk Assessment Methodology	172
2.3.1	Task 3 Summary	172
2.3.2	Risk Assessment Philosophy	173
2.3.3	P&W Recommended Risk Assessment Process	178
2.3.4	Sample Application of Recommended Risk Assessment Process	187
2.4	Task 6: Integration of Generic Methodologies into Management Methodology	194
2.4.1	Management Methodology Recommendation	194
2.4.2	Management Approach	195
2.4.2.1	Case-Limiting Area Definition	195
2.4.2.2	Inspection Interval Determination	197
2.4.2.3	Inspection Recommendation	198
2.4.3	Summary of Management Methodology	198

APPENDICES

- A—Data and Data Plots of da/dN Tests
- B—Heat Treat Study of Inconel 718
- C—Destructive Analysis of JT9D Turbine Exhaust Case (TEC)
- D—Destructive Analysis of JT9D Diffuser Cases After Extended Service

LIST OF FIGURES

Figure		Page
1	PW4000 Cast Nickel Diffuser Case	2
2	JT9D Wrought Nickel Diffuser Case	3
3	Typical Microstructures of AMS 5613 Base Metal Test Material After 1 and 16 Stress Relieves at 1015°F (2 hrs)	14
4	Typical Microstructures of AMS 5613 Weld Test Material After 1 and 16 Stress Relieves at 1015°F (2 hrs)	15
5	Bar Chart Plots of AMS 5613 Base Metal RT Tensile Strengths as Effected by Multiple Stress Relief Cycles and Hours of Exposure to 900°F	17
6	Bar Chart Plots of AMS 5613 Base Metal RT Tensile Ductility as Effected by Multiple Stress Relief Cycles and Hours of Exposure to 900°F	17
7	Typical Microstructures of AMS 5616 Base Metal Test Material (Heat ZCESS) in Hardened-Plus-Tempered, Tempered Plus 1 Stress Relieve, and Tempered Plus 16 Stress Relieves	21
8	Typical Microstructures of AMS 5616 Welds After 1 and 16 Stress Relief Cycles	22
9	Bar Chart Plots of AMS 5616 Base Metal RT Tensile Strengths as Effected by the Number of Stress Relief Cycles and Hours of Exposure to 900°F	24
10	Bar Chart Plots of AMS 5613 Base Metal RT Tensile Ductility as Effected by the Number of Stress Relief Cycles and Hours of Exposure to 900°F	24
11	Typical Microstructure of AMS 5616 Barstock Heat PKRC After One and Eight Stress Relief Cycles at 1050°F (2 hrs)	27
12	Crack Growth (da/dN) Plots of AMS 5613 Tested at 750°F, R = 0.1 and 10 cpm	30
13	Crack Growth (da/dN) Plots of AMS 5613 Tested at 950°F, R = 0.1 With Cyclic Rates of 10 cpm and 2-Minute Dwell at Maximum Stress	31
14	Plots of Crack Growth Test Results of AMS 5613 Tested at 750° and 950°F	32
15	Plots of Crack Growth Rates (da/dN) of AMS 5613 Tested at Room Temperature and 10 cpm to Evaluate the Effects of R Ratio (0.1 vs 0.5) and Stress Relief (0 vs 8)	33
16	Plots of Crack Growth Rates (da/dN) of AMS 5616 Tested at 750°F, R = 0.1 and 10 cpm	36

17	Crack Growth Rate (da/dN) Plots of AMS 5616 Base Metal Specimens in the Hardened-Plus-Tempered Condition Tested at 950°F, R = 0.1 and Under Cyclic Loading of 10 cpm or 2-Minute Dwell at Maximum Stress	37
18	Crack Growth Rate Plots (da/dN) of Stress-Relieved AMS 5616 Tested at 950°F, R = 0.1 and Cyclic Rates of Either 10 cpm or 2-Minute Dwell at Maximum Stress	38
19	Crack Growth Rate (da/dN) Plots of AMS 5616 Tested at 850°F With and Without Dwell Loading	39
20	Typical Microstructures Exhibited by the Contract Program Coarse- and Fine-Grain AMS 5663 Test Material in the Standard Fully Heat-Treated Condition	41
21	Microstructure of Coarse-Grain AMS 5663 After Six Additional Solution Cycles at 1750°F and Six Short-Age Cycles	41
22	Microstructure of Coarse- and Fine-Grain AMS 5663, Fully Aged After 30 Hours of Exposure at the 1750°F Solution Temperature	42
23	Microstructure of AMS 5663 Weld Fusion Zones in the Standard Fully Heat-Treated Condition and After 30 Hours of Exposure at the 1750°F Solution Temperature	42
24	Crack Growth Rate (da/dN) Plots for AMS 5663 With an ASTM 4-5 Grain Size Tested at Various Temperatures	44
25	Crack Growth Rate (da/dN) Plots for AMS 5663 With an ASTM 8-10 Grain Size Tested at Various Temperatures	45
26	Crack Growth Rate (da/dN) Plots of AMS 5663 Tested at 800° and 1100°F After Being Exposed to Six 1-Hour Solution (1750°F) Exposures or Six 5-Hour Solution Exposures	46
27	Crack Growth Rate (da/dN) Plots for AMS 5663 Tested at 800°F/10 cpm, 1000°F/2 mdw, and 1100°F/2-Minute Dwell and R = 0.1	47
28	Crack Growth Rate (da/dN) Plots of AMS 5663 Gas Tungsten Arc Welds Tested at 800°F, R = 0.1 and 10 cpm	48
29	Crack Growth Rate (da/dN) Plots of AMS 5663 Gas Tungsten Arc Welds Tested at 1100°F, R = 0.1 and 2-Minute Dwell at Maximum Stress	49
30	PWA 1469 (Cast+HIP Inconel 718) in the Standard Fully Heat-Treated Condition	51
31	Microstructure of HIP Processed Welds in PWA 1469	51
32	Microstructure of PWA 1469 Base Material and HIP Welds After Eight 5-Hour Exposures at 1750°F	52

33	Microstructure of PWA 1469 Weld Fusion Zones After Being Exposed to Eight 5-Hour Exposures at 1750°F	52
34	Crack Growth Rate (da/dN) Plots of PWA 1469 Base Metal, Welds and HIP Welds Tested at 1100°F, R = 0.1, and Under 2-Minute Dwell at Maximum Stress	54
35	1100°F Crack Growth Rate (da/dN) Plots of Fully Heat-Treated PWA 1469 With a 40-Hour Exposure at 1750°F	55
36	1100°F Crack Growth Rate (da/dN) Plots of PWA 1469 With a 40-Hour Exposure at 1750°F	56
37	Typical Microstructures of HIP Welds in the Fully Heat Treated and Heat-Treated-Plus Exposed to 40 Hours at 1750°F	59
38	Typical Microstructure of Crack Growth Rate Test Specimens Excised From the Outer Pressure Wall of JT9D Diffuser Case BW0976	70
39	Typical Microstructure of Crack Growth Rate Test Specimens Excised From the Outer Pressure Wall of JT9D Diffuser Case CJ3225	70
40	Typical Microstructure of Crack Growth Rate Test Specimens Excised From the Outer Pressure Wall of JT9D Diffuser Case S/N AG9961	71
41	Crack Growth Rate (da/dN) Plots of Specimens Excised From Long-Time Service Cases BW096, AG9961, and CJ3225 Tested at 800°F, R = 0.1 and 10 cpm	72
42	Crack Growth Rate (da/dN) Plots of Specimens Excised From Long-Time Service Cases BW096, AG9961, and CJ3225 Tested at 1100°F, R = 0.1 and 2-Minute Dwell at Maximum Stress	73
43	Crack Growth Rate (da/dN) Plots of Specimens Excised From Long-Time Service Cases BW096 and CJ3225 and Coarse-Grain AMS 5663 With a 1000-Hour Exposure at 1100°F	74
44	Location Map for EDM Slots and S/Gs on the Diffuser Case	77
45	Details for EDM Slots and S/Gs on the Diffuser Case	78
46	EDM Slot Details and Measurements	79
47	Hot-Cyclic Pressure Rig Setup to Test Large Commercial Engine Diffuser Case Outer Pressure Walls	80
48	Crack in Outer Pressure Wall of PW4000 Diffuser Case Cycled for 684 Cycles in the Hot-Cycle Pressure Rig	82
49	Hot-Pressure Rig Diffuser Test Case After Rupture Following 5589 Cycles	83

50	Cross Section of Tt3 Boss Platform Fabricated With Multiple Layers of Welds	84
51	Area Between the Tt3 and Boroscope Bosses	85
52	Tensile Overload and a Combination of Tensile Overload Plus Fatigue Fracture Features Found Throughout the Main Case Fracture	86
53	Examples of Crack Growth Propagation by a Transgranular and Intergranular Paths	86
54	Examples of Secondary Cracks Along Cast Base Metal Grain Boundaries and Delta Plates	87
55	PWA 1469 Hot-Pressure Rig Test Case After 5589 Cycles at 1150°F	88
56	Left Side of Main Fracture With Five Fatigue Thumbprints Indicated by Brackets	88
57	Fractographic Photographs of Fatigue Observed on the Fracture Surface of the Hot Rig Test Case Main Rupture	89
58	Macroetched Outer Surface of Hot-Pressure Test Rig Case Illustrating Structure Near Main Case Fracture	90
59	Macroetched Inner Surface of Hot-Pressure Test Rig Case Illustrating Structure Near Main Case Fracture	90
60	Typical Intergranular Surface Cracks (a) Observed on the Hot-Pressure Rig Test Case in the Vicinity of the Case Rupture Fracture Cracks Proved to be Weld HAZ Grain-Boundary Liquation Cracks and (b) Commonly Found With Welds of Cast Inconel 718	91
61	Crack Extending Out of an EDM Slot on the Inner Surface Embossment of Large Service Boss 34 (Location No. 2)	92
62	Secondary Electron Images of EDM Slot No. 3 After It and the Associated Crack Was Opened Up (a) an Overall View of Slot and Fracture and (b) Illustrates the Line Along Which Crack Length was Measured From the Slot Into the Embossment	94
63	Secondary Electron Images of EDM Slot No. 3 After It and the Associated Crack Were Opened Up (c) White Lines Extending From the EDM Slot Edge Represent Where the Crack Length Was Measured Along the Inner-Wall Surface and (d) Along the Boss Neck	95
64	EPLAS Stress Shakedown Option Used in SURCK	103
65	Comparison of MARC Results to EPLAS for Bolthole	103

66	Bolthole Specimen With Tensile Load	108
67	Bolthole Tension Specimen Stress-Intensity Correlation	109
68	Bolthole Bending Specimen Stress-Intensity Correlation	109
69	JT8D-200 Series CCOC General Features	110
70	The UG Solid Models of the Ps4 Boss Used in the Analysis (Model 1)	111
71	The UG Solid Models of the Ps4 Boss Used in the Analysis (Model 2)	111
72	ANSYS 3D Model of the CCOC Drain Boss	111
73	ANSYS 3D Model of the CCOC Ps4 Boss	112
74	The 2D Axisymmetric ANSYS Model of Two Bosses	112
75	The CCOC Drain Boss in the 3D ANSYS Model	113
76	Schematic of the Test Cycle Shows the Steady-State and Transient Conditions	113
77	Comparison of Transient Temperatures for ACCEL Between Measured (TC) and Simulated (ANSYS) (the Analysis; Open Drain Tube Case) for Three Selected T/C Locations	114
78	Comparison of Transient Temperatures for DECEL Between Measured (TC) and Simulated (ANSYS) (the Analysis; Open Drain Tube Case) for Three Selected T/C Locations	114
79	CCOC Drain and Ps4 Boss 3D Solid Model and Applied BCs	115
80	Maximum Stress Location at the CCOC Rear Flange	116
81	Maximum Stress Location at the Drain Boss Weld	117
82	High Stresses at the Ps4 Boss Weld Region	117
83	UG Solid Model of the JT8D-CCOC Shows the Bosses Features and the Submodels Selections at the Critical Locations on the Weld	118
84	Drain Boss Submodel No. 2 Mesh Density and Temperature Gradient	118
85	JT8D-219 CCOC Maximum Principal Stresses at the Drain Boss Weld Fillet	119
86	JT8D-219 CCOC Maximum Principal Stresses at the Ps4 Boss Weld Fillet	120
87	JT8D-219 CCOC Drain Boss Through Thickness Stress Gradient	121

88	Crack Growth Rate of Steel (AMS 5613) at 750°F, R = 0.1 Used in the Analysis	122
89	JT8D CCOC Typical Rear Drain Boss Crack With Multiorigins	123
90	JT8D-200 CCOC Drain Boss Residual Lives for Different Crack Lengths, Analysis Performed at t = 700°F and Crack Depth a = 0.016"	124
91	JT8D-219 CCOC Drain Boss Crack Propagation Life Through Thickness Calibrated With Field Data	126
92	JT8D-219 CCOC Drain Boss Crack Propagation Life on Surface Calibrated With Field Data	126
93	JT9D Diffuser Case Boss 6 Solid Model and Mesh Density, 36° Sector	128
94	JT9D Diffuser Case Boss 7&8 Solid Model	128
95	Temperature Gradient Near Boss 7&8 at t = 26 sec	129
96	Temperature Gradient Near Boss 6 at t = 28 sec	129
97	Predicted Metal Temperature Near Boss 6 at t = 28 sec	129
98	Predicted Rear Rail Temperature Gradient at Boss 6, t = 28 sec	129
99	Boss 7&8 Metal Temperature at t = 26 sec	130
100	Rear Rail Gradient Near Boss 7&8 at t = 26 sec	130
101	Maximum Principal Stress at the Rear Rail Adjacent to Boss 6	130
102	Maximum Principal Stress at the Rear Rail Adjacent to Boss 7&8	130
103	T9D Diffuser Case, Boss 7&8 Submodels	132
104	JT9D Diffuser Case, Boss 6 Submodels	133
105	Maximum Elastic Principal Stress Results for Boss 7&8 and Boss 6	133
106	Maximum Plastic Principal Stress Results for Boss 7&8 and Boss 6	134
107	Elastic Principal Stress Path Plots for Boss 7&8 and Boss 6—Aft End	134
108	Elastic Principal Stress Path Plots for Boss 7&8 and Boss 6—Forward End	135
109	Plastic Principal Stress Path Plot for Boss 7&8 and Boss 6—Aft End	135
110	Plastic Principal Stress Path Plot for Boss 7&8 and Boss 6—forward End	135

111	Boss 7&8 and Boss 6 Initial Global Model and Crack Mesh	137
112	Elastic Stress-Intensity Factor Results for Corner Crack—Top Segment	138
113	Elastic Stress-Intensity Factor Results for Corner Crack—Forward Segment	138
114	Plastic Stress-Intensity Factor Results for Corner Crack—Top Segment	138
115	Plastic Stress-Intensity Factor Results for Corner Crack—Forward Segment	139
116	Life Calculations for Corner Crack Using Elastic Stress Field	139
117	Life Calculations for Corner Crack Using Plastic Stress Field	140
118	Paris Equation Model for AMS 5663 (Wrought IN 718)	141
119	Twenty-Five Percent NCL and Fifty Percent NCL Stress-Intensity Factor Extraction Points for Edge and Through Cracks	141
120	Elastic Stress-Intensity Factor Results for Edge Crack—Aft Segment	142
121	Elastic Stress-Intensity Factor Results for Edge Crack—Forward Segment	142
122	Plastic Stress-Intensity Factor Results for Edge Crack—Aft Segment	142
123	Plastic Stress-Intensity Factor Results for Edge Crack—Forward Segment	143
124	Maximum Elastic Principal Stress Path Plots for Uncracked and Cracked Models, Boss 6—Aft Segment	144
125	Maximum Elastic Principal Stress Path Plots for Uncracked and Cracked Models, Boss 6—Fore Segment	144
126	Maximum Elastic Principal Stress Path Plots for Uncracked and Cracked Models, Boss 7&8—Aft Segment	145
127	Maximum Elastic Principal Stress Path Plots for Uncracked and Cracked Models, Boss 7&8—Fore Segment	145
128	Principal Elastic Stress Distribution for Cracked Boss 6	146
129	Principal Elastic Stress Distribution for Cracked Boss 7&8	146
130	Elastic Stress-Intensity Factor Results for Through Crack	147
131	Plastic Stress-Intensity Factor Results for Through Crack	147
132	Life Calculations for Through Crack Using Elastic Stress Field	148

133	Life Calculations for Through Crack Using Plastic Stress Field	148
134	Three Phases of Crack Propagation	149
135	Wrought IN 718—Diffuser Case Rear Rail Maximum Principal Stress Gradients	150
136	JT9D-DC Rail SIF Values Comparison Between SURCK and FRANC-3D	150
137	JT9D-DC Rail Corner Crack Propagation Adjacent to Boss 7&8 and Boss 6, Comparison Between SURCK and FRANC-3D Predictions	151
138	JT9D-DC Rear Rail Minimum Residual Life Using SURCK Predictions	152
139	JT9D-DC Rear Rail Typical Residual Life Using SURCK Predictions	152
140	JT9D-DC Rear Rail Minimum Residual Life Using FRANC-3D Predictions	153
141	JT9D-DC Rear Rail Typical Residual Life Using FRANC-3D Predictions	153
142	Paris Equation Model for IN 718 Weld	155
143	JT9D-DC Welded/Repaired Rear Rail FM Analysis, Case BW 1086 Weld Defect Size ~ 0.12" x 0.015"	156
144	JT9D-DC Rear Rail Welded/Repaired FM Analysis, Case AH 0071 Defect Size 0.035 x 0.012"	156
145	JT9D-DC Welded/Repaired Rear Rail FM Analysis, Case BG 3352, Defect Size 0.110" x 0.015"	157
146	EDM Slot 2 and Cyclic Crack Growth	160
147	Crack Growth Correlation EDM Slot 2	160
148	Maximum Stresses at Slot 8 Location Used in the FM Analysis	161
149	Photomicrograph of Slot No. 8 After the Crack Was Broken Open	161
150	Crack Growth Correlation for EDM Slot 8	162
151	EDM Slot 6 Crack Growth Correlation	162
152	Maximum Stresses at the Slot 6 Location Used in the FM Analysis	163
153	Striation Data Obtained From the 4.125" Long Case Crack	163
154	ANSYS Model of the Diffuser Case Section	164
155	FRANC-3D Model Imported From the ANSYS Diffuser Case Model	164

156	Elastic Principal Stresses Between the Tt3/Binocular Bosses	165
157	Plastic Principal Stresses Between the Tt3/Binocular Bosses	165
158	Initial Crack Geometry Nucleated Between the Tt3 and the Binocular Bosses in the Engine Correlation	166
159	FRANC and SURCK Predictions Plotted With the Striation Data From the Engine Test	167
160	Maximum Principle Stress Between the TT/Binocular Bosses at Running Rig Conditions	167
161	Initial Crack Geometry Nucleated Between the Tt3 and the Binocular Bosses in the Rig Correlation	168
162	Cast IN 718 (Aged) Crack Growth Law	169
163	FRANC and SURCK Crack Growth Predictions Plotted Against the Striation Data for the Rig Test	169
164	Case Rupture in the Cyclic Pressure Rig	171
165	Risk Simulation Flowchart	174
166	P&W Recommended Risk Assessment Process Flowchart	179
167	Example of Risk Model Crack Calibration Curve	191
168	Example Plot of Cumulative Risk Factor	192
169	Case Management Process Flowchart	195
170	Case-Limiting Location Example for Damage Tolerance Life Calculation	196
171	Expanded Management Process Flowchart	199

LIST OF TABLES

Table	Page
1 Major Engine Cases	6
2 AMS 5613 and AMS 5616 Field Repair Heat Treat Cycles	7
3 AMS 5613 and AMS 5616 Mechanical Properties Test Program	8
4 AMS 5663 Component Field Repair Heat Treatments	9
5 AMS 5663 Crack Growth (da/dN) Test Plan	10
6 AMS 5663 Weld Crack Growth (da/dN) Test Program	11
7 PWA 1469 Base and Weld Crack Growth (da/dN) Test Program	11
8 Summary of Effects of Multiple Repair Heat-Treatment Cycles on the Mechanical Properties of AMS 5663 and PWA 1469	12
9 AMS 5613 Room Temperature Tensile Properties—Preliminary and Main Evaluations Effect of Multiple Stress Relieves and 900°F Exposures	16
10 AMS 5613 Welds 750°F Notch ($k_t = 2$) LCF Properties Test Results	18
11 AMS 5613 Welds 750°F Notch ($k_t = 2$) LCF Properties Test Data Analysis	18
12 AMS 5616 RT Tensile Properties Effect of Multiple Stress Relieves and 900°F Exposures	23
13 AMS 5616 750°F Notch LCF Properties	25
14 AMS 5616 Base Metal 750°F Notch ($k_t = 2$) LCF Properties Test Data Analysis	26
15 AMS 5616 Welds 750°F Notch ($k_t = 2$) LCF Properties Test Data Analysis	26
16 AMS 5616 Crack Growth (da/dN) Test Plan	35
17 1100°F/2-mdw Crack Growth Rates at 20 and 30 Delta K for Various Forms of Inconel 718	58
18 JT9D TEC S/N CD8893 Metallographic Analysis Areas	61
19 JT9D Diffuser Cases Retired From Service	62
20 Summary: Weld Analysis Long-Time Service JT9D Diffuser Cases	64
21 Mechanical Properties Test Plan Long-Time Service JT9D Diffuser Cases	65

22	Monotonic Mechanical Properties of Long-Time Service JT9D Diffuser Cases	66
23	Smooth ($k_t = 1$) Low-Cycle Fatigue Properties Long-Time Service JT9D Diffuser Cases	67
24	Notch ($k_t = 2$) Low-Cycle Fatigue Properties Long-Time Service JT9D Diffuser Cases	68
25	Analysis of Low-Cycle Fatigue Properties of Long-Time Service JT9D Diffuser Cases	68
26	EDM Test Slots, PW4168 Diffuser Case, Exposed to Eight 5-Hour Heat Treatments	76
27	Pressure Rig Test Log	81
28	FPI Crack Length Measurements of Pressure Test Case EDM Slots	92
29	Crack and Slot Length Measurements	93
30	P&W Experience of JT9D-7 Engine Diffuser Case Cracking Locations	98
31	List of Critical Locations on Diffuser Cases and the Required FEA	101
32	JT8D-219 CCOC Maximum Principal Stresses at the Drain Boss	119
33	JT8D-219 CCOC Maximum Principal Stresses at the Ps4 Boss	119
34	JT8D-219 CCOC Rear Drain Boss Crack Sections Striation Data	124
35	JT8D-219 CCOC Crack Field Data	125
36	Cyclic Pressure Rig Predicted vs Measured Stresses	159
37	Crack Length From Slot Center—Inches	159
38	Stress-Intensity Factors at Various Crack Lengths for the Engine Conditions and the Calculated da/dN Values	166
39	Stress-Intensity Factors at Various Crack Lengths Under the Rig Conditions and the Calculated da/dN Values	168

LIST OF ACRONYMS AND TERMS

a	crack length
ANSYS	Commercial finite element code
APU	Auxiliary power unit
BIE	Boundary integral equation
da/dN	crack growth rate—change in crack length per cycle of operation
EDM	Electro discharge machining—the use of an electrode to machine a part, in this case to place a crack into a piece of hardware
FM	Fracture mechanics
FAA	Federal Aviation Administration
FCG	Fatigue crack growth—progressive growth of a crack due to fatigue loading
FEA	Finite element analysis
FEM	Finite element method
FPI	Fluorescent penetrant indications
FRANC-3D	3-dimensional fracture mechanics code developed by Cornell University
GS	grain size of a material
HIP	Hot isotropic pressure—method of processing casting under high isotropic pressure conditions to reduce casting porosity
I.D.	Inner diameter
LCF	low cycle fatigue
LOF	lack of fusion; incomplete fusion of two surfaces during the welding process
IN 718	Inconel 718 material
k	Stress-intensity factor
N	Cycles

NASTRAN	Commercial finite element code
NCL	Normalized crack length
NDI	Nondestructive inspection—the ability to detect cracks through the use of nondestructive methods, such as fluorescent penetrant, eddy current, or ultrasonic inspection techniques.
O.D.	Outer diameter
P&W	Pratt & Whitney
S/G	Strain gage
SIF	Stress-intensity factor
Sinh	Hyperbolic sine function
Striation Count	A metallographic review of a crack surface that counts the number of repetitive cycles over a measured length
SURCK	Pratt & Whitney in-house linear elastic fracture mechanics code

EXECUTIVE SUMMARY

Pratt & Whitney (P&W) has successfully managed cracking in critical engine cases through field management plans. These plans typically employ the monitoring of crack growth and the incorporation of repair and case modifications. In 1995, P&W began supporting the Federal Aviation Administration's (FAA) investigation into the effect of possible loss in material properties due to aging and multiple repairs under their contract to develop "Crack Growth-Based Predictive Methodologies for the Maintenance of Structural Integrity of Repaired and Nonrepaired Aging Engine Stationary Components."

The two main objectives of the contract were to:

1. determine if aging and multiple repairs impacted case material properties requiring a new FAA regulation for mandatory retirement lives or inspection intervals on static cases to ensure future flight safety.
2. provide a generic methodology the industry could use to develop management plans for the continued airworthiness of high-pressure static cases.

Additional work to determine improved nondestructive inspection and repair techniques was dropped from the contract due to funding restrictions.

Extensive material evaluation was performed as part of this contract. A complete summary of the conclusions of this testing can be found in section 2.1. Testing has shown that aging and multiple-repair cycles have some deleterious effects on these materials. The major effects are summarized here:

- Multiple stress relieves have a small debiting effect on the strength of AMS 5616 (Greek Ascoloy).
- Multiple solutions, ages, and long-time exposure to 1100°F temperature all cause accelerated crack growth in AMS 5663 (wrought IN 718) at temperatures over 1000°F.
- Welds of coarse grain AMS 5663 have 800°F crack growth rates close to that of fine grain baseline AMS 5663.
- Welds of AMS 5663 have crack growth rates at 1100°F under dwell conditions that lie between that of coarse- and fine-grain baseline material.
- Multiple solution heat treatments slightly accelerate the high-temperature (>1000°F) dwell crack growth rate of AMS5663 welds.
- Welded material in cast 718 have crack growth rates that are faster than the baseline cast material at 1100°F dwell by up to a factor of 3-4X.

- Hot isotropic pressure (HIP) welds in cast 718 material have crack growth rates that are faster than the baseline cast material at 1100°F dwell by factors of 8X to >10X. There is also a wide scatter between the two tests of HIP welds.
- Up to 40 hours of re-solution heat treatment accelerates the 1100°F dwell crack growth rate of cast 718 material by a factor of <2X.

Current stress and crack growth prediction methodologies were investigated under the contract. Application of these techniques successfully predicted the crack growth experienced in operating cases as well as that generated during testing of a full-scale cast case under contract funding.

A risk analysis methodology to quantify the expected number of future events, along with the probabilities of occurrence for cracking of pressurized engine static cases has been documented. It provides a methodology that includes the discussion of typical input data elements and their usage, statistical procedures used in creating the model, methods of model calibration with actual experience, typical output elements, and the philosophy of sensitivity studies. An approach to define inspection thresholds, reinspect intervals, and retirement of cases that exceed authorized repair limits is included.

A generic risk management methodology is presented that can be used for the management of critical case structures throughout the industry. The management methodology includes the recommendation for repetitive case inspections for cases whose rupture could hazard an aircraft.

Conclusions and Recommendations:

- There is no immediate need for the retirement of aged cases to insure flight safety.
- Risk management methodology should be applied to critical static cases to determine an appropriate repetitive inspection interval.
- The material data generated under this contract should be used in the risk management methodology that defines the case inspection requirements.
- Current stress and crack growth prediction methods can accurately predict case crack growth.

1. INTRODUCTION.

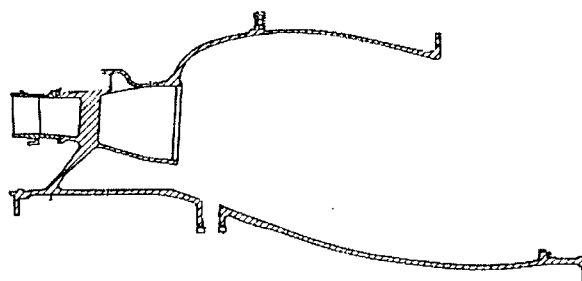
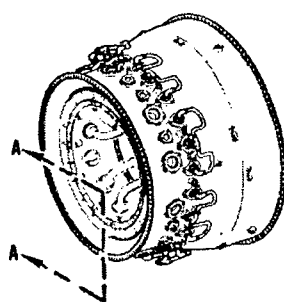
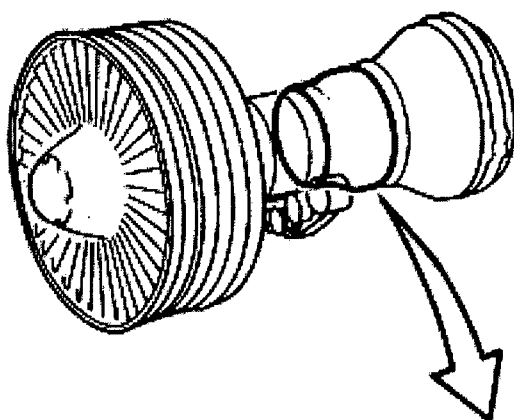
Pratt & Whitney (P&W) entered into a 5-year contract, "Crack Growth-Based Predictive Methodologies for the Maintenance of Structural Integrity of Repaired and Nonrepaired Aging Engine Stationary Components," with the Federal Aviation Administration (FAA). The contract began in October 1994 and was aimed at maintaining flight safety through the management of cases as they age and included the following major tasks:

- Task 1. Material Data Acquisition
- Task 2. Crack Growth Prediction Methodology
- Task 3. Risk Assessment Methodology
- Task 4. Nondestructive Inspection (NDI) Methodology
- Task 5. Repair Methodology
- Task 6. Integration of Generic Methodologies

Subsequent to the beginning of the contract, tasks 4 and 5 were eliminated due to funding issues.

The FAA Draft Advisory Circular, Continued Airworthiness Assessments of Turbine Engines, Propellers, and APUs (Revision 9 – 5/10/95) shows that there have been 31 major case ruptures, resulting in four category 3 and two category 4 events. (Category 3 damage is defined as significant airplane damage with the airplane capable of continuing flight and making a safe landing. Category 4 damage is defined as severe airplane damage involving a crash landing, critical injuries, fatalities, or hull loss.) Currently, unlike rotating hardware, the FAA has no requirement to track time or cycles on these critical engine static parts. In addition, these parts typically undergo multiple repairs, requiring extensive heat treatment procedures to extend their useful operational life. Since total part-time cycles are not typically tracked, the ability to manage the parts, if any future cracking occurs, relies heavily on the ability to accurately predict the future growth of these cracks. Historically, inspection intervals to monitor crack progression have been based on observed or predicted crack growth. The determination of any material property degradation due to these repairs and long-time operation of these cases, its effect on mechanical properties affecting the development and propagation of cracks are an integral part of this contract. The evaluation of the material properties of these parts is conducted to determine if a new FAA regulation is required to impose either mandatory retirement lives or inspection intervals on static cases to ensure future flight safety.

The program is intended to address the flight safety and airworthiness of commercial engine-pressurized cases that are subjected to high-energy ruptures from cracks originating at flaws, welds, or local design features, which presents the greatest flight safety risk of any of the stationary cases or frames. The goal of this effort is to provide a generic methodology for safely managing fracture mechanics and crack growth applicable to the entire commercial fleet. This methodology has been developed using the designs, materials, and experience of the P&W fleet of engines. However, because of its generic form, it can be applied to the engine static cases of all manufacturers. The program addresses wrought, fabricated cases, and cast cases that are currently operating in the airline fleet. Figures 1 and 2 present P&W cast and wrought case configurations that are typical of cases being addressed.



SECTION A-A

FIGURE 1. PW4000 CAST NICKEL DIFFUSER CASE

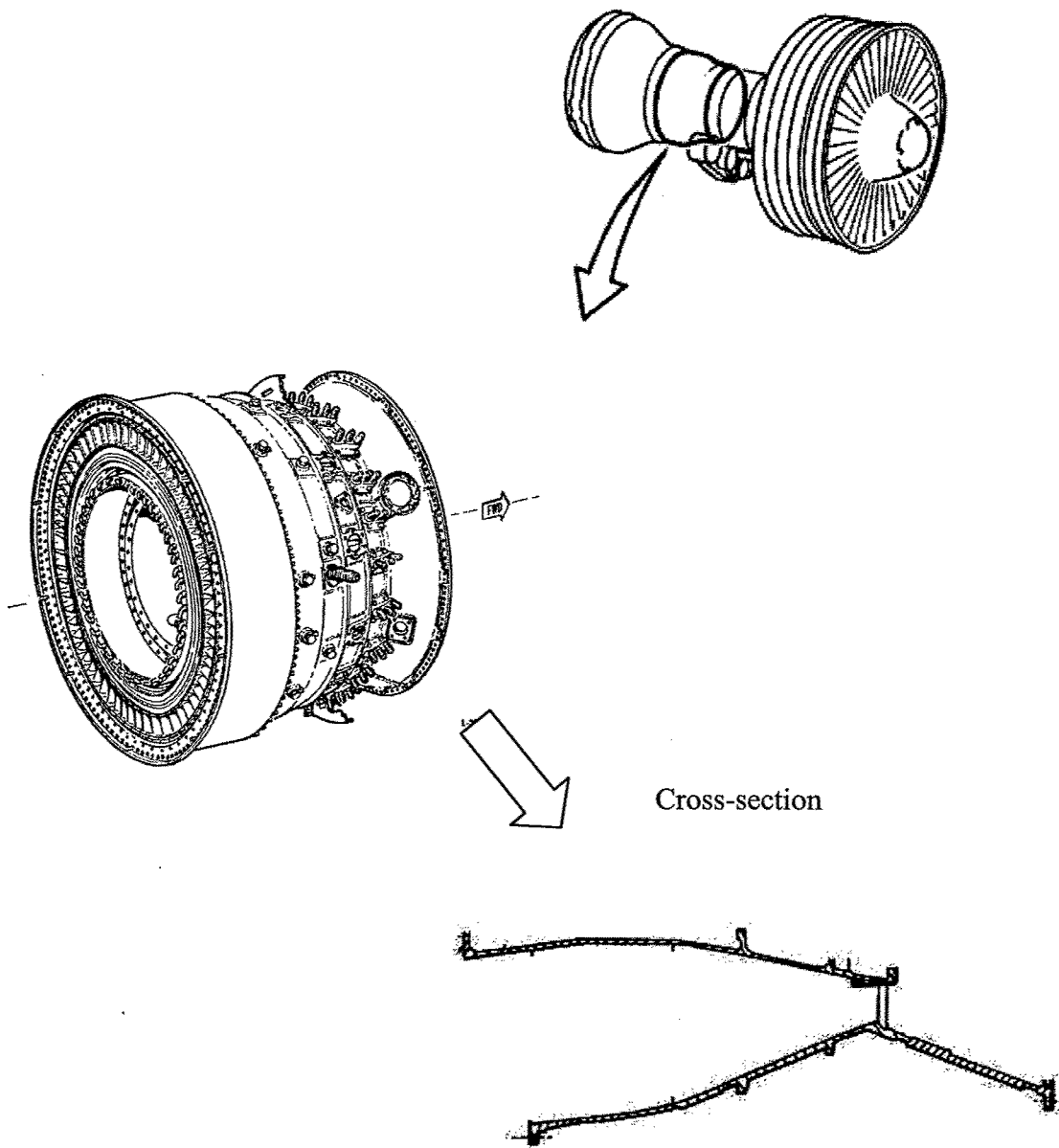


FIGURE 2. JT9D WROUGHT NICKEL DIFFUSER CASE

This contract has developed general strength and fracture mechanics properties for case materials that has been exposed to multiple processing cycles typical of engine cases that have been operated for long periods of time and have gone through several repair cycles.

Information is needed for inclusion in a risk simulation program to quantify the expected number of future case crack events and the probability of occurrence for the representative aging fleet has to be determined. A risk analysis methodology is presented as the basis for predicting the risk of future cracking events that includes the aging material characteristics and is based on P&W risk methodology experience.

Task 1 was aimed at providing the material data required for the development of the program methodology. Specifically, the required basic material fracture crack growth characteristics for baseline and repaired material were developed. Test specimens as well as a full-size case were tested in order to gather data used in the calibration of the stress and crack growth analysis techniques. During this task, the cycling of a PW4000 cast diffuser case was seeded with flaws to more closely simulate crack growth that would be experienced in operation. The effect of multiple repair heat treatments experienced by a case aged in operation for several typically used case materials were evaluated. Task 5 was meant to fully explore industry repair standards to gain a comprehensive understanding of the number of repairs a typical case undergoes during its operational life. While the cancellation of task 5 prevented this in depth review of industry standards, several discussions were held with repair vendors in the industry to identify how many repair cycles a case might undergo. This repair "exposure" was simulated in the material as part of the task.

Task 2 formulated methodologies to calculate case static stress and fracture progression rates. This task consists of two sections. The first addressed the determination of the static case stress fields in which cracks propagate and included the identification of case-critical areas based on P&W experience. The second section presented the calculation method for the crack fracture progression rate at the various limiting locations within the case. An integral part of both sections was the calibration of the methods with P&W service experience and the results of the rig testing that simulates field service operation.

Task 3 formulates a generic risk analysis methodology to quantify the expected number of future events, along with the probabilities of occurrence for cracking of pressurized engine static cases. It documents risk analysis methodology that includes the discussion of typical input data elements and their usage, statistical procedures used in creating the model, methods of model calibration with actual experience, typical output elements, and the philosophy of sensitivity and "what-if" studies. A generic approach for defining inspection thresholds, reinspect intervals, and retirement of cases that exceed authorized repair limits is also included.

This task provides an improved optimization of the recommended field management program process that should lead to increased flight safety with less economic impact.

Tasks 4 and 5 were eliminated subsequent to the contract award due to funding limitations.

Task 6 combines the individual task methodologies into an overall generic methodology that can be used to develop management plans for the continued airworthiness of high-pressure static cases. The methodology shows how to develop overall fleet management plans that are directly applicable to the management of any engine model.

The methodologies that were generated in tasks 1 through 3 have been integrated into this overall generic methodology. This methodology shows how to establish a process to develop management plans to assure the continued safe operation of engine high-pressure cases. It is applicable to all engine cases, regardless of manufacturer, and provides the capability for defining the retirement of cases that exceed authorized, safe operating condition.

2. RESULTS AND DISCUSSION.

Each of the major program tasks is summarized in an individual section of the report.

2.1 TASK 1: MATERIAL DATA ACQUISITION.

The overall objective of task 1 was to provide materials, microstructure characteristics, and mechanical property data to enhance the development of crack growth prediction methodology (task 2) and support integration of the methodology into a field management plan (task 6). Task 1 has six subtasks, which are:

1. Establishment of database needs and identification of a source of program materials.
2. Characterization of effects of multiple repair cycles on non-fracture mechanics (FM) materials mechanical properties.
3. Refinement of materials FM properties database.
4. FM characterization of material exposed to the "maximum" allowable repair cycles.
5. Metallurgical evaluation of long-time service cases.
6. Rig testing (where needed) of full-size components to complement specimen tests.

For purposes of reporting, subtasks 3 and 4 have been combined.

2.1.1 Establishment of Database Needs and Identification of a Source of Program Materials.

2.1.1.1 Introduction.

The first step in establishing what was needed in the database was to select several alloy systems for investigation. P&W has generated extensive mechanical property databases on all alloys committed to production of commercial gas turbine engine static components. The contract program goal was not to develop a management plan for all alloys used by P&W, but rather to develop and demonstrate a methodology for several families of alloys to ensure the established system holds true for more than one type of alloy system. Three criteria were considered when selecting which alloy systems to include in the program.

1. Extensive use—Extensively used alloys, especially when represented in several critical and/or sensitive applications, offer the best value for development of a field management system.
2. Experience—One objective of the program is to validate or adjust design and life prediction systems based on materials' specimen tests with experience gained in the field on actual components. Alloys that have not been used much offer little opportunity to compare the prediction system against field occurrences. It would be especially helpful to have field cracking experience to test the models.

Upon considering these two criteria, titanium alloys were eliminated. Most titanium-static structures in P&W commercial engines are stiffness limited, although they may have local areas with high concentrated stresses. P&W's experience with titanium cases is that they need infrequent repairs and represent a very low risk with long-time service. The steel and nickel cases, on the other hand, often are in static components that have cyclic life limits and require frequent field repairs. A field management system for steel and nickel alloys would provide the most value. A third criterion was a good understanding of the crack growth characteristics of the alloy. Special conditions would be investigated in the program. However, there would be a heavy reliance on existing materials' fracture mechanics databases to develop the management program.

Table 1 lists steel and nickel alloys currently used in mature and newer commercial engines. Until 1980, P&W's major structural cases were weld assemblies comprised of smaller details that were more typically of wrought (sheet, forging) form but occasionally contained small castings. In 1980, P&W introduced its first major one-piece cast structural case, the PW2000 diffuser case. This case is constructed of cast+HIP (Hot Isostatic Pressed) Inconel 718 alloy, referred to as specification PWA 1469. Since then, the use of cast+HIP nickel cases has steadily increased and is now being used in commercial engine diffusers, tangential on-board injection (TOBI), and bearing housing cases.

TABLE 1. MAJOR ENGINE CASES

Engine	Diffuser Case	HPT Case	LPT Case	Turbine Exhaust Case
JT8D	AISI 410 Stainless	A-286	A-286	Greek Ascoloy
JT9D	Wrought Inconel 718	Wrought Inconel 718	Wrought Inconel 718	Greek Ascoloy
PW2037/40	Cast+HIP Inconel 718	Wrought Inconel 718	Wrought Inconel 718	Greek Ascoloy
V2500	Cast+HIP Inconel 718	Wrought Inconel 718	Wrought Inconel 718	Greek Ascoloy
PW4056	Cast+HIP Inconel 718	Wrought Inconel 718	Wrought Inconel 718	Greek Ascoloy
PW4168	Cast+HIP Inconel 718	Wrought Inconel 718	Wrought Waspaloy	Greek Ascoloy
PW4084	Wrought Waspaloy	Wrought Inconel 718	Wrought Waspaloy	H-46 Steel
PW4090/98	Wrought Waspaloy	Wrought Inconel 718	Wrought Waspaloy	H-46 Steel

Four alloy systems, two steels and two nickel, were selected from the matrix in table 1. AMS 5613 (AISI 410 stainless steel) was selected because it represents a lower operating steel temperature of <900°F and because P&W has substantial field data reports relating to the cracking of the JT8D CCOC (combustor chamber outer case). AMS 5616 (Greek Ascoloy) was selected because it represents a higher operating steel temperature of 1000°F+ that is used extensively in the construction of turbine exhaust cases (TEC) for P&W's high-bypass commercial turbofan engines. All models of the JT9D high-bypass turbofan engine have an AMS 5616 TEC, many with extensive service life and with numerous visits to repair and overhaul shops. Thus, both alloys satisfy the first two criteria for program material alloy selection. Both alloys went into service before testing of materials fracture mechanics characteristics was prevalent for static component applications. As a result, the existing fracture mechanics databases (criterion three) for both alloys were limited.

Nickel alloy Inconel 718 was chosen for investigation primarily because of its major role in the construction of diffuser cases. It is a critical component that is a high-pressure vessel with cyclic limits which is critical to engine performance and safety. Inconel 718 would be evaluated in both wrought (AMS 5663) and cast+HIP (PWA 1469) forms. The former is represented in application of the JT9D diffuser with which P&W has a documented history of crack occurrence and many of which have long-time service experience with numerous trips to repair and overhaul shops. AMS 5663 satisfies all three criteria for selection for investigation. PWA 1469, however, satisfies only the first and third criterion. PWA 1469 is a relatively new alloy and, therefore, has little field cracking experience. However, PWA 1469 offers the opportunity to investigate the effects form (i.e., cast vs wrought) has on long-time field stability. Also, the well-developed PWA 1469 database is validated by hot-pressure rig tests.

2.1.1.2 Data Required to Refine the Material Database.

A review of the AMS 5613 and AMS 5616 database systems revealed that very little fracture mechanics testing had been done. The few tests that were conducted were done under specified conditions to address special, but limited, design considerations or unique field situations. It was, therefore, necessary to generate crack growth rate values (da/dN) for both alloys and their welds in the base processed (hardened + tempered) condition. In the field, it is a common repair practice to weld AMS 5613 and AMS 5616 cases, followed by a stress-relieving temper, often using local heating procedures. All AISI 400 grade steel cases have the option of being rehardened with a reaustenization exposure followed by a rapid cool plus a temper. However, this reconstitution heat treat process is rarely used because of the added difficulty of heat-treating a full-size case and the risk that dimensions of the fully machined case may be distorted. Even in original equipment manufacture (OEM), the cases are hardened prior to machining. Current heat treatment procedures for P&W AMS 5613 and AMS 5616 cases are listed in table 2.

TABLE 2. AMS 5613 AND AMS 5616 FIELD REPAIR HEAT TREAT CYCLES

Alloy System	Stress Relieve ¹	Reharden ²
AMS 5613	1015°F (2 hrs)	1750°F (1 hr) + 1015°F (2 hrs)
AMS 5616	1050°F (2 hrs)	1800°F (1 hr) + 1050°F (2 hrs)

Notes: 1. Stress relieve locally or in furnace following weld repair.

2. Rearden + temper prior weld repair followed by a second stress relief.

An overall testing plan for AMS 5613 and AMS 5616 is presented in table 3. Recent test data was not available for either alloy that was exposed to multiple stress relief cycles. The contract plan was to measure the effect multiple stress relief cycles had on the room temperature tensile, 750°F notch low cycle fatigue (LCF), non-dwell-loading da/dN rates at 750°F and 950°F as well as dwell-loading da/dN rates at 950°F. Ten cycles per minute (cpm) was selected for nondwell da/dN testing and a 2-minute hold at high load was selected for dwell testing. All tests would be at $R = 0.1$. These are typical test conditions used for materials being characterized for commercial engine application.

Although it is not uncommon for AMS 5616 cases to see exposure in service to temperatures above 1000°F, AMS 5613 and AMS 5616 rarely see little extended service at temperatures above 900°F. Prior to conducting the test program outlined in table 3, a preliminary test program would be conducted. Hardness and tensile tests would be used to confirm that multiple stress relieves and extended exposures at 900°F do not have a deleterious effect on either alloys' strength. The same stress relief conditions would be used as well as exposures to 900°F for as long as 1,000 hours.

TABLE 3. AMS 5613 AND AMS 5616 MECHANICAL PROPERTIES TEST PROGRAM

Condition ¹	Hardness		RT Tensile		750F Notch LCF ²		da/dN ³	
	AMS 5613	AMS 5616	AMS 5613	AMS 5616	AMS 5613	AMS 5616	AMS 5613	AMS 5616
H+T	X	X	X	X				X
H+T + 1 S/R	X	X	X	X	X	X	X	X
H+T + 8 S/R ⁴	X	X	X	X	X	X	X ⁵	X ⁵
H+T + 16 S/R	X	X	X	X	X	X	X	X

Notes: 1. H+T = Harden + Temper

AMS 5613 - 1750°F (1 hr) oil quench + 1015°F (2 hrs) AC (Air cooled)

AMS 5616 - 1800°F (1 hr) oil quench + 1050°F (2 hrs) AC

S/R = Stress Relieve:

AMS 5613 - 1015°F (2 hrs)

AMS 5616 - 1050°F (2 hrs)

2. AMS 5613 – modified for weld metal only; AMS 5616 - base metal and welds

3. Tests at 750°F - 10 cpm, 950°F - 10 cpm and 950°F - 2 mdw (2-minute dwell)

4. Optional: Test only if material with 16 stress relieves shows significant differences relative to single-stress relief material

AMS 5663 (wrought IN 718) cases are most commonly repaired with a process that requires a full re-solution heat treatment prior to welding, another full re-solution heat treatment after welding, followed by a full precipitation heat treatment. This process places the material in the most optimum form for welding, achieves full postweld stress relieve, and produces material with full properties. An option reserved for small welds in noncritical locations, allows the material to be welded in the fully hardened condition followed by a "short-age cycle." The short-age cycle is an abbreviated form of the standard precipitation heat treat cycle and provides partial stress relief of the weld while imparting the material with full-strength capability. Both processes are outlined in table 4. AMS 5663 has been extensively tested at P&W, including monotonic (tensile and stress rupture) and cyclic (smooth and notch LCF) property tests of material exposed to as many as six re-solution heat treatments (followed by a precipitation heat treatment) and six short-age cycles. Although the effects are well documented, prior evaluation programs failed to include an assessment of the effect multiple repair cycle heat treatments have on the da/dN characteristics of AMS 5663.

TABLE 4. AMS 5663 COMPONENT FIELD REPAIR HEAT TREATMENTS

Process Step	Full HT Option ^{1,3}	Age Only Option ²
1. Preweld heat treat	1750°F (1 hr)	None
2. Weld repair	GTA repair or EB detail replacement	GTA repair
3. Postweld stress relief	1750°F (1 hr)	
4. Precipitation harden	1325°F (8 hrs) FC (Furnace cool) to 1150°F (8 hrs) AC	1400°F (5 hrs) FC to 1200°F (1 hr)

- Notes: 1. Large repairs and all repairs in critical locations
2. Small repairs in less critical (i.e., low stress) locations.
3. Operators have the option to use the short age with the full heat treat option

For this project, a test program was developed to define repair heat treat processing effects on AMS 5663 da/dN properties. This is presented in table 5. Two factors added complexity to the plan. One was that while most details were fabricated from coarse-grained AMS 5663 (typically ASTM 4-5) with "needle" delta phase structure, there were no restrictions regarding the fineness of grain size. Individual details used in construction of larger cases, such as the JT9D diffuser case, can have grain sizes from ASTM 3 to ASTM 12 with the delta phase morphology being either predominantly needle or spheroidal. Evaluations on rotating grade wrought IN 718 had shown that grain size and delta phase morphology have a profound effect on the alloy's da/dN characteristics, especially at higher temperature and under dwell-loading conditions. In order to establish the effects that multiple weld repair heat treat cycles have on da/dN of IN 718, fine grain with spheroidal delta and coarse grain with needle delta material had to be tested. A base needed to be established with the program material to determine where it fell among the P&W materials' database scatter band. This was done in order to separate heat treat effects from normal heat-to-heat scatter. The scatter in rates is significant with wrought IN 718 due to its wide variation in grain size and microstructure details. No other mechanical property tests were planned. Other mechanical properties had been well documented in previous programs.

As the test program progressed, it was modified in several ways. The number of tests at 800°F were reduced, reflecting the relative insensitivity the crack growth rate had on heat treatment effects at this low temperature. The number of tests at 1000°F and nondwell at 1100°F were also reduced. Dwell testing at 1100°F was selected as a major test condition because (1) it represents an upper operating temperature for extended exposures for some P&W wrought Inconel 718 commercial engine components (though not diffuser cases), and (2) it provides a condition against which to compare the cast+HIP form of the alloy. PWA 1469 (cast+HIP Inconel 718) is regularly operated for extended times at and above 1100°F, including diffuser cases. Testing was concentrated on the coarse-grain material because it was the more common form of AMS 5663 in the components of interest for this program.

TABLE 5. AMS 5663 CRACK GROWTH (da/dN) TEST PLAN

Material Condition ¹	Test Temp. (°F)	Cyclic ² Rate	Fine ³ Grain	Coarse ³ Grain
Base (FHT)	800	10 cpm	X	X
	1000	10 cpm	X ⁴	X ⁴
	1000	2 mdw	X ⁴	X ⁴
	1100	10 cpm	X	X
	1100	2 mdw	X	X
	1200	10 cpm	X	X
	1200	2 mdw	X	X
	1250	2 mdw	X	X
FHT + 6 Solutions	800	10 cpm	X ⁴	X
	1100	2 mdw	X ⁴	X
FHT + 30 Solutions	800	10 cpm		
	1100	2 mdw	X	X
FHT + 6 Short Ages	800	10 cpm		X
	1100	2 mdw		X
FHT + 1100F Exp.	1000	2 mdw	X ⁴	X
	1100	2 mdw	X ⁴	X

- Notes: 1. FHT: 1750°F (1 hr) + 1325°F (8 hrs) FC to 1150°F (8 hrs)
6 Solutions: 6 x [1750°F (1 hr) + 1325°F (8 hrs) FC to 1150°F (8 hrs)]
30 Solutions: 6 x [1750°F (5 hrs) + 1325°F (8 hrs) FC to 1150°F (8 hrs)]
6 Ages: FHT + 6 x [1400°F (5 hrs) FC to 1200°F (1 hr)]
1100°F Exposure: 1100°F (1000 hrs)
2. 10 cpm = 10 cycles per minute; 2 mdw = 2-minute hold or dwell at maximum stress
3. Fine: ASTM 10-12, Coarse: ASTM 5-6
4. Later deleted from test plans

Another area needing better definition regarding da/dN characteristics was the AMS 5663 welds. IN 718 weld da/dN baseline data had been established as part of the IN 718 database and includes tests of welds at several test conditions. However, testing of welds exposed to multiple postweld heat treat cycles had not been conducted. Table 6 lists the program's planned tests. Testing would be limited to the two prime test temperatures, 800° and 1100°F (dwell). Welds with a single full (solution + age) postweld heat treat cycle and welds with the maximum of solution heat treat exposures were selected to evaluate the AMS 5663 base material. Multiple short-age heat treatments of the gas tungsten arc (GTA) welds were not included in the evaluation because this option is not as commonly used as the full double-solution process. It was expected that "overaging" would most probably soften the material and that it would not adversely affect crack growth rate values. It may even slow down the crack growth rate. The specimens would be prepared with the "crack," or starting slot, aligned with either the fusion zone (FZ) of the weld and/or with heat-affected zone (HAZ) of the weld.

TABLE 6. AMS 5663 WELD CRACK GROWTH (da/dN) TEST PROGRAM

Material Condition ¹	Test Temp. (°F)	Cyclic Rate	HAZ ²	FZ ²
Weld + FHT	800	10 cpm	X	X
	1100	10 cpm		X
	1100	2 mdw	X	X
Weld + FHT+ 30 Solution	800	10 cpm	X	X
	1100	2 mdw	X	X

Notes: 1. FHT: 1750°F (1 hr) + 1325°F (8 hrs) FC to 1150°F (8 hrs)

30 Solutions: 6 x [1750°F (5 hrs) + 1325°F (8 hrs) FC to 1150°F (8 hrs)]

2. HAZ - Weld Heat-Affected Zone; FZ = Weld Fusion Zone

PWA 1469, cast+HIP IN 718, is a well-defined system that includes evaluations of the effects of multiple solution and multiple short-age postweld heat treatments on the basic monotonic and cyclic properties of the alloy. The original plans were to conduct tests of PWA 1469 at the two prime conditions, 800°F/10 cpm and 1100°F/2 mdw. However, the program was revised to limit the tests to the 1100°F/2 mdw condition. This was done because this program's tests of AMS 5663 confirmed previously generated results that crack growth rates at 800°F were relatively insensitive to heat treat and microstructural variations within a nickel alloy system. Short-age only exposures were also not included because this option is rarely used on PWA 1469 and never in critical highly stressed areas.

Testing would include that of PWA 1469 welds, both HIP and non-HIP. Non-HIP welds are expected to behave similarly to AMS 5663 welds. HIP welds represent repairs made by the casting supplier prior to HIP of the casting. These welds have a unique microstructure that differs from the base metal (BM) and the post-HIP weld structures. Specimens of post-HIP welds would include those with starting cracks in the weld's fusion zone and starting cracks in the weld's heat-affected zone. Table 7 presents the test program laid out for PWA 1469. Four tests at 1100°F and 10 cpm were added to help understand the rig test results discussed in greater detail in the rig test section.

TABLE 7. PWA 1469 BASE AND WELD CRACK GROWTH (da/dN) TEST PROGRAM

Material Condition ¹	Test Temp. (°F)	Cyclic Rate	Base	HIP Weld	Non-HIP Weld	
				FZ	FZ	HAZ
FHT	1100	2 mdw	X	X	X	X
Weld + FHT+ 40 Solution	1100	2 mdw	X	X	X	X

Notes: 1. FHT: 1750°F (1 hr) + 1350°F (8 hrs) FC to 1225°F (8 hrs)

40 Solutions: [8 x 1750°F (5 hrs) + 1350°F (8 hrs) FC to 1225°F (8 hrs)]

2.1.2 Effects of Multiple Repair Cycles on Non-FM Materials Mechanical Properties.

As presented above, non-FM (fracture mechanics) testing in this program was limited to the AMS 5613 and AMS 5616, which were exposed to multiple, full-temper stress relief exposures. Tests included tensile and notch LCF. Details of these evaluations and the results are presented in this section.

Effects of multiple repair heat treat cycles on the properties of AMS 5663 and PWA 1469 were well established prior to initiation of this contract. Although the exposures had not been explored to the degree they would be under this contract program, the effects multiple resolutions and short ages had on the properties of Inconel 718 were sufficiently understood, making additional testing unnecessary. A summary of the results is presented in table 8.

TABLE 8. SUMMARY OF EFFECTS OF MULTIPLE REPAIR HEAT-TREATMENT CYCLES ON THE MECHANICAL PROPERTIES OF AMS 5663 AND PWA 1469

Process	Property	AMS 5663	PWA 1469
Solution + Age	Tensile	~10% strength loss after 6 cycles	No effect up to 40 cycles
	Stress Rupture	~30% life loss after 6 cycles	No effect up to 40 cycles
	Smooth LCF	~40% loss after 6 cycles	No effect up to 40 cycles
	Notch LCF	No effect up to 6 cycles	No effect up to 40 cycles
Short Age	Tensile	< 10% strength loss after 6 cycles	No effect up to 6 cycles
	Stress Rupture	No effect up to 6 cycles	No effect up to 6 cycles
	Smooth LCF	No effect up to 6 cycles	No effect up to 6 cycles
	Notch LCF	No effect up to 6 cycles	No effect up to 6 cycles

Notes: Solution + Age:

AMS 5663: 1750°F (1 hr) + weld + 1750°F (1 hr) + 1325°F (8 hrs) FC to 1150°F (8 hrs)

PWA 1469: 1750°F (1 hr) + weld + 1750°F (1 hr) + 1350°F (8 hrs) FC to 1225°F (8 hrs)

Short Age:

AMS 5663 and PWA 1469: weld repair + 1400°F (4 hrs) FC to 1200°F (1 hr)

2.1.2.1 Effect of Multiple Tempers and High-Temperature Exposure on the Non-FM Properties of AMS 5613—Plans and Preparation.

Prior to receipt of the program test material, a preliminary evaluation was conducted using pieces from a thick forging of heat SGAUH, where SGAUH is the ID of the material. The first batch was used as a preliminary test. The second was used for validation. The purpose of the preliminary test was to confirm that multiple stress relieves would have little effect on the tensile and hardness characteristics of AMS 5613, and by implication, one could expect little effect on the alloy's crack growth rate characteristics. Another objective was to prove that extended service at 900°F also had little effect on the alloy's mechanical properties. The preliminary program material was hardened by an oil quench from 1750°F followed by a 2-hour temper at 1015°F. Pieces of the tempered material were then stress relieved an additional one, two, four, and eight cycles at 1015°F (2 hrs), while additional pieces were exposed to 900°F for 10, 100,

and 1000 hours. Cylindrical threaded grip tensile specimens with 0.25" diameter gages were machined from each section with the principal specimen length oriented in a tangential direction, or parallel to the ring's final rolling direction. The specimens were tested at room temperature and pulled at a strain rate of 0.005 in./in./min.

The main study followed the plan as outlined in table 3. Four rolled rings of AMS 5613 Heat ZCLPT were procured from the Ladish Corporation. Each was 24" in diameter by 4" high with a wall thickness of 0.75". All met the chemistry and mechanical property requirements for AMS 5613. Each were hardened by heating to 1750°F, held for 1 hour, and rapidly cooled by an oil quench. Each ring was then tempered by heat treating at 1015°F (2 hrs) and air cooled. During this procedure, one of the rings was exposed to an overtemp, rendering it unusable. Because of the reduction in the amount of available test material, the fatigue program was modified to include only AMS 5613 welds.

Two hardened-plus-tempered rings were then welded together by semiautomatic GTA technique and AMS 5776 (AISI 410) filler wire. The weld ran circumferentially around the ring's perimeter. The welded ring was then divided into three sections for stress relief processing. One, eight, or sixteen stress relief cycles were performed on the three sections. Each cycle was 2 hours at 1015°F. Notch-fatigue and compact-tension crack growth rate test specimens were machined from the welded ring such that the GTA weld was centered in the gage of each specimen. This was an axial direction for the fatigue specimens, but a tangential, or longitudinal, direction for the compact-tension specimens. The notch ($k_t = 2$) LCF specimens were pin-loaded 0.100" thick, flat specimens with a 0.25" wide gage at the notch tip. Crack growth rate test specimens* were mini-compact-tension specimens with dimensions of 1.25" by 1.20" by 0.25" thickness. LCF tests were conducted at 750°F, $R = 0.1$ at 20 cpm with a maximum concentrated stress of 170 ksi. Interim inspections were made during the course of the testing to gather data on cycles to crack initiation (i.e., 1/32" long crack) as well as cycles to rupture data. Tensile tests were conducted at room temperature with the specimens pulled at a rate of 0.05 in./in./min.

The single hardened-plus-tempered ring was divided into three parts, and the parts were stress relieved for 1, 8, and 16 cycles at 1015°F (2 hrs). Tensile specimens were machined from each stress-relieved section with the specimens' main axis aligned in a tangential direction. The tensile specimens were threaded-grip cylindrical specimens with 0.25" diameter gages. Crack growth rate test specimens* were aligned such that the crack would progress in a tangential direction. For base metal testing, compact-tension crack growth rate specimens had standard dimensions of 1.25" by 1.20" by 0.375" thick. Tensile tests were conducted at room temperature with the specimens pulled at a rate of 0.05 in./in./min. Typical microstructures for the Heat ZCLPT AMS 5613 base metal and weld test material with 1 and 16 stress relieves are presented in figures 3 and 4.

* Testing of compact tension crack growth rate test specimens is discussed in section 2.1.3.



AMS 5613 Base Metal 1 S/R 100X



AMS 5613 Base Metal 1 S/R 500X

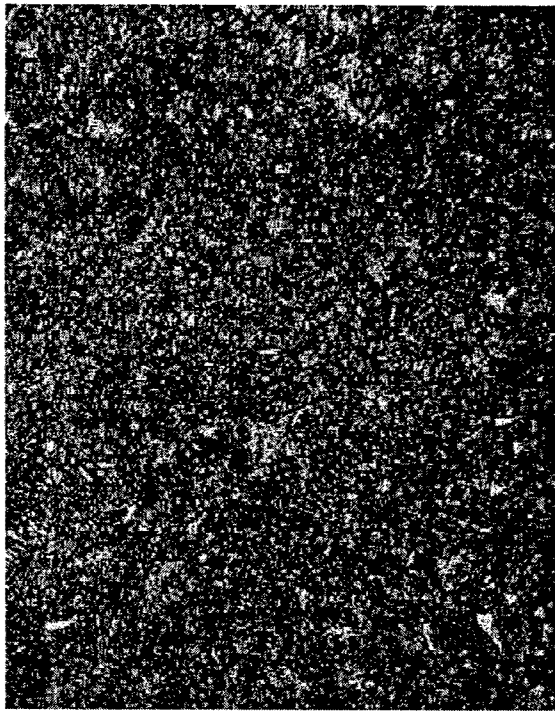


AMS 5613 Base Metal 16 S/R 100X



AMS 5613 Base Metal 16 S/R 500X

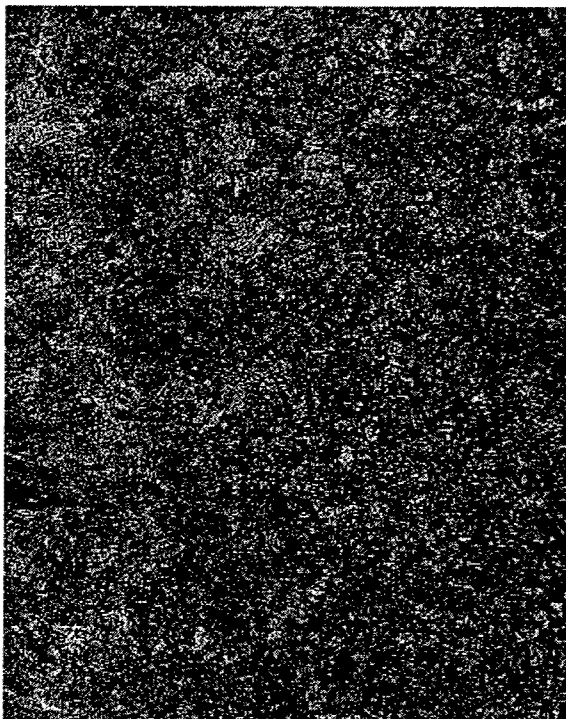
FIGURE 3. TYPICAL MICROSTRUCTURES OF AMS 5613 BASE METAL TEST MATERIAL AFTER 1 (UPPER) AND 16 (LOWER) STRESS RELIEVES AT 1015°F (2 HRS)



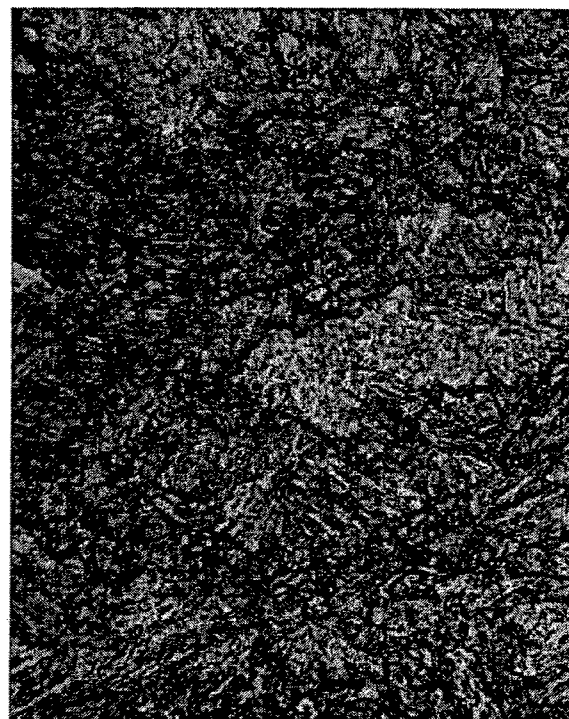
AMS 5613 Weld 1 S/R 100X



AMS 5613 Weld 1 S/R 500X



AMS 5613 Weld 16 S/R 100X



AMS 5613 Weld 16 S/R 500X

FIGURE 4. TYPICAL MICROSTRUCTURES OF AMS 5613 WELD TEST MATERIAL AFTER 1 (UPPER) AND 16 (LOWER) STRESS RELIEVES AT 1015°F (2 HRS)

2.1.2.2 Effect of Multiple Tempers and High-Temperature Exposure on the Non-FM Properties of AMS 5613—Results.

The preliminary evaluation (Heat SGAUH) revealed a greater than expected effect of multiple stress relief cycles on the room temperature strength of AMS 5613. A single stress relief cycle lowered the strength of fully heat-treated (hardened + tempered) AMS 5613 by 13%. Additional stress relief cycles continued to lower the strength of AMS 5613 so that after eight cycles the strength had been lowered by a total of approximately 25%. The effect of multiple stress relief cycles on the alloy's ductility was minor. Exposures at 900°F also lowered the alloy's strength with a 1000-hour exposure bringing the strength down to approximately 15% of strength in the fully heat-treated condition. These effects are presented in table 9 and illustrated in figures 5 and 6.

TABLE 9. AMS 5613 ROOM TEMPERATURE TENSILE PROPERTIES—PRELIMINARY AND MAIN EVALUATIONS EFFECT OF MULTIPLE STRESS RELIEVES AND 900°F EXPOSURES

Condition ¹	Hardness (Rc)	0.2% YS (ksi)	U.T.S. (ksi)	Elongation (%)	Red. of Area (%)
H+T	39.0	150.9	173.7	19.1	58.4
		151.8	175.2	16.9	55.1
H+T + 1 S/R ²	34.0	130.8	151.1	18.8	61.7
		132.1	152.2	20.1	62.7
H+T + 1 S/R ²	33.5	128.4	149.3	19.5	68.1
		129.3	149.7	20.0	68.6
		129.9	151.1	20.2	65.5
		130.9	151.2	19.5	67.4
H+T + 2 S/R	32.5	125.6	145.6	22.0	67.8
		125.7	146.2	20.4	66.2
H+T + 4 S/R	30.0	115.8	136.7	21.3	64.7
		116.9	137.8	21.1	62.0
H+T + 8 S/R	29.0	112.0	133.0	21.7	64.7
		112.3	132.3	21.9	64.0
H+T + 8 S/R ²	28.6	114.9	135.8	21.5	65.8
		115.3	136.1	20.2	64.9
		115.9	136.5	19.4	64.9
		115.9	136.6	21.5	65.5
H+T + 16 S/R ²	26.3	111.6	132.3	21.0	64.4
		112.4	133.3	19.1	62.4
		112.6	132.7	20.7	66.3
		113.3	133.8	20.2	65.3
H+T+900°F (10 hrs)	39.0	148.8	172.5	16.5	60.0
		149.5	172.3	20.8	64.7
H+T+900°F (100 hrs)	36.5	141.8	163.0	17.9	61.1
		143.3	161.2	17.3	59.1
H+T+900°F (1000 hrs)	37.5	127.7	147.9	21.3	64.3
		128.4	148.8	18.9	63.5

Notes: 1. H+T: Harden + Temper = 1750°F (1 hr) oil quench + 1015°F (2 hrs) AC S/R: stress relief = each cycle = 1015°F (2 hrs)
2. Main evaluation, rolled ring Heat ZCLPT; Other data is from the preliminary evaluation with forging SGAUH

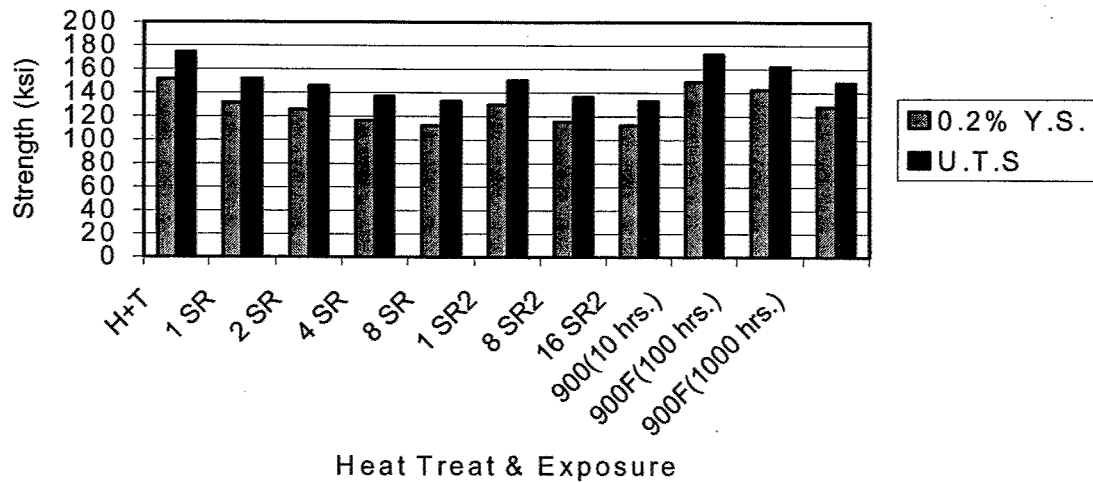


FIGURE 5. BAR CHART PLOTS OF AMS 5613 BASE METAL RT TENSILE STRENGTHS AS EFFECTED BY MULTIPLE STRESS RELIEF CYCLES AND HOURS OF EXPOSURE TO 900°F (SR2 refers to the main study evaluation (Heat ZCLPT).)

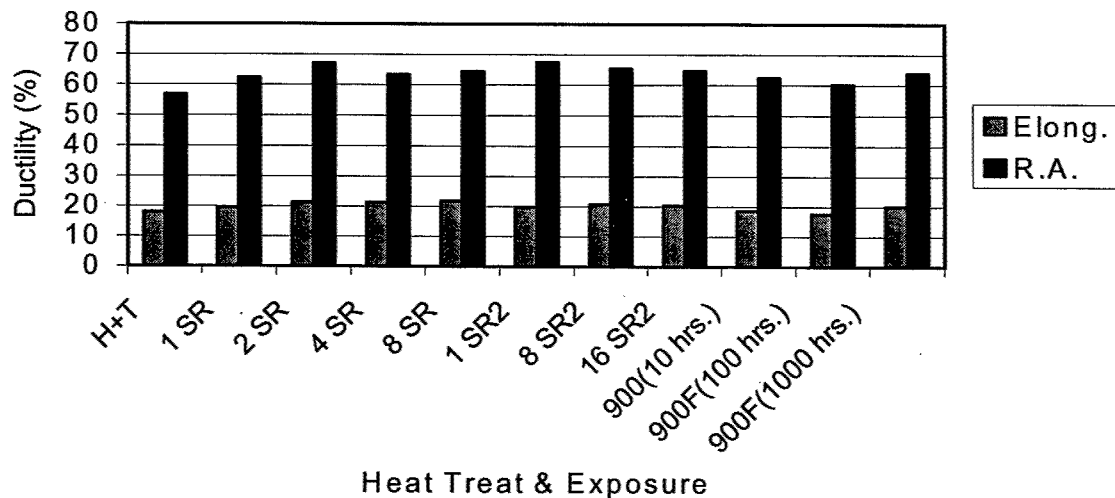


FIGURE 6. BAR CHART PLOTS OF AMS 5613 BASE METAL RT TENSILE DUCTILITY AS EFFECTED BY MULTIPLE STRESS RELIEF CYCLES AND HOURS OF EXPOSURE TO 900°F (SR2 refers to the main study evaluation (Heat ZCLPT).)

Tensile tests of specimens from the forged rings (Heat ZCLPT) produced results similar to that of the preliminary evaluation but to a different degree. The single stress-relieved material was slightly weaker than in the initial study, but additional loss with up to eight stress relief cycles was less than experienced with material from Heat SGAUH. After eight stress relief cycles, strengths were lower by only 9% (U.T.S) to 11% (Y.S.) relative to single stress-relieved material. An additional eight stress relief cycles produced only another 2% loss in strength. As with the preliminary evaluation, effects on ductility were minor. Hardness trends with heat treatment were similar for the two heats of material. These results are presented along with the preliminary evaluation results in table 9 and figures 5 and 6.

Notch LCF testing at 750°F of AMS 5613 welds revealed little effect of multiple stress relieves, as presented in table 10, and Weibull Probability Analysis summaries are shown in table 11. Based on average values and Weibull analysis, both sets of multiple-cycle, stress-relieved AMS 5613 weld specimens displayed superior cyclic lives compared to single-cycle, stress-relieved weld specimens. This was especially true for cycles to a 1/32" crack and less so for cycles to rupture. The larger difference was between one and eight stress-relieved material where minimum cyclic life to a 1/32" crack was three times longer for welds receiving eight stress relieve cycles.

TABLE 10. AMS 5613 WELDS 750°F* NOTCH ($k_t = 2$) LCF PROPERTIES TEST RESULTS

Weld + 1 S/R		Weld + 8 S/R		Weld + 16 S/R	
Cycles to 1/32" Crack	Cycles to Rupture	Cycles to 1/32" Crack	Cycles to Rupture	Cycles to 1/32" Crack	Cycles to Rupture
5,000	13,800	17,500	20,600	7,500	11,300
7,500	16,000	15,500	22,400	12,000	14,300
Not inspected	16,200	20,000	25,500	13,000	15,700
10,000	17,200	16,000	26,100	12,500	18,000
12,500	17,300	14,000	27,300	15,000	18,300
		20,000	31,100	10,000	19,100

* All tests were conducted at 750°F, R = 0.1, 20 cpm and maximum stress 170 ksi (conc.).

TABLE 11. AMS 5613 WELDS 750°F NOTCH ($k_t = 2$) LCF PROPERTIES TEST DATA ANALYSIS

	Weld + 1 SR		Weld + 8 SR		Weld + 16 SR	
Cyclic Life Factor*	Cycles to 1/32" Crk.	Cycles to Rupture	Cycles to 1/32" Crk.	Cycles to Rupture	Cycles to 1/32" Crk.	Cycles to Rupture
Average	8,750	16,000	17,170	25,500	11,670	16,120
W_{CL}	10,000	17,000	18,500	27,500	13,000	17,500
W_{50}	8,850	16,500	17,500	26,000	11,500	16,500
$W_{0.1}$	3,000	12,000	10,000	16,500	6,000	10,000

* Average – mathematical average

W_{CL} - Weibull Probability Analysis Characteristic Life (failure probability = 63.5%)

W_{50} - Weibull Probability Analysis Median Life (failure probability = 50.0%)

$W_{0.1}$ - Weibull Probability Analysis Minimum Life (failure probability = 0.1%)

2.1.2.3 Effect of Multiple Tempers and High-Temperature Exposure on the Non-FM Properties of AMS 5613—Discussion.

No significant differences were observed among the microstructures of the test material regardless of number of stress relief cycles. Although the weld structure was more finely grained than the base metal, the overall microstructure was similar. As stated, the effect of multiple stress relief cycles on the strength of AMS 5613 was greater than expected. The initial large drop in strength between hardened-plus-tempered material and the material with a stress relief may be attributed to incomplete tempering with the original temper. Tempering reactions

initially occur at a fast rate but decelerate over time. Thus, the first stress relief is more effective than subsequent tempers (or stress relieves). After four cycles the material is probably near metallurgical stability. At this point the curve becomes asymptotic for the degree of temper versus time plot. Namely, additional stress relieves have a near negligible metallurgical effect. The reason the degree of response was different between the two heats of material may be explained by the nature of the forged pieces. Small sections of forging were heat treated for all steps of the preliminary evaluation and have been more thoroughly tempered than the larger ring forgings. The drop in strength between one and eight stress relief cycles was within 5 ksi of each other for the two heats. In summary, the trends were the same. Differences in degree of change when reacting to multiple stress relieves can be attributed to heat-to-heat variation and forging material size. Hardness changes followed the tensile strength pattern and thus effects on ductility were negligible.

Exposures at 900°F were less effective as might be expected by the lower temperature. After 100 hours at 900°F, strength and ductility values were slightly better than the material with a single 1015°F stress relief. While after 1000 hours at 900°F, strength and ductility were slightly inferior to that of the single stress-relieved material. In retrospect, the 900°F exposure study should have been performed on the single stress-relieved material, which would better represent actual use of the alloy. Most AMS 5613 components are stress-relieved, weld-assembled constructions.

While the data suggests that multiple stress relief cycles improve the cyclic properties of AMS 5613 welds, it would be prudent to accept there is no debit associated with multiple stress relieves and not claim credit for a cyclic properties gain. The limited amount of LCF data puts any other conclusion at high risk.

2.1.2.4 Effect of Multiple Tempers and High-Temperature Exposure on the Non-FM Properties of AMS 5616—Plans and Preparation.

While waiting for receipt of the program test material, a bar of AMS 5616 from Heat PKRC was used to conduct a preliminary evaluation on the effects of multiple stress relieves on the strength and hardness of AMS 5616. Sections of the rectangular cross section bar were hardened by an oil quench from 1800°F and tempered at 1050°F (2 hrs). Small pieces of the bar were then stress relieved for one, two, four, and eight cycles at 1050°F (2 hrs) while other pieces were exposed for 10, 100, and 1000 hours at 900°F. Threaded grip, 0.25" diameter tensile specimens were machined from the bar sections with the specimen's main axis parallel to the bar's rolling direction. All were pulled at room temperature at a strain rate of 0.005 in./in./min.

The main study followed the plan as outlined in table 3. All test material was excised from rolled rings of AMS 5616, Heat ZCESS, produced by the Ladish Corporation. Material met all chemistry and mechanical property requirements for that AMS 5616. A total of four 24" diameter by 4" high by 0.75" thick rings were procured. Three were hardened by heating to 1800°F, held for 1 hour and rapidly cooled by oil quench. Each ring was then tempered by heat treating at 1050°F (2 hrs) and air cooled. A fourth ring was grain coarsened by solution heat treating it at 2050°F (1 hr) prior to the standard harden-plus-temper heat treatment.

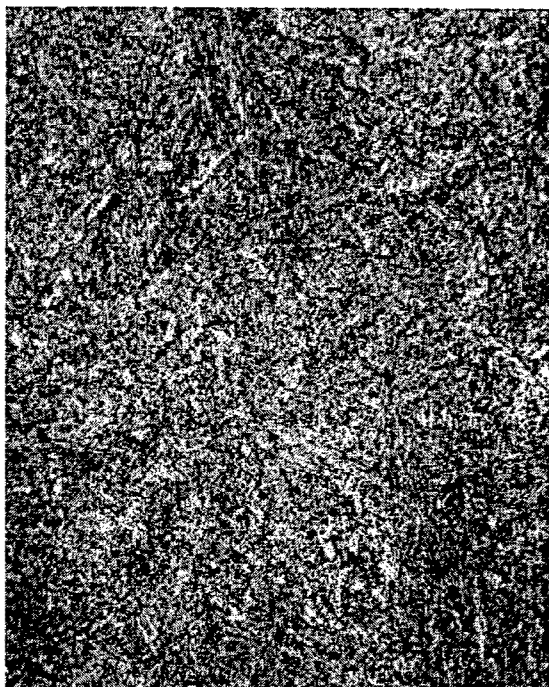
One of the standard hardened/tempered rings was sectioned into four parts and used to supply base metal tensile, notch fatigue, and crack growth rate test specimens. Tensile and crack growth rate specimens were machined from an as hardened-plus-tempered section of the ring. For this ring, all tensile specimens were excised such that the specimen's major axis was tangential, or parallel to the ring's final rolling direction. Compact tension crack growth rate specimens** were removed from the hardened-plus-tempered ring section with orientations parallel and normal to the rolling direction. A portion of the grain-coarsened ring was similarly machined into tangentially oriented tensile specimens and compact tension crack growth rate test specimens with two orientations. Tensile specimens were threaded grip, cylindrical specimens with 0.25" diameter gages. Compact tension specimens were standard, 1.25" by 1.20" by 0.375" thick.

The remainder of the standard hardened/tempered ring was sectioned into three pieces that were stress relieved for 1, 8, and 16 cycles at 1050°F (2 hrs). Tensile and compact tension specimens, that were identical to those excised from the two hardened-plus-tempered rings, were excised from each of the stress-relieved sections. All specimens had a tangential orientation. Notch fatigue specimens were also excised from the three stress-relieved sections with an axial orientation. This was done to make them consistent with the fatigue specimens that would be excised from the welded ring. These specimens were pin-loaded grip 0.100" flat specimens with a 0.25" wide gage at a notch in the gage center that creates a k_t factor of 2.

The remaining two noncoarsened, hardened-plus-tempered rings were welded together by semiautomatic GTA technique with AMS 5817 (Greek Ascology) filler that ran circumferentially around the ring's perimeter. The welded ring was divided into three sections for stress relief per 1, 8, or 16 stress cycles of 2 hours at 1050°F. Notch fatigue and compact tension specimens were excised from each of the stress-relieved sections. The fatigue specimens were axially oriented and identical to the base metal specimens described above. The GTA weld was placed across the middle of the specimen gages. The compact tension specimens were tangentially oriented with the weld centered in the slot for crack growth. For the welds, minicompact tension specimens of 1.25" by 1.20" by 0.25" thick were used.

Test conditions were similar to that used to test the AMS 5613 specimens. Tensile specimens were pulled at room temperature at a strain rate of 0.005 in./in./min., while the notch fatigue specimens were cycled under axial-load control at 750°F, 20 cpm, and an R ratio of 0.1, but at a maximum stress level of 180 ksi. Process inspections were made to detect the fatigue specimens' cycles to a 1/32" crack as well as its rupture cyclic life. Typical microstructures of the AMS 5616, Heat ZCESS, base metal and weld test material are illustrated in figures 7 and 8.

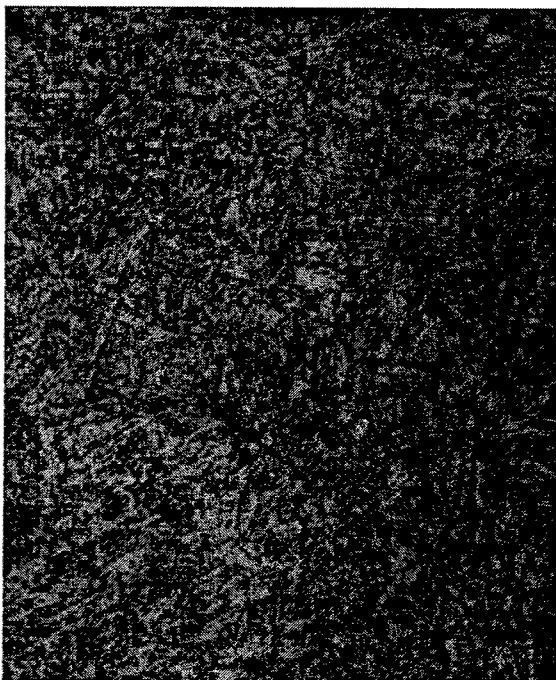
** Testing of compact-tension crack growth rate test specimens is discussed in section 2.1.3.



AMS 5616 B/M H+T ASTM 4.0 500X



AMS 5616 B/M H+T ASTM 2.5 500X

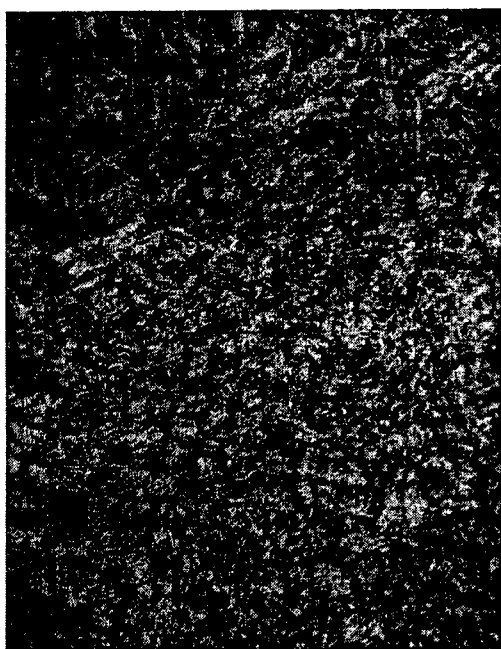


AMS 5616 B/M H+T+ 1 SR 500X



AMS 5616 B/M H+T+ 16 SR 500X

FIGURE 7. TYPICAL MICROSTRUCTURES OF AMS 5616 BASE METAL TEST MATERIAL (HEAT ZCESS) IN HARDENED-PLUS-TEMPERED (UPPER), TEMPERED PLUS 1 STRESS RELIEVE (LOWER LEFT), AND TEMPERED PLUS 16 STRESS RELIEVES (LOWER RIGHT) (Coarsened material is illustrated in upper right photomicrograph.)



AMS 5616 Weld 1 SR 500X



AMS 5616 16 SR 500X

FIGURE 8. TYPICAL MICROSTRUCTURES OF AMS 5616 WELDS AFTER 1 (LEFT) AND 16 (RIGHT) STRESS RELIEF CYCLES

2.1.2.5 Effect of Multiple Tempers and High-Temperature Exposure on the Non-FM Properties of AMS 5616—Results.

Little difference was noted in microstructure among base metal and weld test material or whether the material had received 1 or as much as 16 stress relief cycles. The solution heat-treated ring had an average grain size of ASTM 2.5 compared to ASTM 4.0 for the standard hardened-plus-tempered ring.

All tensile test data is presented in table 12 and illustrated in figures 9 and 10. With regards to tensile strength, both evaluations produced similar results. Multiple stress relief cycles lowered the strength of the hardened-plus-tempered AMS 5616. With the barstock (Heat PKRC), eight stress relief cycles lowered the yield strength by 8.7% and the ultimate strength by 17.0%. With the rolled rings (Heat ZCESS), the losses were 9.5% and 7.2% respectively. An additional eight stress relief cycles lowered both strengths of the rolled ring material by less than another 1%.

With regards to ductility values, the two evaluations produced conflicting results. Multiple stress relief cycles dramatically lowered the ductility of the Heat PKRC barstock. After eight stress relief cycles, elongation and reduction of area values were at a single-digit level, being on average of 83.3% and 92.3% lower, respectively, compared to the values in the hardened-plus-tempered condition. Ductility values of the rolled ring material (Heat ZCESS) actually improved with multiple stress relieves. Relative to the standard hardened-plus-tempered ring material, the coarse-grain ring displayed slightly higher strengths (1-3%), slightly lower elongation (~3%), and slightly higher reduction of area values (~7%). Another observation was that there was significant scatter in ductility values for some of the barstock specimens.

TABLE 12. AMS 5616 RT TENSILE PROPERTIES EFFECT OF MULTIPLE STRESS RELIEVES AND 900°F EXPOSURES

Condition ¹	Hardness (Rc)	0.2% YS (ksi)	U.T.S. (ksi)	Elongation (%)	Red. of Area (%)
S + H+T	40.0	146.2	178.8	14.1	48.9
		149.2	181.5	14.3	50.4
		149.5	180.2	15.1	50.4
		150.3	181.9	16.3	49.6
H+T	37.5	146.0	171.0	17.3	55.6
		146.5	172.9	15.6	14.3
H+T	38.0	146.8	173.9	15.5	51.4
		147.2	174.4	17.5	57.0
		147.4	174.3	14.7	45.5
		148.6	175.6	15.1	31.8
H+T + 1 S/R	36.5	140.5	166.5	12.8	21.4
		142.1	168.5	12.3	26.3
H+T + 1 S/R ²	37.2	144.9	172.5	16.1	53.0
		145.6	173.4	17.2	53.2
		147.4	175.8	17.3	53.2
H+T + 2 S/R	36.0	138.1	160.0	7.3	8.6
		138.3	156.7	4.3	7.5
H+T + 4 S/R	36.0	131.0	131.5	1.3	2.2
		135.2	143.0	3.9	3.3
H+T + 8 S/R	36.0	132.4	133.7	2.0	1.1
		135.4	152.5	3.2	4.3
H+T + 8 S/R ²	36.5	132.8	160.9	18.4	54.1
		133.3	161.7	17.2	55.4
		133.6	161.9	18.4	53.7
		134.4	163.0	18.6	53.6
H+T + 16 S/R ²	34.6	132.9	160.5	17.1	54.8
		133.0	160.4	17.1	53.7
		133.1	160.9	18.3	56.4
		133.2	160.0	17.8	55.2
H+T + 900°F (10 hrs)	39.0	150.4	173.4	13.9	32.5
		150.9	174.4	13.6	17.5
H+T + 900°F (100 hrs)	38.5	154.6	175.3	13.6	24.3
		159.8	175.8	15.7	33.4
H+T + 900°F (1000 hrs)	38.0	153.3	172.9	14.7	35.1
		153.6	172.6	13.6	35.1

- Notes: 1. S + H+T: Solution + H+T = 2050°F (1 hr) AC + H+T
H+T: Harden + Temper = 1800°F (1 hr) oil quench + 1050°F (2 hrs) AC
S/R : Stress relief = Each cycle = 1050°F (2 hrs)
2. Main study with rolled rings of heat ZCESS; other data is with Heat PKRC

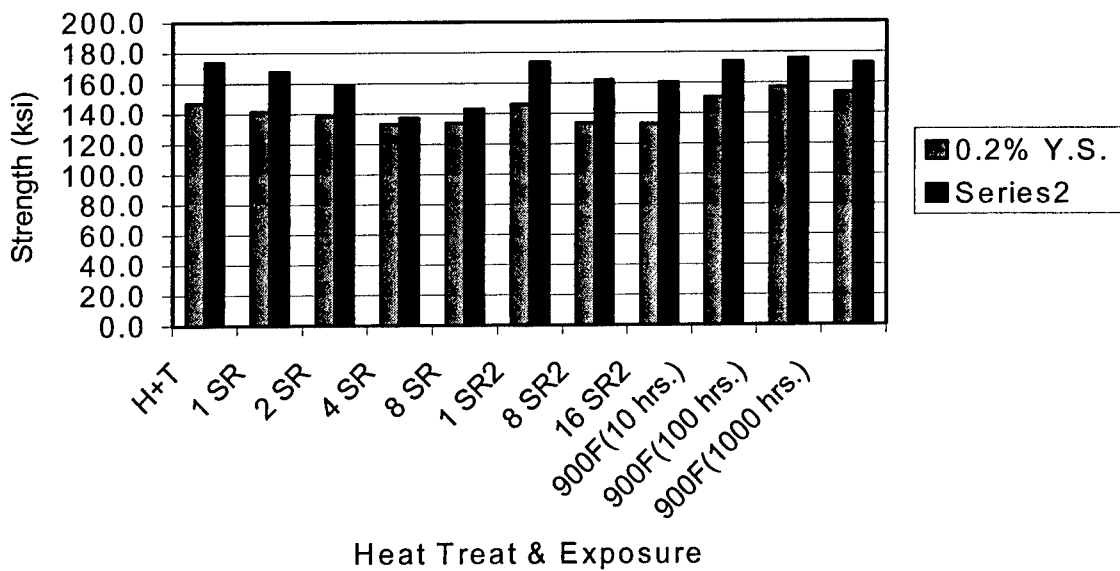


FIGURE 9. BAR CHART PLOTS OF AMS 5616 BASE METAL RT TENSILE STRENGTHS AS EFFECTED BY THE NUMBER OF STRESS RELIEF CYCLES AND HOURS OF EXPOSURE TO 900°F (SR2 refers to the main evaluation (Heat ZCESS), while the other data is from the preliminary evaluation (Heat PKRC).)

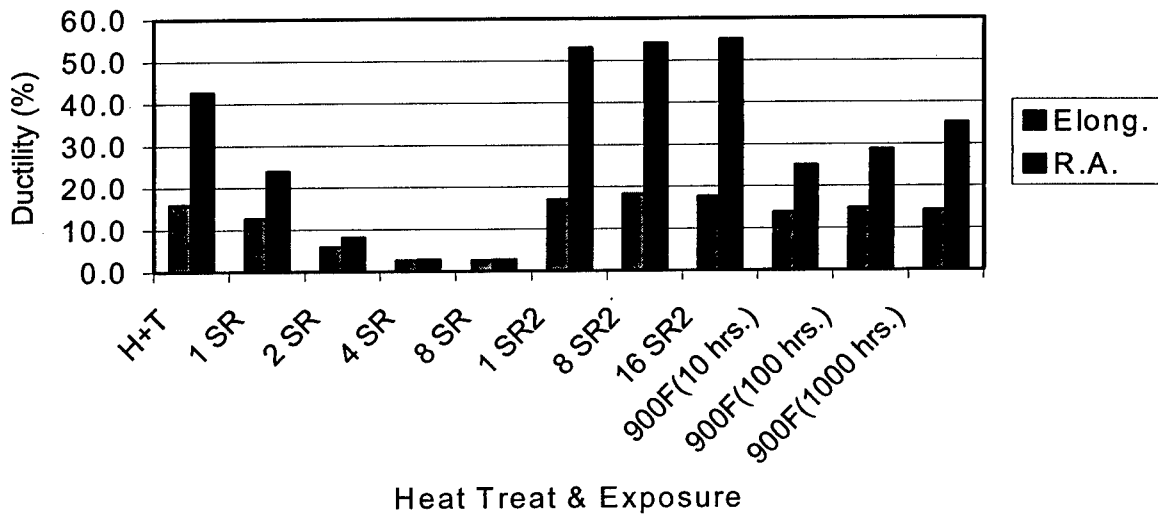


FIGURE 10. BAR CHART PLOTS OF AMS 5613 BASE METAL RT TENSILE DUCTILITY AS EFFECTED BY THE NUMBER OF STRESS RELIEF CYCLES AND HOURS OF EXPOSURE TO 900°F (SR2 refers to the main evaluation (Heat ZCESS), while the other data is from the preliminary evaluation (Heat PKRC).)

Table 13 presents all LCF test data, while analysis of the base metal test results and weld test results are presented in tables 14 and 15, respectively. LCF cyclic lives at 750°F were consistently lower for multiple-cycle, stress-relieved base metal specimens by 13% to 36%. The greater difference was at Weibull probability of failure of 0.1% and less so for average lives. The results were reversed for AMS 5616 welds. Single-cycle, stress-relieved weld specimens displayed cyclic lives that were approximately half that of the similarly heat-treated base metal specimens. However, the multiple-cycle, stress-relieved weld specimens displayed unusually long cyclic life. Four specimens were discontinued without rupture after they reached 100,000 cycles, with no indication of failure. The single-cycle, stress-relieved specimens were surprisingly low lived. Cycles to crack initiation were captured on only one of five specimens because the inspection process was initiated too late to capture a crack of less than 1/32" in length.

TABLE 13. AMS 5616 750°F¹ NOTCH² LCF PROPERTIES

H+T + 1 S/R		H+T + 8 S/R		H+T + 16 S/R	
Base Metal Specimen Tests					
Cycles to 1/32" Crack	Cycles to Rupture ³	Cycles to 1/32" Crack	Cycles to Rupture ³	Cycles to 1/32" Crack	Cycles to Rupture ³
<15,000	19,600	11,200	12,500	<10,000	17,700
15,000	22,000	<15,000	17,900	12,000	19,400
16,500	22,800	12,000	18,500	16,000	20,900
20,000	26,800	15,000	21,800	14,000	21,500
20,000	29,400	17,500	25,600	12,200	22,300
30,000	38,000	19,000	27,600	15,700	24,500
32,500	39,200	23,700	30,300	29,000	35,600
35,000	43,300	28,000	33,700	35,000	43,300
GTA Weld Specimen Tests					
<8,500	12,300	37,500	42,100	12,000	18,600
<5,000	13,600	48,000	56,500	20,000	23,500
<15,000	15,700	63,000	71,600	30,000	37,100
12,500	19,700	100,000+	100,000+	55,000	59,700
No Inspect.	25,300	100,000+	100,000+	67,500	76,000
		110,000+	110,000+	100,000+	100,000+

Note: 1. All tests conducted at 750°F, R = 0.1, 20 cpm and Max. Stress 180 ksi (concentrated)

2. $k_t = 2$

3. 100,000+ indicates specimen test was discontinued at 100,000 cycles without rupture or any indication of cracking

TABLE 14. AMS 5616 BASE METAL 750°F NOTCH ($k_t = 2$) LCF PROPERTIES TEST DATA ANALYSIS

	H + T + 1 SR		H + T 8 SR		H + T + 16 SR	
Cyclic Life Factor*	Cycles to 1/32" Crack	Cycles to Rupture	Cycles to 1/32" Crack	Cycles to Rupture	Cycles to 1/32" Crack	Cycles to Rupture
Average	23,000	30,140	17,675	23,490	17,990	25,650
W_{CL}	25,000	33,500	19,000	23,500	20,000	27,500
W_{50}	22,500	30,000	17,000	23,000	17,000	23,500
$W_{0.1}$	7,800	13,500	6,800	9,000	5,000	11,500

* Average – mathematical average

W_{CL} – Weibull Probability Analysis Characteristic Life (failure probability = 63.5%)

W_{50} – Weibull Probability Analysis Median Life (failure probability = 50.0%)

$W_{0.1}$ – Weibull Probability Analysis Minimum Life (failure probability = 0.1%)

TABLE 15. AMS 5616 WELDS 750°F NOTCH ($k_t = 2$) LCF PROPERTIES TEST DATA ANALYSIS

	H + T + 1 SR		H + T 8 SR		H + T + 16 SR	
Cyclic Life Factor ¹	Cycles to 1/32" Crack	Cycles to Rupture	Cycles to 1/32" Crack	Cycles to Rupture	Cycles to 1/32" Crack	Cycles to Rupture
Average	<10,250	17,320	>74,750	>78,370	>47,420	>52,480
W_{CL}	n.a.	19,000	74,000	87,500	52,000	59,000
W_{50}	n.a.	17,500	67,000	78,000	40,000	48,000
$W_{0.1}$	n.a.	8,000	22,000	25,000	6,000	8,000

* Average – mathematical average

W_{CL} – Weibull Probability Analysis Characteristic Life (failure probability = 63.5%)

W_{50} – Weibull Probability Analysis Median Life (failure probability = 50.0%)

$W_{0.1}$ – Weibull Probability Analysis Minimum Life (failure probability = 0.1%)

2.1.2.6 Effect of Multiple Tempers and High-Temperature Exposure on the Non-FM Properties of AMS 5616—Discussion.

Results from the main study tensile evaluation were more consistent with expectations. Data from several other programs suggests that multiple stress relieves would overtemper the material resulting in a reduction of hardness and strength. However, what was surprising was the significant loss in ductility displayed by the Heat PKRC barstock. With reduced hardness and strength, it is assumed ductility would increase as it did with the rolled ring material (Heat ZCESS). One explanation may be that the barstock had a relatively high amount of nonmetallic contamination that might have made it more sensitive to the multiple heat treatments. It was noticed during the metallographic examination that this material had a relatively high amount of sulfides located at the grain boundaries and after stress relieves the structure took on a more sensitized structure. These features are illustrated in figure 11. The tensile specimens exhibited numerous small secondary cracks associated with grain-boundary inclusions. Thus, ductility displayed by a given specimen was probably controlled by the presence, location, and size of grain-boundary particles rather than the innate strength and hardness of the material. Other evidence leading toward dirt as a cause for the low ductility includes the scatter in ultimate

tensile strength. Additionally, the fact that after four or more stress relief cycles, the barstock's yield strength was 89% to 99% of its ultimate strength supports this assumption of dirt causing the ductility. Multiple fracturing around inclusions not only led to low ductility values, but prevented the specimens from showing full potential for ultimate strength. The 900°F exposures had a less damaging effect, which is probably due to the 150°F lower temperature relative to the stress relief condition. In summary, the data from the preliminary evaluation is questionable and should be discounted. Material from the rolled rings (Heat ZCESS) presents a more accurate representation of the effects of multiple stress relieves on monotonic properties.

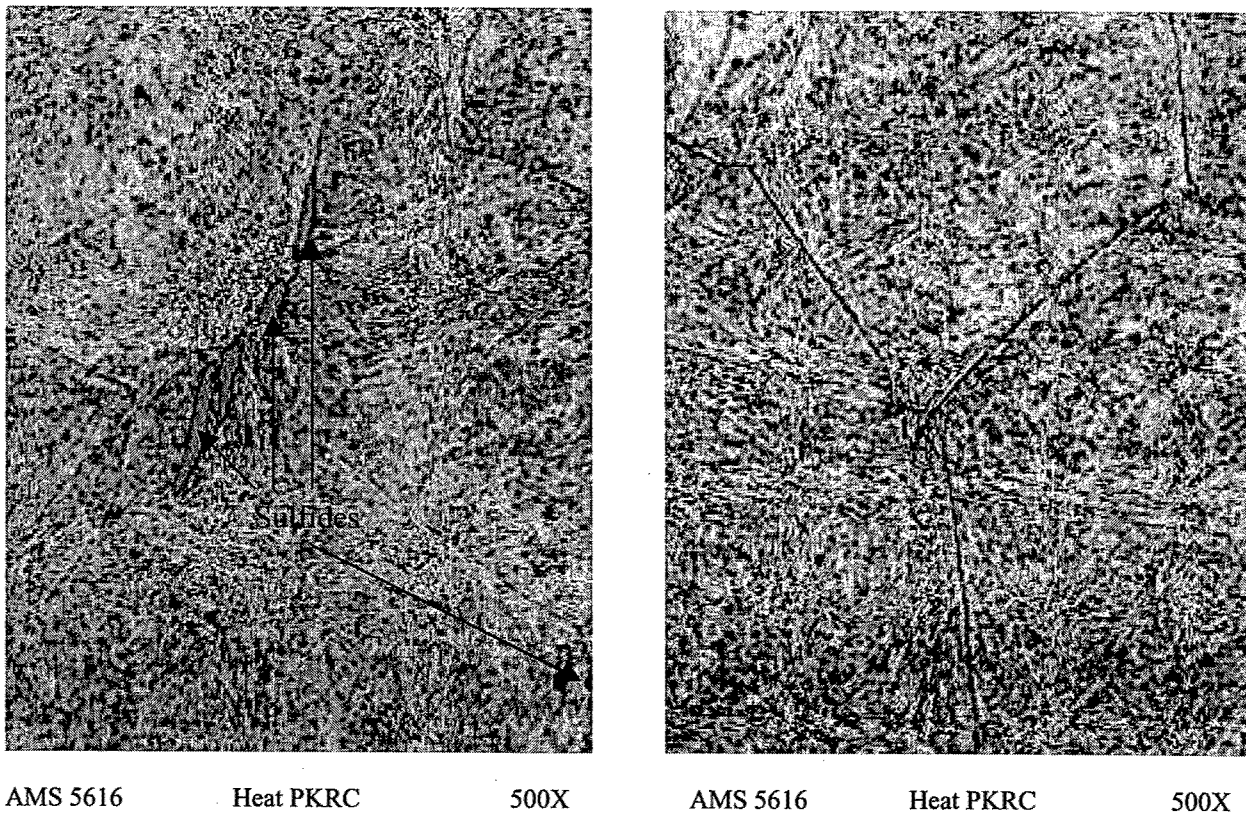


FIGURE 11. TYPICAL MICROSTRUCTURE OF AMS 5616 BARSTOCK HEAT PKRC AFTER ONE (LEFT) AND EIGHT (RIGHT) STRESS RELIEF CYCLES AT 1050°F (2 HRS)
 (Note the presence of sulfides in the grain boundaries and more clearly delineated grain boundaries (right) indicative of a sensitized condition with grain boundaries filled with carbides and other particles, compared to the cleaner structure of rolled ring material (heat ZCESS) illustrated in figure 7.)

No clear pattern evolved from the fatigue testing. Material with 16 stress relief cycles had lower cycles to initiation than eight-cycle, stress-relieved material, but longer rupture lives. Relative to the base of a single stress relief, the losses are minor. Due to the finer structure of the welds, one would expect that they would exhibit better fatigue lives. However, only the welds that had received eight stress relief cycles accomplished this. On a qualitative basis, it can be concluded that multiple stress relief cycles cause no harm to the fatigue resistance of AMS 5616 base metal or its welds.

2.1.3 Materials FM Database Refinement.

As described earlier, tests were planned to complement the existing FM database and evaluate the effects of multiple repair heat treat cycles on the crack growth rates (da/dN) of contract materials. This section reports on the results of that test program. The data that existed within P&W's database prior to this contract program is not presented in this report.

2.1.3.1 Testing Procedures.

All tests were conducted with ASTM compliant compact tension specimens with either straight or chevron starter slots. Three specimen sizes were used in deference to expected material grain size. The smallest specimen, a mini-compact-tension specimen, having dimensions of 1.25" wide by 1.20" long by 0.25" thick was used for the finest grain material such as the welds. A standard compact-tension specimen having dimensions of 1.25" wide by 1.20" long by 0.375" thick was used for the wrought base metal material. An oversize specimen that measured 2.40" wide by 2.00" long by 0.50" thick was used for the coarse-grained cast material. All specimens were tested to rupture, but for most tests, only the region II area of the crack growth profile was generated. For purposes of this program, threshold data was not considered critical. All testing was conducted using the direct current electric potential drop (DCEPD) method for monitoring the crack growth rate. This is an automated test method that uses a constant current passing through a test specimen. A computer monitors the change in potential drop across the crack, provides data acquisition, and test control. As the crack grows, the change in potential is converted into a crack length. Testing was discontinued when the crack length reaches an A/W beyond the limits of the (stress intensity factor) K solution. (A = crack length and W = the specimen width.) Testing within region II was conducted using constant load conditions. Two frequencies were used, 10 cpm (cycles per minute) and with a 2-minute dwell, or hold, at the maximum stress. Once the crack length versus N (cycle) data was collected, it was reduced to produce a da/dN plot.

For purposes of presentation and discussion, a seven-point polynomial curve was fitted through the data to provide for a smooth line that highlighted the data trend. The curve was tested for degree of fit with the data. Greater than 90% compliance with all datum was necessary for the plot to be accepted. Posttest crack length measurements were taken of the fracture surface at both the specimen surfaces and through the crack path center to ensure that plain-strain crack growth had occurred. Results from specimens experiencing tunneling was rejected. Visual crack length measurements were periodically made during the course of each test to verify the accuracy of the potential drop (PD) data acquisition system.

This section will use plots of the data trends without the actual data points. Basically, points are assigned to the fitted curve, which are then entered into a spreadsheet. A plot of these faux points is then presented. These stylized plots provide an easy to read visual presentation of the data and makes comparisons of heat treatments, heats of material, different materials, etc., easier to discuss. However, the plots in this section fail to illustrate the degree of data scatter, which can be significant, especially with large grain investment cast materials. Between fitting a curve to the data and converting it to a spreadsheet chart, the final plot has been significantly smoothed. A plot of actual da/dN datum for each specimen is provided in appendix A. It is

recommended that these plots be viewed to grasp a true knowledge of the degree of scatter experienced during testing.

2.1.3.2 AMS 5613 FM Test Plan.

The test plan for the AMS 5613 (AISI 410 Stainless Steel) material was presented in table 3. In summary, two temperatures (750° and 950°F) were selected with tests being conducted at cyclic rates of 10 cpm at both temperatures and under 2-mdw (2-minute dwell at high load) loading at 950°F. Base metal and weld FZ specimens were both tested at each of the three test conditions.

Base metal specimens were aligned such that the starting slot (and subsequent crack growth) would be in the tangential direction, or parallel to the ring's final rolling direction. Weld specimens, however, were aligned such that the starting slot (and subsequent crack growth) would be through the weld's fusion zone. As shown in figures 3 and 4, the AMS 5613 weld microstructure is similar to the base metal only with a finer grain. The weld heat-affected zones do not present a unique microstructure. Specimens were machined from the three different stress-relieved sections of the single (for base metal specimens) and welded ring (for weld specimens). Though base metal and weld specimens with 1, 8, and 16 stress relief cycles were available for test, only the specimens with 1 and 16 cycles were committed to test. The specimens with eight stress relief cycles would only be tested if a significant difference in crack growth rates surfaced between the single and 16-cycle, stress-relieved specimens.

Three tests at room temperature were added to the tests originally planned for AMS 5613. These tests were added to try and duplicate phenomena experienced with a few JT8D combustor chamber outer cases (CCOC). On two occasions, cracks appeared to grow at room temperature in an intergranular manner. A hardened-plus-tempered and eight-cycle, stress-relieved specimens were each tested at room temperature at 10 cpm and $R = 0.1$. A second hardened-plus-tempered specimen was tested at room temperature at 10 cpm but at an $R = 0.5$ ratio.

2.1.3.3 AMS 5613 FM Test Results.

Figures 12 through 15 present the da/dN plots of test data generated on AMS 5613 rolled ring material (Heat ZCESS). No significant differences in rates were observed among base metal and weld specimens with either 1 or 16 stress relief cycles when tested at 750°F (figure 12). The range in rates fell between a 1.5X band (minimum to maximum rate), which is a typical scatter band for most wrought steel alloys. Similarly, there is little effect of material type and stress relief (1 versus 16 cycles) when tested at 950°F (figure 13). Dwell loading also had no significant effect on the 950°F crack growth rate characteristics of AMS 5613. The scatter range of rates was within a 2X band (minimum versus maximum) up to a concentration of 20 ksi square root inches. At higher values of delta K, the dwell-loaded, single-cycle, stress-relieved base metal specimen was measurably faster than the other specimens. Total scatter range at 40 ksi root square inches was 6X. Interestingly, the 200°F higher test temperature caused, on average, little change in rate at lower values of (< 30) delta k. However, the 200°F higher test temperature caused significant changes at higher values of delta K. The fastest crack growth rate measured at 950°F was 4X higher than the fastest rate recorded for a specimen tested at 750°F. This is illustrated in figure 14 with plots of selected data from both temperature tests.

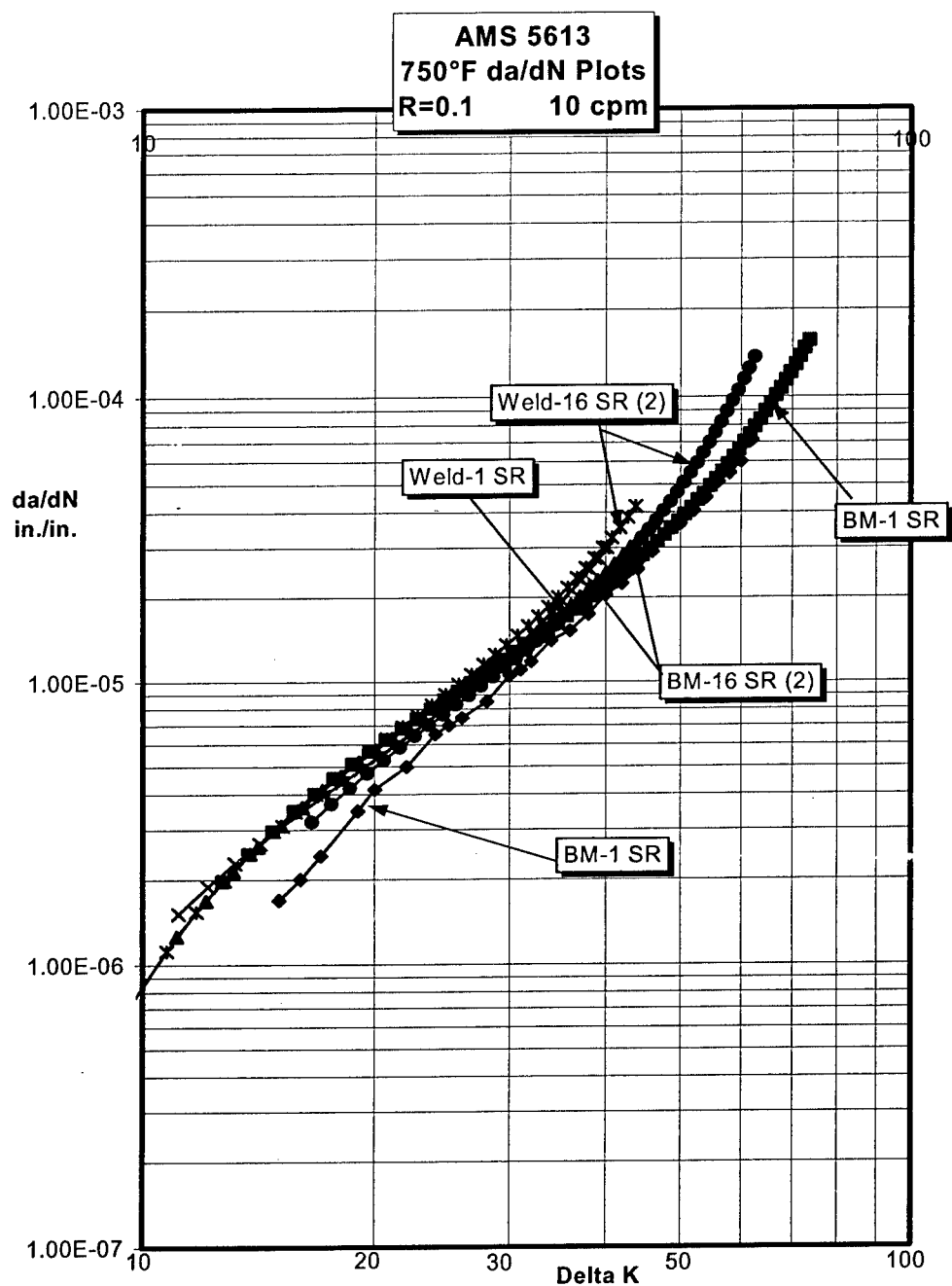


FIGURE 12. CRACK GROWTH (da/dN) PLOTS OF AMS 5613 TESTED AT 750°F, $R = 0.1$ AND 10 cpm (Plots illustrate no significant difference in crack growth rates between base metal (BM) and weld material or any effect of 16, 2-hour stress relieves at 1015°F.)

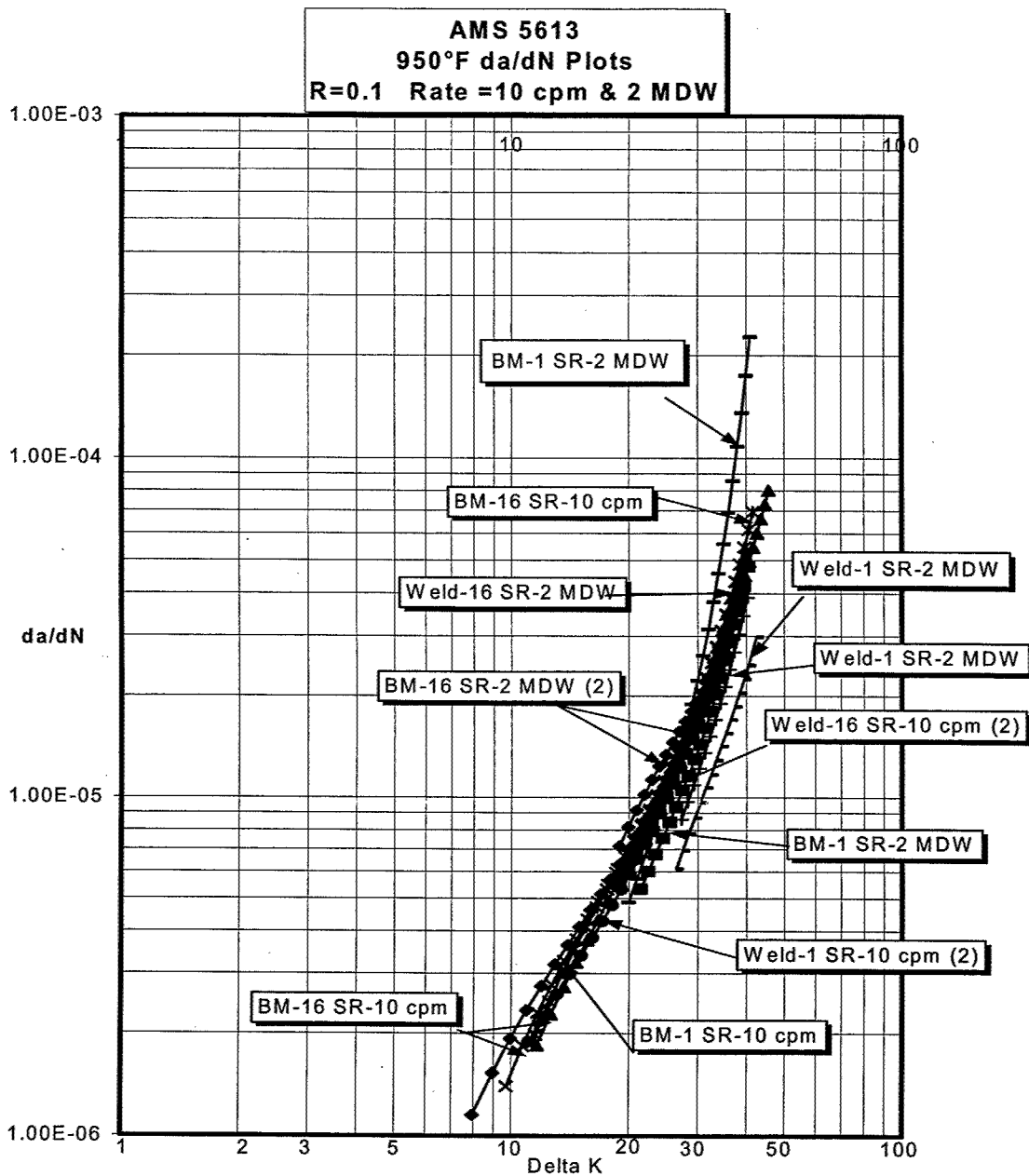


FIGURE 13. CRACK GROWTH (da/dN) PLOTS OF AMS 5613 TESTED AT 950°F, $R = 0.1$ WITH CYCLIC RATES OF 10 cpm AND 2-MINUTE DWELL AT MAXIMUM STRESS

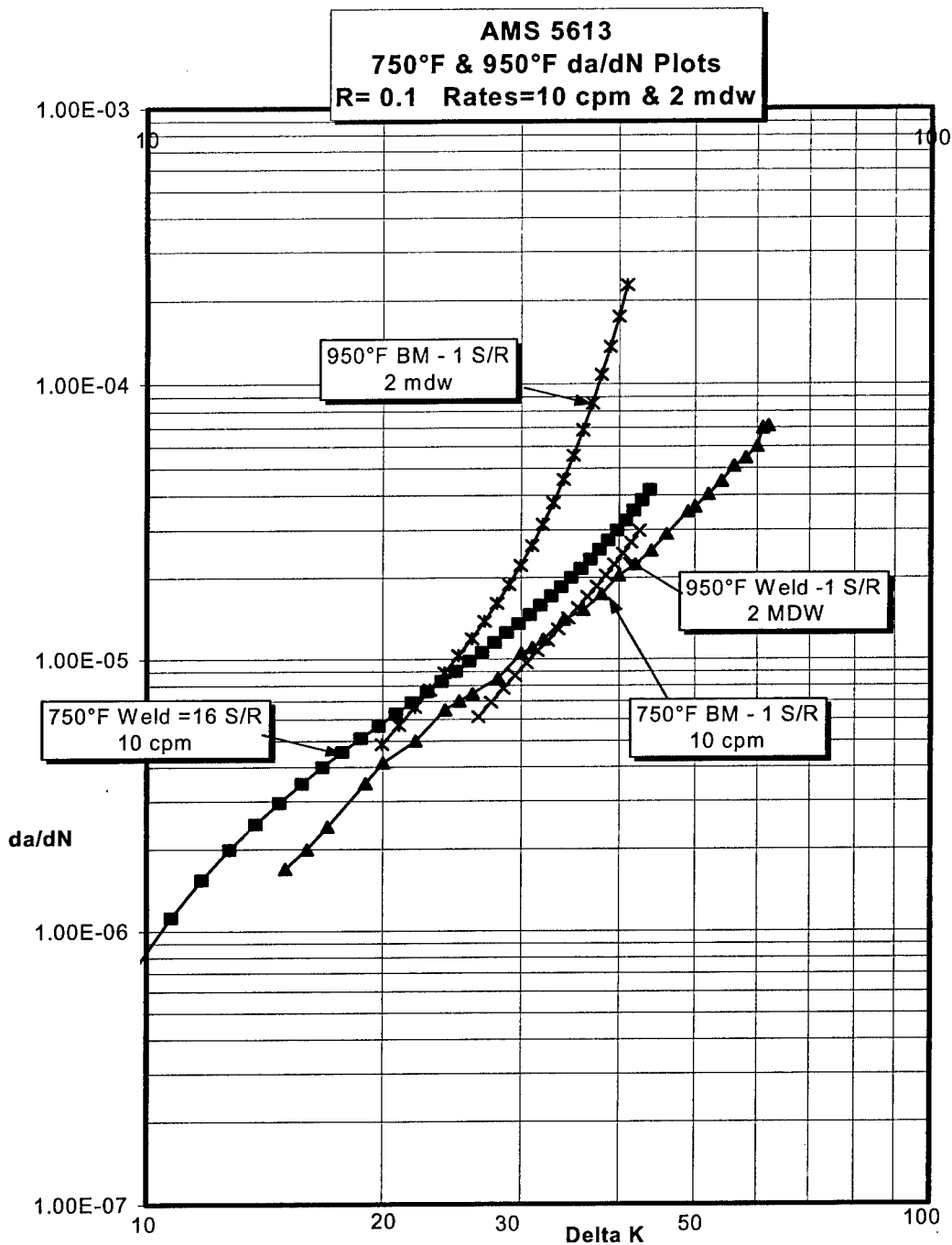


FIGURE 14. PLOTS OF CRACK GROWTH TEST RESULTS OF AMS 5613 TESTED AT 750° AND 950°F (The plots represent the lower (slowest) and upper (fastest) rates at each temperature among the base metal and weld specimen tests. Note the slightly steeper slope (faster acceleration of growth rate) of the 950°F tests, especially the dwell tests.)

Room temperature tests revealed no effect of multiple stress relieve cycles, though the $R = 0.5$ test resulted in a faster crack growth rate, all the specimens exhibited transgranular fracture features. The data is plotted and illustrated against data from a single stress-relieved base metal specimen tested at 750°F in figure 15.

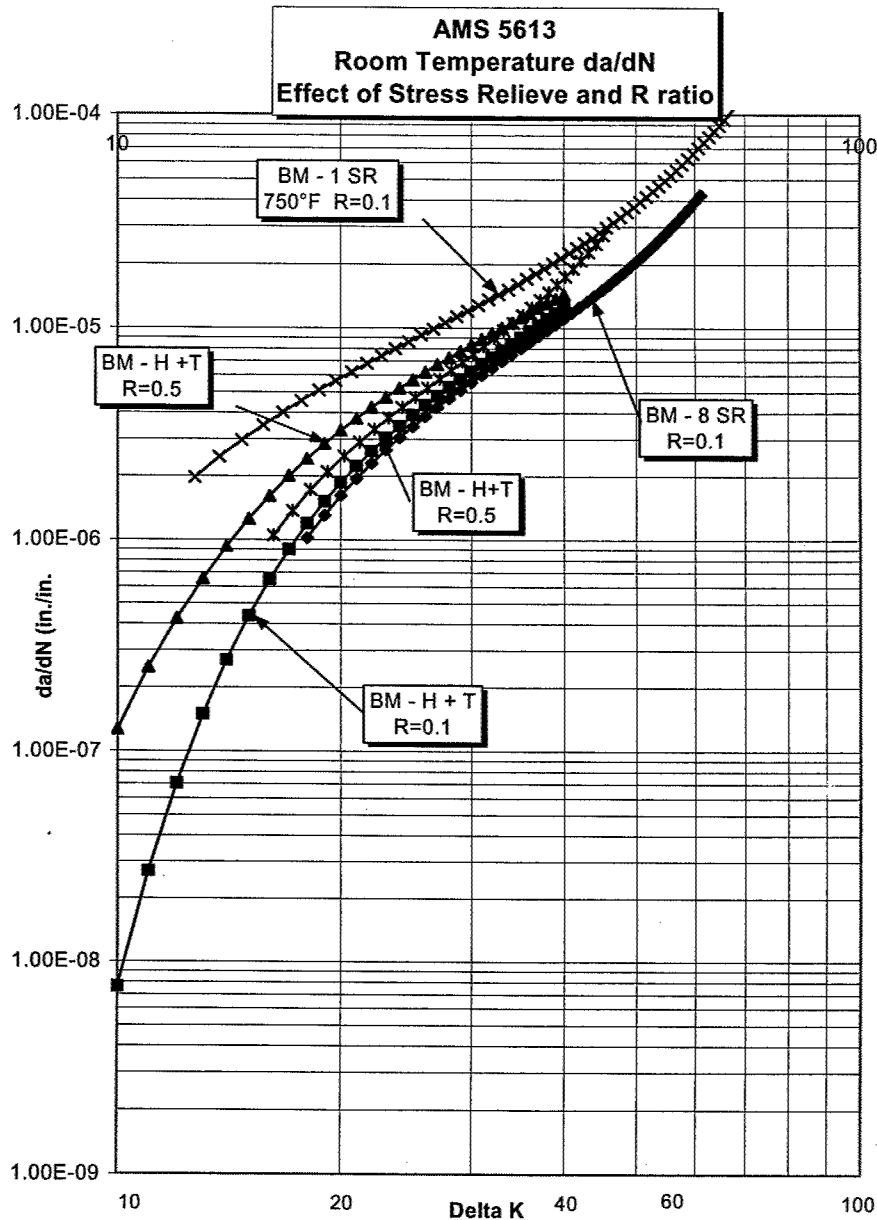


FIGURE 15. PLOTS OF CRACK GROWTH RATES (da/dN) OF AMS 5613 TESTED AT ROOM TEMPERATURE AND 10 cpm TO EVALUATE THE EFFECTS OF R RATIO (0.1 VS 0.5) AND STRESS RELIEF (0 VS 8) (Note the rates relative to 750°F plot used here for reference.)

2.1.3.4 AMS 5616 Base FM Test Plan.

The basic test plan for AMS 5616 was presented in table 3. Many large AMS 5616 components such as high-bypass commercial engine turbine exhaust cases (TEC) were assembled from numerous forged details of varying size, grain size, and experience complex multidirectional loading. Therefore, the crack growth rate test plan for AMS 5616 was designed to include a study of what effect grain size and orientation has on the alloy's crack growth rate. For this part of the evaluation, only hardened-plus-tempered material would be tested and all tests would be at 950°F. The evaluation would however include two grain sizes (ASTM 4 and ASTM 2.5), two orientations (longitudinal and transverse) with respect to a forged ring's major rolling direction, and two load conditions (10 cpm and 2 mdw). In addition, the plan was to include Trueform® specimens. P&W had been substituting Trueform® forgings for conventionally hot rolled rings in select components because the Trueform® process offers manufacturing cost savings. This material was added to the program at temperature tests of 750° and 950°F to determine if this forging process presents variability in the alloy's crack growth characteristics. (The Trueform® material was not procured for this program but donated as leftover from a P&W evaluation program.) There were two changes to the original test plan. First, the 950°F 10-cpm tests were placed on hold. These were only to be tested if the 950°F 2-mdw tests of stress-relieved specimens showed a distinct difference with the results achieved on the hardened-plus-tempered material. Second, two tests would be conducted at 850°F because it was determined this temperature was critical to a major P&W component that was to be analyzed in task 2 of this report.

Base metal specimens were machined from the single fine (ASTM 4.0) and coarse (ASTM 2.5) rings. Specimens with tangential (i.e., longitudinal) and axial (i.e., transverse) orientations were machined from the hardened-plus-tempered (coarse and fine grain) sections. Specimens with tangential orientations were machined from the fine grain ring sections that had been stress relieved for 1, 8, and 16 cycles. Finally, weld test specimens were excised from each of the three different stress-relieved sections of the welded ring. Table 16 presents the final da/dN test plan for AMS 5616.

TABLE 16. AMS 5616 CRACK GROWTH (da/dN) TEST PLAN

Material Condition ¹	Test Temperature	Cyclic Rate	Orientation	Fine ² Grain	Coarse ² Grain	Weld
Base - H+T	850	10 cpm	Transverse		X	
Base - H+T	850	2 mdw	Longitudinal		X	
Base - H+T	950	10 cpm	Longitudinal	X	X	
Base - H+T	950	10 cpm	Transverse	X	X	
Base - H+T	950	2 mdw	Longitudinal	X	X	
Base - H+T	950	2 mdw	Transverse	X	X	
Trueform® - H+T	750 ³	10 cpm	Longitudinal	X		
Trueform® - H+T	950 ³	10 cpm	Longitudinal	X		
H+T + 1 SR	750	10 cpm	Longitudinal	X		X
H+T + 1 SR	950	10 cpm	Longitudinal	X ⁴		X ⁴
H+T + 1 SR	950	2 mdw	Longitudinal	X		X
H+T + 16 SR	750	10 cpm	Longitudinal	X		X
H+T + 16 SR	950	10 cpm	Longitudinal	X ⁵		X ⁵
H+T + 16 SR	950	2 mdw	Longitudinal	X		X
H+T + 8 SR	750	10 cpm	Longitudinal	X ⁴		X ⁴
H+T + 8 SR	950	10 cpm	Longitudinal	X ⁴		X ⁴
H+T + 8 SR	950	2 mdw	Longitudinal	X ⁴		X ⁴

Notes: 1. H+T: Harden + Temper = 1800°F (1 hr) oil quench + 1050°F (2 hrs) AC
S/R: Stress Relief = each cycle = 1050°F (2 hrs)

2. Fine Grain: ASTM 3-5; Coarse Grain: ASTM 2-3

3. Two tests at each condition

4. Optional; to be tested only if necessary

5. Later deleted from the test plan

2.1.3.5 AMS 5616 Base FM Test Results.

Figure 16 illustrates the da/dN plots of the AMS 5616 base metal and welds tested at 750°F at a cyclic rate of 10 cpm. Due to a test rig malfunction, the weld test specimen with a single stress relief cycle was lost and no data was generated. However, results on the other five specimens showed that there were little differences in rates between the stress-relieved (1 and 16 cycles) hot-rolled base metal, a weld with 16 stress relief cycles, and as hardened-plus-tempered Trueform® material.

Plots of eight conventionally (i.e., hot rolled) forged base metal specimens that were tested at 950°F are shown in figure 17. They cover variations in grain size (ASTM 4.0 vs 2.5), orientation (longitudinal versus transverse), load form (10 cpm versus 2 mdw), and forging process (hot roll and Trueform®). Six of the specimens had rates within a factor of 1.5X of each other, which is within normal test scatter. However, two of the dwell-loaded specimens exhibited unusually higher rates at relatively low values of stress intensity. One was a coarse-grained longitudinally oriented specimen and the other a fine-grained transverse-oriented specimen. Although no specific reason could be found to discredit either test, it is believed that both of these tests were anomalies and were not representative of the alloy. This conclusion was strengthened by results subsequently received with stress-relieved specimens that had rates similar to the other six hardened-plus-tempered test specimens. The stress-relieved specimen 950°F test data are plotted

in figure 18. It demonstrates that there were no significant crack growth rate differences among the single and 16-cycle, stress-relieved material, welds, and base metal. The rates were similar to those shown by the fine grain hot rolled as hardened-plus-tempered material (figure 19). Scatter between the slowest and fastest rates were within a factor averaging 1.5X of each other. As expected, the two 850°F tests produced results that fell between the 750° and 950°F crack growth rates of AMS 5616 of the same form and loading conditions.

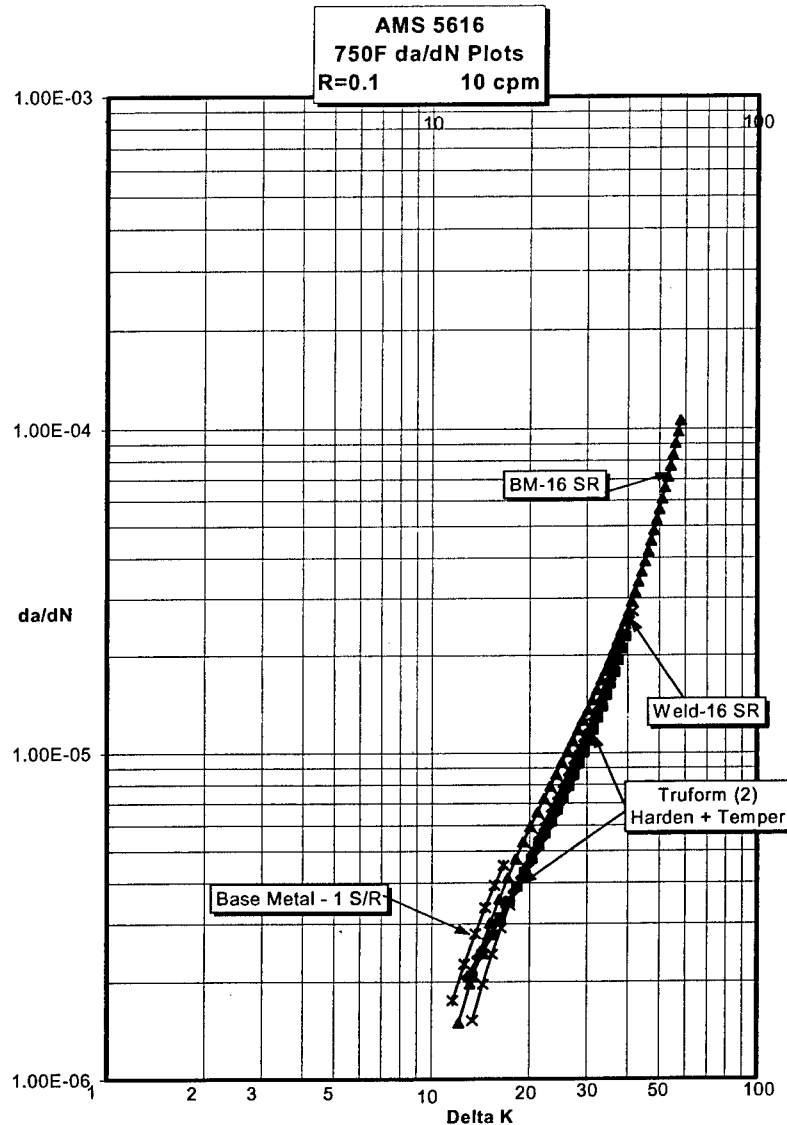


FIGURE 16. PLOTS OF CRACK GROWTH RATES (da/dN) OF AMS 5616 TESTED AT 750°F, $R = 0.1$ AND 10 cpm (Note that there are no significant differences in rates between base metal and weld specimens, conventionally rolled rings and Trueform® rings, and no effect of 16, 2-hour stress relieve cycles at 1050°F.)

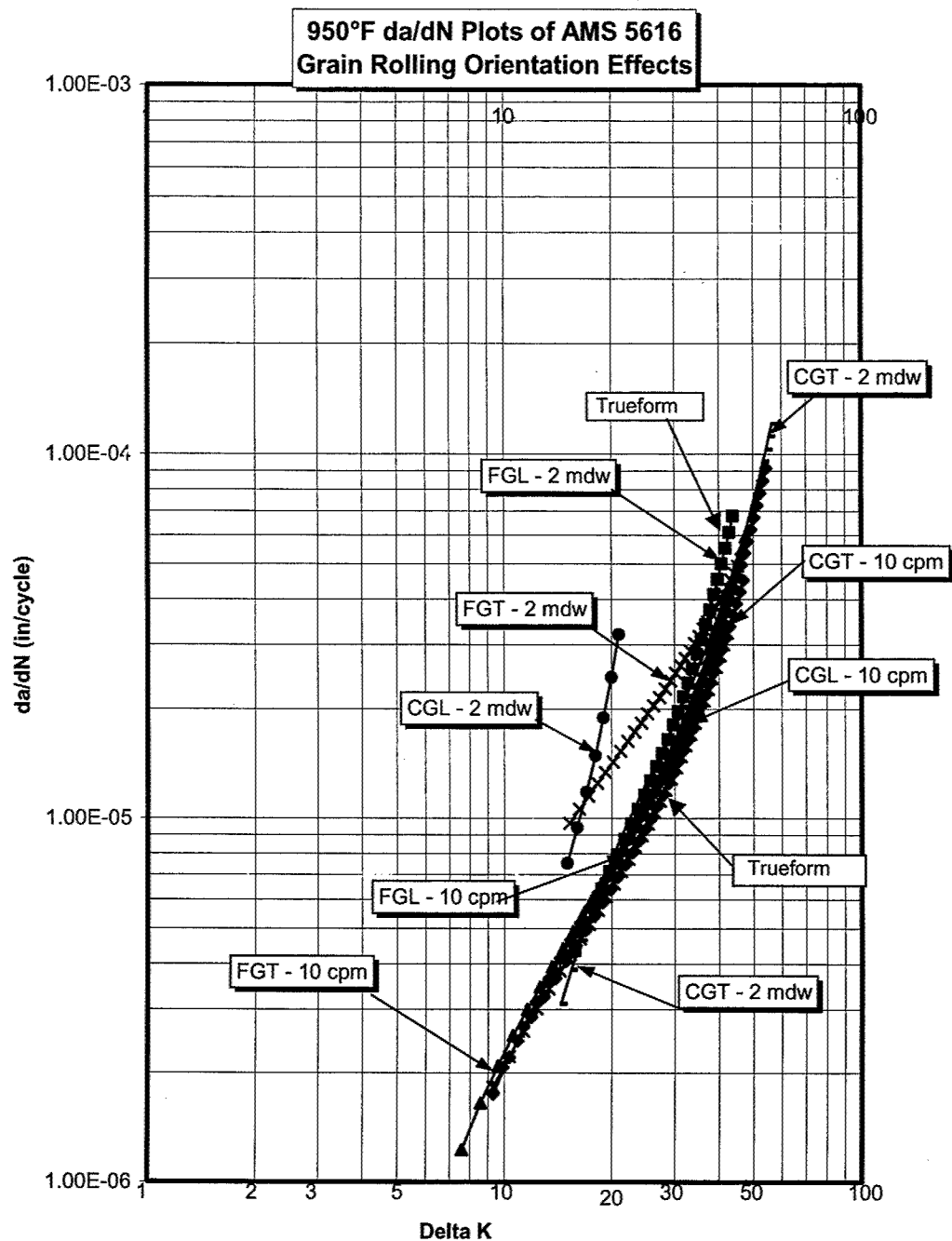


FIGURE 17. CRACK GROWTH RATE (da/dN) PLOTS OF AMS 5616 BASE METAL SPECIMENS IN THE HARDENED-PLUS-TEMPERED CONDITION TESTED AT 950°F, $R = 0.1$ AND UNDER CYCLIC LOADING OF 10 cpm OR 2-MINUTE DWELL AT MAXIMUM STRESS (Note two anomalous plots (CGL-2 mdw and FGT-2 mdw). Otherwise there is little difference among specimens of different grain size, orientation, or forging practice.)

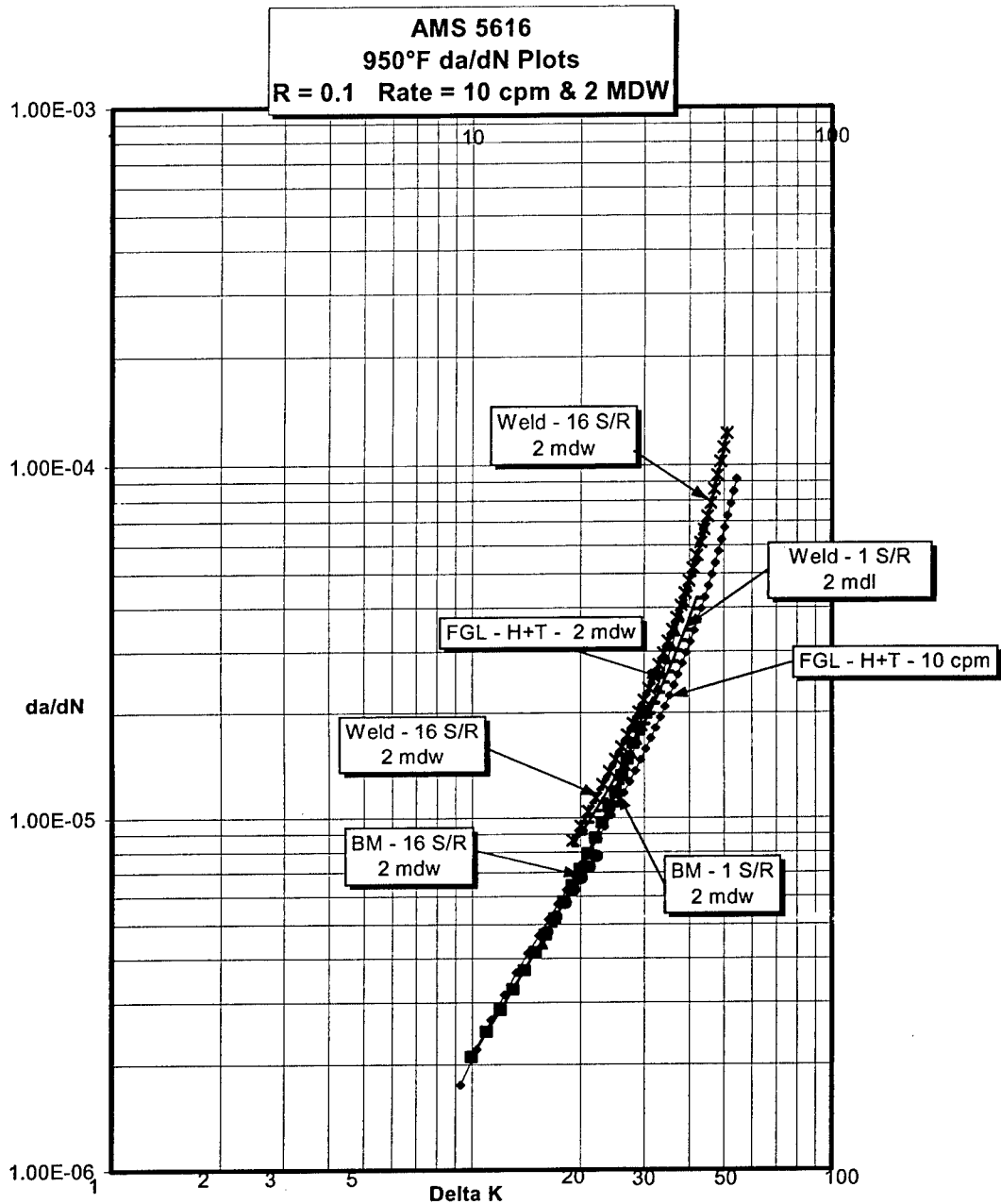


FIGURE 18. CRACK GROWTH RATE PLOTS (da/dN) OF STRESS-RELIEVED AMS 5616 TESTED AT 950°F, $R = 0.1$ AND CYCLIC RATES OF EITHER 10 cpm OR 2-MINUTE DWELL AT MAXIMUM STRESS (The plots illustrate no significant difference in rates between welds and hot rolled-ring forged metal. It also illustrates there is no effect of dwell loading or 16 stress relief cycles. The two hardened-plus-tempered specimens plots are included for reference.)

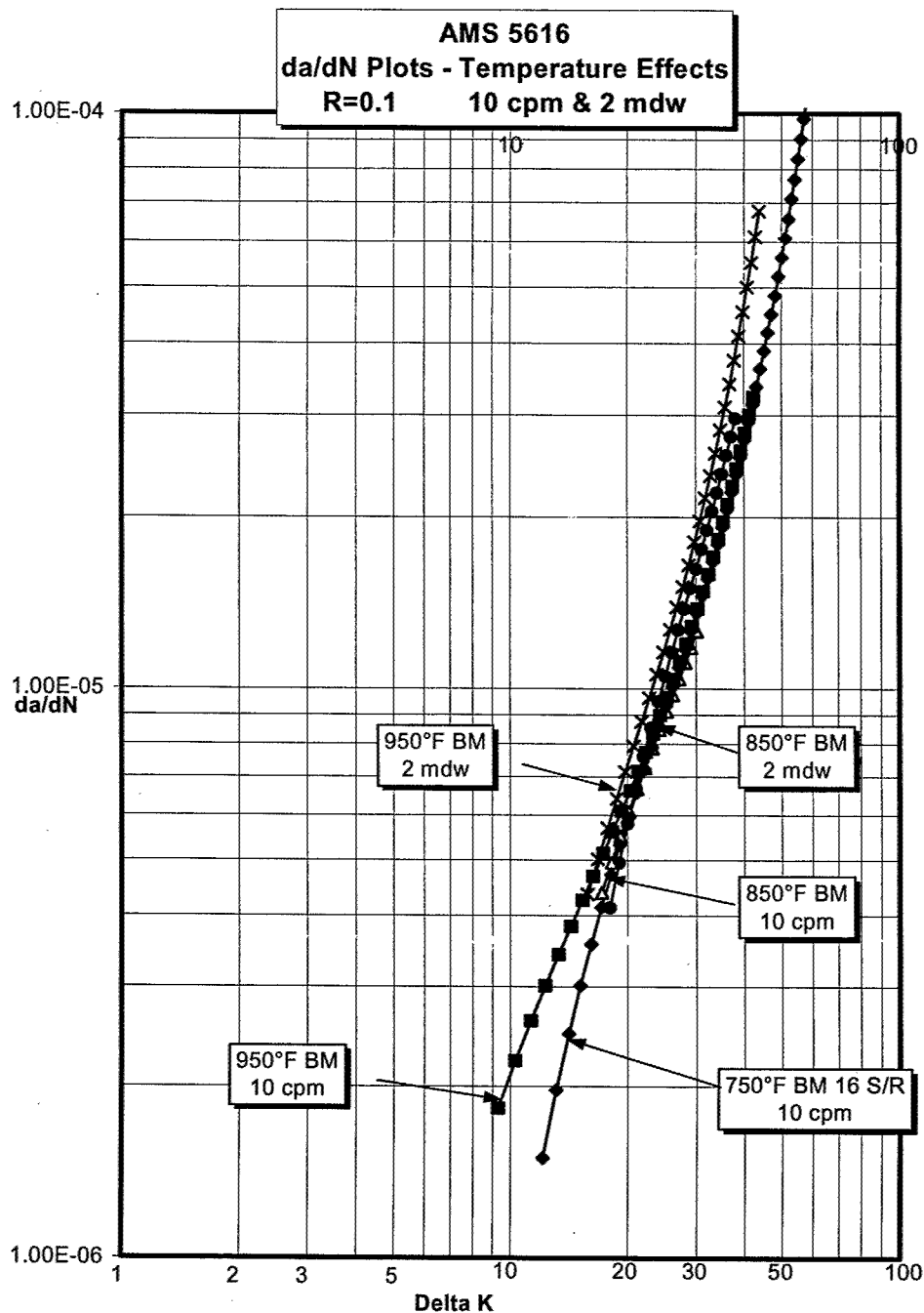


FIGURE 19. CRACK GROWTH RATE (da/dN) PLOTS OF AMS 5616 TESTED AT 850°F WITH AND WITHOUT DWELL LOADING (Note that the eight-cycle, stress-relieved material has rates between those of the 750°F/10 cpm and 950°F/2-mdw stress-relieved base metal rates.)

During the course of the test program a base metal, single-cycle, stress-relieved specimen was mistakenly tested at 1200°F under dwell loading. A data plot is not presented here, but the data is included in appendix A. This is certainly too high a temperature for AMS 5616 application and is included in the data package merely for informative purposes. Little data was collected from the specimen due to its rapid crack growth rate that was an order of magnitude (>10 X) greater than the rate at 950°F.

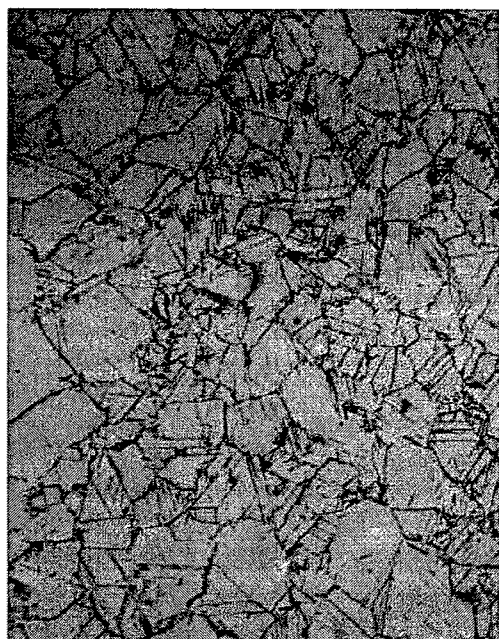
2.1.3.6 AMS 5663 FM Test Plan.

Crack growth rate testing of coarse and fine grain base metal (BM) AMS 5663 was performed to provide a baseline against which to compare results received with specimens processed through simulated multiple-repair heat treat cycles. Test temperatures varied from a low of 800° to a high of 1250°F. Tests were conducted at cyclic rates of 10 cpm and 2-minute dwell. All tests were at $R = 0.1$. Tests were also conducted on GTA fusion welds at 800°F/10 cpm and 1100°F/2 mdw. The coarse grain test material was removed from PW4000 high pressure turbine (HPT) cases of AMS 5663 Heat CKLBCD that had a grain size of ASTM 4 to 6. Fine grain material was excised from barstock with a rectangular cross section and was rolled from Heat PHDMG. This material was determined to have a grain size of ASTM 10 to 12. Standard 1.25" wide by 1.20" long by 0.375" thick compact-tension crack growth rate specimens were machined from both sources so the crack growth would be parallel with the ring or barstock rolling direction.

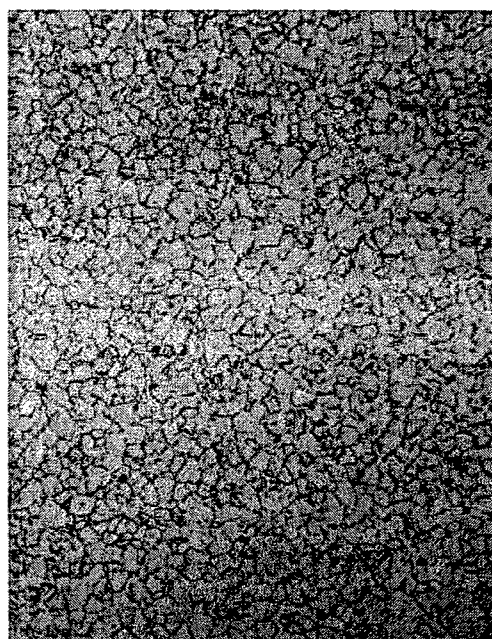
Weld test material was prepared by joining two lengths of the same fine grain barstock described above with a semiautomatic GTA weld (AMS 5382 Inconel 718 filler). Mini-compact-tension test specimens (1.25" by 1.20" by 0.25") were machined from the welded panels with the specimen starting notch aligned either in the center of the fusion zone (FZ) or along one of the heat affected zones (HAZ). Weld FZ are fine grain cast structures, while the HAZ are like the wrought base metal but coarser and with more thermally recrystallized grains. HAZ cracks created by liquation of the base metal grain boundaries are common in the HAZ. The HAZ microstructure is uniquely relative to the FZ and BM microstructure.

To assess the effect of high-temperature engine operation, coarse grain BM specimens were tested at 1000° and 1100°F after 1000 hours of exposure at 1100°F. To assess the effect of multiple-repair heat treat cycles, initially coarse grain BM specimens were exposed to six 1-hour solution cycles at 1750°F, each followed by a full-precipitation age or given six short-age cycles. This expanded the previous evaluation to include crack growth characterization. Later, coarse- and fine-grain BM and weld specimens that had a total of 30 hours of exposure at 1750°F were prepared and tested. This exposure was accomplished through a series of six 5-hour exposures, each followed with a precipitation-aged heat treatment. After a heat treat study that demonstrated such an exposure would create significant amounts of needle delta phase in the coarse grain microstructure, 30 hours was selected. This time frame was also based upon limited input from service repair shops that indicated a 30-hour exposure would represent an extreme amount of exposures for a service case. Results of the heat treat study are presented in appendix B.

Microstructures of various forms and conditions of AMS 5663 that were tested are presented in figures 20 through 23.



AMS 5663 Coarse Grain 200X



AMS 5663 Fine Grain 200X

FIGURE 20. TYPICAL MICROSTRUCTURES EXHIBITED BY THE CONTRACT PROGRAM COARSE- (LEFT) AND FINE- (RIGHT) GRAIN AMS 5663 TEST MATERIAL IN THE STANDARD FULLY HEAT-TREATED CONDITION



AMS 5663 CG + 6 Solutions 200X

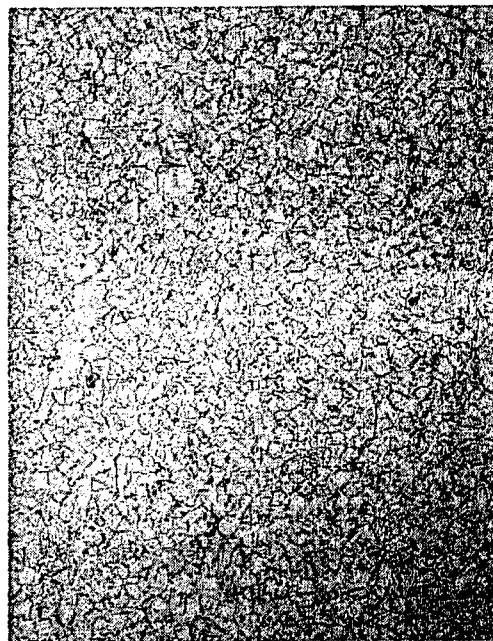


AMS 5663 CG + 6 Short Ages 200X

FIGURE 21. MICROSTRUCTURE OF COARSE-GRAIN AMS 5663 AFTER SIX ADDITIONAL SOLUTION CYCLES AT 1750°F (LEFT) AND SIX SHORT-AGE CYCLES (RIGHT)

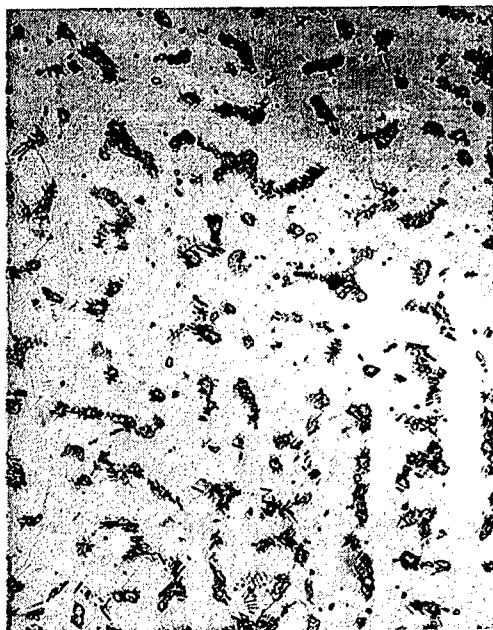


AMS 5663 CG + 30 Sol. Hours 200X

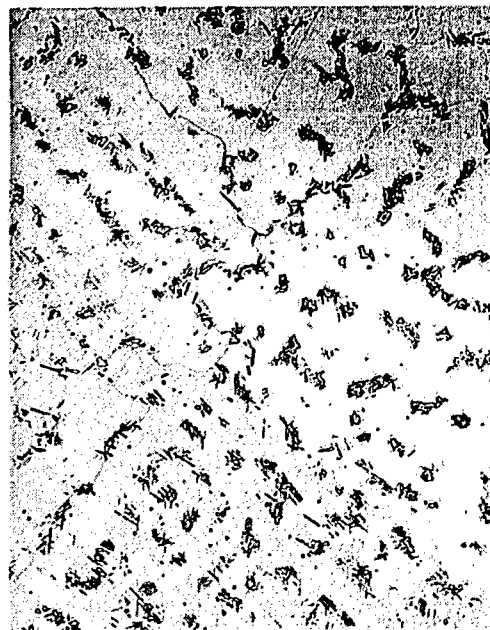


AMS 5663 FG + 30 Sol. Hours 200X

FIGURE 22. MICROSTRUCTURE OF COARSE- (LEFT) AND FINE- (RIGHT) GRAIN AMS 5663, FULLY AGED AFTER 30 HOURS OF EXPOSURE AT THE 1750°F SOLUTION TEMPERATURE



AMS 5663 Weld FZ FHT 500X



AMS 5663 Weld FZ FHT+Exp. 500X

FIGURE 23. MICROSTRUCTURE OF AMS 5663 WELD FUSION ZONES IN THE STANDARD FULLY HEAT-TREATED CONDITION (LEFT) AND AFTER 30 HOURS OF EXPOSURE AT THE 1750°F SOLUTION TEMPERATURE

2.1.3.7 AMS 5663 FM Test Results.

Figures 24 and 25 present the crack growth rates of coarse- and fine-grained AMS 5663 respectively. Fine-grain (ASTM 10-12) base metal specimens had faster rates than coarse-grain (ASTM 4-5) specimens at all temperatures, but the differences increase with test temperature. Under 10-cpm test loading, the fine-grained specimens growth rate grew faster by a factor of 1.7X at 800°F and a factor of 2.4X at 1200°F. The gap in rates was even greater under dwell-loading conditions where the fine-grain material grew at a faster rate by factors of 4X to 14.0X. Overall, the results were consistent with existing data and no anomalies were associated with the program test material. (The 1250°F coarse-grained specimen was lost in testing and was not replaced because the program material was performing consistent with the existing data.)

Exposure to multiple hours at the 1750°F solution temperature had mixed results with the coarse- and fine-grain AMS 5663 (figure 26). Six solution + age heat treat cycles were examined on coarse-grain material that was tested at 800°F/10 cpm and 1100°F/2 mdw. Crack growth rates were similar to the coarse-grain base results generated in this program. However, a 30-hour exposure at 750°F had a significant effect on raising the rate of crack growth rate for the coarse-grain material. This 30-hour exposure was administered as six 5-hour heat treatments followed by the standard-age heat treatment. The same exposure failed to do likewise with the fine-grain material. The fine-grain base material rate under 1100°F/2-mdw conditions was approximately 8X faster than that of the coarse-grain material. The 30-hour exposure failed to alter the 1100°F/2-mdw crack growth rate for the fine-grain material, but raised the rate of the coarse-grain material to the level of the fine-grain stock. Photomicrographs illustrated that extended exposures at the 1750°F solution temperature dramatically increased the volume of needle delta phase in the microstructure while barely changing the microstructure of the fine-grain material (compare figures 20 and 22).

Multiple hours at aging temperatures had an unexpected effect on the crack growth rate of AMS 5663 at high temperature (figure 27). Coarse-grained material exposed for 1000 hours at 1100°F showed, on average, a 4X increase in crack growth rate at the test condition of 1100°F/2 mdw. The crack growth rate of AMS 5663, when tested under dwell conditions at 1000°F, did not increase, even though the material had the same age temperature exposure as the material tested at 1100°F/2 mdw. Exposures of AMS 5663 for up to six cycles of SPOP 465, the short-age field heat treat cycle, had an even more dramatic effect on crack growth rates. For tests at 1100°F/2 mdw, the rate of acceleration of the multiple SPOP 465-exposed material was increased significantly. This observation is supported by the much steeper slope of the data plots. Thus, at lower delta Ks, such as 20 sq. root ksi, the rates of exposed and base material are equivalent, but at 30 sq. root ksi, the crack growth rate of the exposed material was faster by a factor of 7X. Exposure to six cycles of the SPOP 465 short age did not significantly affect the crack growth rate of AMS 5663 when tested at 800°F/10 cpm.

Crack growth rates of Inconel 718 GTA fusion welds fell between that of the coarse- and fine-grain base material rates at both 800°F/10-cpm (figure 28) and 1100°F/2-mdw (figure 29) test conditions. This was true for FZ and HAZ weld specimens. It was also true, for welds that were fully heat treated and for fully heat treated-plus-exposed to six 5-hour exposures at 1750°F. The

spread of rates among the weld samples was greater at the 1100°F test compared to the 800°F test (3X vs 2X), but this is expected. One 30-hour solution-exposed weld showed a faster rate than the other specimens when tested at 1100°F/2 mdw. However, there was no clear pattern of accelerated crack growth rates of welds when exposed to multiple hours at the solution temperature.

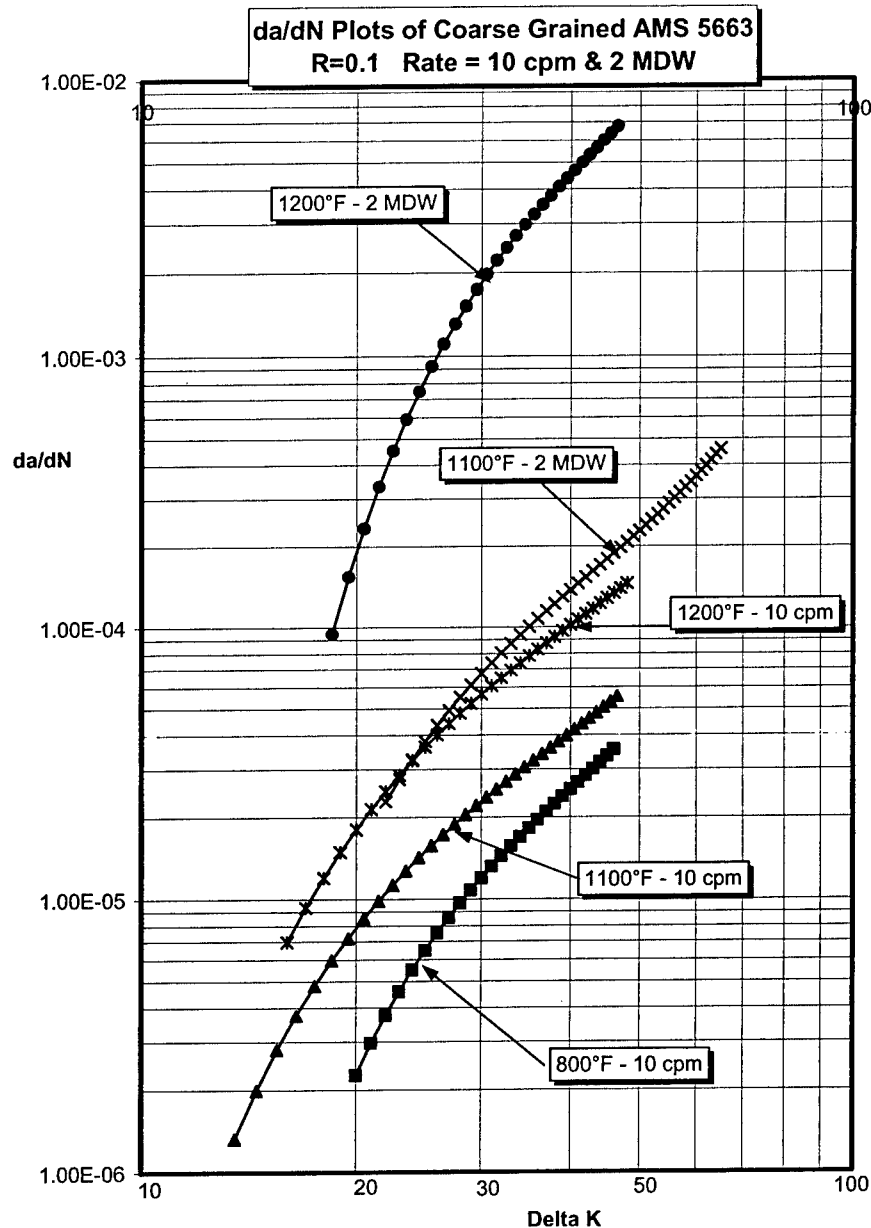


FIGURE 24. CRACK GROWTH RATE (da/dN) PLOTS FOR AMS 5663 WITH AN ASTM 4-5 GRAIN SIZE TESTED AT VARIOUS TEMPERATURES (The results are consistent with existing P&W database data and serves as a baseline against which to compare material with simulated heat treatments.)

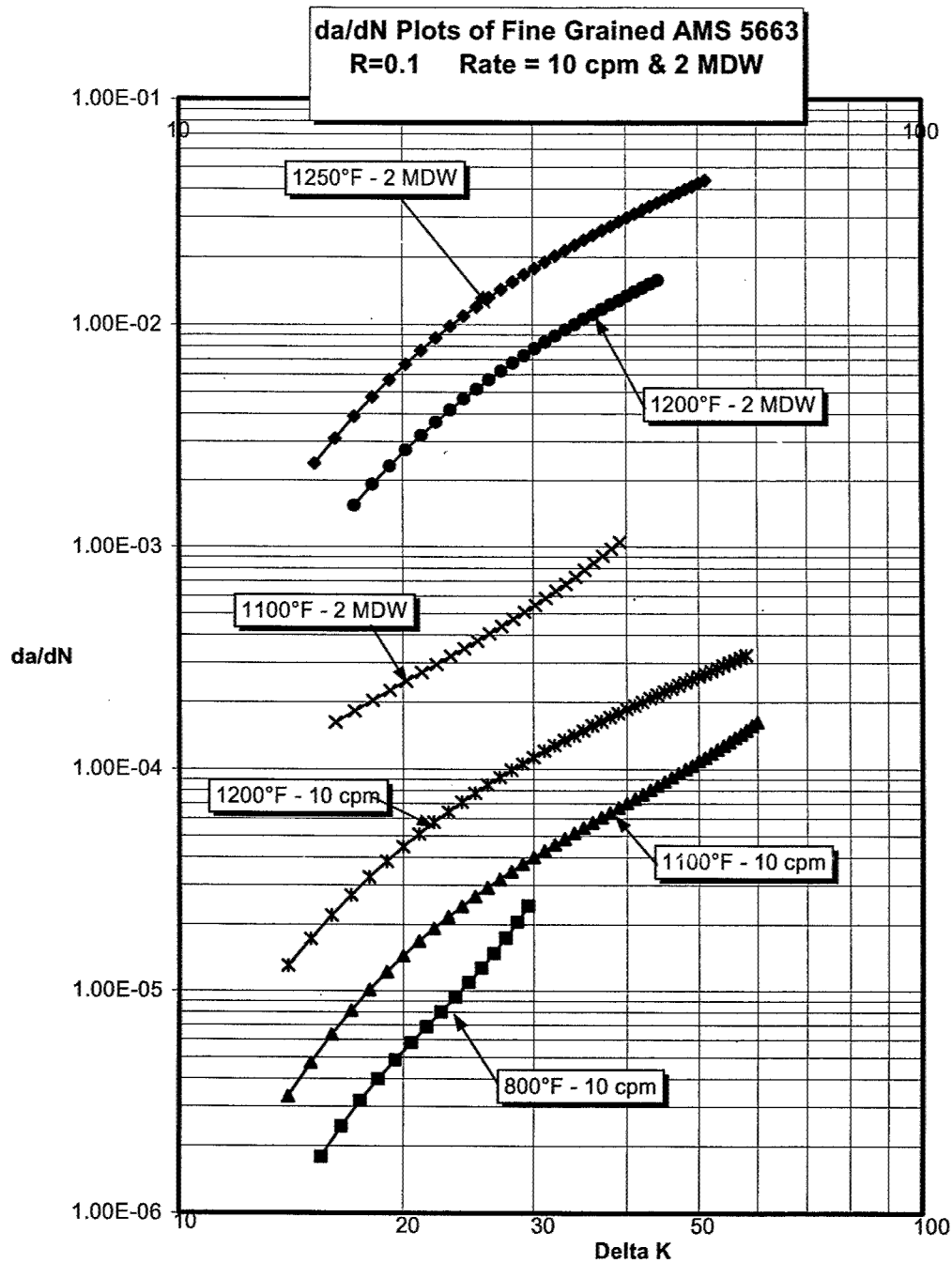


FIGURE 25. CRACK GROWTH RATE (da/dN) PLOTS FOR AMS 5663 WITH AN ASTM 8-10 GRAIN SIZE TESTED AT VARIOUS TEMPERATURES (The results are consistent with existing P&W database data and serves as a baseline against which to compare material with simulated heat treatments. Note the faster rates of the fine-grained material relative to coarse-grained material (figure 24), especially at temperatures at and above 1100°F.)

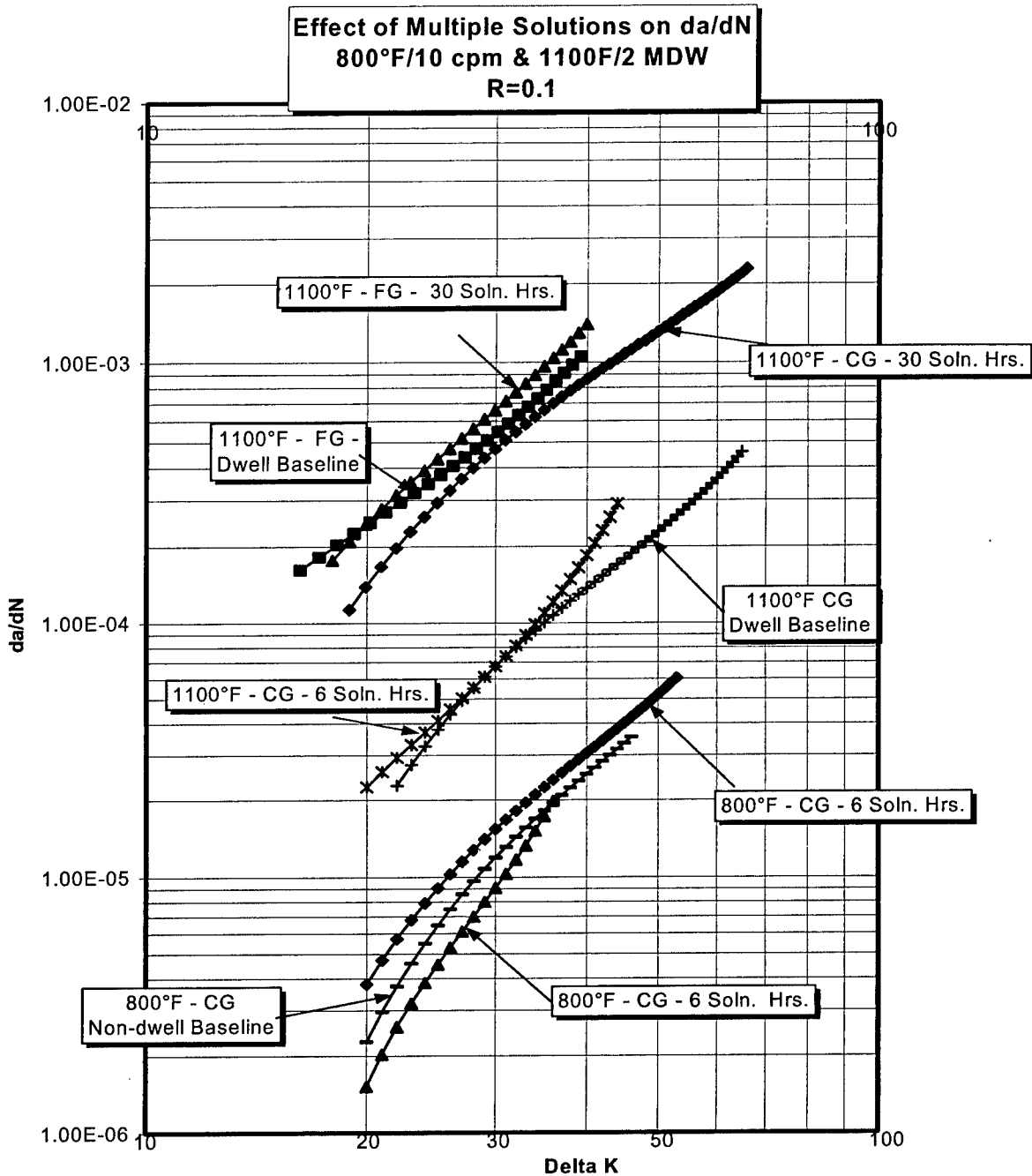


FIGURE 26. CRACK GROWTH RATE (da/dN) PLOTS OF AMS 5663 TESTED AT 800° AND 1100°F AFTER BEING EXPOSED TO SIX 1-HOUR SOLUTION (1750°F) EXPOSURES OR SIX 5-HOUR SOLUTION EXPOSURES (Note the relative ineffectiveness of a 6-hour exposure at both test conditions. The 30-hour exposure dramatically increases the crack growth rate of the coarse material tested under dwell loading at 1100°F but had no effect on the rate of the fine grain material.)

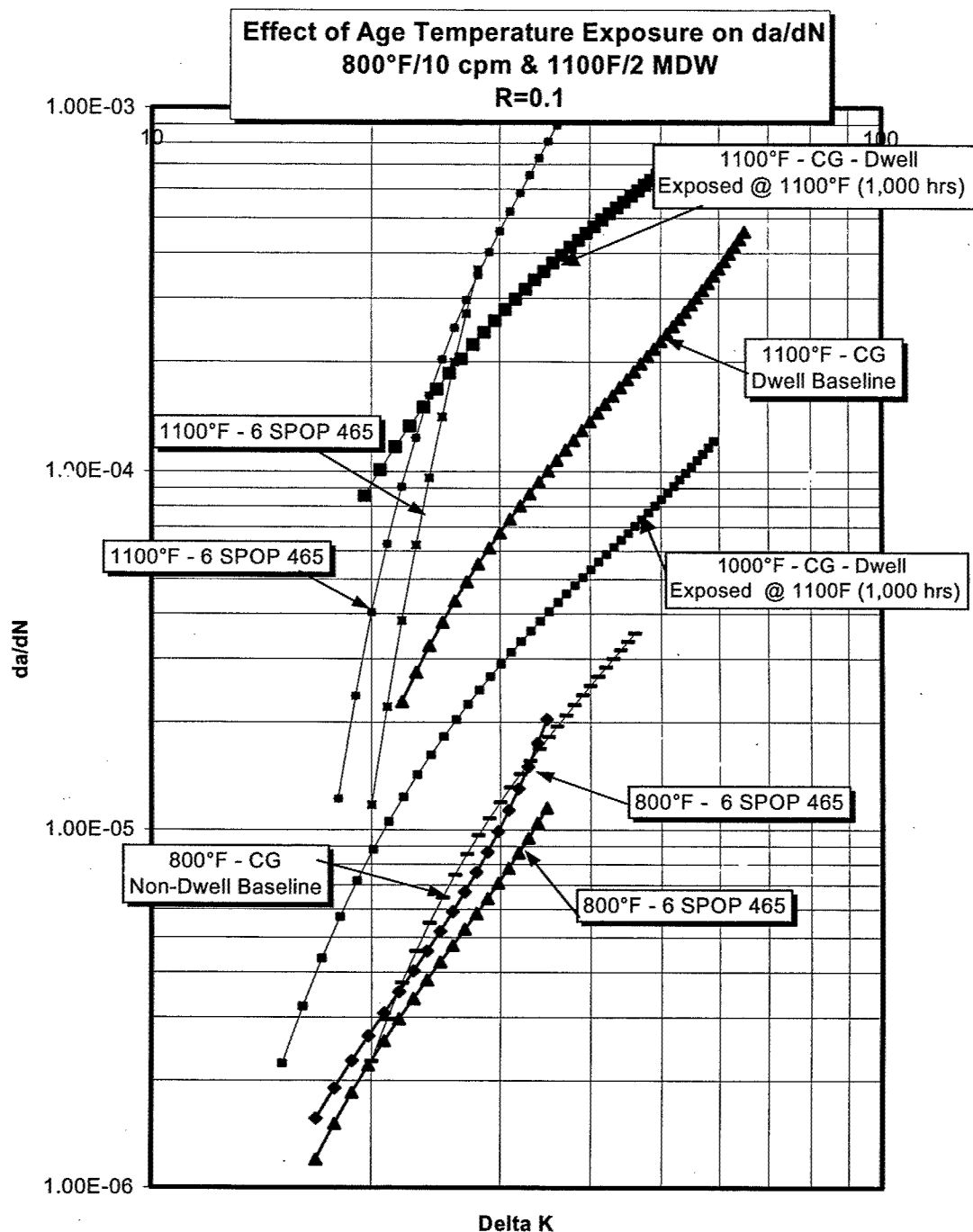


FIGURE 27. CRACK GROWTH RATE (da/dN) PLOTS FOR AMS 5663 TESTED AT 800°F/10 cpm, 1000°F/2 mdw, AND 1100°F/2-MINUTE DWELL AND $R = 0.1$ (Test material was exposed to six field repair short-age cycles (SPOP 465) or 1000 hours at 1100°F.)

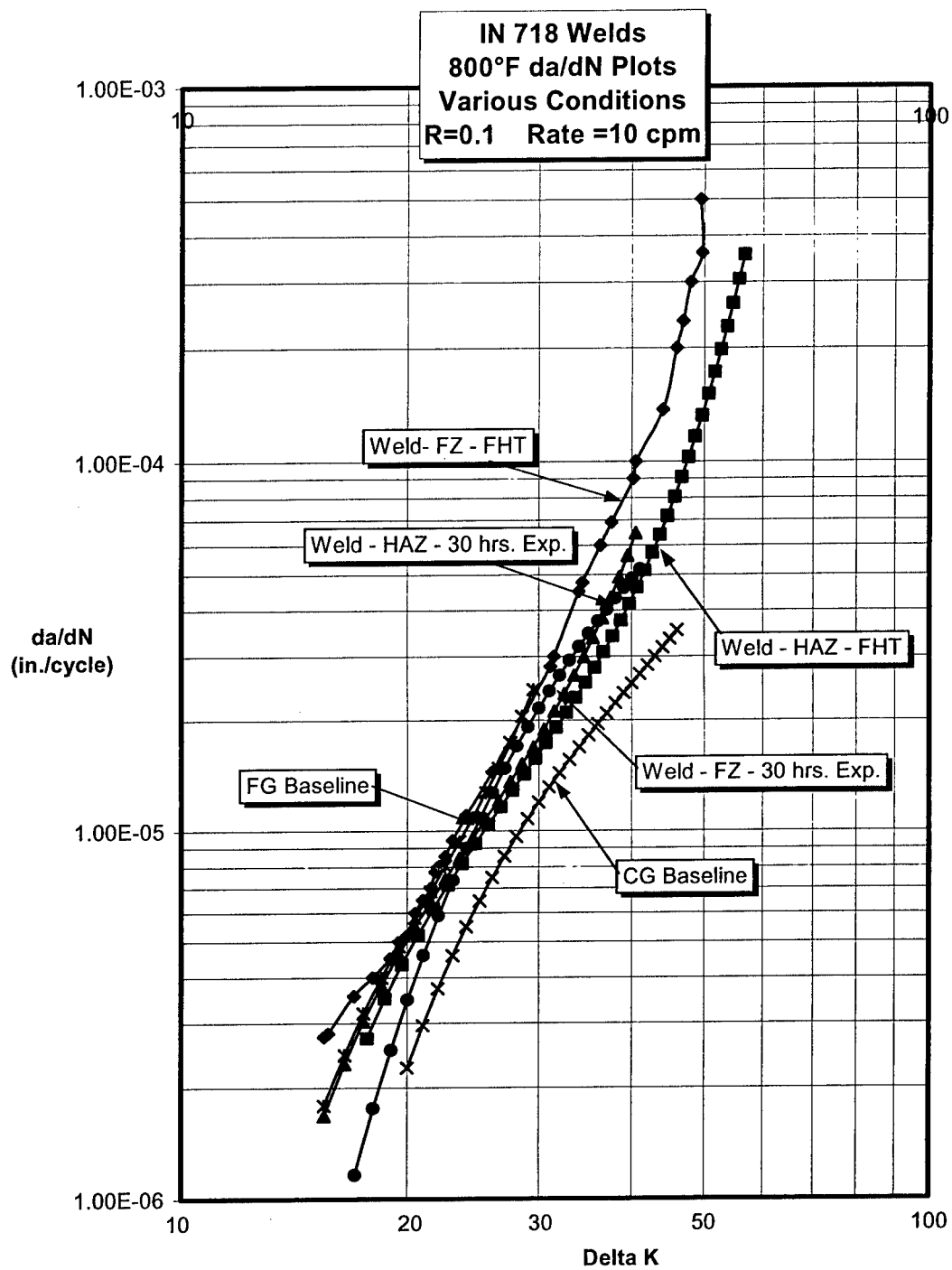


FIGURE 28. CRACK GROWTH RATE (da/dN) PLOTS OF AMS 5663 GAS TUNGSTEN ARC WELDS TESTED AT 800°F, R = 0.1 AND 10 cpm. (Note how all plots, FZ and HAZ, fall between the rates of coarse- and fine-grained base metal.)

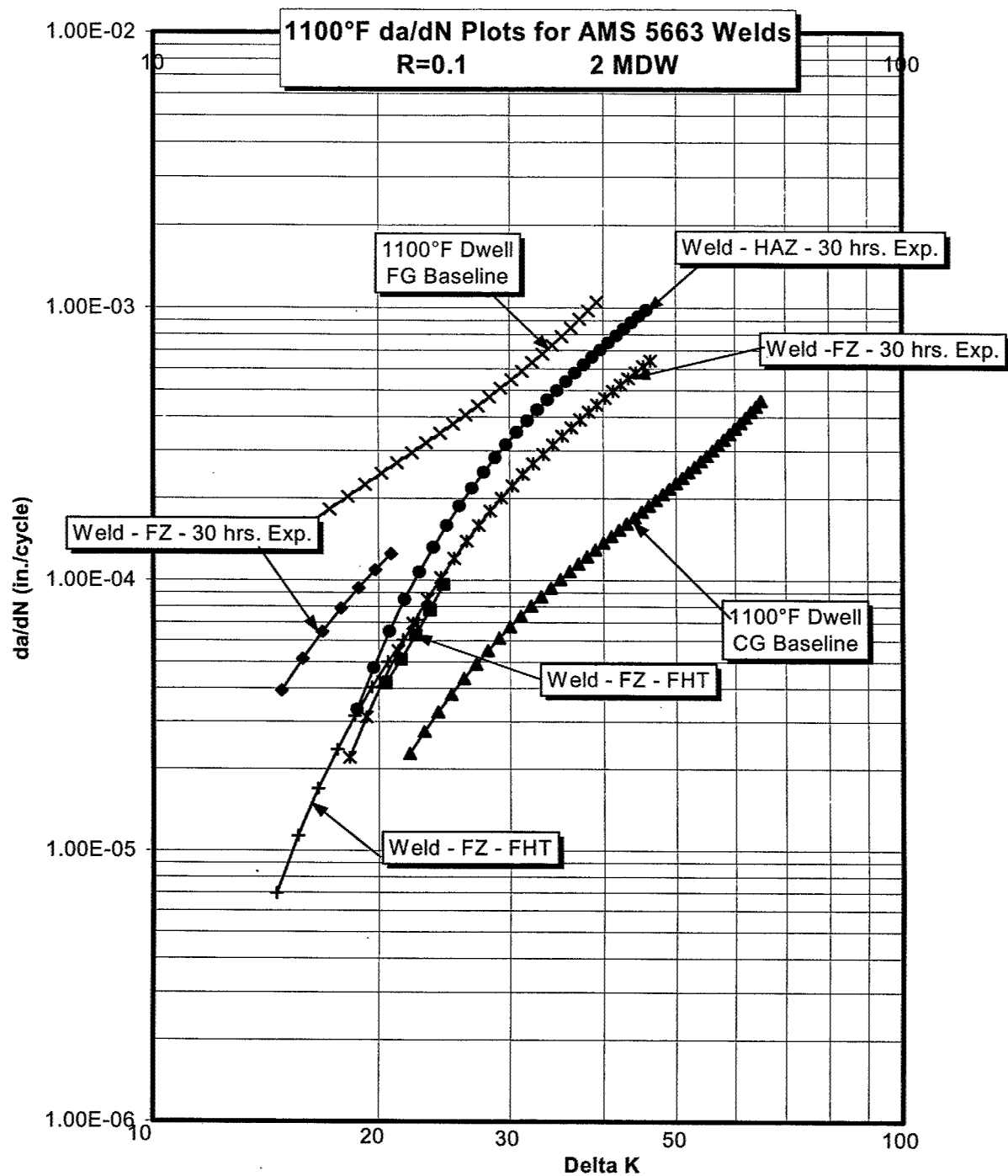


FIGURE 29. CRACK GROWTH RATE (da/dN) PLOTS OF AMS 5663 GAS TUNGSTEN ARC WELDS TESTED AT 1100°F, $R = 0.1$ AND 2-MINUTE DWELL AT MAXIMUM STRESS (Note how all plots, FZ and HAZ, fall between the rates of coarse- and fine-grained base metal.)

2.1.3.8 PWA 1469 Base FM Test Plan.

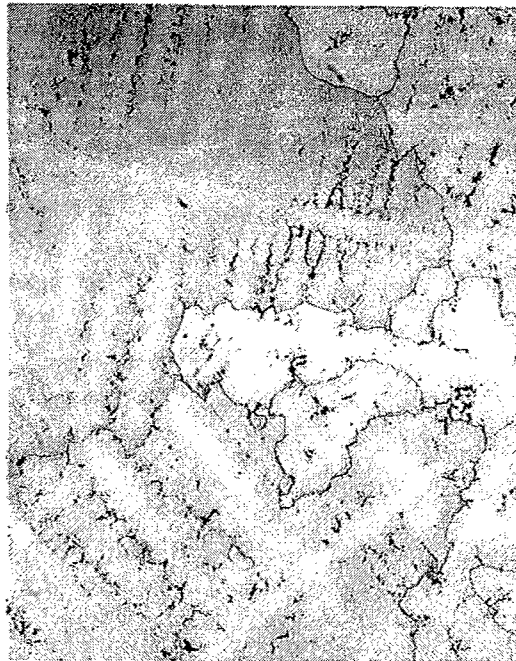
Testing of PWA 1469 (cast+HIP Inconel 718) concentrated on the 1100°F/2-mdw test condition. However, a few 1100°F/10-cpm tests were added in order to facilitate analysis of the hot-pressure test rig case. The high-temperature dwell condition is typical for P&W commercial engine PWA 1469 diffuser case outer-pressure walls. There are two characteristics of the PWA 1469 that made it unique with respect to existing data for the wrought forms of Inconel 718. One is that even for castings with the same grain size, there is considerably more scatter. This is probably due to the crack growth rates of individual specimens being strongly influenced by individual grains within the specimen. Using the largest cross section test specimen mitigates against this effect to some degree. However, when testing large grain castings, single very large-grains can skew the results. The other difference is that the cast plus HIP form of Inconel 718 shows relative insensitivity to dwell loading. The scatter bands of dwell and non-dwell-loading overlap considerably. It is not unusual for dwell-loaded specimens to display rates that are slower than typical non-dwell-loaded specimen rates at 1100°F. Material conditions that were evaluated included base metal, GTA welds, and HIP GTA welds. Each of these three forms were tested in the fully heat-treated and heat treated-plus-exposed conditions. The exposure was eight 5 hour-cycles at 1750°F and each cycle was followed by the standard full precipitation age heat treatment. This exposure would simulate multiple repair process cycles on components such as diffuser cases. Heat treatment particulars that affect the exposure were selected at the conclusion of the heat treat study and are summarized in appendix B. No plans were made to examine the effect of multiple SPOP 465 (short-age) cycles on the crack growth rate of PWA 1469 because the use of this option is severely restricted with respect to PWA 1469 cases.

Nondwell (10 cpm) testing was added in order to facilitate crack growth rate analysis of the hot-pressure rig test case. During the latter portion of the case testing, the rig test moved from a dwell-loaded condition to a straight cycling condition because the pressure could not be maintained. Consequently, four tests were added to the program. All were conducted at 1100°F and 10 cpm. The specimens included two exposed (40 solution hours) base metal, a HIP weld, and a HIP weld that was also exposed.

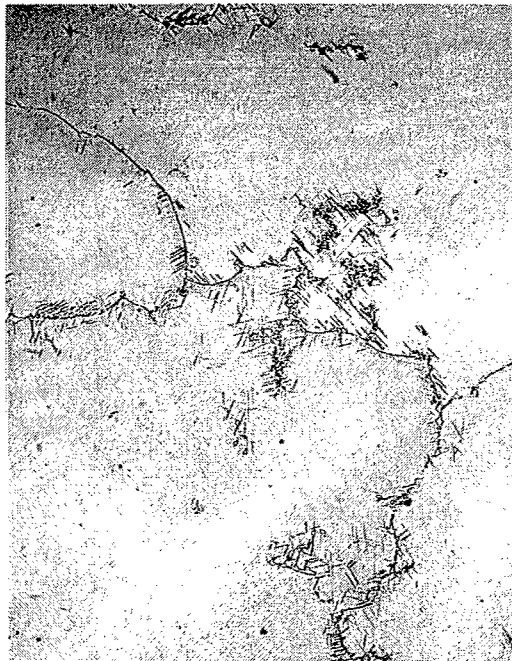
Test material was procured in the form of 4" by 8" by 0.625" thick cast plates (Heat 41214) supplied by Precision Castparts Corp. (PCC). Baseline data was conducted on material that was fully heat treated per PWA 1469, which is detailed below. Post-HIP welds were made after the solution heat treat phase, resolutioned and aged. HIP welds were made just prior to HIP and are exposed to the full PWA 1469 heat treat process. Exposed specimen material was produced by exposing fully heat-treated material to the cycles described above.

Process	Parameters
HIP	2175°F (15 ksi) (4 hrs)
Stabilization	1600°F (10 hrs)
Solution	1750°F (1 hr)
Precipitation Age	1350°F (8 hrs) FC to 1225 (8 hrs)

Microstructures typical of the evaluated material are illustrated in figures 30 through 33.

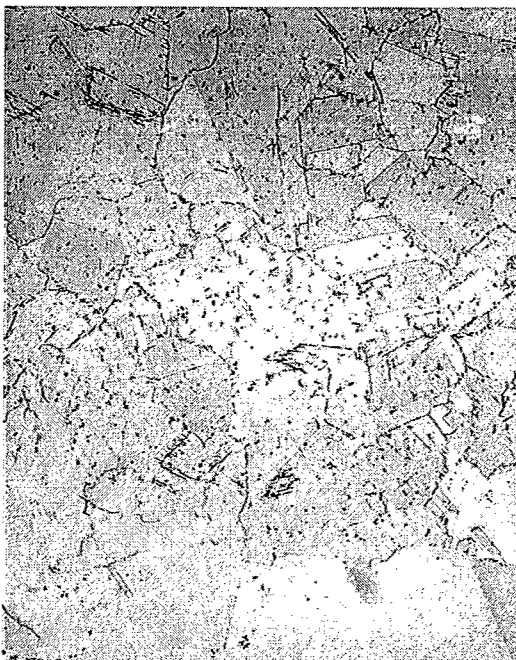


PWA 1469 FHT 50X



PWA 1469 FHT 500X

FIGURE 30. PWA 1469 (CAST+HIP INCONEL 718) IN THE STANDARD FULLY HEAT-TREATED CONDITION

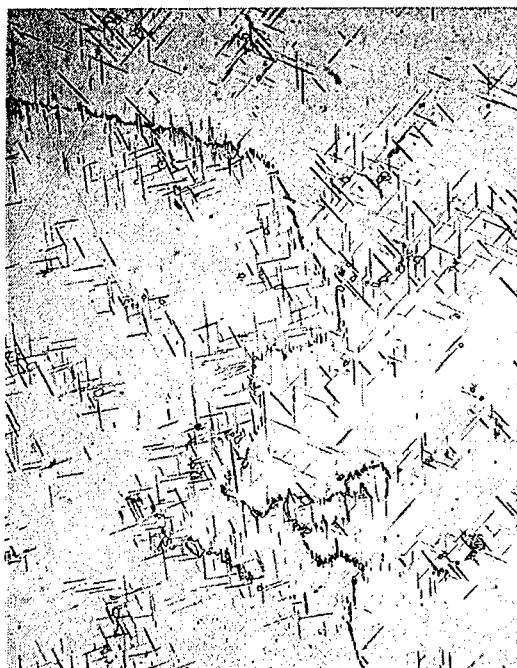


PWA 1469 HIP Weld 50X



PWA 1469 HIP Weld 200X

FIGURE 31. MICROSTRUCTURE OF HIP PROCESSED WELDS IN PWA 1469 (Lower third of left photomicrograph is the coarser grain structure of the cast base metal. The HIP weld structure exhibits wrought like features such as twinning and intragranular needle delta phase.)

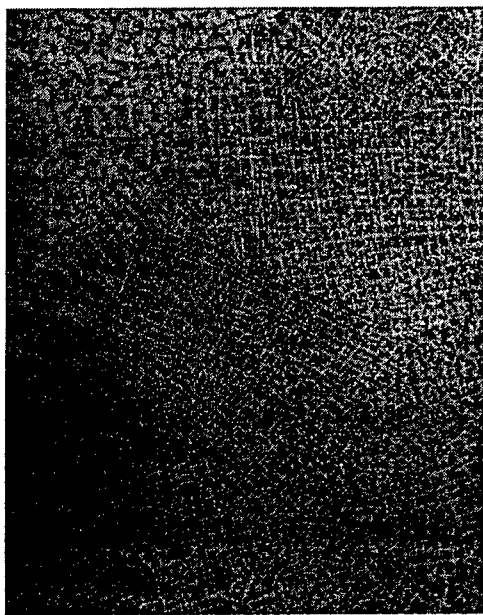


Exposed PWA 1469 Base Material 200X

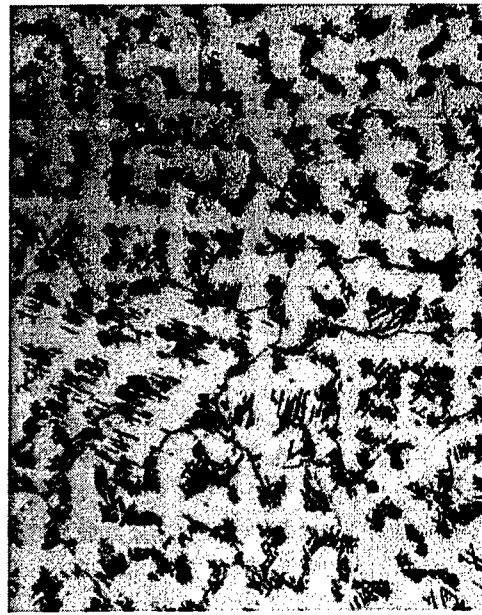


Exposed HIP Weld of PWA 1469 200X

FIGURE 32. MICROSTRUCTURE OF PWA 1469 BASE MATERIAL (LEFT) AND HIP WELDS (RIGHT) AFTER EIGHT 5-HOUR EXPOSURES AT 1750°F



Exposed PWA 1469 Weld FZ 50X



Exposed PWA 1469 Weld FZ 500X

FIGURE 33. MICROSTRUCTURE OF PWA 1469 WELD FUSION ZONES AFTER BEING EXPOSED TO EIGHT 5-HOUR EXPOSURES AT 1750°F (Structure was similar to nonexposed welds except for increased amounts of short needle delta phase at interdendritic areas.)

2.1.3.9 PWA 1469 FM Test Results.

Figure 34 presents test results of base metal, welds, and HIP welds in the as fully heat-treated condition along with a plot of the coarse-grain AMS 5663 1100°F/2 mdw results which will serve as references. Rates of PWA 1469 are approximately 80% of that of the coarse-grain AMS 5663. Both of these baseline plots were within the 1100°F/10 cpm scatter band for PWA 1469. In fact, the two base metal plots were very close to the curve and are used as "typical" for PWA 1469 tested at nondwell conditions. As mentioned, one feature of large-grain cast Inconel 718 is its relative insensitivity to dwell loading.

The non-HIP welds had a faster crack growth rate than the casting baseline by an average factor of 1.5 to 2.0X. This was still slower than the coarse-grain AMS 5663 rates and other AMS 5663 welds. It is difficult to explain this, being that the fusion zone areas of both AMS 5663 and PWA 1469 have identical microstructures. One fusion zone weld specimen was machined with the weld that was not properly aligned in the starting slot. Crack growth of this specimen was primarily through the specimen's base metal portion. When the HIP weld specimen was tested under 10 cpm loading, the crack growth rate was faster than the dwell-loaded base material at lower delta K values. However, the plots converged at higher (40) values. Results of the HIP welds tested under dwell conditions were the most dramatic. The two specimens tested under dwell loading were faster than the HIP baseline by factors of 13X and ~30X. The faster crack growing HIP weld had a rate that matched that of the fine-grain AMS 5663 tested under identical conditions (see figure 25).

Exposures of up to 40 hours at the 1750°F temperature increased the rate of crack growth of the base metal at the 1100°F/2-mdw test condition by a modest factor of 1.5X (figure 35). The exposed base metal specimen tested at 1100°F/10 cpm actually had a slightly faster rate than the exposed metal tested under dwell conditions. These rates were on the high side of the scatter band of nonexposed base metal tested at 1100°F/10 cpm. Thus, all test results of PWA 1469 base metal, exposed and as fully heat treated, fell within a range that currently defines the database scatter band for PWA 1469 at 1100°F.

Exposures of up to 40 hours at the 1750°F solution temperature had mixed results on PWA 1469 welds (figure 36). One exposed fusion zone specimen had a rate that was slightly slower than the nonexposed fusion zone specimen. However, the two exposed HAZ, weld specimens had rates that were 5-6X faster than the nonexposed HAZ specimens. One followed the same plot as the slower nonexposed HIP weld while the other was slightly faster.

Under dwell loading, the two exposed HIP welds were only slightly faster rates than the slower two of nonexposed HIP weld specimens although one had a very steep slope to its plot.

As stated earlier, scatter among PWA 1469 da/dN plots is greater than the wrought materials. These results illustrate trends, but not enough tests were done to use the results to define design curves. Care must be taken against relying too much on the results of a few specimens to establish a design curve. Additional testing of HIP weld is especially warranted to confirm its behavior.

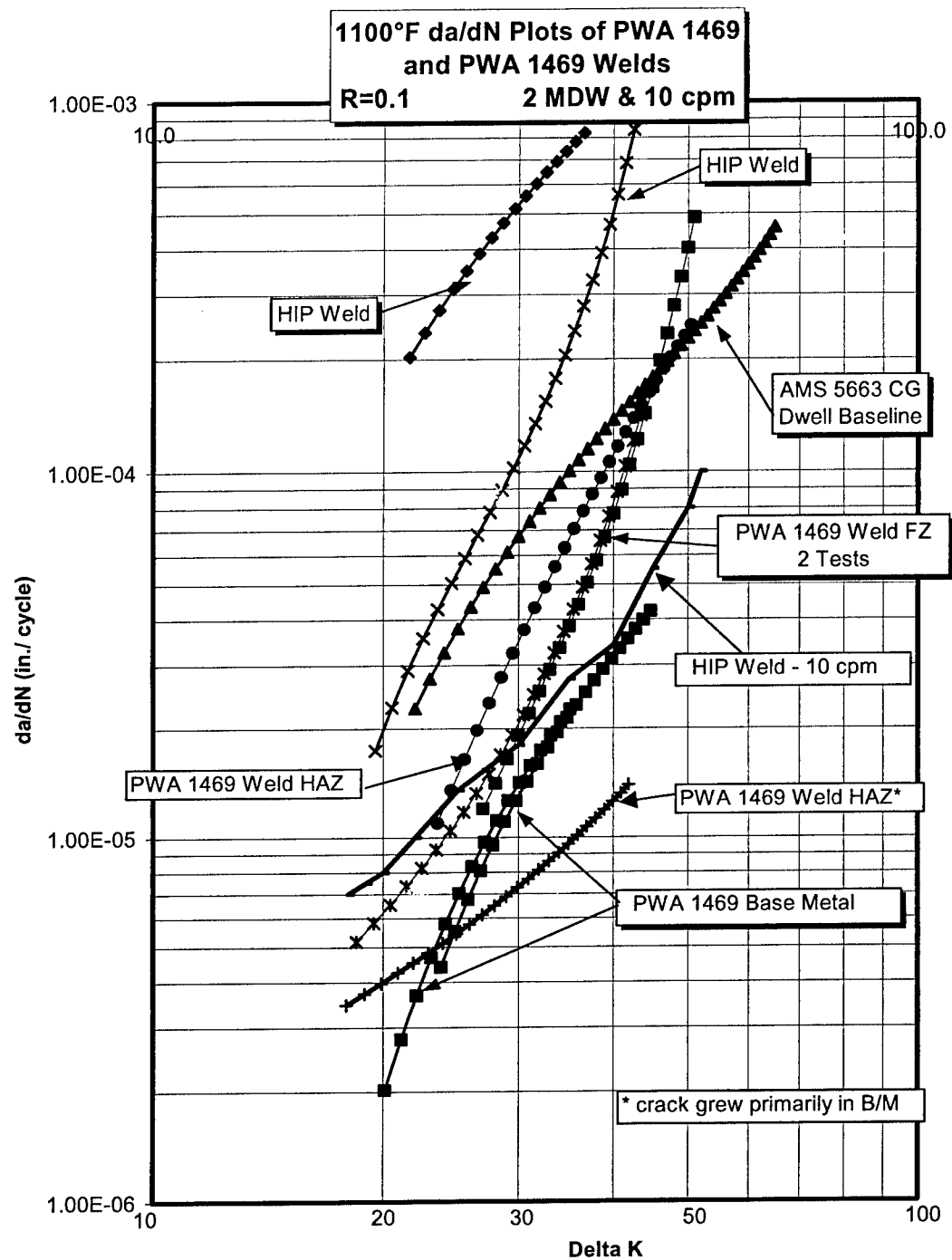


FIGURE 34. CRACK GROWTH RATE (da/dN) PLOTS OF PWA 1469 BASE METAL, WELDS, AND HIP WELDS TESTED AT 1100°F, $R = 0.1$, AND UNDER 2-MINUTE DWELL AT MAXIMUM STRESS (One HIP weld was tested at 10 cpm. Weld cracks were centered either in the weld HAZ or FZ. The AMS 5663 coarse grain 1100°F dwell plot is included for reference.)

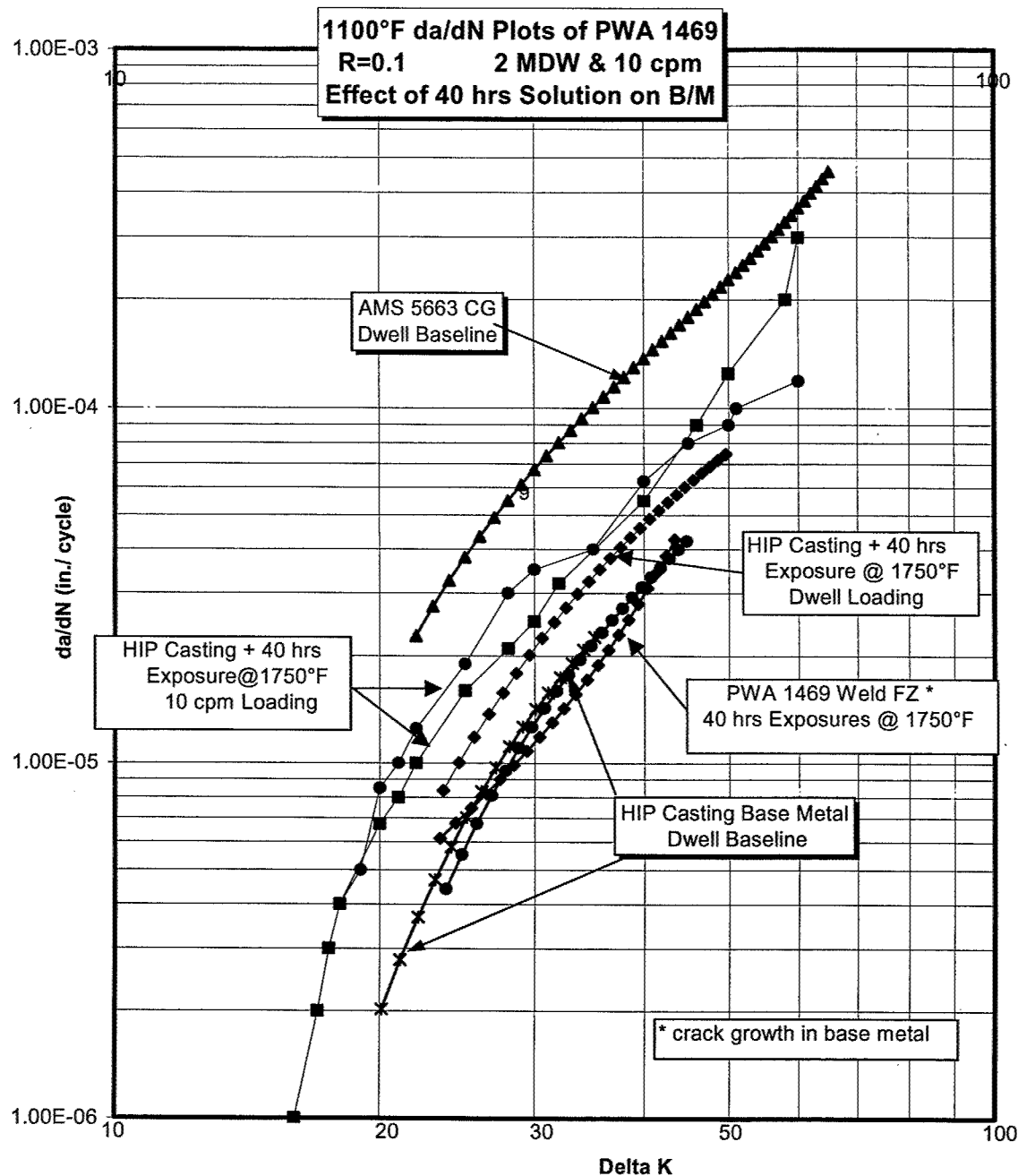


FIGURE 35. 1100°F CRACK GROWTH RATE (da/dN) PLOTS OF FULLY HEAT-TREATED PWA 1469 WITH A 40-HOUR EXPOSURE AT 1750°F (The coarse grain AMS 5663 and base PWA 1469 1100°F dwell plots are included for reference. Note that the exposed specimen run under 10 cpm loading has a faster rate than the dwell-loaded specimens.)

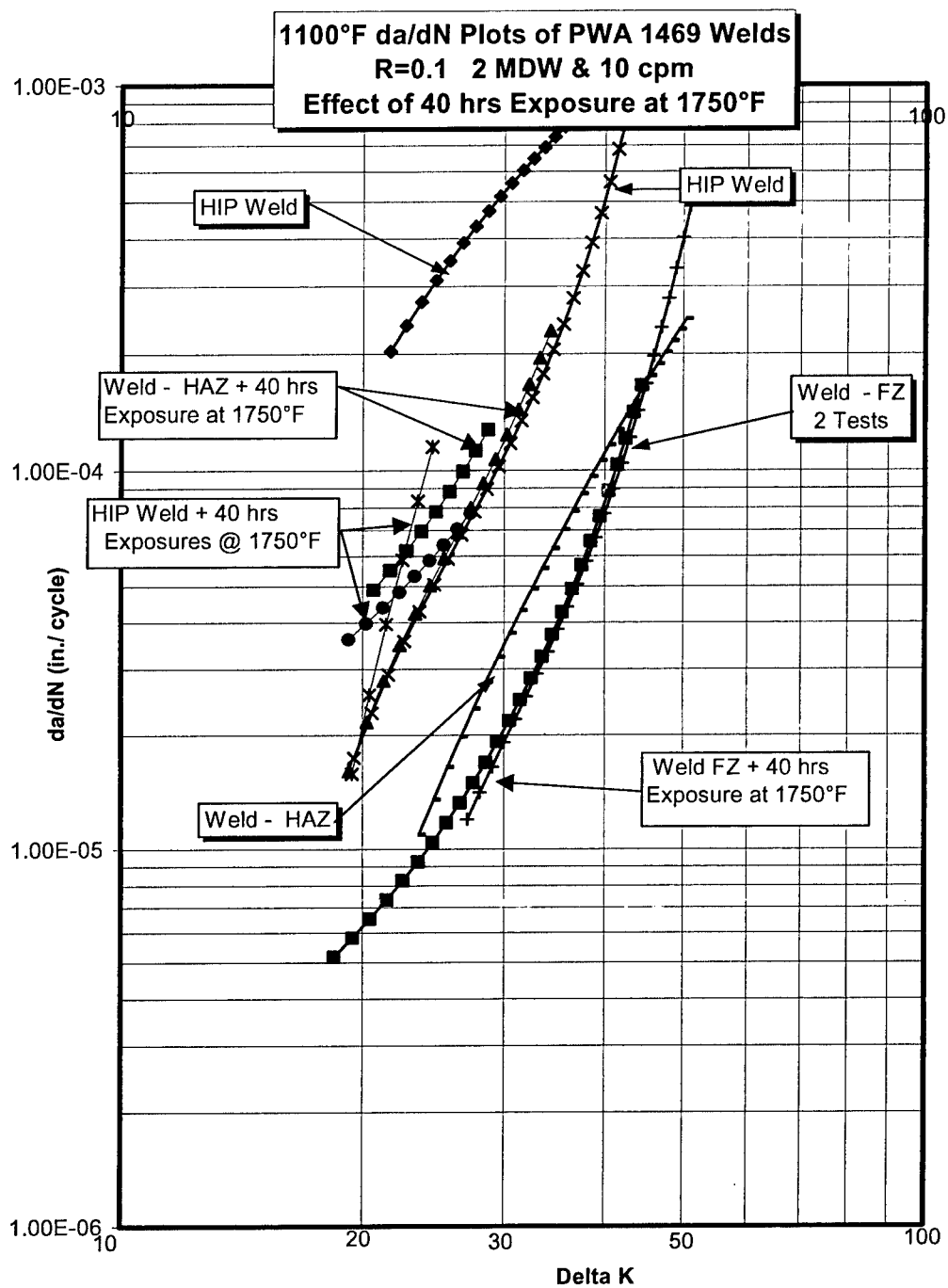


FIGURE 36. 1100°F CRACK GROWTH RATE (da/dN) PLOTS OF PWA 1469 WELDS WITH A 40-HOUR EXPOSURE AT 1750°F (The exposure had an accelerating effect on the non-HIP weld HAZ specimens, but not so on the two other weld specimen types.)

2.1.3.10 FM Data Summary.

Crack growth rate testing of AMS 5613 and AMS 5616 produced no surprises. The results demonstrated that the martensitic microstructure is relatively insensitive to multiple tempers with regard to crack growth rates at the temperatures evaluated. The systems are also insensitive to dwell loading and weld effects. For AMS 5616 within the range evaluated, differences between material orientation with respect to the rolling direction or grain size do not effect the crack growth rates.

Grain size effects on the crack growth rate of wrought Inconel 718 are well known and were confirmed with the AMS 5663 baseline test results as illustrated in figures 24 and 25. Test results achieved with the AMS 5663 welds were consistent with previously generated data. It is generally accepted that AMS 5663 forgings used to construct large static components, such as cases, are generally coarse grained. However, cutup analysis of the long time service cases (see section 2.1.4) have shown that very fine grain details may get into a case assembly.

Two surprises arose from the AMS 5663 testing. One was the rate accelerating effect of a 30-hour solution exposure on coarse-grain AMS 5663 when tested at 1100°F/2 mdw, and the other was the effect that aging temperatures had on the crack growth characteristics of AMS 5663.

- The rate of accelerating effect of a 30-hour exposure was a surprise because it had been reported from earlier programs that multiple-solution exposures that generated more, even in excess, needle delta did not have such an effect. A recheck of the material used in those programs uncovered that the test material had been fine-grain forgings and not the as-reported coarse-grain forgings. Thus, the results of this program were consistent. It is noted that the upper end of the wrought Inconel 718, 1100°F dwell loading, crack growth scatter band is set by very fine grain forged material. Treatments of other forms of Inconel 718 may cause acceleration in the rate of crack growth but rarely creates rates that are faster. This is, except for over-aging, caused by extended exposure in the precipitation aging temperature range for the alloy.
- When this program was started, it was assumed that over-aging would have a minimal effect on the crack growth resistance of AMS 5663. However, both the long-time (1000 hours) exposure at 1100°F and the multiple-repair short ages caused an acceleration of AMS 5663's 1100°F/2-mdw crack growth rate. Of particular concern is when the effect of the short-age heat treat cycle is used without benefit of any resolution. Not only was the rate increased, but the rate of increase accelerated with crack growth. It is believed that multiple age only repair processing is used sparingly, if at all, on critical AMS 5663 components.

One of the objectives of the nonfunded portion of this contract program was to monitor the repair shops to determine exactly what repaired and reconditioned cases actually experience. In light of the dramatic effects the short-age process had on high-temperature crack growth rates, there are a number of actions that should be considered to mitigate against possible risk caused by using this process. One action would be to get the field information originally planned for this program to determine if the process is little or widely used. Second, the process should be evaluated for its

effect on AMS 5663 at temperatures between 800° and 1100°F. The long 1100°F exposure was found not to affect AMS 5663's crack growth rate at 1000°F, but the more damaging short-age process was only evaluated at 800° and 1100°F. More critical AMS 5663 components, such as the JT9D diffuser, operate at temperatures between these two levels. Finally, the process should be tested to determine if it affects the crack growth rate properties of finer grain AMS 5663.

Results of the crack growth rate testing of PWA 1469 generally followed form and were consistent with experience. Long exposures to the solution temperature neither generated significant amounts of needle delta phase nor substantially affected the crack growth rates of base metal and welds. However, the much higher crack growth rates of HIP welds at 1100°F/2 mdw relative to normal welds or the PWA 1469 base were unexpected. An explanation lies in the microstructure exhibited by the HIP welds. A typical HIP weld microstructure is similar to that of thermally recrystallized wrought Inconel 718, with more than typical amounts of twinning. Also, qualitatively, there appears to be less grain boundary delta and more intragranular delta. The structure of two HIP welds and two exposed HIP welds are illustrated in figure 37. Table 17 lists the crack growth rates of the various forms of Inconel 718 at 1100°F/2 mdw with respect to grain size. Not only do HIP welds resemble wrought Inconel 718 by microstructure, but they also behave similarly to wrought Inconel 718 under dwell loading at high temperatures. These rates are strongly influenced by grain size and are more sensitive to the precipitation of excess delta phase. Observing the grain sizes of HIP welds revealed that the thermally recrystallized structure appears to be finer in the center of the weld with coarser thermally recrystallized grains surrounding the center. Thus, the crack growth rate a specimen exhibits is related to how the specimen's starting crack was aligned with the HIP weld.

TABLE 17. 1100°F/2-mdw CRACK GROWTH RATES AT 20 AND 30 DELTA K FOR VARIOUS FORMS OF INCONEL 718

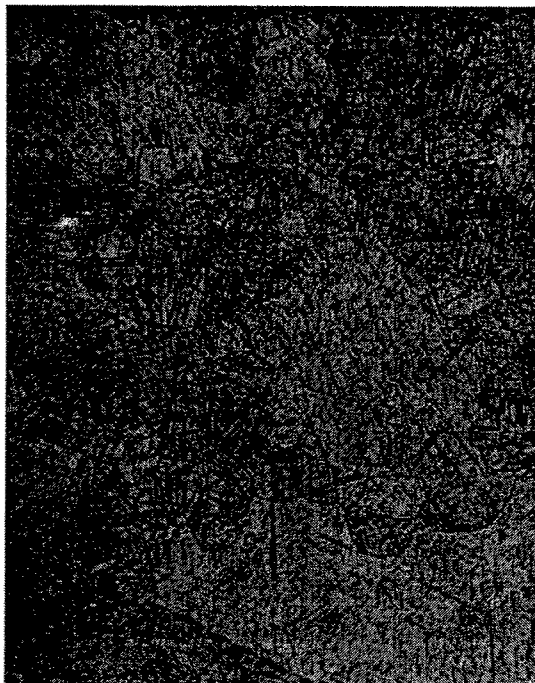
Form – Specimen Number	ASTM Grain Size	20 Delta K	30 Delta K
PWA 1469 Base – 44615	>00	1.8×10^{-6}	1.4×10^{-5}
PWA 1469 Base – 44616	>00	2.0×10^{-6}	1.4×10^{-5}
PWA 1469 Exposed – 46231	>00	4.0×10^{-6}	1.5×10^{-5}
AMS 5663 Coarse-Grain Base – 39809	5	1.5×10^{-5}	6.7×10^{-5}
HIP Weld Exposed – 46118	4(2)	2.0×10^{-5}	-
HIP Weld – 46037	6	2.0×10^{-5}	1.0×10^{-4}
HIP Weld Exposed – 46119	5	3.9×10^{-5}	1.2×10^{-4}
HIP Weld – 46036	7	1.6×10^{-4}	5.2×10^{-4}
AMS 5663 Fine-Grain Base – 40372	9-10	2.5×10^{-4}	5.5×10^{-4}



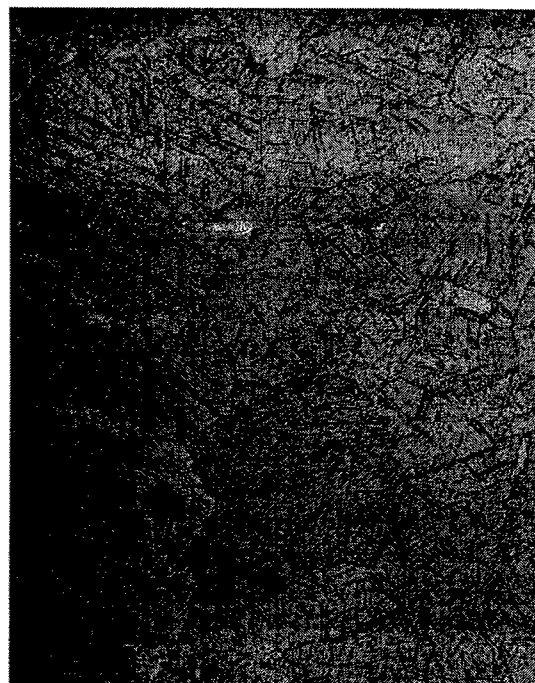
HIP Weld Spec. 46036 100X



HIP Weld Spec. 46037 100X



Exposed HIP Weld Spec. 46118 100X



Exposed HIP Weld Spec. 46119 100X

FIGURE 37. TYPICAL MICROSTRUCTURES OF HIP WELDS IN THE FULLY HEAT TREATED (UPPER) AND HEAT TREATED-PLUS-EXPOSED TO 40 HOURS AT 1750°F (LOWER)

Note appearance of microstructure to coarse grain wrought (AMS 5663) material (figures 20 and 22).

2.1.4 Metallurgical Evaluation of Long-Time Service Cases.

2.1.4.1 JT8D Combustor Cases (AMS 5613).

Numerous JT8D outer combustor cases have been examined over the past few years to evaluate field issues and monitor changes with long-time service. No additional cases were procured, sectioned, or evaluated for this contract because it was felt that documentation of metallurgical and physical changes with the alloy was already sufficient. Some scanning electron microscope (SEM) work was completed in this section of the contract to support the crack growth prediction work that had been conducted in task 2.

2.1.4.2 JT9D TEC (Turbine Exhaust Cases) (AMS 5616).

Two long-time service TEC components were retrieved from the scrap inventory. Both cases were retired due to the extent of cracking that was deemed not economical to repair. The long service life of both cases was a major factor in determining not to repair the two cases. Both were retrieved from Japan Airlines (JAL) with extensive service time, both in cycles and hours as shown below.

LONG SERVICE TIME JT9D TURBINE EXHAUST CASES

Case S/N	Engine	Operator	Service Hours	Service Cycles
CD8893	JT9D-7	JAL	63,887	12,934
BG7045	JT9D-7	JAL	71,102	14,800

2.1.4.3 JT9D TEC Metallographic Examination.

Case S/N CD8893 was selected for cutup analysis. The sectioning plan and photographs that documents the case's typical microstructure are presented in appendix C. No mechanical properties testing was conducted on material from the case, but hardness measurements were made at various locations. A summary of the metallographic investigation is presented in section 2.1.4.4.

2.1.4.4 JT9D TEC Metallurgical Evaluation Results.

All major case details and critical areas were examined. These are listed along with corresponding hardness values in table 18. All samples were mounted in bakelite mounts, polished, and etched with Villella's Etch. Samples were examined for general microstructure and hardness.

Little difference was observed among the various areas examined, save for grain size. Not unexpectedly, the sheet metal struts were finer grained than either the outer- or inner-ring forgings. The outer ring displayed the coarsest grain size and also a more sensitized microstructure relative to the inner ring and struts. The outer ring's level of grain boundary carbide precipitation was greater than what was typically observed when working with smaller forgings or what was considered typical in specification microstructure control

photomicrographs used for stainless and martensitic steels. The case typical structure was consistent with control photomicrographs that call for a metallurgical review, i.e., the structure would neither be rejected nor accepted. On review it would be accepted, providing that the hardness requirements had been met. It would be erroneous to assume the microstructure was the result of engine operation. Another cause, the more probable one, is that the case receives a controlled cooling rate in lieu of being "quenched" from the austenizing temperature. AMS 5616 forgings are typically liquid quenched to minimize intergranular carbide precipitation, and the resultant microstructure is illustrated in the control specifications.

TABLE 18. JT9D TEC S/N CD8893 METALLOGRAPHIC ANALYSIS AREAS

Case Detail	Location	Average Hardness (Rc)	Value of Examination
Outer Ring	Forward Flange	35.5	Critical attachment flange
	Forward Wall	33.8	Hottest operating location
	Engine Mount	33.1	Highest stressed area
	Center Wall	33.3	Typical large ring forging
	Rearward Wall	35.3	Cooler operating wall
	Flange	35.5	Cooler operating flange
Strut	Side Walls and Leading Edge	32.9	Hot-operating sheet metal
Inner Ring	Wall	31.5	Smaller ring forging
Inner Ring	Rear Flange	32.6	Cool-operating flange

The JT9D case is assembled with annealed details and then the entire case assembly is hardened and tempered as a unit. It would be impossible to reach the cooling rates achieved with a true quench, without creating serious distortion of the case. Forced gas cooling is used, representing a slower cooling medium. Thus, some grain boundary carbide precipitation is inevitable during the original case assembly process. Again, hardness measurements are used to determine that the cooling rate was fast enough for the material to meet mechanical properties requirements.

This said, the forward outer ring wall, just behind the forward outer flange, did appear to have more grain boundary carbides than other case areas. This may reflect that this area operates at hotter temperatures. For short periods, the area may experience temperatures as high as 1100°F. Extended exposure at this high-tempering temperature can create the same metallurgical structure. Segregation and carbide stringers were observed, but not more than typically observed in AMS 5616 forged rings. One interesting and disconcerting feature discovered was that large notches were adjacent to the attachment weld between the case and the strut. More information is needed to determine that these are not due to handling of the case after it was retired from service. Several of the notches were inside the hollow of the struts, which precluded their inspection at completion of the welding process. It is important that the notch effect be taken into account in the design.

2.1.4.5 JT9D D/C (Diffuser Case) (AMS 5663).

Seven JT9D Model 7 and 7A diffuser cases were retrieved from the scrap inventory. Japan Airlines operated five of them and British World Airlines (BA) operated the other two. All had been retired due to extended weld repair in critical locations and were considered no longer worthy for further repair or engine operation. Three of the cases were selected for sectioning and analysis. The three cases represent a range of service times, service cycles, and operators. The seven cases are shown in table 19.

TABLE 19. JT9D DIFFUSER CASES RETIRED FROM SERVICE

Case S/N	P/N	Operator	Service Time	Service Cycles
BW1040	784299	JAL	52,542	26,618
AG9961*	781487	JAL	53,487	23,869
CJ3211	784297	JAL	54,539	21,023
AG9947	784299	JAL	55,028	20,281
AH0086	803624	BA	55,622	11,185
CJ3225*	803625	JAL	60,307	19,260
BW0976*	749645	BA	63,092	13,696

* Selected for microstructural and mechanical property evaluation.

2.1.4.6 JT9D Diffuser Metallographic Analysis—Plan.

The JT9D diffuser case is a weld assembly of five subassemblies and 18 details. In total, the welded assembly serves as the casing for both the engine's diffuser and combustion chamber. The most critical and heavily loaded section is the outer-pressure wall, which consists of three AMS 5663 forged rings. Front and back skirt forgings are relatively thin ($<0.100''$ walls) and are welded to the outer center ring forging, which is comprised of a heavily milled detail fabricated from a thick ($>0.250''$) ring. Integral with the final machined center-body ring are a bulk of the service bosses, several inspection port bosses, and all fuel injection nozzle mounting pads. Also, there are numerous external pads that attach a wide variety of tubes and support brackets. The goal of the sectioning plan and metallographic examination was to examine representative samples from each major detail from the inner and outer areas of all three cases. Analysis would include metallographic samples of forged base material, assembly welds, and repair welds. Thus, a more involved cutup analysis was made of the long-time service diffuser cases than was performed on the turbine exhaust cases. To simplify organization of this report, the sectioning plan, illustrations of the case areas, and photomicrographs taken of the samples are presented in appendix D. The following text presents a summary of major findings from the investigation.

Repair options allow for local repair of cracks or other defects and the replacement of whole details. The outer mid-section ring (see appendix D) cannot be replaced, but it can be repaired. Thus, it is the one case detail that can be assured experienced the full life of the case, including all repair heat treatments. All other details may have been replaced at some point in the case's service life so their total service experience is not known.

2.1.4.7 JT9D Diffuser Case Analysis—Results.

This section summarizes metallographic features uncovered during investigation of the three long-time service, JT9D diffuser cases. Please refer to table 19 for data relative to each case's length of service and appendix D for more detail on examined case sections and representative photomicrographs.

Most case areas contained needle-shaped delta phase to a level in excess of microstructural standards for new components. It is assumed that the precipitation of extra delta occurred during solution heat treat cycles associated with field repair processing. The amount of delta suggests the three cases experienced multiple repair cycles. The outer forward skirt of case BW0976 displayed less delta than the other design details of the same case. This suggests that the outer forward skirt may be a replacement detail and was exposed to fewer repair cycles than the rest of the case details. JAL-operated cases (AG9961 and CL3225) displayed slightly less needle delta but more of a delta phase-banded structure. It was also noted that details with a finer-grain structure tended to have less needle delta phase. Necklace structured material (coarse grains surrounded by fine grains) was observed in some rings with most of the delta precipitate in the fine-grained regions. There were areas of especially dense concentrations of delta needles. Delta needles were found at weld HAZ, machined threads, and below the surface in many areas. The presence of residual strains, due to welding and machining, are the probable cause for the extra heavy delta precipitation at the first two locations. However, it is not clear why near surface layers of extreme delta phase concentration occurred. At places, the layer was 0.006" thick.

Heavy oxide scale was not detected, but a surface reaction was observed in several locations on each of the cases. Areas effected by this surface reaction were denuded of secondary phases except for carbides. The reaction layer, varied in depth from 0.0004" to 0.0010". Both original assembly and repair welds had microstructures similar to new welds with perhaps slightly more small delta needles in the interdendritic areas. Weld soundness varied from the presence of no microstructural defects to isolated gas pores to cracks up to 0.030" in length.

Thirty-three weld sections were examined and were comprised of 22 assembly and 11 repair welds. Weld microstructures were very similar to new welds with perhaps slightly more delta needle phase being concentrated in the interdendritic region of the weld metal. Only seven welds, all case assembly type, were free of any defects. Fourteen sections appeared to be of a single weld, although more than one pass was present within the weld; 11 of these were case assembly welds. Gas pores with an average diameter of 0.6 mils were found in seven of the welds. The largest was 1.2 mils. Lack of fusion (LOF) was also observed in six of the welds. Average length of the LOFs was 7.0 mils, but one was 21.0 mils. Only one of the 14 sections contained a crack. However, this was 150 mils long, which was more than twice as large as the next largest defect found during this investigation. Two welds appeared to be made of two adjacent or overlapping weld nuggets, suggesting one weld was a repair of the other weld. Both had gas pores of less than a 1.0 mil diameter but one had dirt or oxide inclusions up to 1.5 mils in length and one had LOF of 15.0 mil in length. Neither had any cracks.

The remaining six welds appeared to be built-up from more than two welds. This suggests that a number of repairs were made on previous welds or adjacent to previous welds. Because of this, it is not easy to distinguish the number of separate welds from multiple passes of the same weld. All six had gas pores (15 total). While the pores were typically approximately 1.0 mil in diameter, there was one pore cluster that measured 60.0 mils in diameter. There were 33 examples of LOF among three of the welds. While the average length of the LOFs was 2.4 mils, one LOF was 39.0 mils in length. The other three welds displayed five cracks—the largest was 45.0 mils in length. Almost all the defects were within fused metal or weld nugget material. IN 718 typically displays HAZ cracks rather than weld nugget defects. However, with multipass welds and rewelds of previous welds, the previous weld or pass becomes the HAZ to the subsequent weld. Table 20 illustrates the trend with more and bigger defects related to multiple-weld cycles.

TABLE 20. SUMMARY: WELD ANALYSIS LONG-TIME SERVICE JT9D DIFFUSER CASES

Defect Size (mil)	Defect Type*	Weld Type - Number of Nuggets
10.0	LOF	Repair - Multiple (>2)
11.0	LOF	Assembly - Single
12.5	LOF	Repair - Multiple (>2)
15.0	LOF	Repair - Double
20.0	Pore	Repair - Multiple (>2)
21.0	LOF	Assembly - Single
30.0	Crack	Repair - Multiple (>2)
30.0	Crack	Repair - Multiple (>2)
39.0	LOF	Repair - Multiple (>2)
45.0	Crack	Repair - Multiple (>2)
60.0	Pore Cluster	Repair - Multiple (>2)
150.0	Crack	Repair - Single

Note: * LOF = lack of fusion; Pore = spherical void, typically a gas pore

Eight of the twelve defects of 10 mils or larger dimension were in multiple nugget repair welds and half of the twelve defects were LOF. However, sizes at and above 30 mils, half the defects were cracks. Multiple nugget repairs remained the primary location for larger defects (five of six). It is generally accepted that 32 mils sets the lower limit for reliable x-ray detection. Four of the defects exceeded this in size, but the inspection history and disposition of the long-time cases was not available, so it is not known if those defects were detected. The number of LOF defects is a concern. LOF defects represent a failure to achieve proper fusion across an interface of the weld being deposited and the solid substrate. This is generally related to poor weld technique or the presence of dirt or contamination that interferes with the bonding action. These results emphasize the need for review of repair shop practices.

2.1.4.8 JT9D Diffuser Case Properties Evaluation.

Evaluations of the two sectioned JT9D diffuser cases were extended to include mechanical properties testing, including tensile tests, smooth and notch fatigue tests, and crack growth rate tests. This was to complement the existing data baseline and simulated repair heat treat tests with data off material that was actually exposed to service operation. The two long-time service cases displayed a variety of microstructures as described above. Testing was conducted on specimens that were excised from all three of the sectioned diffuser cases. Tensile and LCF specimens were excised from the outer pressure wall front and rear skirt details, providing a variety of microstructures. Crack growth rate test specimens were all excised from the outer pressure wall center ring. Specimens excised from scrap HPT cases were used to provide the program with typical coarse grain AMS 5663 material. Table 21 presents the mechanical properties test plan.

TABLE 21. MECHANICAL PROPERTIES TEST PLAN LONG-TIME SERVICE
JT9D DIFFUSER CASES

Mechanical Property	HPT Case	JT9D Case AG 9961	JT9D Case CJ3225	JT9D Case BW0976
Tensile				
Room temperature	2	2	2	1
1200°F	2	2	2	2
Stress rupture				
1200°F/100 ksi	2	2	2	2
Low-cycle fatigue				
1100°F/130 ksi, $k_t=1$	6	6	4	8
1100°F/170 ksi, $k_t=2$	4	6	6	8
Da/dN				
800°F/10 cpm	*	1	1	2
1000°F/2 mdw	*		1	1
1100°F/2 mdw	*	1	1	2

Note: * Baseline testing provided earlier in report.

Tensile, stress rupture, and smooth LCF specimens were standard 0.100" thick smooth-tapered gage specimens with pin-loaded grips and 0.250" wide gages. Notch LCF specimens were 0.100" thick straight gage specimens with pin-loaded grips and edge notches creating a 0.250" wide gage between the notch tips and a k_t equal to a factor of 2. All tensile, stress rupture, and LCF specimens were machined from either the forward or rearward skirt of the three respective cases. Thus, variation in grain size and delta phase concentration was great, as illustrated in appendix D. Tensile and LCF tests were conducted in electrohydraulic driven test rigs with the fatigue specimens run at 30 cpm and at an R ratio of 0.1.

Tensile and stress rupture results are presented in table 22. Test results on specimens excised from the three long-time service cases are consistent with P&W studies that investigated simulated multiple-repair heat treat cycles on the properties of AMS 5663. Tensile yield strengths were lower than typical for AMS 5663 with three of the five room-temperature

specimens. Two of the six 1200°F test results were lower than specification requirements. Ultimate strengths appeared to be less affected, but the British Air case specimens met specification limits by only 5 to 9 ksi. The two Japan Airlines cases with 53,487 and 60,307 hours of service life displayed slightly better strengths. Among specimens from the same case, microstructures that were within current standards of acceptable amounts of delta phase generally had better strength values. However, when comparing results among specimens from all three cases, the relationship to the delta control standard was not always clear.

TABLE 22. MONOTONIC MECHANICAL PROPERTIES OF LONG-TIME SERVICE JT9D DIFFUSER CASES

Room Temperature Tensile Properties					
Specimen Source	Case Location	Delta Structure	0.2% Y.S (ksi)	U.T.S. (ksi)	Elong. (%)
HPT Case	Center Wall	Acceptable	163.4	195.4	19.6
	Center wall	Acceptable	161.2	195.6	20.4
Diffuser AG9961	OPW-Front Skirt	Rejectable	142.0	189.0	21.7
	OPW-Rear Skirt	Acceptable	164.5	193.5	19.3
Diffuser CJ3225	OPW-Front Skirt	Rejectable	148.9	190.4	19.1
	OPW-Rear Skirt	Marginal	151.9	187.7	13.9
Diffuser BW0976	OPW Front Skirt	Marginal	138.8	184.8	16.3
1200°F Tensile Properties					
Specimen Source	Case Location	Delta Structure	0.2% Y.S (ksi)	U.T.S. (ksi)	Elong. (%)
HPT Case	Center Wall	Acceptable	138.8	156.2	21.1
	Center wall	Acceptable	136.9	156.3	20.8
Diffuser AG9961	OPW-Front Skirt	Rejectable	127.3	161.6	22.2
	OPW-Rear Skirt	Acceptable	137.5	158.8	17.9
Diffuser CJ3225	OPW-Front Skirt	Rejectable	130.4	157.9	18.9
	OPW-Rear Skirt	Marginal	131.5	152.4	14.4
Diffuser BW0976	OPW Front Skirt	Marginal	121.2	147.9	20.7
	OPW Front Skirt	Marginal	119.9	148.4	18.7
1200°F/100 ksi Stress Rupture Properties					
Specimen Source	Case Location	Delta Structure	Rupture Life (hrs)	Rupture Location	Elong. (%)
HPT Case	Center Wall	Acceptable	148.3	Outer Q	16.0
	Center wall	Acceptable	193.8	Outer Q	36.0
Diffuser AG9961	OPW-Front Skirt	Rejectable	40.5	Outer Q	5.0
	OPW-Rear Skirt	Acceptable	164.2	Outer Q	19.0
Diffuser CJ3225	OPW-Front Skirt	Rejectable	40.1	Gage	5.0
	OPW-Rear Skirt	Marginal	66.7	Outer Q	5.0
Diffuser BW0976	OPW Rear Skirt	Marginal	45.7	Gage	10.0
	OPW Rear Skirt	Marginal	40.8	Gage	8.0

All the specimens from the three cases met minimum requirements for stress rupture life when tested at 1200°F and 100 ksi. However, the achieved rupture lives for five of the specimens (40.8 to 66.7 hours) were substantially lower than the typical rupture life. The only specimen

that reached a typical rupture life (164.2 hours) was the only one that had a delta phase volume totally within the acceptable range of the current quality standard.

Results of the fatigue testing are presented in tables 23 (smooth) and 24 (notch), while analysis of the data is presented in table 25. Due to a high incidence of grip failures, a smooth LCF baseline was not achieved for this program. However, cyclic lives of specimens excised from the three long-time service cases were approximately half that represented by the existing data. This was true for average and on a minimum (Weibull Probability of Failure of 0.01%) basis. These results are consistent with those of previous in-house studies. However, grouping the results to establish Delta Content Quality control acceptance and rejection standards resulted in no significant differences in average or minimum cyclic lives. It was expected that the higher volume content material would have even lower lives. Most of the specimens whose lives were included in the acceptable category had marginally acceptable microstructures. This means that the amount of needle delta was greater than typical but within quality standards acceptance levels. These results suggest that the influence of excess delta phase may be stronger in debiting smooth LCF resistance than previously believed. The existing data is based essentially on low-delta volume material. This may have to be reviewed for future reference.

TABLE 23. SMOOTH ($k_t=1$) LOW-CYCLE FATIGUE PROPERTIES LONG-TIME SERVICE JT9D DIFFUSER CASES (1100°F/130 ksi)

Specimen Source	Case Location	Delta Structure	Rupture Life (hrs)	Comments
HPT Case	Center Wall	Acceptable	8,700+	Grip Failure
	Center Wall	Acceptable	23,800+	Grip Failure
	Center Wall	Acceptable	24,900+	Grip Failure
	Center Wall	Acceptable	31,100+	Grip Failure
	Center Wall	Acceptable	63,000	
	Center Wall	Acceptable	100,000+	No Failure; Run Out
Diffuser AG9961	Front Skirt	Rejectable	28,400	
	Front Skirt	Rejectable	32,700	
	Rear Skirt	Acceptable	43,200	
	Front Skirt	Rejectable	47,000	
	Front Skirt	Rejectable	53,700	
	Rear Skirt	Acceptable	85,000	
Diffuser CJ3225	Rear Skirt	Marginal	36,300	
	Rear Skirt	Marginal	37,000	
	Front Skirt	Rejectable	50,900	
	Front Skirt	Rejectable	53,200+	Grip Failure
Diffuser BW0976	Front Skirt	Marginal	14,500	Invalid; Rig overload
	Rear Skirt	Rejectable	27,800+	Grip Failure
	Front Skirt	Marginal	36,100	
	Front Skirt	Marginal	36,700	
	Front Skirt	Marginal	38,900	
	Rear Skirt	Rejectable	42,100	
	Front Skirt	Marginal	42,600	
	Rear Skirt	Rejectable	50,200	

TABLE 24. NOTCH ($k_t=2$) LOW-CYCLE FATIGUE PROPERTIES LONG-TIME SERVICE JT9D DIFFUSER CASES (1100°F/170 ksi)

Specimen Source	Case Location	Delta Structure	Rupture Life (hrs)	Comments
HPT Case	Center Wall	Acceptable	41,200	
	Center Wall	Acceptable	46,200	
	Center Wall	Acceptable	56,200	
	Center Wall	Acceptable	100,000+	No Failure; Run Out
Diffuser AG9961	Front Skirt	Acceptable	24,800	
	Front Skirt	Rejectable	37,800+	Grip Failure
	Rear Skirt	Rejectable	40,800	
	Front Skirt	Acceptable	45,100	
	Front Skirt	Rejectable	48,300	
	Rear Skirt	Rejectable	66,900	
Diffuser CJ3225	Front Skirt	Rejectable	19,500	
	Front Skirt	Rejectable	34,600	
	Front Skirt	Rejectable	40,000	
	Front Skirt	Rejectable	43,100	
	Front Skirt	Rejectable	48,900	
	Front Skirt	Rejectable	68,500	
Diffuser BW0976	Front Skirt	Marginal	43,600	
	Front Skirt	Marginal	46,700	
	Front Skirt	Marginal	48,000	
	Front Skirt	Marginal	61,000	
	Front Skirt	Marginal	83,400	
	Front Skirt	Marginal	99,400	
	Front Skirt	Marginal	100,000+	No Failure; Run Out
	Front Skirt	Marginal	100,000+	No Failure; Run Out

TABLE 25. ANALYSIS OF LOW-CYCLE FATIGUE PROPERTIES OF LONG-TIME SERVICE JT9D DIFFUSER CASES

1100F/130 ksi S-LCF	Base	BW0976	AG9961	CJ3225	Acceptable	Rejectable
Average	n.a.	39,114	48,333	44,350	44,412	44,650
W_{CL}	n.a.	42,500	53,000	48,000	47,500	50,000
W_{50}	n.a.	41,000	48,000	45,000	43,000	45,500
$W_{0.1}$	n.a.	29,000	20,000	25,000	35,000	23,000
1100F/170 ksi N-LCF	Base	BW0976	AG9961	CJ3225	Acceptable	Rejectable
Average	60,900+	72,762+	43,950+	42,433	65,200+	43,192
W_{CL}	55,000	81,000	51,000	49,000	73,000	51,000
W_{50}	51,500	71,000	45,000	42,000	63,000	44,000
$W_{0.1}$	30,000	25,000	16,000	12,000	15,000	15,000

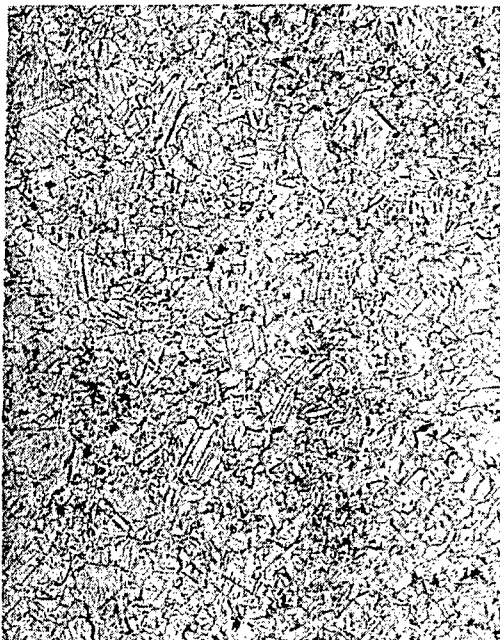
Results of the notch LCF testing present a more significant result. Two of the three cases demonstrated average cyclic lives that were less than the baseline. The baseline was consistent with the established database. When the data is grouped by acceptable or rejectable microstructure relative to delta phase content, both groups displayed average and characteristic lives that were similar to the base specimens. However, on a minimum basis, both groups displayed approximately half the life (15,000 cycles versus 30,000 cycles) of the base specimens. Interestingly, both groups of results contained one unusually low life specimen. Deleting these two points from the data would produce minimum lives that bracket that of the base, 35,000 cycles for acceptable microstructure and 25,000 cycles for rejectable microstructure. Posttest analysis of the specimens and test rigs found no reason to discard those two points. They are merely highlighted to illustrate how close the notch fatigue results achieved with aged case material approached that of the base lives. Previous studies suggested that excess delta was not deleterious to the alloy's notch LCF properties. Results of the notch fatigue testing performed with the aged case material support a review of the previously held position with an expanded program that would take into account the possible interacting influence of grain size and morphology.

It should be noted that while the low-cycle fatigue results were unexpected, they probably do not influence the JT9D case. Studies with excessively high delta phase have shown that the debiting effect on strength and fatigue, until this work was believed to only affect smooth LCF, decreases with decreasing temperature. Generally it is assumed that the effect is negligible at temperatures below 1000°F, which is the temperature regime in which the JT9D diffuser/combustor case typically operates. The results point out that the position regarding excess delta and its affect on Inconel 718 must be carefully scrutinized for higher temperature applications.

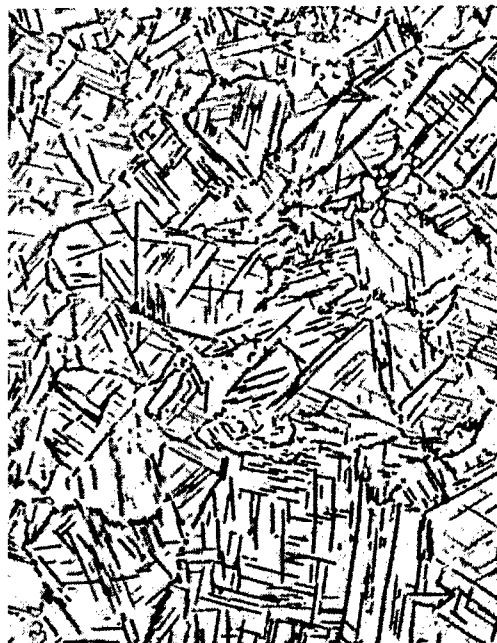
Crack growth rate specimens were excised from the outer center-body forging of the three cases. Thus, it can be assured that the material experienced the total time and cycles listed for each case and was exposed to all the repair associated heat treatments. Typical microstructures for the fracture mechanics test material are presented in figures 38 through 40.

Specimens excised from the BA- and JAL-operated cases exhibited crack growth rates at 800°F/10-cpm conditions that were similar to that displayed by the coarse-grain AMS 5663 baseline material (figure 41). This was so despite the fact that material from the BA-operated case (BW0976) was substantially finer (figure 38) than the baseline material (figure 20).

Crack growth rates of the aged case specimens were substantially faster than the coarse-grain baseline when tested under dwell-load conditions at 1000° and 1100°F (figures 42 and 43). The rates matched or surpassed those demonstrated by the material with six simulated short-age, postweld heat treat repairs and 1000 hours of exposure at 1100°F. Delta concentration within the BA case specimen was significantly greater than the baseline and simulated repair exposure specimens while the delta structure between the two JAL case specimens was more typical. However, one of the JAL cases (AG9961) had mixed grain sizes. Bands of coarse grains led to slower rates at 1100°F/2 mdw (figure 42).



FM Spec. 41160 ~100X

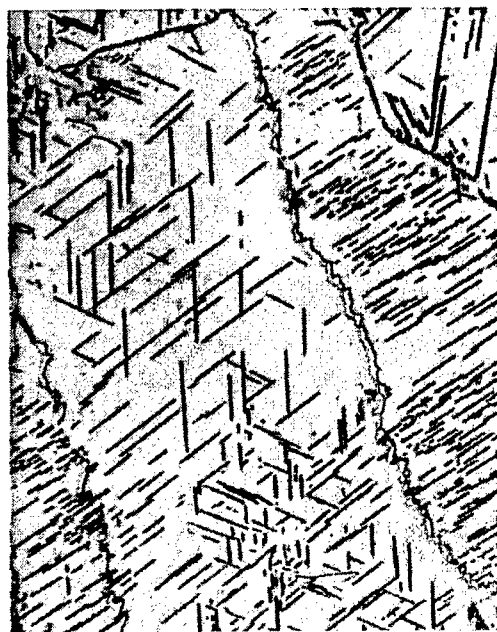


FM Spec. 41160 ~500X

FIGURE 38. TYPICAL MICROSTRUCTURE OF CRACK GROWTH RATE TEST SPECIMENS EXCISED FROM THE OUTER PRESSURE WALL OF JT9D DIFFUSER CASE BW0976 (BA, 63,096 hours and 13,696 cycles)



FM Spec. 41826 ~100X



FM Spec. 41826 ~500X

FIGURE 39. TYPICAL MICROSTRUCTURE OF CRACK GROWTH RATE TEST SPECIMENS EXCISED FROM THE OUTER PRESSURE WALL OF JT9D DIFFUSER CASE CJ3225 (JAL, 60,307 hours and 19,260 cycles)



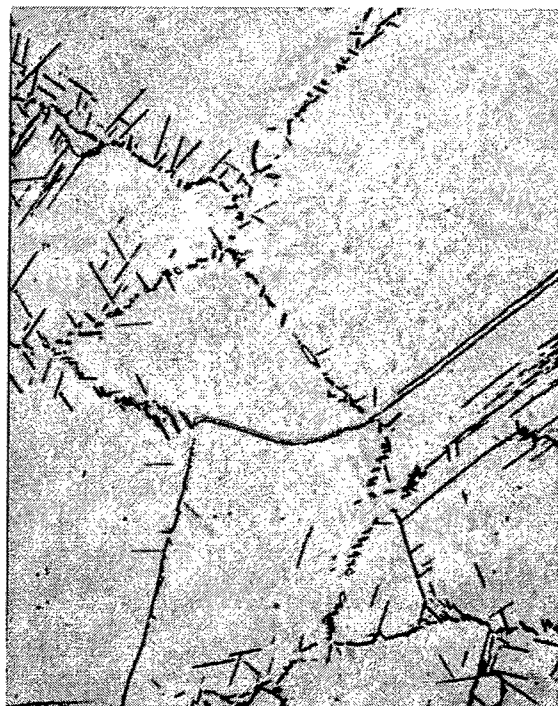
FM Spec. 41824

100X



FM Spec.41824

500X



FM Spec. 41824

~500X

FIGURE 40. TYPICAL MICROSTRUCTURE OF CRACK GROWTH RATE TEST SPECIMENS EXCISED FROM THE OUTER PRESSURE WALL OF JT9D DIFFUSER CASE S/N AG9961 (JAL, 53,487 hours and 23,869 cycles)

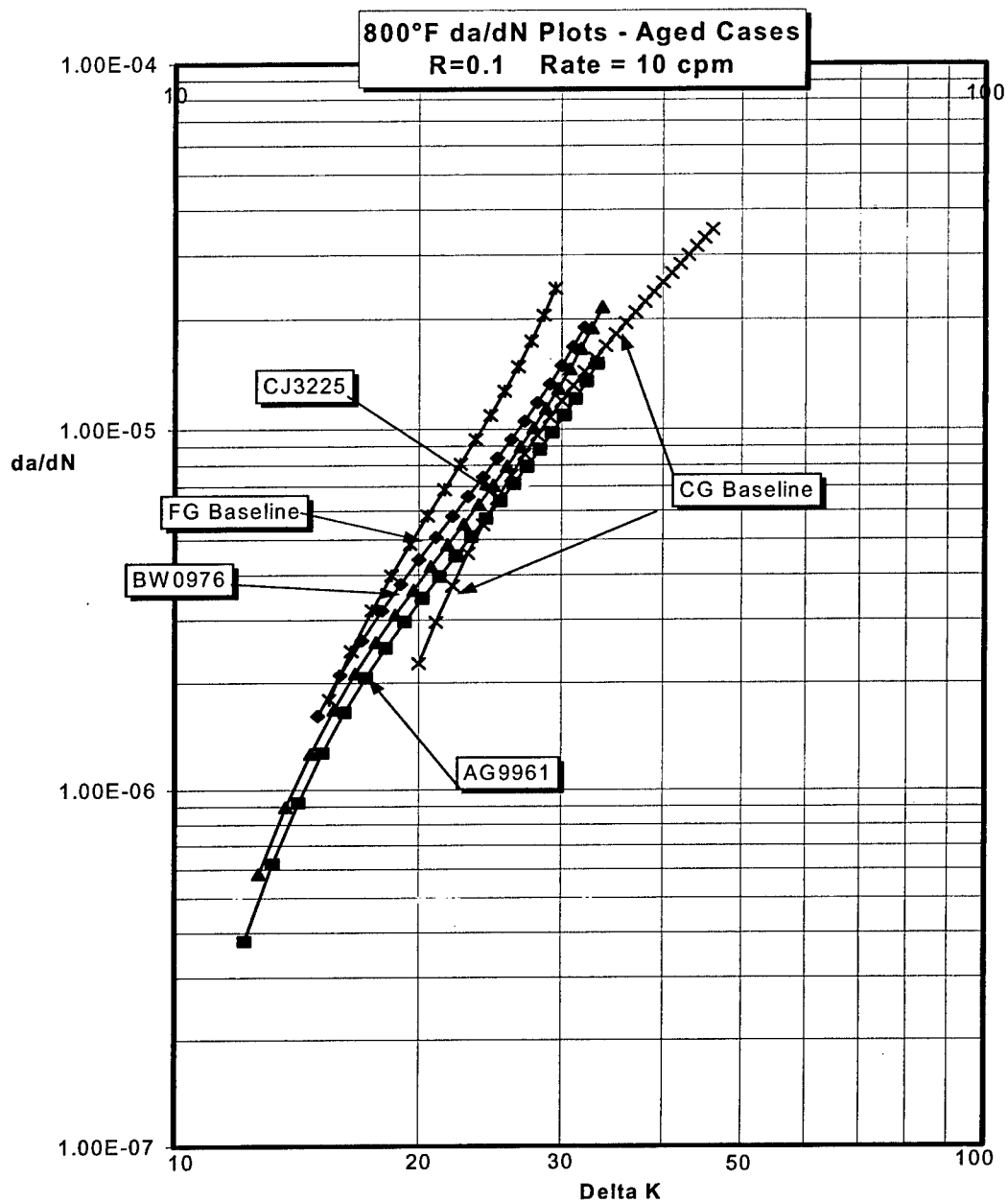


FIGURE 41. CRACK GROWTH RATE (da/dN) PLOTS OF SPECIMENS EXCISED FROM LONG-TIME SERVICE CASES BW096, AG9961, AND CJ3225 TESTED AT 800°F, R = 0.1 AND 10 cpm (Note that all plots fall between the coarse and fine grain AMS5663 baseline plots.)

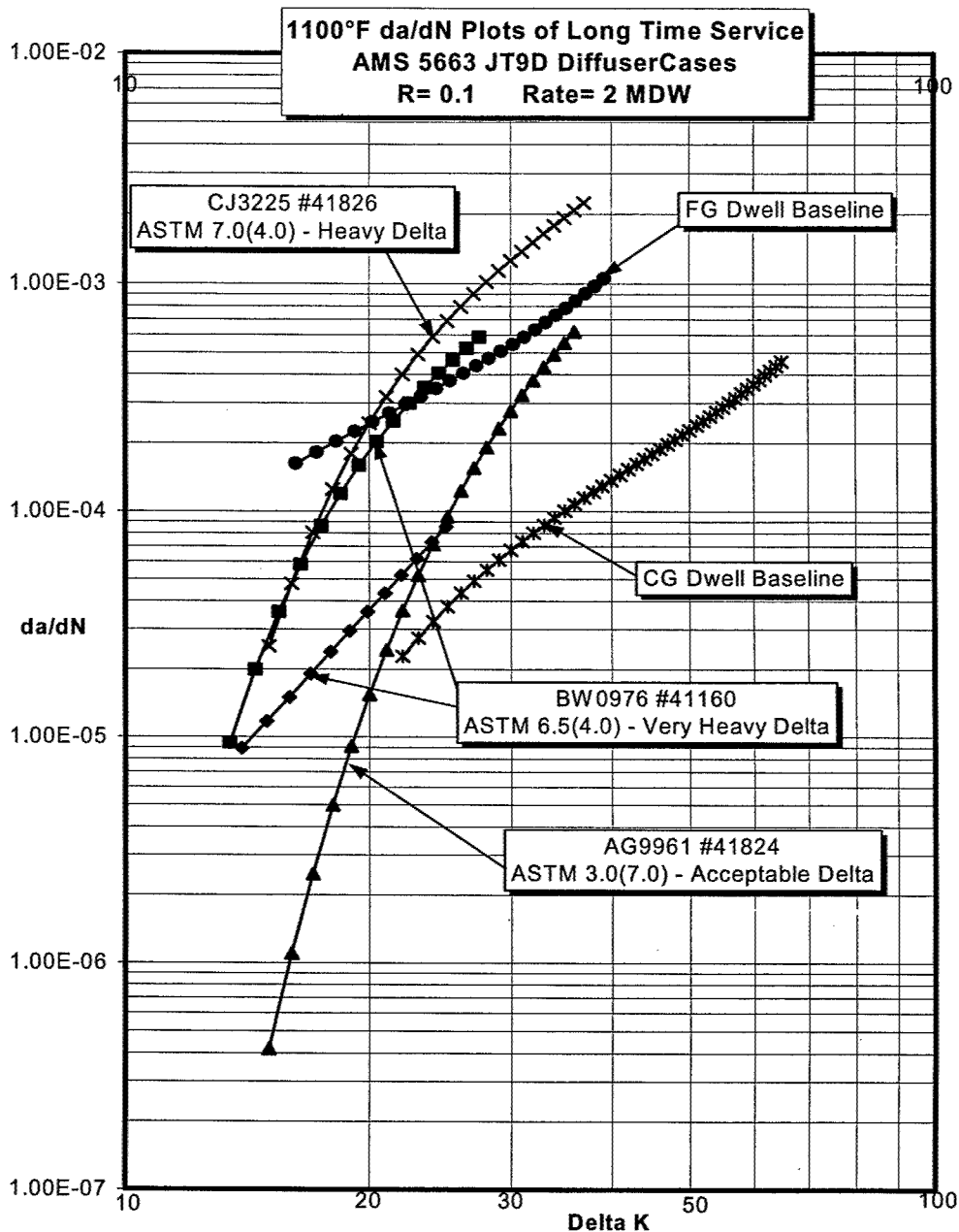


FIGURE 42. CRACK GROWTH RATE (da/dN) PLOTS OF SPECIMENS EXCISED FROM LONG-TIME SERVICE CASES BW096, AG9961, AND CJ3225 TESTED AT 1100°F, $R = 0.1$ AND 2-MINUTE DWELL AT MAXIMUM STRESS (Note that all plots have a steeper slope than both the coarse and fine grain AMS5663 baseline plots. Also, that the faster rates of the case specimens appear more related to grain size than delta content.)

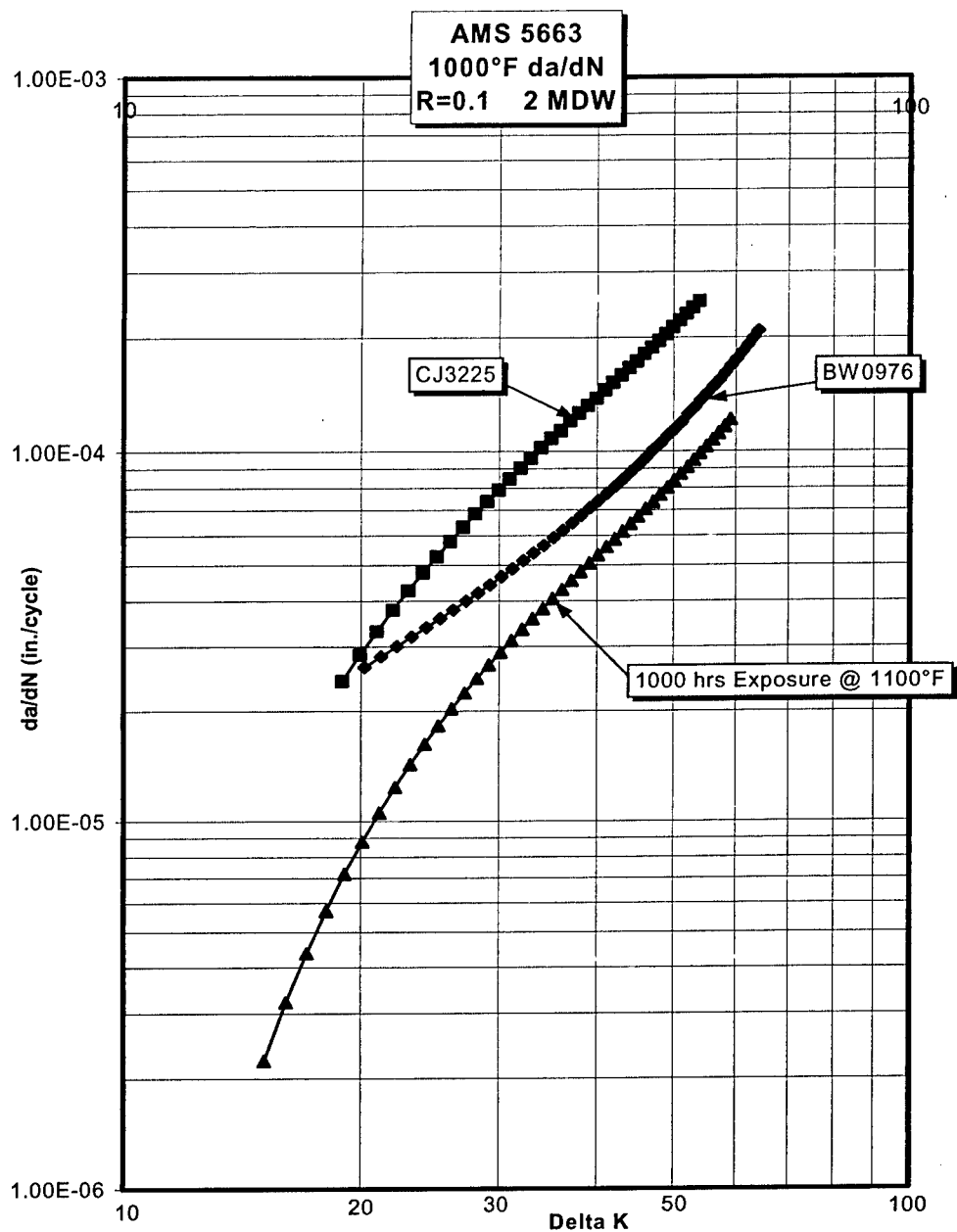


FIGURE 43. CRACK GROWTH RATE (da/dN) PLOTS OF SPECIMENS EXCISED FROM LONG-TIME SERVICE CASES BW096 AND CJ3225 AND COARSE-GRAIN AMS 5663 WITH A 1,000-HOUR EXPOSURE AT 1100°F (All tests were at 1000°F, $R = 0.1$ and 2-minute dwell at maximum stress.)

2.1.4.9 JT9D Diffuser Analysis—Discussion.

Investigation of the microstructures and properties of the three JT9D that experienced extended service generated results that both consisted and conflicted with previous notions. Microstructurally, it was not surprising that several case details had high amounts of needle delta phase since numerous solution heat treatments will produce this. The fact that individual details can be replaced in whole, helps explain variations in delta concentration among different details. However, what was unexpected were the high concentrations of needle delta phase around threads and at local surface spots. Such localized delta concentration could be explained by the presence of local high stresses. The source of the high stresses remains unknown, at least for the surface spots. Results of the tensile testing were consistent with previous studies, but the LCF results require additional analysis. Previous studies had shown that high delta concentrations lowered smooth LCF but did not affect notch LCF. The results of the study in this program suggest that those conclusions may have to be altered. There is insufficient data to conclude this, but the results of this study support further investigation. This should include an evaluation at temperatures between 800° and 1000°F and the effect of microstructure differences (i.e., fine vs coarse grain and equiax vs banded structure).

Further analysis of the crack growth characteristics is also needed. Understanding the variations in rates was made more difficult by the banded structure. It needs to be established at what point the crack growth progresses through coarse- or fine-grain material and through the delta lean or heavy areas.

2.1.5 Cast Nickel Case Rig Test Evaluation.

Introduced in 1980, PWA 1469, a cast+HIP Inconel 718, was the material of choice for the diffuser cases in P&W's four newer commercial engines, the PW2037, V2500, PW4060, and PW4168. Although these cases have a sum total of millions of service hours, some of the individual cases have been in service for tens of thousands of hours. Yet, no retired cases were available for destructive analysis at the start of this contract.

Subtask 6 was to conduct and evaluate the results of a hot-pressure rig test of a full size, commercial engine diffuser case. The rig to be used was designed and constructed specifically to test PWA 1469 diffuser cases, which are really one-piece combination diffuser/combustor cases. Prior to this contract, P&W had subjected cases representing all current (V2500, PW2000, and PW4000) high-bypass commercial gas turbine engines to the rig test. Thus, a solid base of data existed to compare results against. Two types of tests are conducted, one where the test case has no pre-existing cracks and one where small slots are electrodischarge machined (EDM) into the case at strategic and highly loaded areas. The former test was used to validate the PWA 1469 fatigue initiation system and case design, while the later was used to validate the alloy's crack growth rate system. Both these systems are based upon specimen testing where the number of grains across the specimen gage is few and to that extent may exaggerate the effect of any one grain.

The PWA 1469 case in this program would be unique because it would be exposed to multiple-solution heat treatments that would total 40 hours at a 1750°F solution temperature. Thus, the

rig case would complement the specimen testing and help address the problem of determining the effect multiple repair heat treatments have on the crack growth characteristics of PWA 1469.

2.1.5.1 Test Case.

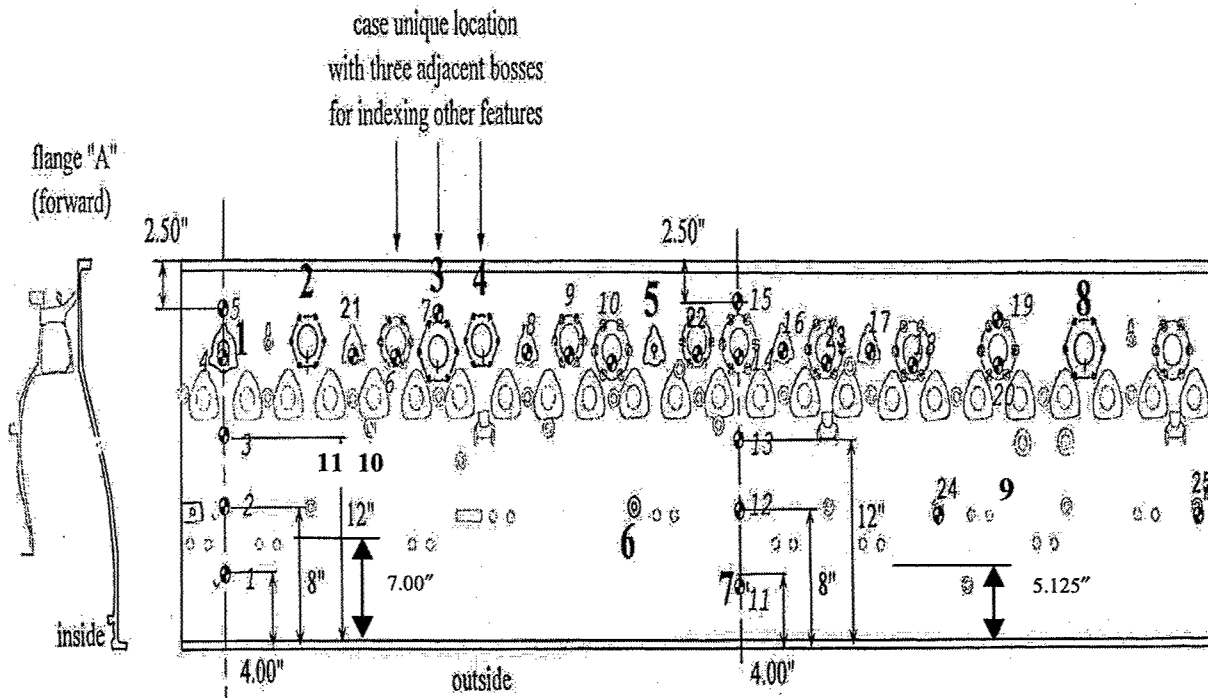
For purposes of this program, a PW4168 case was borrowed from the completed P&W qualification program. This case differed from production cases because it contained a welded-on instrumentation and Tt3 boss. Production engine cases do not have the extra instrumentation boss and the Tt3 boss is an integral-feature cast into the case. Prior to receipt of the case for rig testing, it had run a total of 1600 endurance cycles in a test engine at which time the case developed a crack adjacent to the welded Tt3 boss.

In preparation for test, the inner structure was removed by trepanning the case around the structural cone along a circle approximately 1" inward of the outer pressure wall. The case was then exposed to eight 5-hour exposures at 1750°F followed by a full precipitation heat treatment.

Strain gages were applied to the case and 11, 0.005" to 0.010" wide slots, measuring 0.050" to 0.060" long by 0.025" to 0.030" deep, were EDM into the case wall. Table 26 lists the slots by identity, size, and location, while figures 44 to 46 presents the locations of the EDM slots and strain gages. Slots associated with inside diameter of the boss tube at the embossment radius joining the tube with the case pressure wall. The slots are positioned on the rearward side of the tube. Four slots were located on the outer pressure wall's outer surface; one in base material, one in a repair weld made after the case was HIPped, and the remaining two in repair welds made prior to HIP.

TABLE 26. EDM TEST SLOTS, PW4168 DIFFUSER CASE, EXPOSED TO EIGHT 5-HOUR HEAT TREATMENTS

Number	Location
1	Small service boss inner embossment
2	Medium size service boss inner embossment
3	Large service boss inner embossment
4	Medium size service boss inner embossment
5	Small service boss inner embossment
6	Pressure wall boroscope boss inner embossment
7	Outer pressure wall
8	Large service boss inner embossment
9	Outer pressure wall post-HIP repair weld
10	Outer pressure wall pre-HIP repair weld
11	Outer pressure wall pre-HIP repair weld



1 denotes 8 EDM flaw locations

W/ #9,10,11 in weld areas

1 denotes 20 strain gage locations

24 denotes 5 backup strain gage locations

PWA 1469 (Cast Inco-718)

FIGURE 44. LOCATION MAP FOR EDM SLOTS AND S/Gs ON THE DIFFUSER CASE

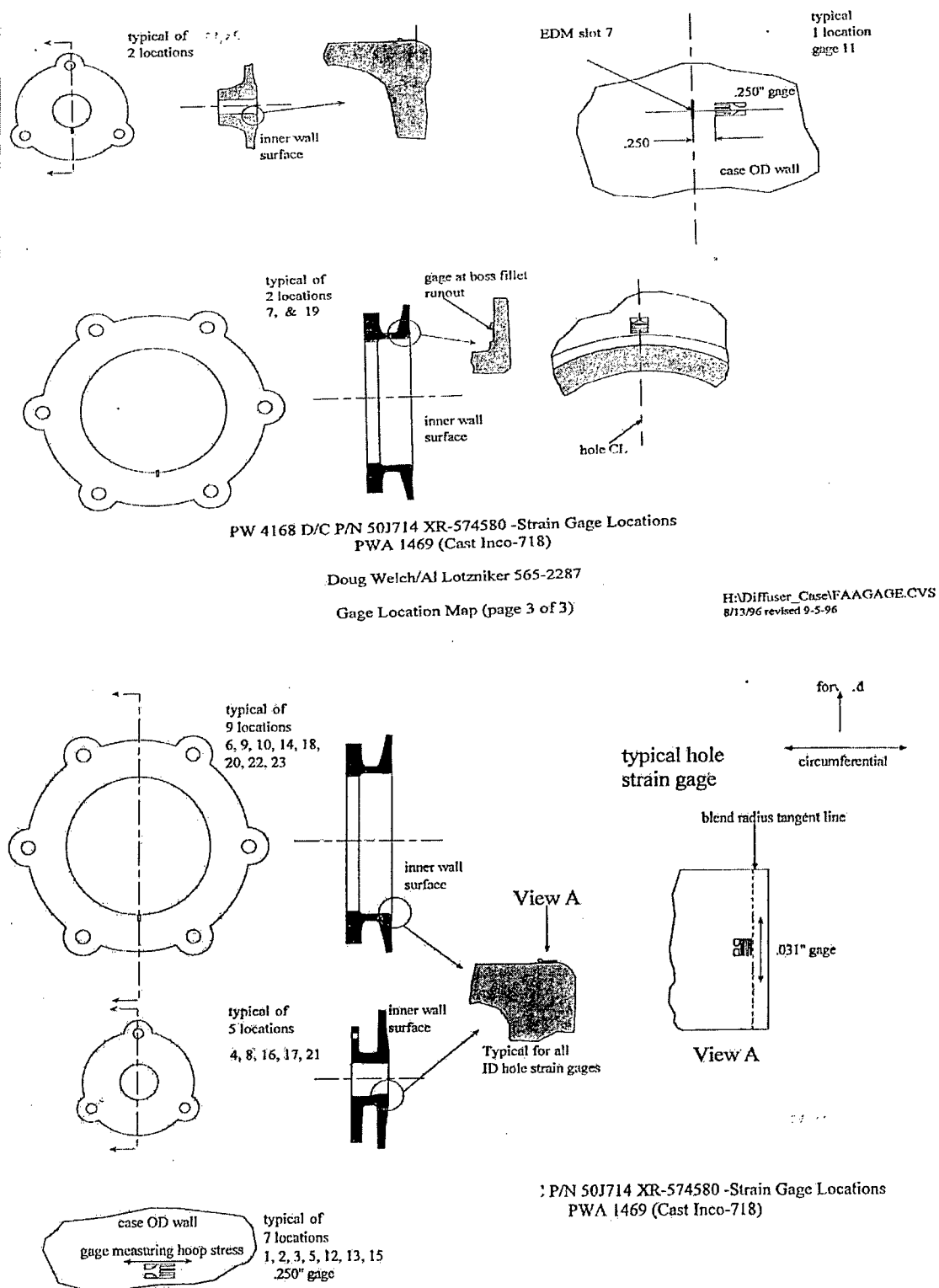
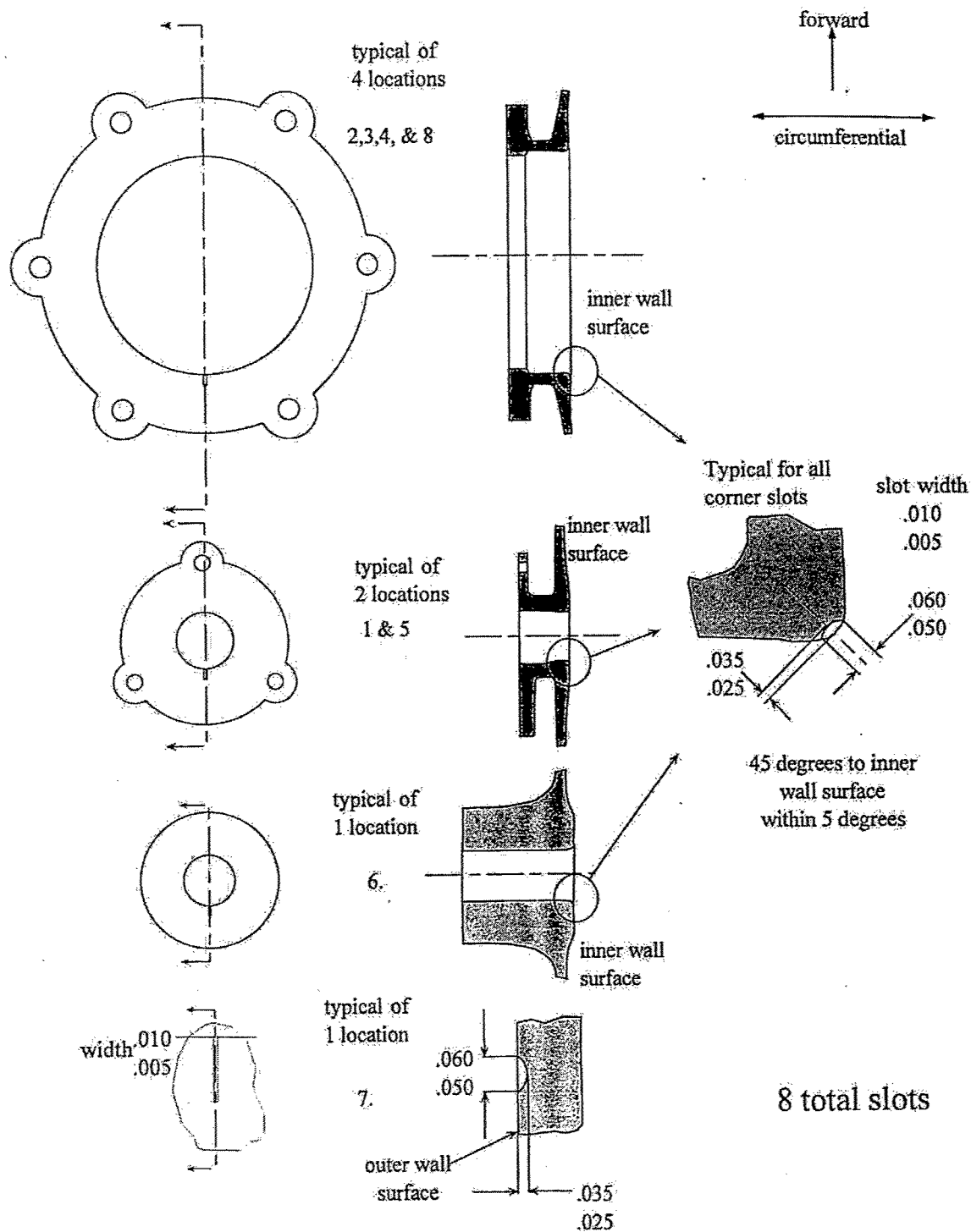


FIGURE 45. DETAILS FOR EDM SLOTS AND S/Gs ON THE DIFFUSER CASE



PW 4168 D/C P/N 50J714 XR-574580 - EDM Slot Locations
PWA 1469 (Cast Inco-718) Job # 11635

FIGURE 46. EDM SLOT DETAILS AND MEASUREMENTS

2.1.5.2 Test History.

The case was installed in the P&W pressure rig facility (figure 47), at which time testing was initiated. A summary of the testing conducted, cycles accumulated, and observations can be found in table 27.

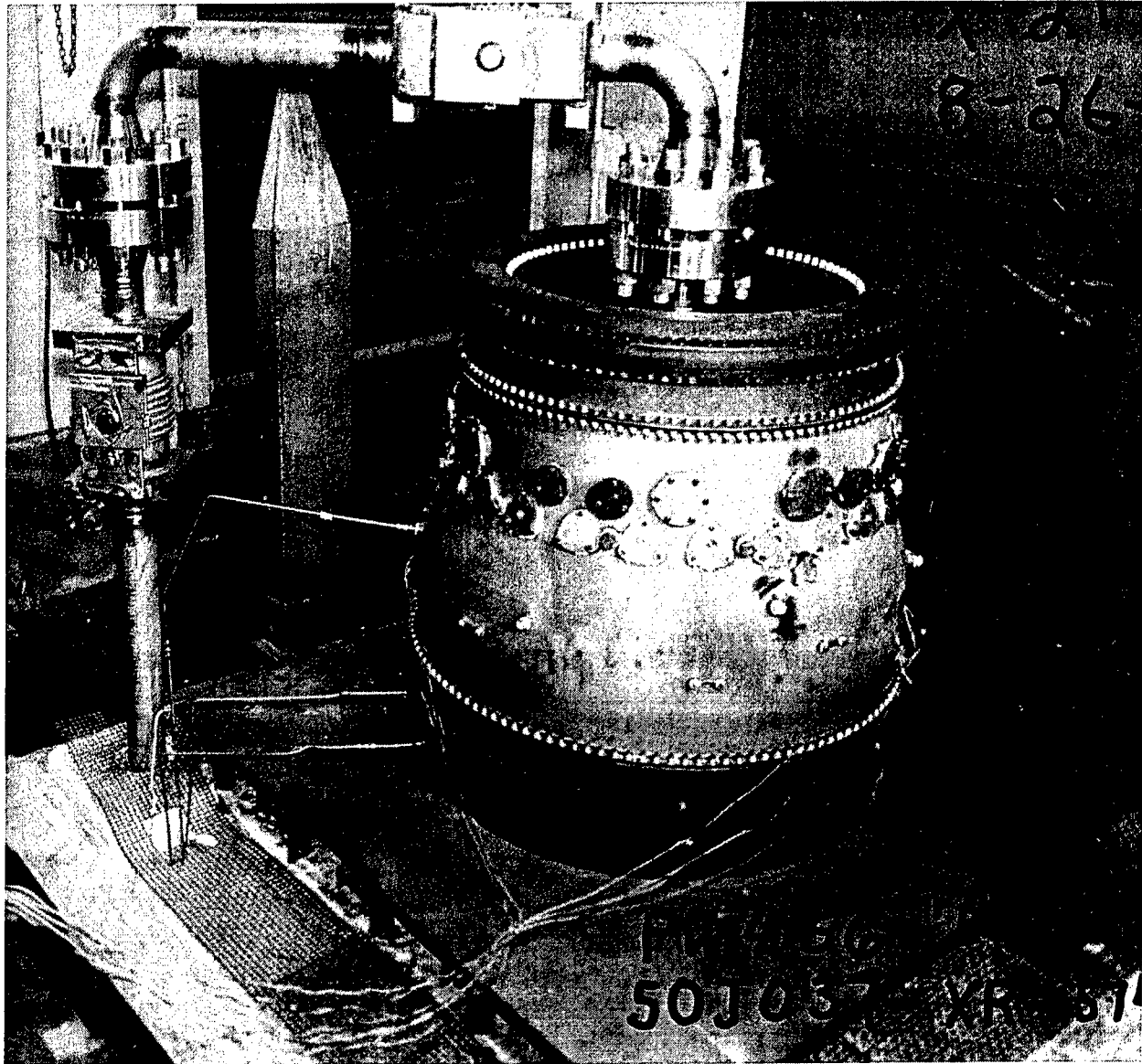


FIGURE 47. HOT-CYCLIC PRESSURE RIG SETUP TO TEST LARGE COMMERCIAL ENGINE DIFFUSER CASE OUTER PRESSURE WALLS (The large pipe extending up on the left and over into the center of the case provides the high-pressure nitrogen gas/air mixture to load the case walls. The various wires attached to the case are for strain gages used to calibrate stress loads prior to test. The entire unit, rig, and test case is encased in a furnace capable of producing high temperatures similar to engine operation.)

TABLE 27. PRESSURE RIG TEST LOG

Rig Cycles	Date	Comments
0	10/16/96	Limited strain gage program completed
684	12/12/96	4- to 5-inch crack found, removed BT EDM and case weld repair
2442	4/17/97	0.990-inch crack found, surface defined by DEA, area patch repaired. Cracks initiated at EDM slots 2, 4, and 6.
2442	11/5/97	Strain gage survey of patch boundary
2594	12/18/97	Excessive leakage, dwell cycling terminated
3606	2/12/98	Crack growth on EDM slots 2, 3, 4, 6, and 8 measured
4600	4/1/98	Crack growth on EDM slots 2, 3, 4, 6, and 8 measured. Indications on edge of patch repair and boss 25 (welded in boss)
5106	5/13/98	Crack growth on EDM slots 2,3,4,6 and 8 measured. Indications on edge of patch repair and boss 25 increased.
5350	6/10/98	OD inspection only, patch repair indications increases in size with maximum individual IND. = 0.415 inch
5589	6/17/98	Case ruptures 11 cycles prior to scheduled inspection

Originally cycling was done with a 1-minute dwell at maximum load, but later in the program, this proved untenable.

The first inspection of the slots was scheduled after 1000 cycles had occurred. However, because 7 of the 11 slots were located on the inner surface embossments, the case had to be completely removed from the test rig so the inspection could occur. After 684 cycles, there were noticeable pressure losses. An inspection of the case's outer surface revealed a crack in excess of 4" between the welded-on Tt3 boss and a nearby borescope inspection boss, (see figure 48). There was no evidence that any of the EDM slots had grown. The crack was excised using wire EDM after which the EDM racetrack-shaped hole was weld repaired, the case reheat treated, and returned to test. In addition to the 5" repair weld, numerous surface welds were placed on the outer surface to correct for distortion created by the large repair weld. It should be noted that a weld of this size would not be permitted on a service case. It was undertaken here to salvage the case for the sake of the test program.

After 1758 additional cycles, the case's outer surface was re-examined and a crack approximately 1" long was discovered at the location of the first repair weld. Attempts to weld repair the area were fruitless. Contributing to the problem was the presence of the postsequence repair weld and the large weld used to attach the Tt3 boss. Continued repairing using puddle welds would create unacceptable levels of distortion. Because of this, it was decided to repair the case using a patch removed from a scrapped case of similar dimension. This is an unorthodox repair procedure that is not permitted on P&W cases. However, it was used with this case to get sufficient cycles to evaluate the crack growth of the 11 slots, a few of which had begun to exhibit crack growth.

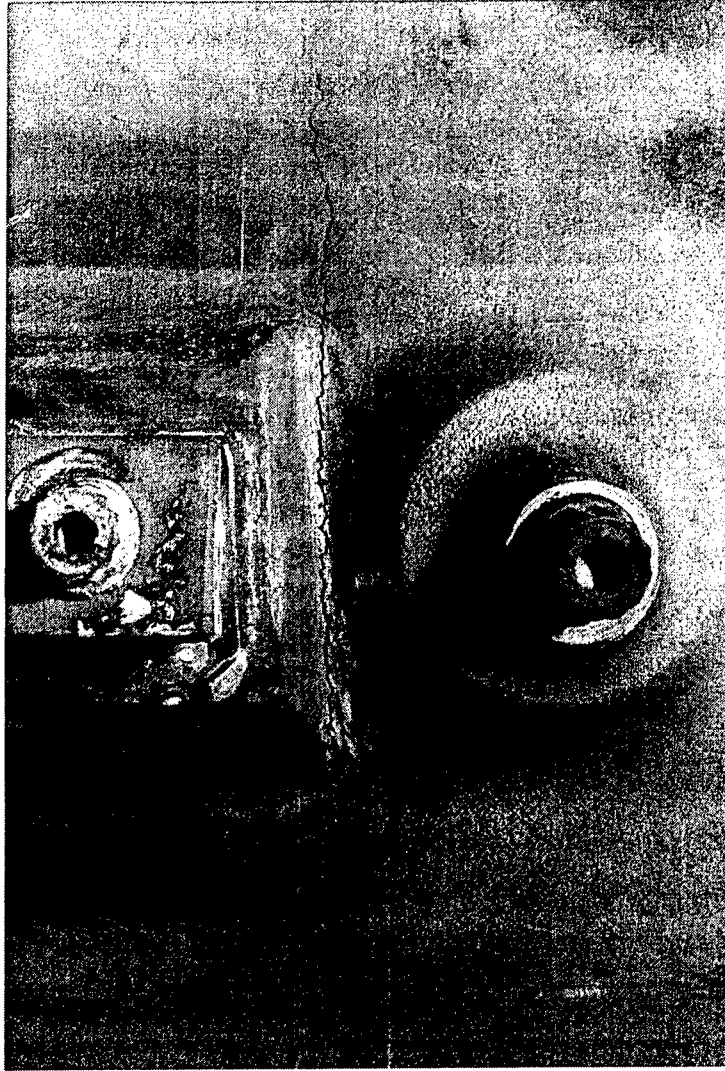


FIGURE 48. CRACK IN OUTER PRESSURE WALL OF PW4000 DIFFUSER CASE CYCLED FOR 684 CYCLES IN THE HOT-CYCLE PRESSURE RIG (The crack runs axially adjacent to an instrumentation boss (left of the crack), the base that was created by the buildup of multiple layers of weld metal.)

Completing the patch repair created distortions of the flanges to a degree that it made holding pressure in the rig difficult. The previous 2442 cycles had been generated with dwell loading. However, after an additional 152 cycles with dwell loading, it was decided to continue the test without dwell loading because it failed. Cyclic loading continued for an additional 2759 cycles with a full inspection (outer- and inner-wall surfaces) after 1012 cycles. Cracks were growing out of several, but not all, EDM slots. With the inspection at 5106 cycles, numerous cracks (0.065" to 0.355" in length) were observed in the vicinity of the patch weld. At 5350 cycles, a cluster of these cracks measured 1.2" long on the outer surface. Although the case was planned to run another 250 cycles, after 238 cycles, the case ruptured, see figure 49.

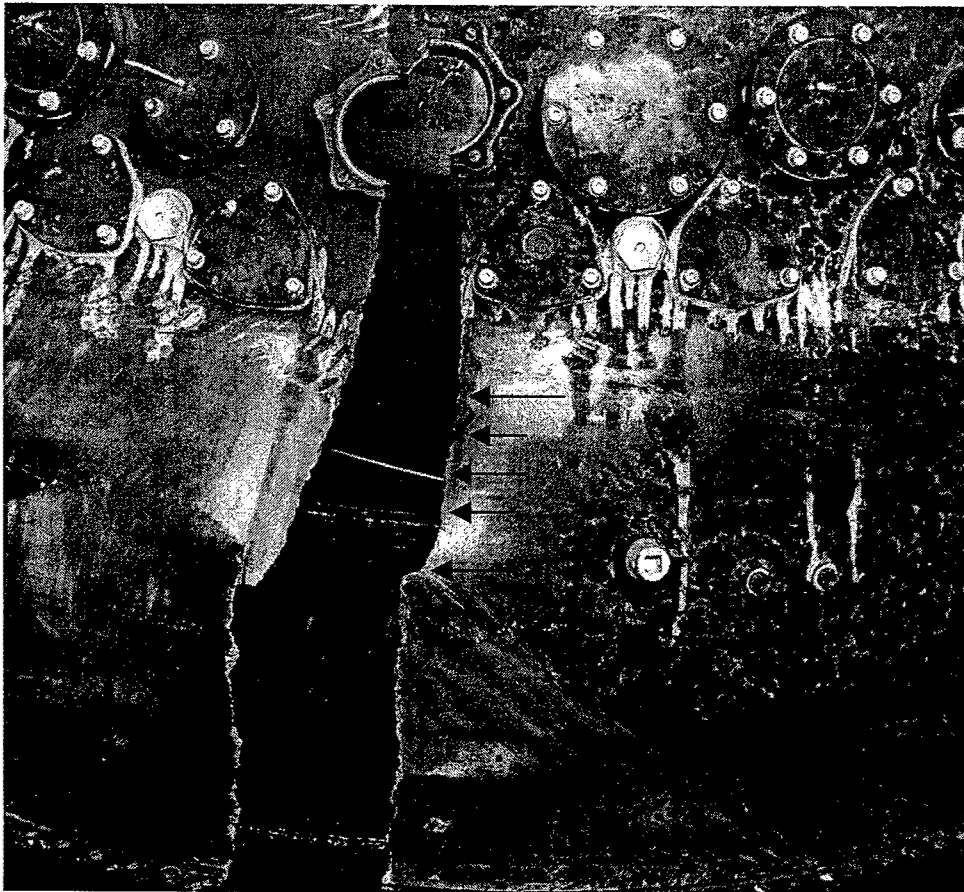


FIGURE 49. HOT-PRESSURE RIG DIFFUSER TEST CASE AFTER RUPTURE FOLLOWING 5589 CYCLES (Arrows mark major fatigue origin points along main fracture but there were numerous smaller crack indications along the fracture path at earlier inspections.)

2.1.5.3 Initial Crack Analysis—684 Cycles.

As previously stated, the case used included welded-on boss configurations that were not consistent with a final commercial application design. This contributed to the early cracking of the case. The crack extended forward and aft of the Tt3 boss (see figure 48) and appeared to initiate in the fillet between the Tt3 boss and adjacent binocular bosses. After removal by EDM from the case wall, the crack was measured and found to extend 2.25" forward of the welded-in instrumentation boss and 1.875" rearward of the same boss for a total length of 4.125". The fatigue "thumbprint" measured approximately 0.050" along the outer surface wall and was 0.080" deep, coming within 0.010" of the wall's inner surface before rapid tensile tearing occurred. The origin of fatigue was centered in the fillet on a tangential line connecting the two bosses that straddled the fillet. Several factors contributed to the initiation of the crack.

1. The proximity of the Tt3 boss to the borescope boss caused stresses in the fillet between the two bosses to be exceptionally high.

2. The Tt3 boss was attached to a platform fabricated by making multiple layers of welds onto the case's inner and outer surfaces. This unusually large weld exhibited lots of LOF between the layers (figure 50), creating numerous sites for fatigue initiation.
3. The fillet between the bosses had been shaped by hand grinding with little effort being made to properly blend or polish the fillet (figure 51).

Using a SEM to analyze the fracture, striations were measured on the crack surface as it grew from the outer to the inner surface of the case (data shown in figure 153). Giving credit for scatter with the striation measuring process may suggest that the case had already been cracked prior to initiation of the hot-pressure rig test. A review of records confirmed that procedures were not followed and that the case was not inspected at the conclusion of its run in an experimental test engine or prior to its placement in the hot-pressure test rig. A more complete analysis of the crack is provided in task 2 of this report.



Tt3 Boss Weld Platform

~4X



Interface Tt3 Platform/Case

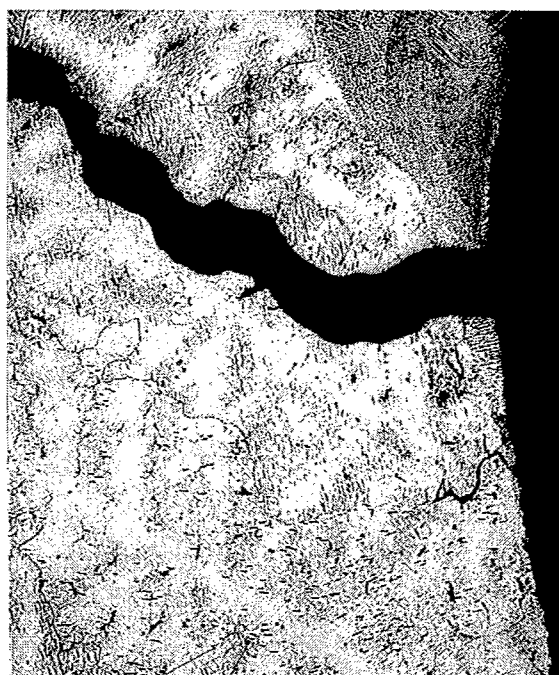
50X

FIGURE 50. CROSS SECTION OF Tt3 BOSS PLATFORM FABRICATED WITH MULTIPLE LAYERS OF WELDS (Note the lack of fusion and HAZ cracks (right) associated with the rather massive welds.)



Tt3/Borescope Boss Fillet

~20X



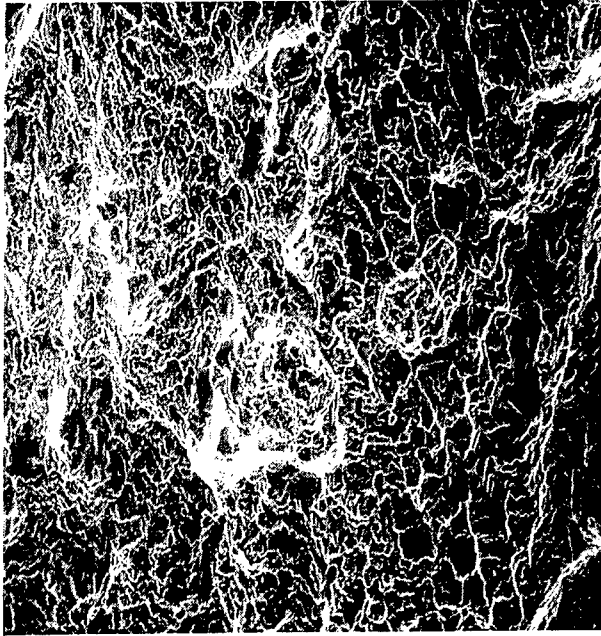
Tt3/Borescope Boss Fillet

50X

FIGURE 51. AREA BETWEEN THE Tt3 AND BORESCOPE BOSSES (Note the heavy grind marks on the outer surface (left) and weld material in the fillet (right). Both were associated with the case rupture fracture.)

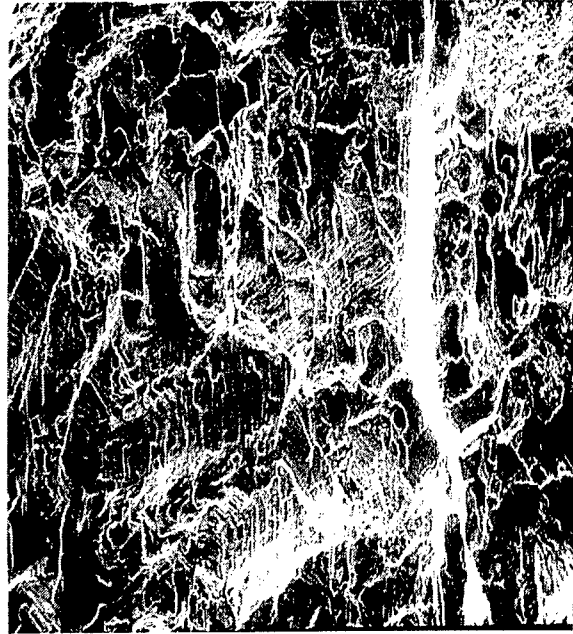
2.1.5.4 Second Crack Analysis—2442 Cycles.

At completion of the second sequence of cyclic testing, a 0.990" long crack was detected near the 5-inch weld repair that was used to fill the EDM slot made in removal of the sequence 1 crack. It proved impossible to identify a single fatigue origin. Along the fracture length were areas of tensile overload (figure 52(a)), fatigue (figure 52(b)), fatigue + overload, and both transgranular (figure 53(a)) and intergranular (figure 53(b)) crack propagation. Multiple initiation sites were detected. These attributed to poor quality of the large repair weld and to the intersecting small surface welds that were used to correct the distortion caused by the large repair weld. Extensive secondary cracking was also observed. Secondary cracks were observed along grain boundaries of the exposed base material (figure 54(a)) and along delta plates (figure 54(b)) in areas of extremely high delta concentrations. Some of these areas exhibited levels of needle delta phase concentration in excess of that observed during the heat treat studies. This was attributed to exposing the case to delta-precipitating temperatures while residual stresses were imposed on the material, accelerating the precipitation process.



a. Tensile Overload

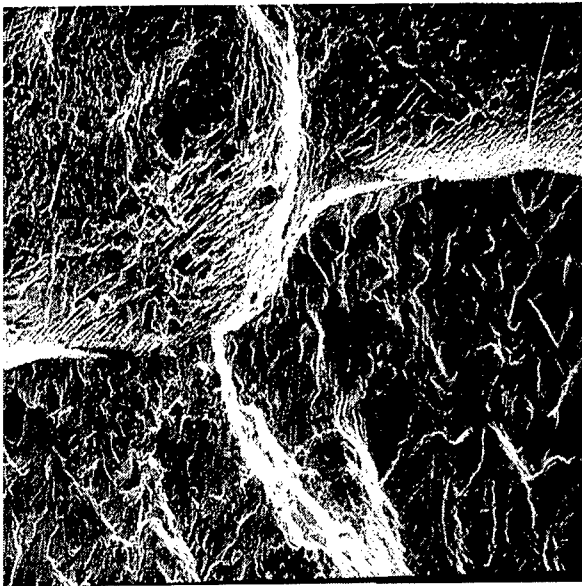
~300X



b. Tensile + Fatigue Fracture

~300X

FIGURE 52. TENSILE OVERLOAD (LEFT) AND A COMBINATION OF TENSILE OVERLOAD PLUS FATIGUE (RIGHT) FRACTURE FEATURES FOUND THROUGHOUT THE MAIN CASE FRACTURE



a. Transgranular Cracking

~300X



b. Intergranular Cracking

~300X

FIGURE 53. EXAMPLES OF CRACK GROWTH PROPAGATION BY A TRANSGRANULAR (LEFT) AND INTERGRANULAR (RIGHT) PATHS

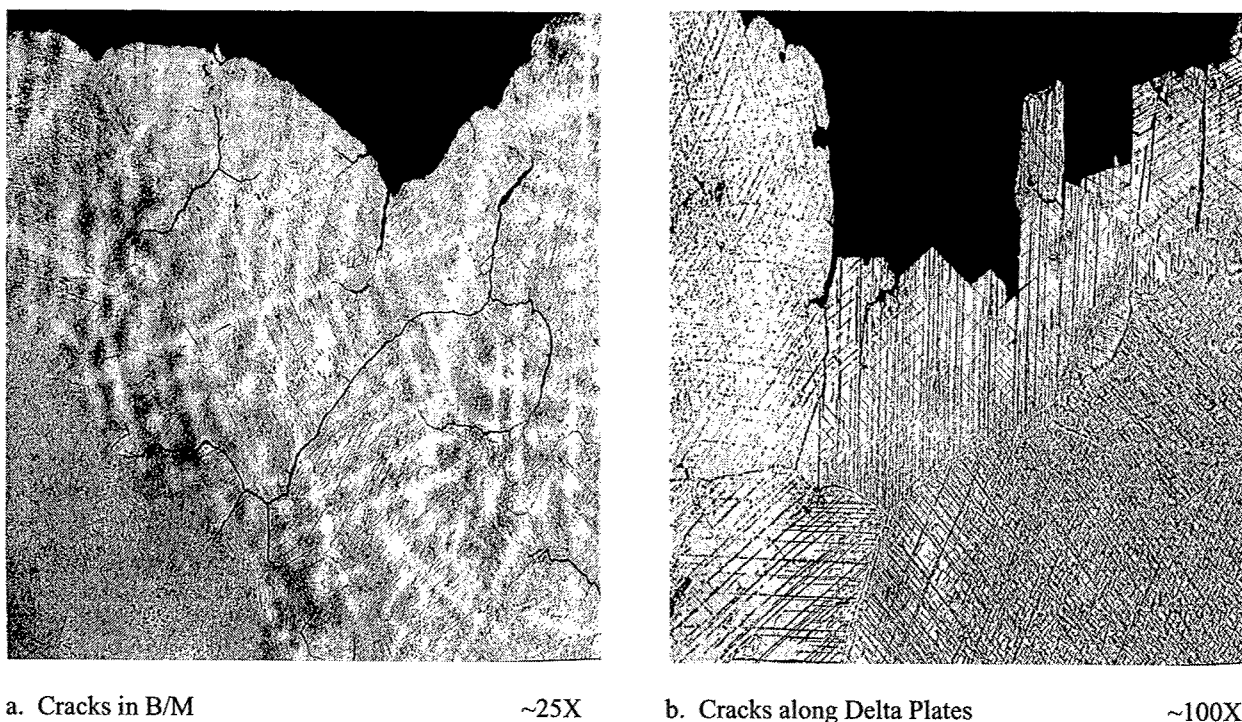


FIGURE 54. EXAMPLES OF SECONDARY CRACKS ALONG CAST BASE METAL GRAIN BOUNDARIES (LEFT) AND DELTA PLATES (RIGHT)

2.1.5.5 Rupture Fracture Analysis—5589 Cycles.

Figure 55 illustrates the main fracture of the ruptured test case. Two other fractures broke the case into three pieces. However, the other two showed no evidence of fatigue, only tensile overload. It was calculated that it required 2667 cycles for the crack to propagate from outer- to inner-wall surfaces based on measurements of the fatigue striation. Considering that the case was operated for 3147 cycles after the patch repair was made, the crack would have been detectable at approximately 480 cycles into the last sequence of cyclic runs. However, the inspection at the completion of 4600 cycles (2158 cycles into the final run) failed to detect any pressure wall indications in the area of the patch repair. After another 506 cycles (5106 total on the case), the same area was marked by 21 indications ranging in length from 0.050" to 0.355". With another 244 cycles of testing (5350 cycles total), several of the indications had linked, so there were three continuous or near-continuous indications over 0.285" in length existed. The largest was 0.460" in length and was in line with several smaller indications, making a total length of 1.2". An attempt was made to get another 250 cycles of test time, but the case ruptured after only another 239 cycles.

Five thumbprints were identified along the main fracture surface. These are indicated in figure 56. All grew from the outer surface inward. The largest measured 1.5625" along the outer surface and extended to the inner surface. The others ranged in length along the outer surface from 0.4375" to 0.5625" and extended from approximately 1/3 to 3/4 of the wall's thickness. Obviously the larger thumbprints represent linking up of the many smaller fluorescent

penetrant indications (FPI) detected at 5350 cycles that measured almost 1.2" in length. A more detailed analysis of the test case's main rupture growth characteristics is presented in task 2.



PWA 1469 Hot Rig Test Case

Main Rupture

5,589 cycles

FIGURE 55. PWA 1469 HOT-PRESSURE RIG TEST CASE AFTER 5589 CYCLES AT 1150°F (The photo illustrates main case rupture with arrows indicating weld boundary of the patch repair welds.)

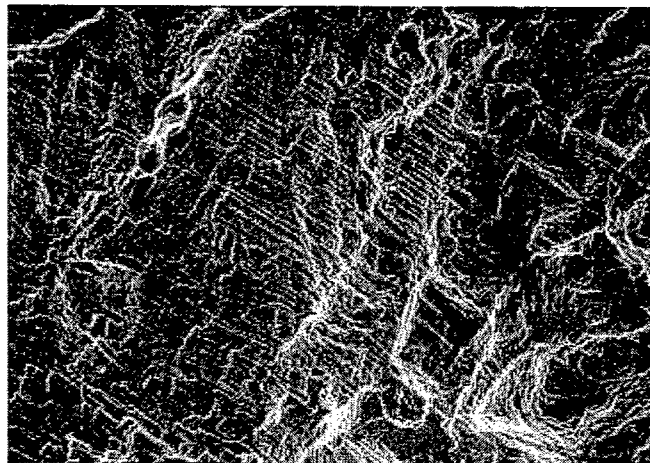


Main Fracture

5,589 cycles

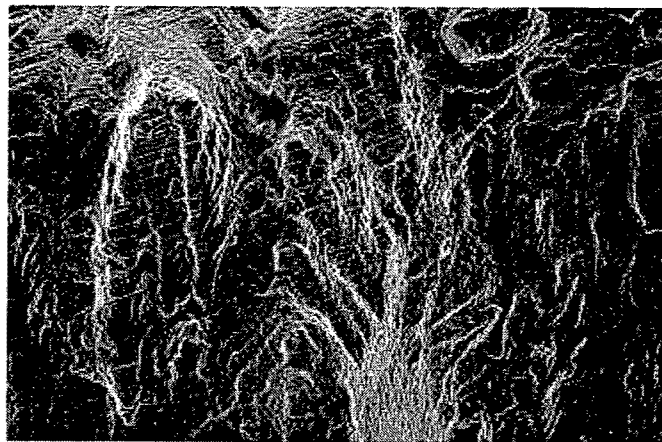
FIGURE 56. LEFT SIDE OF MAIN FRACTURE WITH FIVE FATIGUE THUMBPRINTS INDICATED BY BRACKETS (The largest (no. 1) measured 1.5625" in length and was located in the area where the 1.2" string of indications was observed at 5350 cycles.)

The thumbprints had relatively clear indications of the fatigue crack progression from the outer toward inner surfaces. However, there was also evidence of fatigue in the fracture areas between the thumbprints. Examples of the two areas are illustrated in figure 57. Numerous small intergranular cracks were observed near the main fracture that had the appearance of weld HAZ grain-boundary liquation cracks. A macroetched case section with the main fracture (figures 58 and 59) confirmed that the main fracture was near, but did not initiate or grow to any extent within the patch repair welds. Instead, cracking that led to the case rupture appears to have occurred from the numerous shallow welds. These shallow welds were made on the outer surface in an attempt to mitigate the distortion created by the large patch repair. Figure 60 presents photographic images of a typical surface crack and a HAZ crack emanating from a shallow weld.



a. Major Crack Thumbprint No. 1

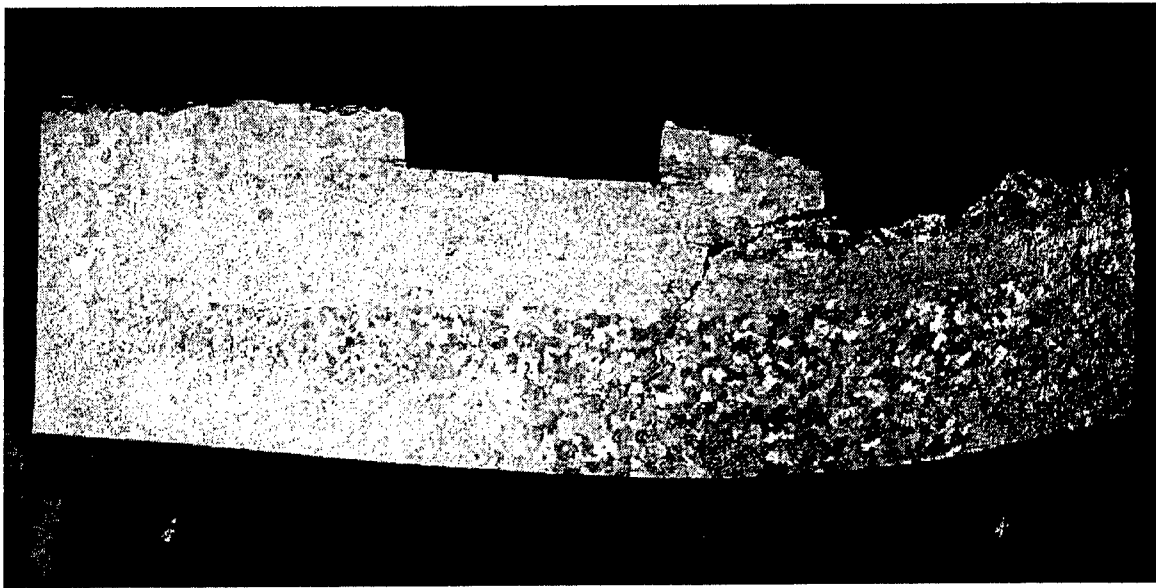
~1,000X



b. Major Crack Between Thumbprints

~1,000X

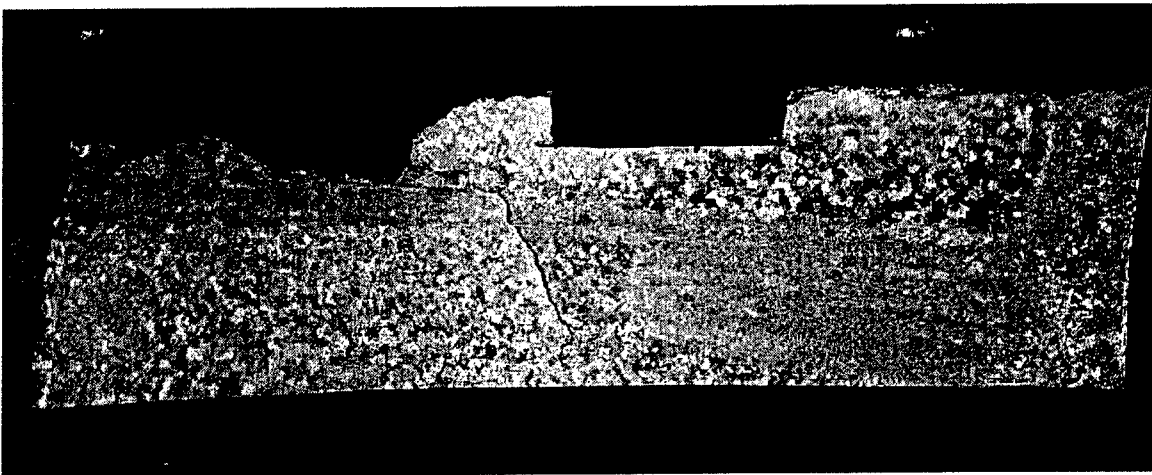
FIGURE 57. FRACTOGRAPHIC PHOTOGRAPHS OF FATIGUE OBSERVED ON THE FRACTURE SURFACE OF THE HOT RIG TEST CASE MAIN RUPTURE (The examples were taken within thumbprint no. 1 (a) and between thumbprints nos. 2 and 3.)



Main Case Rupture

Outer Surface

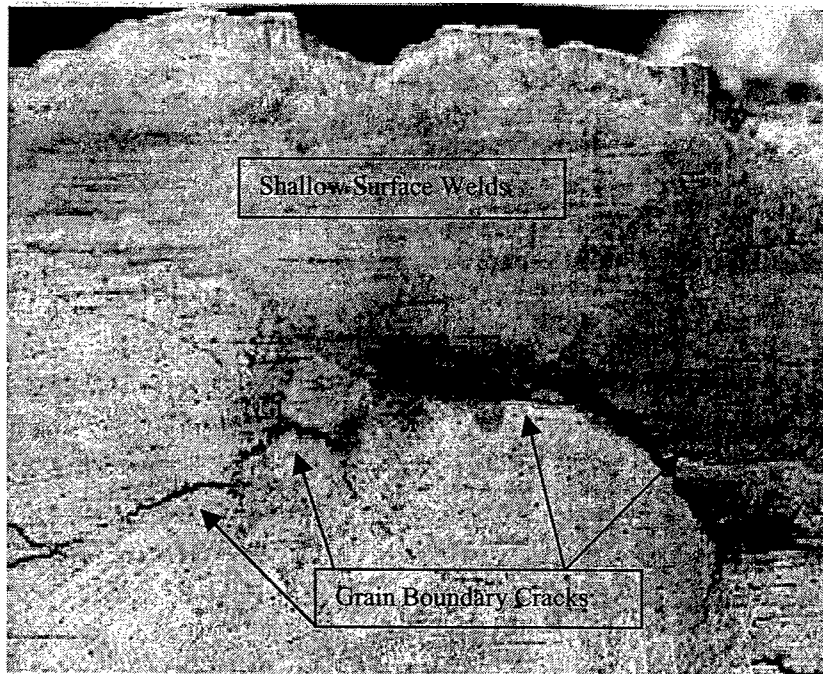
FIGURE 58. MACROETCHED OUTER SURFACE OF HOT-PRESSURE TEST RIG CASE ILLUSTRATING STRUCTURE NEAR THE MAIN CASE FRACTURE
(Largest and probable initial fatigue site was within the section cut out of the center of the illustrated section. Note that it is some distance from the patch repair weld which runs left to right approximately in the middle of the excised section.)



Main Case Rupture

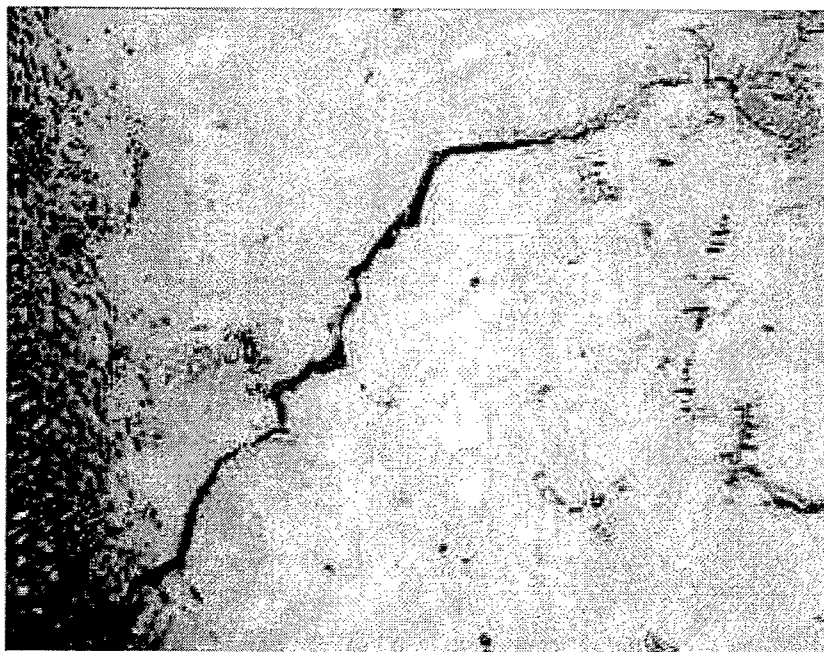
Inner Surface

FIGURE 59. MACROETCHED INNER SURFACE OF HOT-PRESSURE TEST RIG CASE ILLUSTRATING STRUCTURE NEAR THE MAIN CASE FRACTURE
(Note the clear delineation of coarse grains of the cast repair patch up to the fracture surface.)



a. Surface IG Cracks

~10X



b. HAZ crack

~200X

FIGURE 60. TYPICAL INTERGRANULAR SURFACE CRACKS (a) OBSERVED ON THE HOT-PRESSURE TEST RIG CASE IN THE VICINITY OF THE CASE RUPTURE FRACTURE CRACKS PROVED TO BE WELD HAZ GRAIN-BOUNDARY LIQUATION CRACKS AND (b) COMMONLY FOUND WITH WELDS OF CAST INCONEL 718. (These are typically caused by high restraint, poor welder technique or when welds are too large and/or too many such that they overlap each other.)

2.1.5.6 EDM Slot Analysis – 5589 Cycles.

Crack growth was detected at slot location nos. 2, 4, and 6 as early as 2442 cycles into the test or when the second large pressure wall crack was discovered. Five of the EDM slots showed signs of crack growth before the test had completed. Total crack lengths, including that of the EDM slot, are presented in table 28. The crack at location no. 2 grew faster than all the other slots, measuring 0.375" in length at 4600 cycles and 0.495" in length at 5100 cycles.

TABLE 28. FPI CRACK LENGTH MEASUREMENTS OF PRESSURE TEST CASE EDM SLOTS

Test Cycles	Slot No. 2	Slot No. 3	Slot No. 4	Slot No. 6	Slot No. 8
2,442	0.065"	0	0.045"	0.030"	0
3,606	0.170"	0.041"	0.049"	0.072"	0.039"
4,600	0.375"	0.072"	0.059"	0.105"	0.062"
5,100	0.495"	0.080"	0.060"	0.165"	0.065"
5,589	0.985"	0.085"	0.075"	0.165"	0.080"

At completion of the test, cracks were evident at 7 of the 11 EDM slots that were located on the inner surface embossments of the integrally cast bosses. None of the smooth surface, pressure-wall EDM slots, including the three at welds, showed any evidence of crack progression. Figure 61 illustrates the crack observed at location no. 2 at completion of the pressure rig test.



FIGURE 61. CRACK EXTENDING OUT OF AN EDM SLOT ON THE INNER SURFACE EMBOSSEMENT OF LARGE SERVICE BOSS 34 (LOCATION NO. 2.) (The crack has grown into the boss neck, parallel with the inner surface.)

Each of the cracks were photographed and then opened for further analysis. SEM (scanning electron microscope) images were made of each of the opened slots and the depth of crack growth was measured. Measurements were made in three directions from the EDM slot edge. One from the deepest penetrating edge of the slot directly into the boss corner along a line normal to the EDM slot edge. The other two were along the surfaces on either side of the slot; along, or roughly parallel, with the inner surface and outward; or along the neck of the boss. A more accurate measurement of the EDM slot size was also made. An example of the technique used is presented in figures 62 and 63. Results of the measurements are presented in table 29.

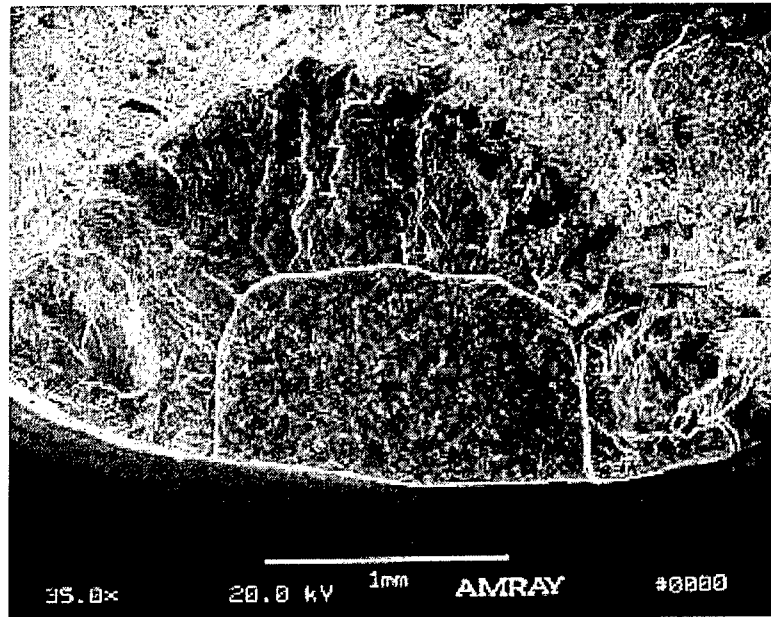
The different total lengths in table 28 and table 29 are due to the fact that the crack length values of table 28 include areas of rapid tensile fracture while those of table 29 are for crack lengths that are limited to fatigue progression.

Not all of the slot fractures were suitable for counting striations. Initially, it appeared that slot nos. 2, 6, and 8 were long enough and had enough identified striations so that they could be counted. However, no. 6 had a significant amount of cleavage fracture mixed in with the fatigue cracking, so no viable measurements were made on this slot. Striation counts were made on no. 8 for a depth of 0.014" inward from the slot, and it was calculated that it took 580 cycles to reach this depth. Slot no. 2 was measured inward for a depth of 0.179" from the slot and 3442 cycles were calculated for the crack to grow to this depth. The cycles calculated for slot no. 2 match the FPI records (table 28). The number of cycles calculated for slot no. 8 were less than the cycles experienced in the test after crack growth from when the slot was first observed. Further analysis of the crack growth out of the EDM slots is provided in task 2.

TABLE 29. CRACK AND SLOT LENGTH MEASUREMENTS

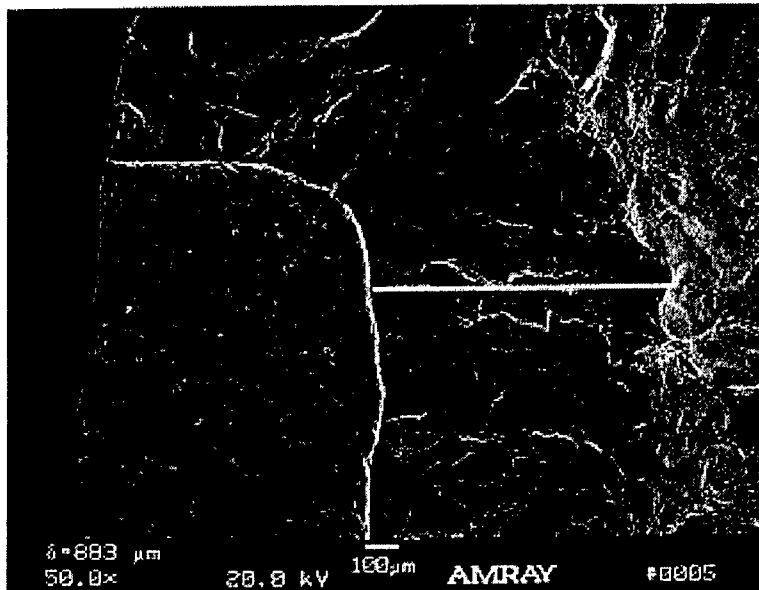
Slot No.	Lengths – mils				Total Crack Length
	Slot Size*	Radial Direction	Along Inner Wall	Along Boss Neck	
1	49.4 x 26.8	10.4	5.2	5.2	0.0598"
2	53.1 x 26.0	28.1	37.5	25.0	0.1687"
3	49.4 x 28.6	24.7	14.8	14.8	0.0790"
4	53.3 x 24.7	23.0	22.0	28.0	0.1030"
5	54.6 x 27.3	6.5	9.0	15.6	0.0792"
6	49.5 x 22.0	37.1	37.1	21.7	0.1083"
8	52.1 x 26.0	14.6	12.5	16.7	0.0813"

*Length x Depth



a. EDM Slot No. 3

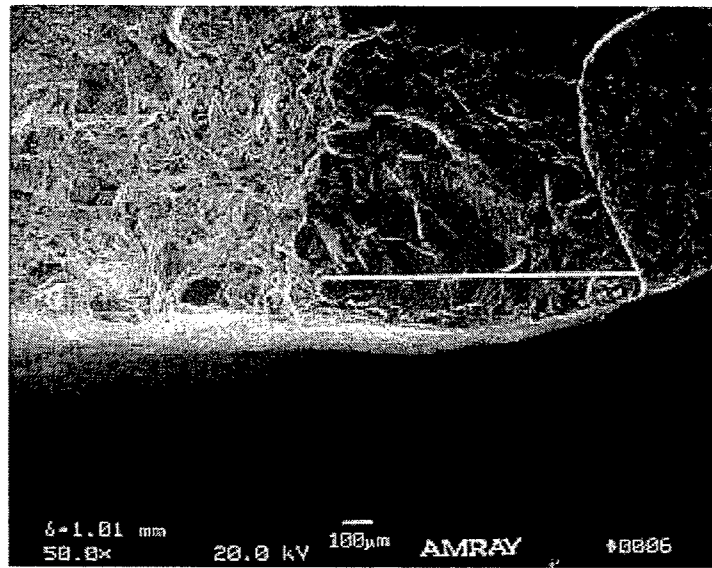
~35X



b. EDM Slot No. 3

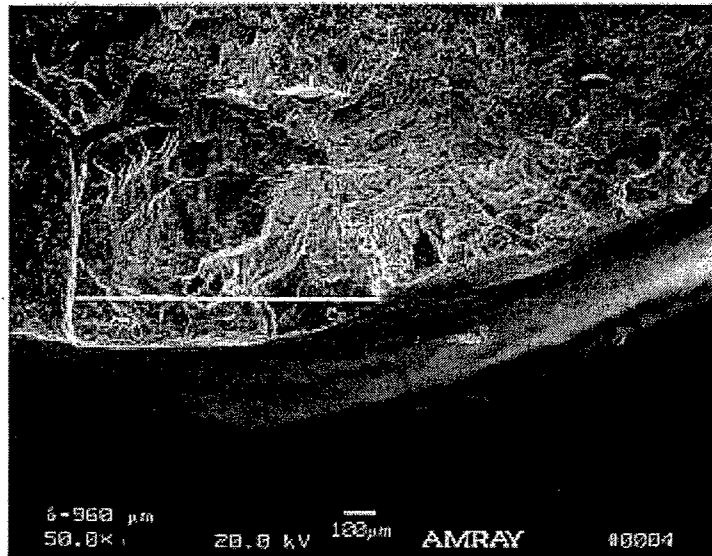
~50X

FIGURE 62. SECONDARY ELECTRON IMAGES OF EDM SLOT NO. 3 AFTER IT AND THE ASSOCIATED CRACK WAS OPENED UP (a) IS AN OVERALL VIEW OF THE SLOT AND FRACTURE AND (b) ILLUSTRATES THE LINE ALONG WHICH THE CRACK LENGTH WAS MEASURED FROM THE SLOT INTO THE EMBOSSEMENT



c. EDM Slot No. 3

~50X



d. EDM Slot No. 3

~50X

FIGURE 63. SECONDARY ELECTRON IMAGES OF EDM SLOT NO. 3 AFTER IT AND THE ASSOCIATED CRACK WAS OPENED UP (c) WHITE LINES EXTENDING FROM THE EDM SLOT EDGE REPRESENT WHERE THE CRACK LENGTH WAS MEASURED ALONG THE INNER-WALL SURFACE AND (d) ALONG THE BOSS NECK

2.1.6 Task-1 Summary.

The objectives set forth for task 1 of this report was to provide the material data required for the development of the program methodology. Specifically, the basic material fracture crack growth characteristics for both the baseline and repaired material were developed; this data was then combined with existing materials' databases. This included data from specimens and a full-size

case. The effect of multiple repair heat treatments experienced by cases in operation was evaluated on several commonly used case materials. Major effects for consideration in methodology development were:

1. Multiple stress relieves have a debiting effect on the strength of AMS 5613 and AMS 5616 but do not impact either alloy's crack growth characteristics.
2. No significant difference can be discerned among the crack growth rates of base AMS 5613 and AMS 5616 and their respective welds, regardless of heat treat processing.
3. The differences in crack growth rates between coarse- and fine- (faster) grain AMS 5663 increases with temperature.
4. Multiple solutions, multiple short-age exposures, and extended exposure at 1100°F all cause accelerated crack growth rates for coarse-grain AMS 5663 at temperatures above 1000°F.
5. Welds of AMS 5663 have crack growth rates between that of coarse- and fine-grain AMS 5663. At 1100°F and under dwell conditions, this can mean as much as a 4X faster rate than the coarse-grain base.
6. Multiple solutions slightly accelerate the high temperature (>1000°F) dwell crack growth rate of AMS 5663 welds.
7. PWA 1469 crack growth rates are significantly slower than that of AMS 5663, especially at high temperature under dwell loading, and are only moderately affected by multiple solutions.
8. Welds of PWA 1469 have crack growth rates at high-temperature dwell loading that are 3 to 4X faster than the base rates but are still slower than coarse-grain AMS 5663 and its welds.
9. Multiple solutions accelerate the crack growth rate of PWA 1469 welds to a point that they are faster than the coarse-grain AMS 5663 base rate at high-temperature dwell loading.
10. HIP welds have high-temperature, dwell-loading rates that are faster than their PWA 1469 base by factors between 8X and greater than 10X. The effect is less dramatic under nondwell loading. The rate appears strongly related to the HIP welds recrystallized grain size.
11. Multiple solutions may have a slight accelerating effect on the high-temperature, dwell-loading crack growth rate of HIP welds.

The materials data generated in task 1 is substantial and will contribute significantly toward the refinement of the component crack growth analysis system and eventual case failure prediction program. However, the task 1 results also highlights some areas requiring additional study in order to make the system as efficient as possible. Some testing and evaluation was omitted from

task 1 for timeliness and budgetary purposes while others were not included because, frankly, their effects were not expected. Suggestions for future study include:

1. Evaluating the properties of AMS 5616 hardened at cooling rates that duplicate those experienced with large commercial engine TEC construction. As discussed in section 2.1.4 and appendix C, the microstructure of the cases demonstrated that the forced-air cooling rate from solution of the cases was slower than experienced with liquid medium-quenched test material. No mechanical properties differences are expected, but this should be confirmed.
2. Evaluating the effect of multiple short-age cycles on the crack growth characteristics of AMS 5663 (coarse and fine grain) at 800° and 1000°F. The effect was very dramatic at 1100°F, but this fails to adequately cover many areas of critical cases such as the JT9D diffuser.
3. Additional crack growth rate testing of HIP and non-HIP welds to better define the causes for scatter among the tests. Microstructural features should be identified to explain the differences. These evaluations need to be extended to include temperatures between 800° and 1100°F, and possibly higher, and need to include testing at dwell and nondwell conditions.
4. Extensive fractographic and metallographic examination of the crack growth test specimens to gain a better understanding of the crack growth mechanisms involved with various forms of Inconel 718. Analysis under this contract support was limited to determining that the specimens were valid for the structure they were intended to test and that the results were not influenced by some pretest undetected flaw.
5. Conducting a repair facility survey and review as originally planned in the nonfunded task 5 of this contract. The main objective of that task was to quantify what service cases experience over their lifetime. Input was provided by several shops at the beginning of this contract, but this was only based on the best recollection of engineers and managers regarding their experience. Because it is not required, documentation of a case's history while in a repair shop (i.e., repair cycle, number of repeat cycles, heat treat variations, etc.) is not maintained.

2.2 TASK 2: CRACK GROWTH PREDICTION METHODOLOGY.

This task addresses two of the key ingredients required to manage static cases; the ability to predict the stress the part is experiencing and the ability to predict the growth rate of any cracks that develop in the hardware. Three different P&W cases were analyzed to cover the various manufacturing methods and materials: a JT8D wrought and welded steel outer combustion chamber case, a JT9D wrought INCO718 welded diffuser case, and a cast INCO718 PW4000 diffuser case.

An integral part of this section is the use of P&W service experience and rig testing to calibrate the prediction processes. Crack growth data has been taken from cases that have cracked during field operation, as well as from the pressure rig testing of the cast case as part of this contract, and used to determine the capabilities of the analytical tools. The results of this task cover initial

screening and analysis guidelines, compilation of operational crack growth data, evaluation and usage of several crack growth prediction methodologies, and the actual analyses and comparison of predicted crack growth data for each of the three case configurations. The material data generated in task 1 was used in the evaluation of the crack growth of the aged cases.

2.2.1 Guidelines for Critical Area Determination.

One of the key ingredients for reducing the risk of case rupture is to identify critical areas in a case that could experience cracking and subsequent crack progression.

Experience has shown that certain areas of these cases are more likely to develop cracks due to local geometric features or manufacturing methods. Cracks in these areas could progress to a size where the risk of failure is higher than in other areas of the cases. The purpose of this task is to establish a set of guidelines to be followed to identify these critical areas of cases that should be examined for crack growth potential. Identification of these critical areas will be based upon experience at P&W with cases that have seen service experience as well as cases that have been tested in pressure rigs or similar test fixtures in-house.

A survey of all high pressure cases at P&W was conducted to identify areas where cracking has occurred. Table 30 is a sample compilation of this information for a typical engine case. This experience covers a broad range of engines, yielding a substantial amount of information, identifying critical case areas that should be reviewed, and analyzed for potential cracking problems. This information has been compiled into the following list of key areas in cases that should be reviewed and analyzed.

TABLE 30. P&W EXPERIENCE OF JT9D-7 ENGINE DIFFUSER CASE
CRACKING LOCATIONS

Engine	Material	Construction	Crack Location	Narrative	Identification Characteristics
JT9D-7	Wrought INCO718	ECM'd center body, three piece welded-ring strut ring	Rear Rail adjacent to boss	Cracks develop in O.D. of rail due to rail thermal gradient. Local k_t due to presence of boss aggravates the stress. Cracks progress down rail, into case wall, and propagate axially. Repaired cracks initiate from weld defects.	<ul style="list-style-type: none"> • Deep Rail • Fillet transition between a thick and thin section • Thick section tied to a thin section • Weld defects
			Front Rail adjacent to boss	Cracks develop in O.D. of rail due to rail thermal gradient. Local k_t due to presence of boss aggravates the stress. Cracks progress down rail, into case wall, and propagate axially. Repaired cracks initiate from weld defects.	<ul style="list-style-type: none"> • Deep Rail • Fillet transition between a thick and thin section • Thick section tied to a thin section • Weld defects
			Flange Boltholes	Cracks develop in O.D. of bolthole due to thermally induced hoop stress and local k_t of hole. Cracks propagate from edge of hole through flange strap.	<ul style="list-style-type: none"> • Deep Rail • Hole
			Circumferential weld	Cracks develop in weld heat affected zone. Cracks propagate circumferentially.	<ul style="list-style-type: none"> • Weld Bead/Heat affected zone
			O.D. Strut Leading edge & I.D. strut T.E. location	Cracks develop adjacent to weld bead where strut is welded to case standup.	<ul style="list-style-type: none"> • Weld bead/heat affected zone • Thick to thin section transition • Strut to standup mismatch

- Rails. Deep rails can be subjected to thermal gradients that can produce high levels of stress. These rails would be used in the areas of flanges, stiffening rails, and retention rails for vanes or other static structure.
- Holes. Holes are an obvious area of concern due to the effect of producing a local stress concentration. Additional problems arise when embossments are used to reduce the local-stress concentration of the hole if these embossments are large or cause the local case area to become overly stiff. Obvious critical areas to review are flange holes, case wall embossed holes as incorporated in service or inspection ports, and any types of attachment or air passage holes.
- Fillets. Fillets provide a transition between thick and thin case sections and are an area of concern due to their local stress concentration effects. They are typically located in areas where thick to thin section transitions can produce local stress problems, due to the stiffness or thermal fight such as at the embossment-to-case wall transition, flange-to-case wall transition, or where local geometry features, such as airfoil struts, join to the case walls.
- Weldments. Weldments produce a wide variety of problems that should be reviewed for cracking potential. Welds have an inherent local stress concentration due to the weld bead geometry. The welding of embossments into thin case walls has the potential for local stress problems due to the misalignment between the case wall and the welded-in detail. The centerline mismatch can produce high local-bending stresses in the part. The weld process itself has the potential to produce crack initiation sites due to lack of cleanliness, microcracking, voids, or other manufacturing-induced defects.
- Casting Flaws. Case integrity is also affected by flaws that occur in case material that are inherent to the casting process. Examples of flaws would be casting porosity, material contamination, or tears. The difficulty in dealing with casting flaws is that they can occur randomly throughout the case structure, making the entire case as a possible site for crack initiation. This requires that cast cases be treated in a different method from wrought cases that are not as prone to subsurface defects. The stress field, throughout the casting, must be controlled to a level that will tolerate the potential defects without reducing the case structural integrity.
- Special Manufacturing Methods. The usage of special manufacturing methods such as electrochemical machining or electrodischarge machining can produce areas that are more prone to cracking than the standard turned or milled manufactured surfaces. These areas should be reviewed for material degradation and geometric features that are unique to the manufacturing method, which could produce a cracking problem.

2.2.2 Define Level of Analysis for Critical Areas.

Different analytical methods can be used to determine the level of operating stress in various critical areas of static cases. Experience dictates the level of analytical sophistication required for these areas. The analytical techniques used range from simple hand calculations to determine

background stress to very detailed three-dimensional finite element analyses aimed at determining the local stress field. This task will identify the level of analysis required for the various critical areas identified in task 2.1 such that sufficient stress detail is obtained to calculate the progression of cracks in these areas while maintaining a cost-effective evaluation procedure.

Most analyses begins with a simplified approach to identify the most critical areas and then determines if a more complex and time-consuming detailed analysis is required. A simplistic example would be a hole in the case wall. The simplified approach of calculating the pressure-induced stress with a hand calculation of P_r/t and combining this with a stress concentration calculation from a K_t handbook would be acceptable for low levels of pressure-induced stress. However, if the pressure-induced stress is significant, or the stress at the hole is influenced by the presence of embossments or other geometric details, a finite element analysis of the area would be more appropriate.

The following guidelines present the minimum analysis requirements for case-critical areas. The ability to model and analyze detailed case structures quickly and efficiently using three-dimensional finite element analysis techniques have been developed to a point where this is the preferred methodology to be used. These methods are summarized in table 31.

- Smooth Pressure Wall. Most case analysis should begin with a simple two-dimensional finite element analysis of the case structure to identify the overall level of background operating stress in the case due to pressure and thermal gradients. This simplified level of analysis is normally sufficient to determine whether flaws in the pressure wall of the vessel could be critical. The results from this analysis can also be used with handbook stress concentration factors to determine if any of the simpler geometric features could be life limiting.
- Rails. The evaluation of the stress field in rails will typically require a two-dimensional finite element analysis. This allows the analyst to account for geometric features, such as fillets or holes, that are typically found in these rails. Rails that are adjacent to geometric features that create large stiffness variations, such as large embossments, may require a more detailed three-dimensional analysis technique.
- Holes. Holes typically require a finite element analysis of some level of sophistication for evaluation. Two-dimensional finite element analysis should be sufficient to obtain the stress distribution around a hole in a flange or rail while a more detailed three-dimensional finite element analysis is normally required for embossed holes.
- Fillets. Fillet stress levels and die out can normally be obtained through the use of two-dimensional finite element analysis techniques. Fillets at the base of embossments or in areas with adjacent structures that may affect the flow through stress would require a three-dimensional finite element analysis for proper stress evaluation.
- Weldments. Evaluation of the stress field in a weldment relies on accurate definition of the mating pieces and the local geometry of the weld. This area can be analyzed using a two-dimensional finite element calculation method; however, weld process variations

makes accurate modeling of this condition difficult. The evaluation of a weldment is best done through finite element analyses combined with historical data obtained on the weld process and its affect on stress and life.

- Special Manufacturing Methods. Special manufacturing techniques bring the unique challenge of understanding the stress field in this area and determining if it is a critical area. The use of detailed or simpler analysis techniques will be dependent on what manufacturing method is being used. However, these methods normally produce details that fall within one of the already identified critical areas that could use the recommended analysis technique for that area. An example of this would be the machining of a case outer wall using electrochemical machining. In this case, the process normally produces raised ridges with fillet radii on the case wall. The evaluation of the stress field in this area would be done using the recommendations for the pressure wall and fillet areas. Each unique situation must be addressed on an individual basis to determine the required level of analysis sophistication.
- Castings. Casting flaws can occur randomly throughout a cast case although certain areas such as gating locations, thick sections, or transition areas may be more prone to having flaws. The possibility of the random occurrence of this flaw requires knowledge of the stress levels in all of the critical areas discussed in this section. Each individual area should use the required stress analysis techniques to ensure that this happens.

TABLE 31. LIST OF CRITICAL LOCATIONS ON DIFFUSER CASES AND THE REQUIRED FEA

Critical Area	Minimum Required Level of Analysis
Smooth Pressure Wall	2-D Finite Element Analysis
Rails	2-D or 3-D Finite Element Analysis
Holes	2-D or 3-D Finite Element Analysis
Fillets	2-D or 3-D Finite Element Analysis
Weldments	2-D or 3-D Finite Element Analysis
Castings	Local requirements apply
Special Manufacturing Methods	Local requirements apply

2.2.3 Crack Growth Prediction Methods.

In addition to characterizing material properties for high-time components with multiple repair cycles, the ability to accurately calculate stress-intensity factors is required to predict crack growth and the level of risk involved in their continued operation. This contract has used both linear elastic, and fracture mechanics techniques in addition to evaluating and applying more complex solution techniques.

2.2.3.1 Linear Elastic Fracture Mechanics.

P&W, as well as the rest of the industry, have used linear-elastic, fracture mechanics codes like NASGRO, BIGIF, or AFGROW that idealize the model of the cracks to evaluate crack growth in engine static components. P&W uses an internally developed code, SURCK, that uses widely

accepted, stress-intensity formulations (SIF), developed by J. C. Newman and I. S. Raju, in addition to other geometry specific formulations. This provides SURCK with stress-intensity solutions considered state of the art for crack configurations operating in elastic stress fields. SURCK's capabilities include modeling of embedded-through and part-through cracks in finite plates and in holes in finite plates and has demonstrated excellent correlation with specimen data. Loading capabilities include constant-amplitude load cycling, modified rainflow-cycle pairing, crack closure, Willenborg load interaction models, and mission damage accumulation. Typical output from this program describes the cyclic growth of a crack from a prescribed initial crack length to a critical crack length. Subsequent remaining life versus flaw size is summarized for individual cycles and for the complete mission.

Most life-critical areas on gas turbine engine components occur in holes, notches, or other geometrical stress raisers where the state of stress is elastic-plastic E/P. SURCK includes an elastic stress to plastic stress "shake-down" capability that provides a more accurate calculation of the true stress state which breeds cracks in locally yielded regions.

Correlation of this complete system shows a significant improvement in accuracy over previous design systems. Every crack growth rate (CGR) model developed for use in SURCK is derived from a simple, well-calibrated ASTM CGR specimen test. Correlation of these models to notch component subelements under constant-amplitude and mission loading consistently shows good accuracy.

The most significant development effort for SURCK has been on SIFs and stress field modeling for a surface crack under an arbitrary stress field. To address this problem, SURCK uses more accurate SIF formulations for cracks in gradient stress fields and load interaction models, which reduces the conservatism found in other life prediction programs. Computational efficiency is achieved in SURCK by using a "crack-length" integration technique instead of a "cycle-by-cycle" method. This allows multiple analysis simultaneously, which is necessary when performing full mission analysis on several life-critical component locations.

SURCK operates on elastic stress distributions defined over the plane of a crack and acting normal to that plane. These distributions are assumed to be isothermal as a function of position in the plane. In general, temperature will vary with time.

Elastic stress distributions may be input explicitly if the analyst so chooses. However, for most problems, it is possible to describe the variation in the distribution of stress at a notch over time. This variation might consist of one or more values of "nominal" stress, which varies with time along with a description of one or more stress gradients. The magnitudes of these stress gradients vary with position but not with time. The total elastic stress field is constructed from the gradient(s) and nominal stress value(s) via the principle of elastic superposition. The distribution associated with a particular component is formed from the product of the gradient and nominal stress value for that component and the total stress is the sum of the various components. The use of stress gradients can significantly shorten the input requirements for the analysis.

Concentrated elastic stress fields in engine hardware typically operates at levels above the proportional limit of the material. As illustrated in figure 64, the elastic stress must be converted to a combined elastic-plus-plastic stress field. There is an elastic-plastic shakedown (EPLAS) option in the SURCK program that can be used to determine the combined stress state based on the user-supplied elastic stress field and material stress-strain response. This response is described by a Ramberg-Osgood fit of the elastic modulus, proportional limit, 0.2% yield stress, and ultimate stress and strain. Using von Mises yield assumptions, the shakedown stress state is determined iteratively (via Newton-Raphson scheme) through simple force balance, which thereby ensures global equilibrium. Figure 65 shows a comparison of EPLAS results to a plasticity analysis using the MARC finite element program. EPLAS is shown to compare well with the MARC results for a PWA 1216 bolthole specimen loaded to 100 ksi net section stress considering room-temperature cyclic material properties. For most applications, life prediction accuracy improves when cyclic stress-strain properties are inputed.

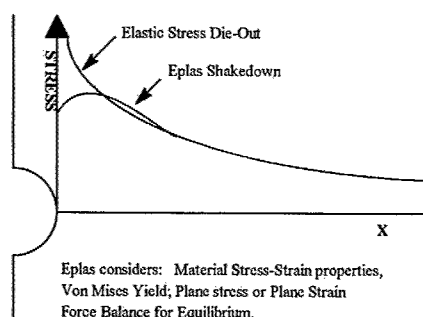


FIGURE 64. EPLAS STRESS SHAKEDOWN OPTION USED IN SURCK

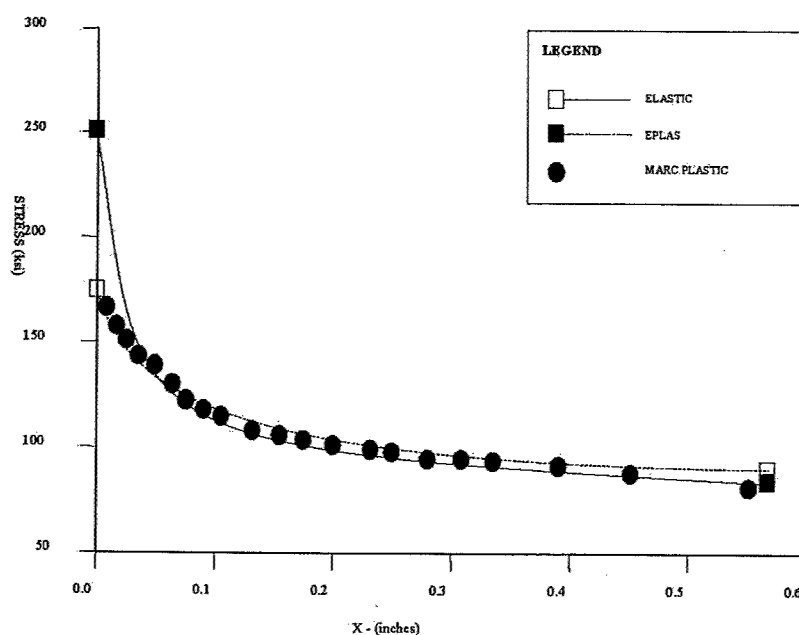


FIGURE 65. COMPARISON OF MARC RESULTS TO EPLAS FOR BOLTHOLE

2.2.3.2 Explicit Fracture Code Evaluation.

There are locations on many engine components that do not readily lend themselves to fracture analysis using conventional models of cracks in plates (as used in SURCK, NASGRO, BIGIF, etc.). This can be due to complex geometry, multiaxial stress states, constrained thermal stresses, or multiple load paths. There are often field problems arising for which the stress-intensity solutions, which are found in these codes, are overly conservative.

P&W has pursued several methods of implicitly determining stress-intensity factors (K) using finite element analysis (FEM)-based approaches (ANSYS crack tip elements) and other dedicated fracture codes. The FEM based approaches have always turned out to be extremely manpower intensive and require a high level of expertise. Therefore, in the first part of task 2, three explicit fracture codes have been evaluated that will reduce the labor overhead associated with explicit K calculations.

After surveying the explicit fracture codes available, the three codes that were selected for evaluation were BEASY, SAFE-3D, and FRANC-3D. BEASY is a commercially available boundary-element code developed by Computational Mechanics Inc. SAFE-3D is a hybrid finite element/boundary-element code that was developed by the United Technology Research Center (UTRC). FRANC-3D is a boundary-element code developed at Cornell University, by the Cornell Fracture Group (CFG), funded in part through the National Aeronautics and Space Administration (NASA) and the National Science Foundation and available for download free of charge from CFG's web site at www.cfg.cornell.edu.

Since all three of these codes are still evolving, the capabilities and shortfalls discussed in this report are based on a snapshot in time. This effort spanned most of 1998. The code evaluation addressed ease of use, applicability to a wide range of problems, and loading conditions. The results of the usability review are provided below. Of the three codes, FRANC-3D was the only one found to have the capability to handle the wide variety of problems encountered in turbine engine components. Thus, it was the only code where accuracy of results was evaluated.

2.2.3.3 SAFE-3D Evaluation.

At the time of evaluation, the SAFE-3D code was a planar crack growth code and was an outgrowth of the SAFE-2D code developed during the 1980s at United Technology Research Center. An update to the code was planned for mid 1999, which would include nonplanar crack propagation. A meeting was held with UTRC to review the capabilities of the SAFE-3D fracture code. SAFE-3D uses a hybrid finite element/boundary-element approach to determine crack propagation rate and direction.

SAFE-3D code uses two input files to create a SAFE-3D data file for analysis. The first input file is a PATRAN neutral file that contains the nodes, elements, material properties, boundary conditions, and loads for the geometry being analyzed. This data is converted by SAFE-3D into a data file for the NONSAP finite element code used to determine the stress state as the crack progresses. The second input file defines the crack location, orientation, and initial geometry along with the material crack growth rate law (note: only the Paris law is currently supported). This information is used to define a boundary-element mesh for the surfaces of the crack. The

boundary-element solution is used to determine the stress-intensity factors around the crack boundary.

The data file created from these two input files is run using a nonlinear analysis with the number of time steps and crack growth increment (specified as a percentage of original crack length) per time step as specified by the user. The number of cycles required to grow the crack to the specified increment is then back calculated using the specified crack growth law.

If it is determined that the crack has grown through an element in the finite-element breakup, the stiffness matrix is reformulated and reanalyzed to update the tractions for the boundary elements.

The following observations were made on the code capability, limitations, and problems:

1. The required conversion of the PATRAN model neutral file to a NONSAP structural model may create compatibility problems relative to elements, loads, and boundary conditions. Element library, MPCs, RBEs, gap elements, etc., need to be investigated to determine if they can be supported by NONSAP. The optimum solution would be for SAFE-3D to use NASTRAN or ANSYS as the FEM solver instead of NONSAP.
2. The loading capability in the current version is very limited with no support for rotational inertia loads or thermals loads.
3. No reasonable (user-friendly) means is available to evaluate the SAFE model after conversion from the neutral file. The program generates many warning messages concerning data in the neutral file that has not converted. The warnings do not tell you what data is being ignored. There is no way to postprocess the stress and deflection results to determine if the model is behaving as intended.
4. Nonplanar crack growth capability is needed with a menu of the crack-turning calculation options.
5. It needs tabular and plot output capability for a versus N and K versus crack size. Also needs user-friendly output showing crack advancement and deflected structure plots.
6. Current user-specified increment of crack size for life prediction may result in integration steps that are too coarse for an accurate life prediction for cracks in steep stress gradients and in near-threshold of da/dN curve; need a "smart" algorithm in the code to test and refine step size as needed.
7. Based on sample case runs, computer time to run expected 3D FM models might be extremely high on available resources. This may be due to the NONSAP FEA solver or the SAFE-3D code itself. The Small beam model ran 20-30 minutes.
8. Anisotropic-material property capabilities in SAFE-3D are needed to address single crystal materials. Note that none of the codes evaluated had this capability.
9. No current mission crack growth predictions.

2.2.3.4 BEASY Evaluation.

Investigation into the BEASY 3D crack growth capability showed that while the code was found to be less computationally intensive than FRANC-3D and SAFE-3D, it has some limitations that made it unsuitable for gas turbine component analysis at this time. Like SAFE-3D, the current version of BEASY does not support thermal or centrifugal loading. FRANC-3D handles centrifugal loading directly and thermal loads using crack face tractions from FEA. BEASY cannot automatically propagate surface cracks because it lacks the ability to remesh the boundary surfaces.

There are also several usability issues that makes BEASY a less attractive choice. The process for defining a crack requires you to input the coordinates of points in space along the crack front. FRANC-3D provides a crack face library where all you have to do is define the origin of the crack along with its size and orientation. The program then calculates the points along the crack front automatically. In some instances (i.e., spline fit crack fronts), BEASY requires you to manually go into the database and modify it. This can lead to errors that may be hard to trace.

2.2.3.5 FRANC-3D Evaluation.

P&W has outsourced several complex fracture analyses to Fracture Analysis Consultants (FAC), Inc. over the last few years. These analyses have been performed using FRANC-3D. The code has subsequently been improved and expanded on by its developers who have now formed Fracture Analysis Consultants, Inc. The code is based on a boundary integral equation formulation with its own solid modeler. P&W has installed the code and has exercised it on several models of various complexities. The code has been successfully used by FAC for predicting crack growth in diffuser cases and fuel nozzles and disk structures.

The following observations are based on these trials and discussions with Dr. Wawrznek at FAC:

1. Creating a FRANC-3D model

- The code has an excellent user-friendly interface and the graphical user interface (GUI) can be accessed via with a drop-down menu.
- In addition to the internal solid modeler, a translator has been developed to create the FRANC-3D solid model geometry from ANSYS or PATRAN files. The code will also read the results file from an ANSYS or NASTRAN analysis to allow interpolation of the FEM element stress results to be used in the creation of crack face tractions for the FRANC-3D submodel. The results are then combined via superposition to determine stress-intensity factors in the cracked body.
- FEM thermal loads are translated as part of the crack face tractions discussed above. Thermals cannot be handled in a stand-alone FRANC-3D analysis.
- Excellent documentation is readily available on the web, with a Concept & User Guide, Menu & Dialog Reference, and Tutorial Examples.
- Supportability has been excellent with prompt updates for glitches found in the program.

2. FM Capabilities

- Easy to put an initial crack in a model by using either a selection from the flaw library or manually describing the flaw geometry. The flaw can then easily be rotated and translated to the desired location.
- The program will split the volume at the crack location and define the crack face surfaces. These surfaces can be viewed graphically to verify proper placement.
- The code provides both an automatic and interactive means to advance cracks. A maximum crack growth increment for the point on the crack front with the highest K value can be specified at each step. The growth of the rest of the crack front is currently calculated by scaling the maximum growth increment by the ratio of K_{local}/K_{max} raised to the Paris law power. The option to scale, using a hyperbolic sine law, is being added to FRANC-3D.
- For crack growth life calculations, the code has capabilities of using several crack growth rate equations (SINH, Paris, and Foreman).
- K histories can be plotted at either the maximum K location or along user-defined trajectories for every crack front analyzed.
- The next version will do mission crack growth analysis using calculated K vs a history.

3. Excellent postprocessing capabilities

- Color contour displays can be made of stresses and displacements of the cracked body.
- X-Y plots and tables of all three crack front stress intensities (Ks) as a function of the normalized crack front location.
- Visual representation of the next crack front based on the user-supplied growth increment prior to tearing the crack for the next crack step. This allows you to modify your input if it looks like the crack is taking too big of a step.

4. FRANC-3D currently has only isotropic property modeling capability, but FRANC-2D has orthotropic-elastic property and toughness modeling capabilities. The next generation of FRANC-3D will include orthotropic capabilities (see below).

2.2.3.6 Fracture Code Preliminary Evaluation Summary.

Based on the capabilities of the codes as evaluated in 1998, FRANC-3D was the best suited for the types of problems generally encountered on turbo machinery. The largest shortfall in the other two codes was the lack of general loading capability (especially rotational inertia and thermals). Additionally, the FRANC-3D user interface and the ability to import geometry from

ANSYS and NASTRAN finite element models resulted in reduced manpower to generate models and postprocess results.

2.2.3.7 FRANC-3D Validation.

Documentation for extensive validation testing of the FRANC-3D code is available on the Cornell Fracture Group web site at www.cfg.cornell.edu under the software menu. P&W, using FRANC-3D, ran several test cases for comparison with known closed-form or curve-fit FEM solutions. Of special interest, are the runs made with the model loaded explicitly in FRANC-3D compared to the runs made with the same models but using the stresses from a finite element model as crack face tractions. The concern, when using crack face tractions, is using stress distributions from an uncracked FEA model to apply crack face tractions. These tests showed that the load redistributes in the FRANC-3D model, and the results matched within 8% for very large crack sizes ($a/W = 0.7$).

The results for the following two simple test cases illustrate the advantages of an explicit 3D fracture code. The results presented below are for a rectangular bolthole specimen with a corner crack loaded in simple tension (figure 66) for the first case and in bending for the second case.

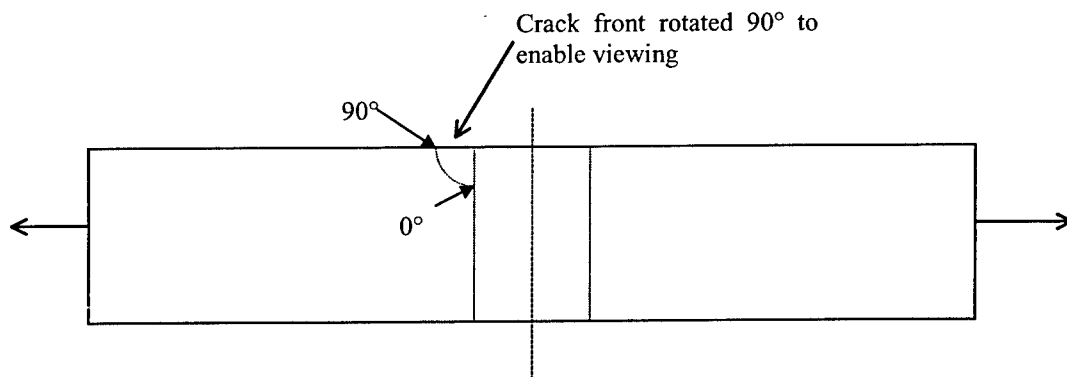


FIGURE 66. BOLTHOLE SPECIMEN WITH TENSILE LOAD

In both cases, predefined crack fronts with a 1:1 aspect ratio ($a/c=1.0$) were modeled to obtain K solutions as a function of crack length. The tensile load on the first case results in a simple stress die out in one direction. The results for four angular locations around the crack front for a bolthole in tension are shown in figure 67. In these plots, 0° is in the barrel of the bolthole and 90° is on the surface of the specimen.

For this simple case, the FRANC-3D results agreed with the Neuman and Raju model and are in line with the other in-house models used for univariant stress field die outs. As an additional test of FRANC-3D's capability to use the stress field from an FEM analysis to convert to crack face tractions, the results from an ANSYS bolthole tension model were used to duplicate the data shown in figure 67. The results showed that there was less than 8% error up to fairly large crack lengths ($a/t = 0.6$). These results were very encouraging since there was some concern about using the stress field for an uncracked body to predict the response for parts where the cracks may get fairly large before becoming unstable.

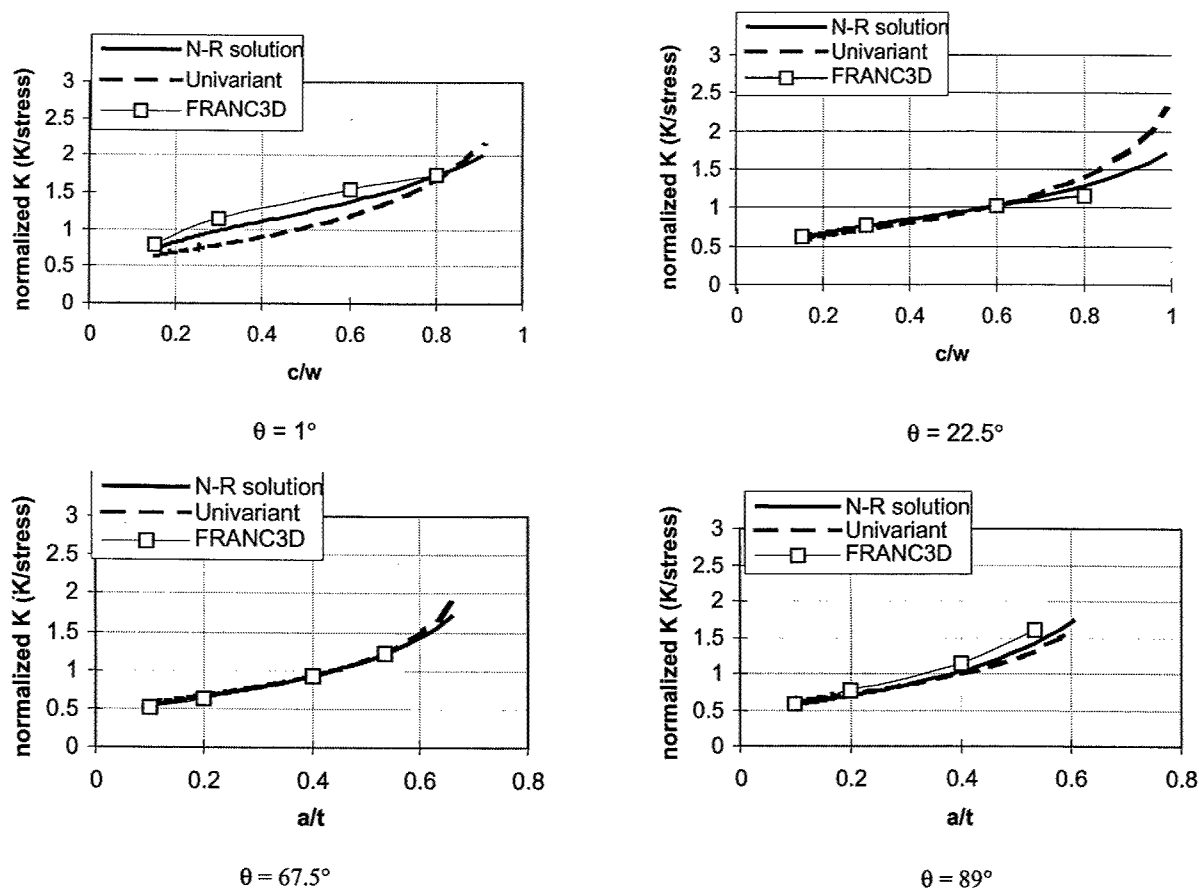


FIGURE 67. BOLTHOLE TENSION SPECIMEN STRESS-INTENSITY CORRELATION

The more difficult case is the bolthole specimen in bending where there is a strong bivariate stress gradient. For this condition, the Neuman and Raju results are in error (per telecon with Neuman) and are not shown. The in-house bivariate solution (based on the slice synthesis approach) and average K method are used as a comparison. The results from this model are shown in figure 68.

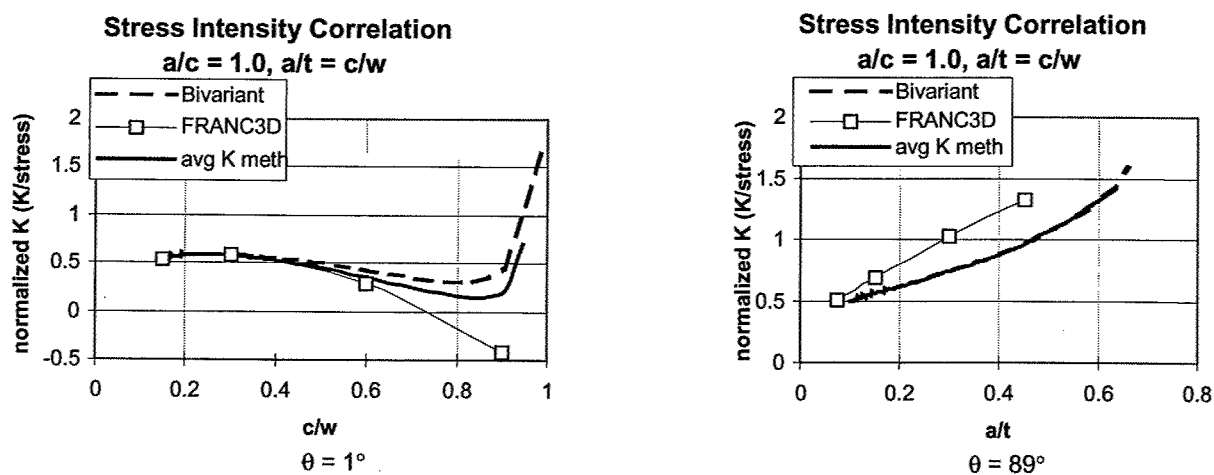


FIGURE 68. BOLTHOLE BENDING SPECIMEN STRESS-INTENSITY CORRELATION

These results show that for small crack lengths ($< 0.6 c/w$) in the barrel of the hole ($\theta = 1^\circ$) the various solutions correlate well. However, for longer crack lengths, the FRANC-3D solution is the only one that shows the stress intensities going negative as the crack advances into the compressive stress field. Obviously, these are forced crack fronts that would not naturally grow at a 1:1 aspect ratio into a compressive stress field. The stress intensities predicted by FRANC-3D, as the crack advances from the hole across the face of the coupon ($\theta = 89^\circ$), are somewhat higher than the other predictions, which shows that FRANC-3D is accounting for the higher stress in the remaining ligament. This simple test case shows the value of an explicit K calculation capability.

2.2.4 Prediction of Case Stress and Crack Growth.

Analysis of three P&W static high-pressure cases has been conducted to evaluate the ability of FRANC-3D and SURCK to predict crack growth in “aged” case material. The calculations have been compared to operational engine crack growth data for wrought Inconel 718 and steel cases and for a heat-treated (to simulate multiple repairs over time) cast Inconel 718 case, which were run in the P&W cyclic pressure rig.

2.2.4.1 Aged Steel Alloy Case Analysis.

A typical wrought steel case, the P&W JT8D-200 Combustor Chamber Outer Case (CCOC), was chosen to be analyzed. The case was made of two steel alloys (AMS 5613 and AMS 5616). The drain, the Ps4 boss, and the rear flange were welded to the case wall. The case has experienced cracking at the boss weld and flange boltholes during service operation. The analysis plan consisted of generating finite element models; conducting thermal, stress, and fracture mechanics analyses; and comparing the predicted residual life to the case field experience for calibration.

2.2.4.1.1 Case Models and Meshing.

The full CCOC is shown in figure 69. Two Unigraphics (UG) solid models of the cases are shown in figures 70 and 71. The solid models of the case include the drain, the Ps4 bosses, and the rear flange.

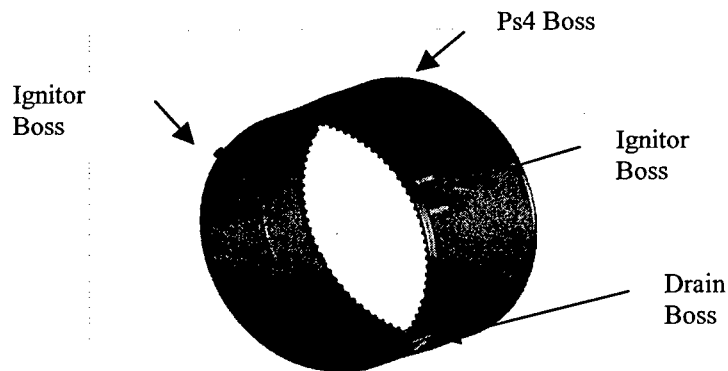


FIGURE 69. JT8D-200 SERIES CCOC GENERAL FEATURES

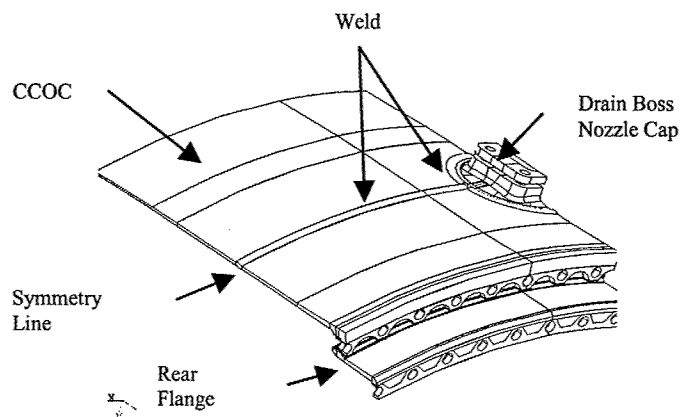


FIGURE 70. THE UG SOLID MODELS OF THE Ps4 BOSS USED IN THE ANALYSIS (MODEL 1)

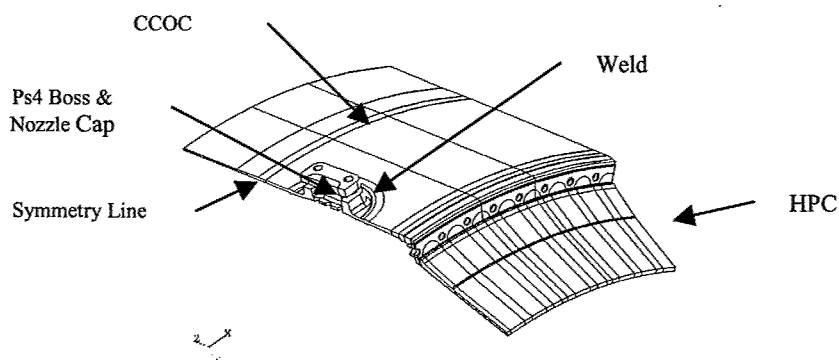


FIGURE 71. THE UG SOLID MODELS OF THE Ps4 BOSS USED IN THE ANALYSIS (MODEL 2)

The solid models were used to create ANSYS models that were used to perform the thermal and the structural analyses. The ANSYS models were meshed using 20-node brick elements for the case and 10-node tetrahedral elements for the bosses. Mesh density and elements types are shown in figures 72 and 73.

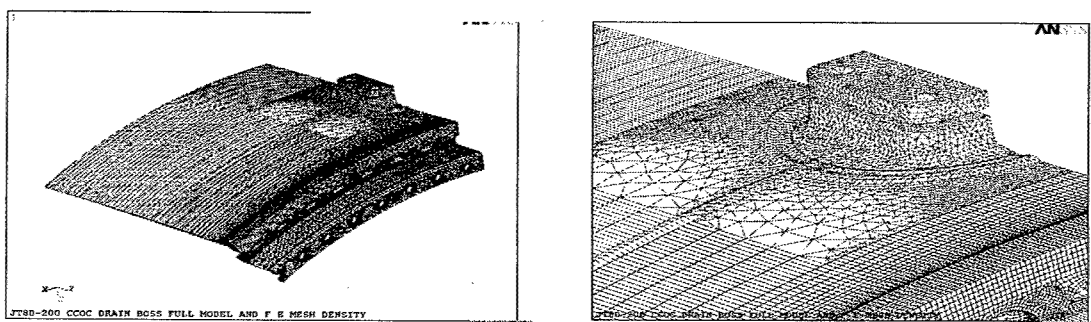


FIGURE 72. ANSYS 3D MODEL OF THE CCOC DRAIN BOSS (MODEL 2)

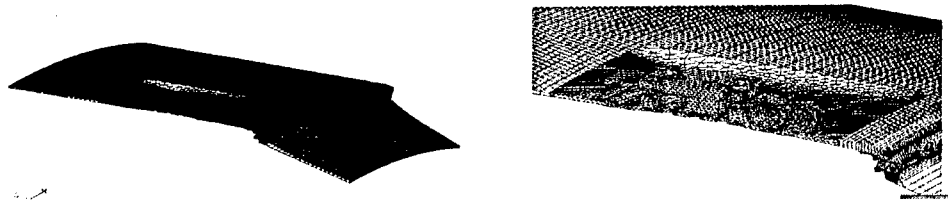


FIGURE 73. ANSYS 3D MODEL OF THE CCOC Ps4 BOSS

2.2.4.1.2 Thermal Analysis.

Transient thermal analysis of the CCOC was performed using a 2D axisymmetric model of the whole case and a 3D model of the drain boss. Thermal boundary conditions were calibrated to previously measured temperature data obtained from two engine tests. The CCOC was instrumented with 13 thermocouples (T/Cs) (10 metal and 3 air). Some of the locations of the T/Cs are shown in figures 74 and 75. The 2D axisymmetric model was used to calibrate the case wall temperature while the 3D model was used to calibrate drain boss metal temperatures. Steady-state and transient T/C readings were taken during the tests for a simple idle to takeoff engine cycle. This cycle is illustrated in figure 76. The boundary conditions were tuned until the simulated temperature matched the engine test results.

Figures 74 and 75 show the 2D model and a comparison of the predicted steady-state metal temperatures with the T/C measurements for the drain boss area. A comparison of the predicted and measured temperature during the mission at the drain boss locations is shown in figures 77 and 78.

Figure 74 shows the two bosses (Ps4 and drain boss) that are represented by two non-axis-symmetrical rectangles. A comparison between the measured and simulated steady-state temperatures for three selected T/C locations is also included.

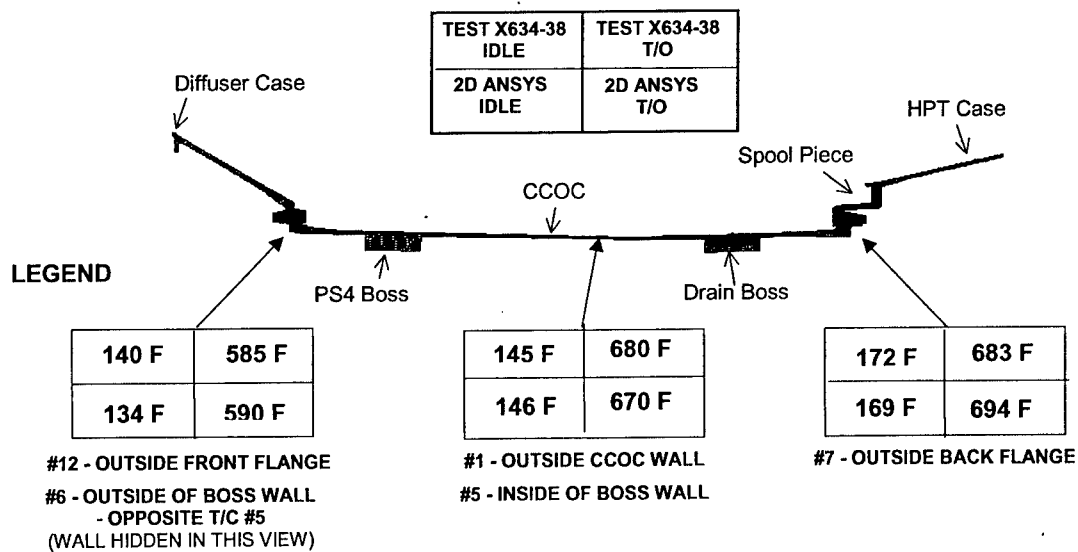


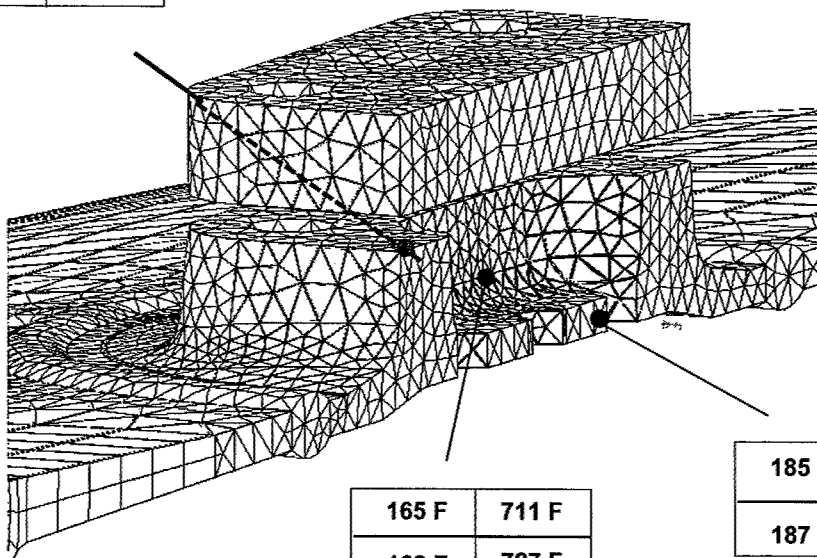
FIGURE 74. THE 2D AXISYMMETRIC ANSYS MODEL OF TWO BOSSSES

Figure 75 shows the 3D model of the drain boss of the downstream half of the CCOC, with a comparison between measured and simulated steady-state temperatures (both the open and closed drain tube case), at the locations for the three T/Cs attached on the boss.

#6 - OUTSIDE OF BOSS WALL
- OPPOSITE T/C #5
(WALL HIDDEN IN THIS VIEW)

149 F	615 F
148 F	631 F

ENGINE TEST X634-38 IDLE	ENGINE TEST X634-38 T/O
3D ANSYS BOSS TEMP. IDLE	3D ANSYS BOSS TEMP. T/O



165 F	711 F
168 F	727 F

185 F	787 F
187 F	805 F

#5 - INSIDE OF BOSS WALL

#4 - BOTTOM INSIDE OF BOSS

FIGURE 75. THE CCOC DRAIN BOSS IN THE 3D ANSYS MODEL

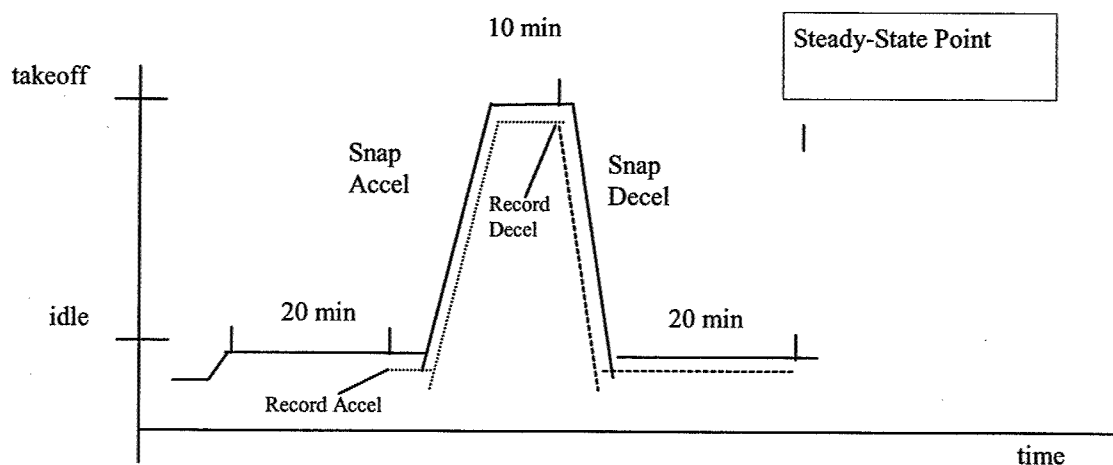


FIGURE 76. SCHEMATIC OF THE TEST CYCLE SHOWS THE STEADY-STATE AND TRANSIENT CONDITIONS

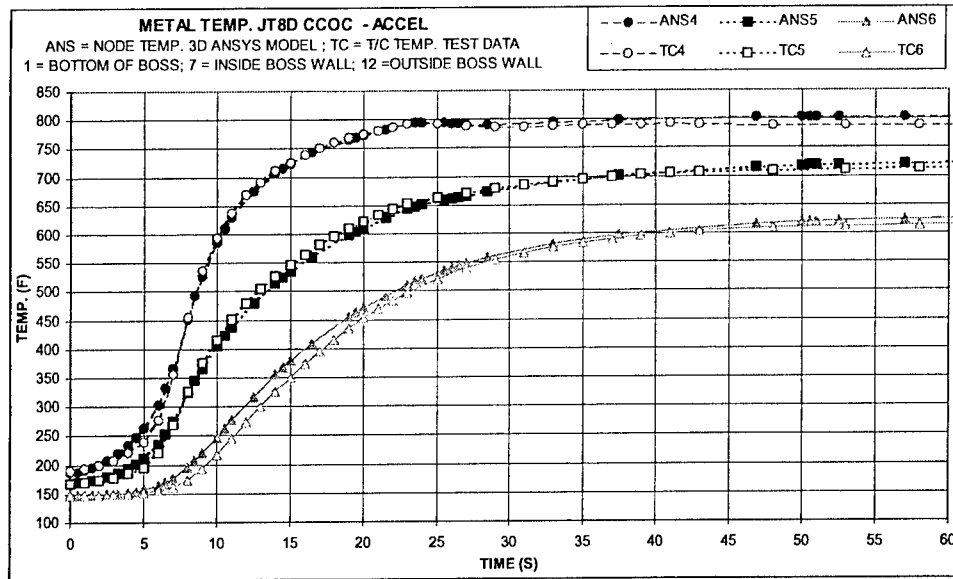


FIGURE 77. COMPARISON OF TRANSIENT TEMPERATURES FOR ACCEL BETWEEN MEASURED (TC) AND SIMULATED (ANSYS) (THE ANALYSIS; OPEN DRAIN TUBE CASE) FOR THREE SELECTED T/C LOCATIONS (The simulation was performed using the 3D ANSYS model of the rear half of the CCOC.)

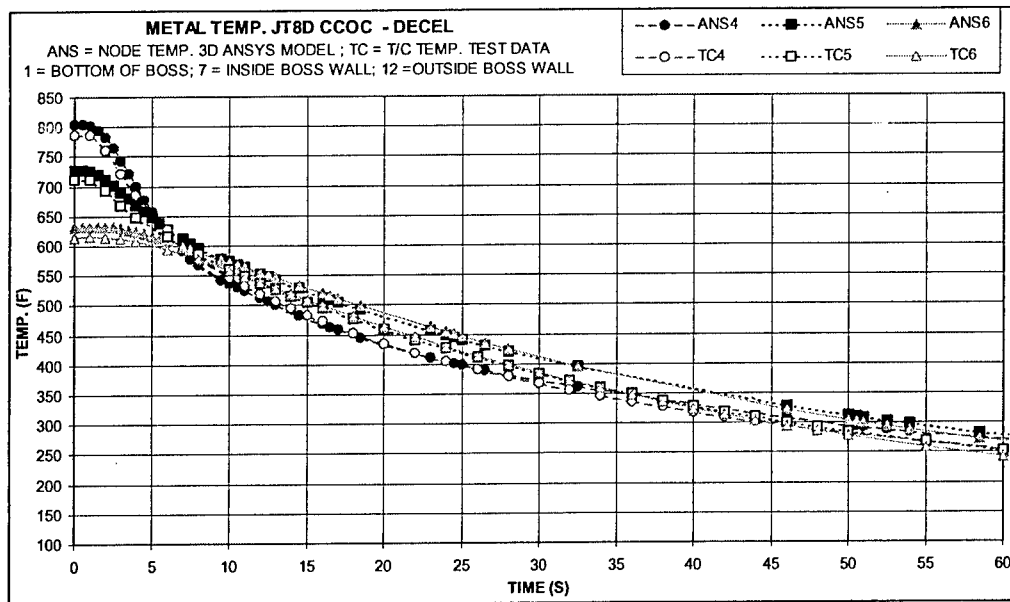


FIGURE 78. COMPARISON OF TRANSIENT TEMPERATURES FOR DECEL BETWEEN MEASURED (TC) AND SIMULATED (ANSYS) (THE ANALYSIS; OPEN DRAIN TUBE CASE) FOR THREE SELECTED T/C LOCATIONS (The simulation was performed using the 3D ANSYS model of the rear half of the CCOC.)

2.2.4.1.3 Structural Analysis.

A finite element structural analysis (ANSYS) was performed on the CCOC drain boss and Ps4 boss, with the models shown in figure 79. The case operating pressures and displacement boundary conditions shown in figure 79 were used. Axial case loading acting on the CCOC boundaries was also simulated at the rear flange surface.

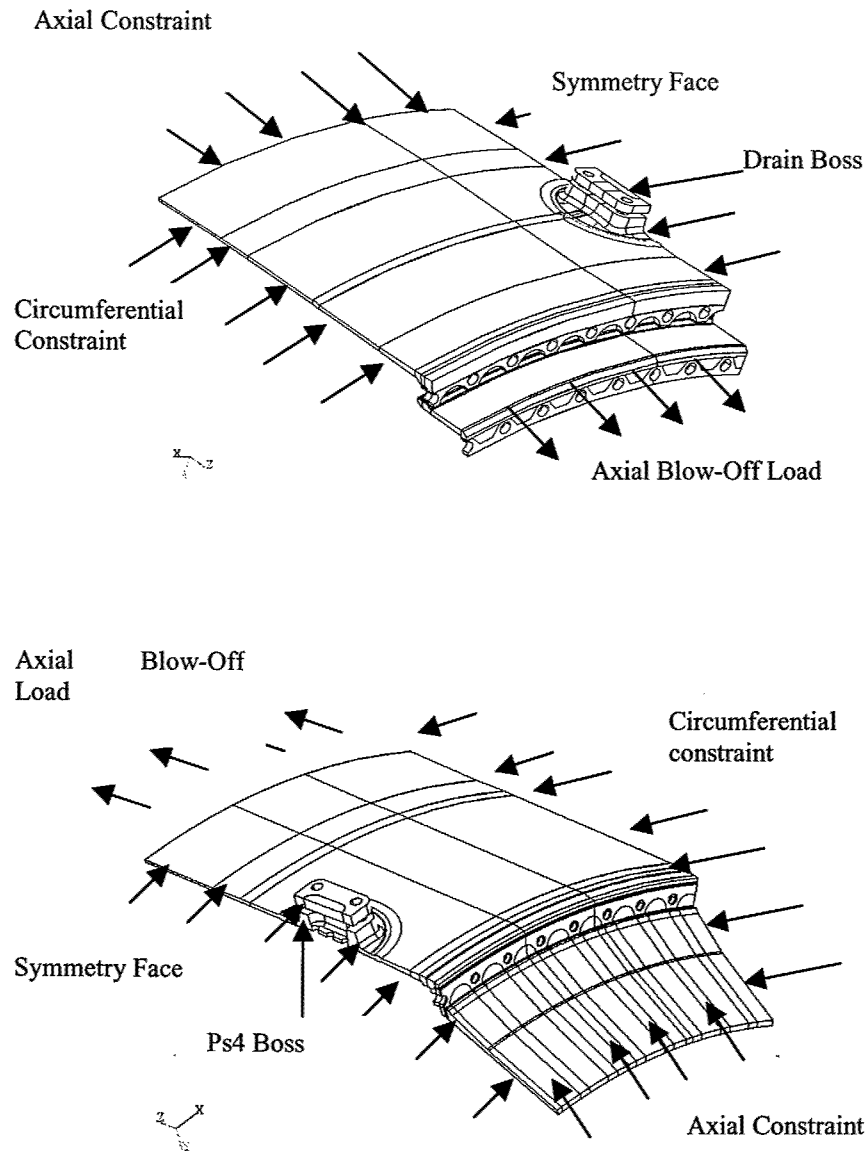


FIGURE 79. CCOC DRAIN AND Ps4 BOSS 3D SOLID MODEL AND APPLIED BCs

2.2.4.1.4 Stress Results.

Results of the stress analysis show that maximum stresses at the CCOC critical locations occur at 10 and 78 seconds into the engine acceleration. These times correspond to the maximum thermal

gradient on the boss. The maximum stress location of the flange was at the flange inner fillet and had a value of 116 ksi, as shown in figure 80, and in the boss areas at the weld fillet as indicated in figures 81 and 82. The analytical predictions agree well with the location of the CCOC field-cracking experience. Submodels of the drain boss and Ps4 boss were analyzed to acquire the maximum concentrated stresses of the two bosses at the weld toe. Figure 83 shows the submodels cuts at the critical locations of the bosses. A typical weld-to-case wall fillet radius of 0.005" was implemented in all submodels. Figure 84 shows the mesh density of the submodels. An analysis was performed using the displacement boundary conditions from results of the 3D full models at the operating points of 10 and 78 sec. Results from the submodel analyses are presented in tables 32 and 33. The maximum stress of the drain boss is predicted as 136.8 ksi at the operating time of 78 sec and 129.5 ksi for the Ps4 boss at the same operating time. Maximum principal stress distributions of the drain and Ps4 bosses are shown in figures 85 and 86.

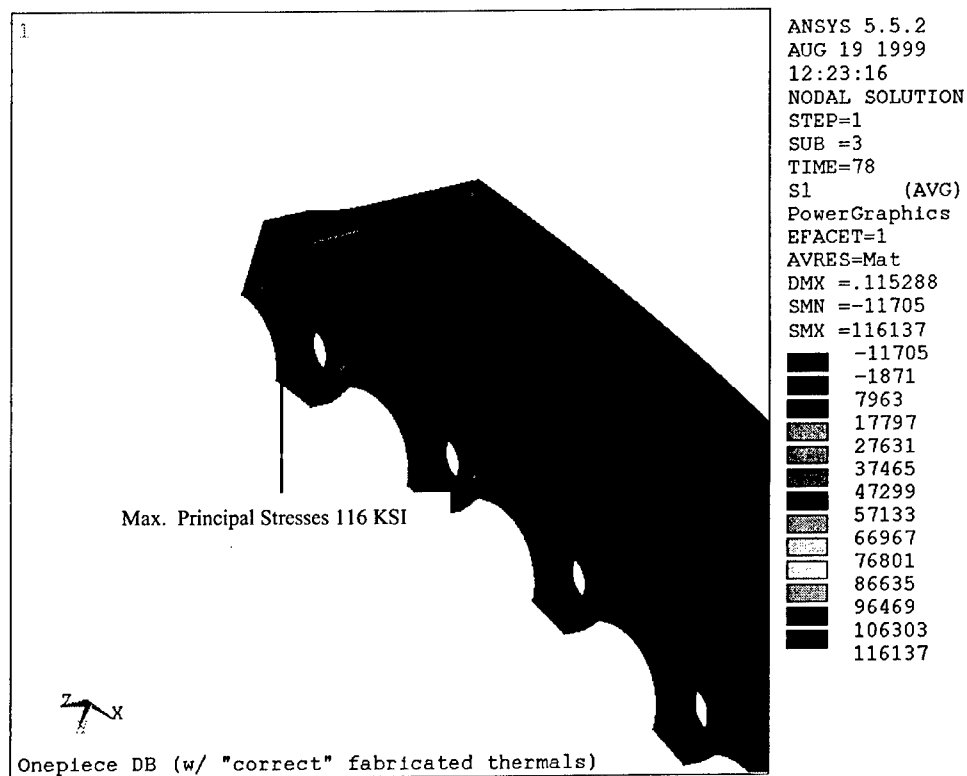


FIGURE 80. MAXIMUM STRESS LOCATION AT THE CCOC REAR FLANGE

Maximum principal stresses at the boss weld fillet

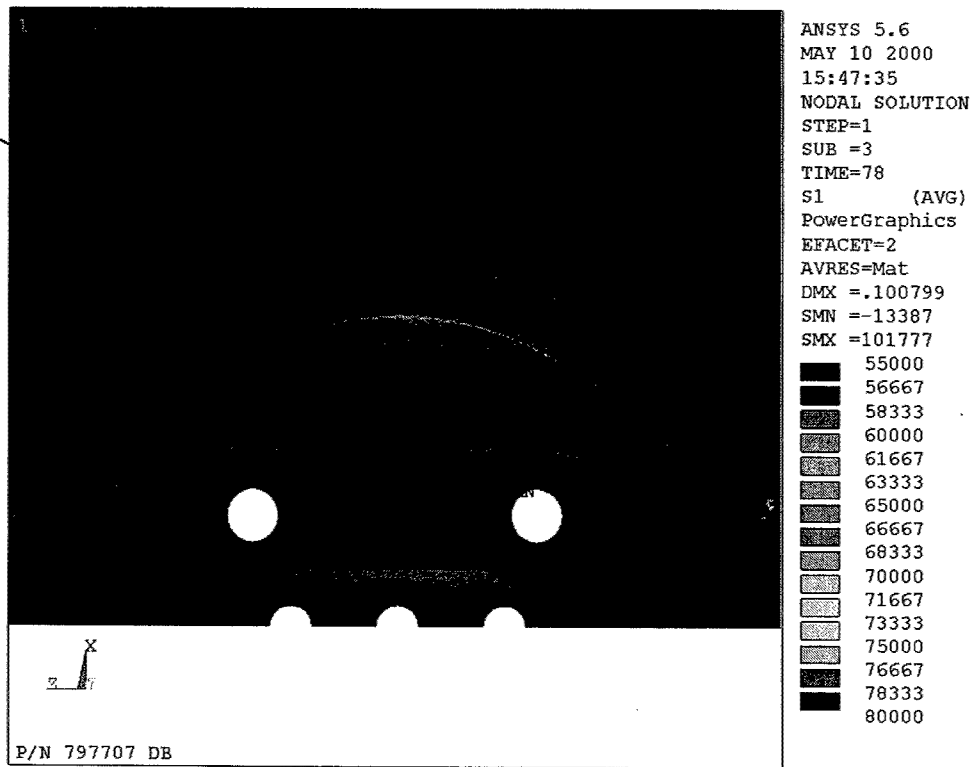


FIGURE 81. MAXIMUM STRESS LOCATION AT THE DRAIN BOSS WELD

Maximum stresses at the boss weld fillet

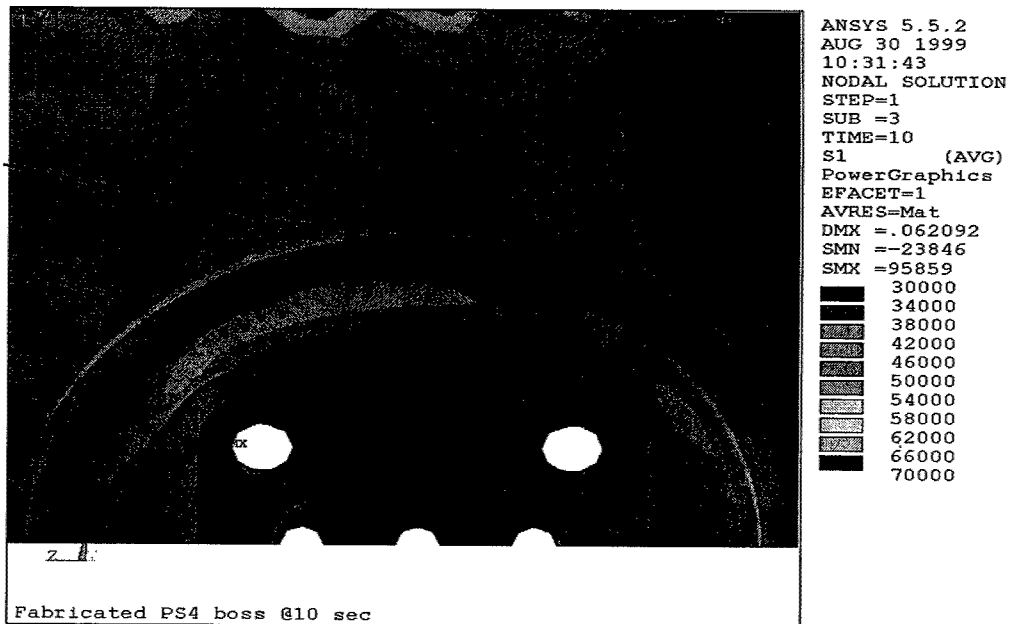


FIGURE 82. HIGH STRESSES AT THE Ps4 BOSS WELD REGION

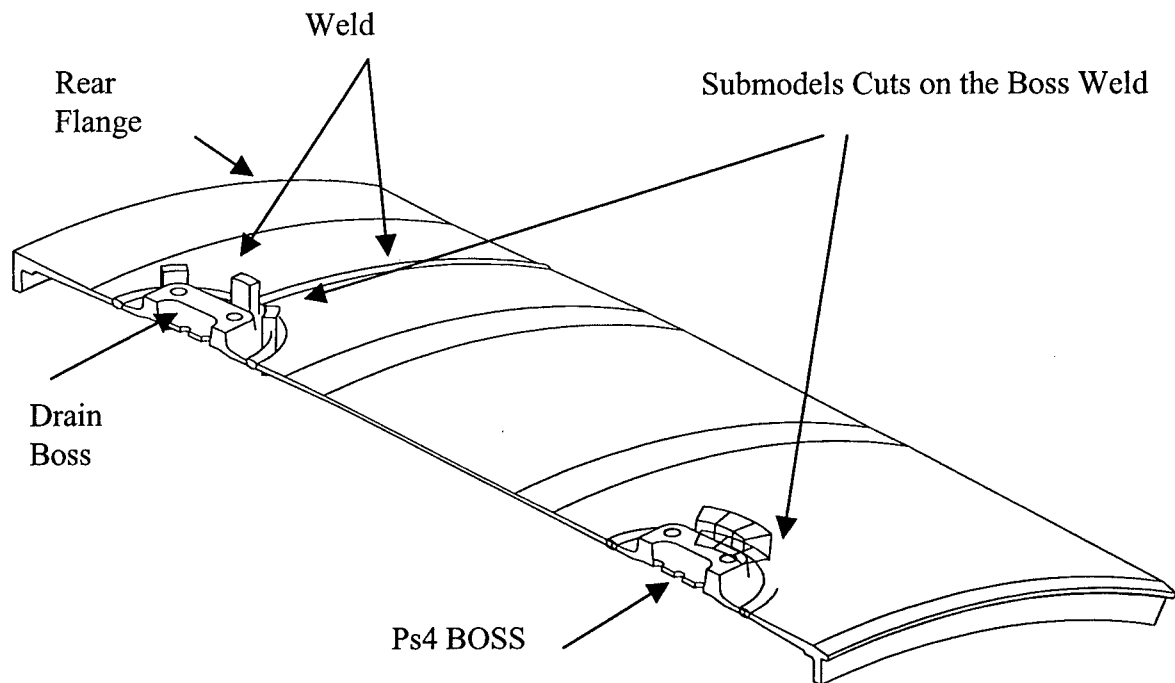


FIGURE 83. UG SOLID MODEL OF THE JT8D-CCOC SHOWS THE BOSSES FEATURES AND THE SUBMODELS SELECTIONS AT THE CRITICAL LOCATIONS ON THE WELD

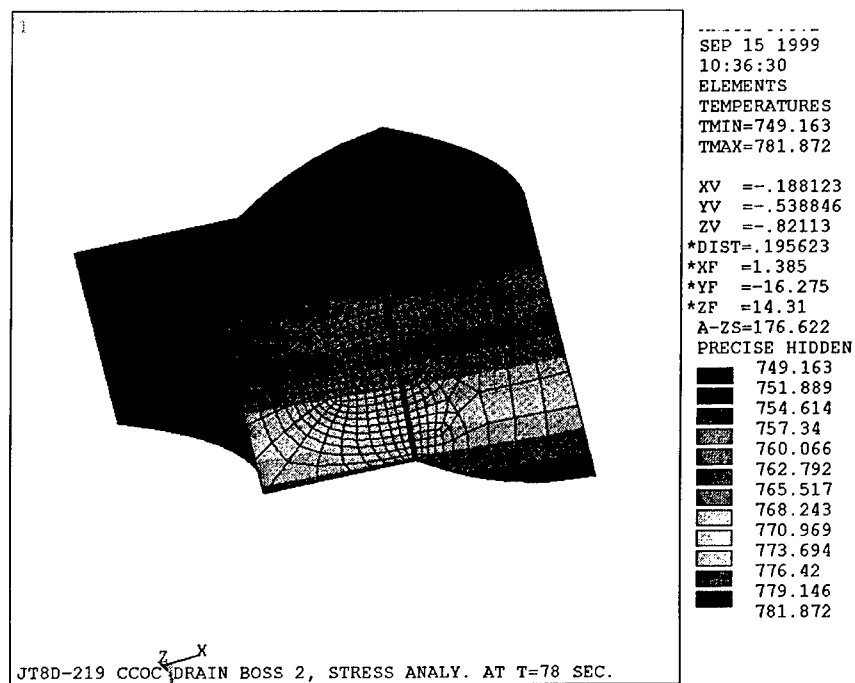


FIGURE 84. DRAIN BOSS SUBMODEL NO. 2 MESH DENSITY AND TEMPERATURE GRADIENT

TABLE 32. JT8D-219 CCOC MAXIMUM PRINCIPAL STRESSES AT THE DRAIN BOSS

Mission Time (sec)	Temp. Range (F)*	Prin. Stress (ksi)	Nom. Stress (ksi)	Location
10	375-----441	104.9	52.9	Submodel 1
78	746-----779	104.2	55.0	//
10	375-----445	135.9	63.1	Submodel 2
78	749-----781	136.8	63.0	//
10	373-----440	106	53.0	Submodel 3
78	744-----778	93.1	44.0	//

* Temperature range is the temperature gradient at this time from ID to OD of the case at this location.

TABLE 33. JT8D-219 CCOC MAXIMUM PRINCIPAL STRESSES AT THE Ps4 BOSS

Mission Time (sec)	Temp. Range (F)*	Prin. Stress (ksi)	Nom. Stress (ksi)	Location
10	357-----455	121.7	56.5	Submodel 1
78	679-----767	129.5	58.0	//
10	349-----442	118.3	54.6	Submodel 2
78	676-----782	126.2	57.2	//

* Temperature range is the temperature gradient at this time from ID to OD of the case at this location.

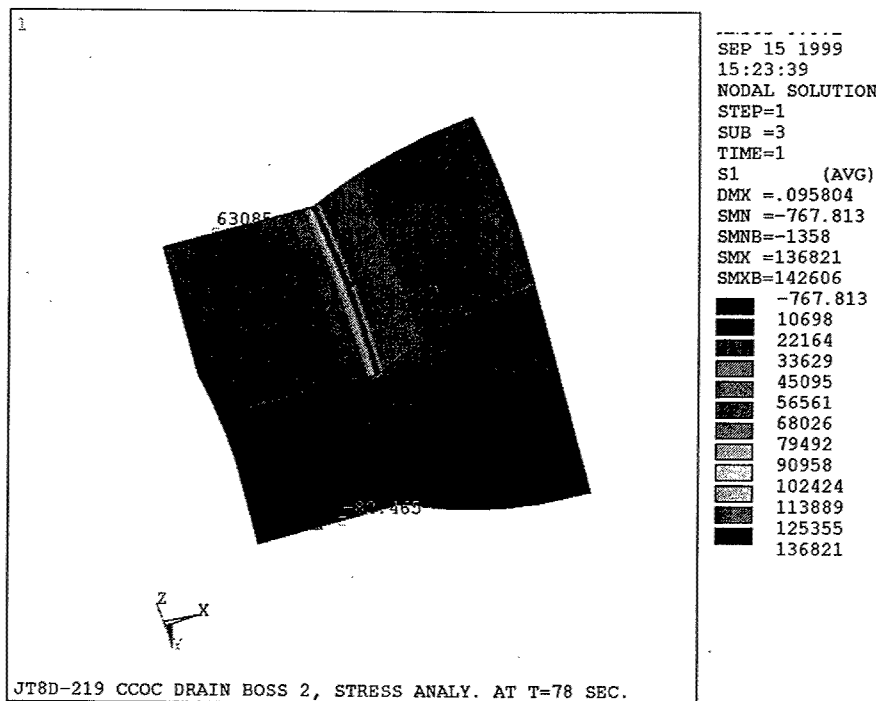


FIGURE 85. JT8D-219 CCOC MAXIMUM PRINCIPAL STRESSES AT THE DRAIN BOSS WELD FILLET

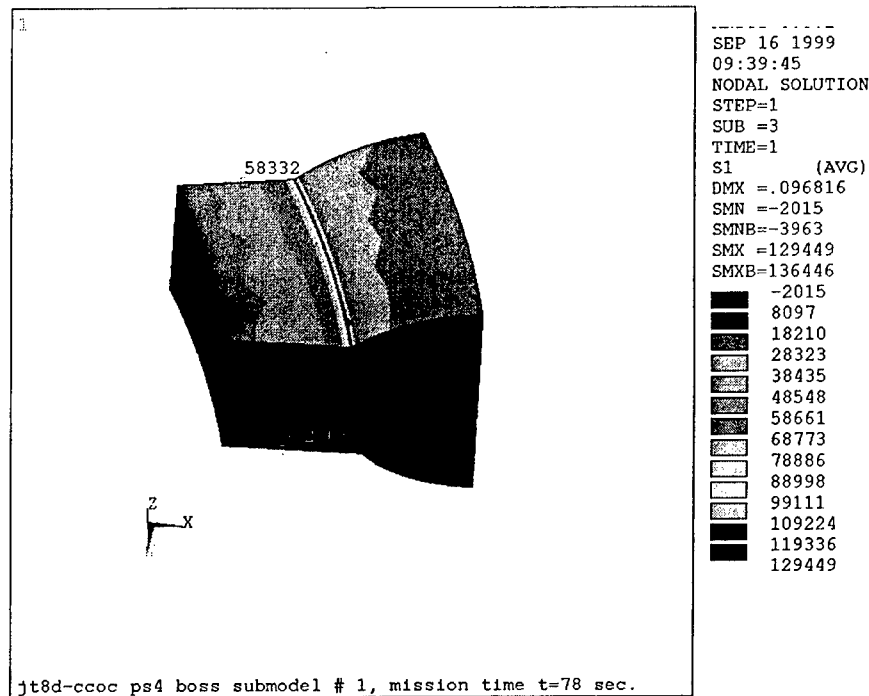


FIGURE 86. JT8D-219 CCOC MAXIMUM PRINCIPAL STRESSES AT THE Ps4 BOSS WELD FILLET

2.2.4.1.5 Fracture Mechanics Analysis.

A fracture mechanics analysis using SURCK was carried out to predict case residual life. It used the predicted CCOC drain boss stresses and the aged material crack growth properties from task 1.

2.2.4.1.6 Stress Gradient.

The stress gradient through the thickness of the case, as shown in figure 87, shows a peak stress at the outer diameter (OD) fillet radius (a high state of bending) of 136.8 ksi. That falls quickly to about 60 ksi after 0.008" below the surface and continues to decrease linearly to the inner diameter (ID) of the case wall. This stress gradient was used in SURCK to predict the case crack propagation.

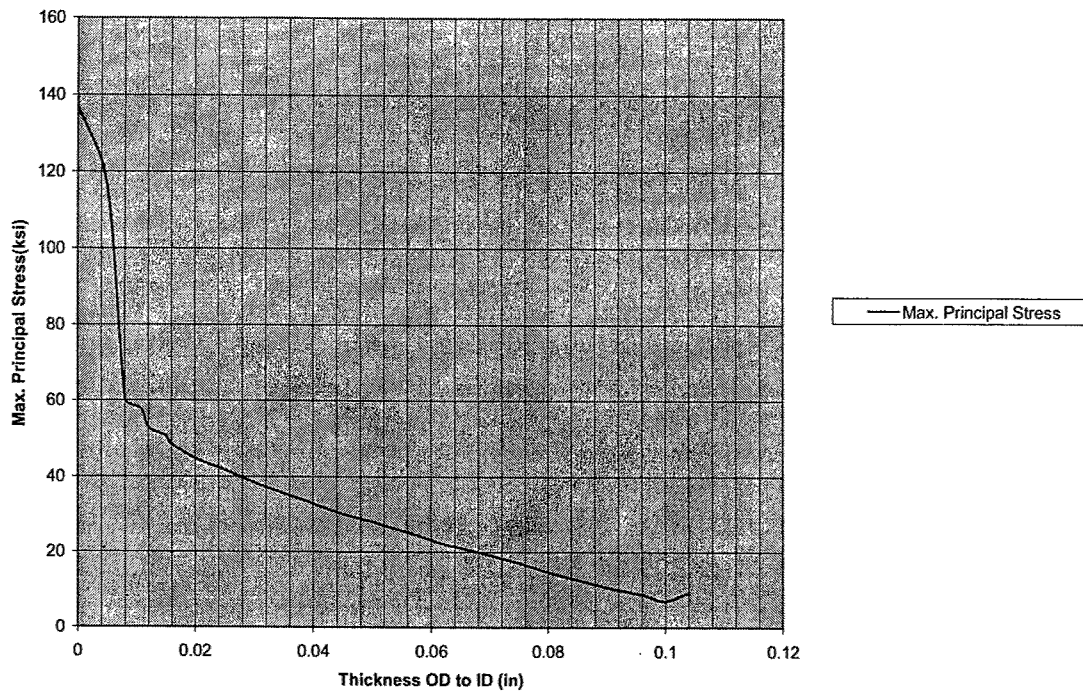


FIGURE 87. JT8D-219 CCOC DRAIN BOSS THROUGH THICKNESS STRESS GRADIENT

2.2.4.1.7 Material Crack Growth Properties.

The FAA Contract Material Specimen testing conducted in task 1 resulted in four different crack growth rates properties for steel alloys at 750°F and R = 0.1. The da/dN vs ΔK data was curve fit using the hyperbolic sine equation. The following are the typical crack growth rates of the wrought and weld steel alloys deduced from task 1 results.

1.	Base metal	$C1 = 0.5,$	$C2 = 3.583,$	$C3 = -1.414,$	$C4 = -5.026$
2.	Base metal, Aged	$C1 = 0.5,$	$C2 = 3.797,$	$C3 = -1.369,$	$C4 = -5.114$
3.	Weld metal	$C1 = 0.5,$	$C2 = 4.186,$	$C3 = -1.481,$	$C4 = -4.982$
4.	Weld metal, Aged	$C1 = 0.5,$	$C2 = 4.049,$	$C3 = -1.337,$	$C4 = -5.161$

The C's coefficients are the Sinh laws constants to be substituted in the hyperbolic sine equation:

$$\text{Log } da/dN = C1 * \sinh (C2 * (\text{Log } \Delta K) + C3)) + C4$$

These laws are plotted in figure 88. Aged steel alloys represented by laws 2 and 4 were used to calculate the remaining life of cracked CCOC at the critical locations.

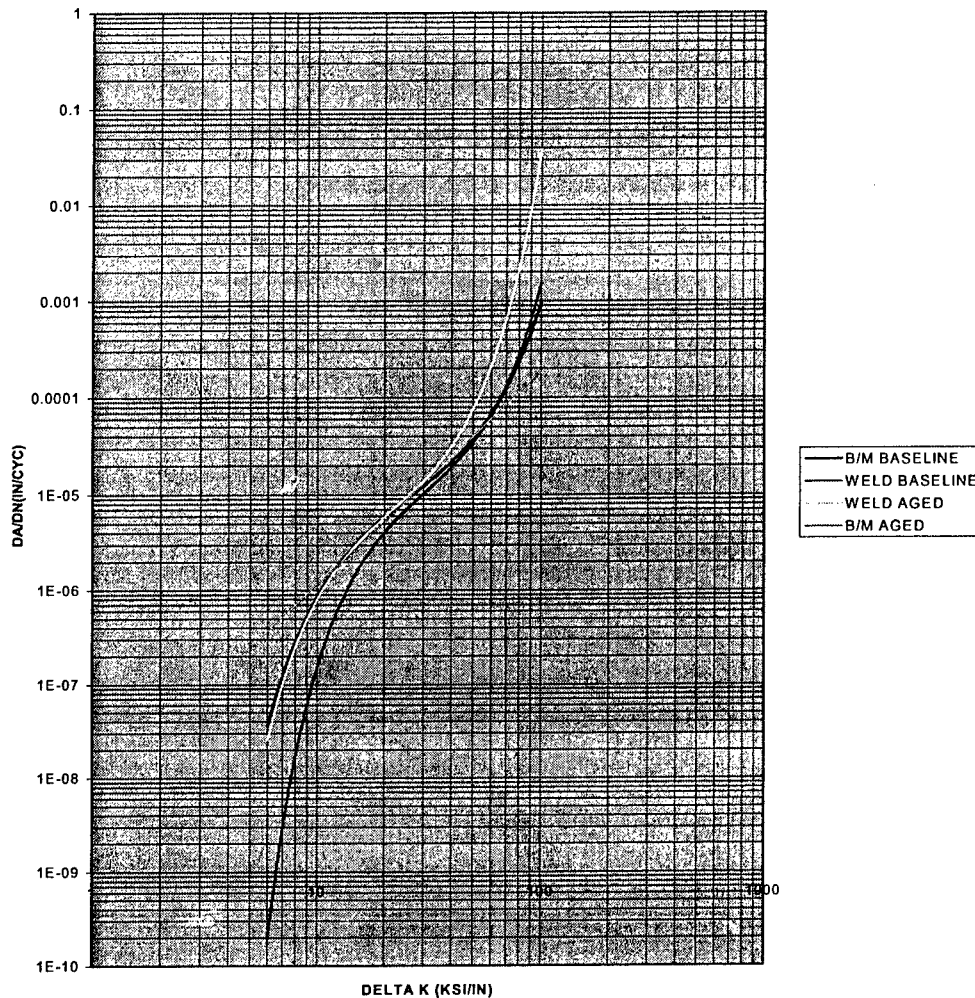


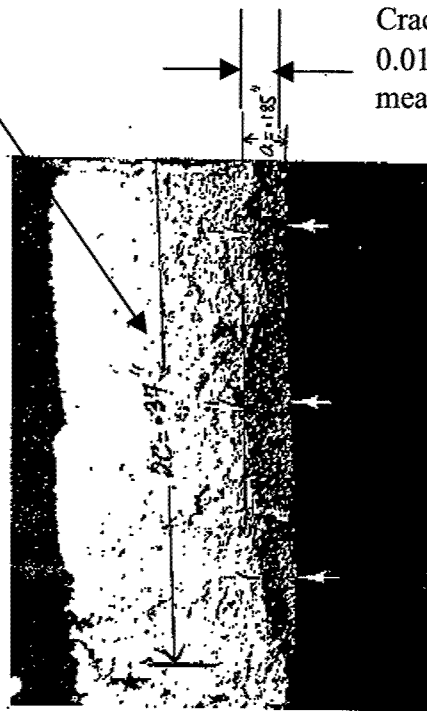
FIGURE 88. CRACK GROWTH RATE OF STEEL (AMS 5613) AT 750°F, $R = 0.1$ USED IN THE ANALYSIS

2.2.4.1.8 Effect of Multiorigin Cracks on Residual Life.

Initial crack aspect ratio has a significant effect on the calculated case residual life. The simulation of the crack geometry should be based as much as possible on observed crack geometry or past experience with cracks in similar locations and stress fields. Microstructural evaluation of a typical CCOC drain boss area crack (figure 89) showed multiple origins with a surface length of 0.375" and a depth of 0.0185". This is the crack geometry used in the CCOC residual life calculations. To show the sensitivity of residual life to initial crack geometry assumptions, various aspect ratio cracks were analyzed for a crack depth of 0.016". The results of the analysis are shown in figure 90. The residual life to rupture varies by a factor of up to 4/1 between a high and low aspect ratio crack.

Crack length of
0.375"
measured

Crack depth of
0.0185"
measured



MAG: 0.75X - LEFT
16X - RIGHT

Crack
locations

Weld Boss

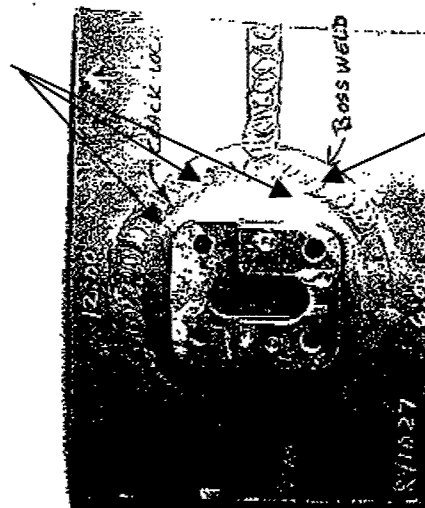


FIGURE 89. JT8D CCOC TYPICAL REAR DRAIN BOSS CRACK WITH MULTIORIGINS

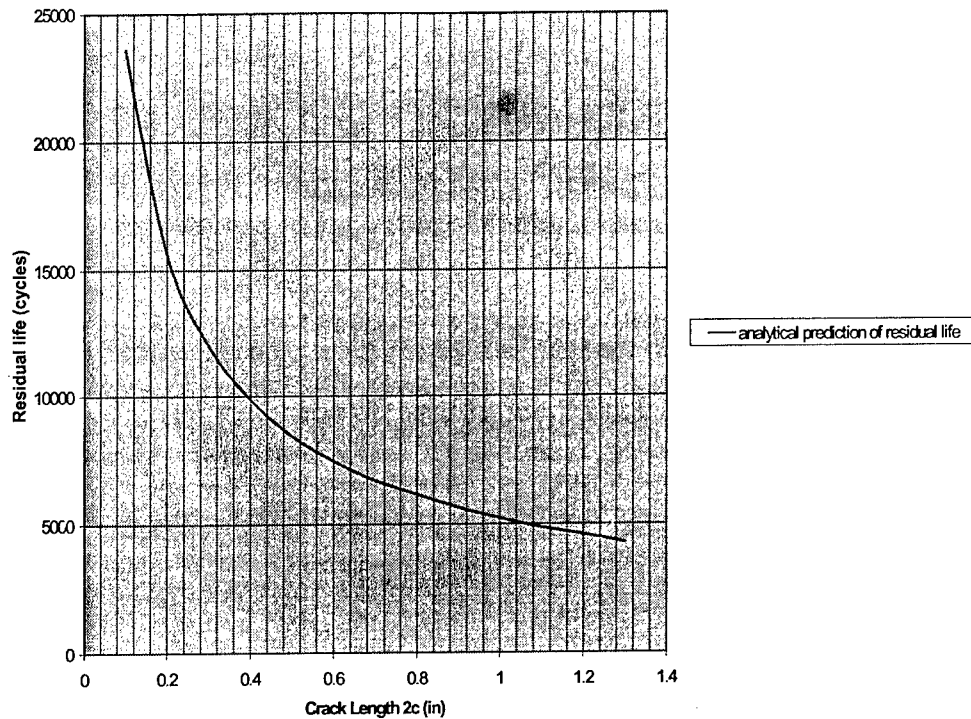


FIGURE 90. JT8D-200 CCOC DRAIN BOSS RESIDUAL LIVES FOR DIFFERENT CRACK LENGTHS, ANALYSIS PERFORMED AT $t = 700^{\circ}\text{F}$ AND CRACK DEPTH $a = 0.016''$

2.2.4.1.9 Measured Field Case Crack Data.

The JT8D CCOC drain boss operational data used in the crack growth calibration process are presented in tables 34 and 35. Table 34 contains striation data (crack progression rates) taken from actual fractured cracks measurements of the welded drain boss, while table 35 contains a summary of case service information. Information shown includes case total service lives, inspection rates, measured cracks length, and the number of cycles since its last shop visit or last weld repair.

This data will be compared with the predicted crack progression cycles, i.e., crack depth vs number of cycles and the crack length vs number of cycles.

TABLE 34. JT8D-219 CCOC REAR DRAIN BOSS CRACK SECTIONS STRIATION DATA

S/N	Depth	Striation Counts
VF5900	0.04"	2325
VF5900	0.05"	3181
VF5900	0.104"	5200
WS9446	0.08"	6263
RY1027	0.022"	1460

TABLE 35. JT8D-219 CCOC CRACK FIELD DATA

Date	S/N	CCOC TC	CSLI	Loc.	Crack Size	Initiation Estimate Cycles
	UM2789	16,806		Drain	0.025"	16,806
	VF5899	19,083		Drain	1.0"	15,383
10/15/98	RY1033	24,294	6978	Drain	RUP	17,316
10/16/98	VF5900	17,650		Drain	2.5" thru	12,450
11/23/98	UM2727	19,687	8730	Drain	3.0" thru	14,487
1/6/99	RU1488	25,119	6549	Ps4		18,570
1/10/99	WS9446	16,437	5575	Drain	0.75"	13,737
1/19/99	VF5892	18,975		Drain	1.0"	15,275
1/20/99	VF5922	18,727		Drain	2.0"	13,527
1/23/99	VR9674	18,408		Drain	2.0"	13,208
1/28/99	VF5981	16,884	7833	Drain		11,684
3/29/99	WM2788	15,724		Drain	2.0"	10,524
Aug-99	RT2626	14,692		Drain	2.5"	9,492
9/21/99	KN1267	24,059		Drain	3.0" thru	18,059
10/21/99	UM2380	13,873	6260	Drain	5.0"	7,613
11/1/99	UM2844	11,998		Drain	3.1" thru	5,998

2.2.4.1.10 Crack Residual Life in Aged Base Metal.

A review of CCOC cracking shows that cracks initiate and propagate inside the base metal, adjacent to the weld bead of the drain boss. The crack growth model for welded, aged steel alloy at 750°F was used to calculate crack propagation for a crack progressing through the case wall. The analysis was carried out using surface crack option in SURCK with an initial aspect ratio of 0.0185" x 0.370". Predicted crack growth vs cycles is plotted in figure 91. A total life of 4850 cycles was predicted for the crack to pass through the case thickness and transition to a through-wall crack with a surface length of 2 inches. Predicted propagation life was calibrated using striation data from three cracked field cases, which is also plotted in figure 91. Good agreement exists between the predicted and measured data. Figure 92 plots the crack length instead of crack depth. A second fracture mechanics analysis was performed in which a center crack was analyzed to simulate the through thickness cracks propagation along the case wall. The center crack analysis predicted 700 cycles for the crack to propagate and reach critical crack length. The total crack growth life from initiation to rupture is predicted to be 5550 cycles, which agrees well with operational experience.

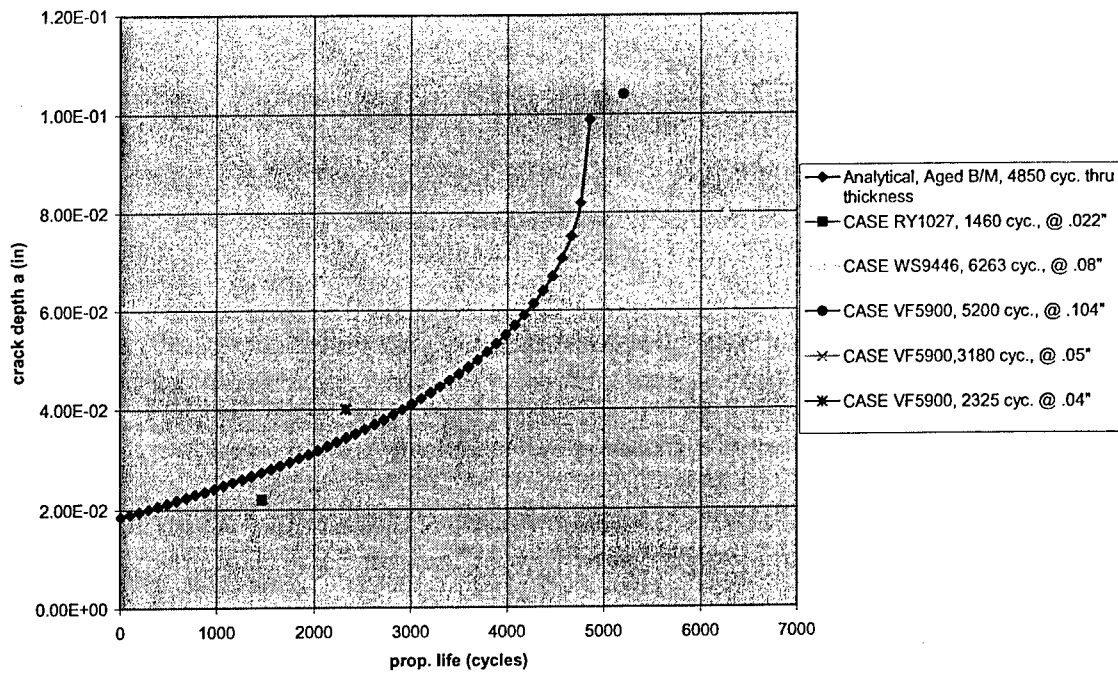


FIGURE 91. JT8D-219 CCOC DRAIN BOSS CRACK PROPAGATION LIFE THROUGH THICKNESS WERE CALIBRATED WITH FIELD DATA

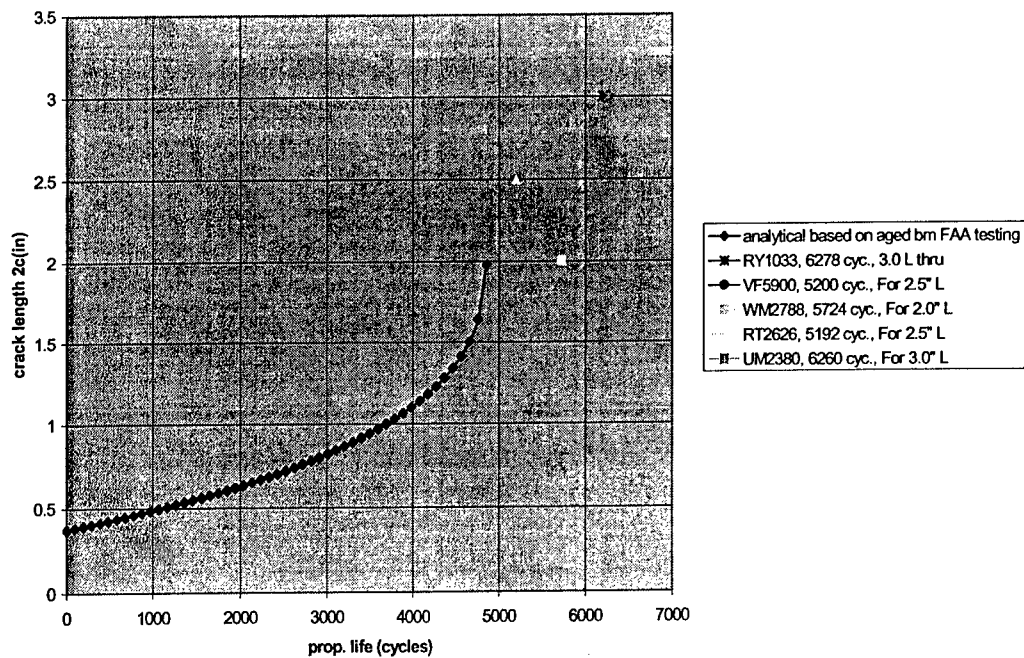


FIGURE 92. JT8D-219 CCOC DRAIN BOSS CRACK PROPAGATION LIFE ON SURFACE CALIBRATED WITH FIELD DATA

2.2.4.1.11 Results.

- Use of detailed 3D finite element analysis and the appropriate level of crack growth analysis sophistication produced crack growth predictions that correlated well with actual operational case experience.
- Crack growth data suggests that the cracks begin propagating from shallow, high aspect ratio cracks. These cracks link up in the high bending stress field. Crack growth data for this analysis was generated from cracked welded embossments in operational cases.
- Good correlation was obtained in predicting the crack residual life of field cracks data in steel alloy cases. This correlation used the crack growth rates of aged baseline and welded steel alloys generated by this program in task 1, material fracture testing.

2.2.4.2 Wrought Nickel Alloy Case Analysis.

The JT9D diffuser case, designed in the early 1970s, is constructed of several wrought Inconel 718 (AMS 5663) pieces that are welded together. This case experienced significant cracking during its millions of hours of operation, which provides crack growth data that is used in calibrating analytical crack growth predictions. This data consists of cracking that occurred in the base alloy case, in weld repairs that have taken place over time, and data from several case ruptures which initiated from weld defects. The crack growth data available in the base material, as well as in the welded and aged conditions, will be used to evaluate analytical crack growth predictions from the FRANC-3D and SURCK computer codes.

2.2.4.2.1 Thermal and Stress Analysis.

Since this case was designed before the availability of detailed finite element analysis codes, a detailed thermal and stress analysis was conducted by BELCAN Engineering of Cincinnati, OH. For this case, major cracking and ruptures occurred from rail locations adjacent to two embossment areas, identified as boss 6 and boss 7&8. Two separate finite element models were created to analyze the diffuser case at these critical locations; one for the diffuser case, including a 36-degree sector around boss 6 (figure 93), and the other for a 72-degree sector around the boss 7&8 locations (figure 94). These models were prepared in Unigraphics and meshed in ANSYS 3D solid-brick elements at the section around the bosses. Shell elements were used for the remainder of the diffuser case assembly. The models were generated with sufficient mesh density in critical areas to ensure model accuracy. Because of the complexities of model geometry, it was necessary to break the models into subregions to allow these regions to be meshed independently. This reduced the mesh generation time. These subregions were later connected by constraint equations at appropriate locations, which mathematically connected these regions to allow for the proper heat conduction and load distribution to transmit between regions.

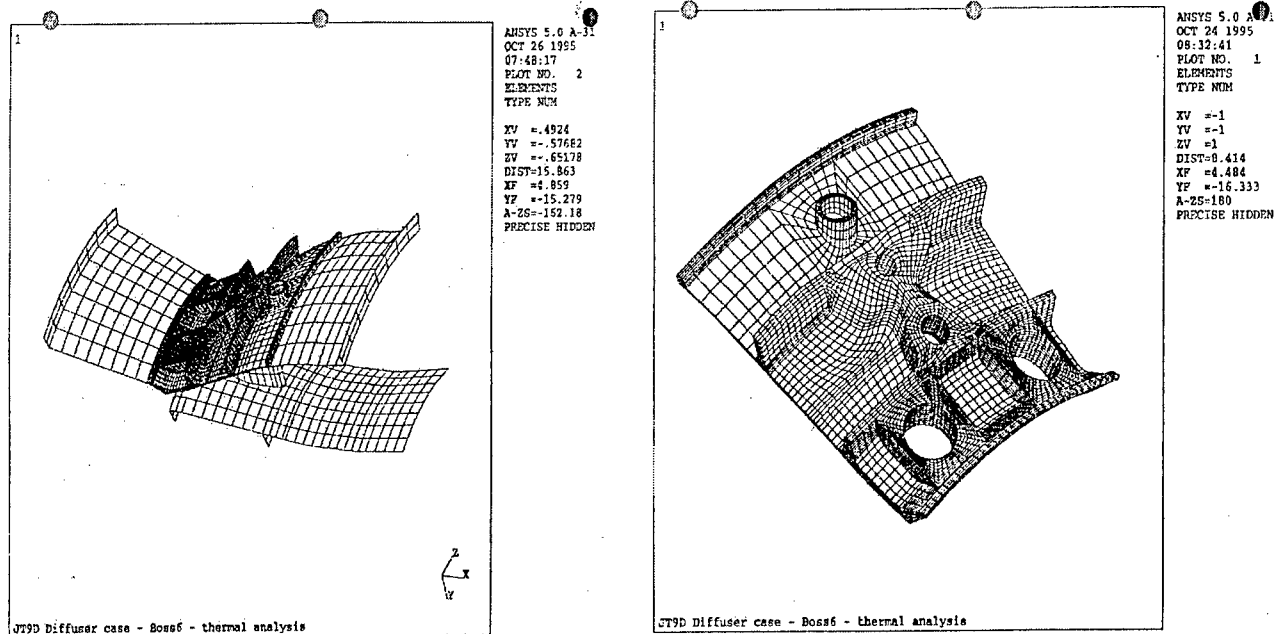


FIGURE 93. JT9D DIFFUSER CASE BOSS 6 SOLID MODEL AND MESH DENSITY, 36° SECTOR

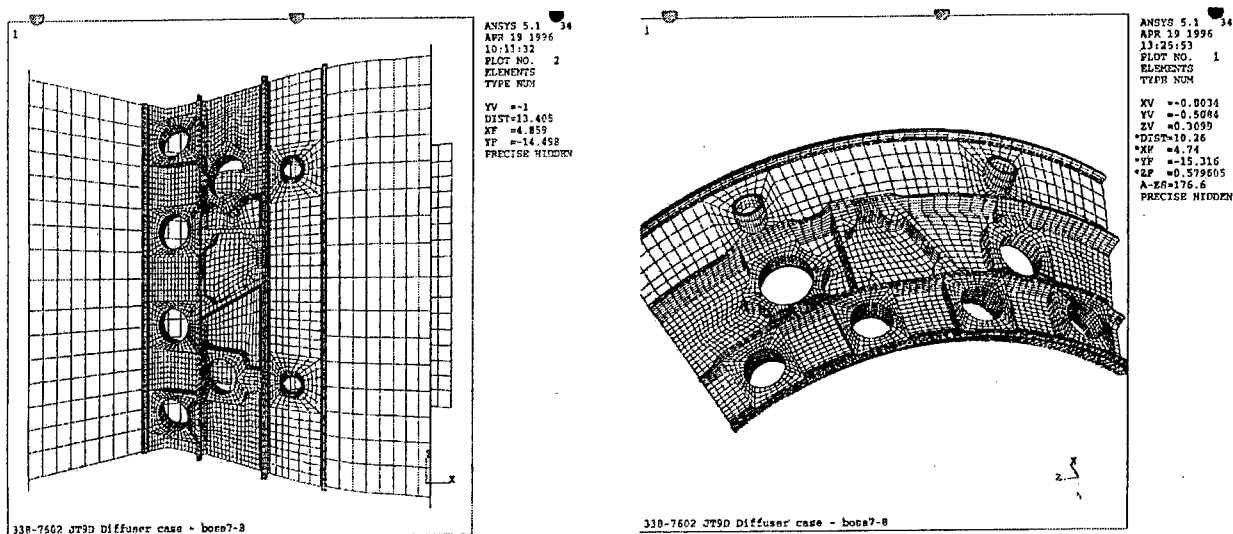


FIGURE 94. JT9D DIFFUSER CASE BOSS 7&8 SOLID MODEL

Heat transfer coefficients and convective gas temperature boundary conditions were included in the model to analyze an engine transient event from idle to takeoff power.

The transient thermal analysis showed the worst-case transient time point, as defined by the largest temperature gradient occurring from the inside diameter to the outside diameter of the aft rail, occurred 28 seconds into the acceleration for boss 6 and boss 7&8 locations. Figures 95 and 96 show the transient rail temperature results.

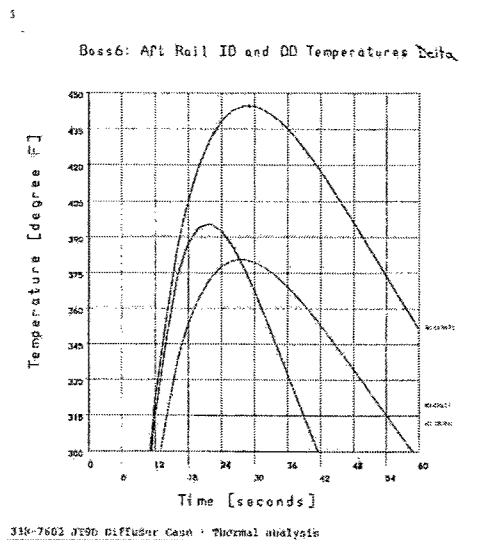


FIGURE 95. TEMPERATURE GRADIENT
NEAR BOSS 7&8 AT $t = 26$ sec

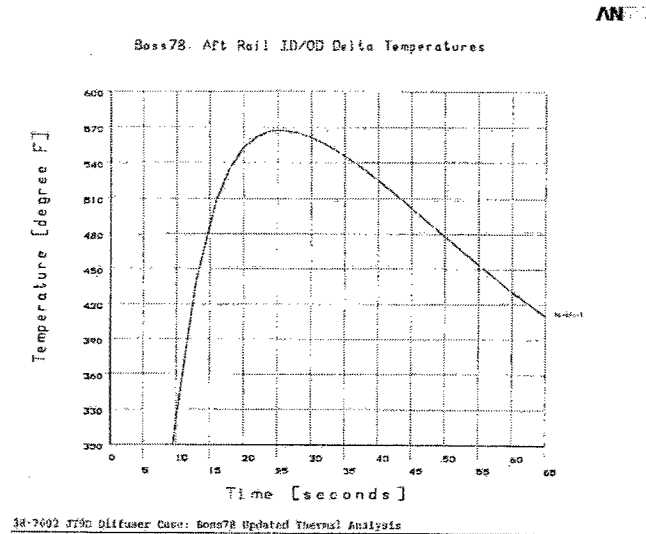


FIGURE 96. TEMPERATURE GRADIENT
NEAR BOSS 6 AT $t = 28$ sec

Figures 97 through 100 show the results of the transient thermal analysis at the limiting gradient points that were used in the stress analysis.

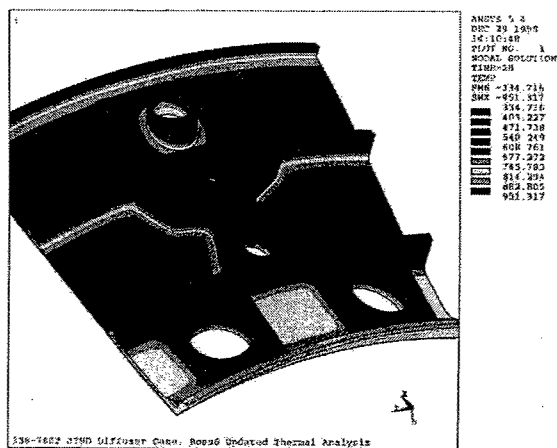


FIGURE 97. PREDICTED METAL
TEMPERATURE NEAR BOSS 6 AT
 $t = 28$ sec

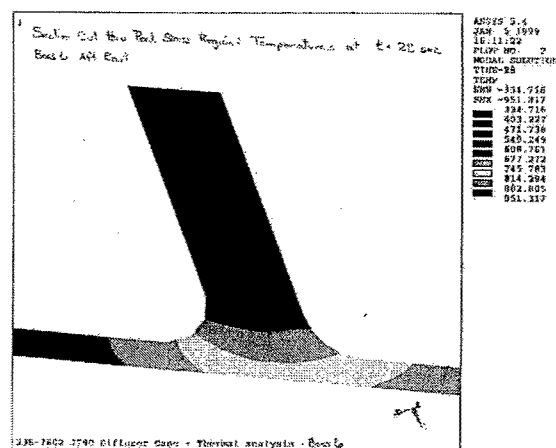


FIGURE 98. PREDICTED REAR RAIL
TEMPERATURE GRADIENT AT
BOSS 6, $t = 28$ sec

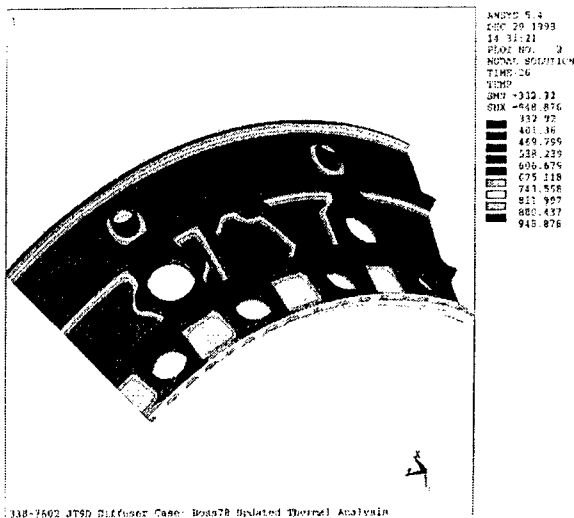


FIGURE 99. BOSS 7&8 METAL TEMPERATURE AT $t = 26$ sec

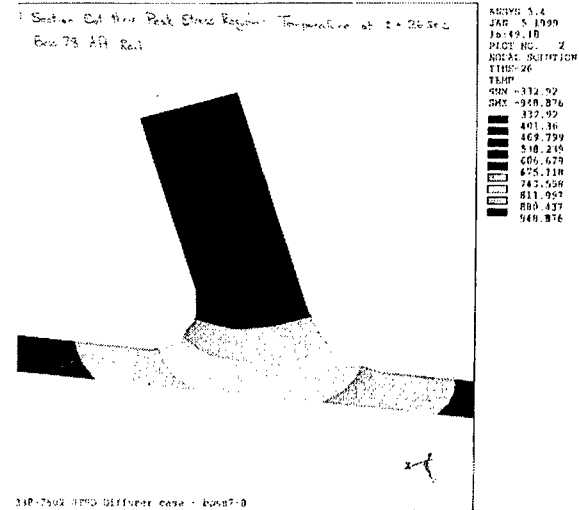


FIGURE 100. REAR RAIL GRADIENT NEAR BOSS 7&8 AT $t = 26$ sec

The structural analysis was performed using metal temperatures from the thermal analysis results, the appropriate case internal pressure, and axial loading. Results of the analyses are presented in figures 101 and 102. Figure 101 shows that the predicted maximum principal stress occurs at the top of the rear rail adjacent to the corners of boss 6 and has a value of 192 ksi. Figure 102 shows the predicted rear rail maximum principal stress of 197 ksi between bosses 7&8. There is a high stress gradient through the rail due to high thermal gradients. Because the calculated peak stresses are significantly above the yield point for the material, ($F_{ly} \sim 140$ ksi), the design approach involved doing a nonlinear plastic finite element analysis at the maximum load condition and performing crack growth predictions using plastic stresses. A kinematic-hardening rule was used to characterize the plastic behavior of AMS 5663. This rule assumes that the initial yield surface translates, with respect to the origin, as a rigid body during plastic flow. Upon identifying the critical locations and the critical load points of the mission, the plastic analysis was only carried out for the boss submodels and not for the entire model. Both elastic and plastic stress results for the boss submodels were used in FRANC-3D fracture mechanics analysis.

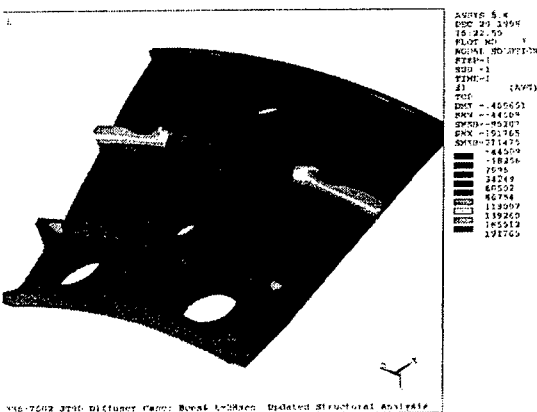


FIGURE 101. MAXIMUM PRINCIPAL STRESS AT THE REAR RAIL ADJACENT TO BOSS 6

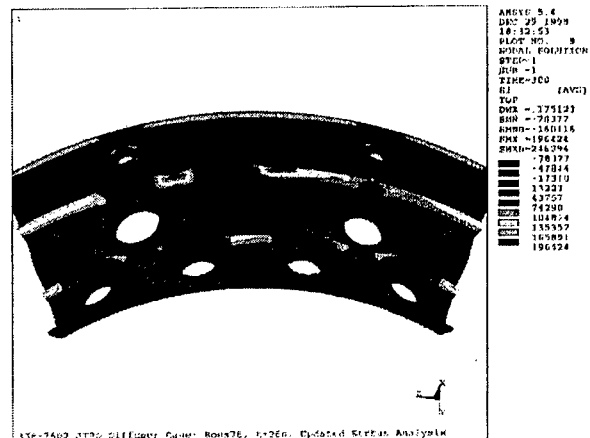


FIGURE 102. MAXIMUM PRINCIPAL STRESS AT THE REAR RAIL ADJACENT TO BOSS 7&8

2.2.4.2.2 Fracture Mechanics Analysis—FRANC-3D.

The fracture mechanics code FRANC-3D discussed in an earlier section was used to calculate the stress intensities in the vicinity of a crack front and predict the crack growth rates in the wrought IN 718 material.

2.2.4.2.3 Fracture Analyses of Cracks in Elastic-Plastic Stress Fields.

In evaluating the JT9D boss 7&8 cracking problem, it became apparent that an FM analysis using elastic stresses was inappropriate because the calculated peak stress of 190 ksi was significantly over the material yield strength of ~140 ksi. Current design procedure for predicting crack growth in stress concentration features with SURCK involves using an elastic-plastic (E/P) stress shakedown procedure to reduce the conservatism. This procedure has been formally established and validated for many materials with notched, subelement specimens. These crack growth tests were at temperatures and loading conditions representative of component operating conditions. These tests are carried out so peak notch stresses are well above the material yield strength.

The following is a description of the current design procedure for crack growth predictions in locally yielded material. It is based on the assumption of cyclically stable (elastic) material behavior after contained yielding has occurred.

1. The elastic stress die out (for maximum loading) in a critical notch feature is calculated by FEA, which is used in an E/P shakedown algorithm with material stress-strain modeling to calculate resultant E/P stress die out.
2. The residual stress die out is calculated and used with elastic stress die outs
 - to calculate crack stress intensities for load cycling and
 - to predict crack growth life using a material crack growth rate model.
3. Comparing predicted crack growth with actual notched specimen, crack growth data validates modeling.

The proposed approach evaluated here for 3D FM analyses to use E/P stresses:

1. An elastic and E/P FEA of a critical region for maximum load condition.
2. Input elastic and E/P stresses as crack face tractions in a FRANC-3D models.
3. Calculate crack stress intensities for elastic stresses, K_{el} 's and E/P stresses, $K_{E/P}$'s.
4. Calculate crack stress intensities for residual stresses ($K_{res} = K_{el} - K_{E/P}$).
5. Predict crack growth life with P&W FM code using K_{res} 's and K_{el} 's.
6. Validate with a prediction of the field experience of the JT9D Diffuser Case at boss 6 and boss 7&8 locations.

2.2.4.2.4 FRANC-3D Model Preparations Submodeling.

A submodeling technique (cut boundary displacement method) was used to considerably reduce the size of the models and eliminate elements such as shells and links, which are not suitable for translation to FRANC-3D. The submodeling approach puts displacements on the cut boundary of the coarse model as boundary conditions for the individual submodels. The submodel sizes were selected to incorporate the regions of maximum stress and critical geometric features (bosses, rails) that could influence the crack growth. After the cut boundary interpolation and solution were finished, arrays of path plots along key regions were analyzed to correlate with the full model. Figures 103 and 104 show the submodels selected for boss 6 and boss 7&8. Figures 105 and 106 show maximum elastic and plastic principal stress results for both cases. Figures 107 to 110 show principal stress path plots along the axial and forward ends of the cases. These plots start at the top of the rails at the critical locations.

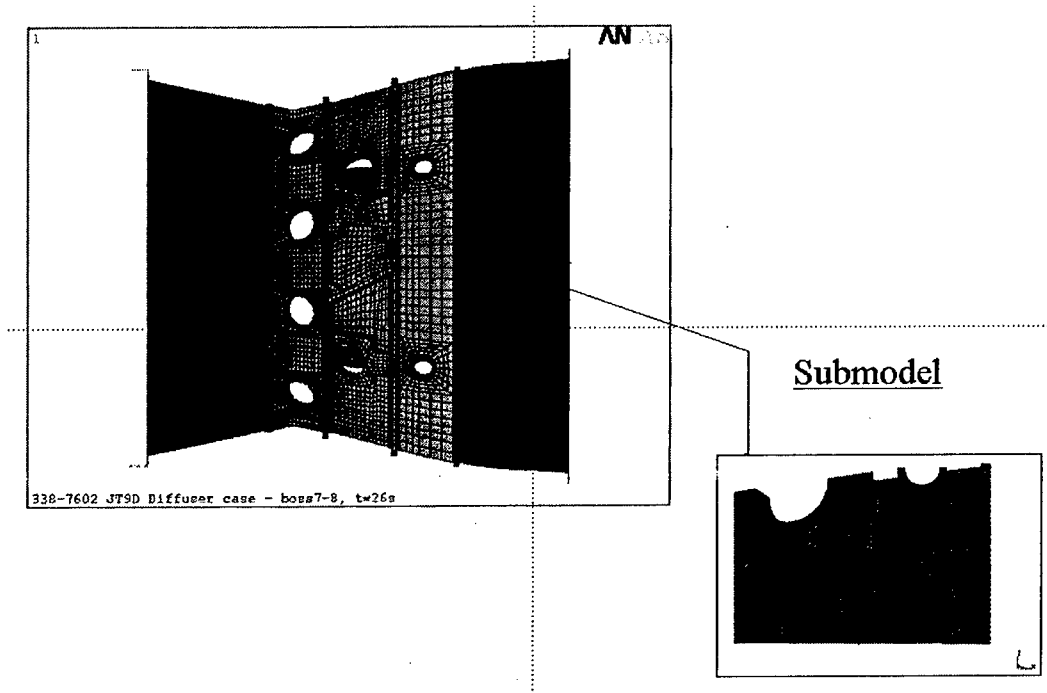


FIGURE 103. JT9D DIFFUSER CASE, BOSS 7&8 SUBMODELS

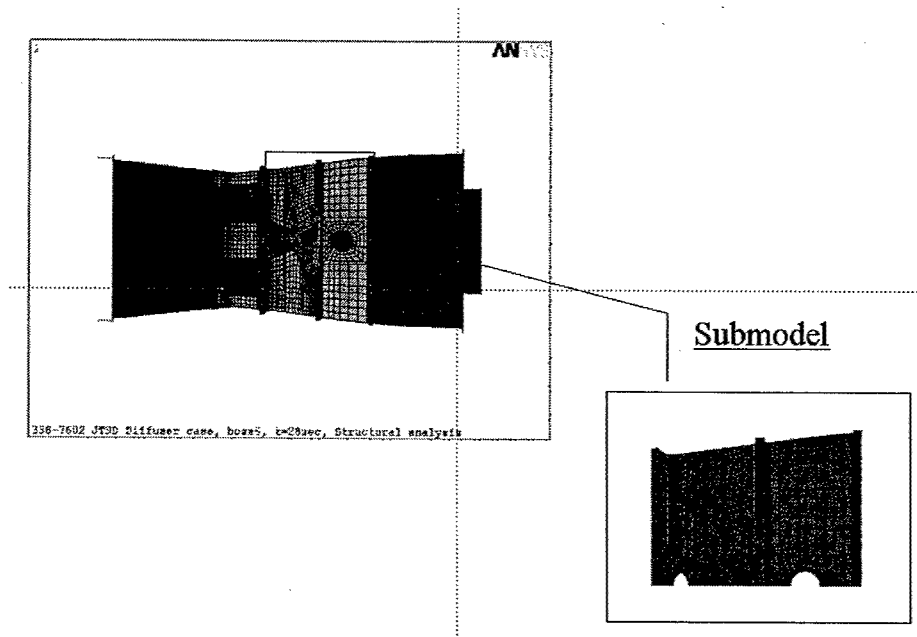


FIGURE 104. JT9D DIFFUSER CASE, BOSS 6 SUBMODELS

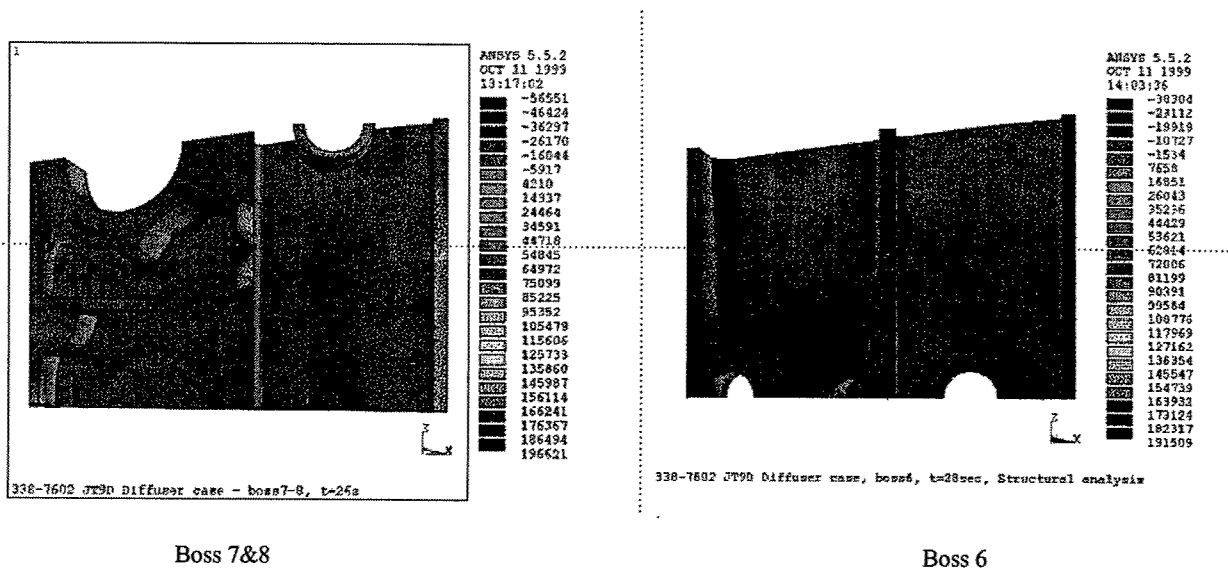
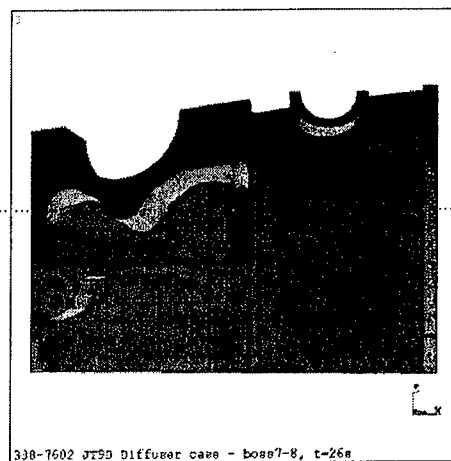
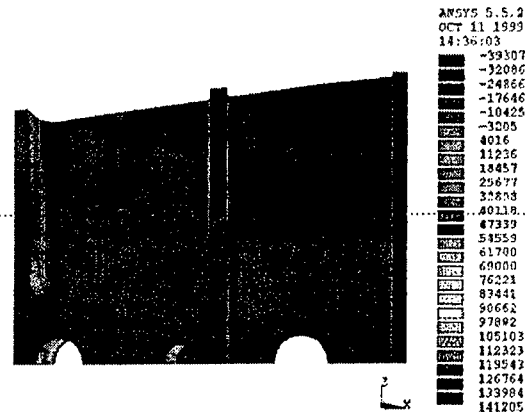


FIGURE 105. MAXIMUM ELASTIC PRINCIPAL STRESS RESULTS FOR BOSS 7&8 AND BOSS 6



Boss 7&8



Boss 6

FIGURE 106. MAXIMUM PLASTIC PRINCIPAL STRESS RESULTS FOR BOSS 7&8 AND BOSS 6

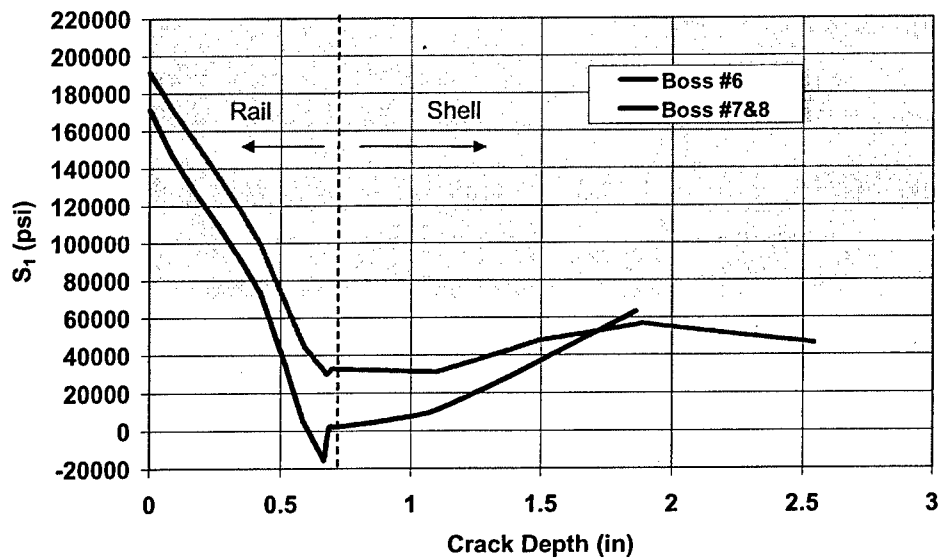


FIGURE 107. ELASTIC PRINCIPAL STRESS PATH PLOTS FOR BOSS 7&8 AND BOSS 6—AFT END

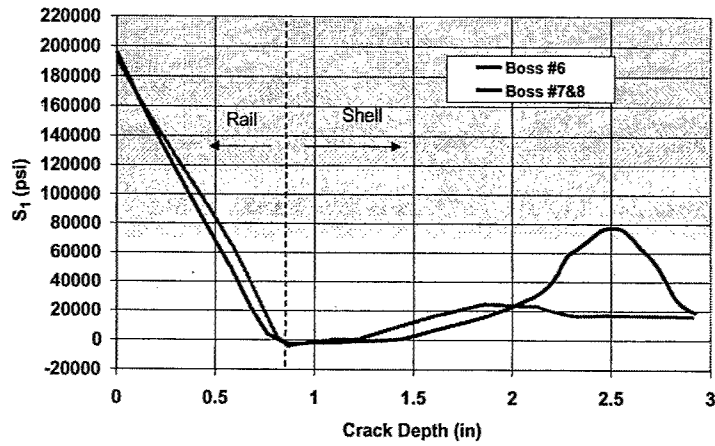


FIGURE 108. ELASTIC PRINCIPAL STRESS PATH PLOTS FOR BOSS 7&8 AND BOSS 6—FORWARD END

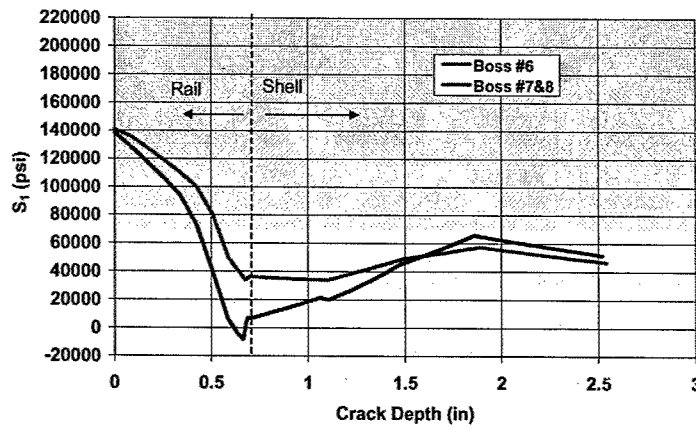


FIGURE 109. PLASTIC PRINCIPAL STRESS PATH PLOT FOR BOSS 7&8 AND BOSS 6—AFT END

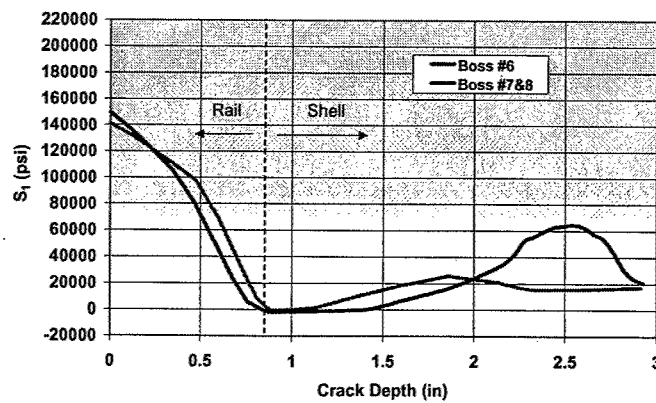


FIGURE 110. PLASTIC PRINCIPAL STRESS PATH PLOT FOR BOSS 7&8 AND BOSS 6—FORWARD END

A preliminary uncracked model was analyzed by applying an internal pressure of 300 psi and comparing it with ANSYS results of similar models. This was done to ensure that the model was behaving properly and that boundary conditions were accurate. Internal pressures were applied as tractions directed along the opposite direction of the face normal. Mesh discretization was accomplished by subdividing the faces and the edges into line segments. The vertices of the edge subdivision would subsequently become the nodes of the mesh. FRANC-3D supports both quadrilateral- and triangular-shaped elements. An array of mesh algorithms allows for mapped and arbitrary mesh configurations. In the arbitrary mesh feature, one practical option allows for user-specified node definitions. Fine mesh discretization was used around critical features and through the thickness of the shell, where maximum stresses were expected to occur. Symmetry boundary conditions were applied in the hoop direction of the cases and the models were constrained in the axial direction at the aft end. AMS 5663 material properties input were $E = 29.1 \text{ Msi}$, $\nu = 0.271$, and density = $7.68\text{E-}03 \text{ lb.s}^2/\text{in}^4$. Solutions were always performed via boundary element solver (BES) with either the in-core or out-of-core option (batch mode). For models with less than 3000 elements, the Gaussian in-core solver, offered by BES, provided a speedy solution. For larger models, the out-of-core QR solver gave the fastest response. Solution times increase rapidly with gradual increases in the number of elements, which is important to discretize the model efficiently. The mesh should be sufficiently dense around critical regions (i.e., cracks, rails, bosses) but fairly coarse in regions away from these features. Displacements and stress results from the Gaussian elimination in-core solver compared favorably with the FEA analyses for boss 6 and boss 7&8 for a 300-psi run.

2.2.4.2.5 Crack Growth Simulation Methodology.

Based on field experience, cracks originate in the top of the back rail due to great variations of temperatures (from 400°F at the top of the rail to 900°F at the ID of the case). The presence of large embossments next to the rails aggravates the stress configuration. Typically, cracks extend down the rail and penetrate the case inner wall. For boss 6, the cracks propagate axially to reach a critical length of approximately 4 inches. Even though peak stresses in the boss 7&8 are higher than the stresses in boss 6, there is no history of failures at this location.

The 10- x 10-mil corner cracks were nucleated at established points of peak stresses for both cases. The cracks were oriented precisely perpendicular to the principal stress direction (hoop). The flaw nucleation was performed in FRANC-3D by using a built-in library of flaws. This procedure required the input of one crack location and orientation to automatically create crack faces. The next step involved computing the crack face tractions, which was done internally in the program, by interpolating the finite element stresses (stored in the .fstr file) at the location of each crack face node and multiplying by the crack face normal.

After placing the cracks, it is required to remesh the model. In general, it is recommended to use a high density of quadrilateral elements along the crack front. In certain instances crack faces must be subdivided to facilitate the meshing procedure. Additional refining was also done to the regions of the model near the crack front. Whenever mapped meshing was not available, arbitrary meshing with automatically generated plus user-defined internal points provided the best discretization. Figure 111 shows initial crack locations and mesh density for boss 7&8 and boss 6.

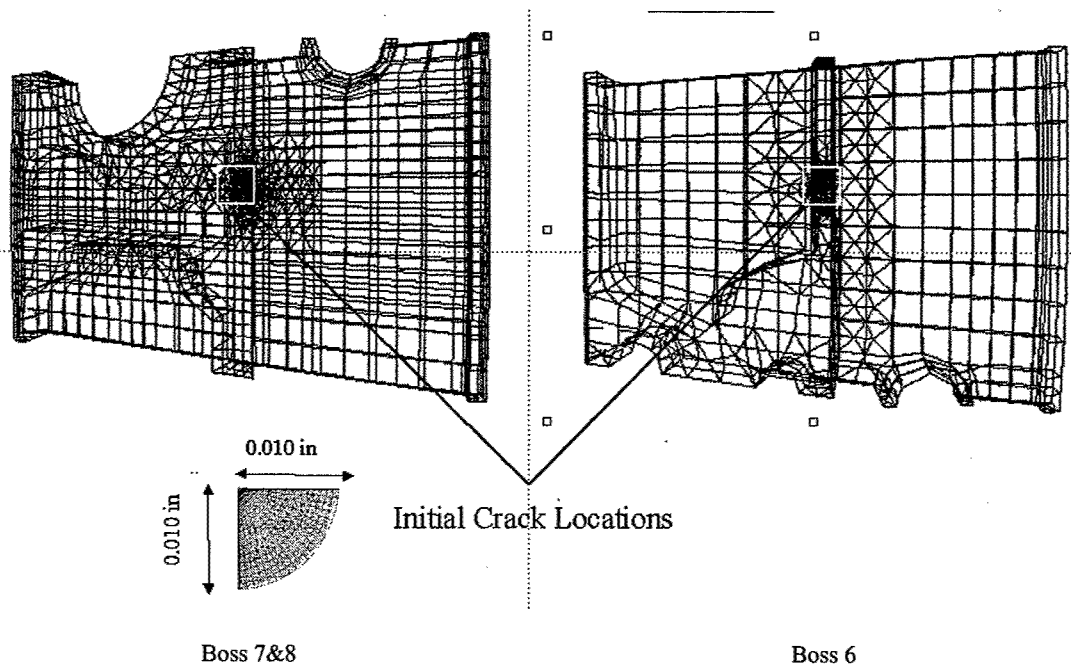


FIGURE 111. BOSS 7&8 AND BOSS 6 INITIAL GLOBAL MODEL AND CRACK MESH

The stress-intensity factors were calculated within FRANC-3D using crack field displacement correlations. The direction of the crack growth was determined using 2D mixed-mode I and II theories. Fracture propagation was controlled by the relative magnitudes of the stress-intensity factors at the crack front, and local extensions were determined by the following expression:

$$Extension = Extension_{max} \times \left[\frac{K}{K_{max}} \right]^b \quad (1)$$

$Extension_{max}$: value determined by the user

K_{max} : maximum stress intensity factor at the crack front

K : local stress intensity factor

b : Paris law power

2.2.4.2.6 Corner Crack Analysis—FRANC-3D.

Stress-intensity factors were calculated for different propagated crack sizes and the results are presented at three different stages: (1) corner crack, using an initial crack size of 10 x 10 mils.; (2) edge crack, after the crack penetrates the aft side of the rail; and (3) through crack, where the crack has penetrated the case wall and propagated axially to reach an axial length of 2 inches.

Figures 112 to 115 show the corner crack stress-intensity factor history for each boss obtained in FRANC-3D with elastic and plastic stress fields. In order to eliminate surface constraint issues and provide more stable results, life calculations use SIF values at 25% normalized crack length (NCL) from both ends (forward and top). SIF values for both cases are very close since the stress values and crack geometry are similar.

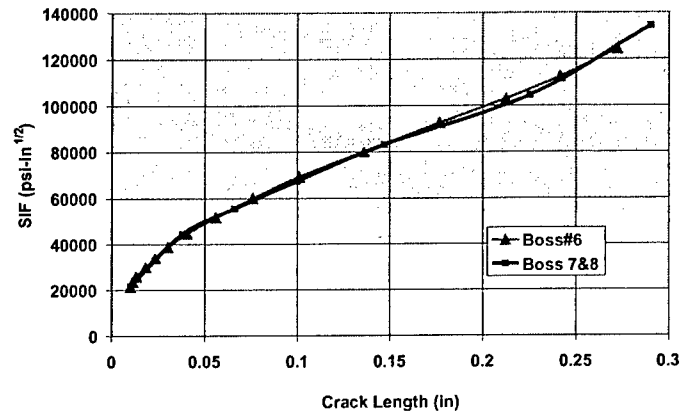


FIGURE 112. ELASTIC STRESS-INTENSITY FACTOR RESULTS FOR CORNER CRACK—TOP SEGMENT

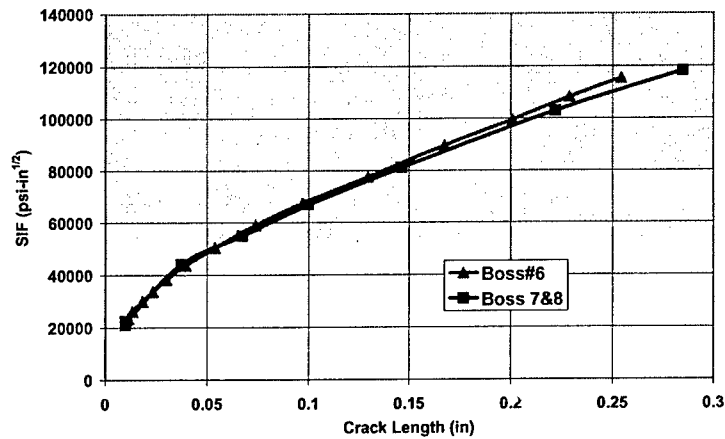


FIGURE 113. ELASTIC STRESS-INTENSITY FACTOR RESULTS FOR CORNER CRACK—FORWARD SEGMENT

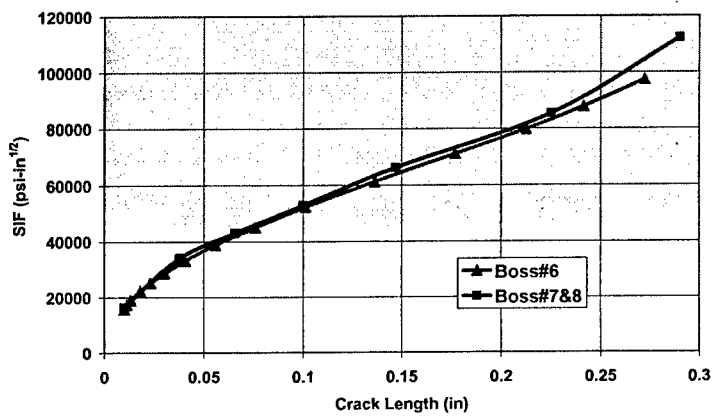


FIGURE 114. PLASTIC STRESS-INTENSITY FACTOR RESULTS FOR CORNER CRACK—TOP SEGMENT

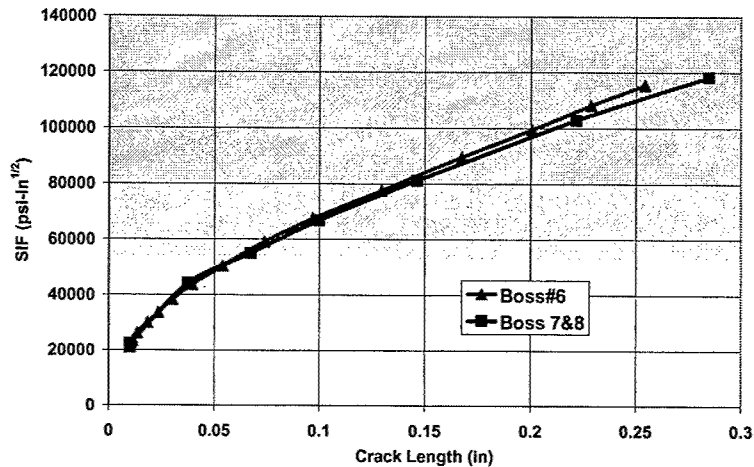


FIGURE 115. PLASTIC STRESS-INTENSITY FACTOR RESULTS FOR CORNER CRACK—FORWARD SEGMENT

Elastic stress distributions along the forward side of the rails were explicitly input into SURCK to simulate the corner crack propagation process. Since peak stresses on the top of the rail reach levels above the proportional limit of the material (140 ksi at 400°F), an elastic-plastic stress shakedown procedure was introduced using the plasticity option within the code, eliminating the conservatism of a purely elastic prediction. Results were compared with fatigue life predictions using K_I vs crack depth values from elastic and plastics runs of FRANC-3D. Figures 116 and 117 show crack depth versus number of cycles charts for the elastic and plastic solutions. Fracture life predictions are conservative for elastic situations compared to FRANC-3D results (1359 cycles and 1,655 cycles for boss 7&8 and boss 6 respectively versus 1739 cycles and 1893 cycles from FRANC-3D). SURCK predicts significantly lower lives when using elastic-plastic stress shakedown (3452 cycles and 3587 cycles for boss 7&8 and boss 6 respectively versus 5313 cycles 4423 cycles from FRANC-3D). Both codes predict more cycles for a corner crack at boss 6 location.

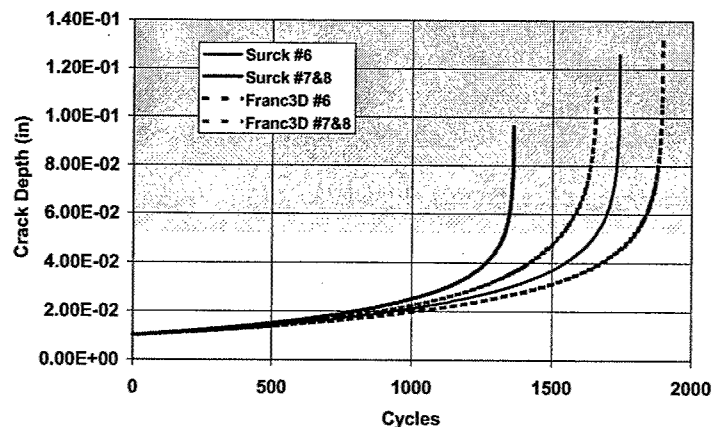


FIGURE 116. LIFE CALCULATIONS FOR CORNER CRACK USING ELASTIC STRESS FIELD

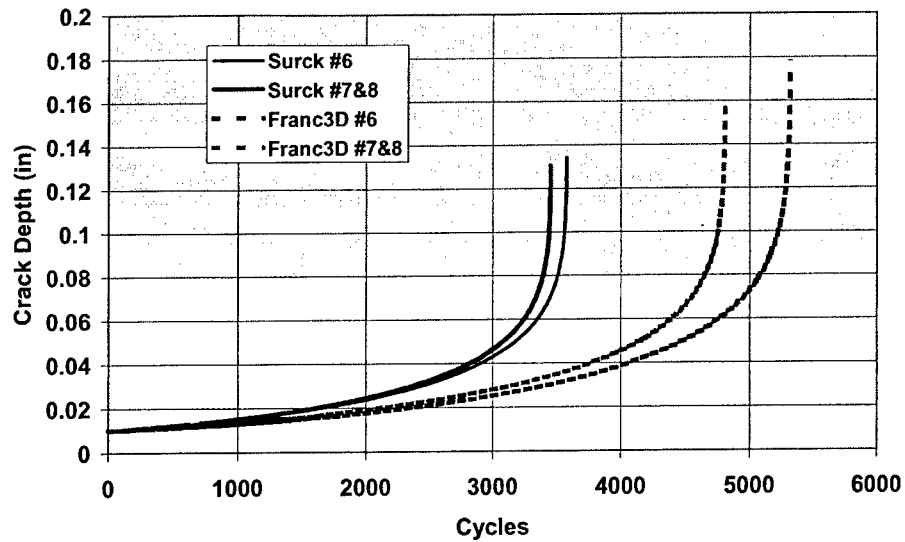


FIGURE 117. LIFE CALCULATIONS FOR CORNER CRACK USING PLASTIC STRESS FIELD

2.2.4.2.7 Edge Crack Analysis—FRANC-3D.

The corner cracks transitioned to an edge crack after 15 steps of propagation for boss 6 and 13 steps for boss 7&8 and remained in the same radial plane. Life predictions were based on the Paris Crack Growth Model, which assumes a power law relationship between the stress-intensity factor range and the crack growth rate. The Paris Model for PWA 5663 at 800°F is shown in figure 118 and represented by the expression:

$$\frac{da}{dn} = 6.12 \times 10^{-11} (\Delta K)^{3.594} \quad (2)$$

Stress-intensity factor values for edge cracks of boss 6 and boss 7&8 correspond to 25% NCL points from both the aft and forward segments. However, once the crack penetrated the inner wall and propagated axially, the values were obtained from 50% NCL to ensure consistency, as shown in figure 119. Figures 120 to 123 show the stress-intensity factors for edge cracks using elastic and plastic/elastic stress values as crack face tractions.

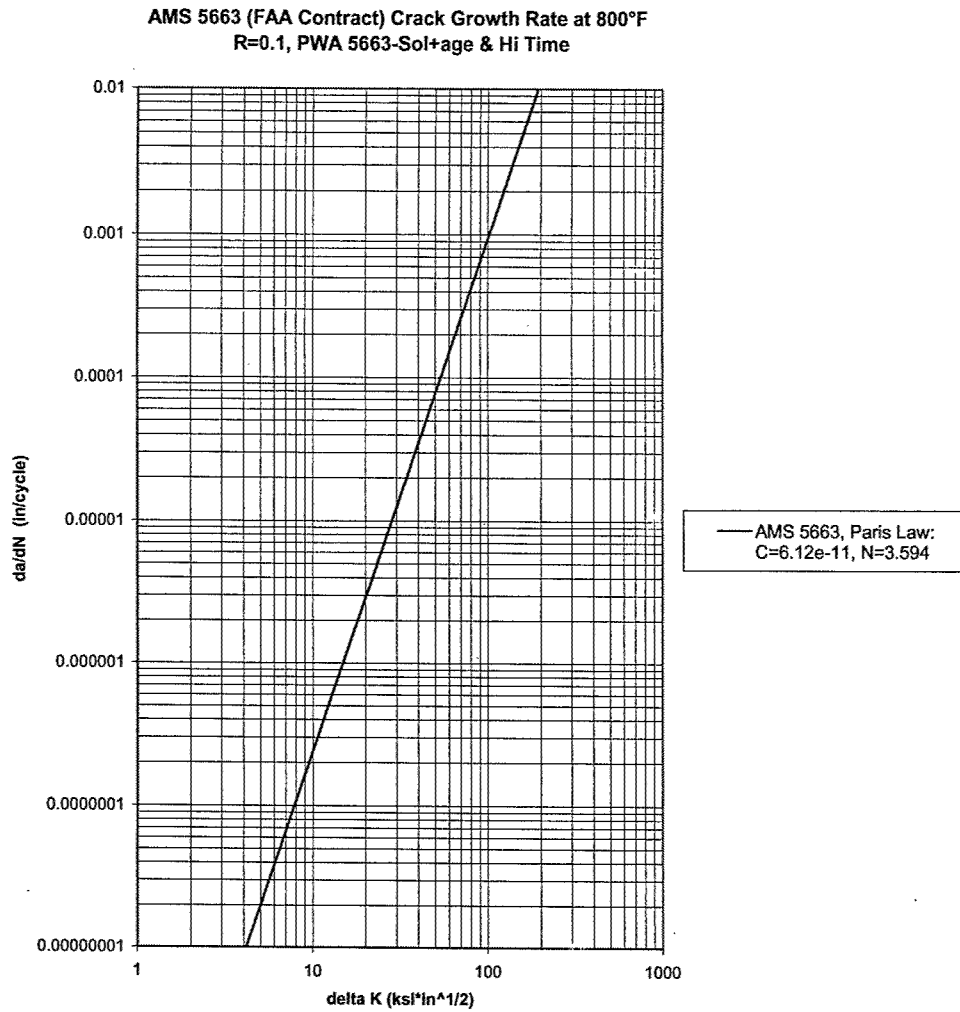


FIGURE 118. PARIS EQUATION MODEL FOR AMS 5663 (WROUGHT IN 718)

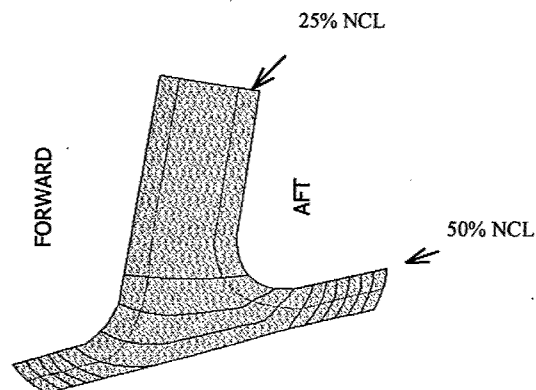


FIGURE 119. TWENTY-FIVE PERCENT NCL AND FIFTY PERCENT NCL STRESS-INTENSITY FACTOR EXTRACTION POINTS FOR EDGE AND THROUGH CRACKS

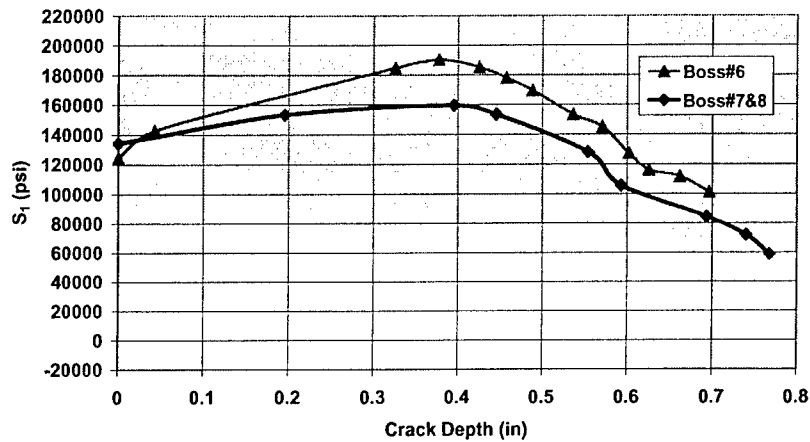


FIGURE 120. ELASTIC STRESS-INTENSITY FACTOR RESULTS FOR
EDGE CRACK—AFT SEGMENT

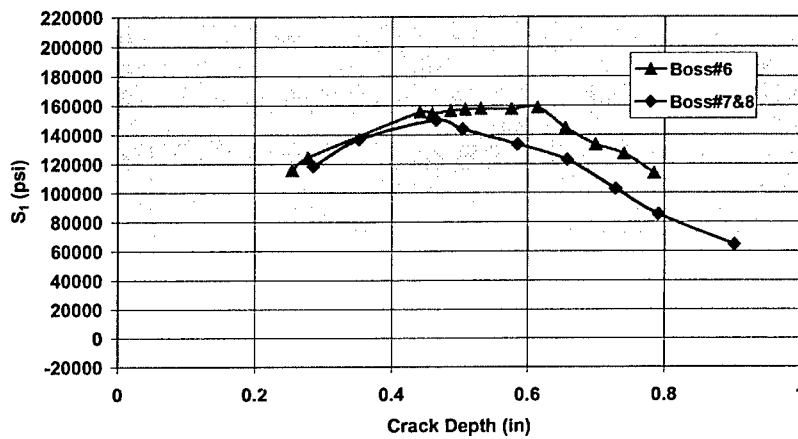


FIGURE 121. ELASTIC STRESS-INTENSITY FACTOR RESULTS FOR
EDGE CRACK—FORWARD SEGMENT

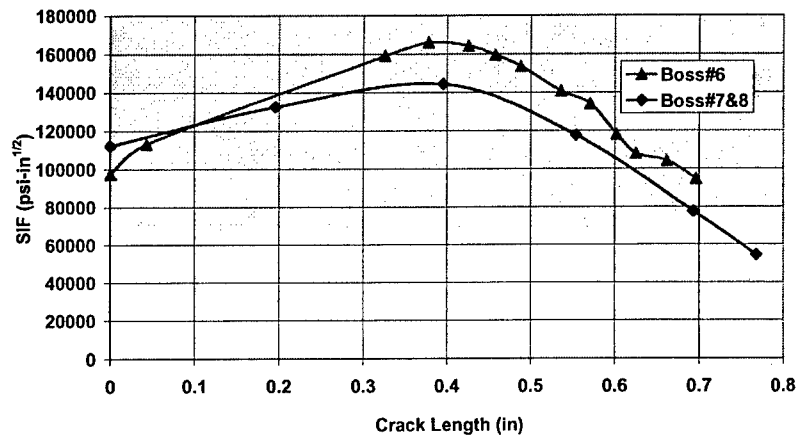


FIGURE 122. PLASTIC STRESS-INTENSITY FACTOR RESULTS FOR
EDGE CRACK—AFT SEGMENT

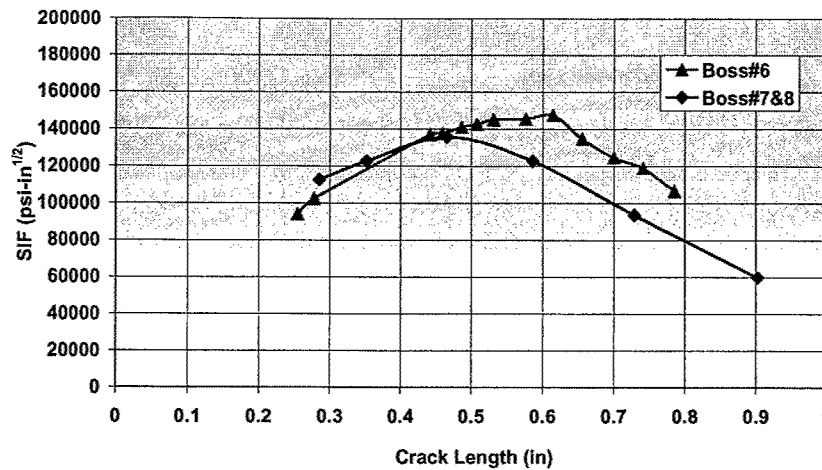


FIGURE 123. PLASTIC STRESS-INTENSITY FACTOR RESULTS FOR
EDGE CRACK—FORWARD SEGMENT

Rapid crack growth, and no additional life, is predicted during the period of transition between a corner crack and a through crack due to the high K values at the rails. Field data support this result with no crack striation data being detected in this region of the crack. As the cracks propagate down the rails, K values on boss 7&8 dropped approximately 50%, whereas the values at boss 6 do not experience a significant decrease. In an attempt to understand this, a finite element analysis was performed on each boss with a surface crack nucleated at the top of the rail, in the highest stress region, penetrating 0.420 in. towards the wall.

Resulting path plots of these analyses show a better redistribution of stresses away from the rail. These stress profiles were used in SURCK with the plastic shakedown option activated to calculate the crack residual lives of the rear rail near boss 6 and boss 7&8. Results are plotted for both sides of the rail as shown in figures 124 to 127, and they are also plotted in the form of a contour plot in figures 128 to 129. The mechanical load from the cracked rail in boss 7&8 redistributes smoothly among the large embossments surrounding the crack. This reduces the crack face tractions and considerably slows the crack growth. Load originally carried by the cracked boss 6 redistributes to the shell, causing high localized tensile stresses, in the order of 70 ksi, perpendicular to the crack faces. As a consequence, the crack in boss 6 rapidly penetrates the inner wall and its crack front exhibits a sharp curvature. The crack front of boss 7&8, in comparison, presents a longer, less rounded front. Initially, axial through crack lengths are 0.600 in. and 0.900 in. for boss 6 and boss 7&8 respectively.

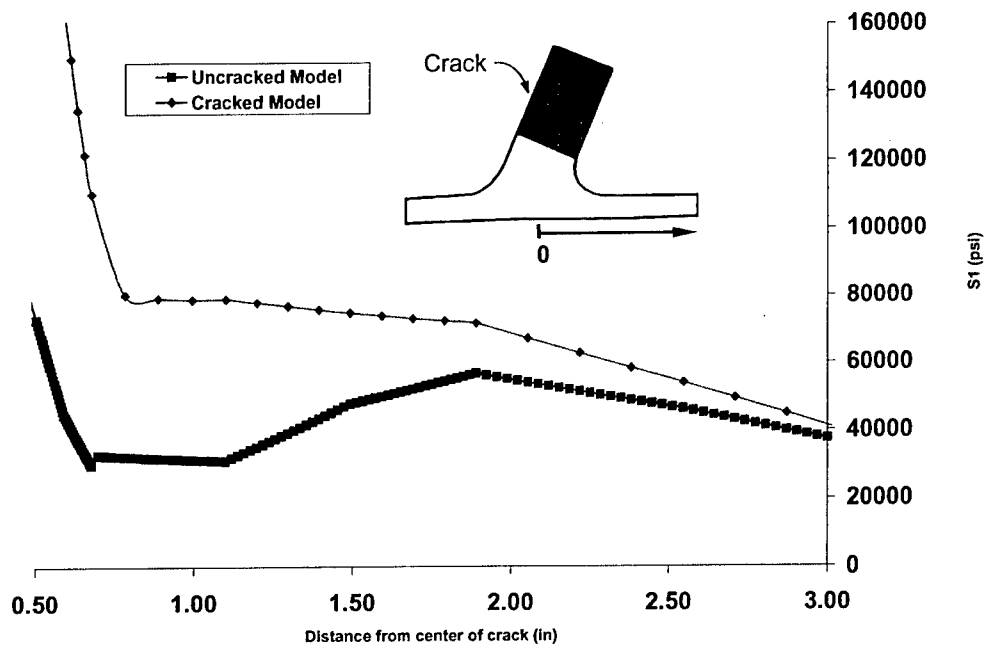


FIGURE 124. MAXIMUM ELASTIC PRINCIPAL STRESS PATH PLOTS FOR UNCRACKED AND CRACKED MODELS, BOSS 6—AFT SEGMENT

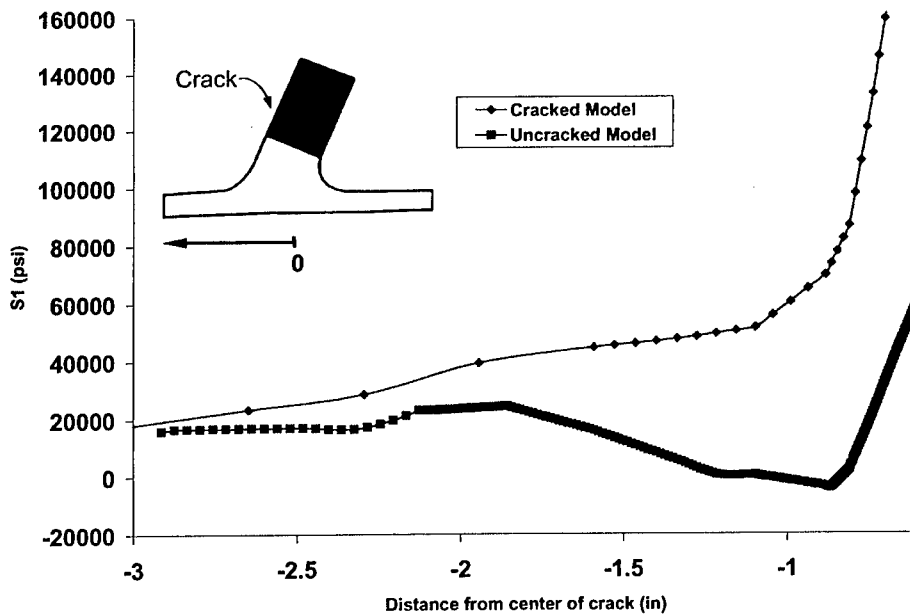


FIGURE 125. MAXIMUM ELASTIC PRINCIPAL STRESS PATH PLOTS FOR UNCRACKED AND CRACKED MODELS, BOSS 6—FORE SEGMENT

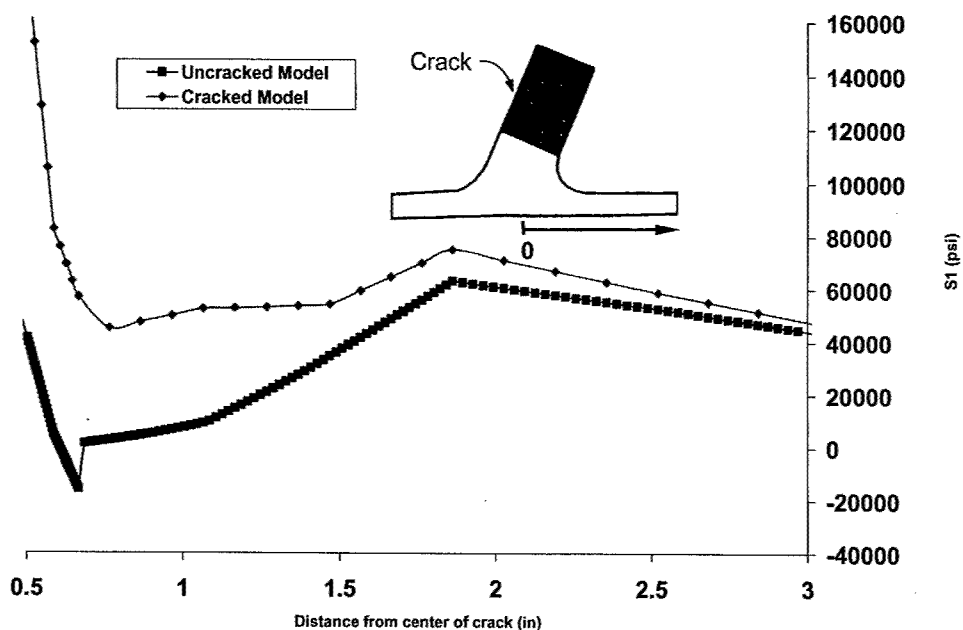


FIGURE 126. MAXIMUM ELASTIC PRINCIPAL STRESS PATH PLOTS FOR UNCRACKED AND CRACKED MODELS, BOSS 7&8—AFT SEGMENT

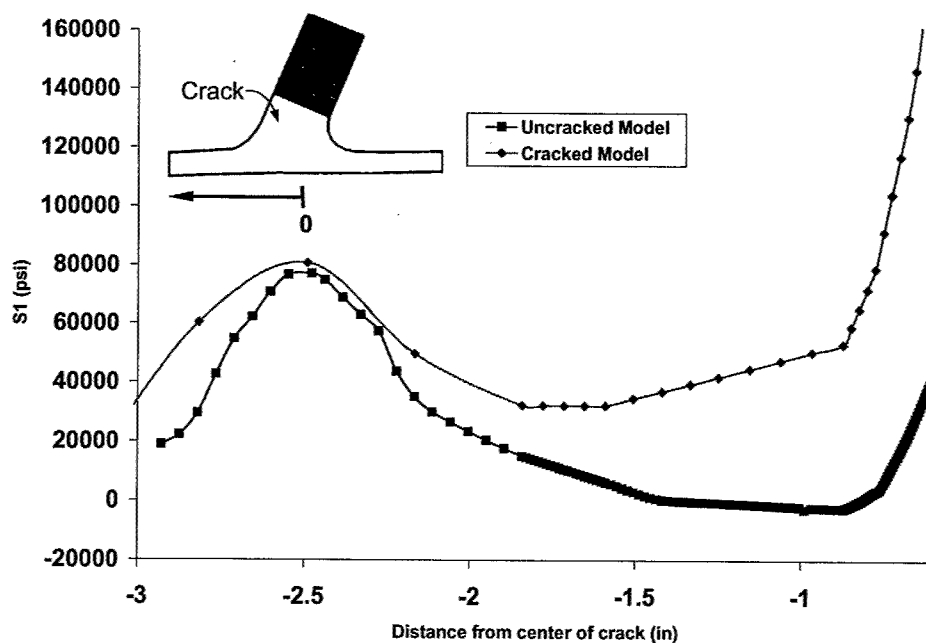


FIGURE 127. MAXIMUM ELASTIC PRINCIPAL STRESS PATH PLOTS FOR UNCRACKED AND CRACKED MODELS, BOSS 7&8—FORE SEGMENT

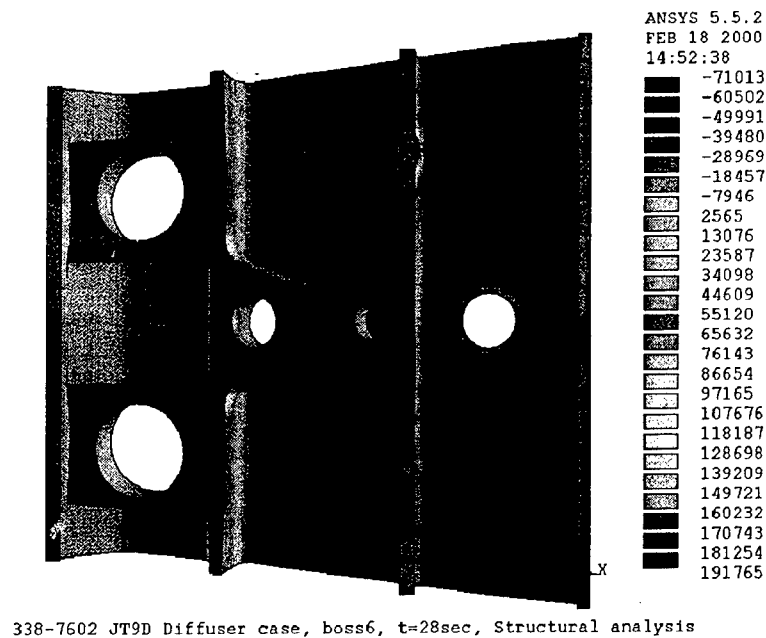


FIGURE 128. PRINCIPAL ELASTIC STRESS DISTRIBUTION FOR CRACKED BOSS 6
(0.290 × 0.400 surface crack on rail)

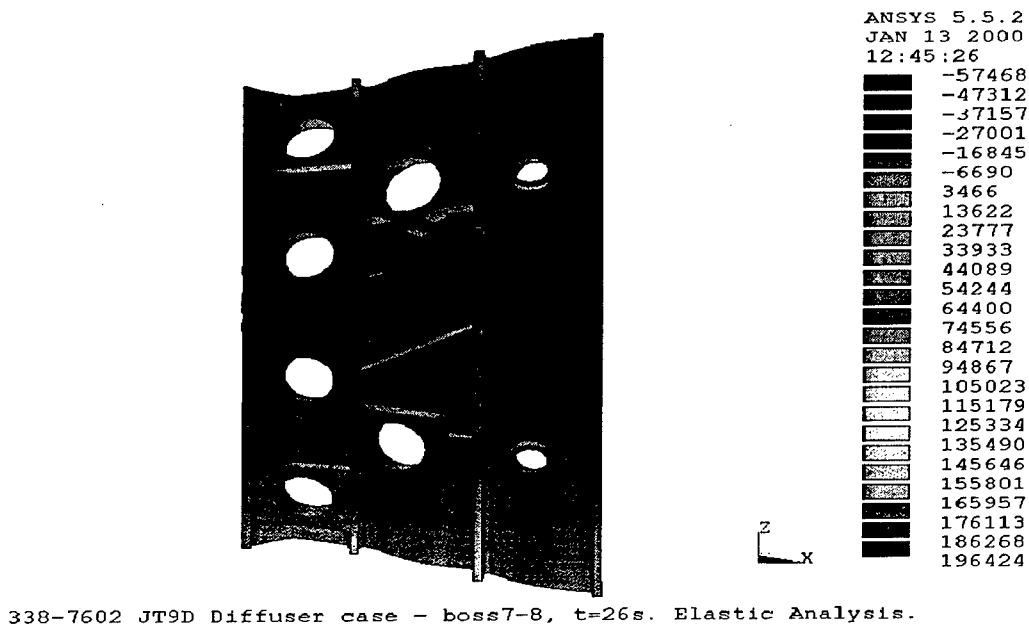


FIGURE 129. PRINCIPAL ELASTIC STRESS DISTRIBUTION FOR CRACKED
BOSS 7&8 (0.290 × 0.400 in. surface crack on rail)

2.2.4.2.8 Through Crack Analysis—FRANC-3D.

Stress-intensity factors for the through-crack analyses are shown in figures 130 and 131. There is no significant difference between the elastic and plastic solutions, since the diffuser case wall stress is not above the material yield strength. Cracks were manually propagated to an axial length of 2 inches. If the cracks were propagated to a larger dimension, the calculations of the SIF would be affected by the boundary conditions of the submodel in the aft side causing the calculations to be overly conservative. Additionally, FRANC-3D only deals with linear elastic model superposition and a concern exists regarding the use of crack face tractions interpolated from an uncracked finite element model. Such a procedure would produce lower K_s once the crack size extends beyond reasonable boundaries (although previous studies have shown acceptable results for larger cracks, $a/W=0.7$, than the ones used in this study with $a/W \sim 0.3$). The next version of FRANC-3D will incorporate FEM capabilities and perform load superposition, resolving this issue.

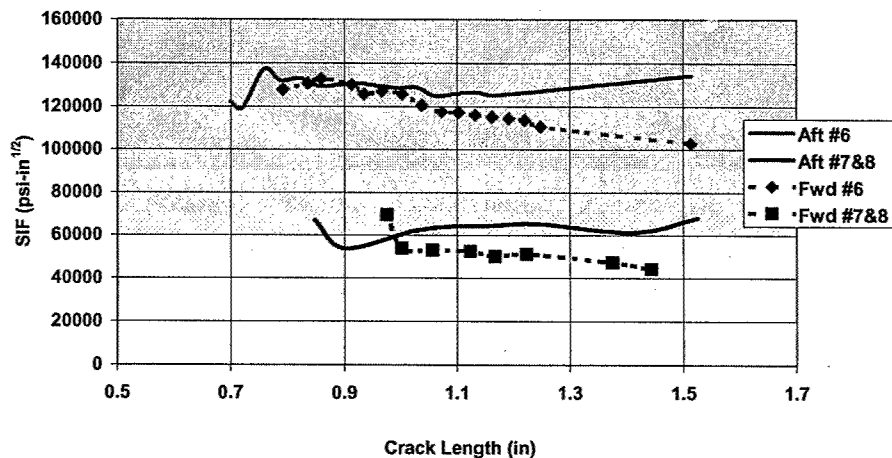


FIGURE 130. ELASTIC STRESS-INTENSITY FACTOR RESULTS FOR THROUGH CRACK

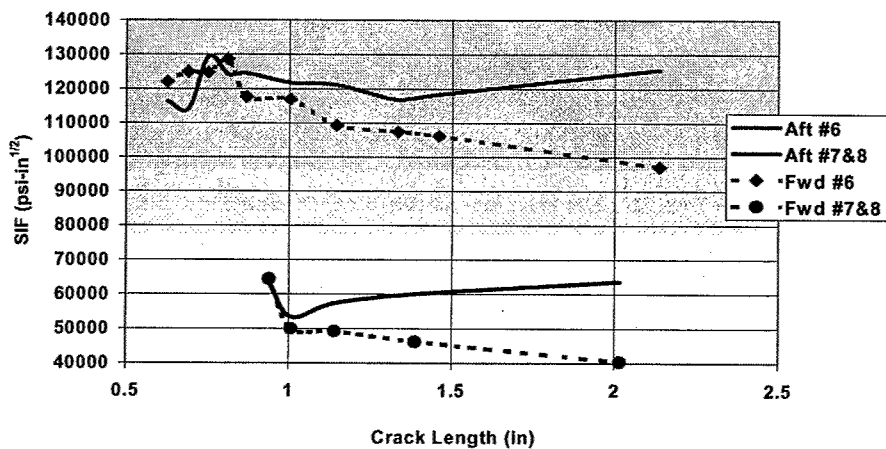


FIGURE 131. PLASTIC STRESS-INTENSITY FACTOR RESULTS FOR THROUGH CRACK

Due to the load redistribution discussed in the previous section, K values for boss 6 were twice as large as that for boss 7&8, while the cracks grow axial in the aft and forward directions. However, in both cases, the shifting of the load to the embossments cause the values to drop slightly as the cracks propagate to the forward side. Stress values gradually increase in the critical aft section, approaching shell mechanical stresses, and produce a minor rise in the SIF values on this region. Life calculations, performed using the Paris Crack Growth model with fracture toughness of the material equal to $150 \text{ ksi-in}^{1/2}$, predict approximately 10 times more cycles for boss 7&8 than for boss 6, as shown in figures 132 and 133. This prediction is consistent with extensive operational experience, which has shown that although large cracks occur adjacent to both boss 6 and boss 7&8, case wall cracks adjacent to boss 6 can lead to rupture, whereas no ruptures have occurred at boss 7&8.

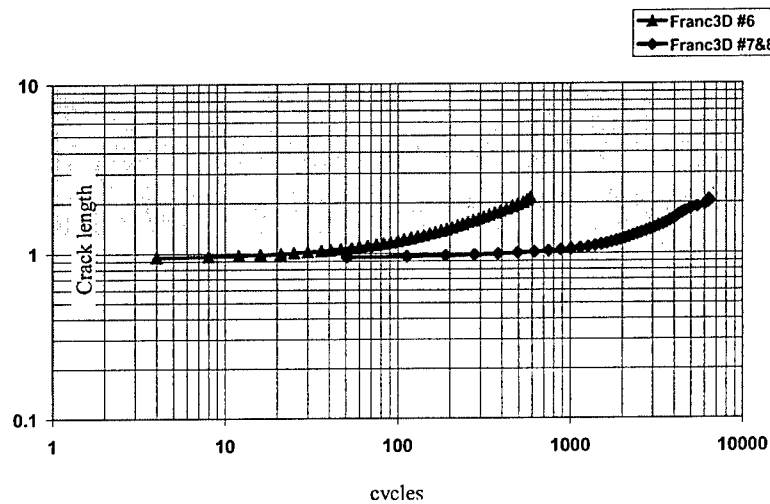


FIGURE 132. LIFE CALCULATIONS FOR THROUGH CRACK USING ELASTIC STRESS FIELD

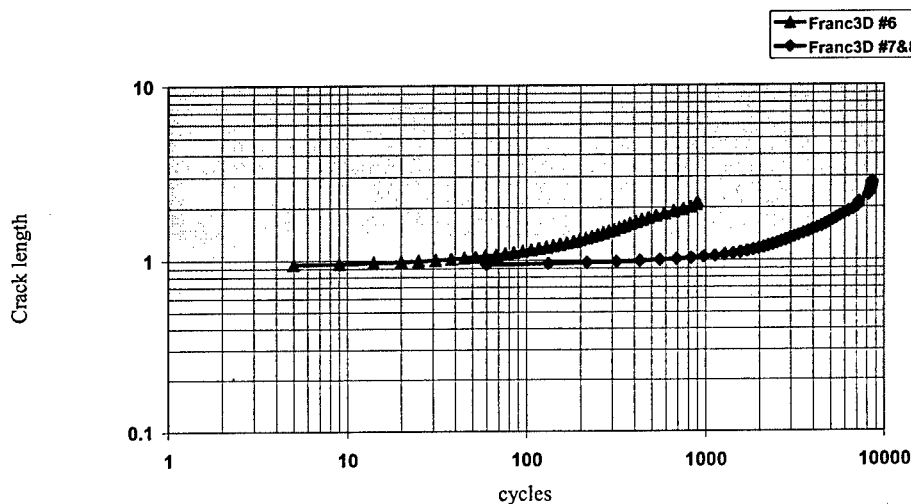


FIGURE 133. LIFE CALCULATIONS FOR THROUGH CRACK USING PLASTIC STRESS FIELD

2.2.4.2.9 Results.

FRANC-3D crack growth predictions agree well with the observed crack propagation in operational cases. FRANC-3D was able to redistribute the thermally driven stresses in the rail/boss area in a JT9D diffuser case and accurately predict the observed large difference between case wall crack propagation at the two boss areas of the case.

2.2.4.2.10 Fracture Mechanics Analysis—SURCK.

The P&W linear elastic fracture mechanics code used in the steel case evaluation was applied to the wrought nickel case to compare with the results from the FRANC-3D analysis. The analysis plan followed here is similar to the one used in the FRANC-3D analysis, evaluating three phases of crack growth, the corner crack, edge crack, and axial crack analyses, as shown in figure 134.

The same stress field and material properties used in the FRANC-3D analysis were also used in this analysis to allow for direct comparison between the two calculation methods.

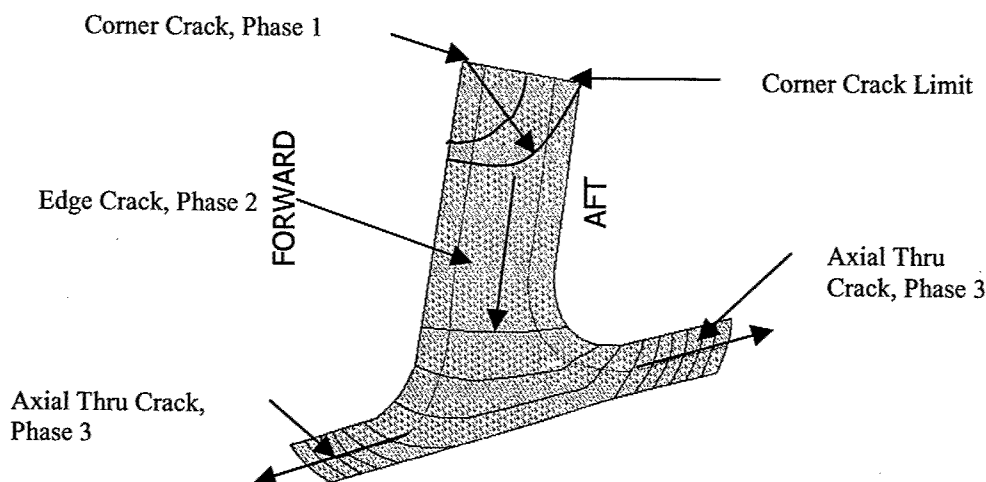


FIGURE 134. THREE PHASES OF CRACK PROPAGATION

2.2.4.2.11 Corner Crack Analysis—SURCK.

The analysis simulated a corner crack adjacent to boss 6 and boss 7&8, using the results from the ANSYS analysis of the rail (figure 135). The calculated SURCK-predicted stress-intensity factors at the crack tip are shown in figure 136. The predicted crack propagation life using SURCK and FRANC-3D fracture mechanics codes are shown in figure 137. The predictions are compared to actual measured crack growth data (striation counts) taken from operating engines in the base metal at the rear rail adjacent to boss 7&8 and other boss locations. The typical predictions for both methods agree well with the field data considering that there is a significant scatter factor between typical and minimum Inconel 718 material properties. Analysis shows that the SURCK code predictions are conservative when compared to the FRANC-3D predictions.

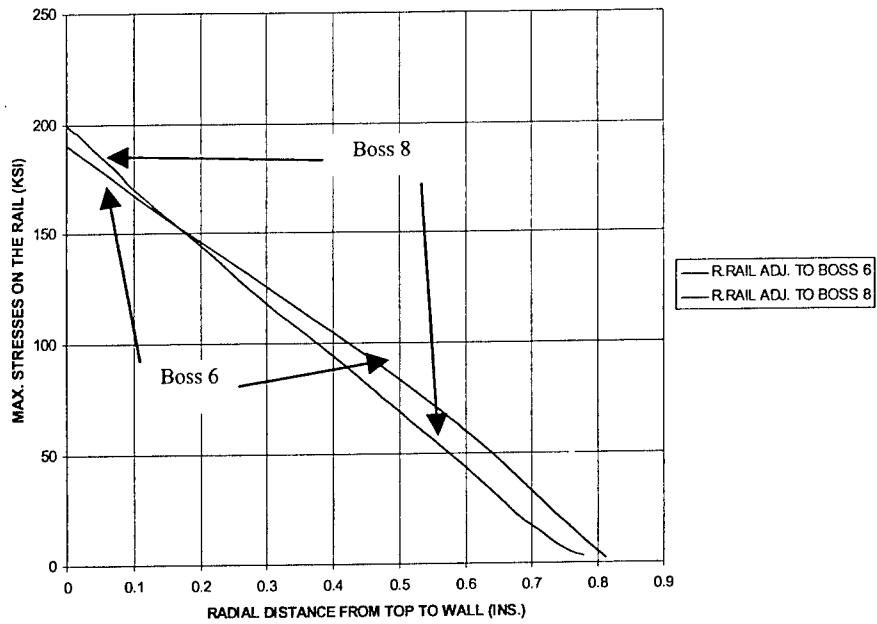


FIGURE 135. WROUGHT IN 718—DIFFUSER CASE REAR RAIL MAXIMUM PRINCIPAL STRESS GRADIENTS

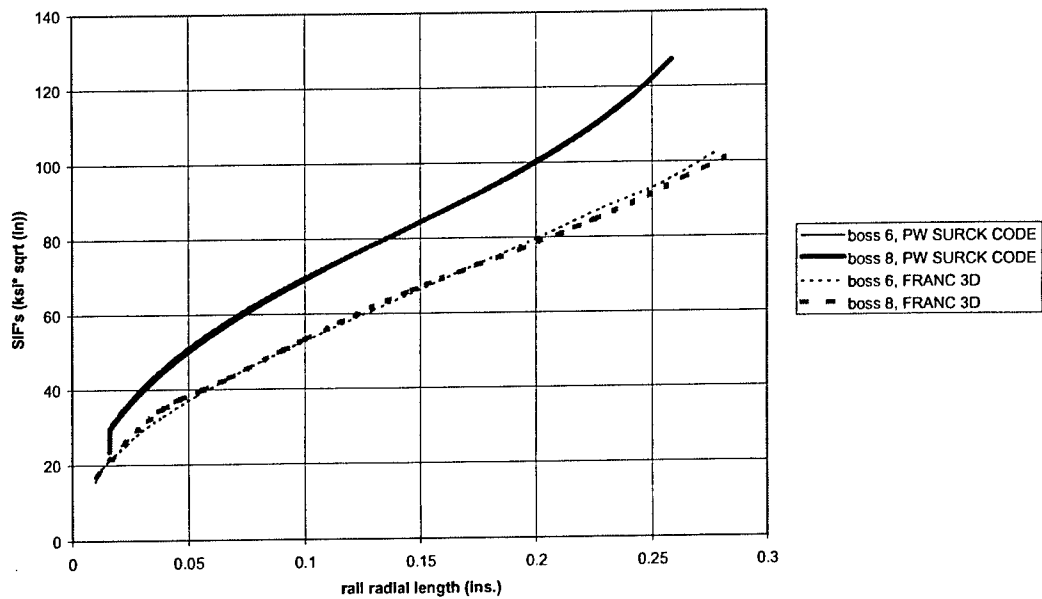


FIGURE 136. JT9D-DC RAIL SIF VALUES COMPARISON BETWEEN SURCK AND FRANC-3D

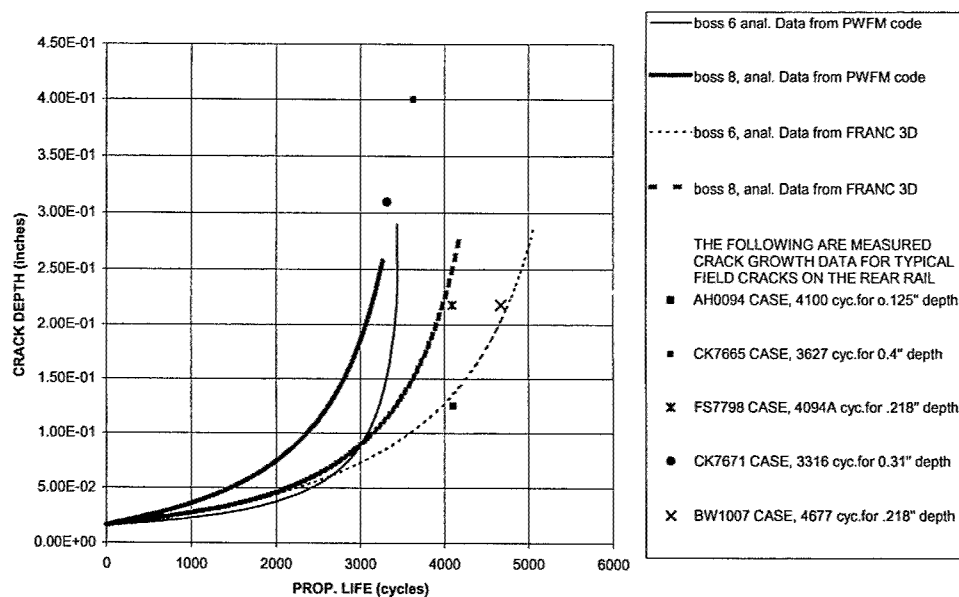


FIGURE 137. JT9D-DC RAIL CORNER CRACK PROPAGATION ADJACENT TO BOSS 7&8 AND BOSS 6, COMPARISON BETWEEN SURCK AND FRANC-3D PREDICTIONS

2.2.4.2.12 Edge Crack Analysis—SURCK.

As the corner crack propagates and reaches the aft side of the rail, it transitions from a corner to an edge crack (figure 134) and has propagated approximately 1.0" down the rail. High SIF values are predicted for this 1" long crack. As in the FRANC-3D calculation, the SIF values exceeded the fracture toughness of the material and resulted in a negligible accumulation of cycles in that region. Field data and reports support this result with no crack striation data detected in this region.

2.2.4.2.13 Through Crack Analysis—SURCK.

Following the edge crack analysis, a through thickness wall crack analysis was performed. The stress gradients calculated for the case wall on both sides of the rail were applied to the crack model. Crack propagation life predictions, are presented in figures 138 and 139. Figure 138 was based on minimum life predictions, while figure 139 was based on typical predictions. In these two plots, the predicted crack propagation life cycle for the case wall were combined with the corner crack propagation life in one single plot showing the total life profile from corner crack propagation at the top of the rail to a critical through wall crack. The curves are discontinued in the middle, where the edge crack transitions from a corner crack to a through wall crack where no crack propagation was predicted. The small curve to the left is the corner crack propagation along the rear rail and the longer one is the axial growth along the case wall. The residual life predictions from SURCK for typical and minimum lives were then compared with field data. The minimum predictions in figure 138 are compared with calculated minimum lives based on field data, while the typical predictions in figure 139 are compared with actual field measured cracks. The analysis shows reasonable agreement with engine data, although the typical data

appears to be underpredicted once the crack goes through the case wall. In addition, SURCK does not predict a significant difference in either life or critical crack size between boss 6 and boss 7&8 as seen in operation, since it cannot account for load redistribution as the crack propagates.

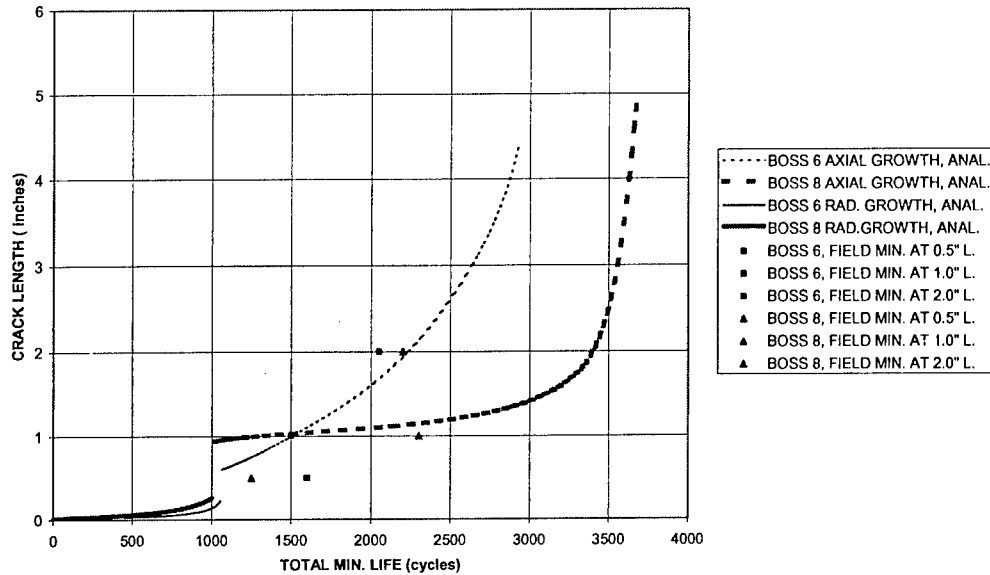


FIGURE 138. JT9D-DC REAR RAIL MINIMUM RESIDUAL LIFE USING SURCK PREDICTIONS

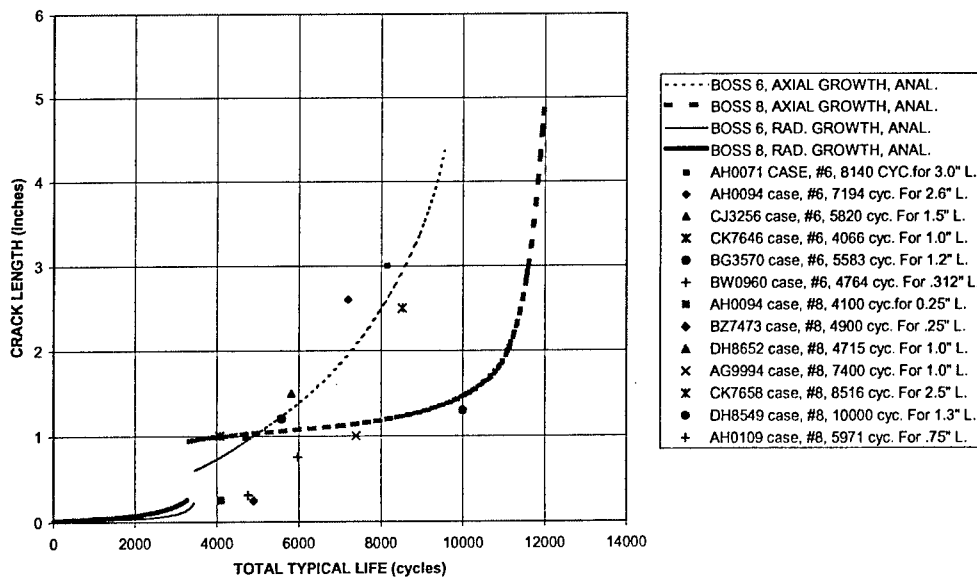


FIGURE 139. JT9D-DC REAR RAIL TYPICAL RESIDUAL LIFE USING SURCK PREDICTIONS

A similar calibration was performed using FRANC-3D life predictions with the results plotted in figures 140 and 141. Figure 140 shows the minimum predicted residual life for the crack starting at the top of the rail and progressing to a through wall crack. Figure 141 presents the typical predictions. FRANC-3D does a better job than SURCK in predicting the observed differences between the critical crack sizes at the two boss locations because FRANC-3D can account for the load redistribution to the adjacent bosses and rail as the crack grows.

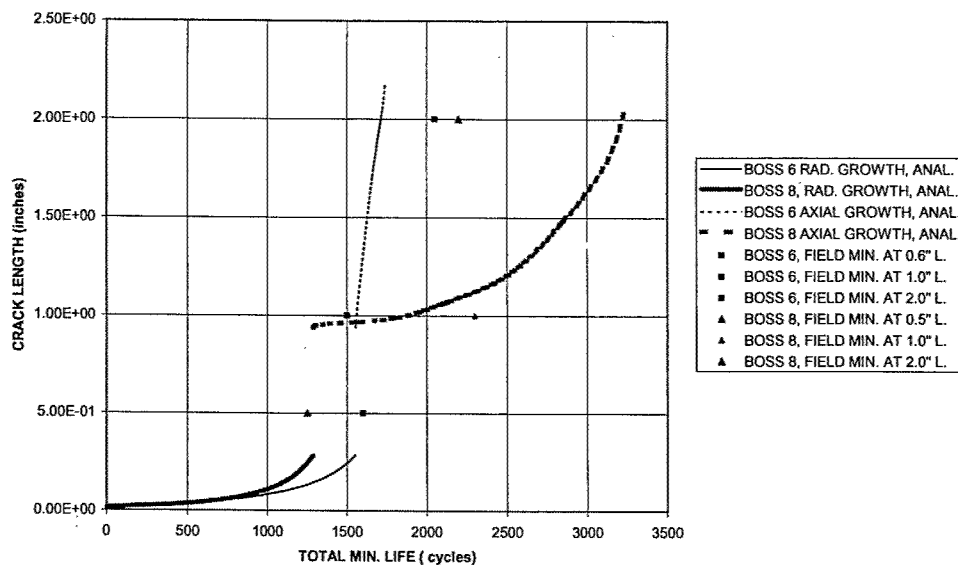


FIGURE 140. JT9D-DC REAR RAIL MINIMUM RESIDUAL LIFE USING FRANC-3D PREDICTIONS

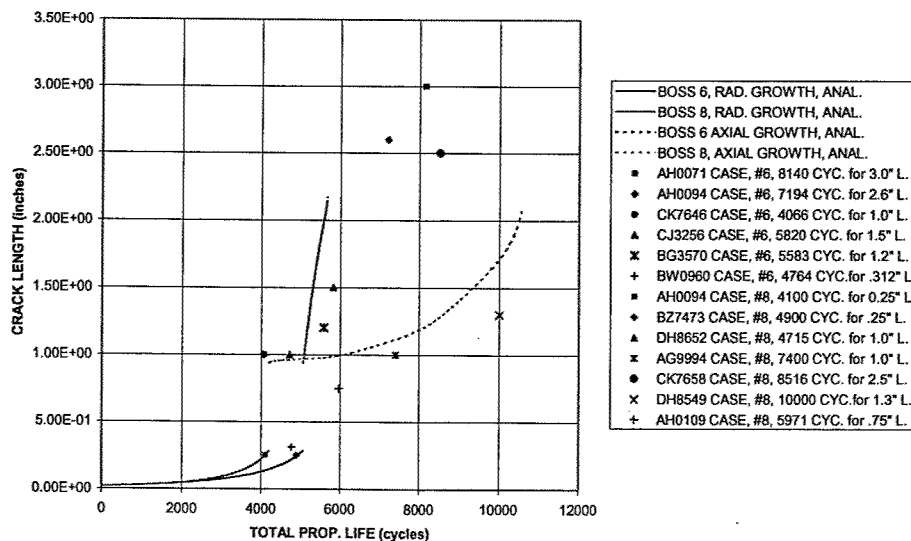


FIGURE 141. JT9D-DC REAR RAIL TYPICAL RESIDUAL LIFE USING FRANC-3D PREDICTIONS

2.2.4.2.14 Fracture Mechanics Analysis—Weld IN 718.

This task covers the ability to predict the residual life in a welded IN 718 component. Some JT9D diffuser case rails are weld repaired in service and have re-cracked due to the high levels of stress present as well as from the weld defects. The variability of the weld defects makes prediction of crack growth in these components difficult since total residual life is a strong function of defect size, location, and orientation. The best method of managing welded cases is to develop a reliable weld repair capability that minimizes defects and provides a high degree of defect detectability. The original scope of this contract included tasks to develop improved welding and inspection techniques. However, the tasks were eliminated due to funding considerations. Knowing that weld defects can be present or that the case may re-crack due to the locally high stress levels makes it important to have the ability to predict crack growth in welded locations.

P&W's JT9D-7A diffuser cases with welds at the rear rail near boss 6 were considered as the test case in this analysis. Upon examining several operational cracked cases, the actual defect size and location along with any striation information from the cracks were recorded. The crack residual life was calculated for each case using the welded material crack growth properties and the predicted lives compared to the actual measured life (striation data) and plotted.

2.2.4.2.15 Crack Growth Properties.

Crack growth rate results were obtained from tests conducted on IN 718 TIG weld specimens. These specimens were exposed to standard postweld heat treatment and aged (30 hrs exposure) solution test results at 800°F and R = 0.1 are presented in figure 142 and are modeled by Paris Law:

$$da / dN = 2.365E - 11 (\Delta K)^{3.974} \quad (3)$$

The previously calculated stress gradients of the rail adjacent to boss 6 were used in the analysis. SURCK was used to calculate the residual life of each diffuser case taking into account the different crack size (weld defect) of each case. The following analyzed cases were selected based on availability of measured crack geometry and striation data for comparison with analytical predictions.

IN 718 weld (FAA Contract) Crack Growth Rate at 800°F
R = 0.1, Post weld+ 30 hrs. Exp.

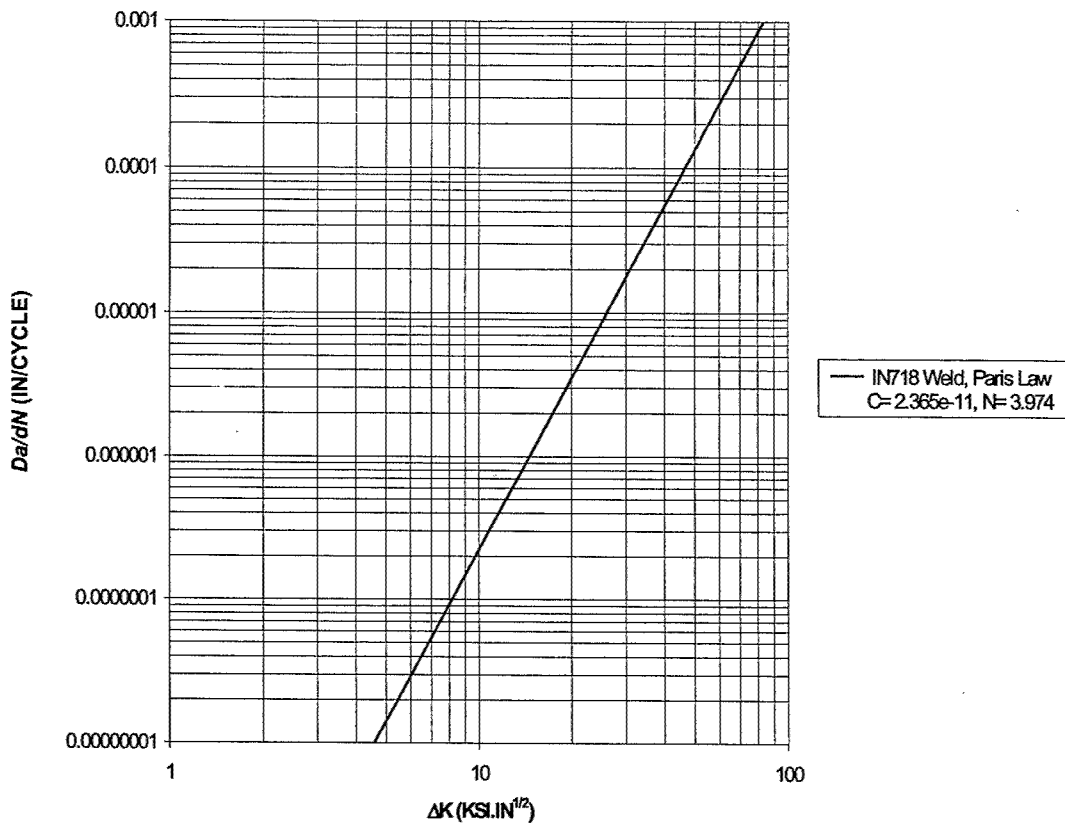


FIGURE 142. PARIS EQUATION MODEL FOR IN 718 WELD

2.2.4.2.16 Welded IN 718—Case BW 1086.

Case BW 1086 is a JT9D-7 diffuser case that had accumulated 904 cycles since its last weld repair when investigation found a 14.75" crack between boss 6 and 7 during an engine removal due to surge and over temperature. The crack had progressed in LCF from a 0.120" x 0.015" weld defect on the front face of the rail. Results of the analysis predict a residual life of ~ 800 cycles along the rear rail as shown in figure 143. The measured crack growth (striation counts) in the rail has been added to figure 143 and shows good agreement with the predictions.

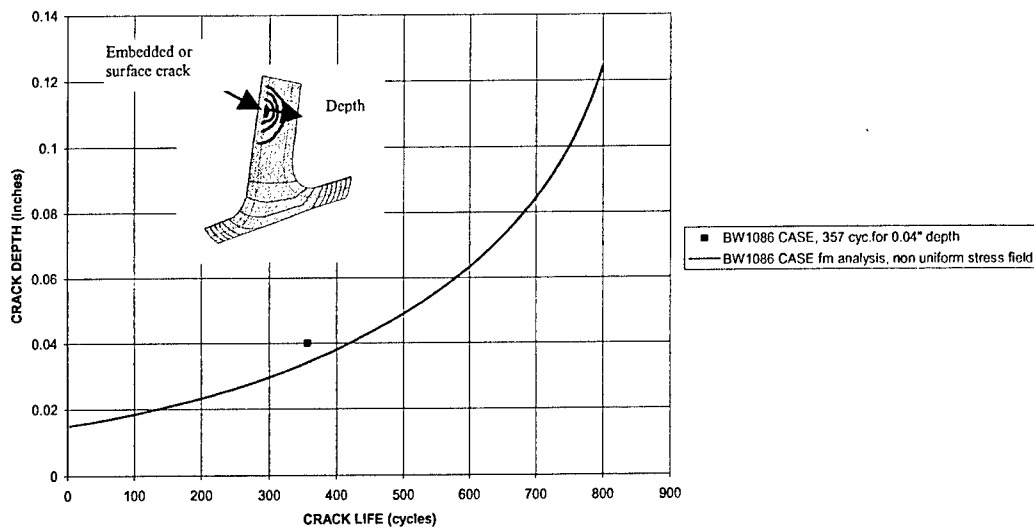


FIGURE 143. JT9D-DC WELDED/REPAIRED REAR RAIL FM ANALYSIS, CASE BW 1086 WELD DEFECT SIZE $\sim 0.12'' \times 0.015''$

2.2.4.2.17 Welded IN 718—Case AH 0071.

Case AH 0071 is a JT9D-7A diffuser case that accumulated 3264 cycles since its last weld repair, and exhibited an 8" axial crack through the rear rail and through the adjacent walls of the case. The crack was due to LCF that progressed from origins at subsurface- and surface-connected weld abnormalities adjacent to boss 6. The weld defect size was approximately $0.035'' \times 0.012''$. The analysis predicts that this case had a life of 2323 cycles for this crack to transition through the rail as shown in figure 144. Measured field data (striation counts) were plotted on the same graph for comparison. Analytical predictions are in good agreement with measured field data.

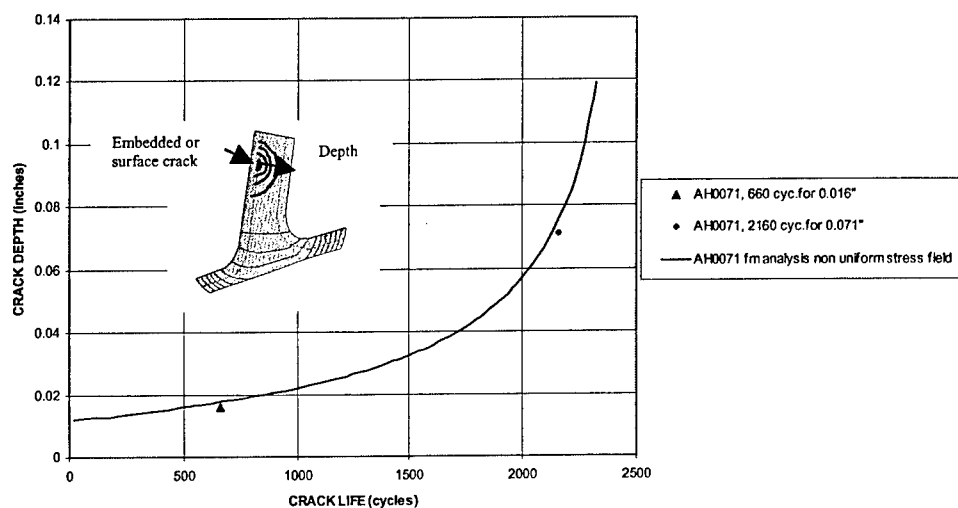


FIGURE 144. JT9D-DC REAR RAIL WELDED/REPAIRED FM ANALYSIS, CASE AH 0071 DEFECT SIZE $0.035'' \times 0.012''$

2.2.4.2.18 Welded IN 718 - Case BG 3352.

Case BG 3352 is a JT9D-7A diffuser case that accumulated 11,669 cycles in service. A crack that propagated in LCF was initiated from a weld defect approximately 0.110" x 0.015" in size on the front surface of the rear rail. Analysis predicts that this case has a crack growth life of 859 cycles to progress through the rail width axially (results are plotted in figure 145). Measured field data (striation counts) showed that the case had between 700 to 1000 cycles (average 850 cycles) of crack progressions on the rail before it changed to an overload tensile progression. The measured distance of LCF progression is 0.05". Analytical prediction is conservative with respect to the field data.

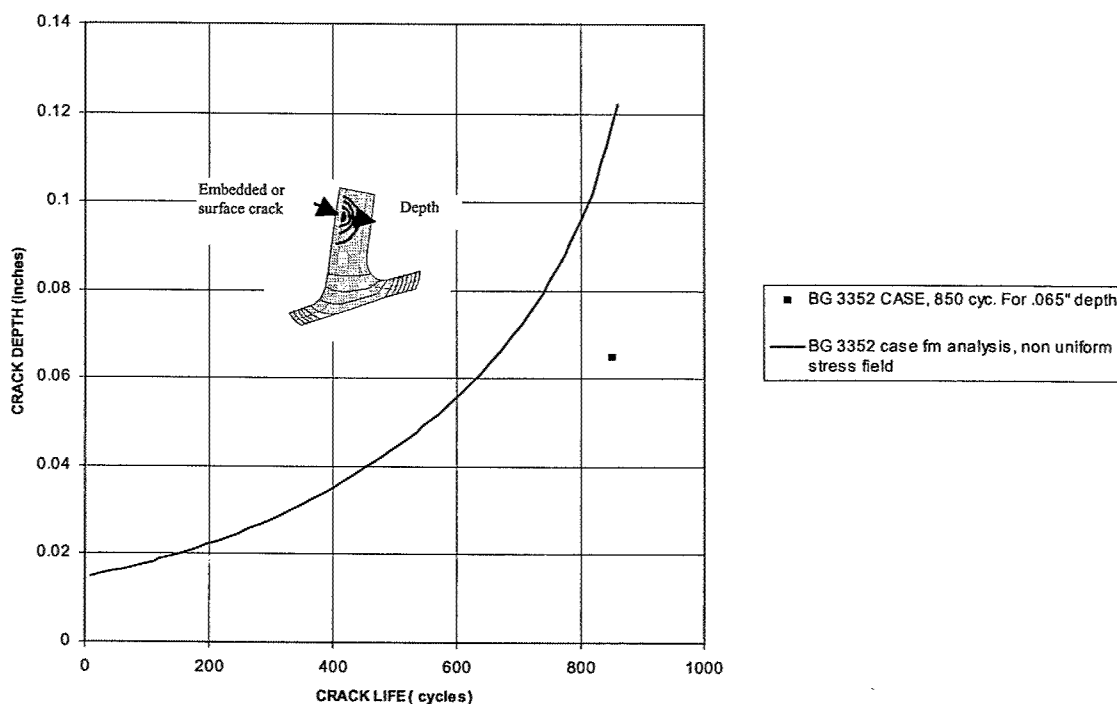


FIGURE 145. JT9D-DC WELDED/REPAIRED REAR RAIL FM ANALYSIS, CASE BG 3352, DEFECT SIZE 0.110" x 0.015"

2.2.4.2.19 Results.

Three-dimensional finite element stress analysis predicts critical locations of the diffuser case rear rail adjacent to boss 6 and boss 7&8 as shown by field experience.

Crack growth rate and life predictions calibrate well with actual operational case cracking as demonstrated by comparing the minimum and typical crack predicted propagation lives to actual data. The linear elastic fracture mechanics predictions are typically conservative with respect to the actual crack growth, especially in areas of high thermally driven stress. The FRANC-3D code is less conservative in its predictions.

The crack growth characteristics of embedded weld flaws can be predicted if the location and size of weld defects are known. Since inspection techniques may not always locate an existing weld flaw, conservative estimates of location and size should be used in the analysis.

2.2.4.3 Aged Cast Nickel Alloy Case Analysis.

As described in task 2, a cast Inconel 718 PW4000 diffuser case previously tested for 1600 cycles at P&W was procured for use in the cyclic-pressure rig test. Prior to testing, the case was given a furnace heat treatment for 40 hours at 1750°F to simulate the effect of multiple repair cycles. Eleven EDM slots were placed in the case to generate crack growth information in the pressure rig facility at a constant temperature of 1150°F and a cyclic pressure of 585 psig. Periodic inspections were performed and crack growth data was collected for use in calibrating the crack growth characteristics of a full-size cast case.

To evaluate design changes and experimental requirements, the case was modified at P&W. An instrumentation boss was added by electron beam (EB) weld buildup and then ground to final shape. This modified area was believed to have cracked during the original 1600 cycles of engine operation and grew to a through wall crack during pressure rig cycling.

The case started cycling in the pressure rig with test conditions consisting of 6 seconds at load and 2 minutes at no load, producing a nominal wall stress of 45 ksi. The case accumulated 684 cycles before a pressure gas leak started from the case precluding further testing. The cause of the leak was found to be a 5.00" long through wall axial crack between the fillets of the welded-in test instrumentation boss and a cast bracket support boss.

The crack was excised from the case and thoroughly examined to determine the cause of cracking and estimate the rate of crack growth. This provided additional crack growth data that could be used in the calibration process. The case was weld repaired to allow for continued cyclic running and gathering of crack growth information in the EDM slots. After an additional 1758 cycles (2442 cycles total), a 0.990" crack was found in the repaired area. A patch was welded into the case and an additional 3147 cycles accumulated before the case ruptured. Dwell testing was terminated after 2594 cycles because case pressure could not be maintained due to the distortion of the flange caused by the welding process.

2.2.4.3.1 Rig Case Stress Evaluation.

A limited strain gage program was performed on the case before the cyclic pressure tests began. Strain gages (figure 45) were placed as described in task 1. A NASTRAN analysis of the case was also performed. Table 36 shows a comparison between the predicted stress and those measured during the strain gage test.

TABLE 36. CYCLIC PRESSURE RIG PREDICTED VS MEASURED STRESSES

EDM Slot	Boss Description	Predicted Stress (ksi) from NASTRAN	S/G Stress (ksi)	S/G Stress (ksi)	S/G Stress (ksi)	S/G Stress (ksi)	S/G No.
1	No. 3 oil scavenge boss	90	84.2	90.4	out		4,8,17
2	Customer Bleed Boss	111	85.2	out			20,18
3	Large Service Boss	113	98.3	out			10,14
4	Customer Bleed Boss	102	100.9	79.6	82.7		6,9,22
5	Ps4 Tobi Sense Boss	90	80.6	out	78.6	90.4	16,17,21,8
6	Borescope Boss	93	78	96.3			24,25
7	Pressure Wall-Cast		37.7	35.5			1,11
8	Large Service Boss	122	98.3	85.2	out	66.8	10,20,18,23
9	P. Wall-post HIP Weld	45	37.7	33.9	35.5	41.6	1,2,11,12
10	P. Wall-post HIP Weld	45	37.7	33.9	35.5	41.6	1,2,11,12
11	P. Wall-post HIP Weld	45	37.7	33.9	35.5	41.6	1,2,11,12
No slot	Boss Fillet Runout	31-40, 26.8	25.1	27.4			7,19
No slot	Forward Press. Wall	31-40, 26.8	35.3	27.4			5,15
No slot	Aft. Of FNP	46.2-53.0, 40.8	47.2	43.7			3,13

2.2.4.3.2 EDM Slot Crack Growth Correlation.

Out of the 11 EDM slots created, only three slots (2, 6, and 8) experienced crack growth during the cycling of the rig. The history of crack growth measurements on these slots during the rig test is presented in table 37. Crack growth at the bore and the wall sides of an EDM is shown in figure 146.

TABLE 37. CRACK LENGTH FROM SLOT CENTER—INCHES

Rig Cycles	EDM2 Bore	EDM2 Wall	EDM6 Bore	EDM6 Wall	EDM8 Bore	EDM8 Wall
2242	0.055	0.05	0.056	0.026		
3606	0.125	0.085	0.086	0.038	0.042	0.049
4600	0.22	0.195	0.091	0.066	0.054	0.058
5106	0.255	0.28	0.141	0.076	0.056	0.061
5589	0.454	0.545	0.182	0.098	0.072	0.071

EDM slot 2 was placed on the fillet radius of a customer bleed boss and is shown in figure 146 along with subsequent crack growth from the slot. This location was selected to obtain crack growth data because it is at the location of a stress concentration and thus a possible location of cracking in the field. Figure 147 presents a comparison of EDM slot 2 crack growth data with analytical predictions from the linear elastic SURCK code. The 2D stress field in conjunction with a corner crack model correlates reasonably well with the crack lengths from FPI measurements. The 1125°F crack growth law used in the analysis has been interpolated from 1100° and 1175°F specimen testing under nondwell conditions. The testing previously reported did not include dwell period during EDM slot crack growth due to the effect of leakage (from distortion due to weld patch repair) and the inability of the furnace to hold temperature with excessive rig through flows. Minimizing the time the case was pressurized limited both heat loss and temperature drop.

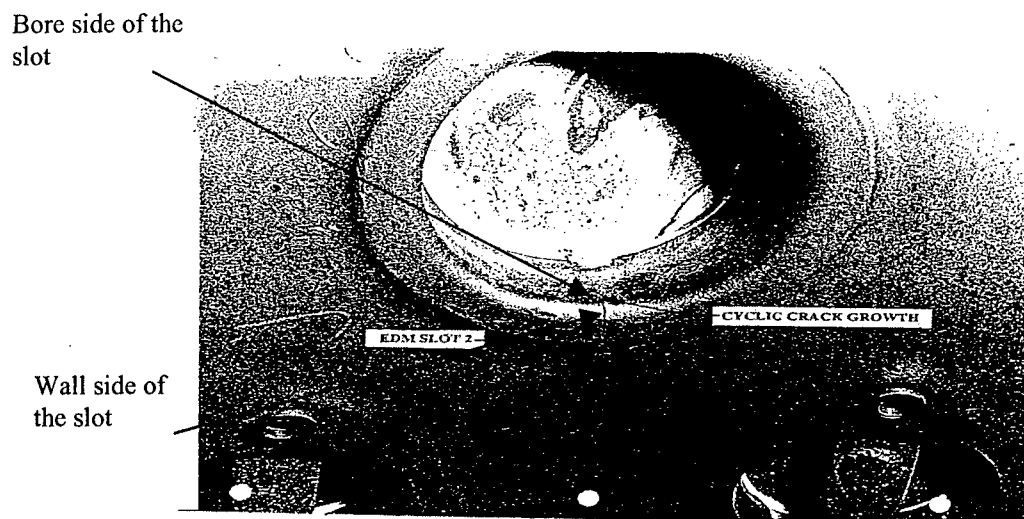


FIGURE 146. EDM SLOT 2 AND CYCLIC CRACK GROWTH

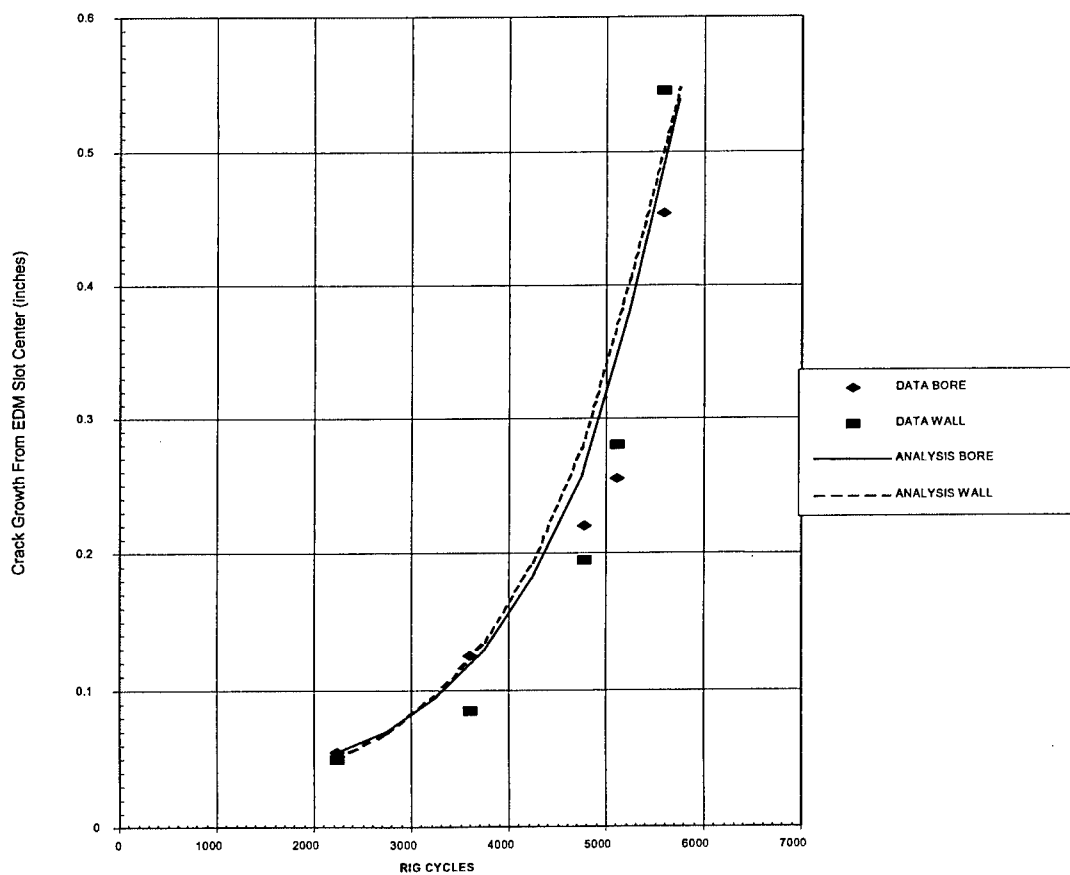


FIGURE 147. CRACK GROWTH CORRELATION EDM SLOT 2

The crack growth prediction of slot 8 (large service boss corner location) was made by using the corner crack formulation in SURCK along with a 2D stress distribution derived from a NASTRAN analysis. Stress results are shown in figure 148, while figure 149 shows the fractured section of slot 8. Figure 150 compares the predicted crack growth results with the measured growth. The correlation appears reasonable until the last data point. Considering a da/dN scatter factor of 1.5 exists for this material, this data point would be covered in the material property scatter.



FIGURE 148. MAXIMUM STRESSES AT SLOT 8 LOCATION USED IN THE FM ANALYSIS

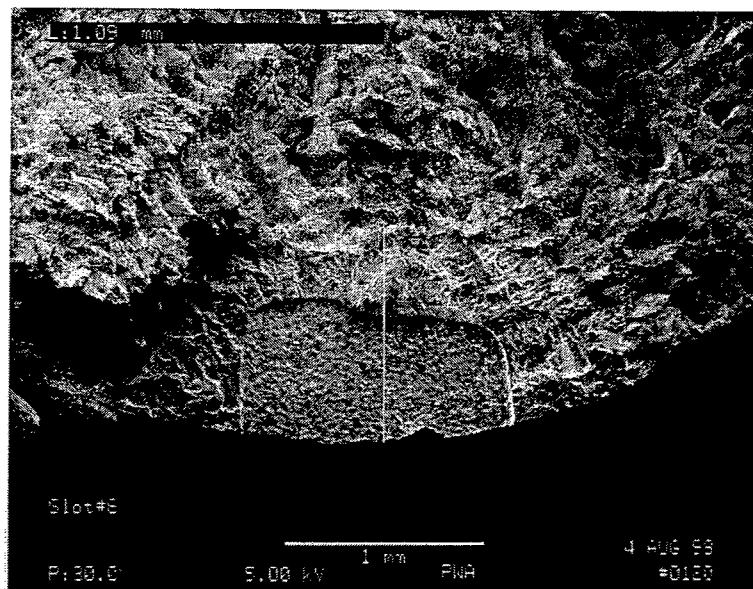


FIGURE 149. PHOTOMICROGRAPH OF SLOT 8 AFTER THE CRACK WAS BROKEN OPEN (Fracture beyond these points was primarily by tensile overload.)

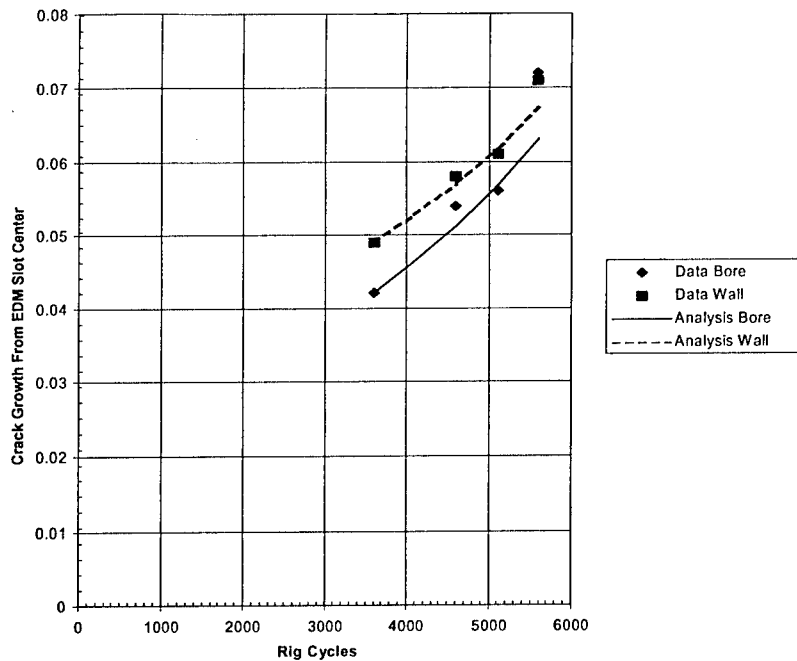


FIGURE 150. CRACK GROWTH CORRELATION FOR EDM SLOT 8

EDM slot 6 was placed on the corner of a borescope boss hole and predictions and striation data are shown in figure 151. Predicted stresses from a simplified NASTRAN model are shown in figure 152. A fracture mechanics model similar to that used in the models for EDM slots 2 and 8, which correlate reasonably well, is grossly optimistic in this case, even considering the scatter within the material data. Considering that the correlation for the other EDM slots was acceptable, it is believed that the lack of correlation in slot 6 is due to the relatively crude geometry definition used in the NASTRAN model, giving inaccurate stress levels. It is believed that a full 3D stress analysis of the area would have produced more acceptable results.

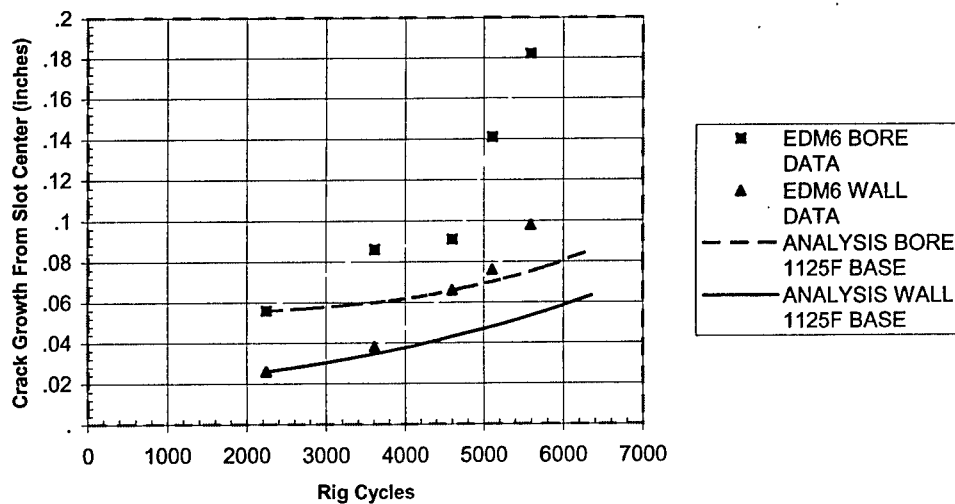


FIGURE 151. EDM SLOT 6 CRACK GROWTH CORRELATION

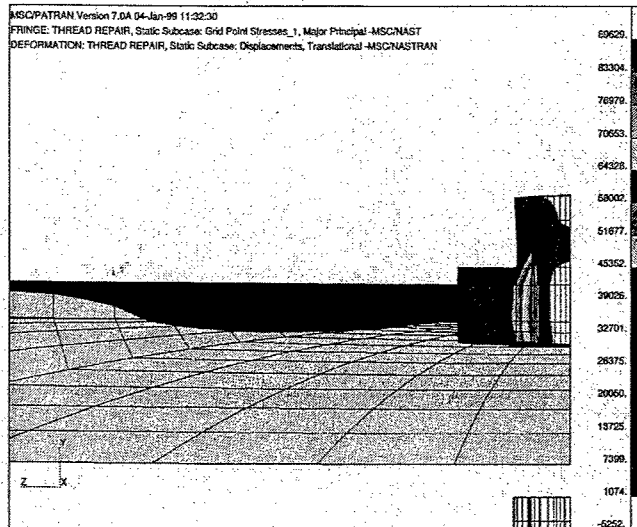


FIGURE 152. MAXIMUM STRESSES AT THE SLOT 6 LOCATION
USED IN THE FM ANALYSIS

2.2.4.3.3 Case Wall Crack Growth Analysis.

The striation data, shown in figure 153, taken from the 4.125" long crack show the rate of crack propagation through the thickness of the case wall. Although unexpected, this crack incident provided additional crack growth data to be used in the crack growth analysis evaluation. Although the crack occurred from a boss produced from a nonproduction process, it is a good representation of what could occur in a field-operated case if good design practices are not followed.

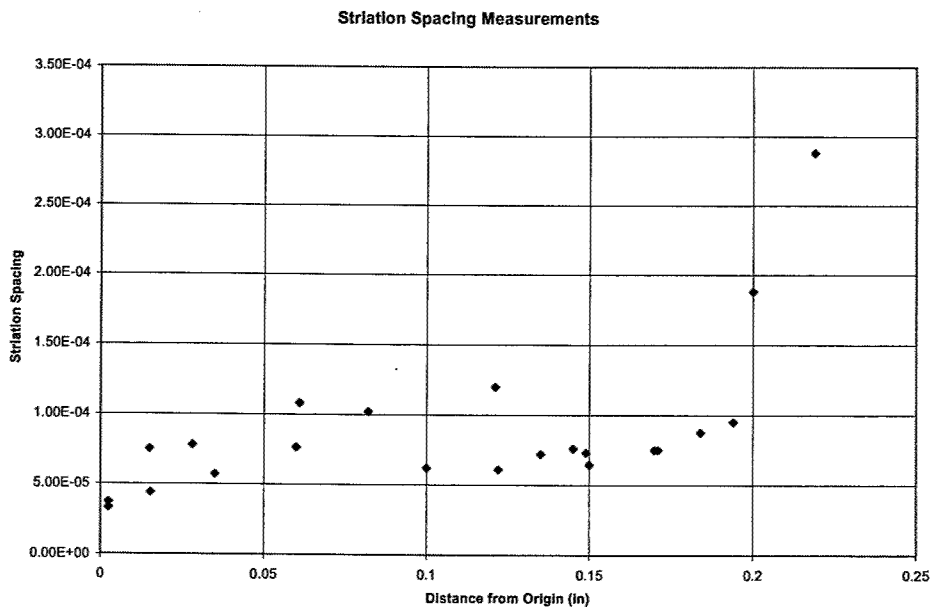


FIGURE 153. STRIATION DATA OBTAINED FROM THE 4.125" LONG CASE CRACK

The striation data (figure 153) represent crack growth from the engine conditions as well as from the rig cycling. A break in the data occurs near the 0.122 in. depth area. It is assumed that the engine striations end and the rig striations begin at or near this point.

The 15 degree ANSYS sector model (figure 154) was converted to a FRANC-3D boundary element model (figure 155). The boundary conditions were applied and the model was meshed in FRANC-3D. Since the crack propagated under two different states of stress, engine and rig, two separate analyses were conducted.

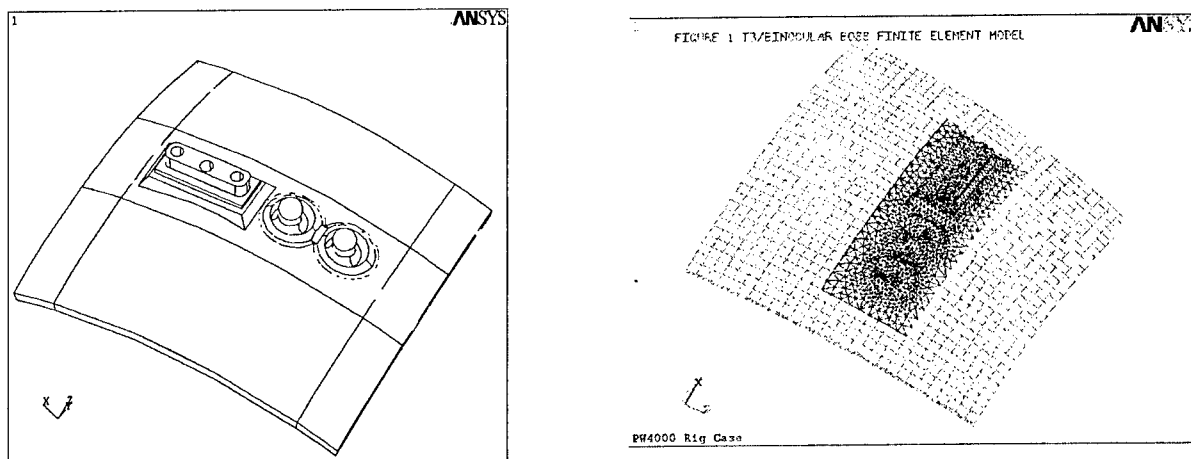


FIGURE 154. ANSYS MODEL OF THE DIFFUSER CASE SECTION

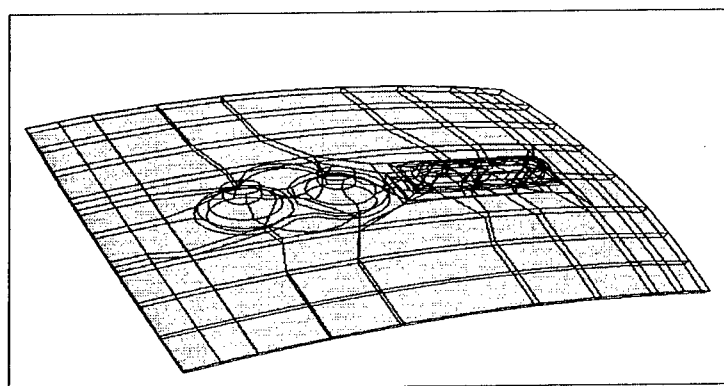


FIGURE 155. FRANC-3D MODEL IMPORTED FROM THE ANSYS DIFFUSER CASE MODEL

2.2.4.3.4 Analysis Under Engine Conditions.

The ANSYS analysis of the case was used to predict the state of stress at the limiting engine condition. Since the stress calculated between the bosses in the elastic analysis was well above the yield strength of the case material ($\sigma_{\max} = 260$ ksi), an ANSYS plastic analysis was performed. The maximum calculated stress in this condition reduced to 160 ksi. Results of the elastic- and plastic-stress analyses are shown in figures 156 and 157.

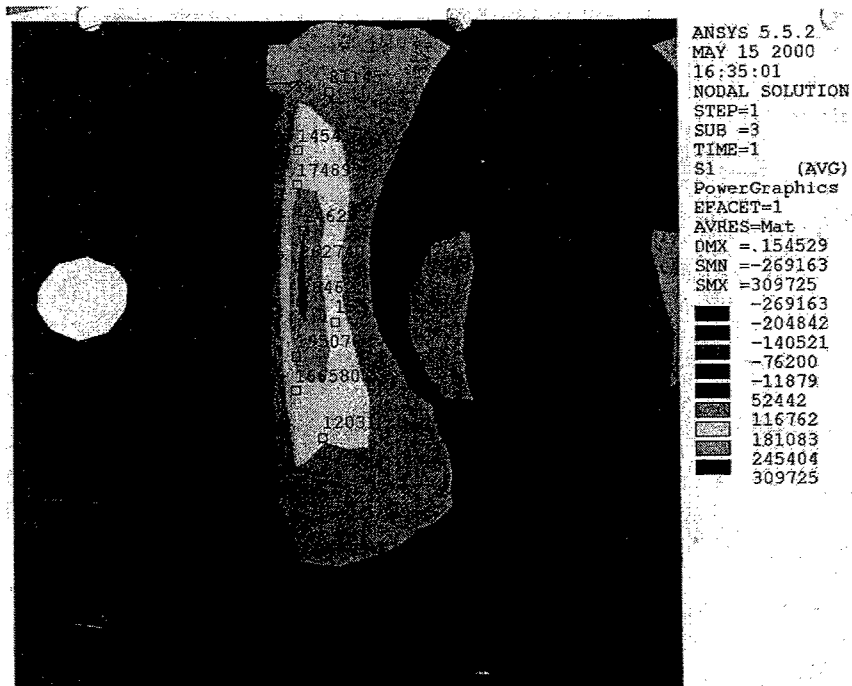


FIGURE 156. ELASTIC PRINCIPAL STRESSES BETWEEN THE
Tt3/BINOCULAR BOSSES

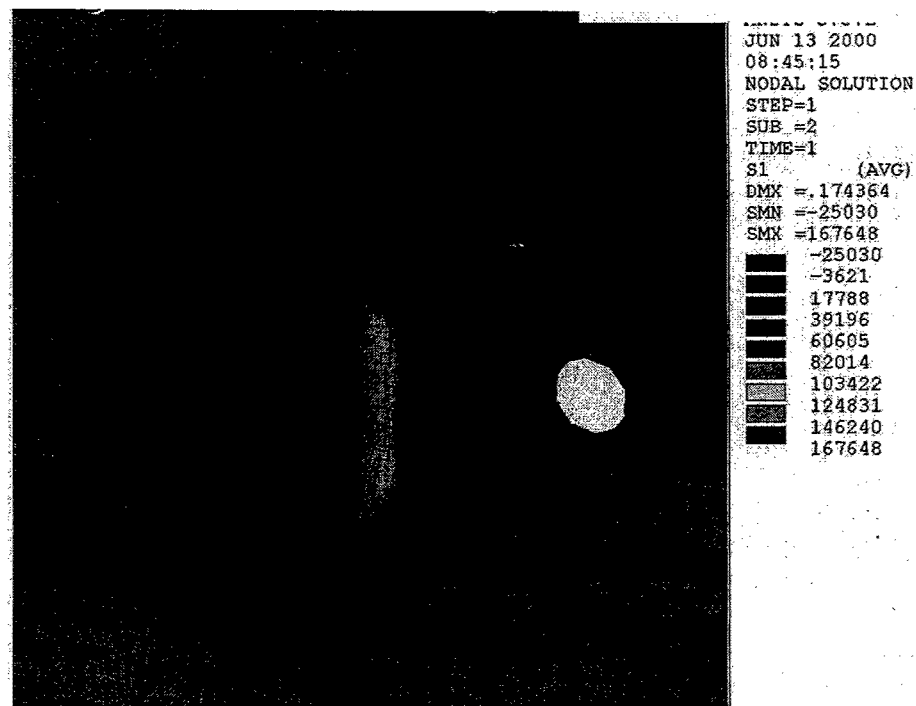


FIGURE 157. PLASTIC PRINCIPAL STRESSES BETWEEN THE
Tt3/BINOCULAR BOSSES

The weld left a heat-affected zone in the diffuser case where it is believed many microcracks were linked together to form a long, shallow crack. FRANC-3D analysis simulated this with the initial crack in the model, as shown in figure 158.

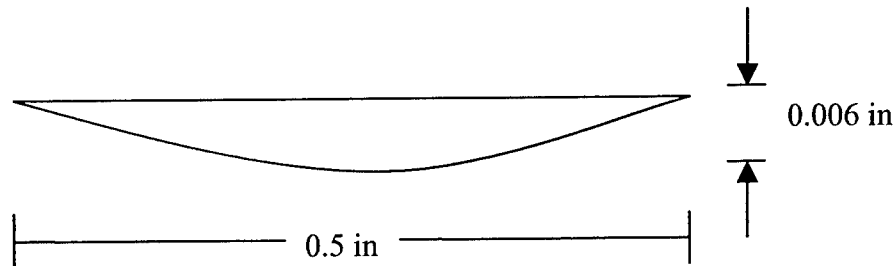


FIGURE 158. INITIAL CRACK GEOMETRY NUCLEATED BETWEEN THE Tt3 AND THE BINOCULAR BOSSES IN THE ENGINE CORRELATION

The crack in the FRANC-3D model was extended, remeshed, and solved a total of eight times until the crack depth was near 0.122 in., as seen in the hardware. The maximum SIF value was recorded for each crack front and is shown in table 38.

TABLE 38. STRESS-INTENSITY FACTORS AT VARIOUS CRACK LENGTHS FOR THE ENGINE CONDITIONS AND THE CALCULATED da/dN VALUES

Crack Length (in)	Stress Intensity Factor (ksi)	da/dN (in/cycle)
0.006	14.9	1.30E-6
0.020	26.6	8.63E-6
0.033	33.6	1.84E-5
0.048	46.9	5.48E-5
0.062	52.2	5.98E-5
0.073	53.0	8.15E-5
0.088	53.5	8.40E-5
0.102	54.8	9.09E-5
0.118	55.9	9.70E-5

Since the crack growth in the case occurred during engine operation prior to the case undergoing the 40-hour heat treatment process, a “nonaged” material Paris Law was used. This equation, developed by P&W, is shown below.

$$\frac{da}{dN} = 1.95 \times 10^{-10} \cdot (\Delta K)^{3.26}$$

This resulted in the crack growth values shown in table 38. These predictions, as well as predictions made using the P&W SURCK code and plastic ANSYS stresses, are plotted in figure 159 for comparison.

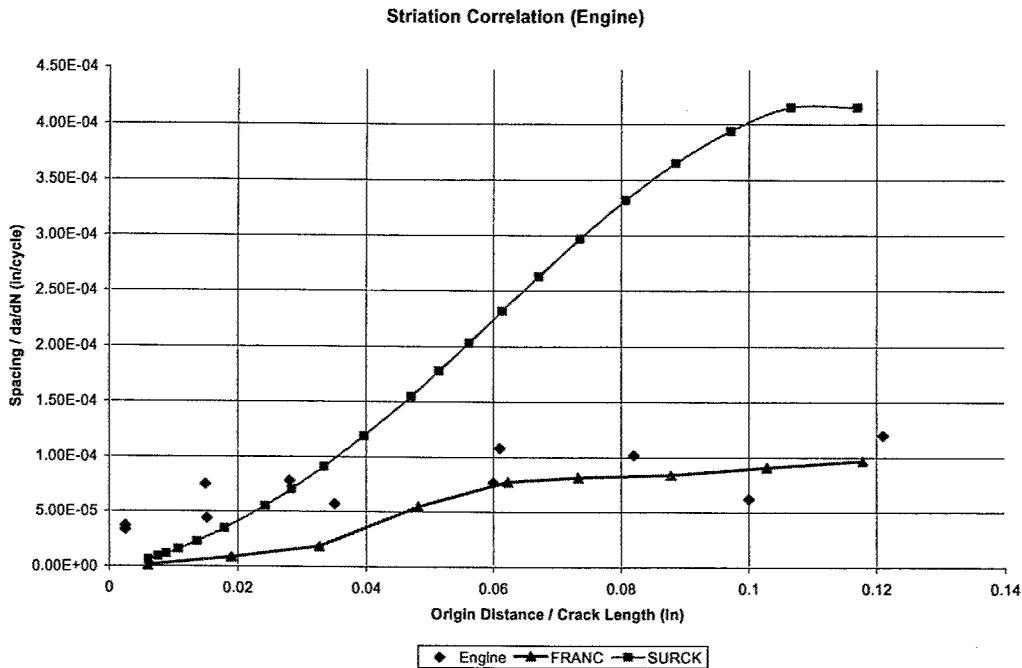


FIGURE 159. FRANC AND SURCK PREDICTIONS PLOTTED WITH THE STRIATION DATA FROM THE ENGINE TEST

2.2.4.3.5 Analysis Under Rig Test Conditions.

The ANSYS finite element model was resolved for the rig conditions of 1150°F and an internal pressure of 435 psi. A maximum stress of 102 ksi was predicted as shown in figure 160. The nodal solution was input into the FRANC-3D model.

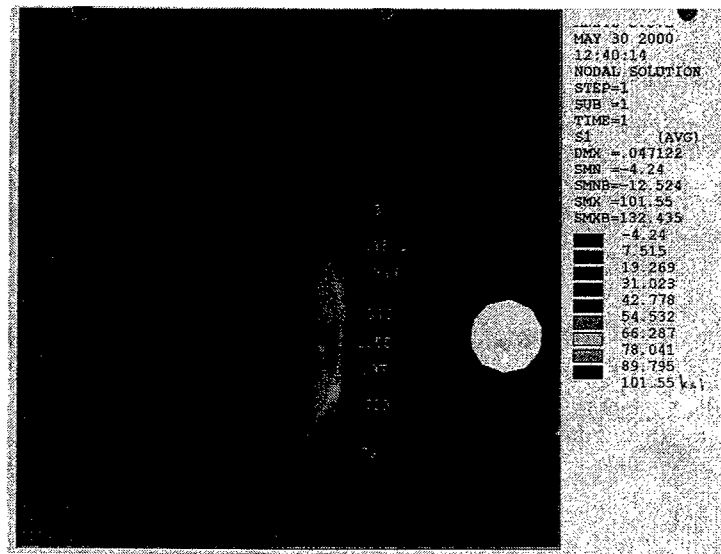


FIGURE 160. MAXIMUM PRINCIPLE STRESS BETWEEN THE TT/BINOCULAR BOSSES AT RUNNING RIG CONDITIONS

Figure 161 shows the initial crack assumed to be present during the cycling of the rig based on the metallurgical review of the crack.

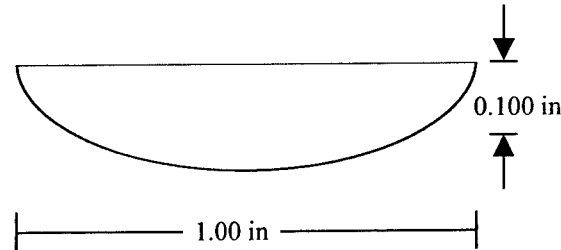


FIGURE 161. INITIAL CRACK GEOMETRY NUCLEATED BETWEEN THE Tt3 AND THE BINOCULAR BOSSES IN THE RIG CORRELATION

As in the engine analysis, the crack was propagated and the stress-intensity factor was predicted as a function of crack depth. Nodal stresses used to attach crack face tractions came from the isothermal ANSYS run. da/dN values were calculated from the hyperbolic-sine law developed in task 1 from the testing of material that underwent similar heat treatments. The results are shown in table 39, and the crack law used for this analysis is shown below. A plot of the aged and nonaged crack growth laws used in this analysis is shown in figure 162.

$$\log\left(\frac{da}{dN}\right) = 0.5 \cdot \sinh[5.512(\log(\Delta K) - 1.532)] - 4.389$$

A SURCK analysis was also conducted using the stresses taken from ANSYS, the same initial crack, and the same hyperbolic sine law to compare to the FRANC-3D result. In figure 163, the striation data, SURCK prediction, and the FRANC-3D predictions are plotted for comparison.

TABLE 39. STRESS-INTENSITY FACTORS AT VARIOUS CRACK LENGTHS UNDER THE RIG CONDITIONS AND THE CALCULATED da/dN VALUES

Crack Length (in)	Stress-Intensity Factor (ksi)	da/dN (in/cycle)
0.100	34.2	4.15E-05
0.107	35.5	4.59E-05
0.120	36.2	4.84E-05
0.131	37.1	5.18E-05
0.145	37.7	5.43E-05
0.157	39.4	6.17E-05
0.171	40.6	6.74E-05
0.183	42.8	7.92E-05
0.195	45.2	9.50E-05
0.207	48.8	1.25E-04

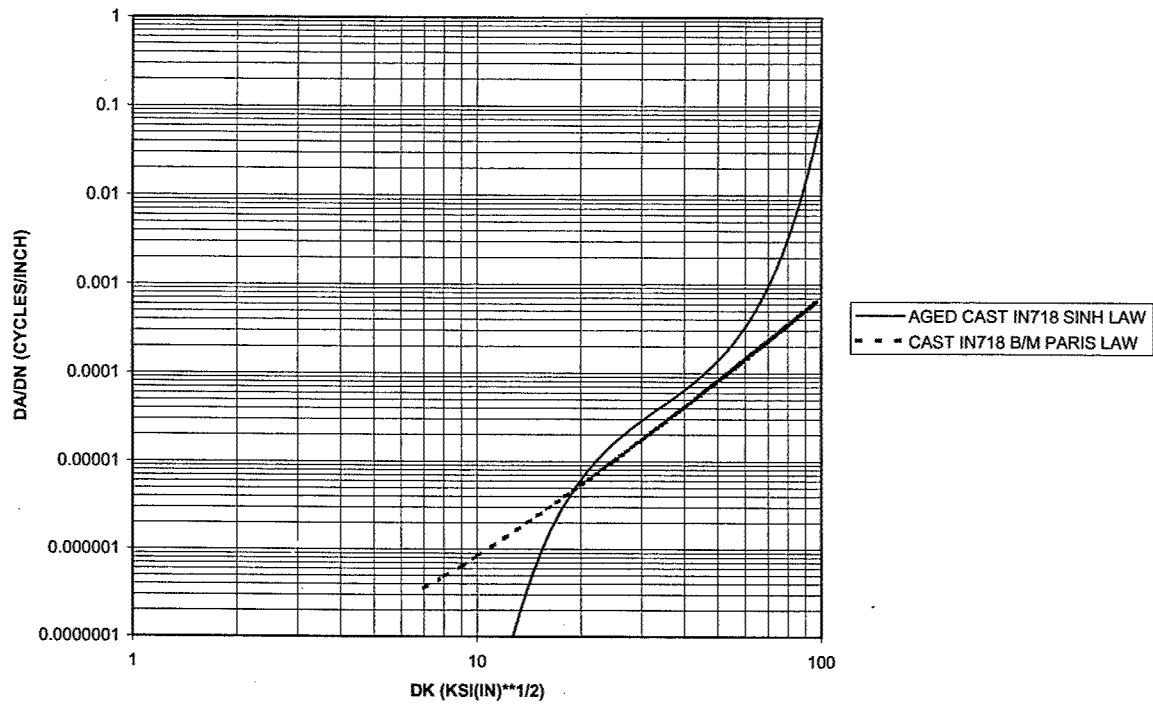


FIGURE 162. CAST IN 718 (AGED) CRACK GROWTH LAW

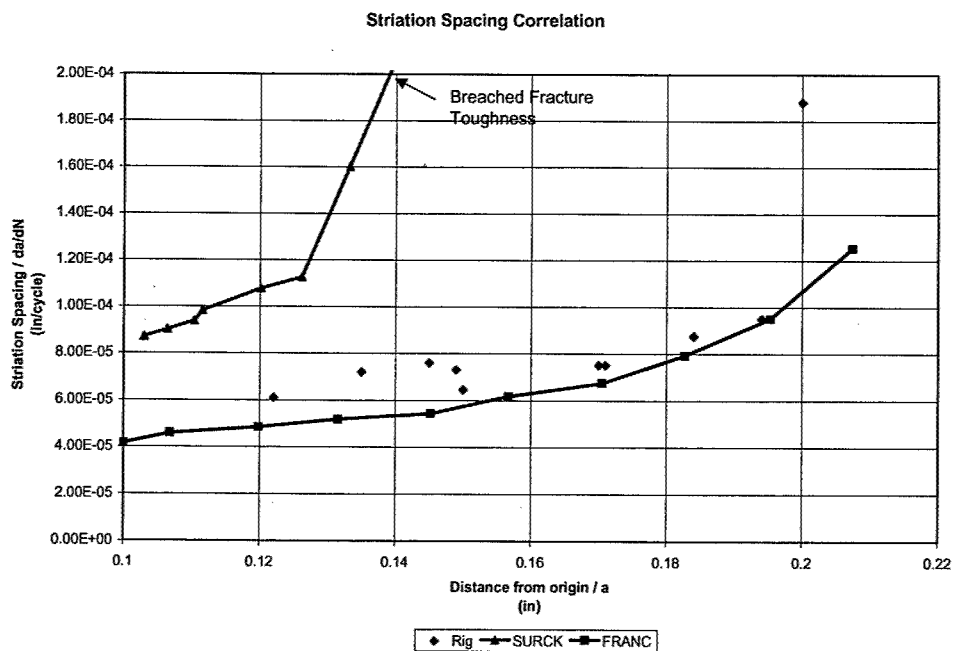


FIGURE 163. FRANC AND SURCK CRACK GROWTH PREDICTIONS PLOTTED AGAINST THE STRIATION DATA FOR THE RIG TEST

2.2.4.3.6 Engine Condition Results.

A good test of the capability of FRANC-3D program was its ability to calculate crack growth of the cast case wall crack under engine-operating conditions. The test produced high stresses driven by thermal gradients in an actual engine environment. The FRANC-3D prediction correlated well with the test data. Initially, propagation is at a slower growth rate than the data shows, which may be attributed to the heat-affected zone created by welding of the boss. The predicted propagation rate increases until the crack reaches 0.05" depth where the predicted and demonstrated crack growth agree. This result is most likely due to the redistribution of the thermal stresses as the crack grows through the thickness. This effect is not accurately accounted for in the linear elastic SURCK prediction and thus results in a very conservative crack growth prediction. It appears that FRANC-3D does a reasonable job of accounting for this effect.

2.2.4.3.7 Rig Condition Results.

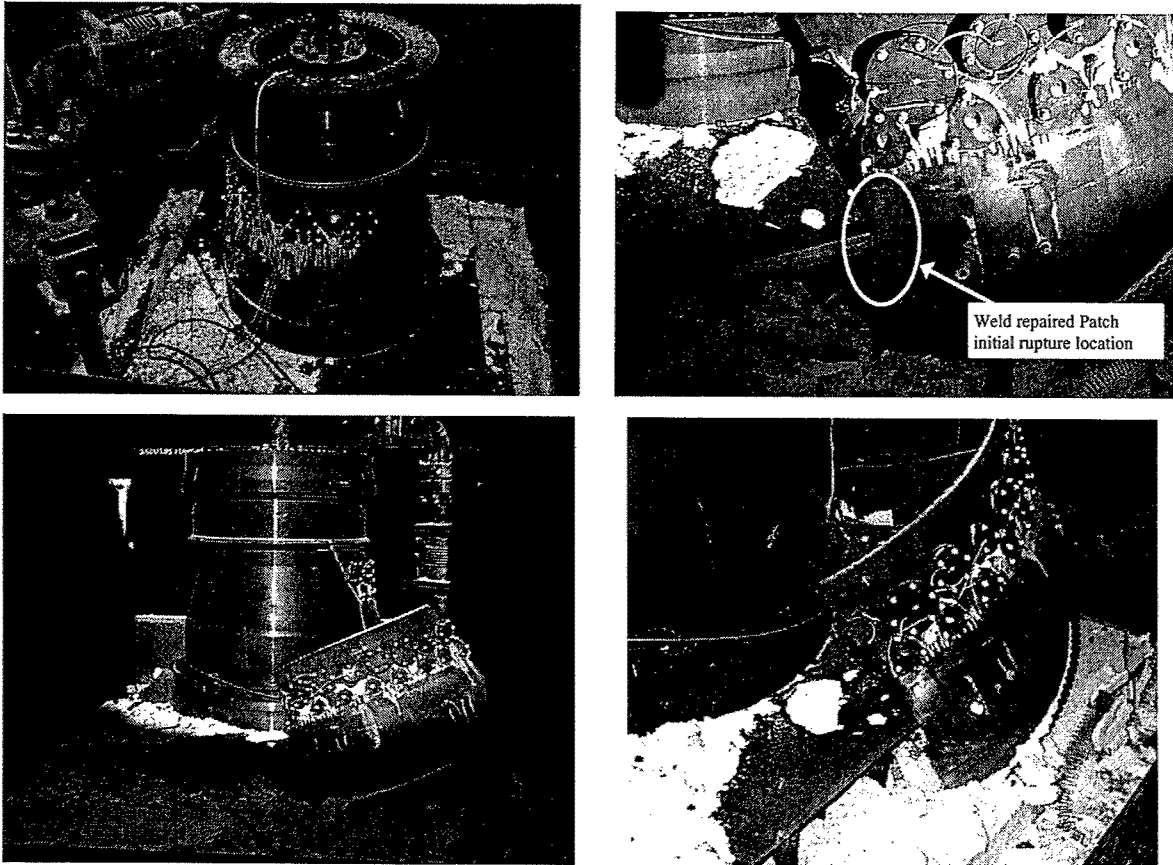
The limited crack growth data obtained from the EDM slots was accurately predicted for two of the three slots. The lack of correlation on the third slot is believed to be due to a relatively coarse finite element breakup in the stress analysis that may not have captured the true state of stress.

The rig conditions produce a simpler state of stress for the case wall crack than what was caused by the engine conditions. The stress is produced only by the mechanical pressure loading since the case is at a constant temperature of 1150°F, with no thermal gradients. The FRANC-3D predicted crack growth correlates well with the actual crack progression striations and exhibits a shape similar to the data. Generally, the prediction is slower than that seen by the striations (prediction shows more life than observed) but is within the normal material scatter. The linear elastic SURCK code proved to be very conservative relative to the actual data.

2.2.4.3.8 Rig Failure.

The rig failure location was determined to be in cast material adjacent to the weld-repaired patch. This was an area of large distortion caused by the welding process, which makes it very difficult to predict the stress. Because of this difficulty, a detailed crack growth prediction for this area was not done as part of the contract.

The rupture of the case, shown in figure 164, emphasizes the amount of energy present in these high-pressure cases and the amount of damage possible due to a case rupture. The patch weld repair done on this case would not have been allowed in a service case. This emphasizes the importance of conducting proper repairs on high-pressure cases.



PW4168 FAA Aged D/ C (R-61549), Case Rupture at 5,588 cycles
6/17/98 96-639-7052

Faarupt.DOC

FIGURE 164. CASE RUPTURE IN THE CYCLIC PRESSURE RIG

2.2.5 Task 2 Conclusions.

State-of-the-art stress, crack growth prediction methodologies, and aged material crack growth properties have been applied to operational engine cases. The following conclusions have been determined:

- Use of detailed 3D finite element analysis and the appropriate level of crack growth analysis sophistication produces crack growth predictions that correlate well with actual operational case experience.
 - 3D finite element analysis accurately predicts the critical cracking locations for the wrought nickel diffuser, the welded steel, and the cast nickel rig cases that were analyzed.
 - Linear elastic fracture mechanics predictions can typically be conservative with respect to actual crack growth, especially in areas of high thermally driven stress.

- FRANC-3D crack growth predictions agree well with the observed crack propagation in operational cases. FRANC-3D was able to redistribute the thermally driven stresses in the rail/boss area in a JT9D diffuser case and accurately predict the large observed difference between case wall crack propagation at the two boss areas of the case. It also predicted the crack growth in the cast diffuser case operating at engine conditions.
- The crack growth characteristics of embedded weld flaws can be predicted if the location and size of the weld defects are known. Since inspection techniques may not always locate an existing weld flaw, conservative estimates of location and size should be used in the analysis.
- Crack growth data from cracked, welded embossments in operational cases suggest that the cracks begin propagating from shallow, high aspect ratio cracks due to the linkup of multiple crack origins in the high bending stress field.
- Use of the crack growth rates of aged baseline and welded alloys generated by this program in task 1 resulted in good correlation of predicting the crack residual life of operational cracked cases.
- The rupture of the cast diffuser case in the pressure rig emphasizes the amount of energy present in these high-pressure cases. Although a repair of this type would not be allowed in an operational diffuser case, the rupture shows the importance of controlling weld repairs in these cases.

2.3 TASK 3: RISK ASSESSMENT METHODOLOGY.

The goal of this task is “to formulate a generic risk assessment/analysis methodology to quantify the expected number of future events along with the probabilities of occurrence for cracking of pressurized engine static cases.” Task 3 documentation explains, in detail, the P&W recommendations for fulfilling this goal.

2.3.1 Task 3 Summary.

A team of P&W commercial risk analysts was formed and addressed the specific items in the contracted work plan. Some of the most significant accomplishments of the team are as follows:

1. The team reviewed/examined the current P&W commercial risk assessment process and decided that, with some improvements, it would fulfill the contract needs. The team
 - a. added a checklist for inputs to ensure all aspects were examined.
 - b. added a checklist for outputs to ensure that the appropriate material from the risk simulation results is summarized.
 - c. formulated a standard presentation format, defining what material should be presented to what audience.

- d. decided to have a third party preview any presentation material for content.
 - e. decided that the risk simulation program could be used, but would need some major enhancements to reduce the programming time and increase repeatability. Consideration was given to:
 - improving the algorithms or develop/find new ones for improved accuracy.
 - simulating crack propagation from a nonlinear distribution.
 - incorporating additional material properties and service environmental variables.
 - incorporating the probability of detection of cracks by size to allow refined determination of inspection plans.
 - engine operational variables.
 - calibration of the risk model to match the field experience using a past risk analysis of a case problem.
2. P&W recommends a special version of the risk simulation program for possible scenarios of aging engine cases. It should handle multiple locations of a feature that have the same life. Two possible versions would be:
 - a. One that replaces/repairs parts at all locations if one or more cracked parts are found, or
 - b. Another that replaces/repairs only the cracked parts.
 3. The risk assessment process for aging engine cases analyzes the most life-limiting features separately to develop a field management plan of inspections/replacements that encompasses all concerned features.

2.3.2 Risk Assessment Philosophy.

Why do Risk Analysis? To optimize inspection/modification/retirement programs designed to control safety-related engine field problems by:

- Meeting risk goals/limits
- Ensuring spare part availability
- Ultimate Goal: Provide flight safety while minimizing impact on the airlines and the traveling public

What is Risk Analysis? A tool for decision-making or selecting a field management plan. Commonly, it uses a computer simulation procedure to quantify the expected number of future

events along with the probabilities of occurrence. This simulation is for a specific problem as a function of specific operational/maintenance constraints. The risk simulation model

- uses statistically based Weibull analysis and Monte Carlo techniques.
- is reality-orientated as much as possible.
- uses engineering judgment.
- addresses unknowns conservatively.
- represents the sum of knowledge about the specific problem.
- quantifies expected number of future events (risk factor) along with the probability of occurrence.

Figure 165 is a flowchart that demonstrates what goes into the Risk Simulation Program. It is important that the model calibrates to actual experience. For example, the model is able to predict/simulate the actual number of cracks/fractures and the time it takes the crack or fracture to develop. The first step in this program is developing a risk simulation model, possibly using Fortran. All the desired outputs must then be defined, and from that the risk analyst can determine what inputs are required. Figure 165 displays a variety of possible inputs.

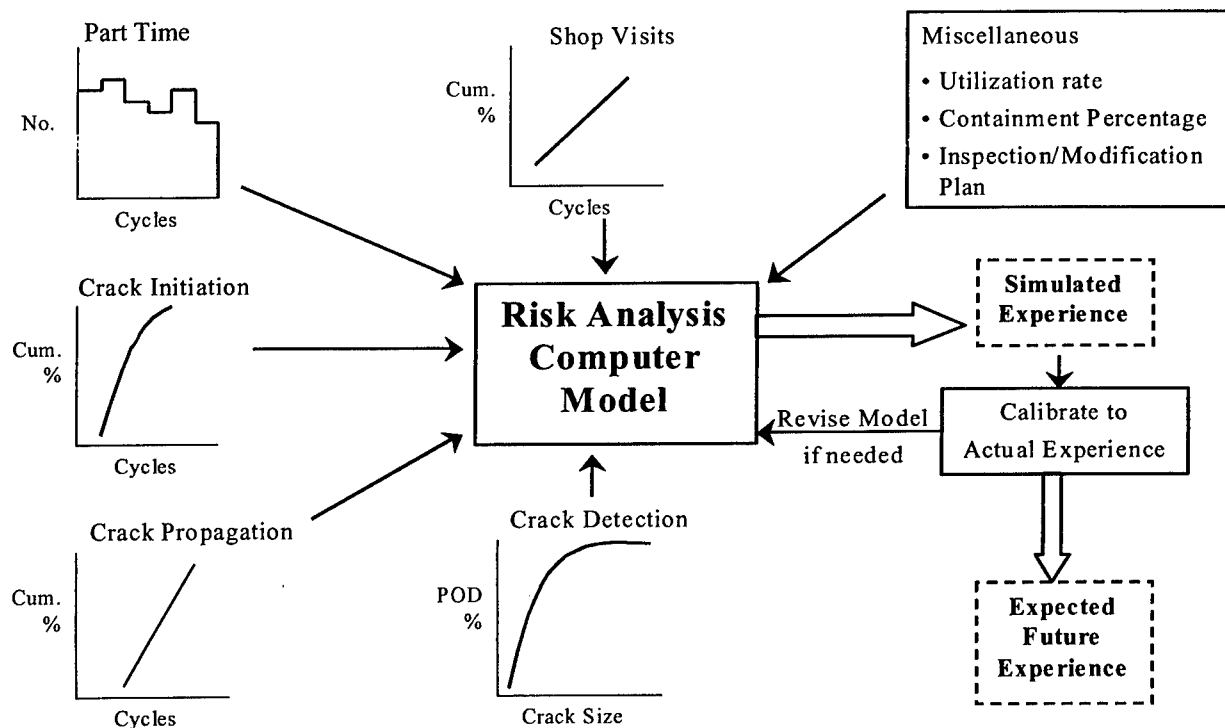


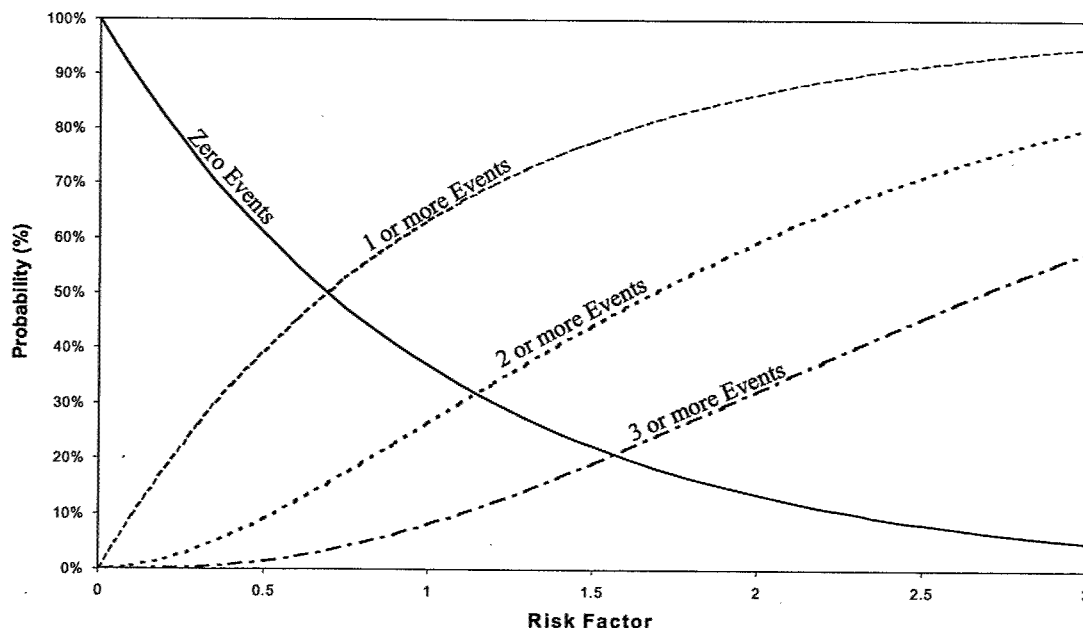
FIGURE 165. RISK SIMULATION FLOWCHART

An important part of developing an accurate simulation program is to ensure that the total number of "if" statements cover all possible paths taken by the input. One approach is to simulate

- the part's time (hours or cycles).
- the number of hours/cycles the part accrues.
- the part's crack initiation (crack has grown to some level of detectability).
- the part's crack propagation (crack grows from detectable to fracture).
- the next shop visit for which the part can be inspected.

Once these are determined, an inspection is simulated where crack size and probability of detection (POD) can be used, if available. If the part is not cracked during this inspection, it goes to the next shop visit or inspection opportunity. If it is found cracked, the program calculates the calendar time (recommended in months) from simulation start, and records the time the crack occurred. If it is simulated that the part fails before the next inspection, the same procedure is done for failures.

Event probability is directly related to risk factor (expected number of events) as shown by the plot below. For example, for a risk factor of 0.50, the chance of zero events occurring is 60% and so the chance of one or more events is 40%. The plot below is also used in the FAA Advisory Circular Draft 39-XX, known as Continued Airworthiness Assessment Methodology (CAAM), in Appendix 4, section 11, figure 2 for discussing event probability.



When deciding which field management plan to implement, consideration should be given to the various factors that are important to the customer and the manufacturer. Some of the factors that should be considered are:

- Cost to implement

- Schedule interruptions
- Maintenance shop workload
- Specialized maintenance/inspection training and tools

Risk analysis is a proven tool for decision-making. Some of the key factors that make a risk analysis the recommended tool for choosing a field management plan are as follows.

- Provides projection of future events along with probability evaluations.
- Based on computer simulation and statistical analysis techniques.
- Results are used to optimize inspection/modification/retirement programs to control safety-related problems.
- Recommended programs meet risk factor goals.
- Operator input and feedback are important.
- Regulatory actions are frequently based on risk analysis results.

Flight safety can be provided/maintained without using risk analysis. Providing for flight safety while minimizing economic impact requires using risk analysis in making decisions. The use of risk analysis requires risk factor and the definition of risk factor goals. The risk factors:

- are based on the average risk analysis results.
- apply to specified inspection/modification/retirement scenario.
- usually cover a time period required for problem resolution but may be applied to specified time period (e.g., 20 years).

Realistic risk factor goals are required. As was mentioned earlier, 0.5 risk factor = 0.5 expected number of events = 60% chance of zero events or 40% chance of one or more events. If the risk analysis simulation is run 100,000 iterations for a part and the risk factor is 0.5 for the chosen inspection/modification/retirement plan, then the table below demonstrates the simulated number of possible events and their associated probabilities. For example, there is a 1.264% chance of exactly three events occurring for the chosen plan, while the probability of four or more events occurring = 1.0 and the probability of three events or less = 1.0 - 0.99825 = 0.00175.

- The number of simulated events is 50,001, so the average simulated events (risk factor) = $50,001/100,000 = 0.5$ with associated probabilities as to the number of events.

No. of Events	No. of Iterations With Specified No. of Events	Events Simulated	Cumulative Events Simulated	Probability	Cumulative Probability
0	60,653	0	0	0.60653	0.060653
1	30,327	30,327	30,327	0.30327	0.90980
2	7,582	15,164	45,491	0.07582	0.98561
3	1,264	3,792	49,283	0.01264	0.99825
4	158	632	49,915	0.00158	0.99983
5	16	80	49,995	0.000158	0.999986
6	1	6	50,001	0.0000132	0.999999

The major elements of a risk analysis are as follows.

- Definition of an "Event"—the failure mode could be a flange unzipping or a case-boss crack propagating to case rupture
- Assignment of risk factor goal, customer-dependent—the FAA policy is less than 1.0 risk factor for a CAAM Level 3+ event and less than 0.10 for CAAM Level 4 event
- Definition of simulation model characteristics—will there be inspections/modifications/retirements, is there POD (probability of detection) vs crack growth data, is there a Chapter 5 life, ...?
- Statistical analysis to define part(s) lives and other input items—crack/fracture Weibull lives, shop visit distribution, current fleet hour/cycle histograms, ...
- Definition of operational/maintenance constraints—inspection reliability (on-wing and shop), part accessibility, modification capability
- Incorporation of structural analysis considerations—need crack initiation and propagation life information and, if possible, crack growth data and defect size distribution
- Creation of a computer simulation model—the Monte Carlo simulation should be robust enough to account for all common inputs and reduce the need to customize it for "uncommon" risk analyses
- Calibration of simulation model—match actual field experience
- Definition of candidate inspection/modification/retirement scenarios—define and determine the risk factors for various initial inspection and repetitive inspection interval and modification schedule aimed at minimizing risk and customer impact and accounting for spare part availability
- Output useful in the decision-making process.
 - Risk Factors = predicted number of events

- Effects of alternate actions—sensitivity study of various inspection/modification/retirement plans
- Parts requirements—replacement availability or tooling capability

A risk analysis of aging cases has some unique aspects. There are multiple features that could fail, and if repairable, they may have multiple lives.

- It is recommended that each feature be analyzed separately, selecting the most life-limiting features for risk analyses. It is not recommended that a simulation be constructed to try to handle all the features of an engine part. Running dissimilar features independently gives the analyst the opportunity to evaluate the risk for each feature and the associated field management plan to minimize risk.
- Perform a comparison of the inspection/modification/retirement scenarios from the various risk analyses to develop a field management plan that encompasses all needed inspections/modifications/retirements for all concerned features while meeting the risk goals. Risk factors for the various features are not additive. The risk analyses are not to be combined, just the necessary inspection/modification/retirement plans to minimize customer impact.

2.3.3 P&W Recommended Risk Assessment Process.

Figure 166 is a flowchart of P&W's recommended risk assessment process, defining the various departments and steps involved in the process. The details of each step in this process is discussed below.

Step 1: A Problem Requiring a Risk Analysis is Identified

A problem is identified in one of two ways.

- A field event, or shop finding, has occurred where a part has cracked or fractured.
- A limited life has been discovered for a part.

In either case, a risk analysis is needed to determine an appropriate field management plan in order to minimize the probability of a safety-related event. As mentioned earlier, aging engine cases may have more than one feature at risk. Therefore, it is recommended that each feature be analyzed separately, selecting the most life-limiting features for risk analyses, then perform a comparison of the inspection/modification/retirement scenarios from the various risk analyses to the develop a field management plan that encompasses all the needed inspections/modifications/retirements for all concerned features while meeting the risk goals.

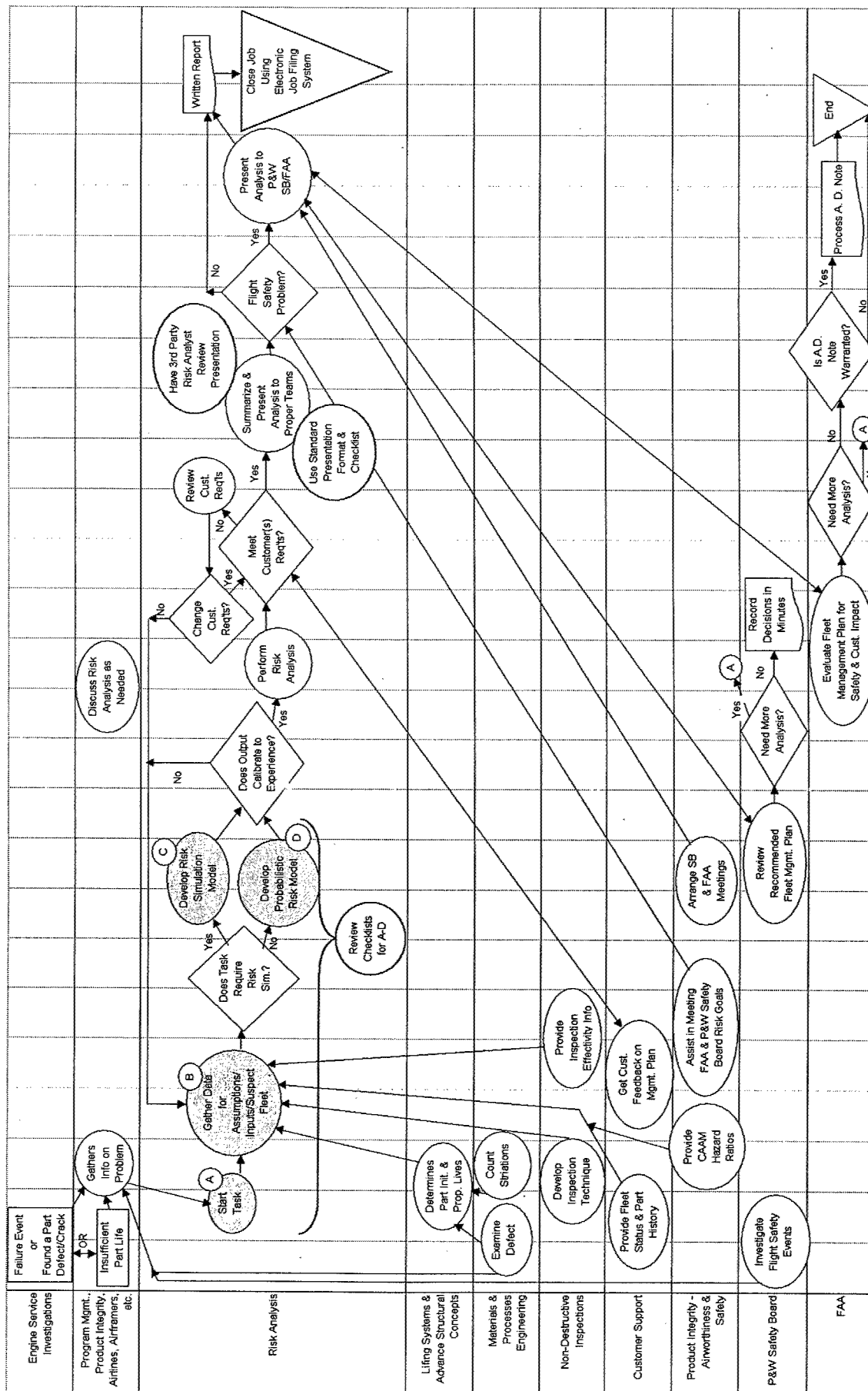


FIGURE 166. P&W RECOMMENDED RISK ASSESSMENT PROCESS FLOWCHART

Step 2: Upfront Data Must Be Gathered

Functional groups gather the data to determine the part failure mechanism and other supporting data in preparation for starting a risk analysis.

Step 3: The Risk Analysis Group Initiates a Task

The risk group starts the task by participating in meetings or other communications to gain an understanding of the problem. The risk analyst needs to:

- define an event, such as crack, fracture, in-flight shut down (IFSD), uncontainment, ...
- define what customer requirements can be addressed at this time, such as:
 - cost to implement
 - schedule interruptions
 - maintenance shop workload
 - specialized maintenance/inspection training and tools
- define the characteristics of an event, i.e., what types of inputs are available/needed, such as:
 - probability of detection distribution vs single value POD,
 - theoretical vs field data-based lives for crack initiation and propagation,
 - choice of appropriate life distributions (Weibull/Maximum Likelihood Estimates (MLE)/ Log-Normal/ ...) based on historical data,
 - type of crack growth, such as HCF, LCF, and corrosion,
 - types of proposed inspection/modification/retirement plans as well as current field practices, or
 - containment concerns as well as CAAM level risks, if necessary.

Step 4: Gather Data for Assumptions/Inputs/Suspect Fleet Information

The following checklist is provided to help mistake-proof this activity.

Required Input for Risk Simulation, based on information below, historical data, or engineering judgment: Clear Definition of Suspect Fleet - Models, Stages, Parts, Part Numbers,
Part Population Status (age) in Hours or Cycles
Part History - Past Problems/Experience of the Same Part or Similar Parts
Part Initiation and Propagation Lives
Inspection Technique and Reliability
CAAM Hazard Ratios and Uncontainment Rates from Past Industry Data
Part Certified Lives
Engine Utilization Rates (hours and cycles per month)
Engine Shop Visit/Overhaul Distribution
Part Accessibility during Shop Visit/Overhaul
Inspection Distribution
Wearout Progression Data (w Inspections) & Failure Data, such as Cracks, Corrosion, Vibration, Defects, ...
Scrap Distribution
Fix Availability Date and Incorporation Rate
Spare Part Sales
Number of Parts per Engine and Life Differences, if any
Part Retirement for Other Causes

Required Input for Probabilistic Approach:

Determine Needed Portions/Ratios of Equations
Gather Needed Distributions for Probabilistic Approach
Gather Needed Parametric Relations for Probabilistic Approach

Step 5: Decision Made to Use Probabilistic Approach or Risk Simulation

A probabilistic risk analysis can be as simple as using occurrence rates to predict the number of events over a period of time, or as complex as calculating the risk factor from the current part time until corrective action is taken using a failure Weibull distribution. However, a risk simulation is recommended if time is a factor in determining when the part would fail, i.e., typical aging (older parts are more likely to fail) or infant mortality (parts fail early in their life). A simulation is especially needed for complicated inspection/modification/retirement plans, or where there is a known relation between crack growth (part time vs length) and POD. Details of the risk simulation are discussed in section 2.3.2.

Step 6a: Development of a Risk Simulation Model

What is a Simulation Model?

Monte Carlo simulation is a very general method of analyzing problems, which are probabilistic in nature, and is highly recommended for risk analysis. The analysis involves defining a mathematical model of the system being studied and operating it repeatedly in order to observe the range of system outcomes. The model typically involves many input parameters, each defined by a probability distribution. The model also defines how the input parameters combine to produce specific potential system outcomes.

The inputs to an aviation safety model might include the failure distributions of contributing failure modes, reliability of fault monitoring and accommodation provisions, scheduled inspections and repair intervals, effectiveness of maintenance actions, effectiveness of crew actions, expected range of flight conditions, etc. Although the output format of a Monte Carlo simulation is often tailored to the specific problem being studied, a typical output would be a prediction of the number of hazardous events for the next year, 5 years, or until fleet retirement.

For fleet problems or limited life findings requiring corrective action, the Monte Carlo method can be used to judge the acceptability of various proposed corrective actions as well as implementation schedules. The system model may be changed as needed to reflect proposed changes in equipment design, revised inspection or maintenance schedules, constraints on flight conditions, etc. The proposed changes to the model can be phased in a defined schedule, if it is desired to judge the benefit of various accelerated implementation schedules. To judge the effectiveness of the proposed corrective action and implementation schedule, the Monte Carlo output (e.g., number of hazardous events) is compared to the original analysis.

Monte Carlo simulation is a stochastic technique, meaning that the outcome is a probabilistic function of the inputs. The simulation typically involves hundreds or thousands of "trials" of system operation. For each trial, a specific value for each input parameter is randomly selected from the specific probability function for that parameter. The "random" selection of each input is accomplished through a random number generator, which is included in most computer programming languages or mathematical modeling software packages.

All initial runs of the simulation should be with a small number of iterations and extra output to a file to check that the simulation is running properly and to verify that the input yields reasonable results. Be careful to have as much data-based input as possible and little subjective input.

Elements of a Simulation:

Analyzing a problem with Monte Carlo simulation involves several steps as described below.

1. Clearly define the problem to be analyzed.
2. Identify the parameters which contribute to or influence the problem.
3. Define each parameter with a probability distribution.

4. Develop flowchart to describe the relationship between the output event (problem) and the input parameters.
5. Define the content and format of the output desired from the simulation.
6. Develop a computer program that corresponds to the system flowchart and summarize results in the desired format.
7. Operate the computer program, obtain the results, and communicate the results to individuals and groups responsible for further action or decision-making related to the problem.

Probability Distributions:

Each input parameter to the Monte Carlo simulation must be defined by a probability distribution. All probability distributions can be grouped into two major categories.

1. Discrete distributions are used when the parameter values must be constrained to specific values. One example would be the effectiveness of an inspection, where the possible outcomes are "defect found" or "defect missed." Another example would be the number of flights for a specific aircraft for a particular day, where the possible outcomes are zero, one, two, three, etc.
2. Continuous distributions are used when the parameters can take any value in a specified range. One example would be component time to failure, where the failure time can be any value greater than zero. Other examples include the flight time for a specific flight, the length of a crack, the growth rate of a crack, or the diameter of a shaft.

Characteristically, parameters that are counted are discrete, while those that are measured are continuous. As shown in figure 165, the simulation model uses various distributions as input. For example, the "Part Time" is a discrete distribution while the "Crack Initiation" is continuous.

Step 6b: Development of a Probabilistic Risk Model

Fleet Risk Measurement:

The material in this section is just basic probability calculations and does not explain the use of Poisson or binomial distributions. It addresses a simplistic approach for fleet risk analysis and is essentially an application of the probability evaluation to an entire fleet. The results of a fleet risk analysis are typically expressed as total events that happen for the fleet per 12 months or total events for the fleet until fleet retirement/problem elimination.

Prediction Based on Observed or Calculated Event Rates:

When probability calculations are based on observed event rates, there is an inherent assumption that the contributing events are random in nature. If the event data is fitted to a Weibull distribution, the slope should be about 1.0. This indicates that the risk for an individual engine is

not affected by the age of the engine or an engine component. So each engine, regardless of its age or history, has an identical risk when expressed on a “per flight hour” or “per flight” basis.

If the risk for an individual engine is considered constant and the risk for each engine in the fleet is considered equal, then the fleet risk is a function only of the individual engine risk and the period of time that the fleet is exposed to that risk. As an example, consider a case where a fuel pump problem has been identified, which can lead to an engine shutdown. The probability of an engine shutdown (IFSD) due to this fuel pump problem is 5×10^{-6} per engine flight hour, based on recent field experience. This example also assumes that the problem is related to hours of operation, not flights. If the fleet consists of 500 aircraft, each with two engines that operate for 8 hours a day, the fleet operating time for one day is equal to:

$$(500 \text{ aircraft}) \times (2 \text{ engines/aircraft}) \times (8 \text{ flt hrs per day/engine}) = \\ 8000 \text{ engine flight hours per day of exposure to risk}$$

If a corrective action plan is to be implemented at a rate of 50 aircraft per month over a 10-month period, the average exposure per aircraft is 5 months. Thus, the total fleet exposure to the fuel pump problem is:

$$(5 \text{ months}) \times (30 \text{ days/month}) \times (8000 \text{ engine flight hours/day}) = 1,200,000 \text{ engine flight hours}$$

The fleet risk of an IFSD due to this problem, expressed as the expected or predicted number of fleet events, is then:

$$(5 \times 10^{-6} \text{ events/engine flight hour}) \times (1,200,000 \text{ engine flight hours}) = 6.0 \text{ events}$$

Thus, if the corrective action plan is implemented according to the proposed schedule of 50 aircraft per month, six IFSDs can be expected before the entire fleet is corrected.

Step 7: Calibrate Risk Output to Field Experience

Early in the risk assessment process, the risk analyst should decide what parameter to use for calibration. This is handled differently for simulated vs probabilistic risk assessments.

Calibration of Probabilistic Risk Assessment:

In most cases, field experience is used to calculate rates for probability equations. Whatever the source of the rates/probabilities before calculating the likelihood of future events, calculate what would have been expected to-date. Make sure the input has been carefully reviewed by all the appropriate people for accuracies. If the to-date prediction matches the field experience, go to step 8, if not

- If the to-date prediction is greater than that experienced after careful input review, a calibration factor of the ratio of experience over predicted needs to be applied to predictions of future events.

- If the to-date prediction is less than that experienced after careful input review, similarly a calibration factor of the predicted over the experience is needed for future predictions.
- If there have been no field events experienced to-date and
 - the to-date prediction is greater than one, calibrate to one assumed event, or
 - the to-date prediction is less than one, either calibrate to one assumed event (may be too conservative) or use the probability equation as is, if thorough assessment of the input shows it to be reliable.

Calibration of Simulated Risk Assessment:

For example, suppose there are five cracked parts found with no ruptures due to this “problem,” and as part of the input, structural engineering provides calculated crack initiation and propagation information. Assume that the simulation predicts that there should have been 15 cracks found to-date. One or more of the inputs must be adjusted to lower the prediction to five cracks to match the actual experience. If it is agreed that all input, other than the lives, is reliable, then the crack initiation life distribution needs to be increased until it predicts just five cracks found to-date. If the simulation underpredicts, the crack initiation life distribution needs to be decreased. If the simulation predicts more than one rupture, (none have occurred) then the crack propagation life distribution should be increased until one “assumed” rupture is predicted. If less than one rupture is predicted to-date, either the propagation life distribution should be decreased until one “assumed” rupture is predicted or use the lives “as is.”

The above paragraph calibrates under the assumption that all other input, except for the lives, are accurate. Even slight input inaccuracies may have an impact on the risk analysis results, but if adequate care is taken in their definition, then calibration is usually a matter of adjusting the lives.

Step 8: Prediction of Future Events With the Risk Analysis

During the calibration, the fleet size and inspection conditions are at least two of the inputs that may be different for the “going forward” risk. The fleet size may have increased or will be increasing over the time at risk. The inspection reliability often goes up due to awareness or improved inspection technique(s). The inspection frequency may change, usually increasing, to reduce the risk. All the inputs, covered in step 4, need to be re-examined for future capability, i.e., have shop visit rates or monthly utilization changed and has the suspect fleet size decreased. The goal is to develop a field management plan that results in acceptable risk, as defined by the engine manufacturer and federal aviation regulatory agencies.

The recommended first-risk scenario is for “no corrective action for 20 years.” The FAA, in most cases, wants to know how high the risk is if nothing is done differently (to reduce risk) for the next 20 years to obtain a baseline of the scope of the problem. The risk analyst must make sure that all conditions are simulated properly, such as replacement part lives and fleet size changes. If the risk analysis shows that no corrective action is necessary to meet acceptable risk levels, then the risk analyst is done and moves on to step 9.

However, if the “no corrective action” scenario results in unacceptable levels of risk, the risk analyst then runs various scenarios to obtain an acceptable level of risk. This is achieved by varying input parameters such as the inspection technique or frequency, by developing a reoperation incorporation plan, or through part retirement. The risk analyst must also consider airline capabilities (shop capacity, inspection equipment and its use) as well as part availability when determining inspection intervals and/or reoperation incorporation rates.

Step 9: Verify That Results Meet Customer’s Requirements

The risk analyst must verify that the risk analysis results meet all customer needs. These customers are the management within the engine manufacturer, the aviation regulatory agencies, and the airlines. The various customers may have slightly varying requirements that the risk analyst should be aware of as the risk analysis is performed.

Foremost among factors that determine what field management plan/scenario to accept is safety. The required risk levels of safety must be achieved. Other customer factors/requirements that need to be considered include inspections (techniques that shops/inspectors are certified to perform and frequency capability for either on-wing or in the shop) and the possible reoperation incorporation rate, again depending on part availability and shop capacity.

Step 10: Summarize and Present Analysis to Proper Teams

Results should be reviewed with the proper teams, such as internal management/safety boards, aviation regulatory agencies, and airlines. It is recommended that the analysts use a standard presentation format for these reviews, where the format and level of detail may differ for various customers. First, have a third-party review the material for content and consistency in format. The typical order of reviews would start with some level of management within the engine manufacturer’s engineering department. Then conduct reviews with the aviation regulatory agencies and the airlines. There may be multiple reviews with some of the customers to first present preliminary results with updates forthcoming. Regular communication is recommended, but be sure to stress whether the risk analysis results are preliminary or final. Eventually, it is essential for the risk analyst to get the customer to buy-in on the recommended field management plan.

Step 11: Determine if the Internal Safety Board Review is Required

If there is a flight safety concern with this problem, the internal management flight safety board/team may need to review the plan. The engine manufacturer’s safety/airworthiness department must aid the risk analyst in determining if this problem is a flight safety concern. Involvement by the airframers and/or the aviation regulatory agencies may be required for accurate determination. This involvement may need to occur earlier in the risk assessment process. Once it has been determined whether this field problem could result in a flight safety event, the risk analyst will use the appropriate levels of risk as the goal of the field management plan. Once management teams have reviewed the proposed field management plan, the internal safety board should review and approve the plan.

Step 12: Document the Report

A written report should be used as the final documentation of the risk assessment once all the needed customer approvals have been acquired. Depending on the engine manufacturer's filing system requirements, this final written report could simply be the presentation material or it might be a more formal document, including all the details from the root-cause investigation to the approved field management plan.

Step 13: Close the Risk Analysis Job with an Electronic File

An electronic file should be used to store all appropriate information about the job in one area. It is recommended that the final written reports be stored in a filing system of all risk analysis jobs. This will allow the risk analysts to search past jobs or perform updates to recent jobs. This does not exclude the use of hardcopy files, where details of input data collection, Weibull plots, and preliminary runs, etc., may be stored.

2.3.4 Sample Application of Recommended Risk Assessment Process.

While the purpose of this report is to address aging engine cases, the following fictitious example demonstrates that the application of this recommended risk assessment process can be used for any engine part with multiple features (such as similar-life bosses or bolts) with the same lives. This example will follow the process detailed in the previous section.

Step 1: A Field Problem is Identified

Operator A has found an aircraft engine part cracked in the field. There are three of these per engine. This part could be in a case with three bosses, each boss having the same or similar life. The field representative was informed and sent a wire to the engine manufacturer, who forwarded the information to the engineering department for investigation.

Step 2: Gather Data

The needed personnel met to decide what data is needed and the best way to gather it. They found that one of the three identical parts had developed a crack due to low-cycle fatigue (LCF), which in turn could propagate to failure. The team determined that the cracked boss is able to be repaired if the crack is small enough. This is the third such crack event to-date with no ruptures. A risk analysis is needed to help develop a field management plan.

Step 3: Initiate a Task

The risk analyst needs to:

- Define an event, such as crack, fracture, In-Flight Shut Down (IFSD), uncontainment. For this problem, the crack is defined as an LCF crack in any one of the three locations, and a fracture is the result of crack growth until the case ruptures.

- Define what customer requirements can be addressed at this time, such as:
 - Cost to implement—the operators must perform an inspection at engine removal and replace/repair the case if found cracked.
 - Schedule interruptions—it is hoped that the risk analysis will support a field management plan that only requires a normal shop visit but on-wing inspections may be needed.
 - Maintenance shop workload—not expected to be significantly more than normal.
 - Specialized maintenance/inspection training and tools—possibly a borescope probe.
- Define the characteristics of an event, i.e., what types of inputs are available/needed, such as:
 - Probability of detection distribution vs single value POD—a single POD was used = 95%, based on rig tests.
 - Theoretical vs field data-based lives for crack initiation and propagation—the field data (three cracked bosses found to-date) demonstrates that initiation occurs between 12,000 and 20,000 cycles, which agrees with the calculated crack initiation life. Propagation was calculated by structural analysis.
 - Choice of appropriate life distributions (Weibull/Maximum Likelihood Estimates (MLE)/ Log-Normal/ ...) based on historical data—the initiation distribution is uniform, while the propagation is a Weibull with a slope of 7.2 and a $B_{63.2}$ of 4,500 cycles. The calculated repair lives are also defined by Weibull distributions.
 - Type of crack growth, such as HCF, LCF, and Corrosion—this crack progresses in LCF.
 - Types of proposed inspection/modification/retirement plans as well as current field practices—an FPI is a possible field management option unless the risk analysis determines otherwise.
 - Containment concerns as well as CAAM Level risks, if necessary—it has been determined that 50% of the case ruptures will result in a nacelle uncontained event, and that 25% of the nacelle uncontained events will be CAAM Level 3 events. No CAAM Level 4 events are expected.

Step 4: Gather Data for Assumptions/Inputs/Suspect Fleet

The risk analyst uses the following checklist:

Checklist Items	Used for Risk Analysis
Clear definition of suspect fleet—models, stages, parts, part numbers,	2 models and only 38 remaining engines are suspect
Part population status (age) in hours or cycles	Between 5000 and 9000
Part history—past problems/experience of the same part or similar parts	None could be found
Part initiation and propagation lives	(see step 3 of 2.3.4)
Inspection technique and reliability	FPI with 95% insp. reliability
CAAM hazard ratios and uncontainment rates from past industry data	50% uncont. and 25% CAAM Level 3 hazard ratio
Part certified lives	None
Engine utilization rates (hours and cycles per month)	Varies by operator
Engine shop visit/overhaul distribution	Between 1500 and 4000 cycles
Part accessibility during shop visit/overhaul	100%
Inspection distribution	Same as overhaul distribution
Wearout progression data (w inspections) and failure data, such as cracks, corrosion, vibration, defects, ...	(see step 3 of 2.3.4)
Scrap distribution	None
Fix availability date and incorporation rate	Immediate
Spare part sales	Not needed
Number of parts per engine and life differences, if any	3 parts per engine – similar lives
Part retirement for other causes	None

Step 5: Determine the need for Probabilistic Approach or a Risk Simulation

This decision is simple due to the various distributions for the input, such as Weibull distributions, with slopes greater than 1.0—a risk simulation approach is needed.

Step 6: Development of a Risk Simulation Model

It is recommended that risk analysts create a base simulation program so that most of the aging cases simulation jobs can use the same program with a few small modifications to the input file. Although the model below looks simple, developing the code with all the needed checks (IF statements and comparisons) is a difficult task. However, whatever time it takes to develop the code is well worth it because the base model can be used most of the time. Once the risk simulation program has been developed, all that is left is setting up the input file with the information gathered in steps 3 and 4.

Here is an example of an input file for calculating risk factors for an aging case from the input above. The intent of showing this file is just to give the user an idea of the complexity of organizing the input for the risk simulation.

```

RISK INPUT FOR AN EXAMPLE OF CASE CRACKING
INIT END DRAW REP TRUN HIST INSP LSV UTL REL NPART
-----"-----"-----
  0 1 0 1 0 0 0 1 1 2 5
SEED ITER NENG SHOP REL THRESH DRAW SV ACC STOP REP
-----"-----"-----
12349 5 38 1.0 0000. 1000. 1.0 9999.
 38 9 1000.
 0
 0 0 0 0 0 6 6 28 2
 0
INIT PROP END CERT GRWTH PDET (INITIAL DATA)
-----"-----"-----
  2 0 2 2 3 3
PROB NO. MONTHS (PROGRAM END)
-----"-----"-----
0.0 240.
1.0 240.
1.0 1.0
0.0 12000.
1.0 20000.
7.2 4500.
PREV 1ST REIN (INSPECTIONS)
-----"-----"-----
  4 4 4
0.0 1500.
0.5 2500.
0.9 3500.
1.0 4000.
0.0 1500.
0.5 2500.
0.9 3500.
1.0 4000.
0.0 1500.
0.5 2500.
0.9 3500.
1.0 4000.
UTL MEAN UTL SD NO. PERIODS PRINTED
-----"-----"-----
100. 0.0 240
HIST ADJ MO DY YR ADJ 1ST INSP
-----"-----"-----
0.0 01 01 01 0.0 0

WING REL INSP CAP
-----"-----"-----
.95 99999.
CERT PCT CERT LIFE
-----"-----"-----
0.0 99999.
1.0 99999.
PCT USED CRK SIZE
-----"-----"-----
0.0 .032
0.5 0.06
1.0 0.10

```

CRK SIZE SHOP REL WING REL AFTER MO.

CRK SIZE	SHOP REL	WING REL	AFTER MO.
0.032	.80	.50	0.
0.06	.90	.70	0.
0.10	.95	.95	0.
0.032	.90	.50	18.
0.06	.95	.90	18.
0.10	.98	.95	18.

Now the risk model is ready for calibration and then for use in determining a field management plan.

Step 7: Calibrate Risk Output to Field Experience

Once the simulation code and the input file are ready and accurate, it is very important that the risk analyst determine if the events that have occurred to-date can be predicted. A calibration run of the simulation must be conducted to demonstrate that the model (simulation and input) is able to reproduce the events in the field, if any. If there have not been any events, the risk analyst should consider assuming that a crack or rupture has occurred to-date. If there were ten boss cracks found between mid-1995 and early 1998 with no ruptures, the remaining fleet of 38 engines, plus the 10 event engines, would be taken back in calendar time (simulation subtracts appropriate number of engine cycles) to before the first crack. The simulation would then be run forward in calendar time (simulation add engine cycles per monthly utilization) to the date of the last crack found. The results should only show that the risk model predicts the right number of cracks found during that period of time and that they should agree with the correct time frame. The comparison below shows a good match between the actual and predicted cracks. (See figure 167.)

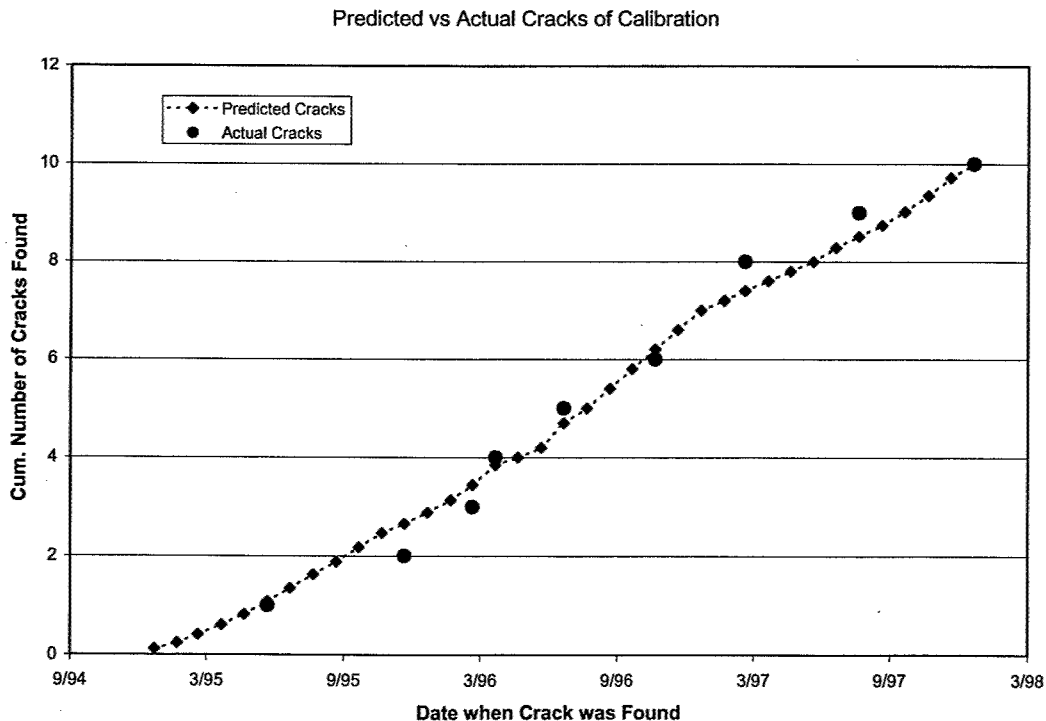


FIGURE 167. EXAMPLE OF RISK MODEL CRACK CALIBRATION CURVE

The risk model shows that the crack events have been calibrated well. Since no fractures have occurred, the risk analyst either assumes one fracture and calibrate/adjust the propagation lives or uses the current propagation lives as long as they do not overpredict. That is, predict more than one assumed event. Once the risk model has been properly calibrated to the field experience and the team agrees to the adjustment of the input parameters, such as lives, the risk analysis of future events can be conducted.

Step 8: Perform the Risk Analysis.

The simulation on the remaining 38 engines is run forward in time to determine the 20-year uncorrected risk, which is the recommended baseline scenario (see figure 168). For this example, the risk of a case rupture is 2.4 over the next 20 years, assuming that FPIs are done at each module teardown. Since the engine nacelle uncontainment rate is only 50% of the fractures and only 25% of those become CAAM Level 3 events, 1.2 engine nacelle uncontainments and 0.3 CAAM Level 3 events are expected.

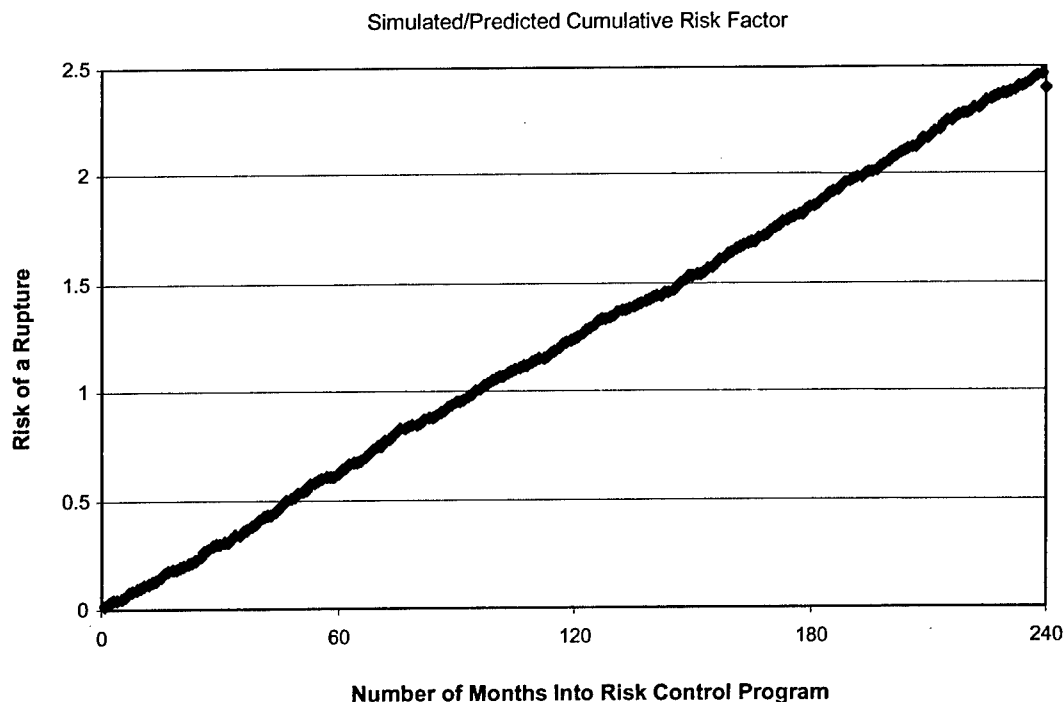


FIGURE 168. EXAMPLE PLOT OF CUMULATIVE RISK FACTOR

Step 9: Meet Customer's Requirements

The external customers for this problem are the operators and the FAA. Internal customers would consist of the appropriate levels of management and the engine manufacturer's safety board.

- The FAA policy guideline for CAAM Level 3 events is 1.0. The risk analysis predicts 1.2 CAAM Level 3 events, so additional action is needed to meet the FAA's requirement.

Going back to step 8, the risk analyst examines another scenario where an on-wing inspection would be performed every 1000 cycles. The resulting risk factor drops down from 2.4 to 0.8 ruptures, 0.4 nacelle uncontainments, and 0.1 CAAM Level 3 events.

- The operators do not want a field management plan that has increased the maintenance burden such as additional inspections or early removals. However, the risk analysis for no additional action shows an unacceptable risk, the scenario with the on-wing inspections has acceptable risk, so the risk analyst will propose a field management of on-wing inspections every 1,000 cycles, starting at 12,000 cycles (min. crack initiation). This puts a small increased burden, but it might be scheduled with some other on-wing inspection or C-check.

Since the proposed field management plan should be acceptable to the external customer based on the internal customer support insight, the risk analyst needs to get the buy-in of the working team and management.

Step 10: Summarize and Present Analysis to Proper Teams

It is recommended that a standard presentation format be used when presenting risk analysis results to management teams, safety boards, the FAA, etc. In this project, all the inputs and assumptions in steps 3 and 4 are covered first and then the calibration results, including the "Actual vs Predicted" plot. Finally, the risk factors are discussed in detail, along with a timeline plot, uncontainment risk, and CAAM risk.

Step 11: Determine if the Internal Safety Board Review Required

This would be the appropriate time to get the management team responsible for flight safety issues to review the proposed field management plan.

Step 12: Write Report

It is recommended that after all approvals are finalized, the final presentations to management teams, safety boards, and the FAA be among the documentation that is included in the final report.

Step 13: Close the Risk Analysis Job Using an Electronic Filing System

It is recommended that all final documentation be stored electronically using a system that protects all stored documents and allows recovery of previous analyses for updates or follow-ups. For this example, the input file, which simulation program was used, and final presentations with plots will be stored in the filing system for closing the job. This will provide an archive of past jobs that can be used for updates or as reference to new jobs.

2.4 TASK 6: INTEGRATION OF GENERIC METHODOLOGIES INTO MANAGEMENT METHODOLOGY.

Each of the previously reported tasks covered the investigation of several important parameters required to safely manage engine high-pressure cases from the time they are released into service, and in fulfillment of this contract goal, as they continue to operate and age. The contract investigation has identified several effects that accelerate crack growth in these alloys. For example, aging and multiple repair heat treatments accelerate the propagation of cracks in the wrought nickel case alloy at high temperatures, however, at lower temperatures there does not appear to be any impact. Using the lower temperature material characterizations developed for the aged material accurately predicts current P&W case cracking experience. This suggests that current management plans are sufficient to manage this cracking mode.

If a new higher temperature cracking mode was identified in the future or if other manufacturers used this material at higher temperatures, the material crack growth characteristics at those temperatures would need to be used. It was also found that the process of HIPping of welds in the cast nickel alloy increased the crack growth rate. Casting defects identified during the initial production process are typically repaired by HIPping. These defects occur randomly in the casting and would not necessarily occur at a location that develops durability cracking problems requiring case management. However, to ensure flight safety, it is recommended that the effect of HIPped welds on long-term case durability be evaluated.

In addition, incorporating these individual parts into a recommended future overall management plan for these important static structures has also been considered as part of this contract. The continued safe operation of engine high-pressure cases can be ensured by using several management approaches. One might take the approach that the case should be retired at a predetermined, predicted life-cycle point or at the first indication of cracking, which is typically done with rotor structures. These methods could adversely affect the airline industry economically because of the high cost of most large structural cases. This would also be contrary to the historical precedent of cases being operated for long periods of time, undergoing significant repairs and providing safe and long-time operation. Static cases have demonstrated high damage tolerance lives, which allows the case to operate in a cracked condition without the fear of creating a flight safety hazard. Since most older static cases have not had their operational number of cycles tracked over time, it would be difficult to implement a "hard time" life retirement plan on older cases. The management methodology proposed here addresses these concerns and provides a mechanism so that these cases can operate safely. The methodology can also be applied to new case design and to current service cases that experience cracking during operation.

2.4.1 Management Methodology Recommendation.

Due to the large amount of stored energy, high-pressure static cases, like diffuser cases, have the potential to create a hazardous condition to the airplane if rupture occurs. Therefore, these cases should undergo repetitive inspections that would detect any crack prior to reaching critical size in order to prevent rupture from taking place. P&W proposes that any static case whose failure that would lead to a hazardous condition be repetitively inspected to ensure safe operation. The inspection interval could be defined either implicitly through the analysis of the damage

tolerance life for the case at the design limiting location or probabilistically by using the risk assessment methodology discussed in section 2.3. In general, using the risk methodology approach should allow for longer inspection intervals and less burden on the airline operator, which is the PW recommended approach. This inspection interval could vary over the life of the part that might include the effect of crack initiation during the initial inspection interval and be based solely on crack propagation on subsequent intervals and include a recommended case retirement life. The repetitive inspection interval could range from an on-the-wing periodic inspection at specific intervals to a mandatory teardown of an engine, or it may be defined as whenever the case is conveniently available in the overhaul shop at the piece part level. The interval will be defined as that required to prevent hazarding the aircraft from a case rupture. It is recommended that cases be inspected as a minimum, whenever the case in question is "split off" from the mating cases.

2.4.2 Management Approach.

The case management process flowchart is shown in figure 169. The following paragraphs discuss the key ingredients required to establish a safe case inspection interval. The methodology proposed can also be applied to aging cases covered specifically by this contract and to new case designs.

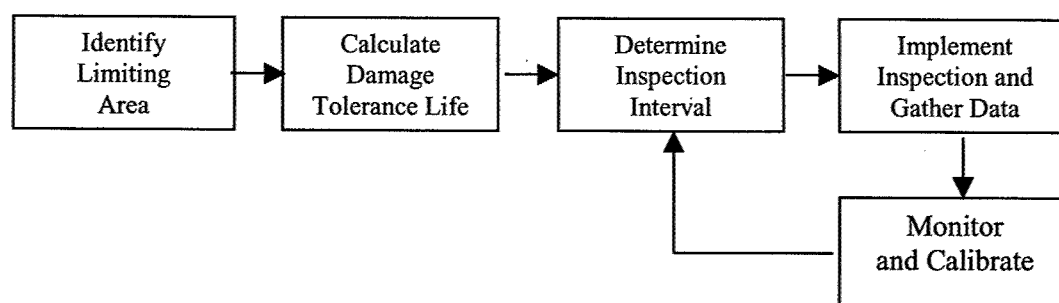


FIGURE 169. CASE MANAGEMENT PROCESS FLOWCHART

2.4.2.1 Case-Limiting Area Definition.

Section 2.2 identified several areas, features, and repairs on static cases where an initial crack or flaw had developed. This can lead to crack propagation and subsequent risk of case failure. The case manufacturer must be aware of these critical features, some of which are pointed out in section 2.2.1, and determine which ones are limiting. In the design of modern gas turbines, several locations may be equally limiting due to optimization of the case structure and multiple failure points may need to be considered. Critical locations, as defined by high-stress areas caused by geometric or thermal discontinuities that can lead to cracking, as well as defects that originate in the manufacturing or repair process, like casting or welding flaws, also need to be considered. On older case structures already in service, critical features may be identified either by the application of current finite element and life prediction methodologies or through obtaining field operational data that identifies areas prone to cracking. As new information on the effects of material aging becomes known, they can also be taken into account.

In determining the case-limiting area (or areas), the time to crack initiation and any subsequent residual time to case rupture needs to be considered. A simplistic presentation of this can be seen in figure 170. Although location B has a longer life to crack initiation, it also has a higher crack propagation rate and very well may define a lower inspection interval requirement to ensure no case rupture.

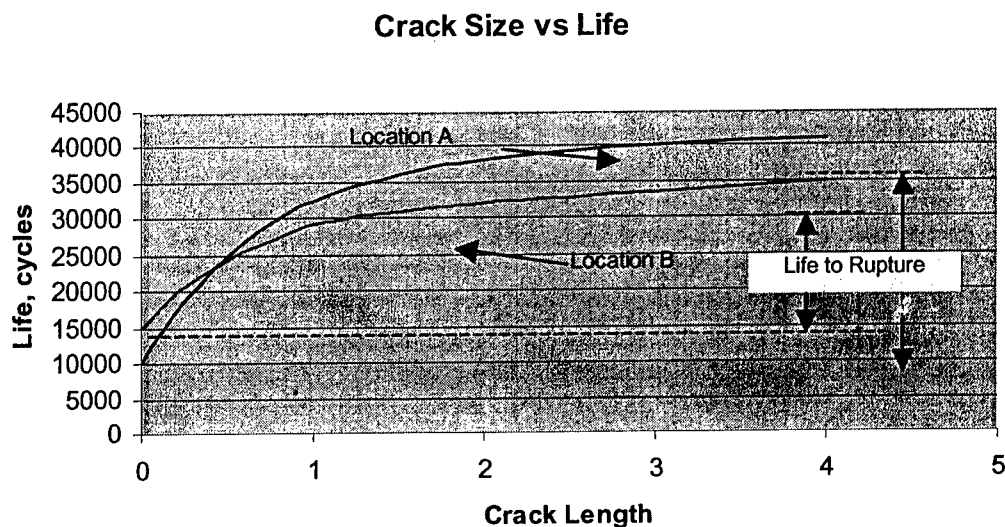


FIGURE 170. CASE-LIMITING LOCATION EXAMPLE FOR DAMAGE TOLERANCE LIFE CALCULATION

Task 2 has shown that modern stress and damage tolerance analysis techniques can accurately predict the rate at which the cracks grow for various case structures and locations for a range of commonly used case materials. This work has shown that linear fracture mechanics techniques, as found in most commonly available industry and commercial codes, i.e., the P&W SURCK code, typically produce conservative estimates of crack growth rates and fracture lives. The use of more detailed fracture mechanics analysis methods such as the FRANC-3D code or finite element methods may offer the ability to calculate more accurate damage tolerance lives that can allow for longer intervals between inspection. It is important that whatever methodology is used to calculate these lives be well calibrated with experience. This experience can be based on actual data obtained from cases that crack in airline operation or from testing of similar components in the manufacturer's test engines or rigs. Since these cases typically experience long periods of operation and undergo several repairs requiring thermal cycling over their life span, the effect of long-time thermal exposure on material properties must be considered. This was done as part of this contract and accounted for in the life calculations.

Task 2 also shows the need to identify the size and locations of case defects that may lead to cracking. This is required to accurately estimate the residual damage tolerance life of the case. As shown in the welded damage tolerance evaluations in task 2, the size and location of defects caused during the weld repair process is a critical factor in the determination of residual crack growth life. Determination of weld defect location and size in these life determinations must be

well documented and estimated through either experience, or if not available, through conservative estimates of defect size based on similar weld repairs or inspection capability.

2.4.2.2 Inspection Interval Determination.

Once the damage tolerance life for an initiated crack or manufacturing/repair defect has been calculated, a safe inspection interval for the case needs to be established. When establishing an interval, several factors need to be considered in order to ensure continued flight safety. P&W recommends the application of the risk methodology discussed in task 3 as the best method to calculate this inspection interval since most of these characteristics can vary significantly. It should be noted that in addition to the risk management methodology providing a safe inspection interval, it also provides the means to determine if continual inspections are adequate to provide flight safety or if a case retirement program is warranted. Any material degradation due to aging or multiple repairs can also be accounted for.

Some of the factors that need to be considered in any inspection interval determination include:

- Crack initiation/ flaw size distribution
- Material capability and scatter in growth rate
- Inspection method reliability
- Defect distribution
- Operational variations in power

The majority of these factors can be described as probability distributions that can be easily accounted for in the risk methodology to determine a safe inspection interval. As an alternative approach, a safe inspection interval could also be established without the use of the risk methodology. This approach typically provides a more conservative estimate in order to account for extremes in the parameters. The following example shows how conservative an interval might be if the probability distributions are not accounted for, but the worse-case variations in parameters are:

Parameter	Scatter factor
Crack growth rate	2/1 (typical/minimum)
Flaw distribution	3/1 (typical/minimum on life)
Inspection reliability	95%

Example: Predicted typical damage tolerance life = 20,000 cycles

Minimum crack growth life = $20,000/2 = 10,000$ cycles

Maximum flaw size effect: $10,000/3 = 3,333$ cycles

Inspection reliability effect: $3333/2 = 1666$ cycles

(allows 2 opportunities to detect a crack)

Required Inspection Interval = 1666 cycles to cover worst-case combination of parameters. This approach would provide a conservative inspection interval to detect one crack in a million cases (probability = $0.001 \times 0.001 = 0.000001$).

Statistically combining all probability distributions in a risk simulation for 20 years, assuming 1000 engines, yields an acceptable inspection interval of 2700 cycles, approximately 60% higher.

This simple example shows how typical variations in these parameters can lead to large reductions in the inspection interval of the case, and if the probability distributions for the various parameters were accounted for, conservatism could be removed.

One criticism of using the risk methodology approach that is frequently discussed is the uncertainty some of the parameters that describe the probability distributions. While all parameters may not be thoroughly known exactly for every case, most of the parameters, such as material scatter factor, can be established from components of similar construction within the manufacturer's experience base, or if not known, estimated with conservative distributions based on other experience. A key element in this approach is the continual monitoring and calibration of the risk system over time.

2.4.2.3 Inspection Recommendation.

Historically, airline operators have not tracked the cyclic usage of these critical case structures, or if tracked, records have been poorly compiled. An integral part of a management plan for critical cases is to record the cyclic life usage, repairs, and inspections over the life of the part. If management of these critical cases is to be meaningful, P&W recommends the following actions be taken for any static case whose failure would lead to a hazardous condition.

- A repetitive case inspection should be established using the risk methodology detailed in task 3 to ensure flight safety.
- Case inspection requirements should be placed in the Chapter 5 life limitation section of the engine manual.
- Case life cycles should be monitored and recorded in a method that can be easily reviewed.
- Case repair history should be recorded and monitored.

The results of case inspections need to be reviewed to calibrate the analysis used to establish the inspection interval. This data not only helps ensure that the inspection interval is acceptable to maintain flight safety, but also provides the data required to determine if the interval can be extended to help minimize the amount of inspections required of the airline operator.

2.4.3 Summary of Management Methodology.

The management process flowchart shown in figure 169 has been included here (figure 171) with the details of the various issues included.

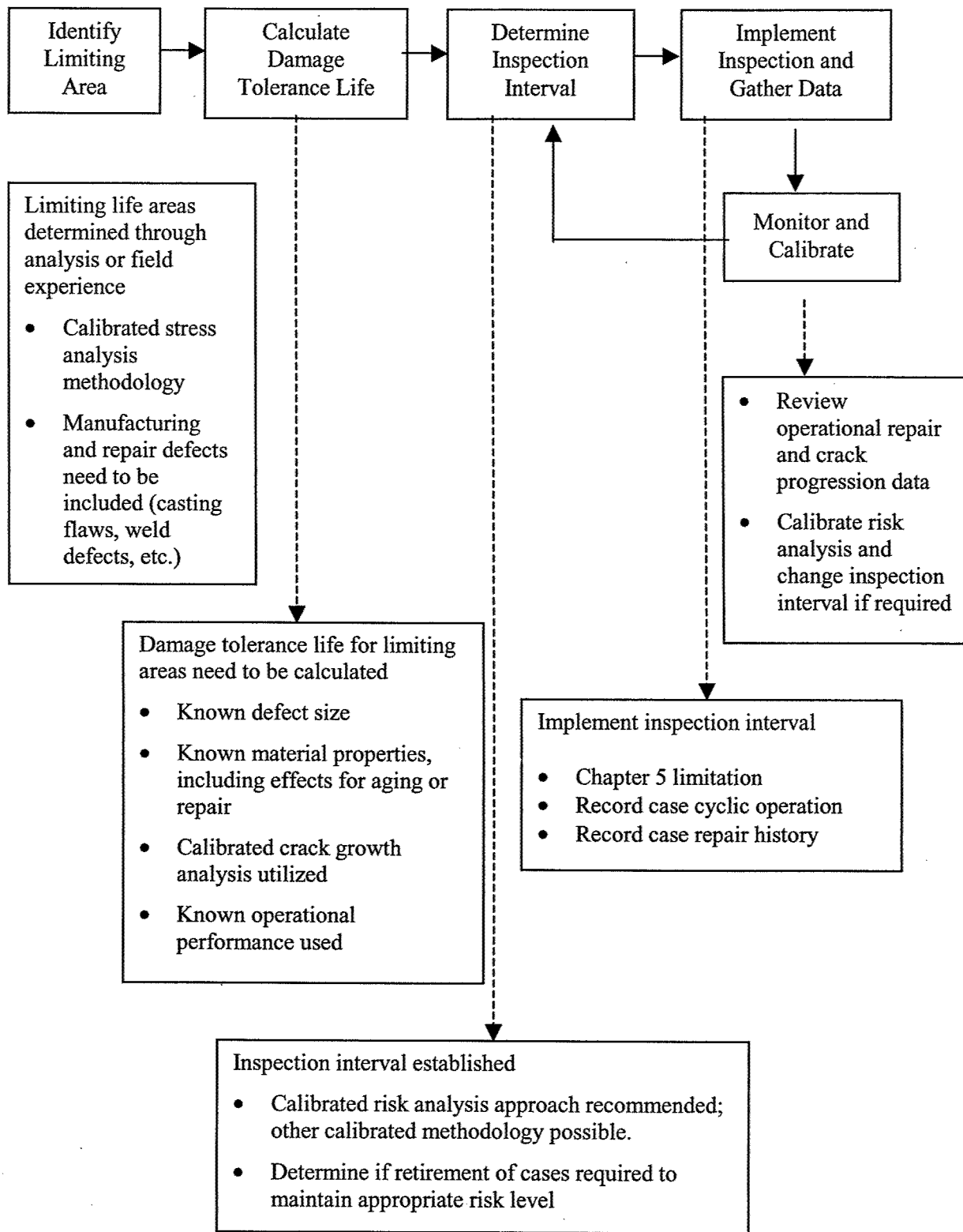


FIGURE 171. EXPANDED MANAGEMENT PROCESS FLOWCHART

APPENDIX A—DATA AND DATA PLOTS OF da/dN TESTS

A.1 AMS 5613 da/dN PLOTS.

Chart No.	Material Source	Condition ²	Specimen Number	Test Temp. (°F)	Cyclic Rate	Comments
A-1	A	A	42556	750	10 cpm	Baseline
A-2	A	A	42557	950	10 cpm	Baseline
A-3	A	A	42558	950	10 cpm	Baseline
A-4	A	A	42559	950	2 mdw	Baseline
A-5	A	A	42560	950	2 mdw	Baseline
A-6	A	B	42562	750	10 cpm	Weld Baseline
A-7	A	B	42563	950	10 cpm	Weld Baseline
A-8	A	B	42564	950	10 cpm	Weld Baseline
A-9	A	B	42565	950	2 mdw	Weld Baseline
A-10	A	B	42566	950	2 mdw	Weld Baseline
A-11	A	C	43346	750	10 cpm	Effect of multi-SR's on BM
A-12	A	C	43347	750	10 cpm	Effect of multi-SR's on BM
A-13	A	C	43348	950	10 cpm	Effect of multi-SR's on BM
A-14	A	C	43349	950	10 cpm	Effect of multi-SR's on BM
A-15	A	C	43350	950	2 mdw	Effect of multi-SR's on BM
A-16	A	C	43351	950	2 mdw	Effect of multi-SR's on BM
A-17	A	D	43352	750	10 cpm	Effect of multi-SR's on Welds
A-18	A	D	43353	750	10 cpm	Effect of multi-SR's on Welds
A-19	A	D	43354	950	10 cpm	Effect of multi-SR's on Welds
A-20	A	D	43355	950	10 cpm	Effect of multi-SR's on Welds
A-21	A	D	43357	950	2 mdw	Effect of multi-SR's on Welds
A-22	A	A	45107	RT	10 cpm	RT Fracture Eval.
A-23	A	E	43335	RT	10 cpm	RT Fracture Eval.
A-24	A	A	45108	RT	10 cpm	RT Fracture Eval.; R=0.5
A-25	A	E	43336	RT	10 cpm	RT Fracture Eval.; R=0.5

- Notes: 1. Rolled Ring; Heat ZCESS
2. A: Harden+Temper+1 Stress Relief Cycle
B: Harden+Temper+Weld+1 Stress Relief Cycle
C: Harden+Temper+16 Stress Relief Cycles. D: Harden+Temper+Weld+16 Stress relief Cycles
D: Harden+Temper+8 Stress Relief Cycles

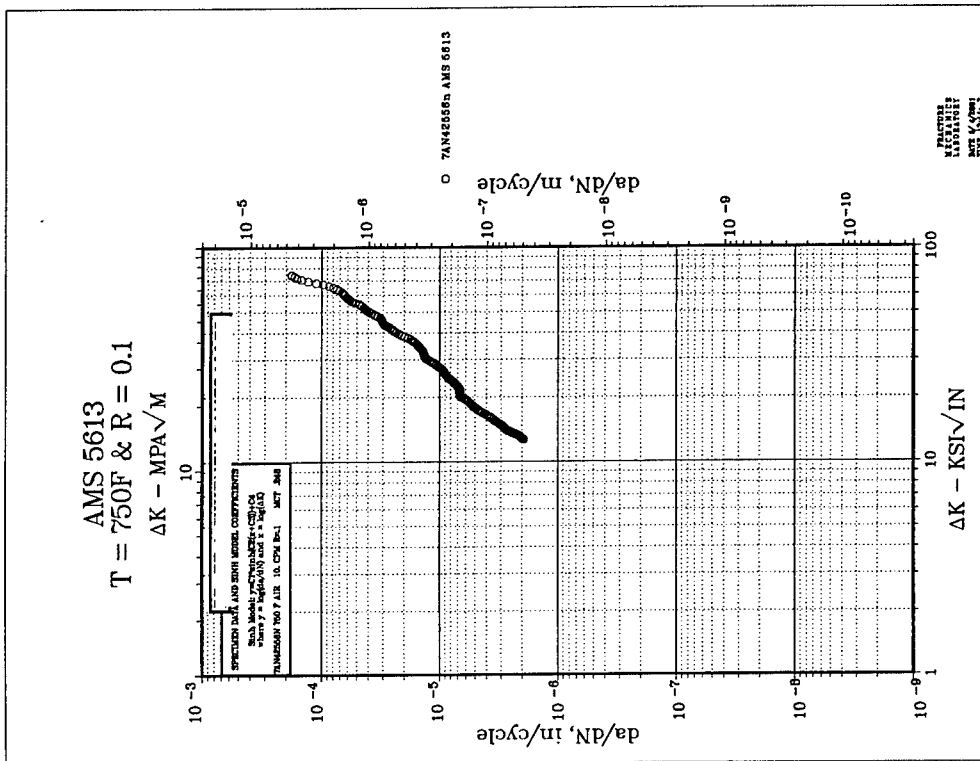


Chart A-1

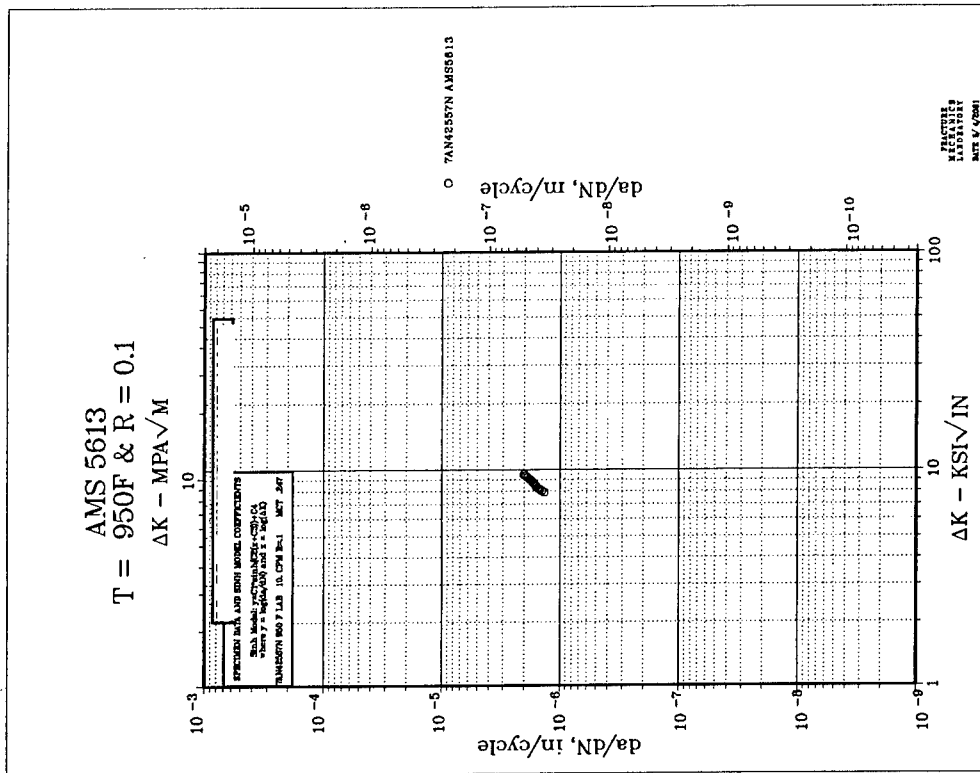


Chart A-2

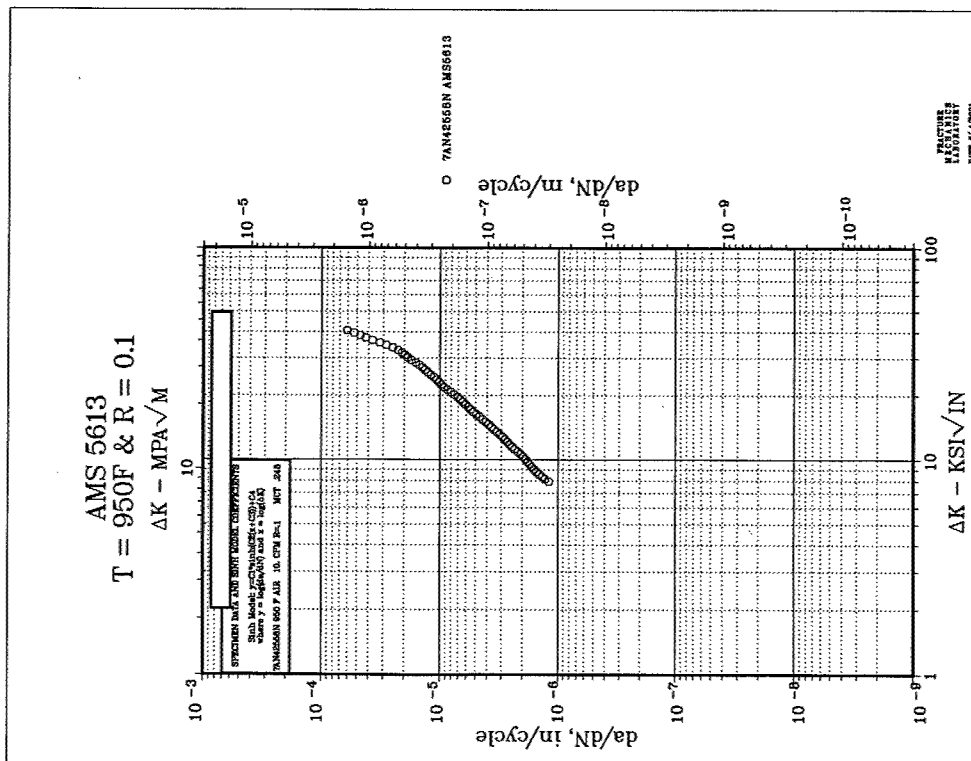


Chart A-3

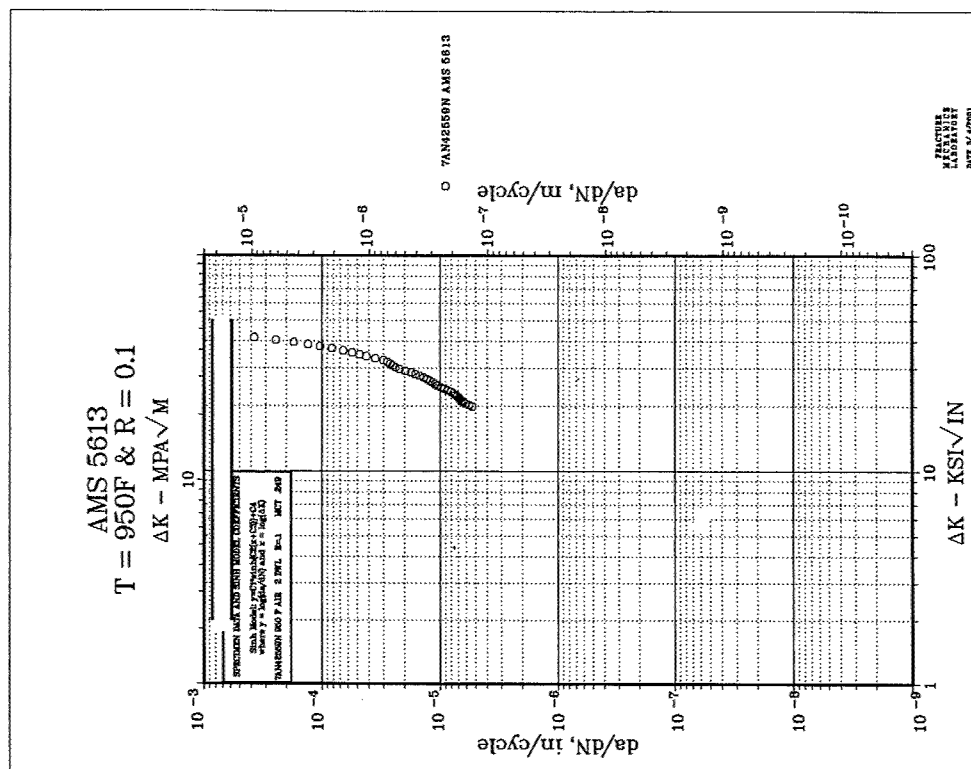


Chart A-4

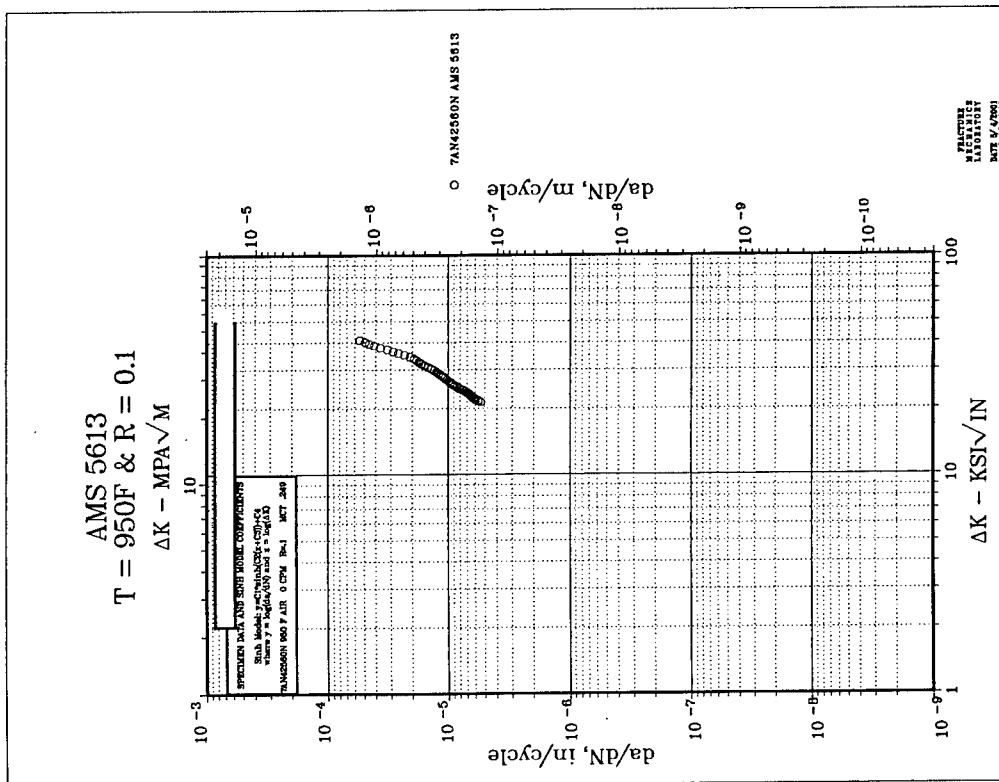


Chart A-5

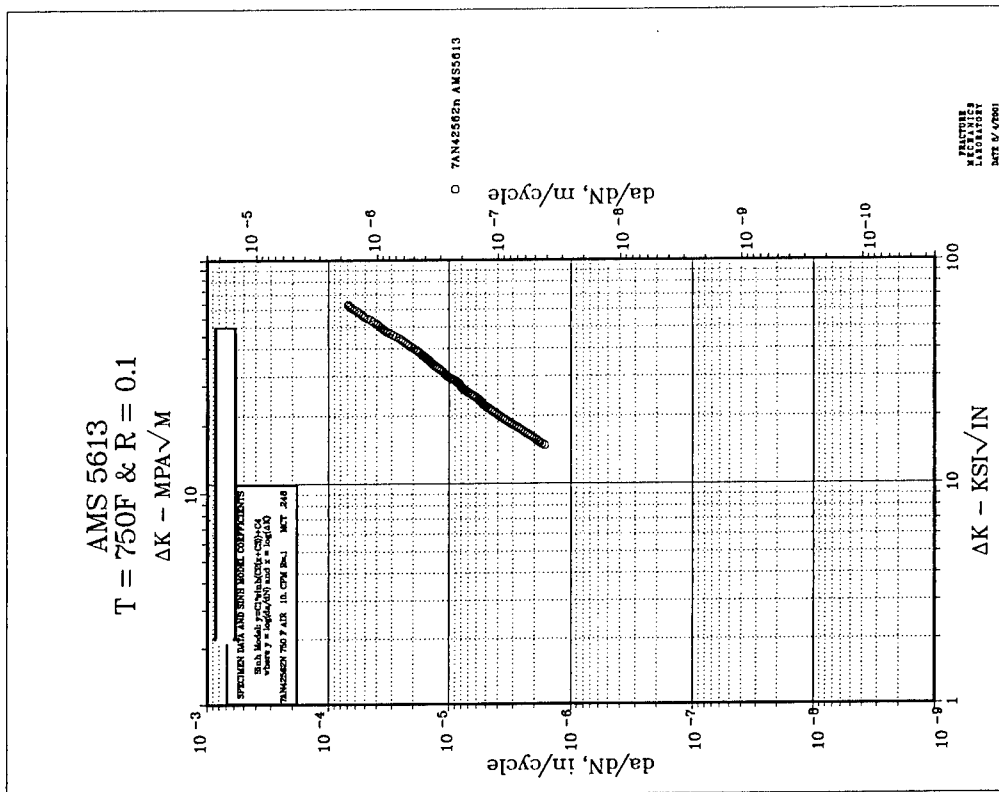
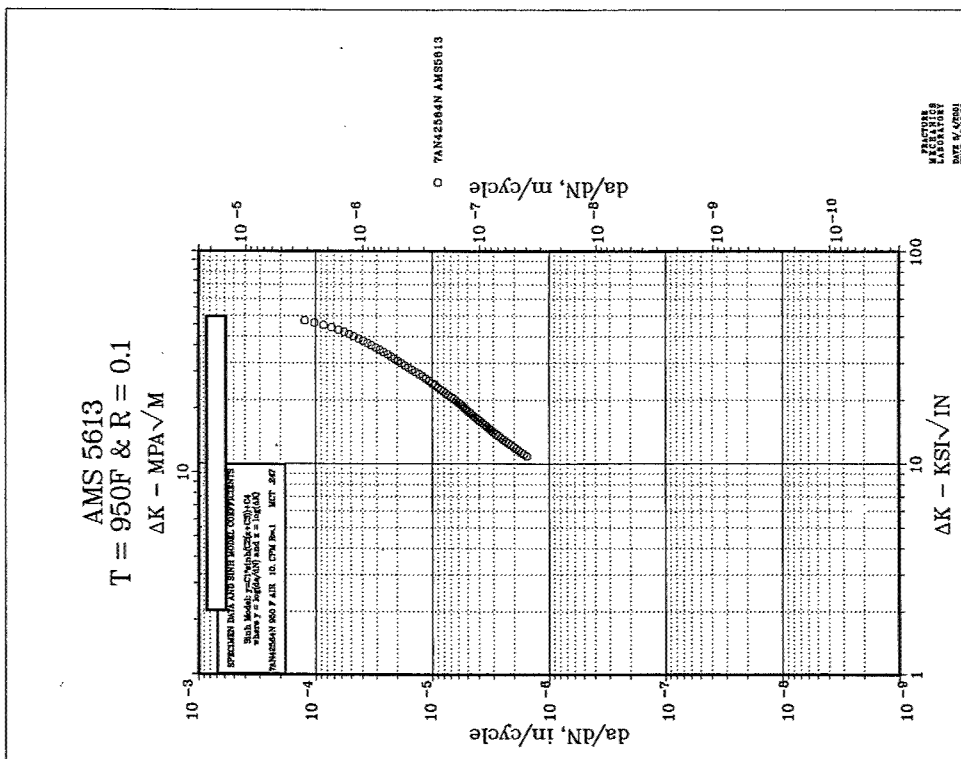
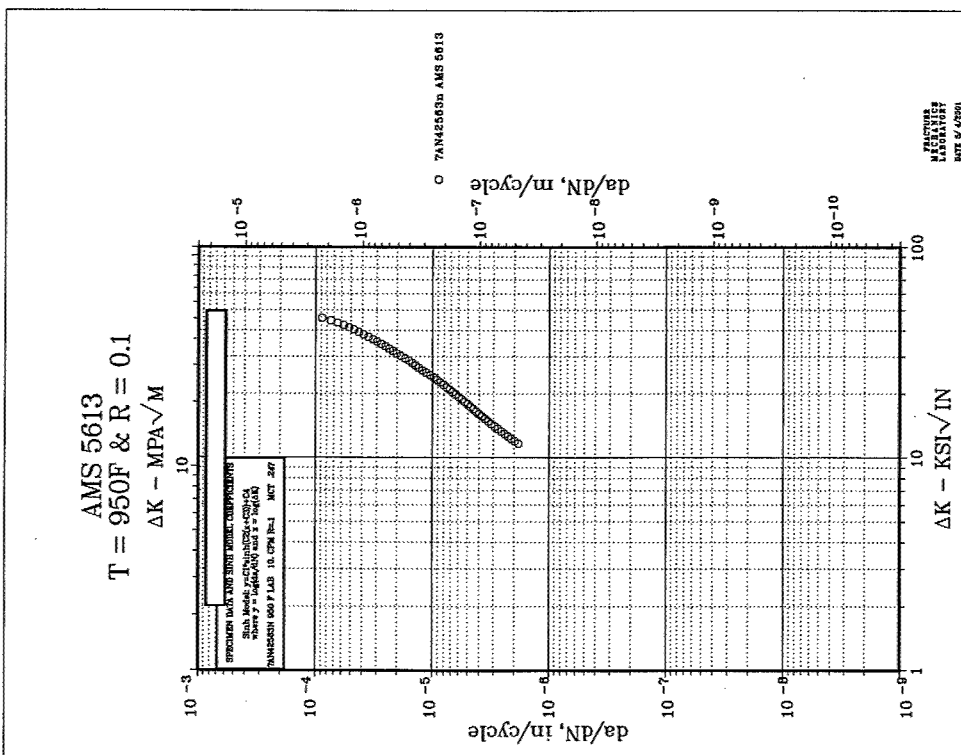


Chart A-6



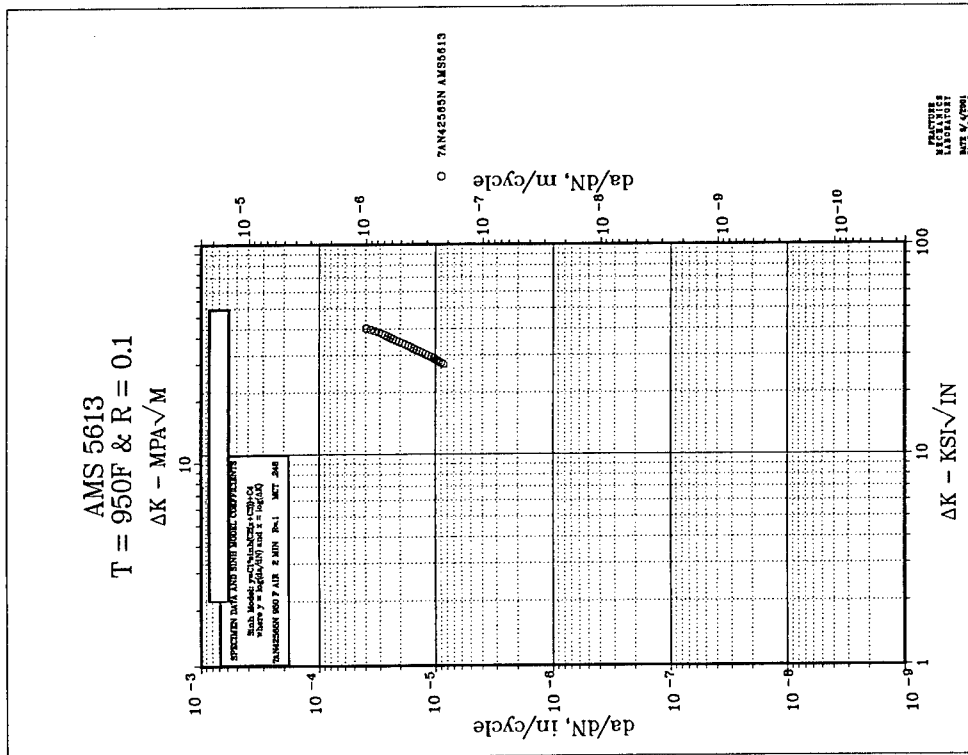


Chart A-9

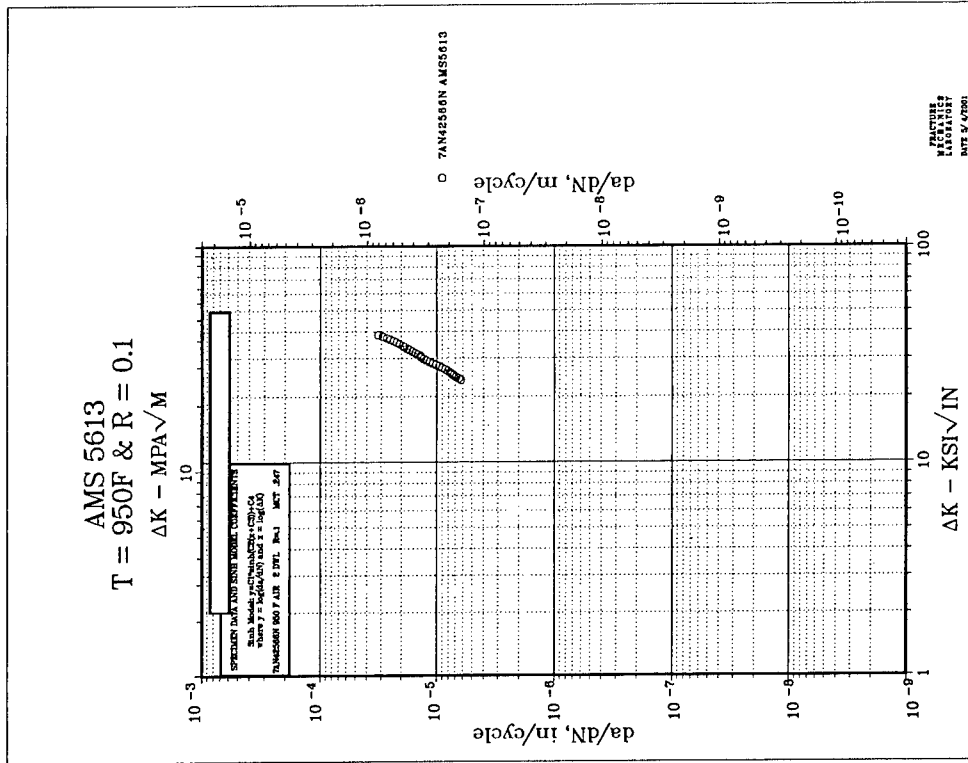


Chart A-10

AMS 5613
T=750 F & R=0.1
 ΔK , MPa \sqrt{M}

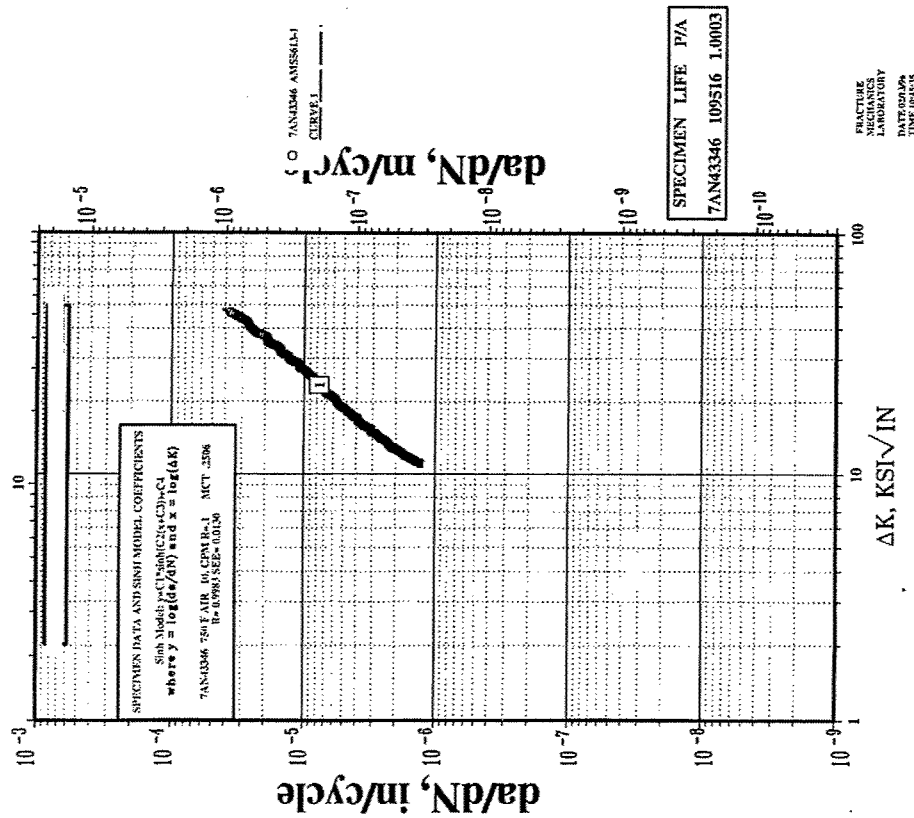


Chart A-11

AMS 5613
T=750 F & R=0.1
 ΔK , MPa \sqrt{M}

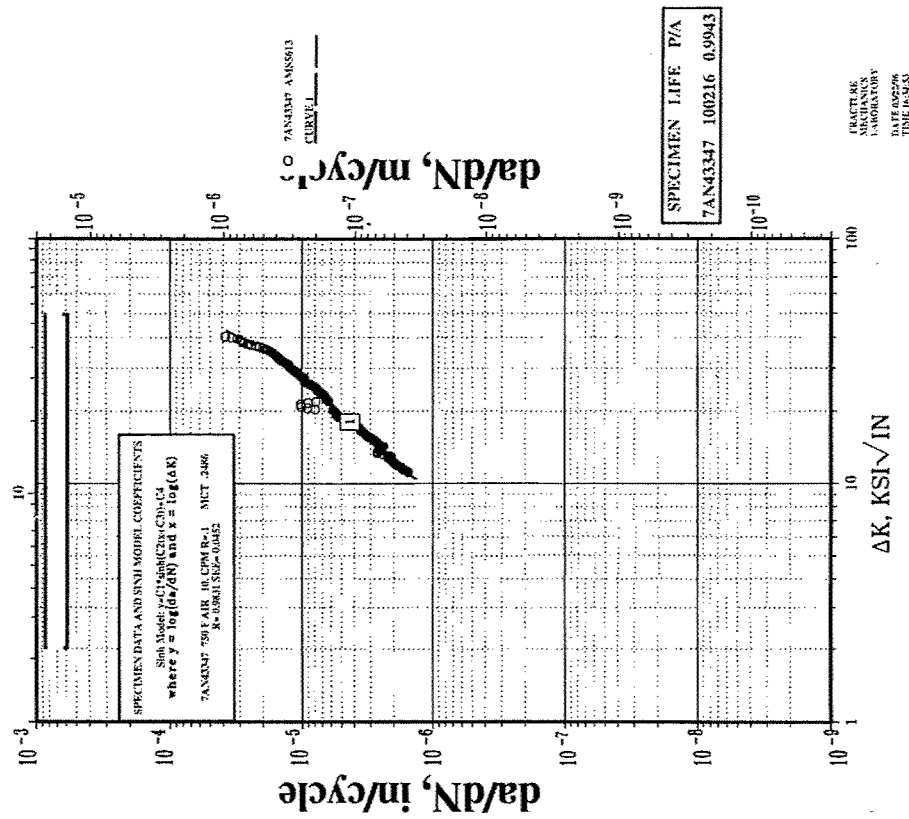


Chart A-12

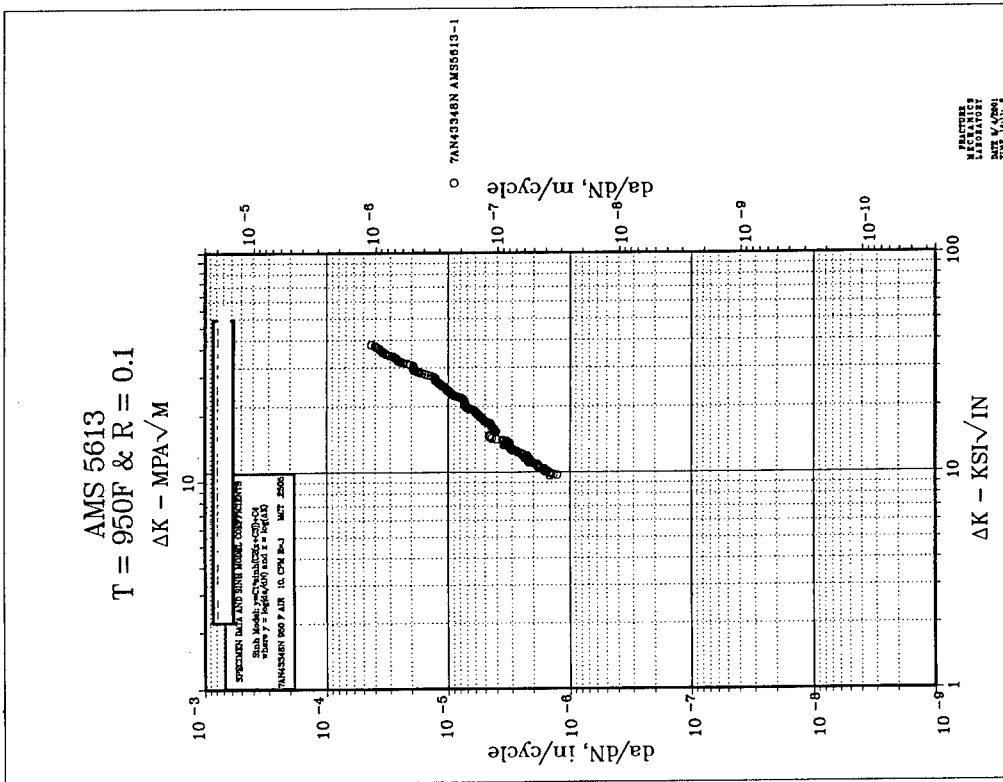


Chart A-13

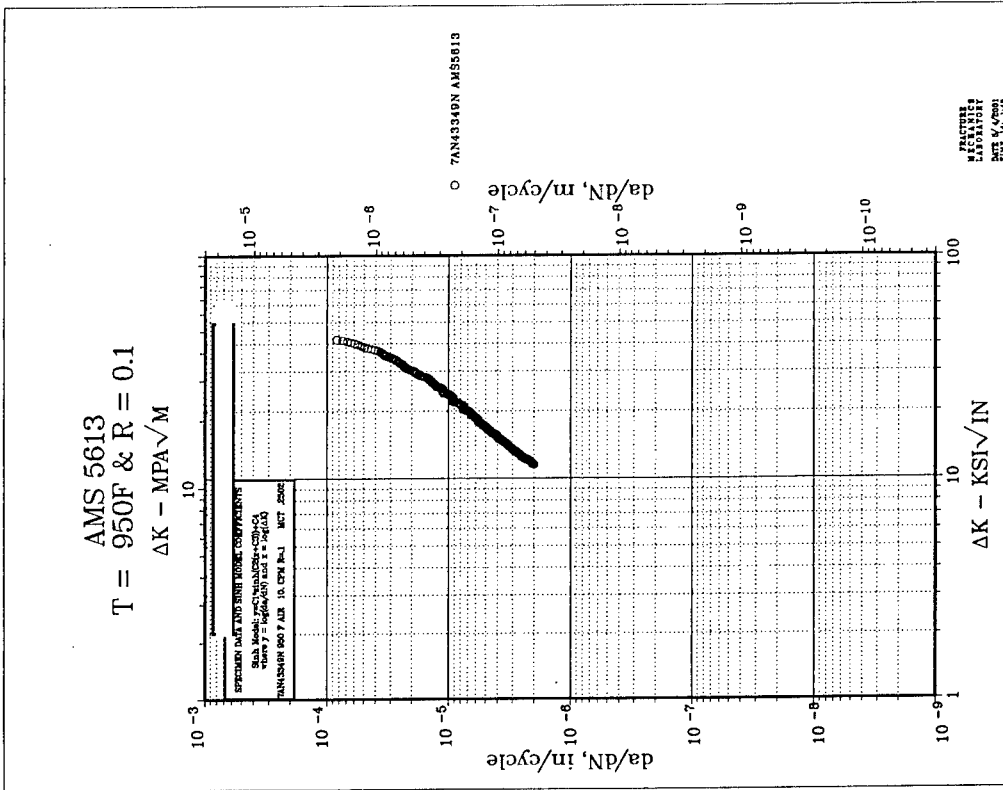


Chart A-14

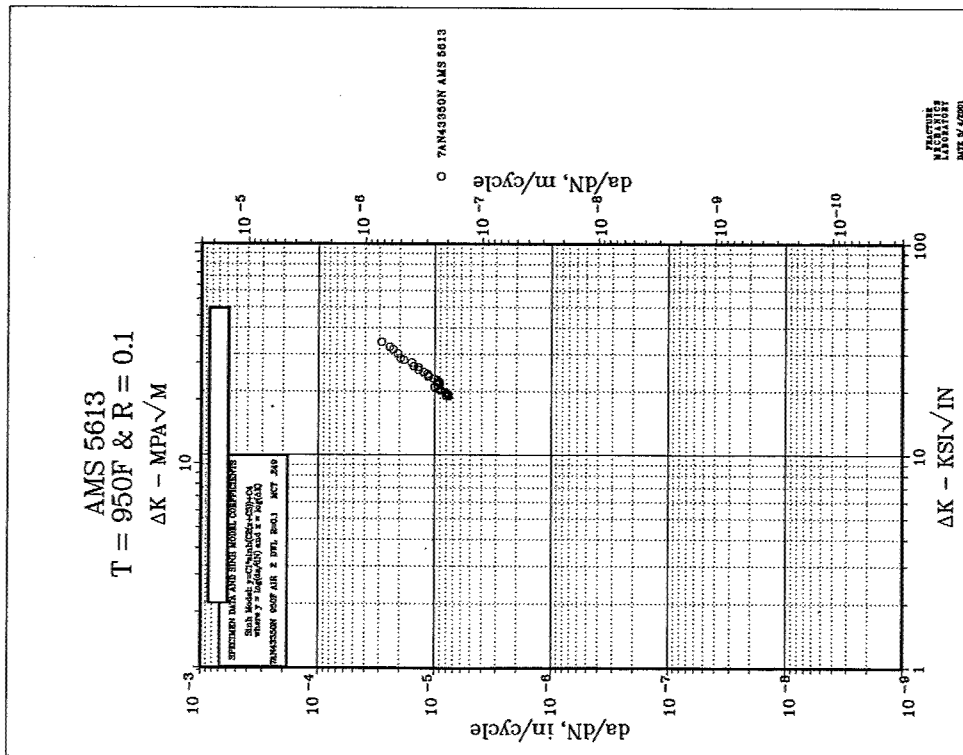


Chart A-15

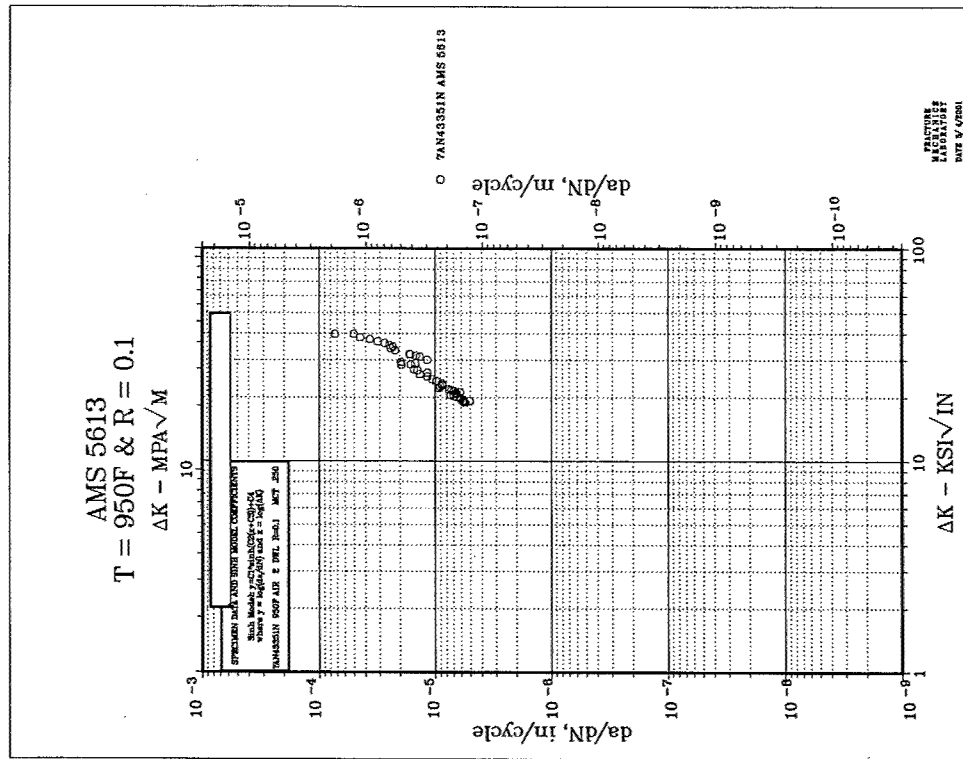
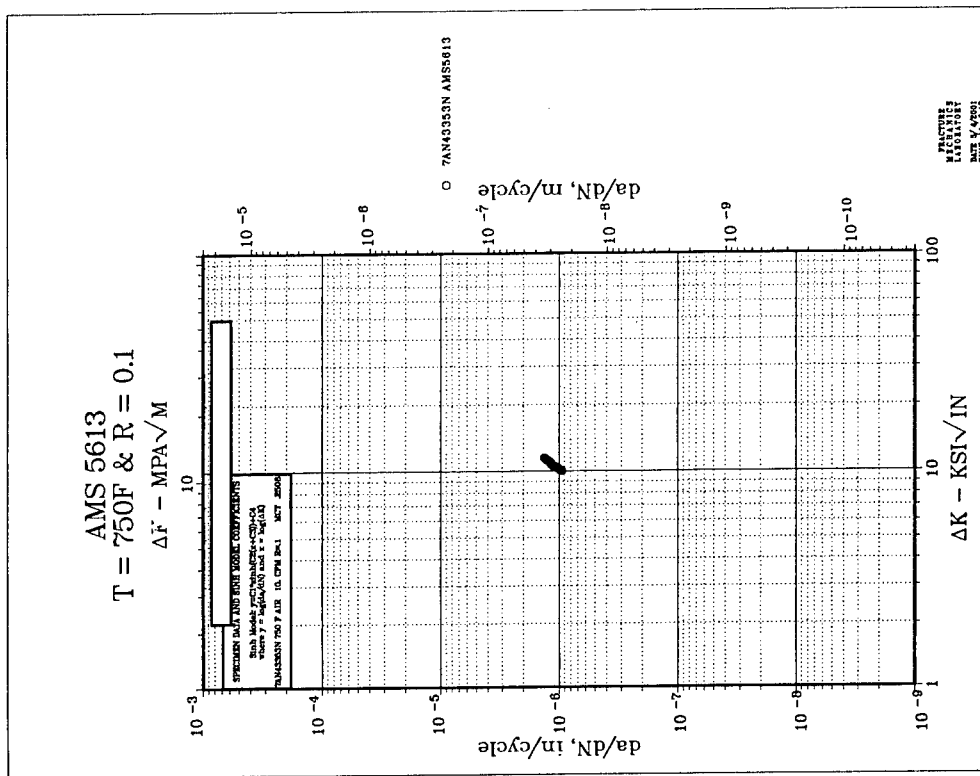
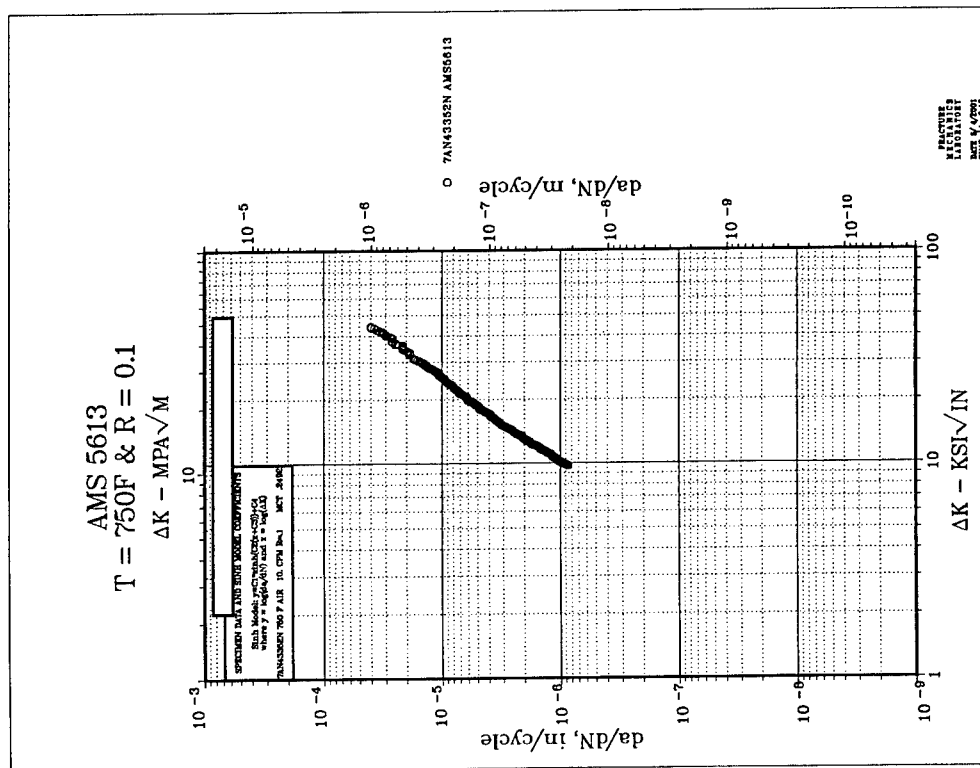
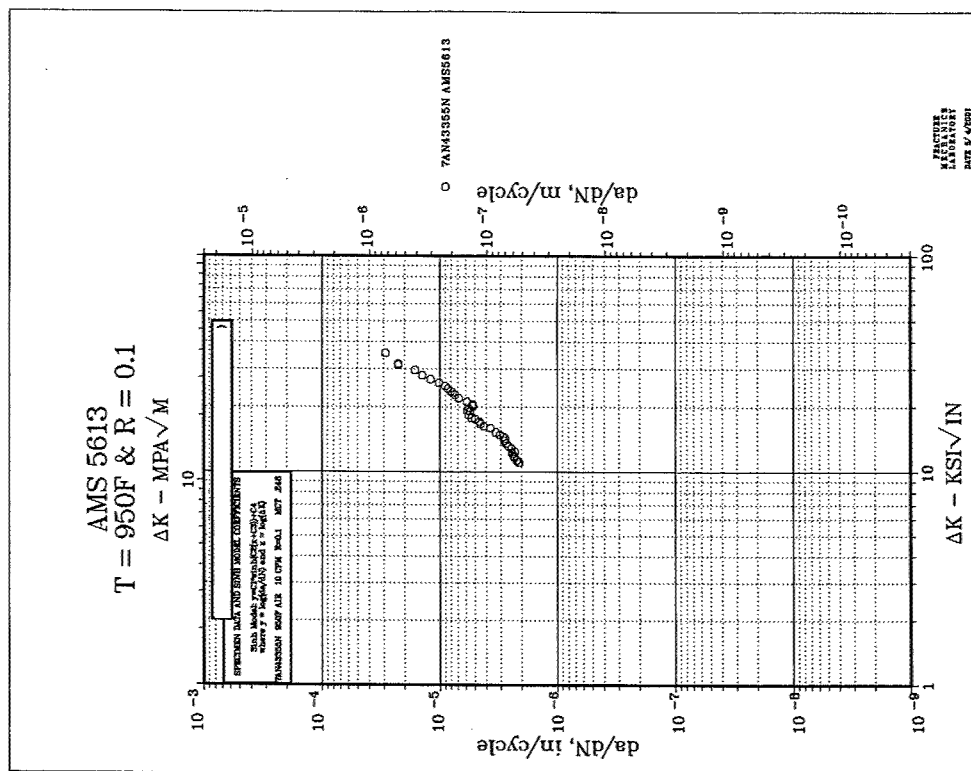
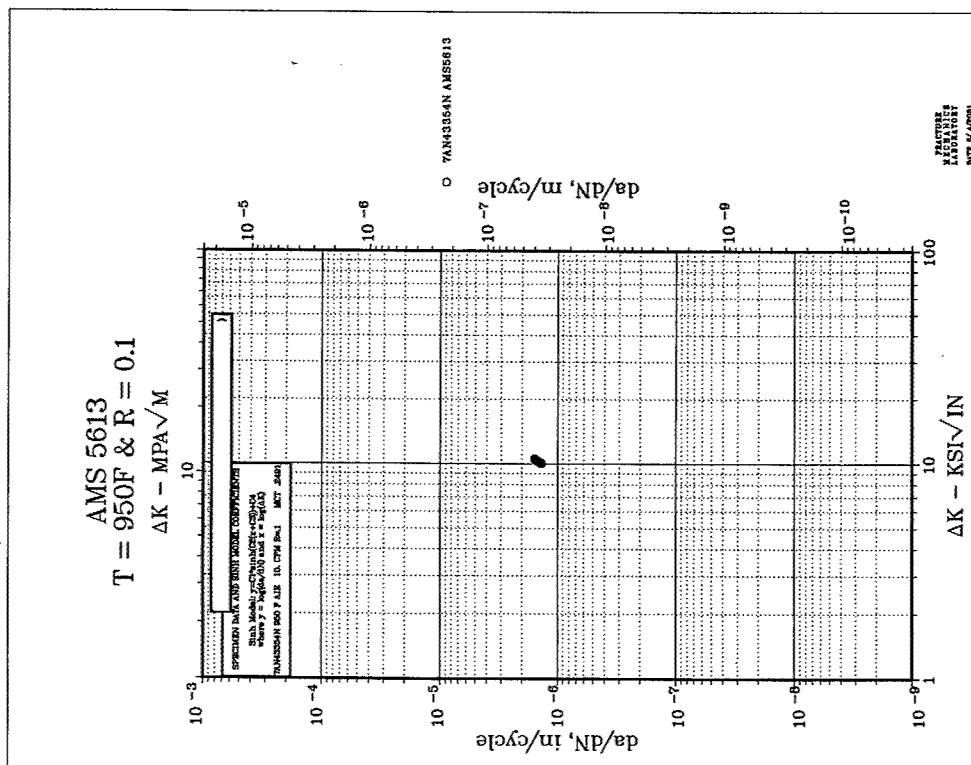


Chart A-16





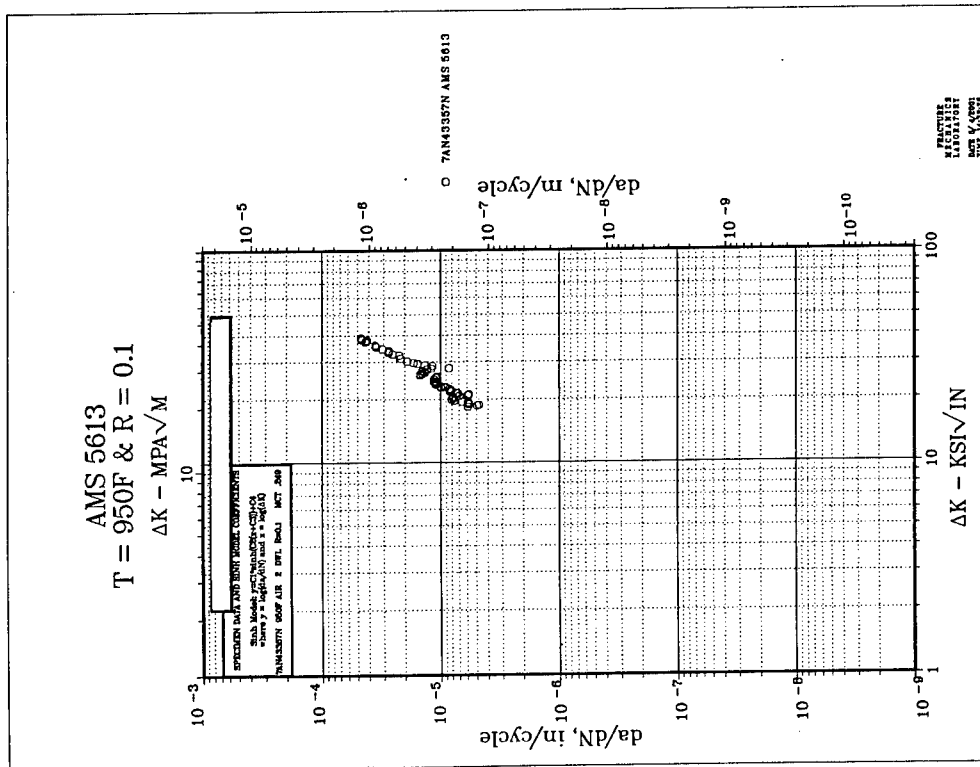


Chart A-21

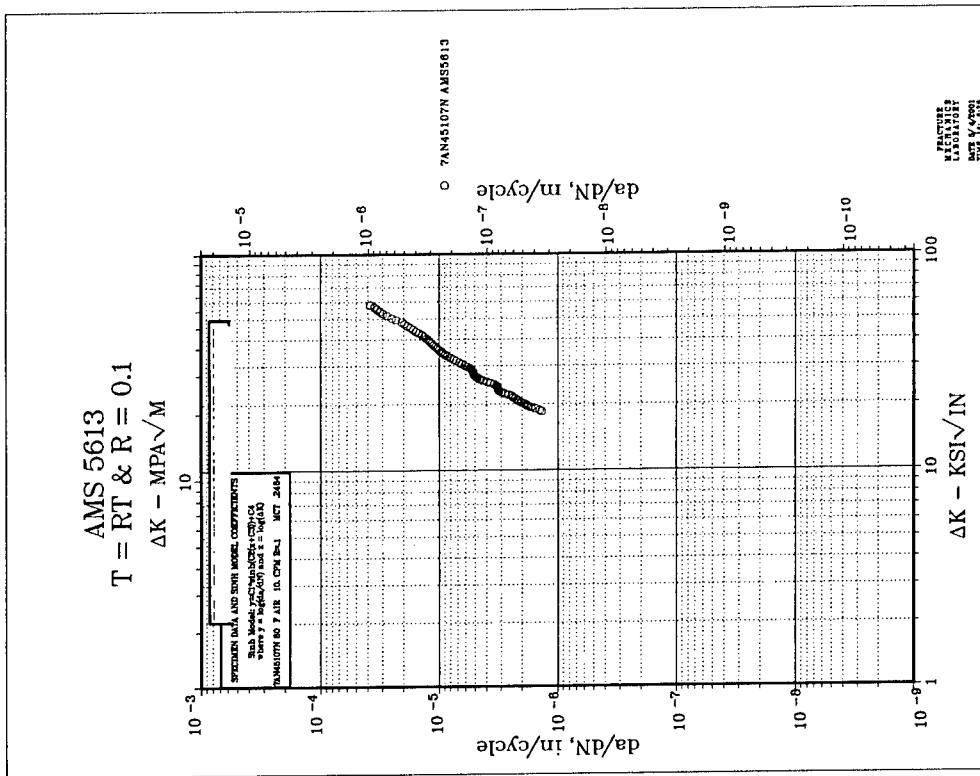


Chart A-22

AMS 5613
T=80 F & R=0.1
 ΔK , MPa \sqrt{M}

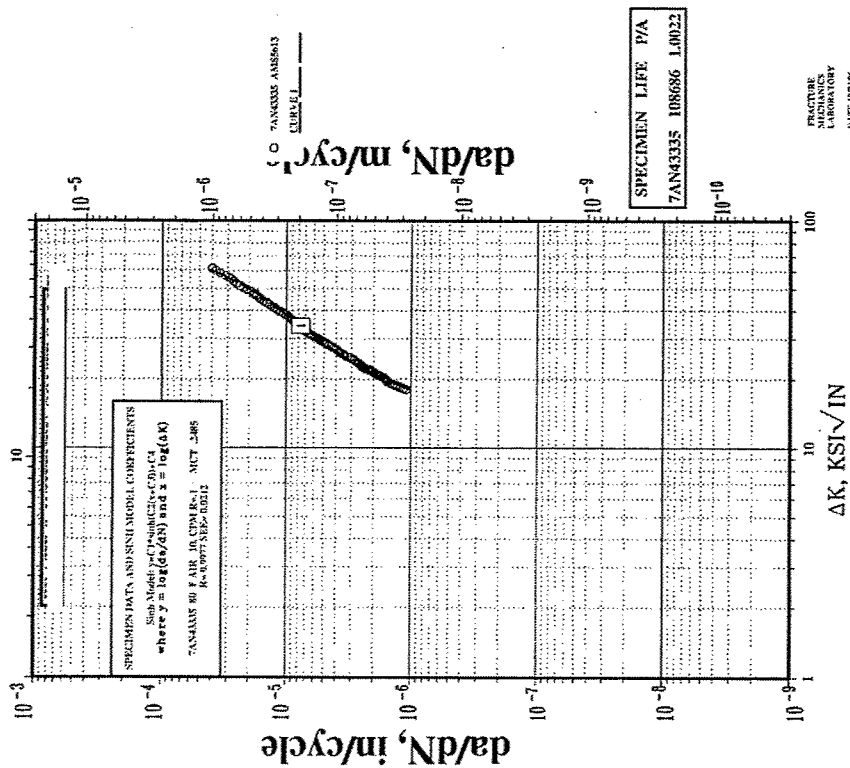


Chart A-23

AMS 5613
T = RT & R = 0.5
 ΔK - MPa \sqrt{M}

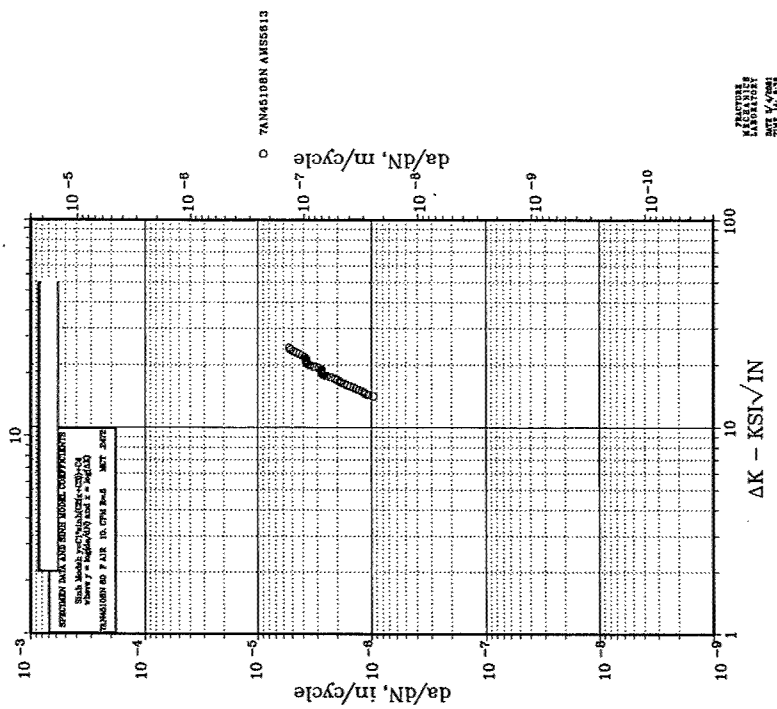


Chart A-24

AMS 5613
T=80 F & R=0.5
 ΔK , MPa \sqrt{M}

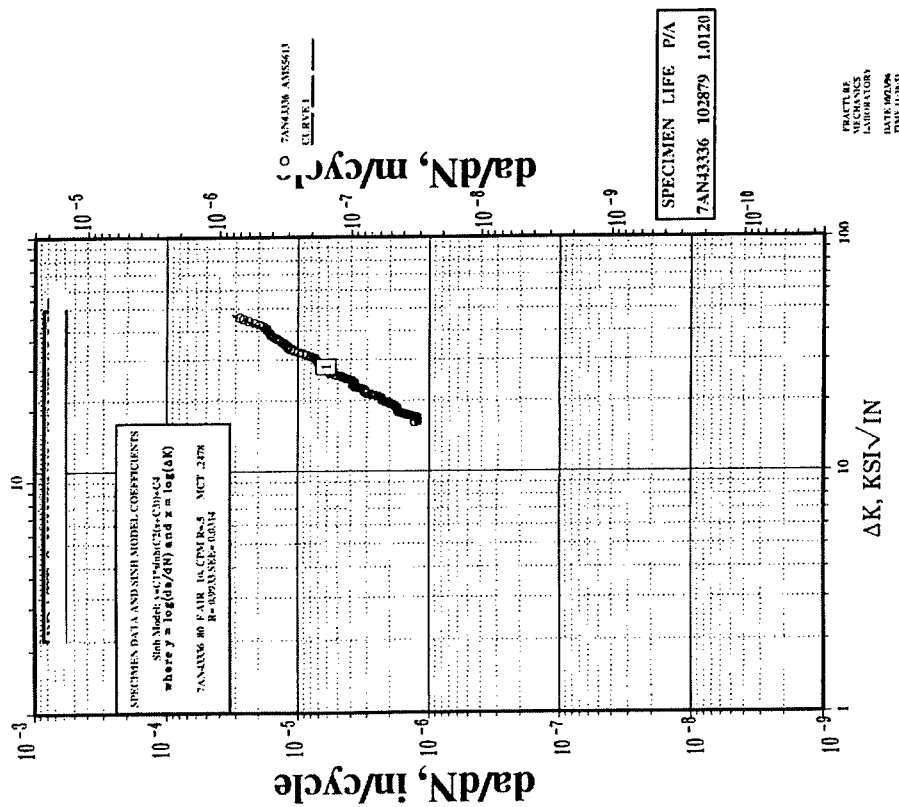


Chart A-25

A.2. AMS 5616 da/dN PLOTS.

No.	Material Source ¹	Condition ²	Specimen Number	Test Temp.(°F)	Cyclic Rate	Comments ²
A-26	A	A	41434	750	10 cpm	Trueform Baseline
A-27	A	A	41436	750	10 cpm	Trueform Baseline
A-28	A	A	41435	950	10 cpm	Trueform Baseline
A-29	A	A	41437	950	10 cpm	Trueform Baseline
A-30	B	A	40846	950	10 cpm	GS/Orientation Eval.; FG-L
A-31	B	A	40848	950	10 cpm	GS/Orientation Eval.; FG-T
A-32	B	A	40847	950	2 mdw	GS/Orientation Eval.; FG-L
A-33	B	A	40849 ⁵	950	2 mdw	GS/Orientation Eval.; FG-T
A-34	B	A	40850	950	10 cpm	GS/Orientation Eval.; CG-L
A-35	B	A	40852 ⁶	950	10 cpm	GS/Orientation Eval.; CG-T
A-36	B	A	40851 ⁵	950	2 mdw	GS/Orientation Eval.; CG-L
A-37	B	A	40853	950	2 mdw	GS/Orientation Eval.; CG-T
A-38	B	B	42336 ⁴	750	10 cpm	Baseline ⁴
A-39	B	B	42337	950	2 mdw	Baseline ⁴
A-40	B	C	42339	750	10 cpm	Weld baseline
A-41	B	C	42341	950	2 mdw	Weld baseline
A-42	B	D	43124	750	10 cpm	Effect of multi-SR's on BM
A-43	B	D	43125	950	2 mdw	Effect of multi-SR's on BM
A-44	B	E	43127	750	10 cpm	Effect of multi-SR's on BM Welds
A-45	B	E	43128	950	2 mdw	Effect of multi-SR's on BM Welds
A-46	B	A	44805	850	10 cpm	850F Eval.; CG-T
A-47	B	A	44804	850	2 mdw	850F Eval.; CG-L
A-48	B	B	42340	1200	2 mdw	1200F test

Notes: 1. Rolled Ring Heat ZCLPT

2. A: Harden+Temper

B: Harden+Temper+1 Stress Relief Cycle

C: Harden+Temper+Weld+ 1 Stress Relief Cycle

D: Harden+Temper+16 Stress Relief Cycles

E: Harden+Temper+Weld + 16 Stress Relief Cycles

3. FG= fine grain, CG = coarse grain, L = longitudinal orientation, T = transverse orientation

4. Rig failure; no data

5. Questionable test results.

6. Electronic record of data was lost.

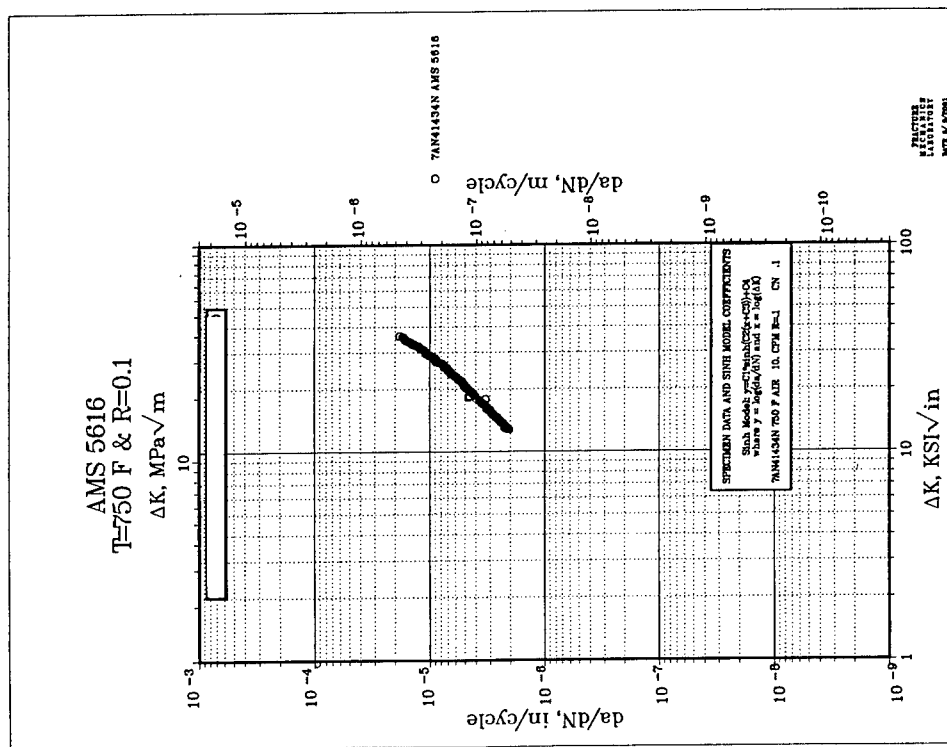


Chart A-26

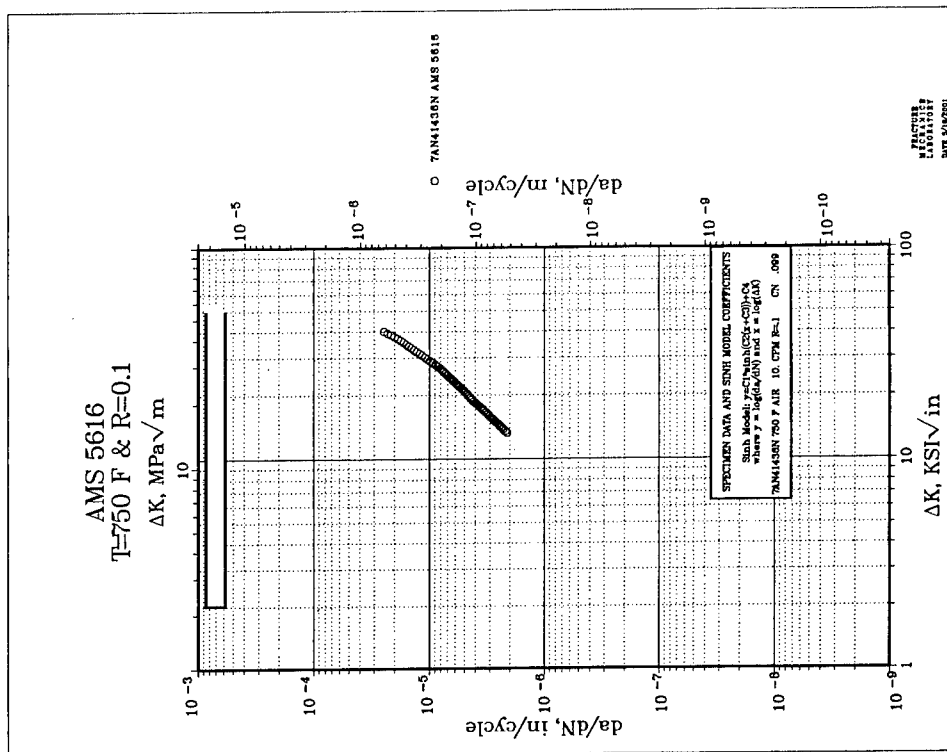


Chart A-27

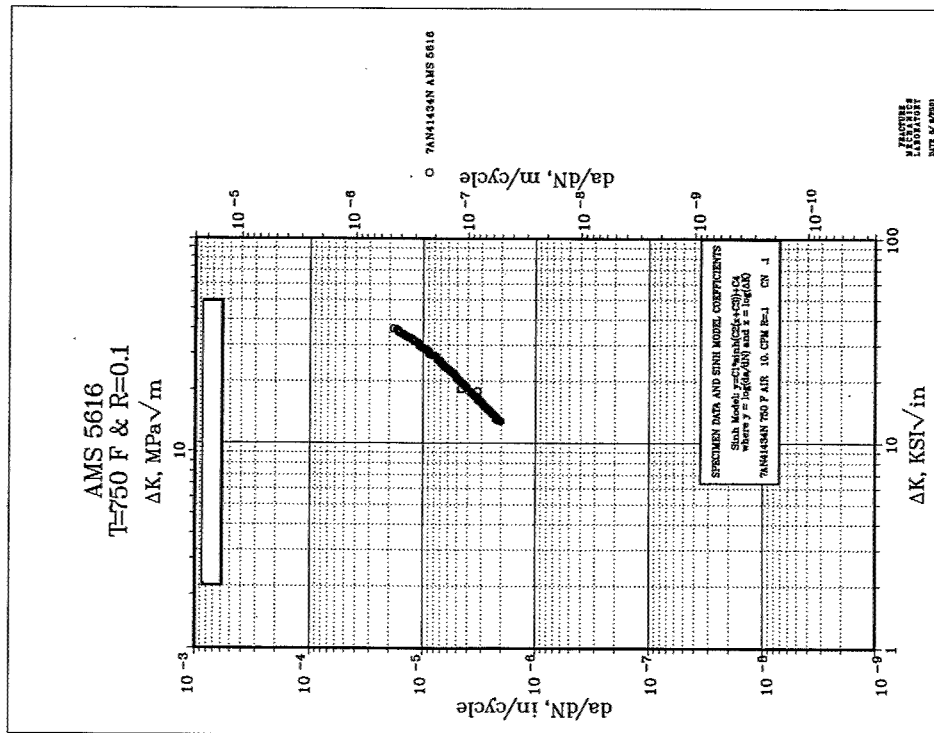


Chart A-28

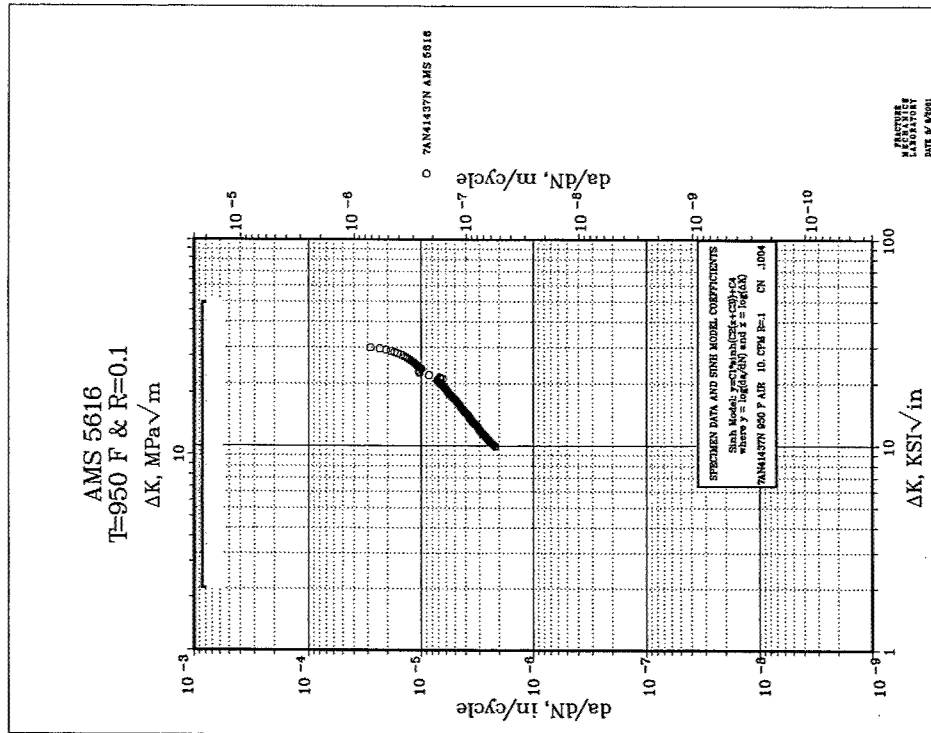


Chart A-29

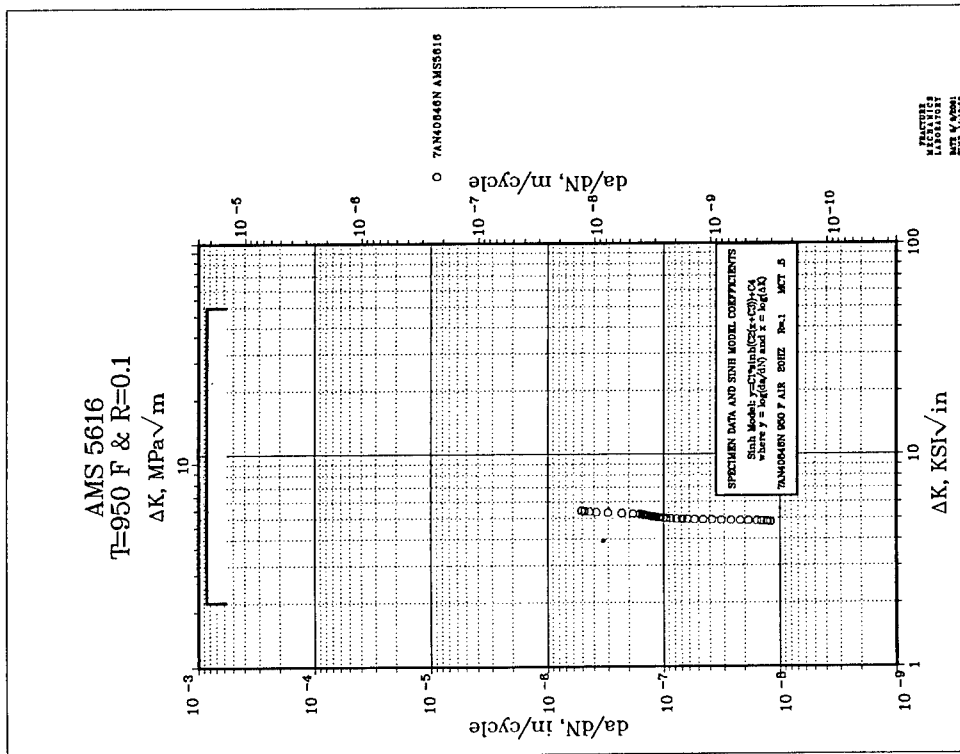


Chart A-30

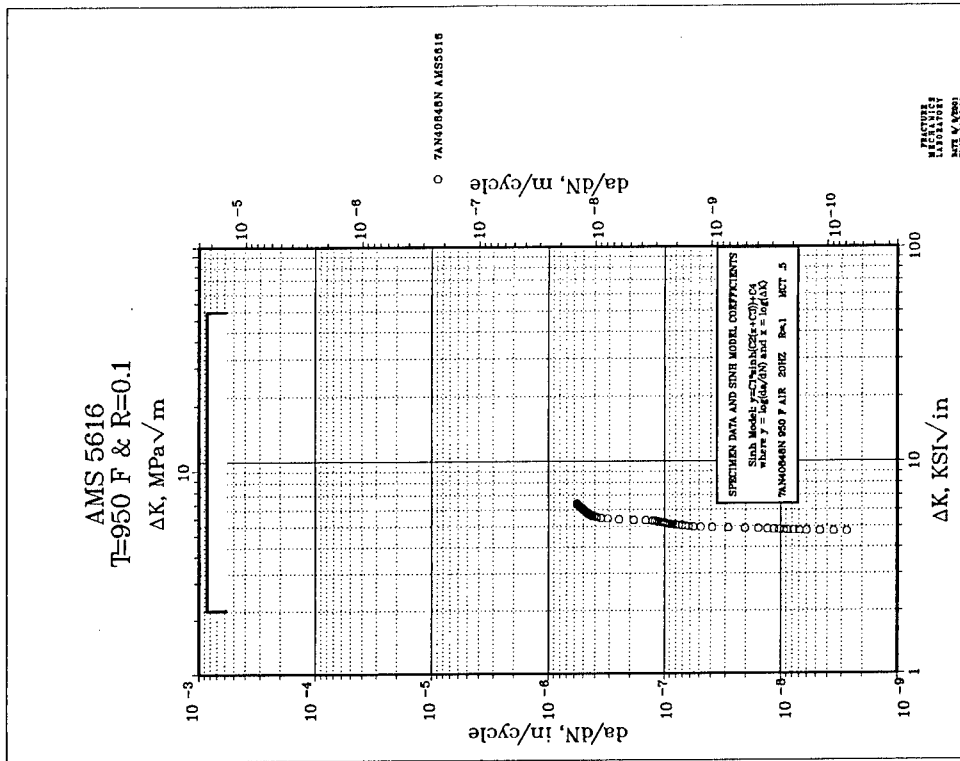


Chart A-31

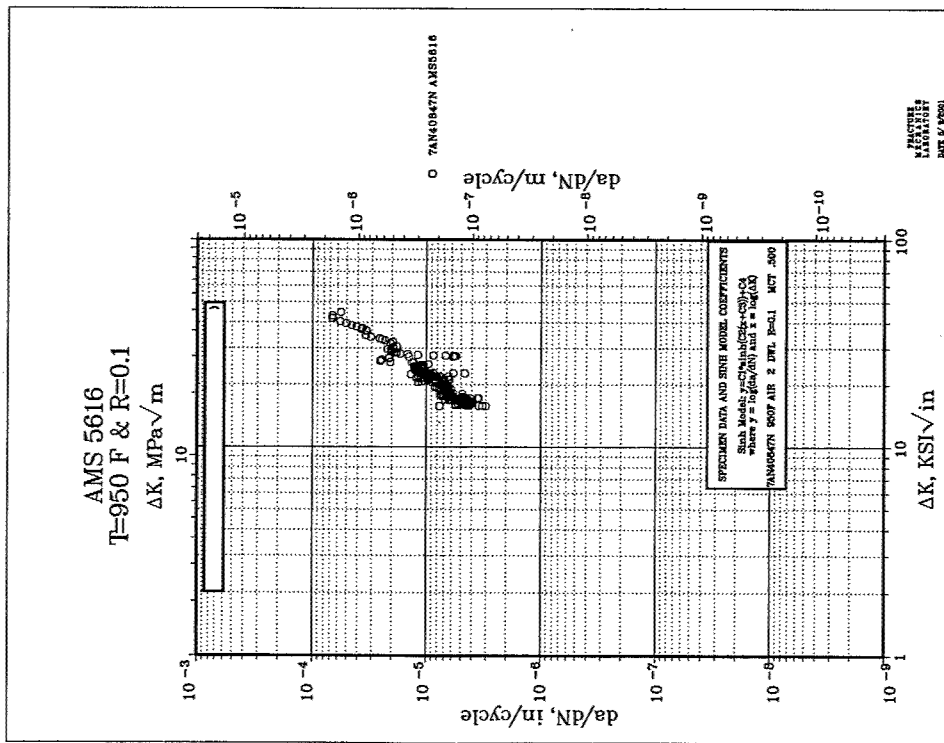


Chart A-32

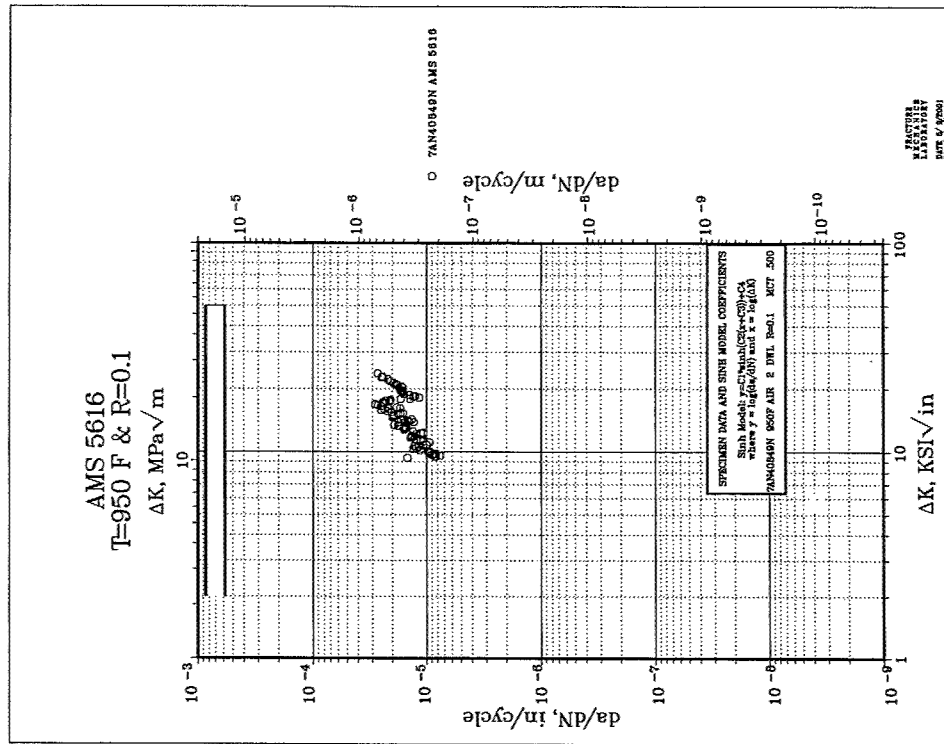


Chart A-33

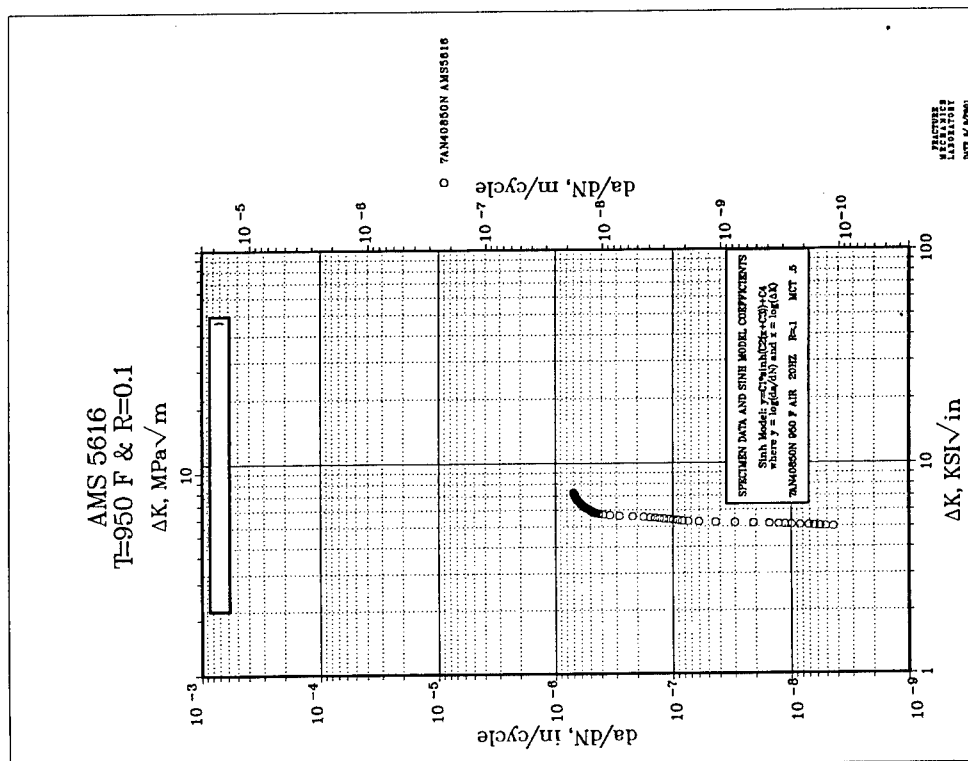


Chart A-34

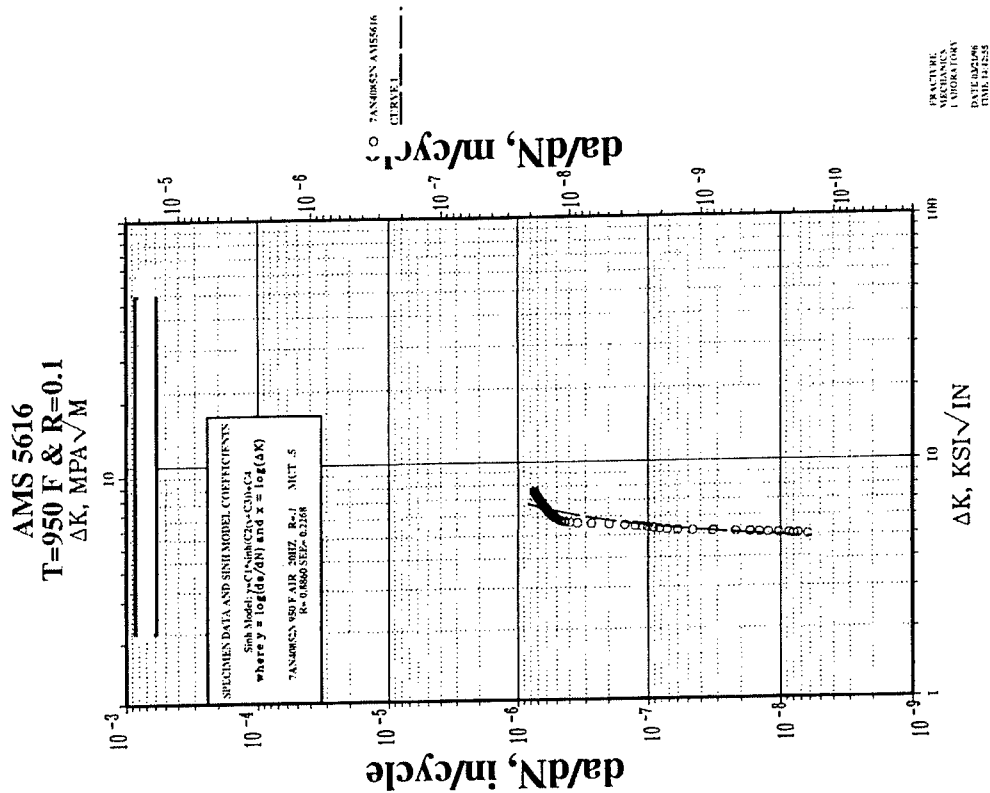
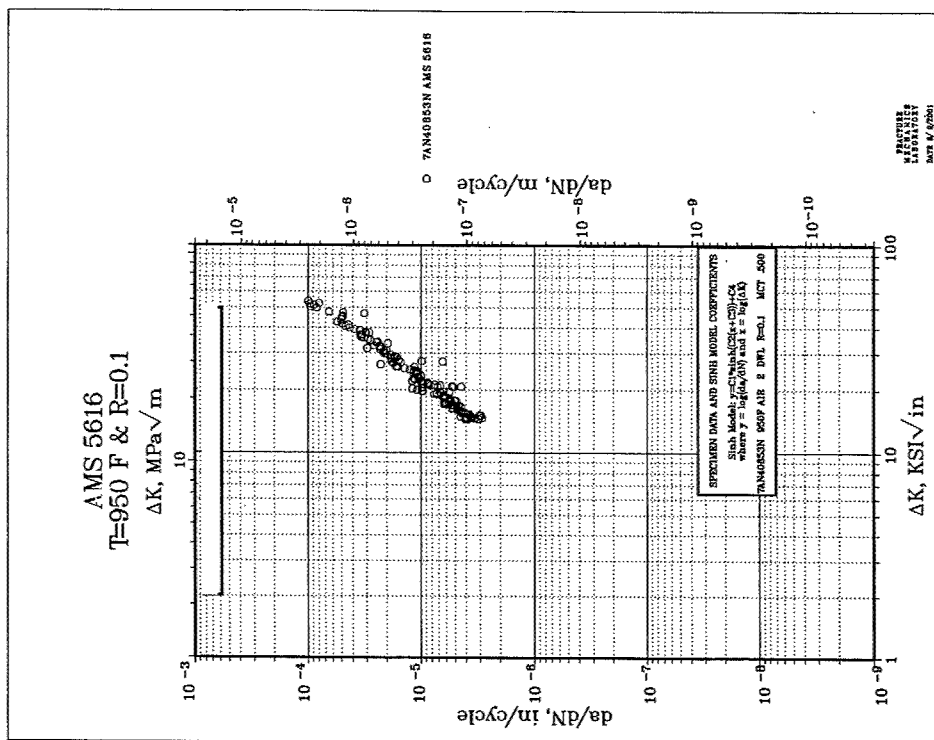
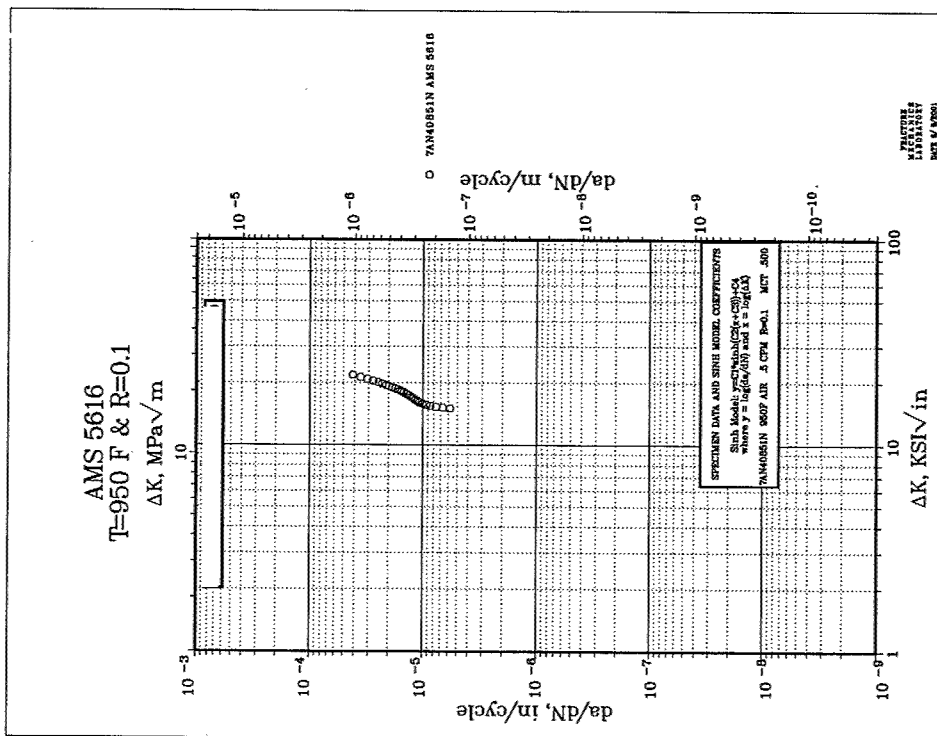


Chart A-35



AMS 5616
T=750 F & R=0.1
 ΔK , MPa \sqrt{M}

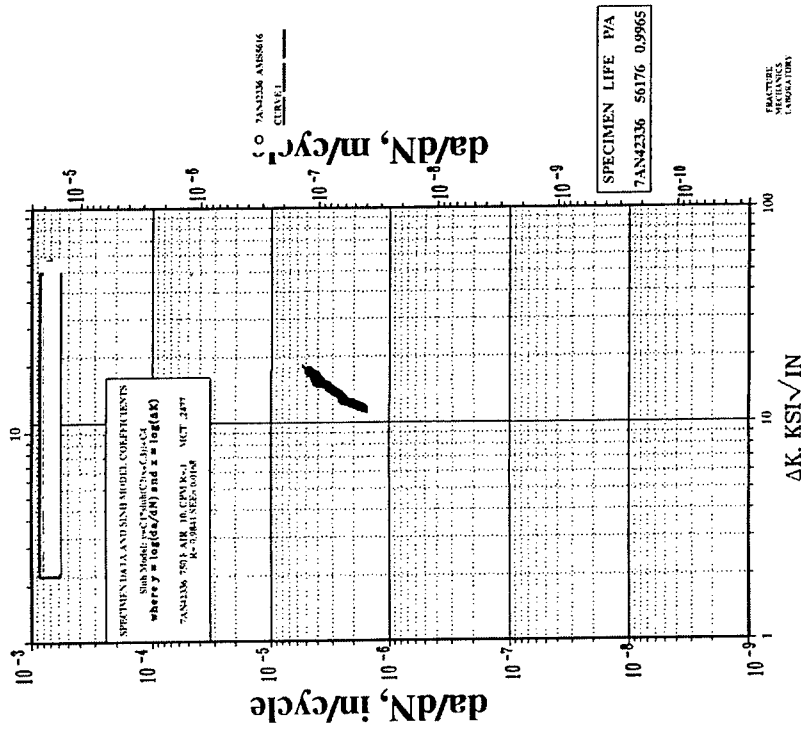


Chart A-38

AMS 5616
T=950 F & R=0.1
 ΔK , MPa \sqrt{m}

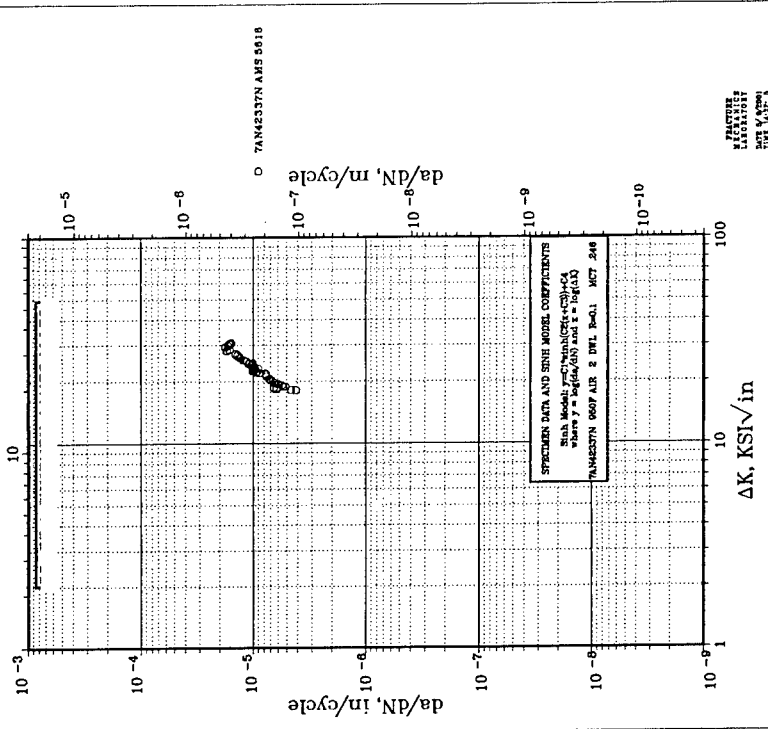


Chart A-39

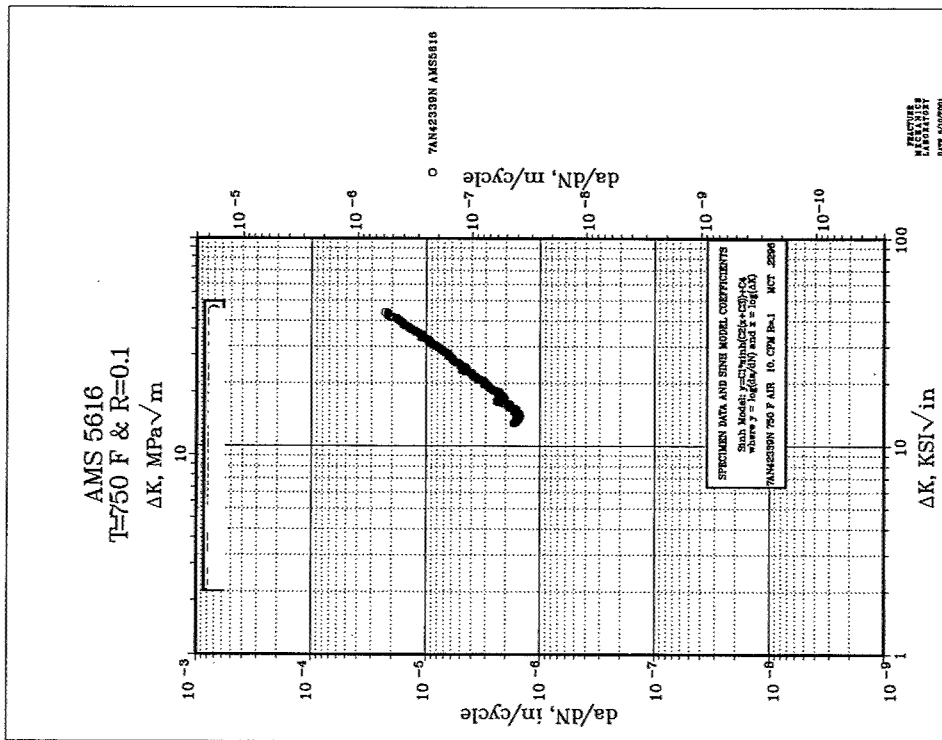


Chart A-40

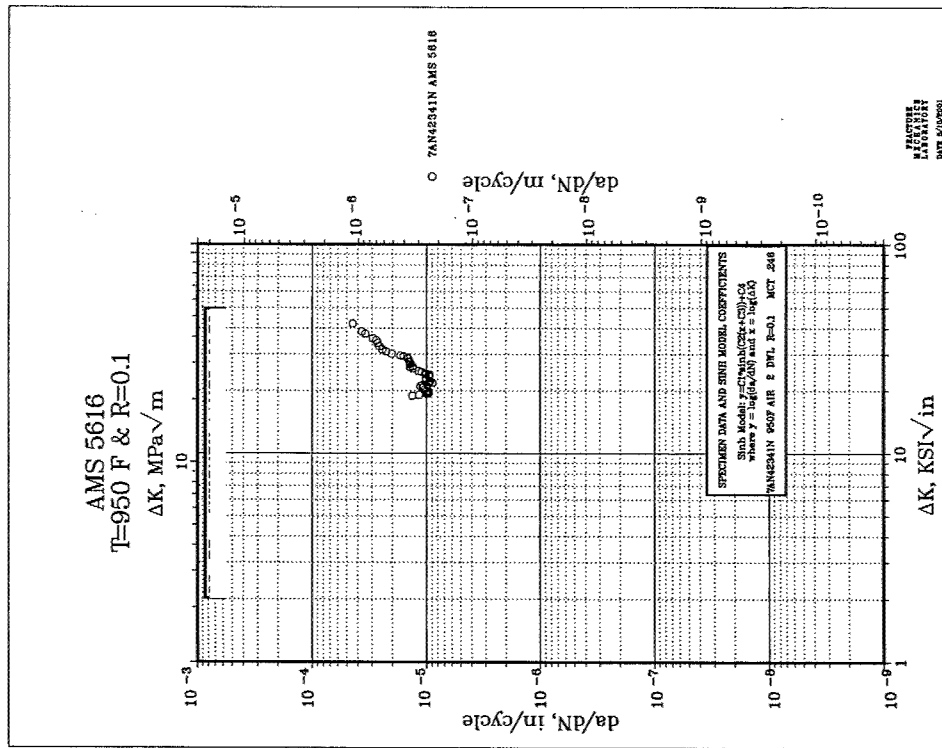


Chart A-41

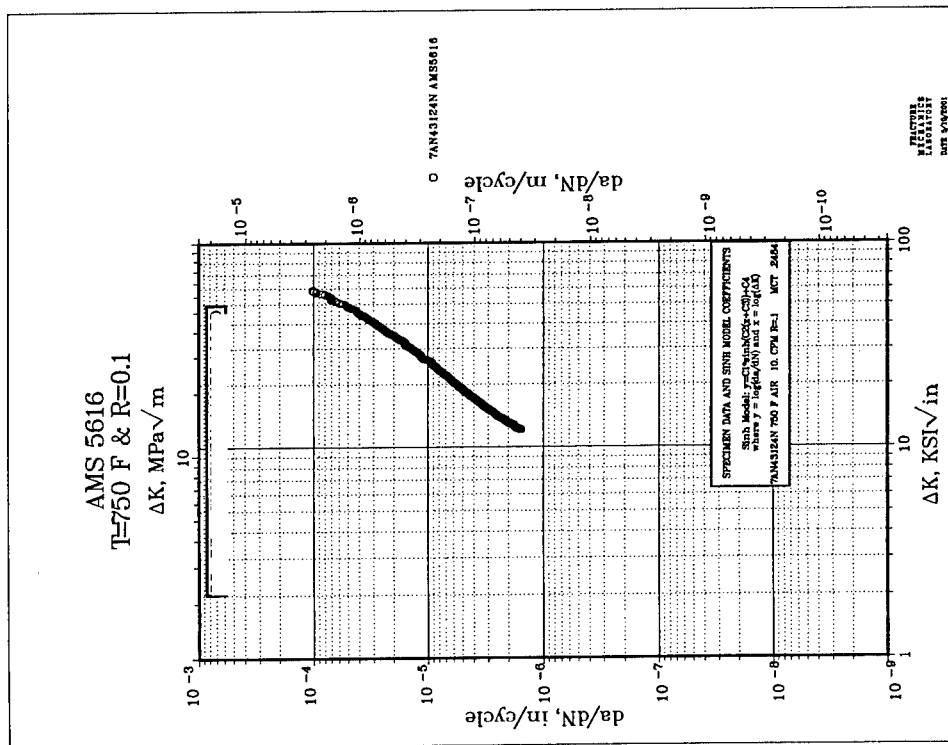


Chart A-42

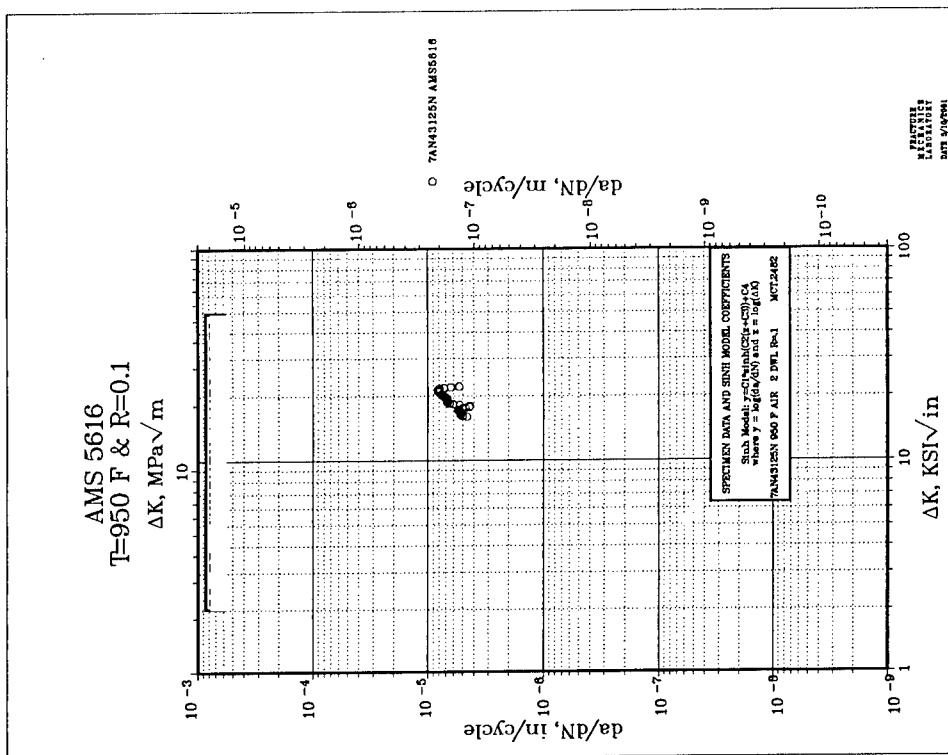


Chart A-43

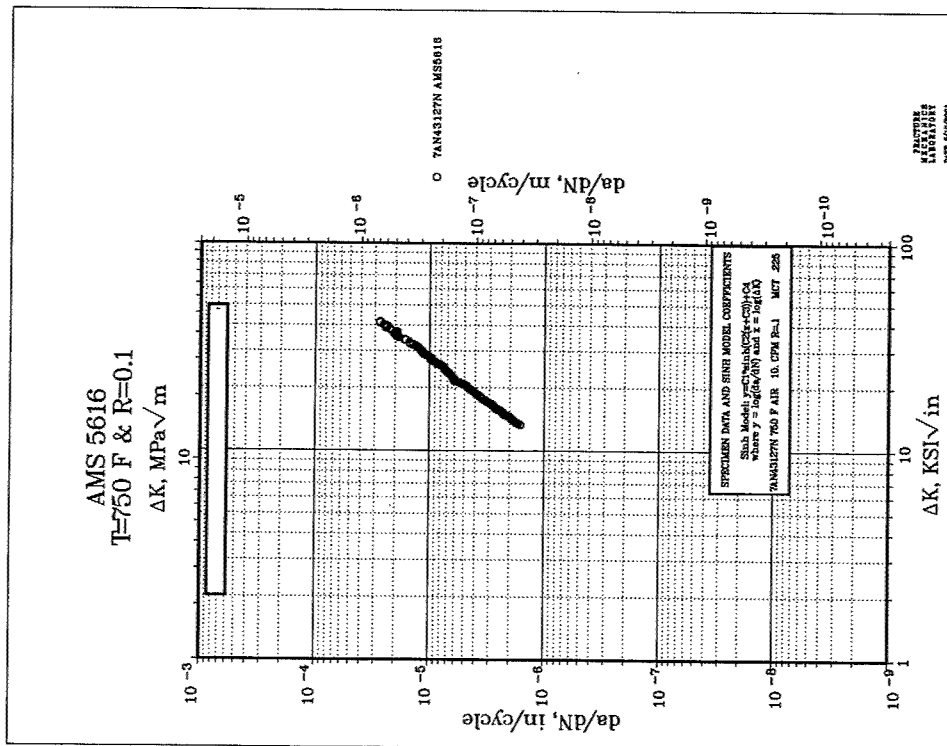


Chart A-44

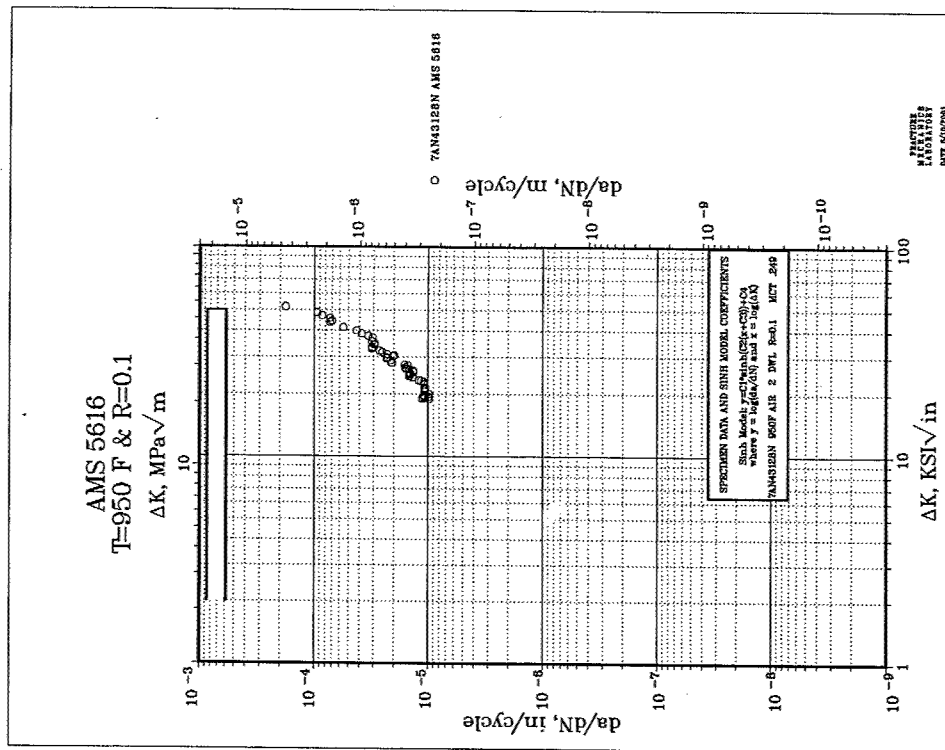


Chart A-45

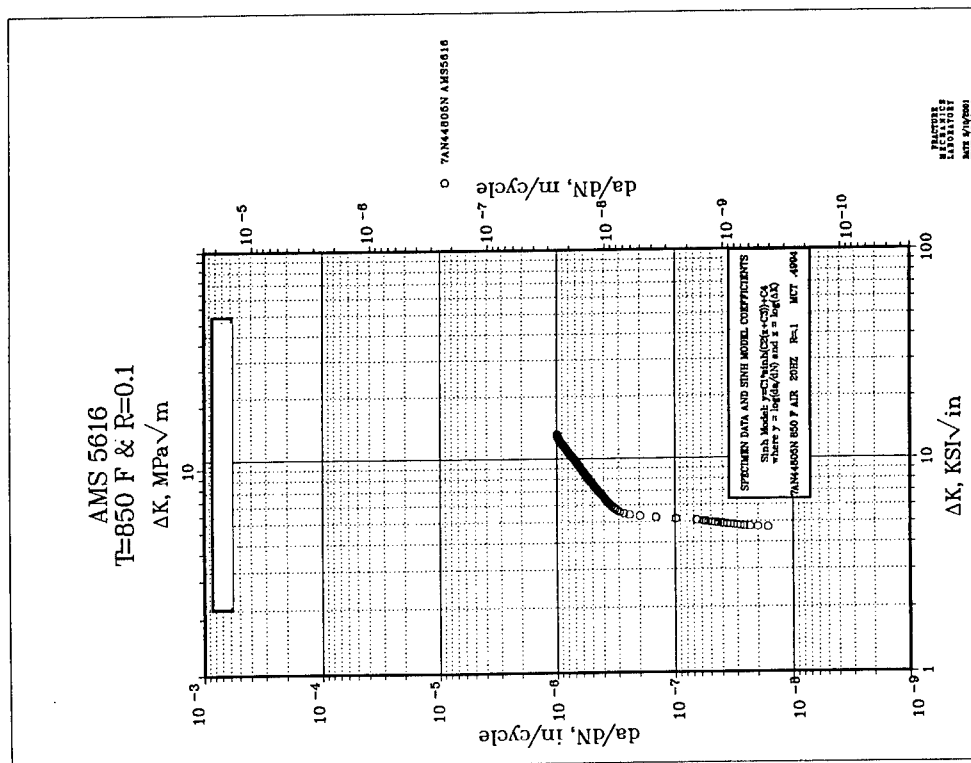


Chart A-46

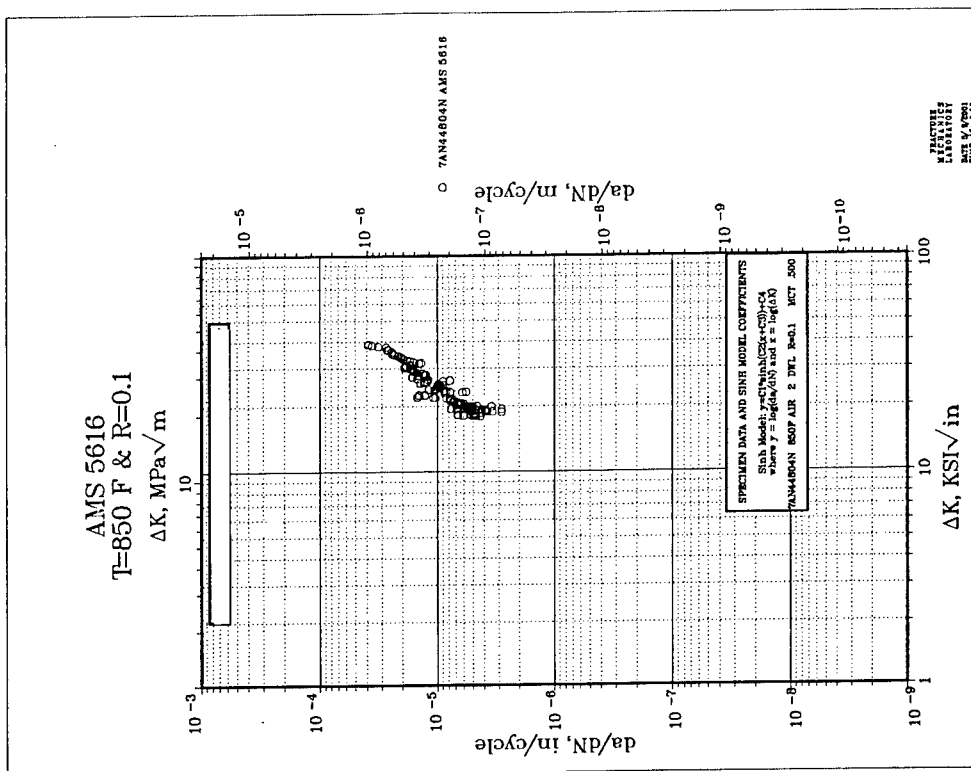


Chart A-47

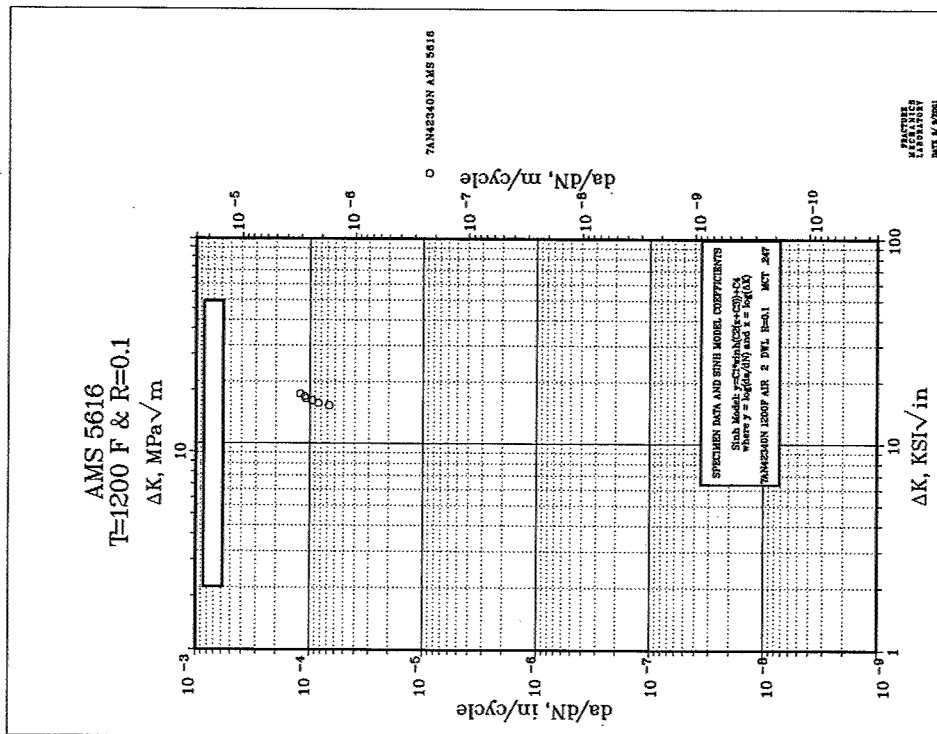


Chart A-48

A.3 AMS 5663 da/dN PLOTS.

Chart No.	Material Source ¹	Condition ²	Specimen Number	Test Temp.(°F)	Cyclic Rate	Comments
A-49	A	A	39810	800	10 cpm	Coarse Grain Baseline
A-50	A	A	41153	1100	10 cpm	Coarse Grain Baseline
A-51	A	A	39809	1100	2 mdw	Coarse Grain Baseline
A-52	A	A	41154	1200	10 cpm	Coarse Grain Baseline
A-53	A	A	41155	1200	2 mdw	Coarse Grain Baseline
A-54	A	A	41156 ³	1250	2 mdw	Coarse Grain Baseline
A-55	B	A	40371	800	10 cpm	Fine Grain Baseline
A-56	B	A	41161	1100	10 cpm	Fine Grain Baseline
A-57	B	A	40372	1100	2 mdw	Fine Grain Baseline
A-58	B	A	41162	1200	10 cpm	Fine Grain Baseline
A-59	B	A	41163	1200	2 mdw	Fine Grain Baseline
A-60	B	A	41164	1250	2 mdw	Fine Grain Baseline
A-61	A	B	40182	800	10 cpm	Effect of 6 Sol. Hours
A-62	A	B	40183	800	10 cpm	Effect of 6 Sol. Hours
A-63	A	B	40186	1100	2 mdw	Effect of 6 Sol. Hours
A-64	A	C	45840	1100	2 mdw	Effect of 30 Sol. Hours
A-65	B	C	45843	1100	2 mdw	Effect of 30 Sol. Hours
A-66	A	D	40184	800	10 cpm	Effect of 6 Short Ages
A-67	A	D	40185	800	10 cpm	Effect of 6 Short Ages
A-68	A	D	40188	1100	2 mdw	Effect of 6 Short Ages
A-69	A	D	40189	1100	2 mdw	Effect of 6 Short Ages
A-70	A	E	41755 ⁵	1000	2 mdw	Effect of long exposure
A-71	A	E	41754	1100	2 mdw	Effect of long exposure
A-72	B	F	42334	800	10 cpm	Weld FZ Baseline
A-73	B	F	42335	1100	2 mdw	Weld FZ Baseline
A-74	B	F	42549	800	10 cpm	Weld HAZ Baseline
A-75	B	F	42550 ⁶	1100	2 mdw	Weld HAZ Baseline
A-76	B	G	42812	800	10 cpm	Effect of 30 Sol. Hours on FZ
A-77	B	G	42814	1100	2 mdw	Effect of 30 Sol. Hours on FZ
A-78	B	G	42815	1100	2 mdw	Effect of 30 Sol. Hours on FZ
A-79	B	G	42816	800	10 cpm	Effect of 30 Sol. Hours on HAZ
A-80	B	G	42818	1100	2 mdw	Effect of 30 Sol. Hours on HAZ
A-81	B	G	42819	1100	2 mdw	Effect of 30 Sol. Hours on HAZ

- Notes: 1. A: PW4000 HPT Case Heat CKLB CD B: Barstock: PHDMG
2. A FHT: Solution + Age B: FHT + 6 X (1 Hr. Sol. + Age)
C: FHT + 6 X (5 hrs. Sol. + Age) D: FHT + 6 X Short Age Cycle
E: FHT + 1100F (1,000 hrs.) F: Sol. + Weld + FHT
G: Sol. + Weld + FHT + 6X(5 hrs. Sol. + Age)
3. Test rig problem; No data generated.
4. Invalid test progression; Data not usable.
5. Electronic data file lost.
6. Crack initiated in HAZ; progressed primarily in FZ.

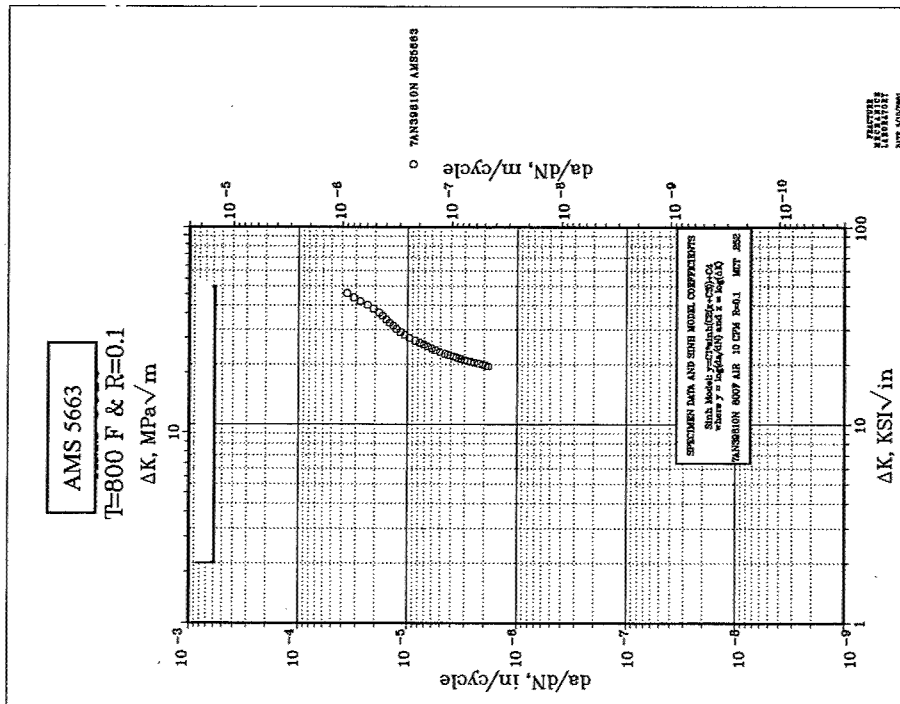


Chart A-49

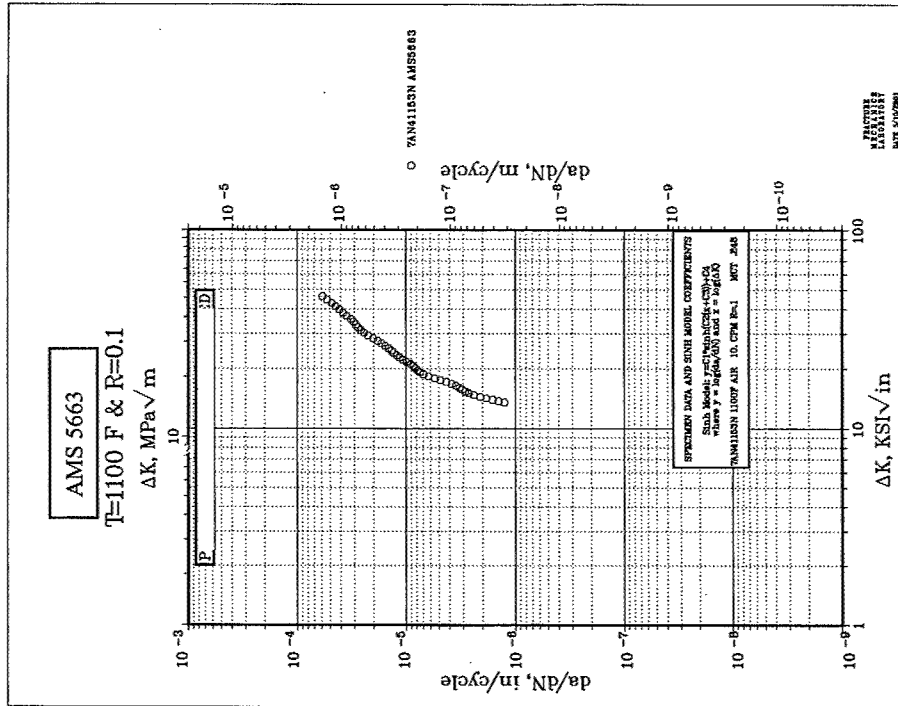


Chart A-50

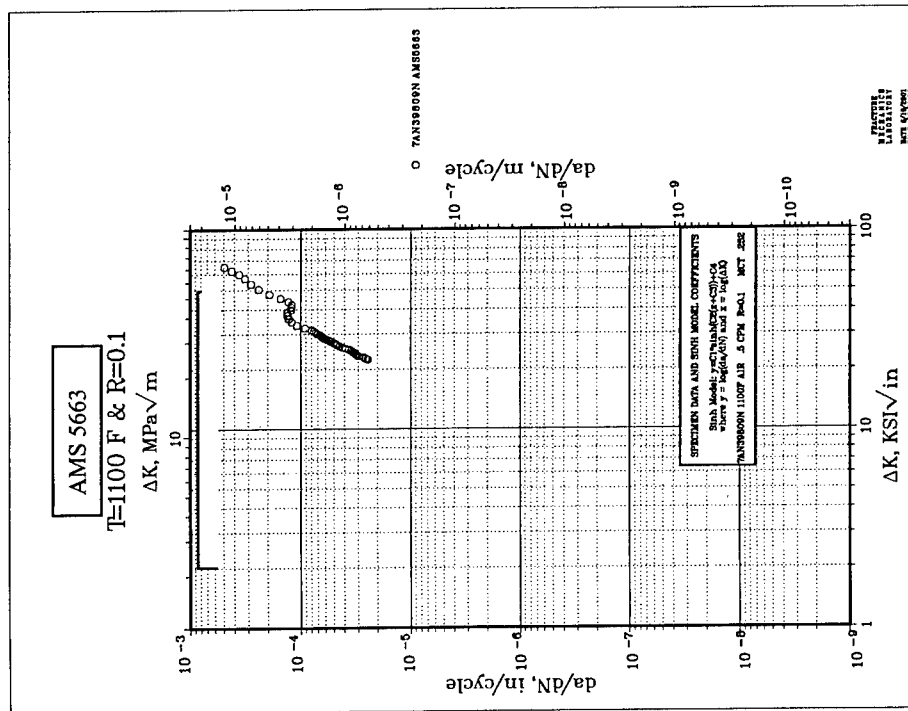


Chart A-51

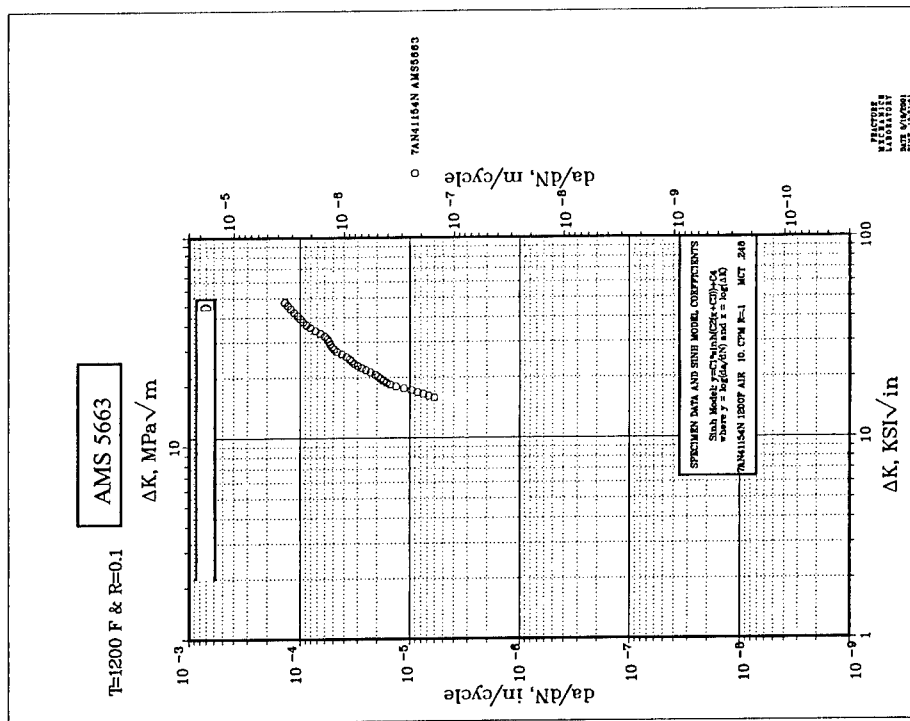


Chart A-52

AMS 5663
T=1200 F & R=0.1
 ΔK , MPa \sqrt{m}

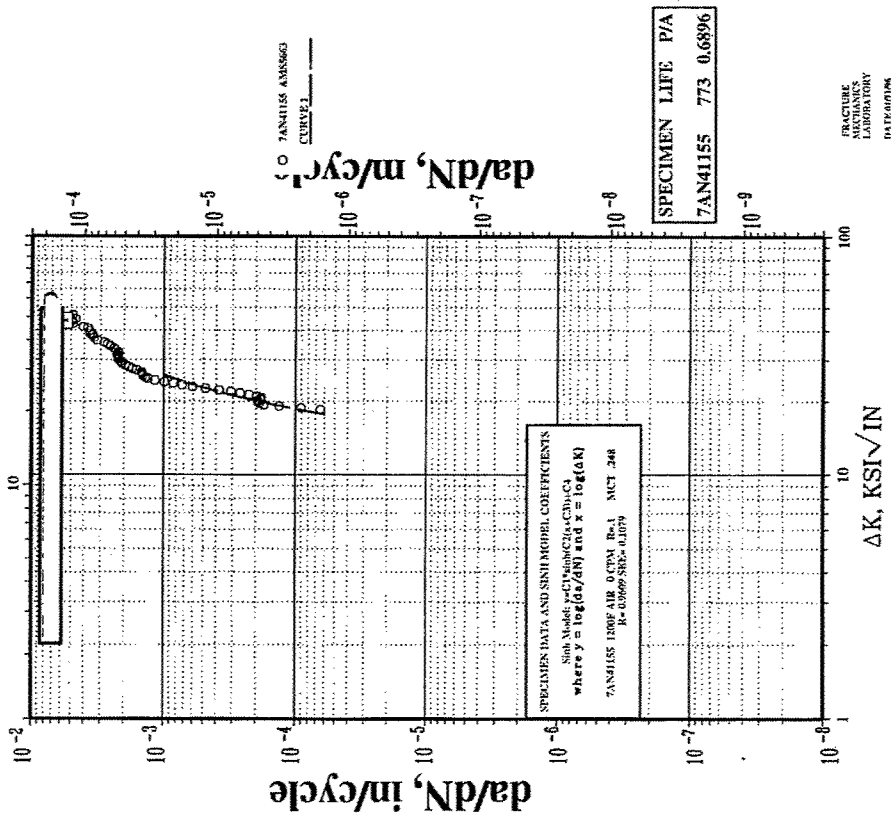


Chart A-53

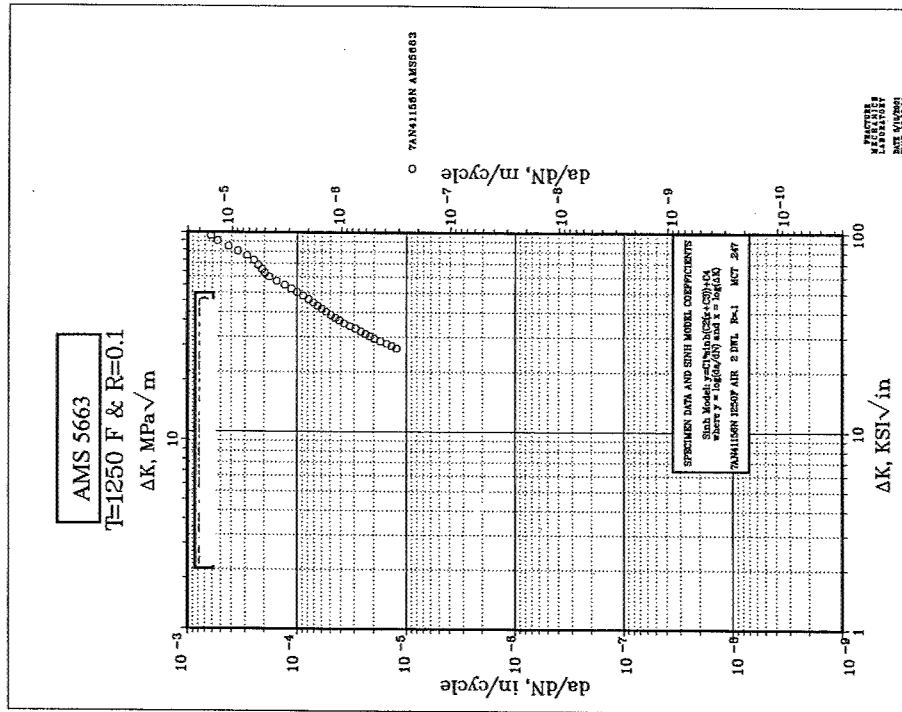


Chart A-54

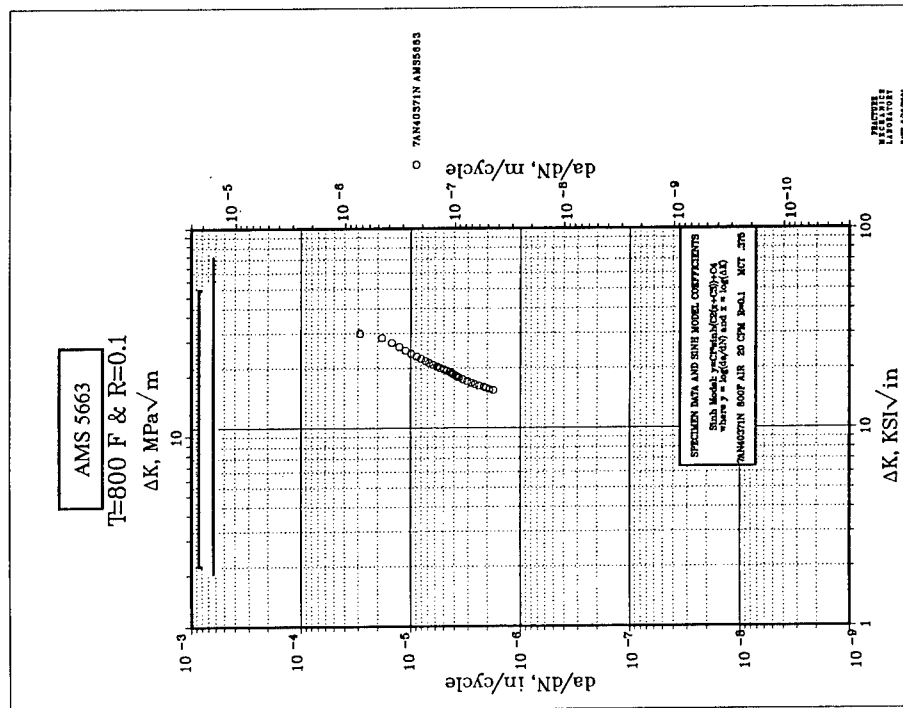


Chart A-55

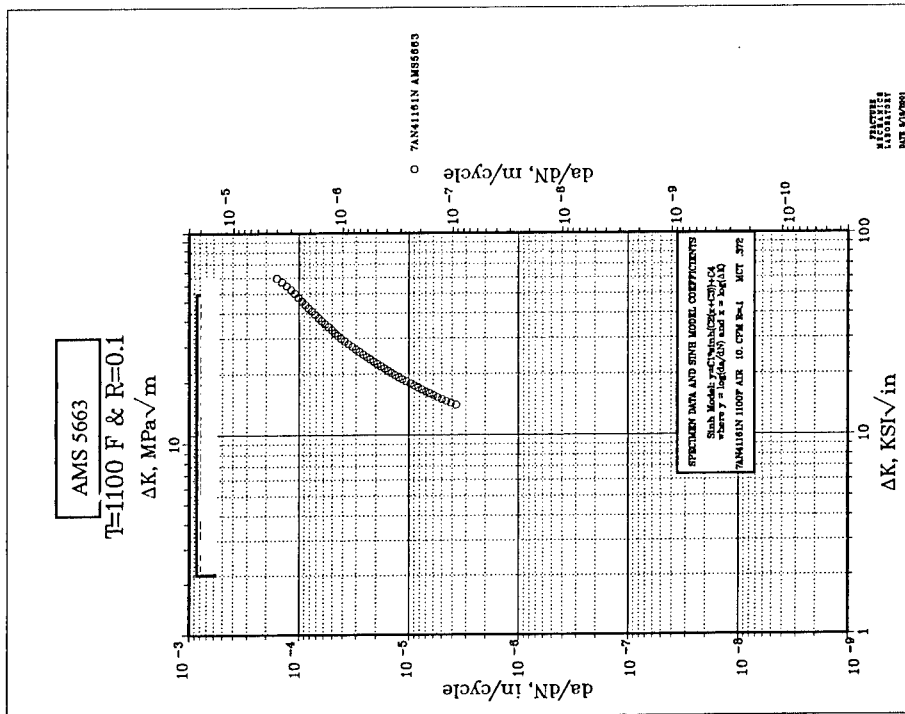


Chart A-56

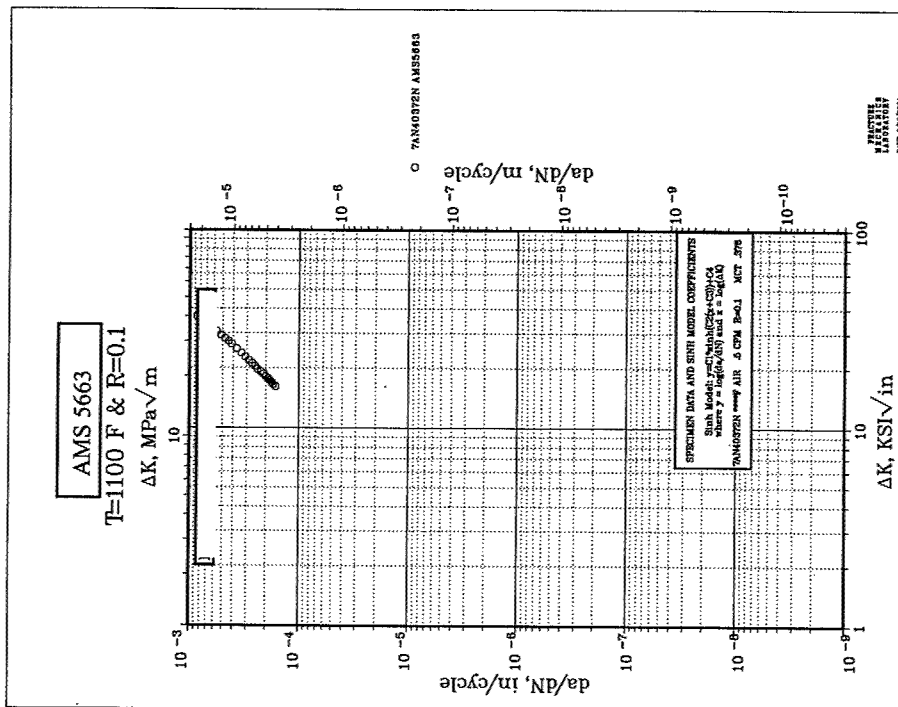


Chart A-57

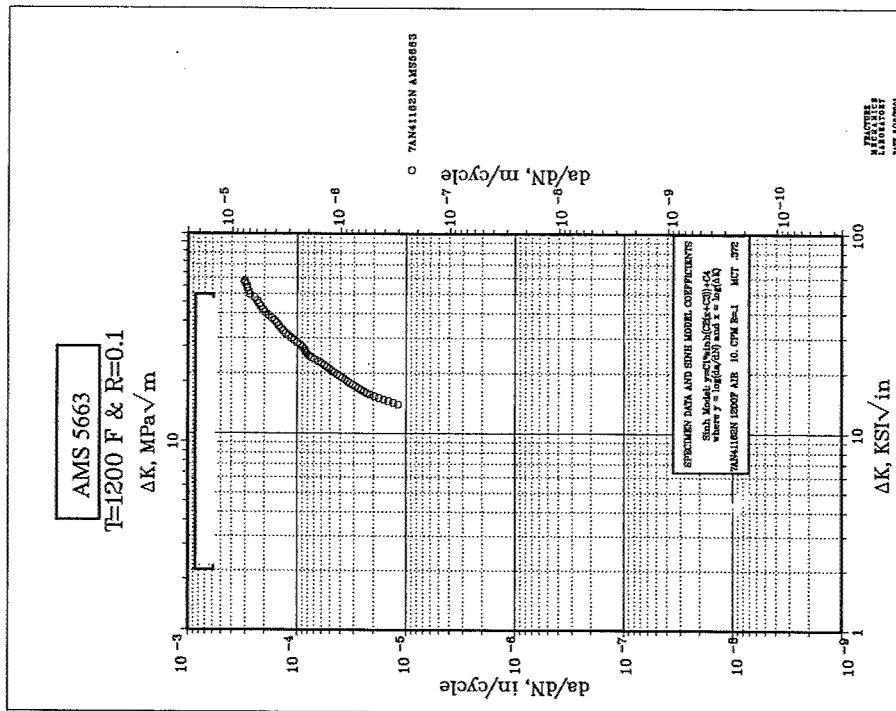


Chart A-58

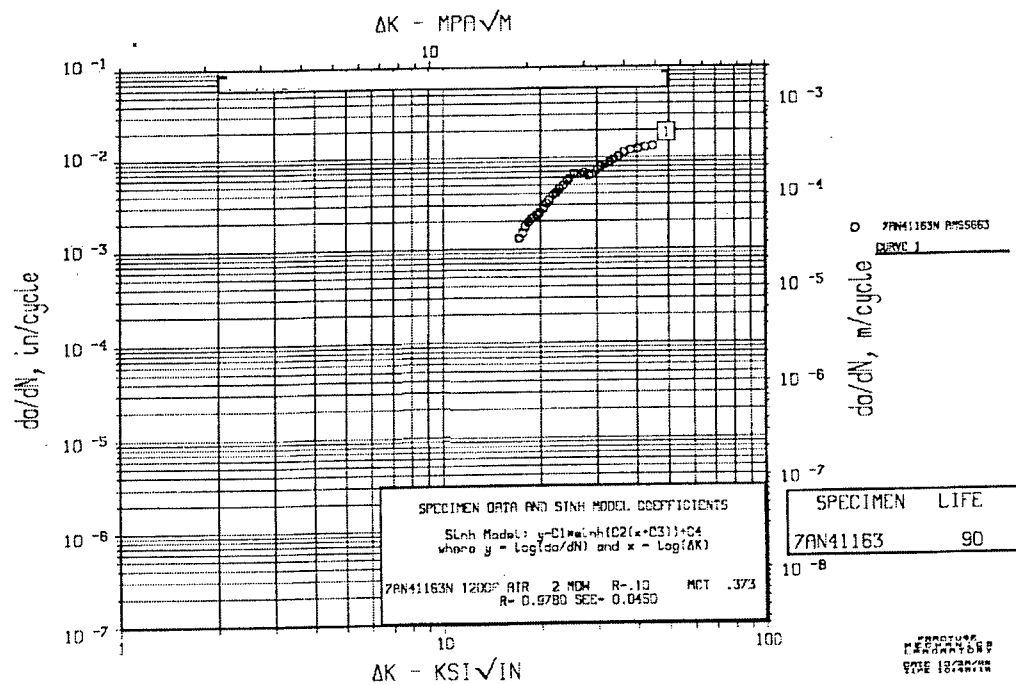


Chart A-59

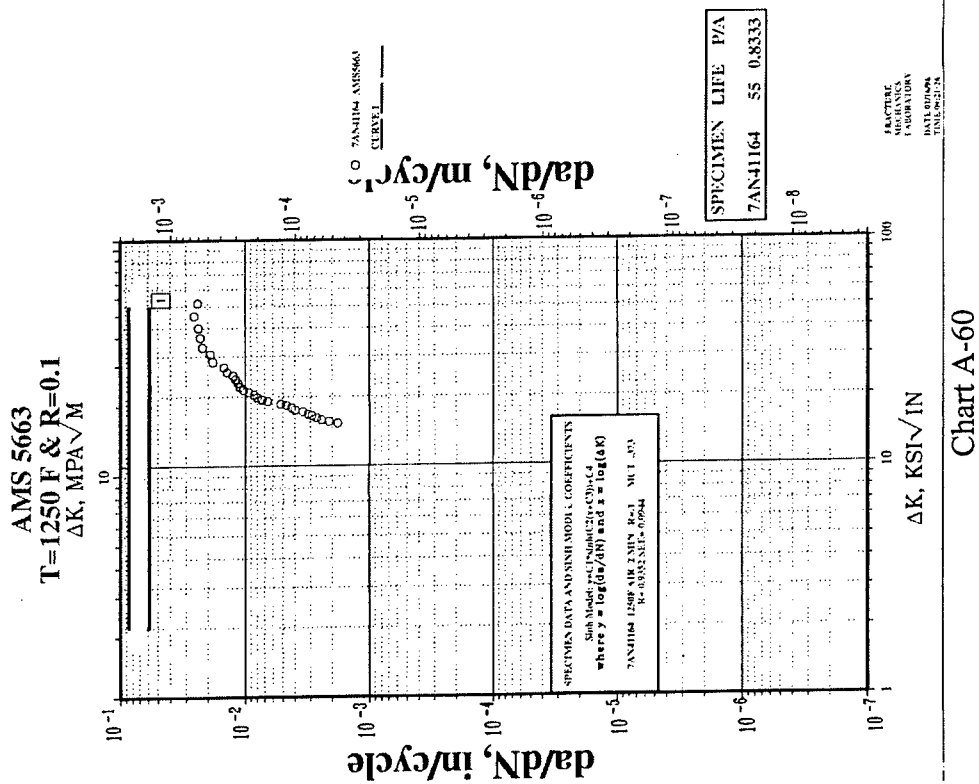


Chart A-60

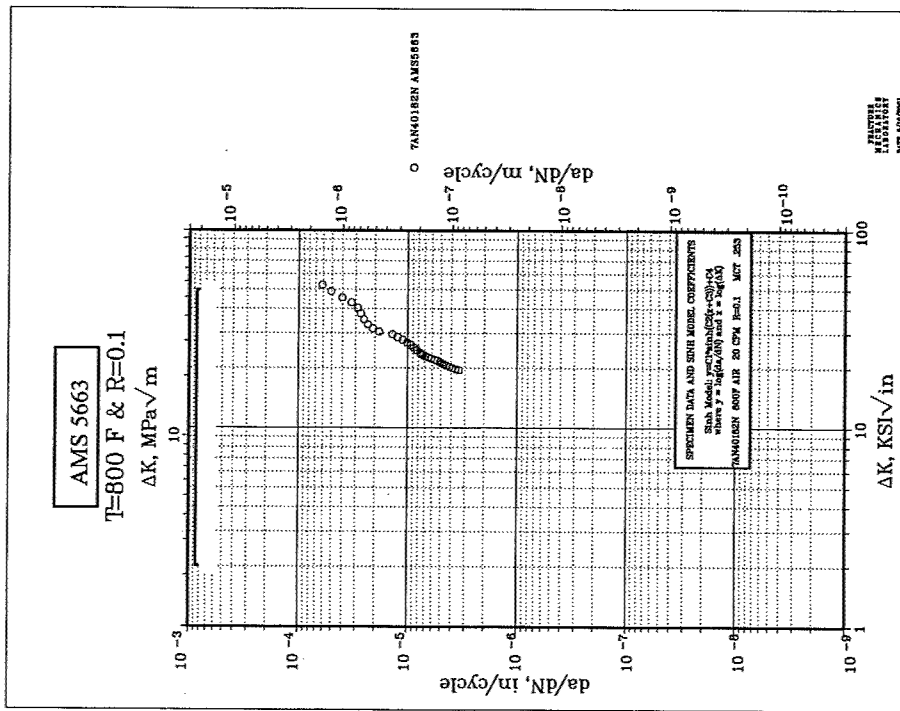


Chart A-61

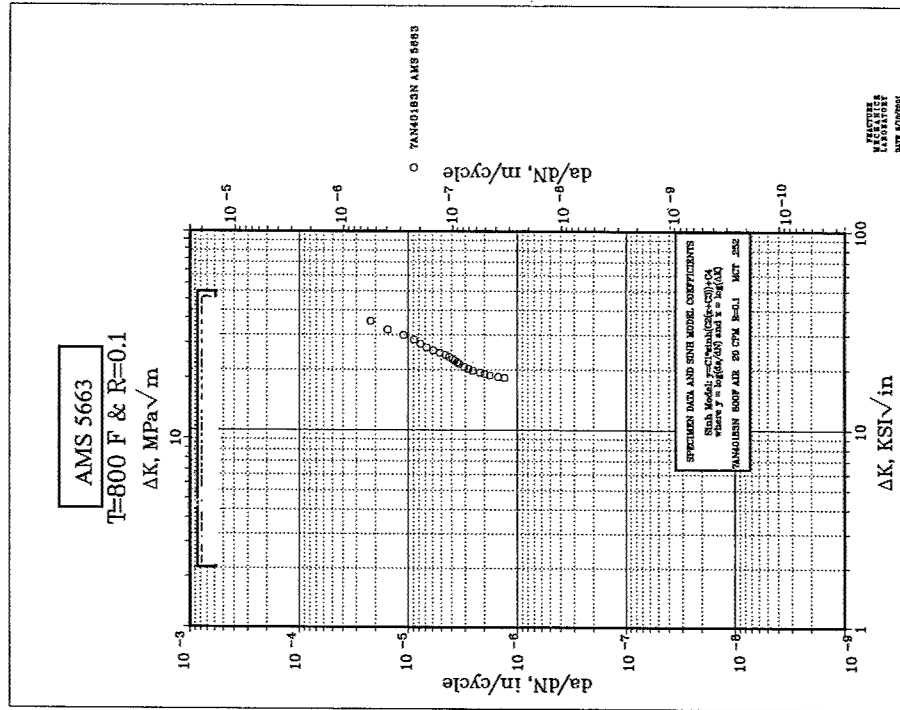
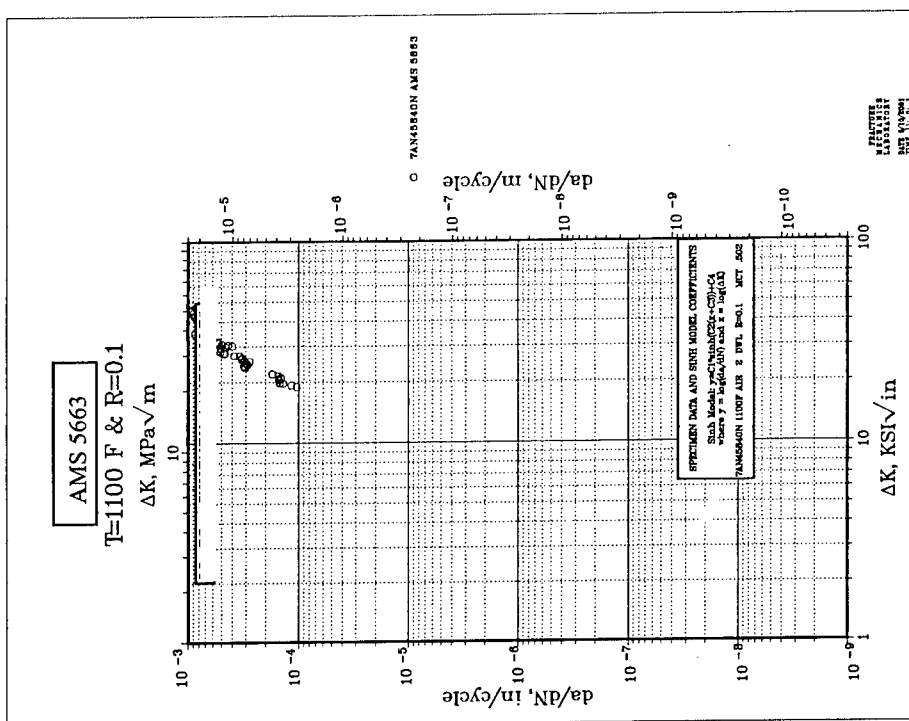
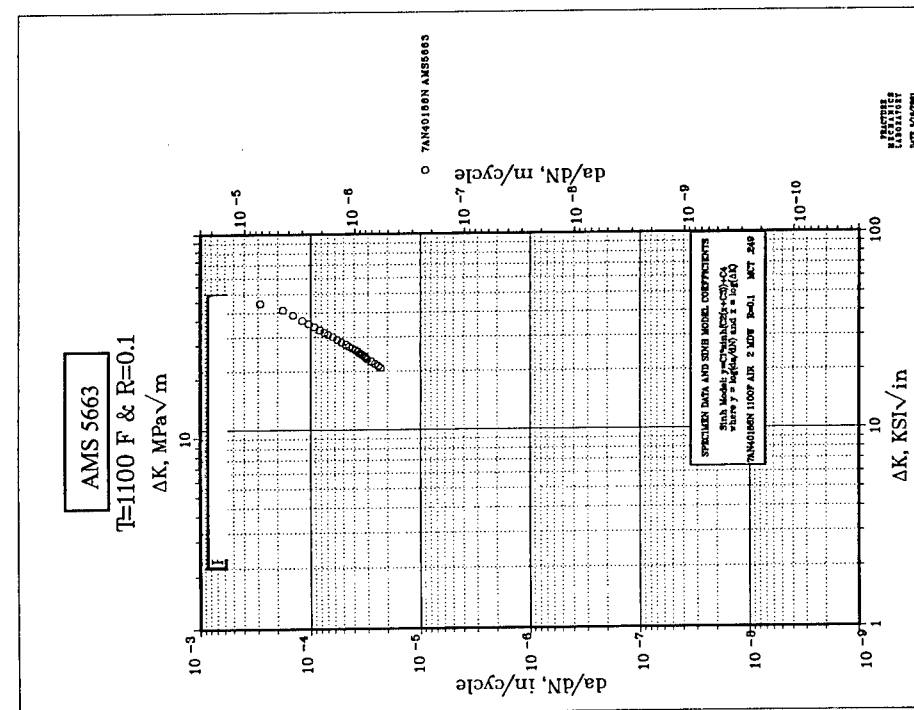


Chart A-62



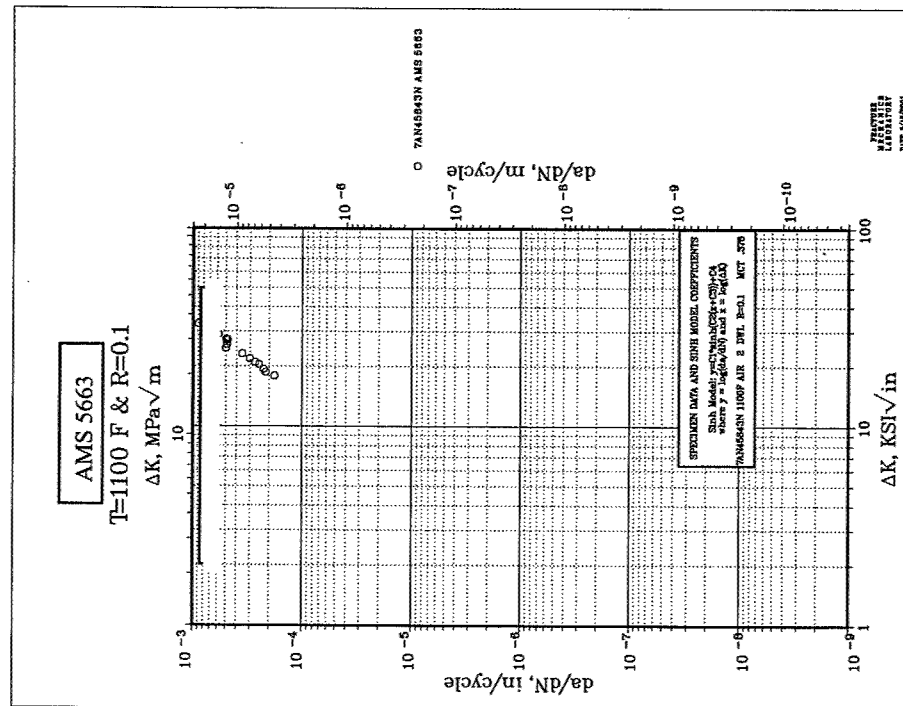


Chart A-65

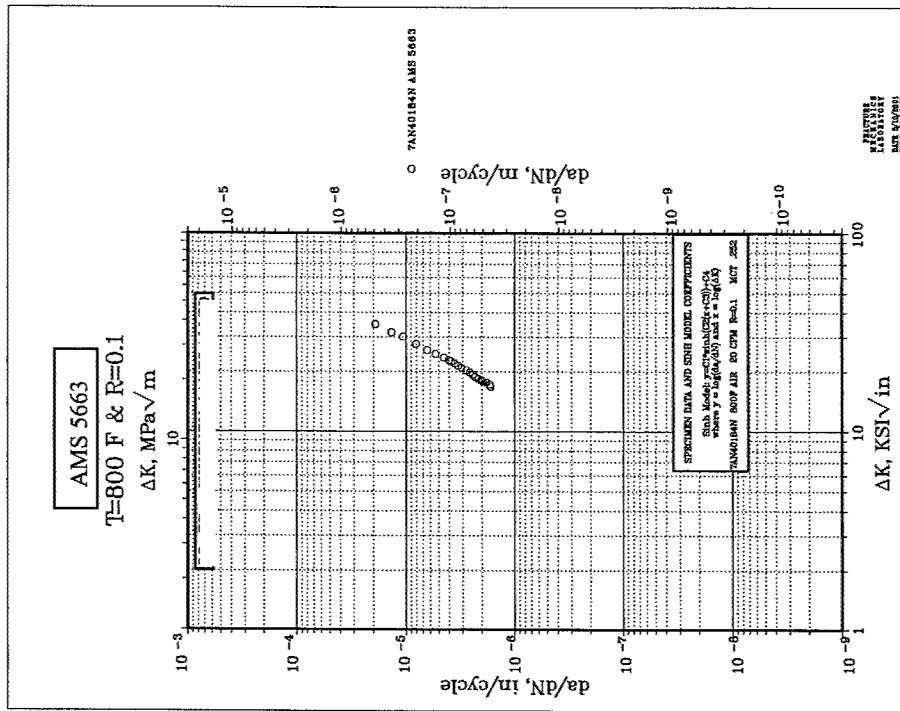


Chart A-66

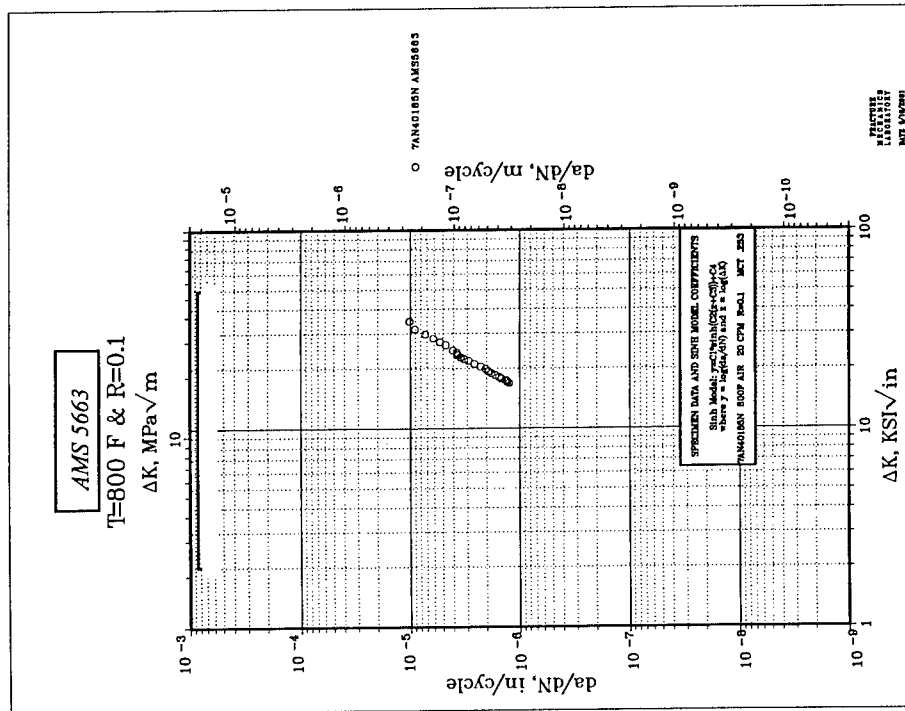


Chart A-67

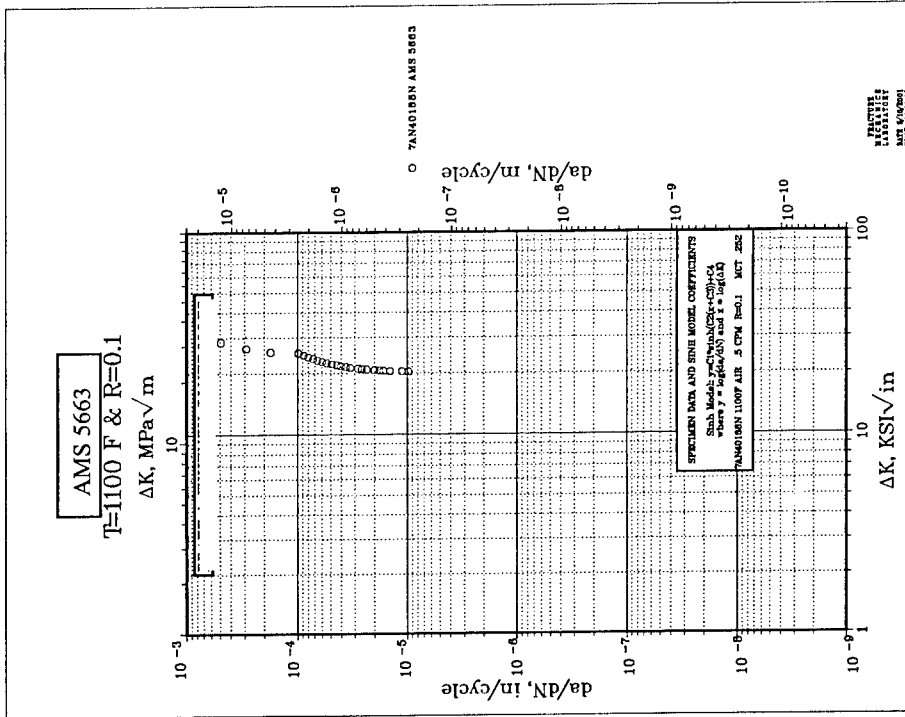


Chart A-68

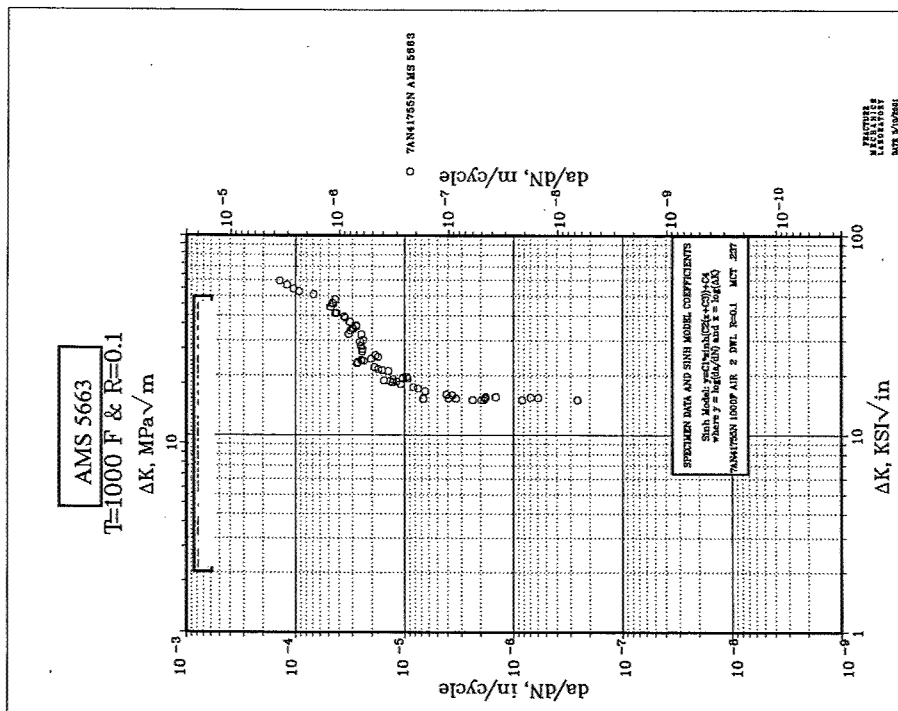


Chart A-70

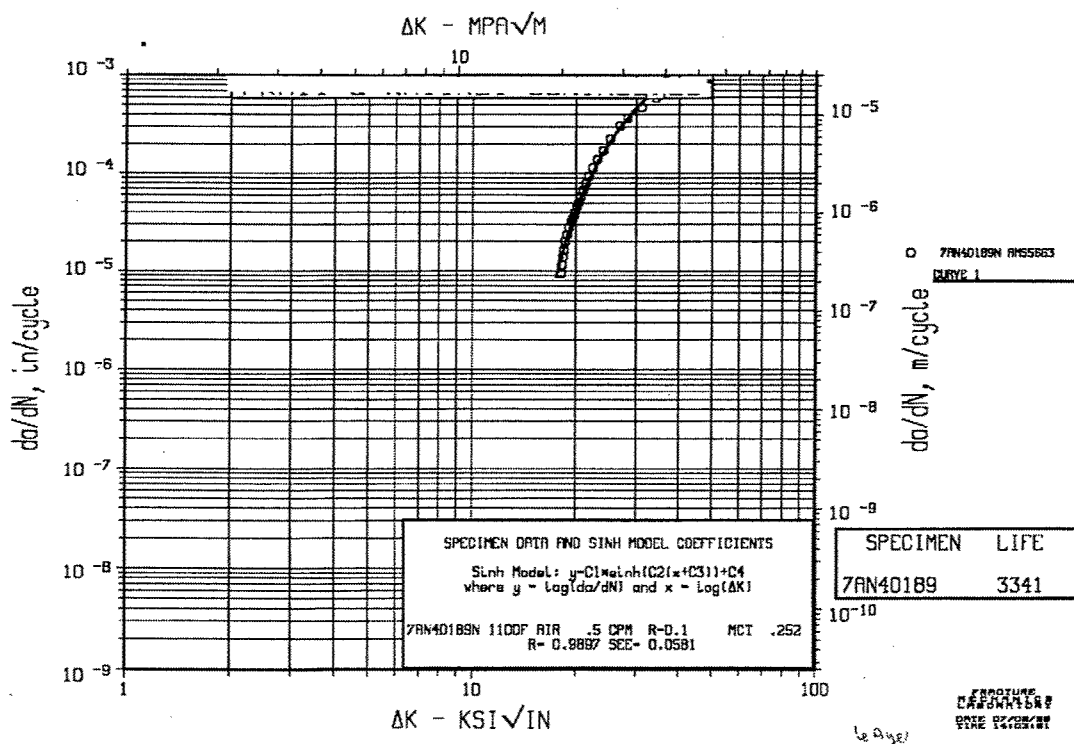


Chart A-69

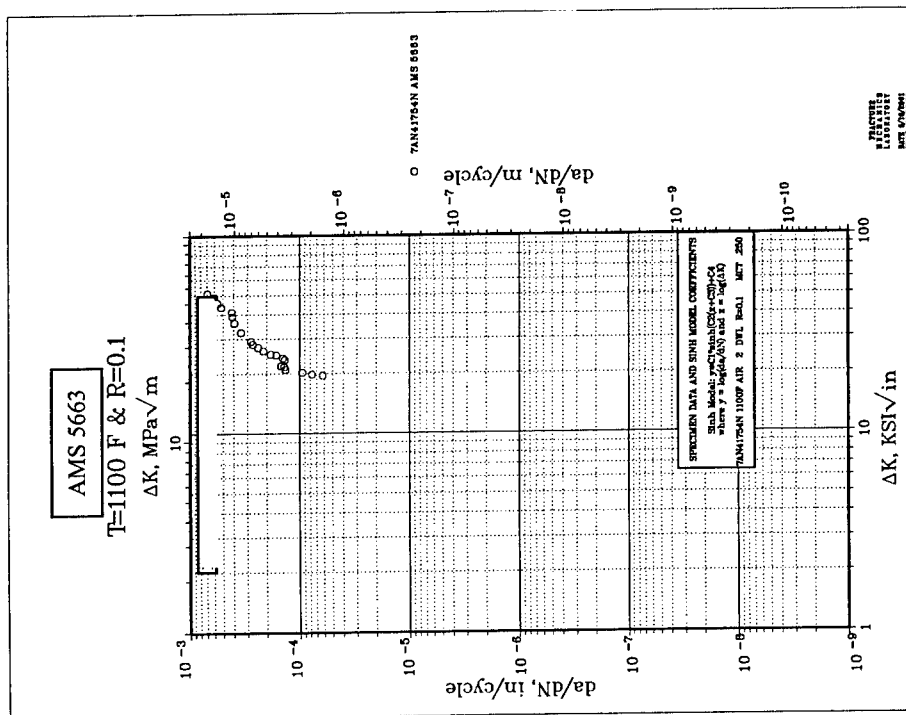


Chart A-71

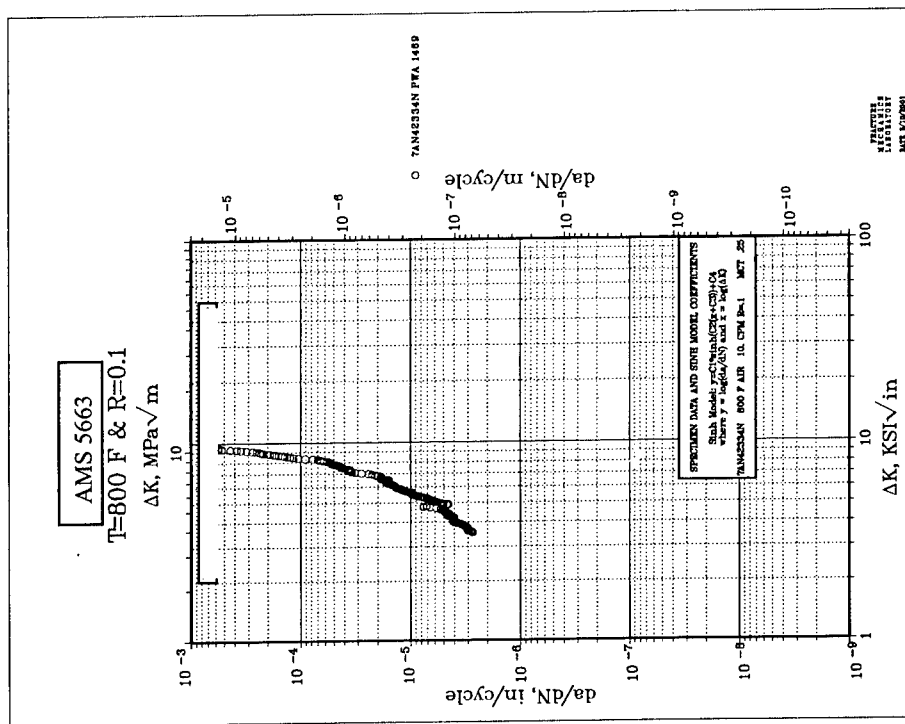


Chart A-72

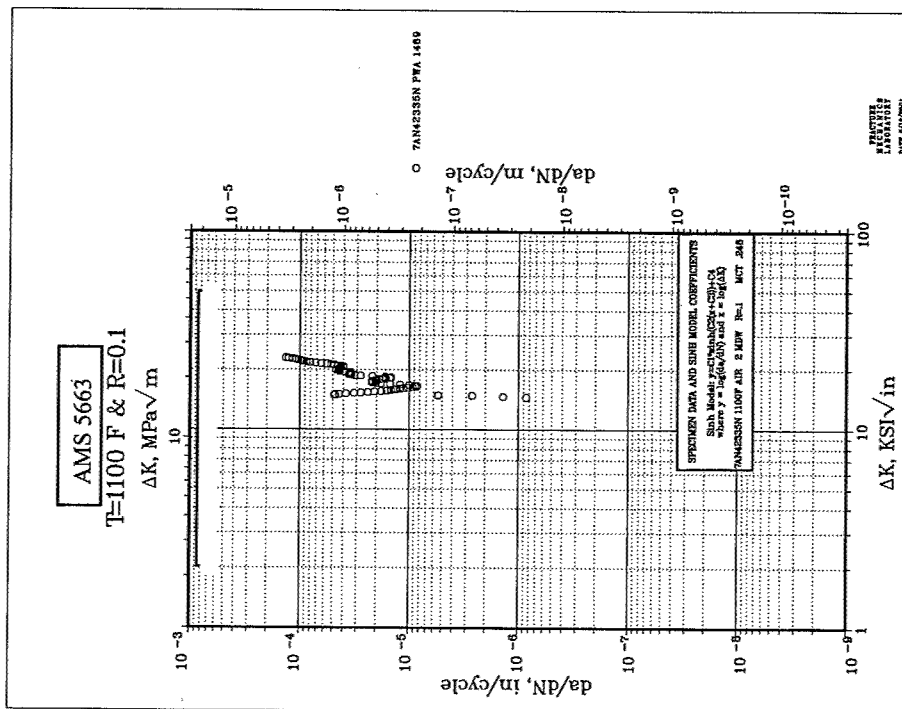


Chart A-73

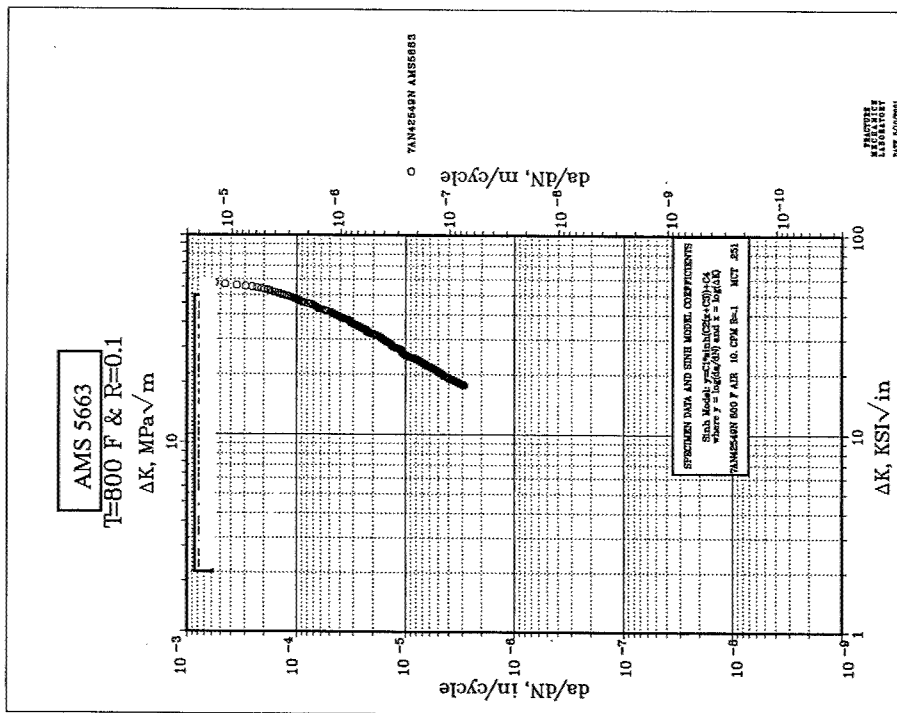
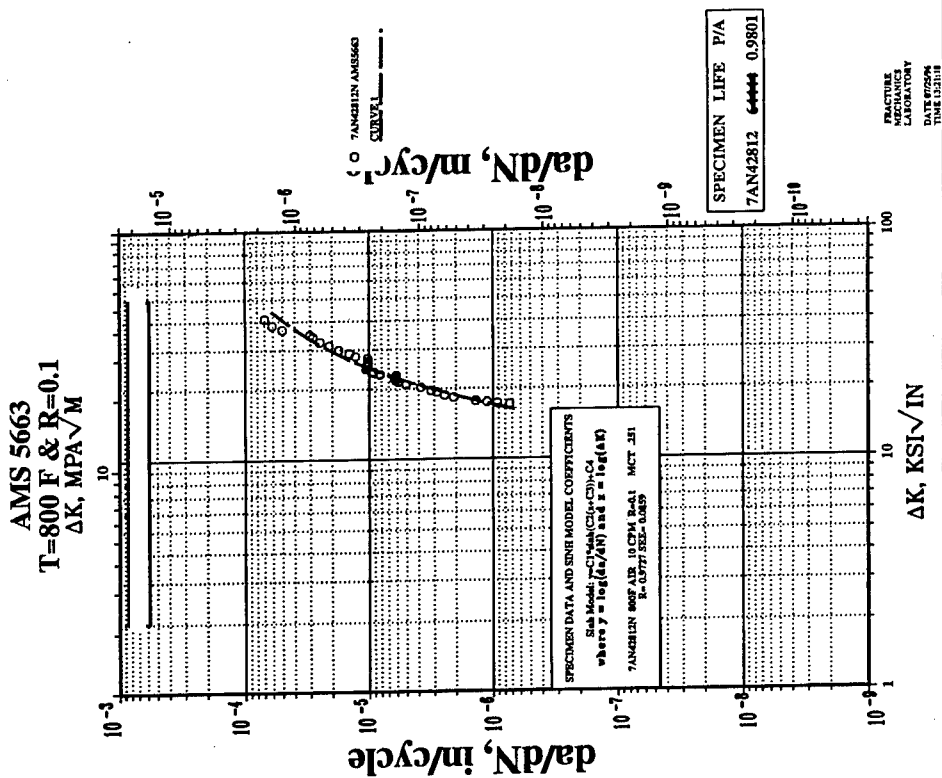
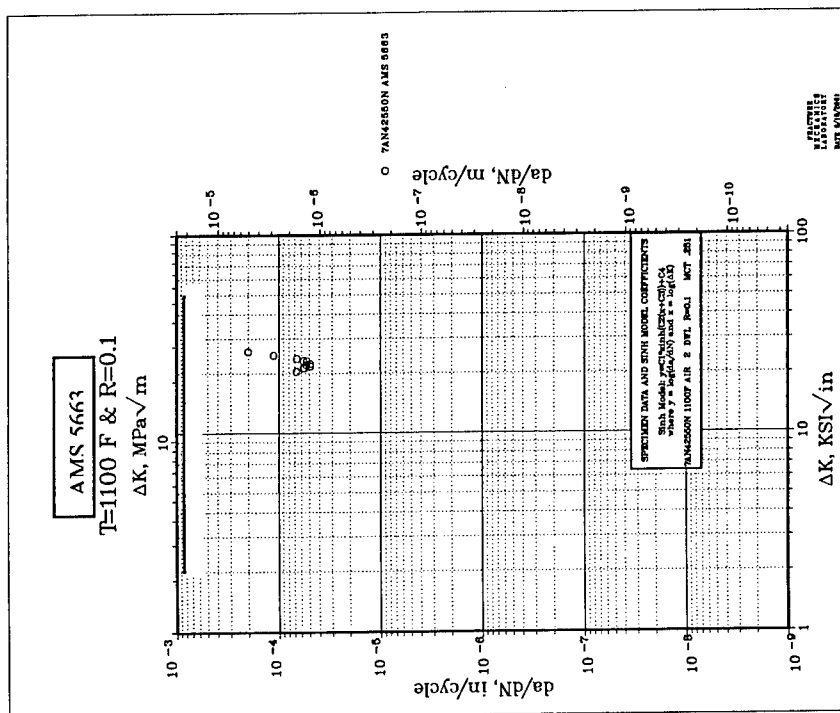


Chart A-74



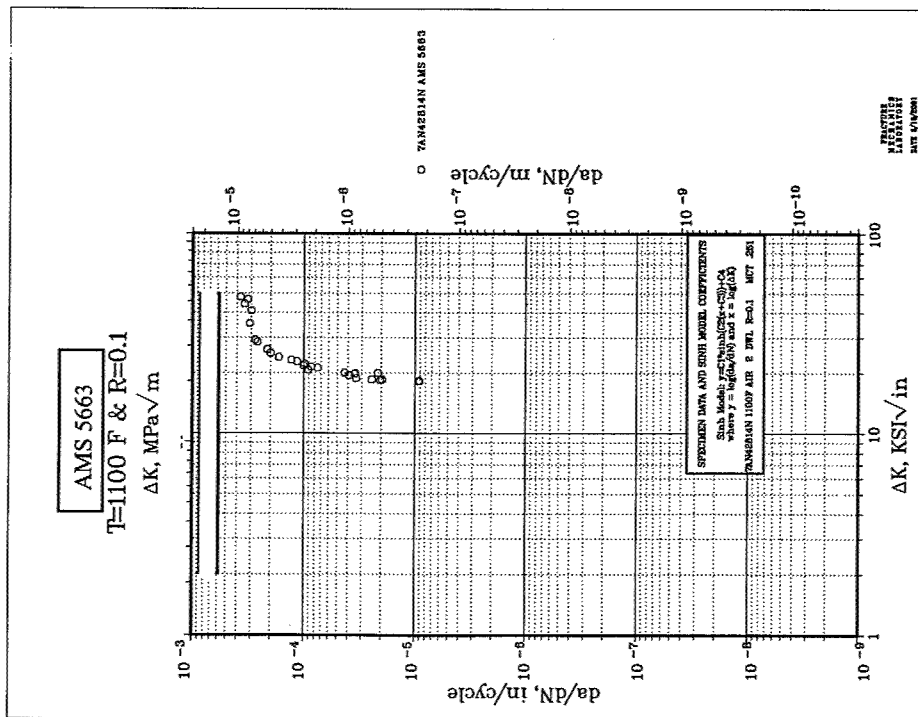


Chart A-77

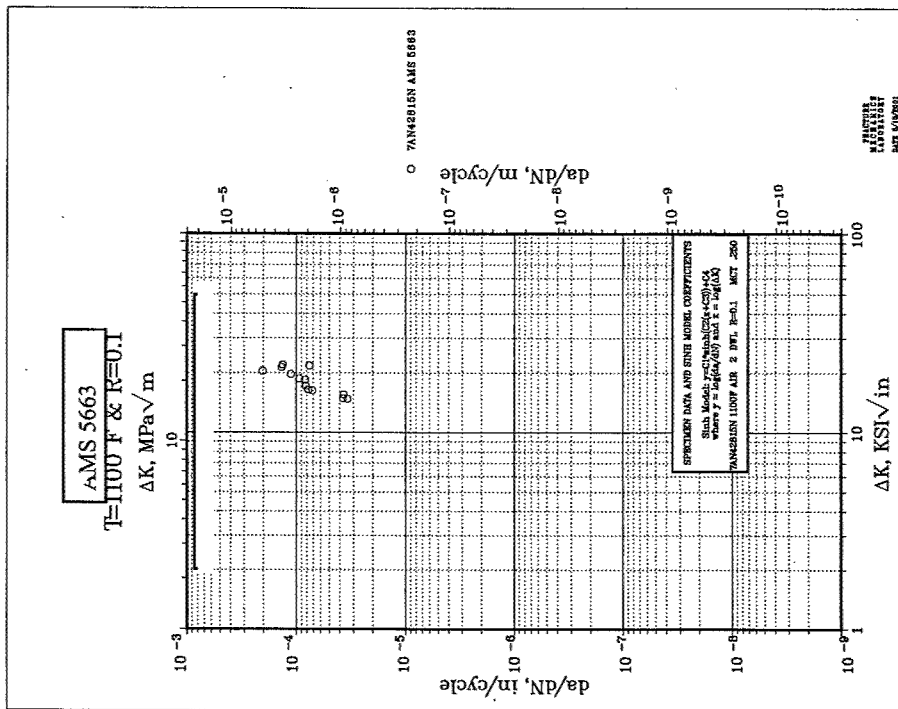


Chart A-78

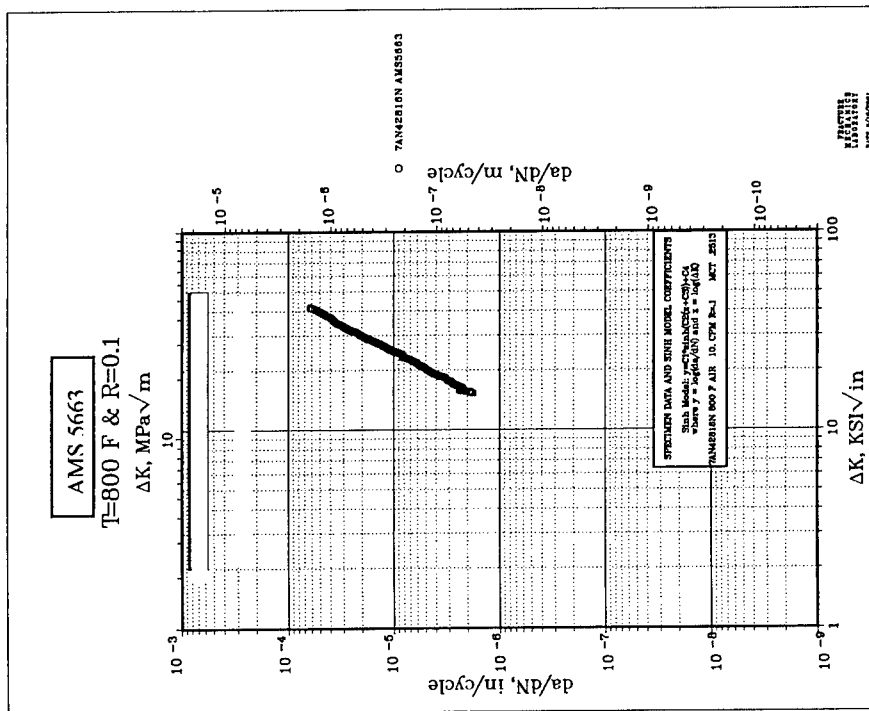


Chart A-79

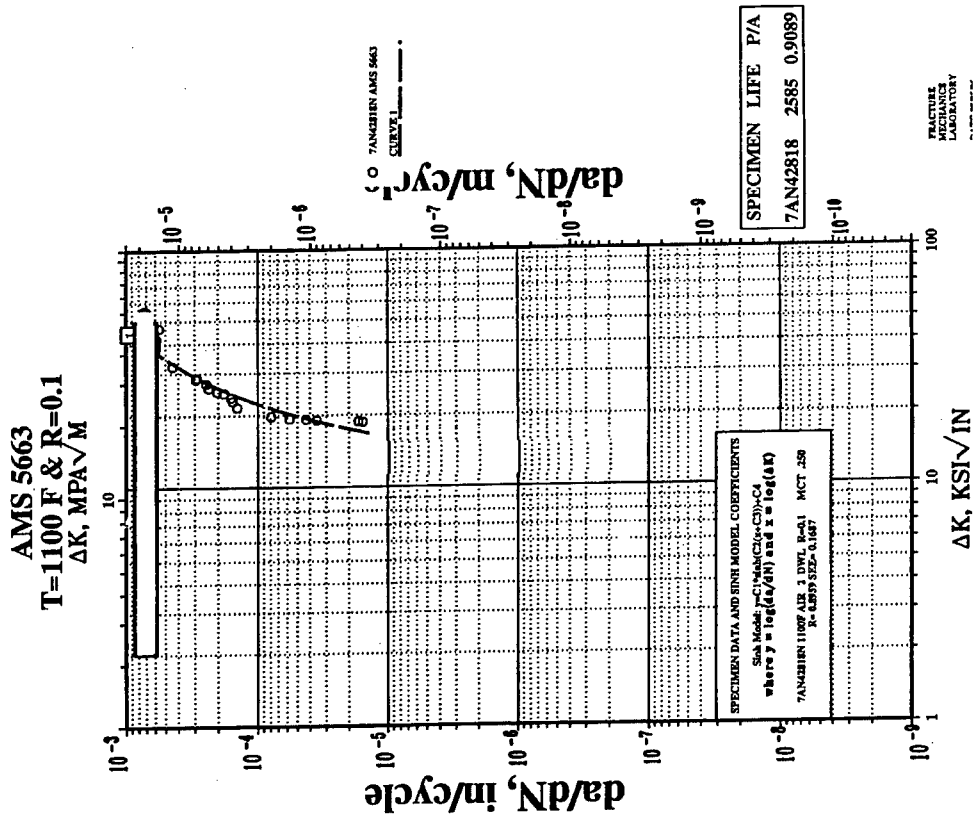


Chart A-80

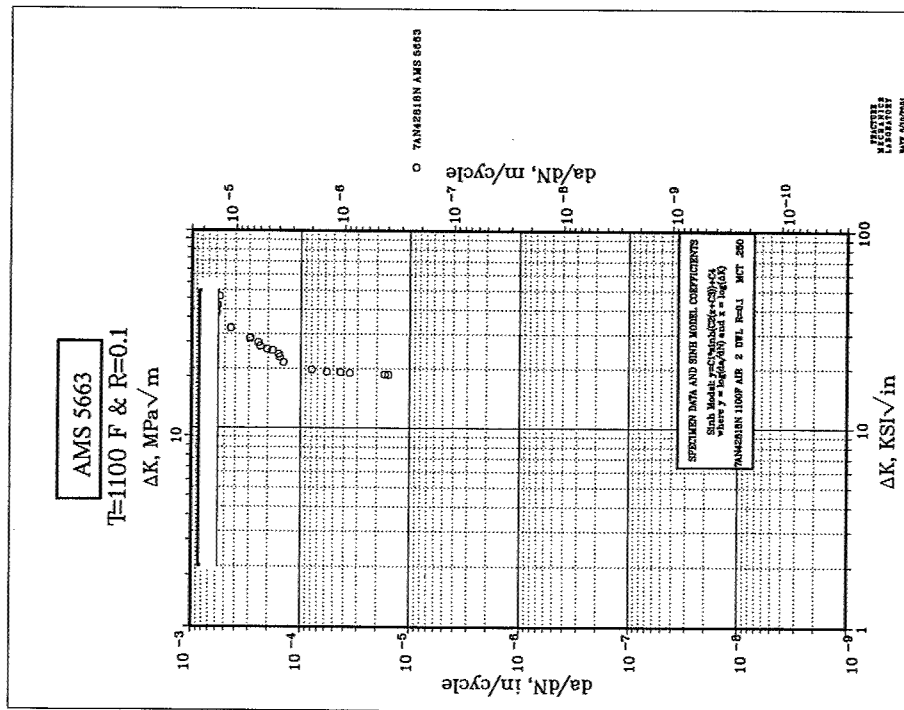


Chart A-81

A.4. PWA 1469 da/dN PLOTS.

Chart No.	Material Source ¹	Condition ²	Specimen Number	Test Temp.(°F)	Cyclic Rate	Comments
A-82	A	A	44615	1100	2 mdw	Baseline
A-83	A	A	44616	1100	2 mdw	Baseline
A-84	A	B	9029	1100	10 cpm	Effect of 40 hrs. solution
A-85	A	B	9030	1100	10 cpm	Effect of 40 hrs. solution
A-86	A	B	46230	1100	2 mdw	Effect of 40 hrs. solution
A-87	A	B	46231	1100	2 mdw	Effect of 40 hrs. solution
A-88	A	C	46038	1100	2mdw	Weld FZ Baseline
A-89	A	C	46039 ³	1100	2 mdw	Weld FZ Baseline
A-90	A	C	46041	1100	2 mdw	Weld HAZ Baseline
A-91	A	C	46042 ⁴	1100	2 mdw	Weld HAZ Baseline
A-92	A	D	46113	1100	2 mdw	40 Sol. Hrs. on weld FZ
A-93	A	D	46114	1100	2 mdw	40 Sol. Hrs. on weld HAZ
A-94	A	D	46115	1100	2 mdw	40 Sol. Hrs. on weld HAZ
A-95	A	E	9031	1100	10 cpm	HIP Weld Baseline
A-96	A	E	46036	1100	2 mdw	HIP Weld Baseline
A-97	A	E	46037	1100	2 mdw	HIP Weld Baseline
A-98	A	F	9032 ⁶	1100	10 cpm	40 Sol. Hrs. on HIP weld
A-99	A	F	46118	1100	2 mdw	40 Sol. Hrs. on HIP weld
A-100	A	F	46119	1100	2 mdw	40 Sol. Hrs. on HIP weld

Notes: 1. A: Cast Plates by Precision Castparts Corp. Heat: 41214

2. A: FHT: Stabilized + Solution + Aged

B: FHT + 8X (5 hrs. Sol. + Age)

C: Stabilized + Solution + Weld +FHT

D: C + 8 X (5 hrs. Sol. + Age)

E: Weld + HIP + FHT

F: Weld + HIP + FHT + 8 X (5 hrs. Sol. + Age)

3. Poor data fit; Not used for comparisons.

4. Crack grew primarily in base metal.

5. Grip failure; No Data

6. Invalid; Crack grew out of plane. R= .7 test.

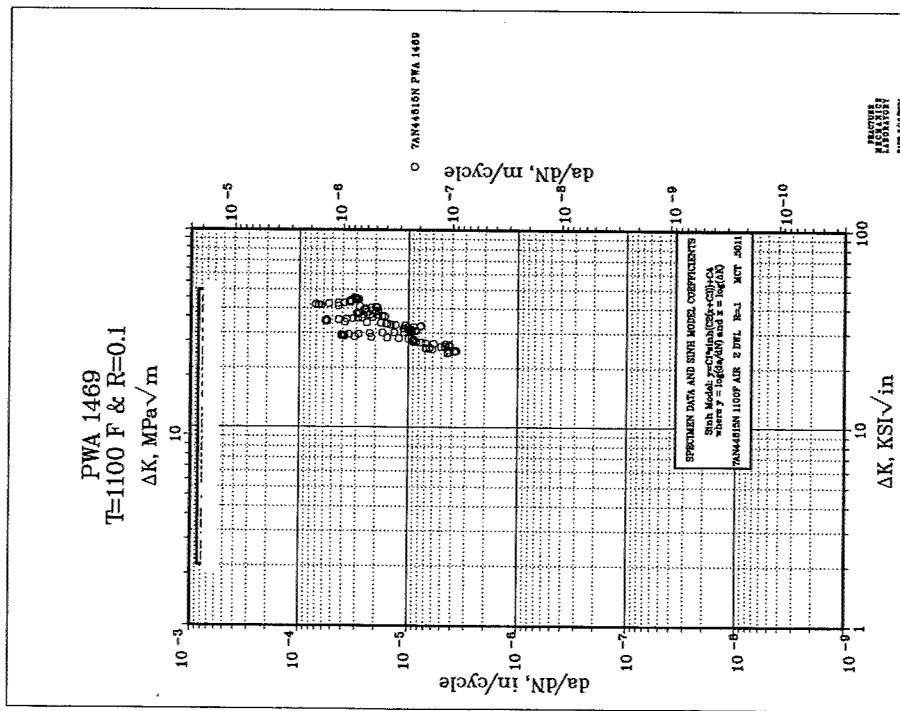


Chart A-82

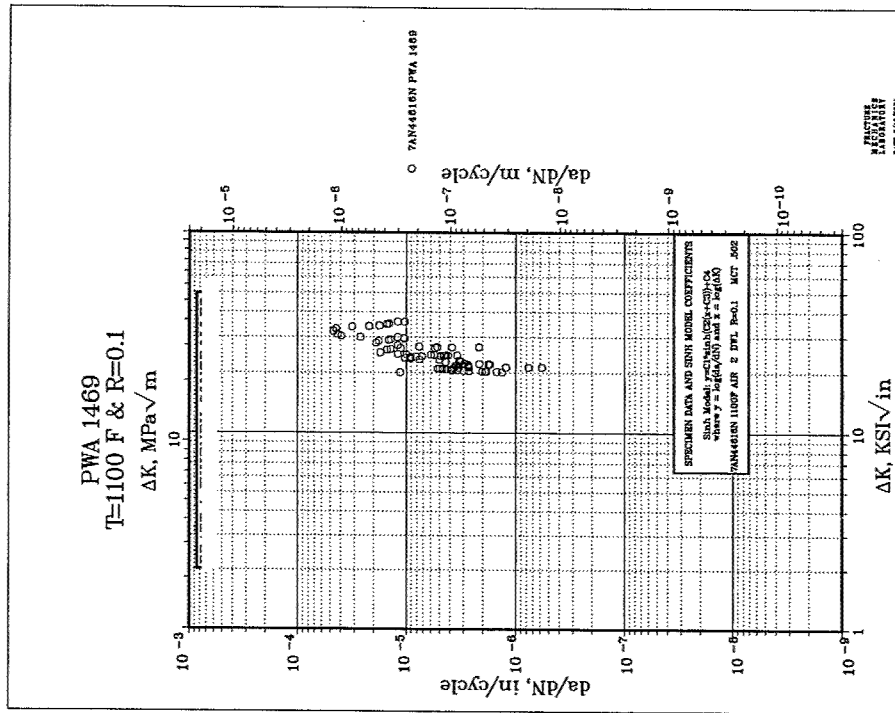
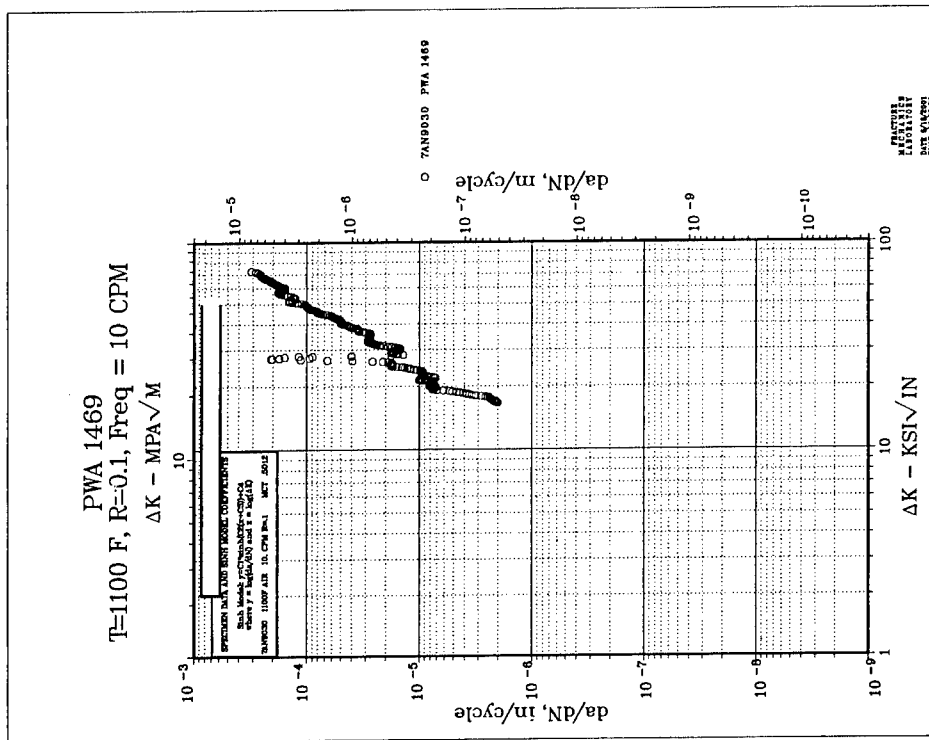
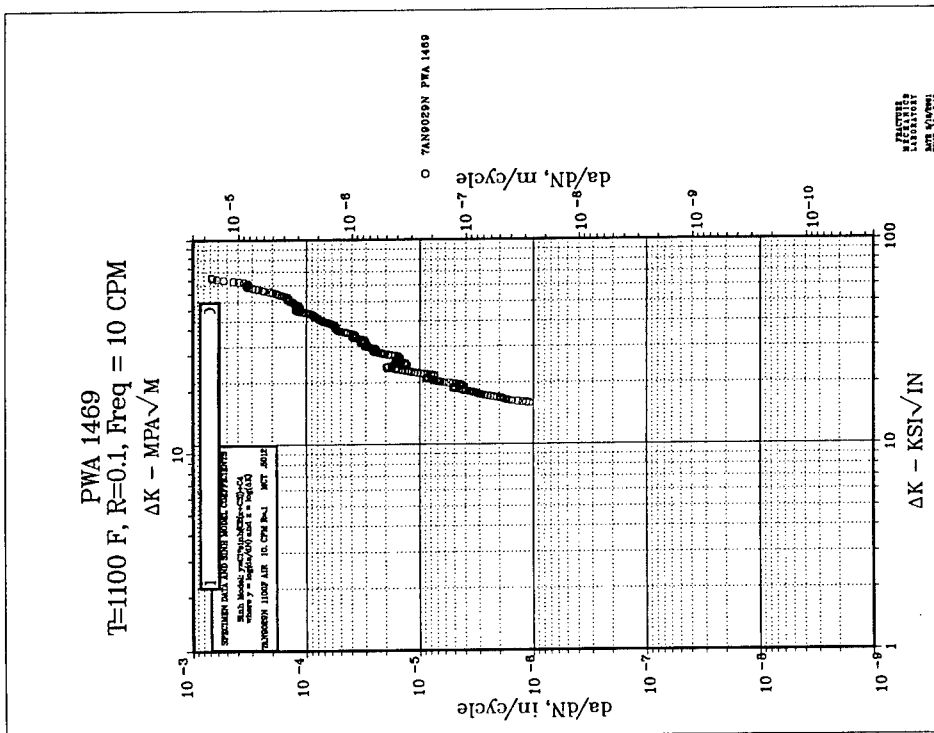


Chart A-83



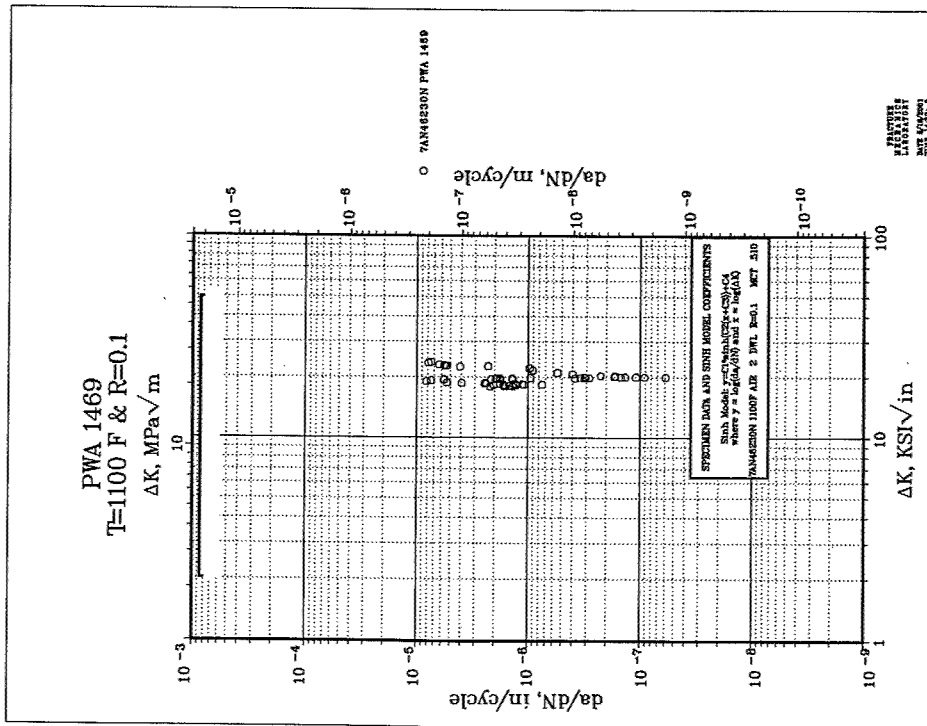


Chart A-86

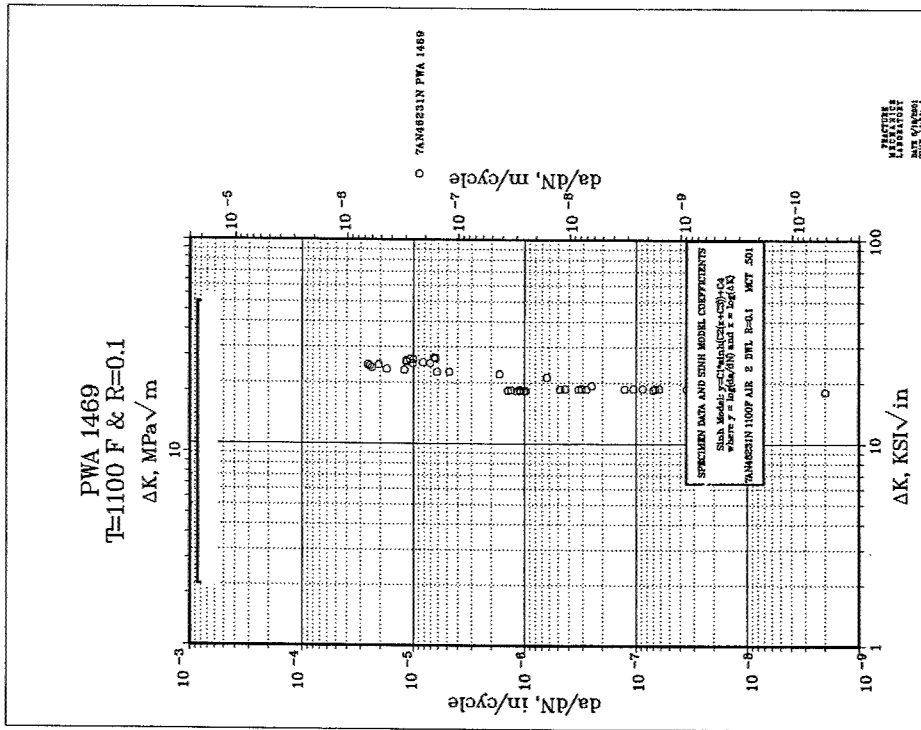


Chart A-87

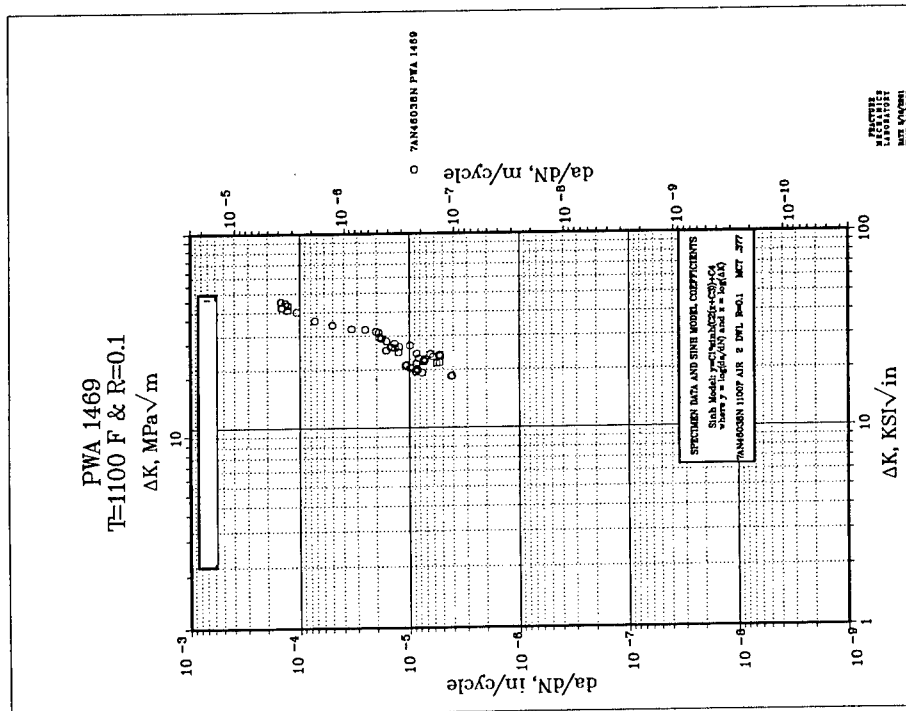


Chart A-88

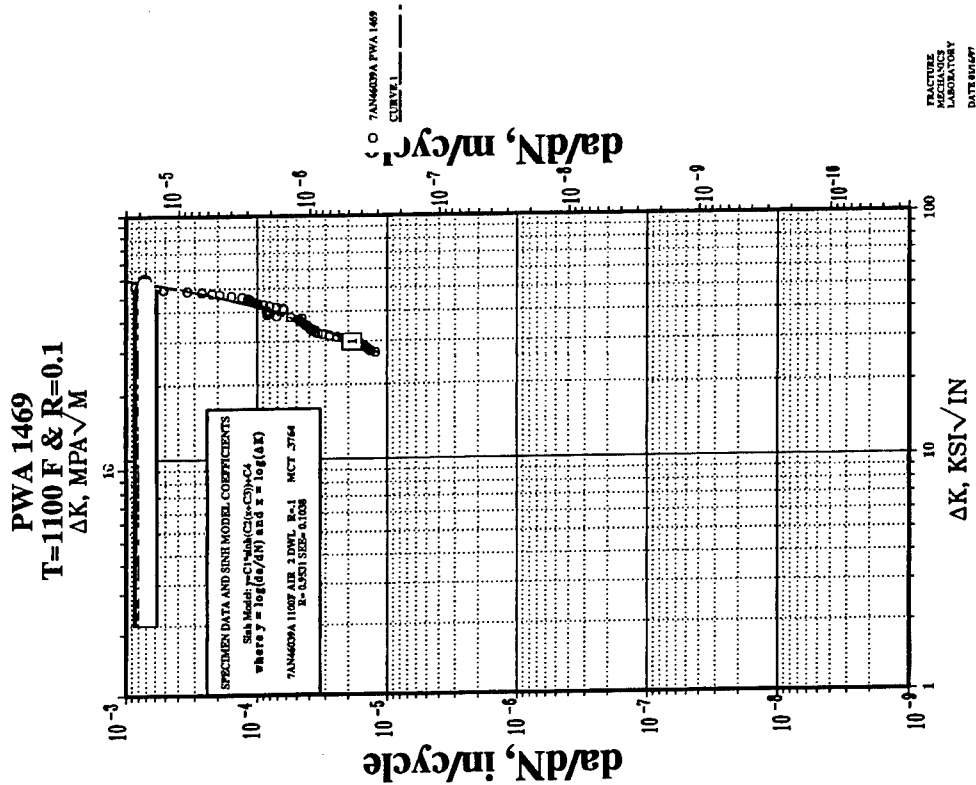


Chart A-89

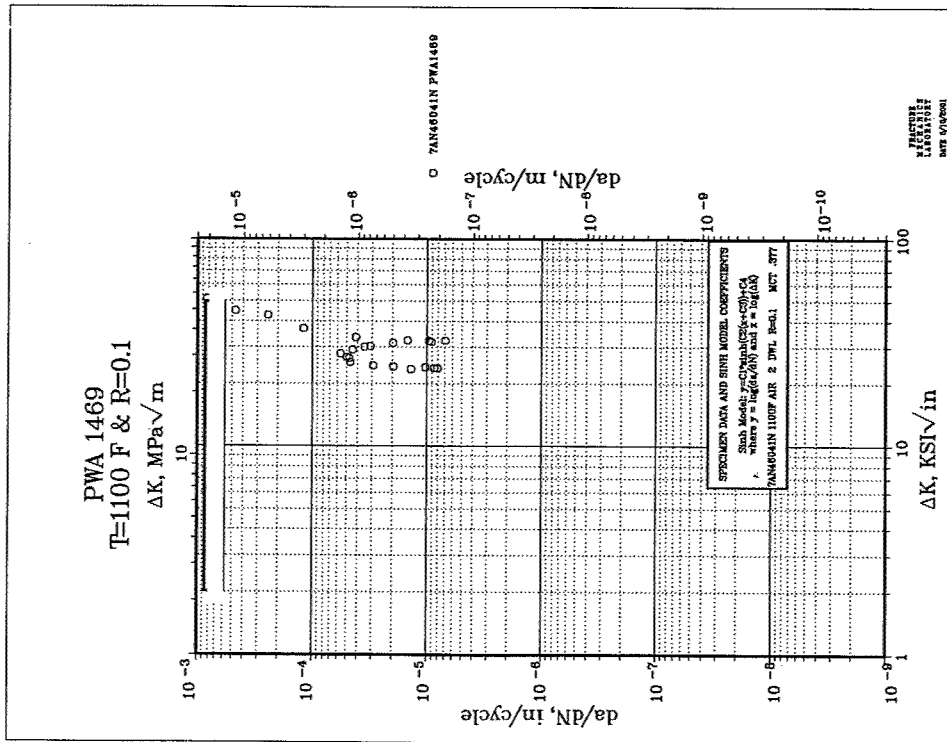


Chart A-90

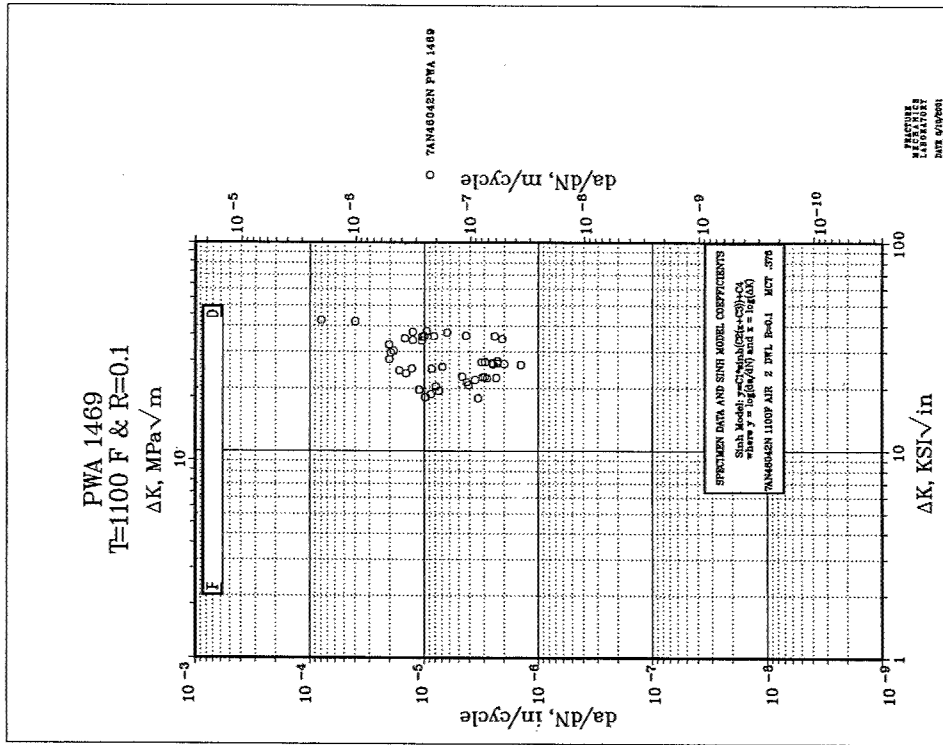


Chart A-91

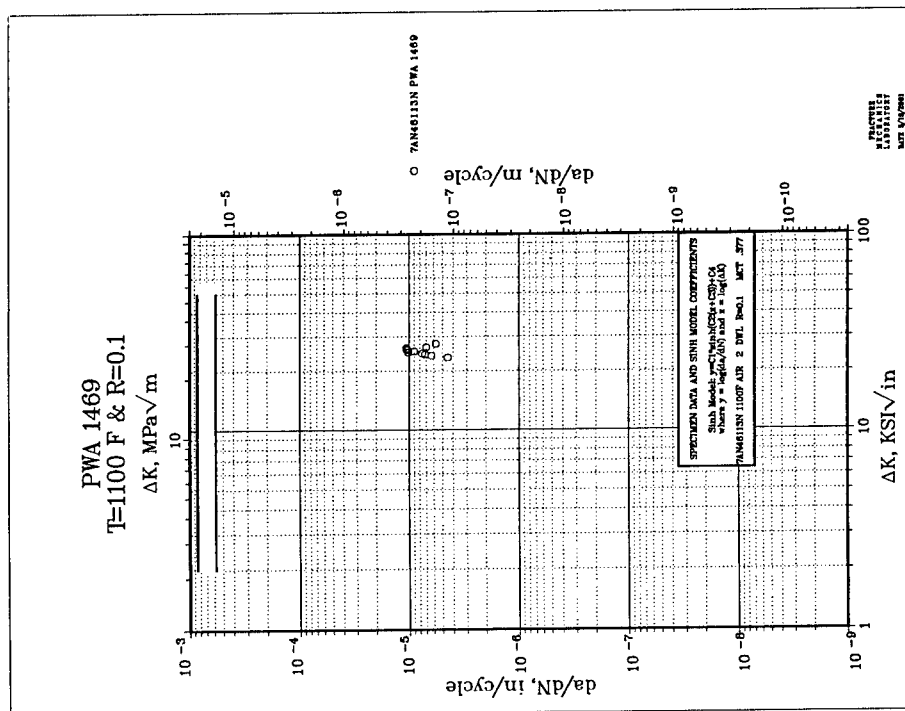


Chart A-92

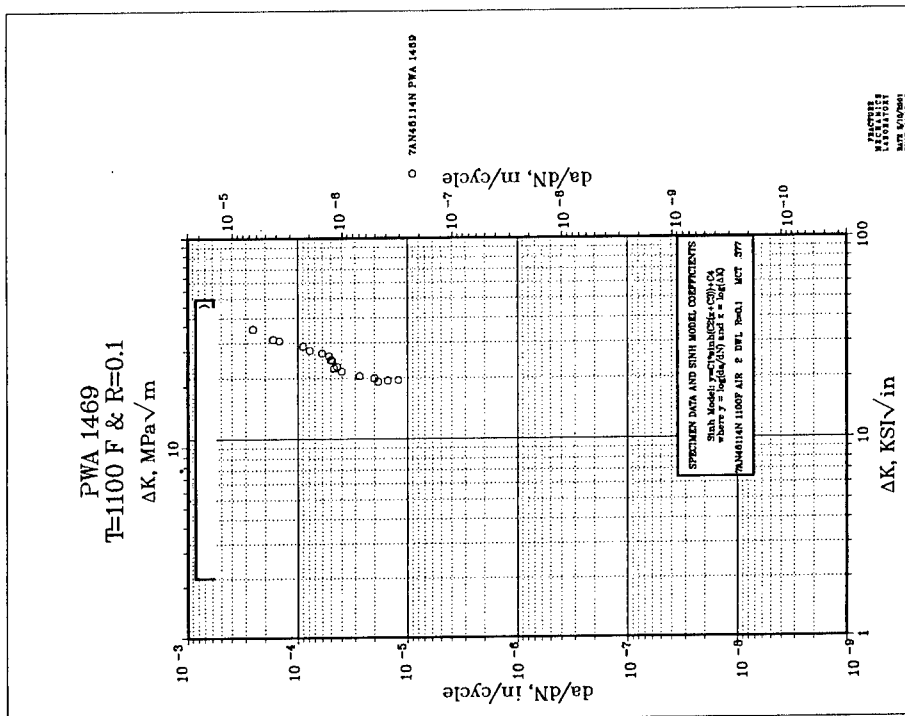
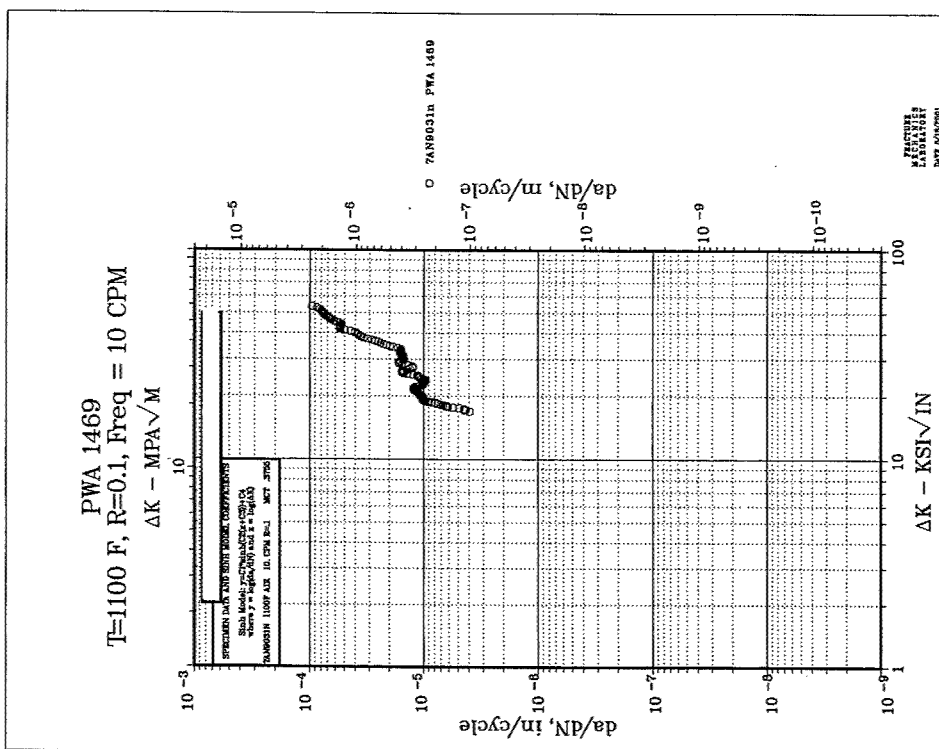
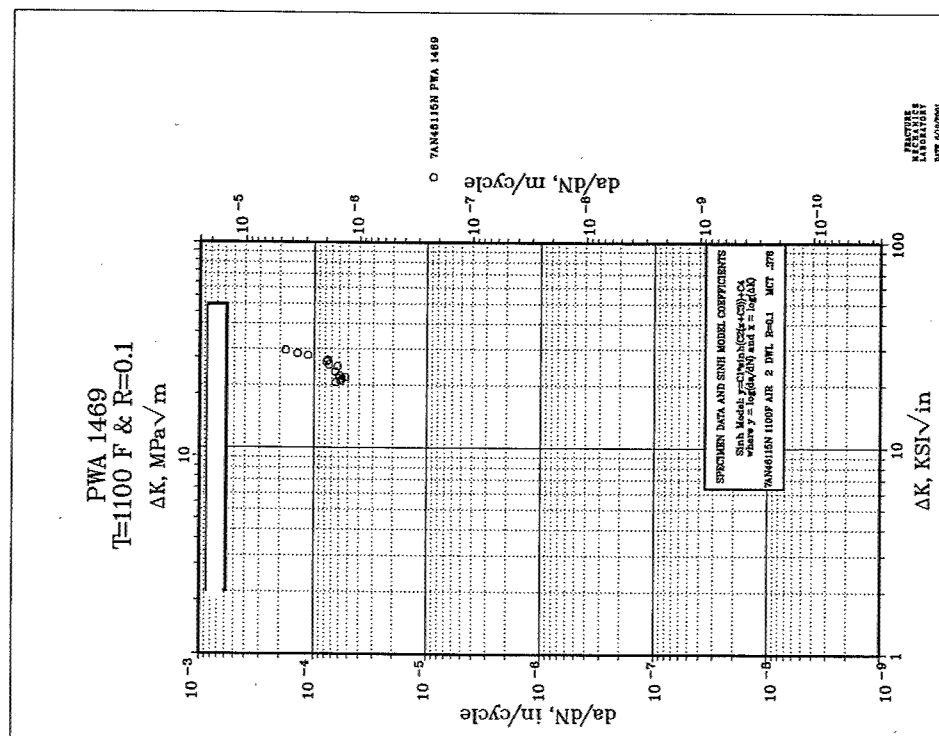


Chart A-93



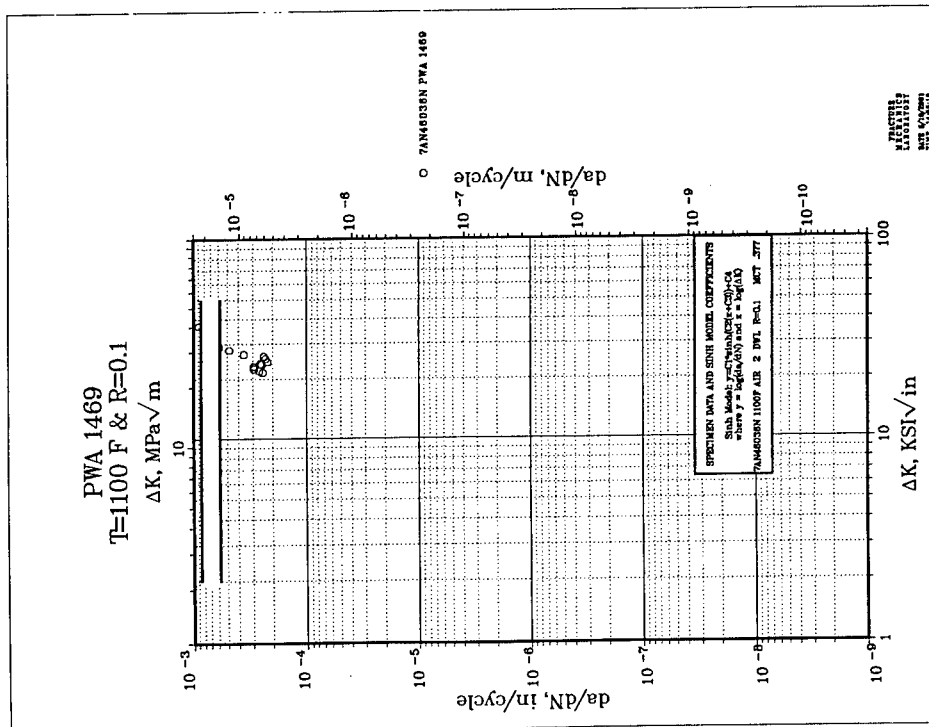


Chart A-96

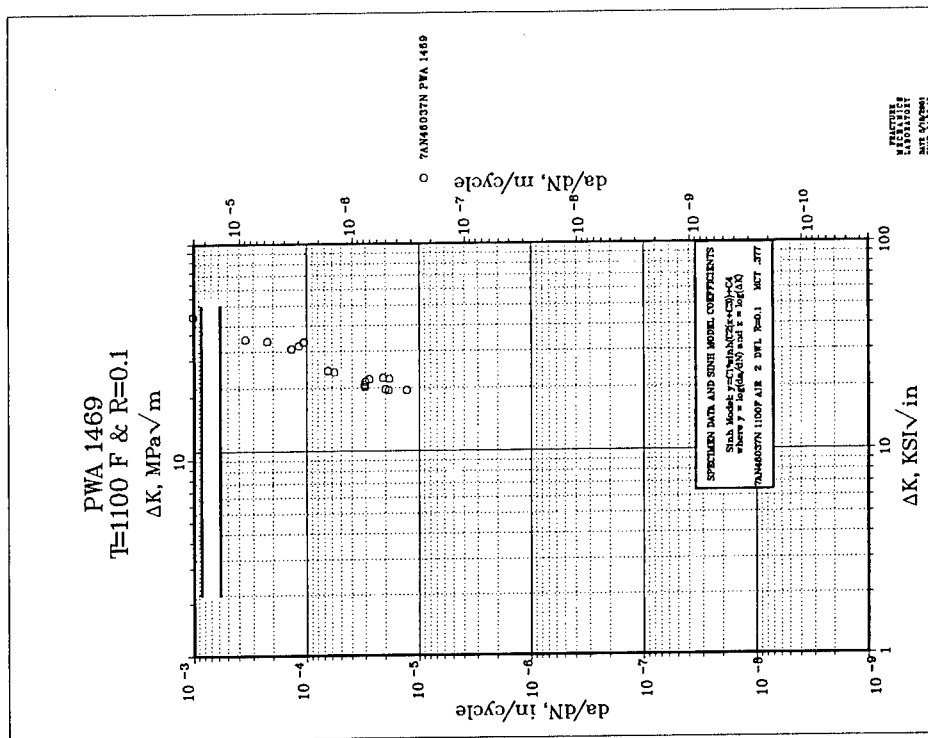


Chart A-97

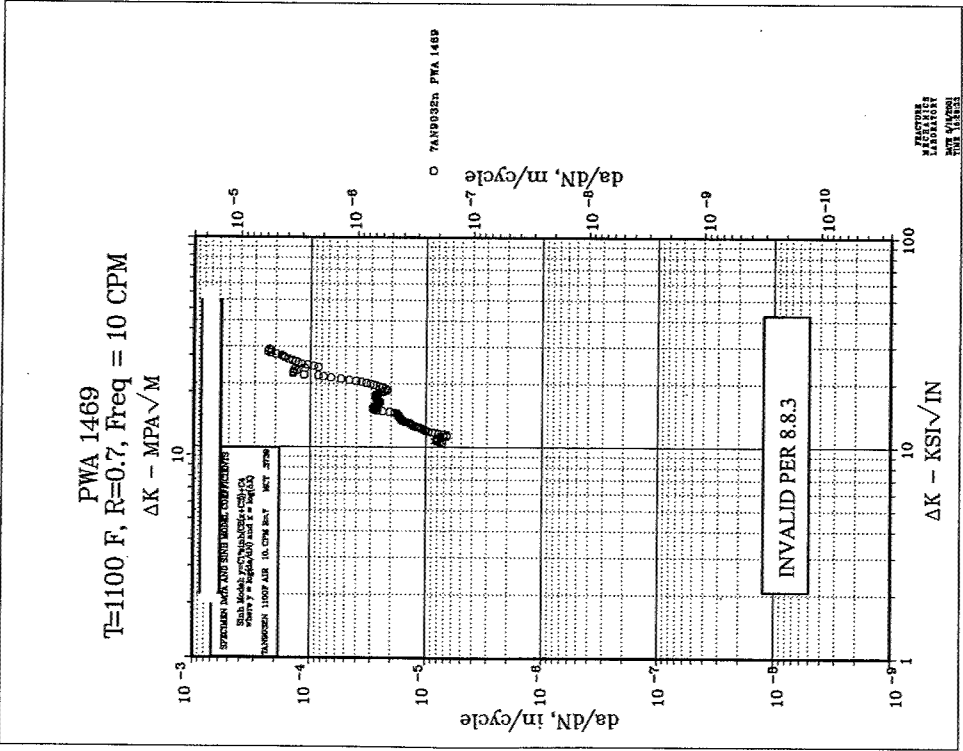


Chart A-98 Invalid Test

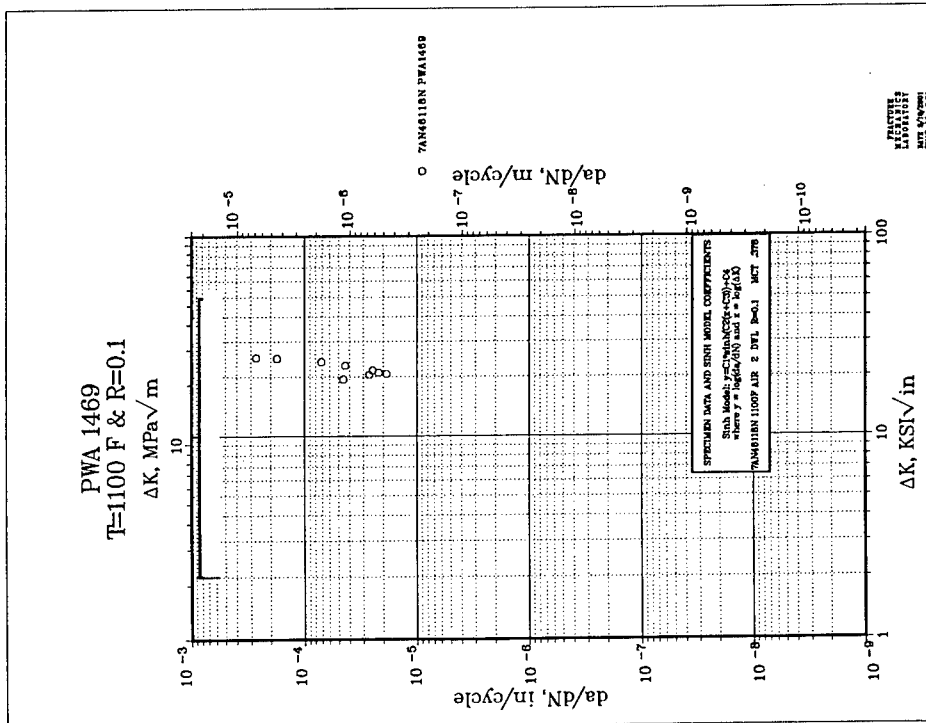


Chart A-99

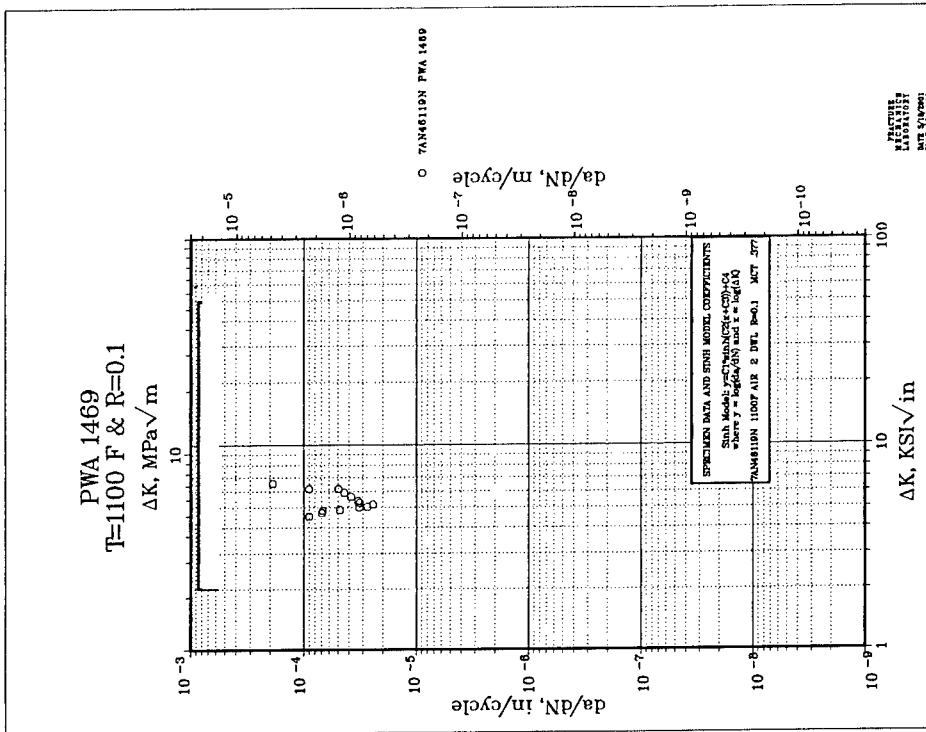


Chart A-100

A.5 JT9D DIFFUSER SPECIMENS da/dN PLOTS.

No.	Material Source ¹	S/N ²	Specimen Number	Test Temp.(°F)	Cyclic Rate
A-101	OPW Center	BW0976	41159	800	10 cpm
A-102	OPW Center	BW0976	43383	1000	2 mdw
A-103	OPW Center	BW0976	41158	1100	2 mdw
A-104	OPW Center	BW0976	41160	1100	2 mdw
A-105	OPW Center	AG9961	41823	800	10 cpm
A-106	OPW Center	AG9961	41824	1100	2 mdw
A-107	OPW Center	CJ3225	41825	800	10 cpm
A-108	OPW Center	CJ3225	43383	1000	2 mdw
A-109	OPW Center	CJ3225	41826	1100	2 mdw

Notes: 1. JT9D Diffuser Case Outer Pressure Wall Center Ring

2. BW0976 Operated by British Airlines for 63,092 hours/13,696 cycles
 AG9961 Operated by Japanese Airlines for 53,487 hours/23,869 cycles
 CJ3225 Operated by Japanese Airlines for 60,307 hours/19,260 cycles.

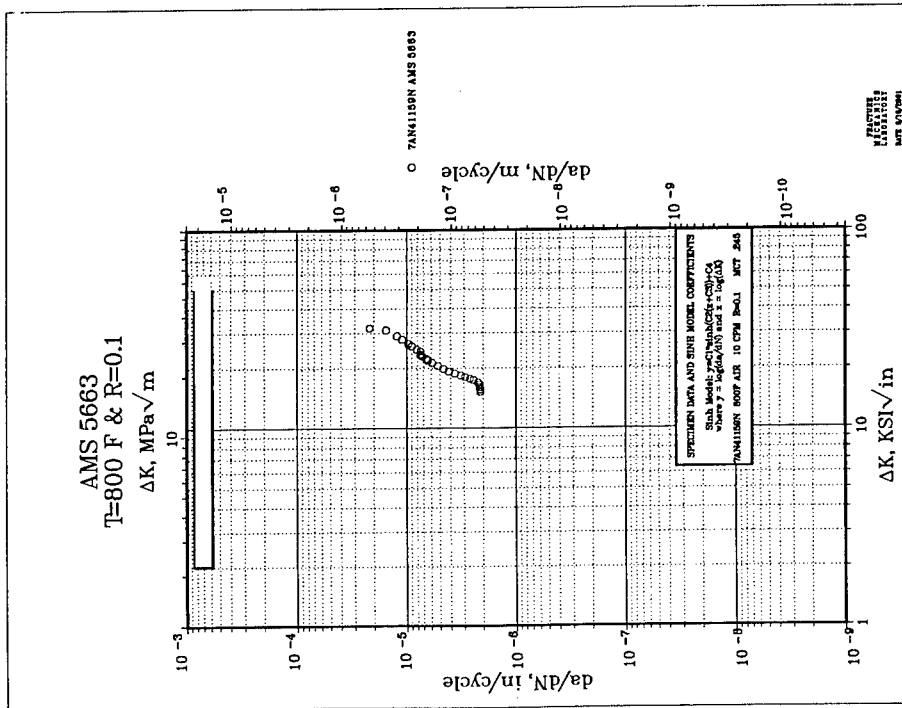


Chart A-101

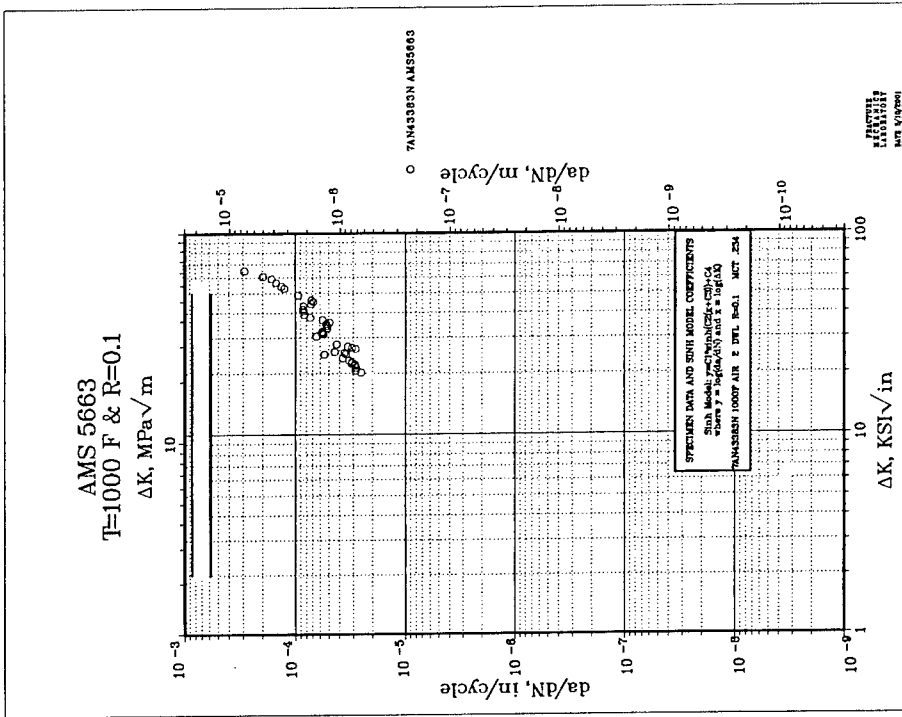


Chart A-102

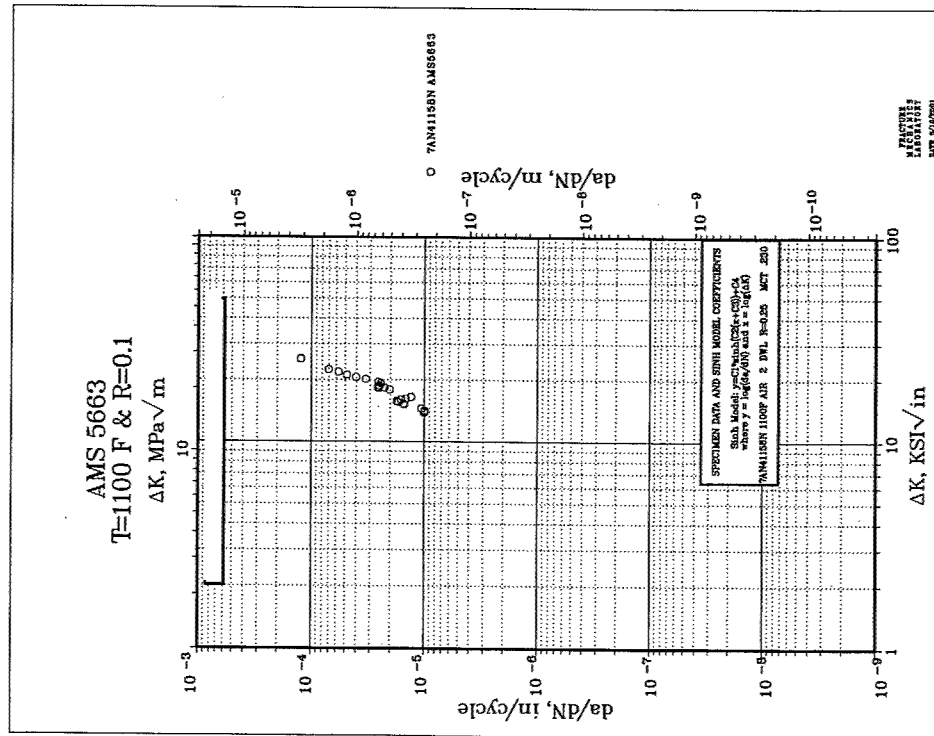


Chart A-103

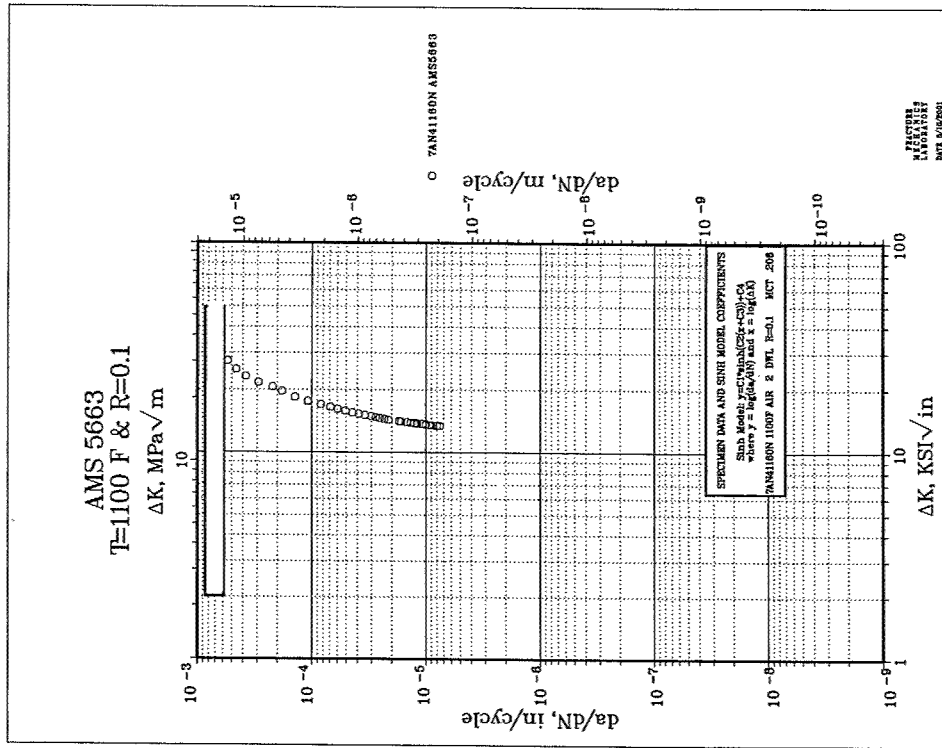


Chart A-104

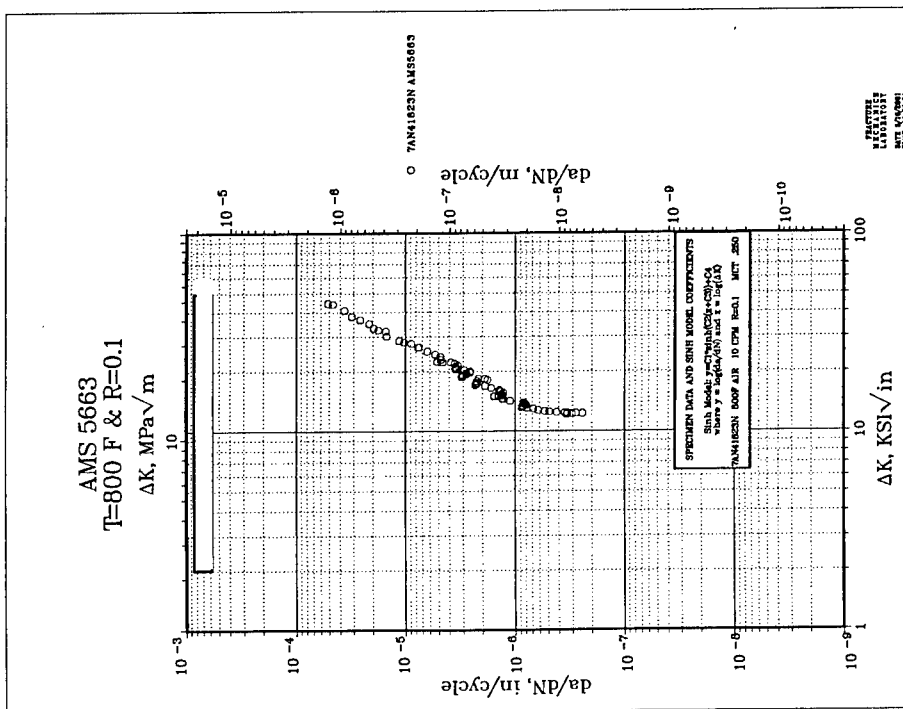


Chart A-105

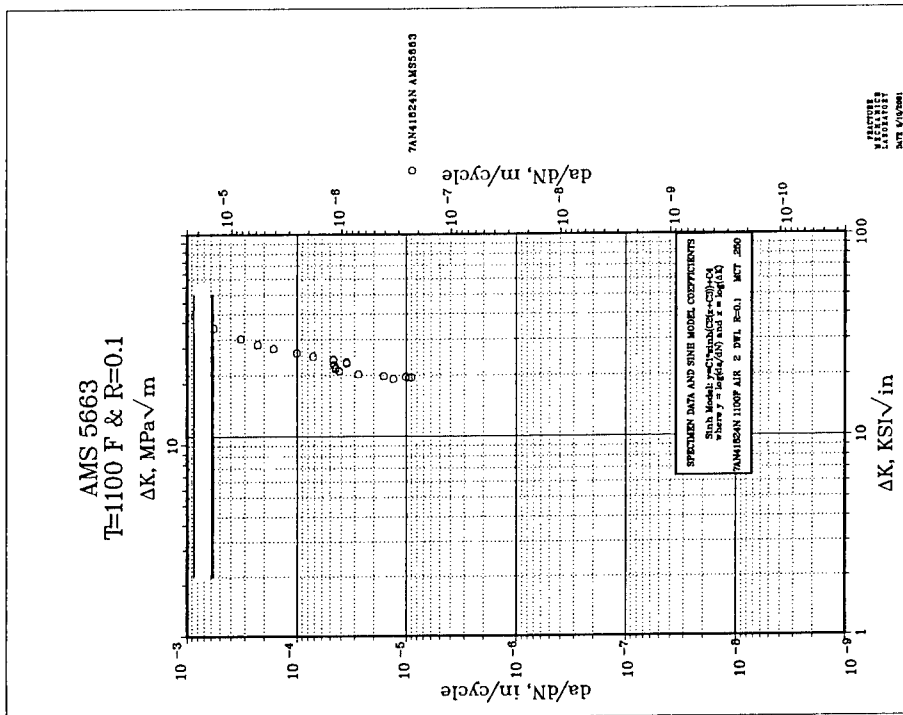


Chart A-106

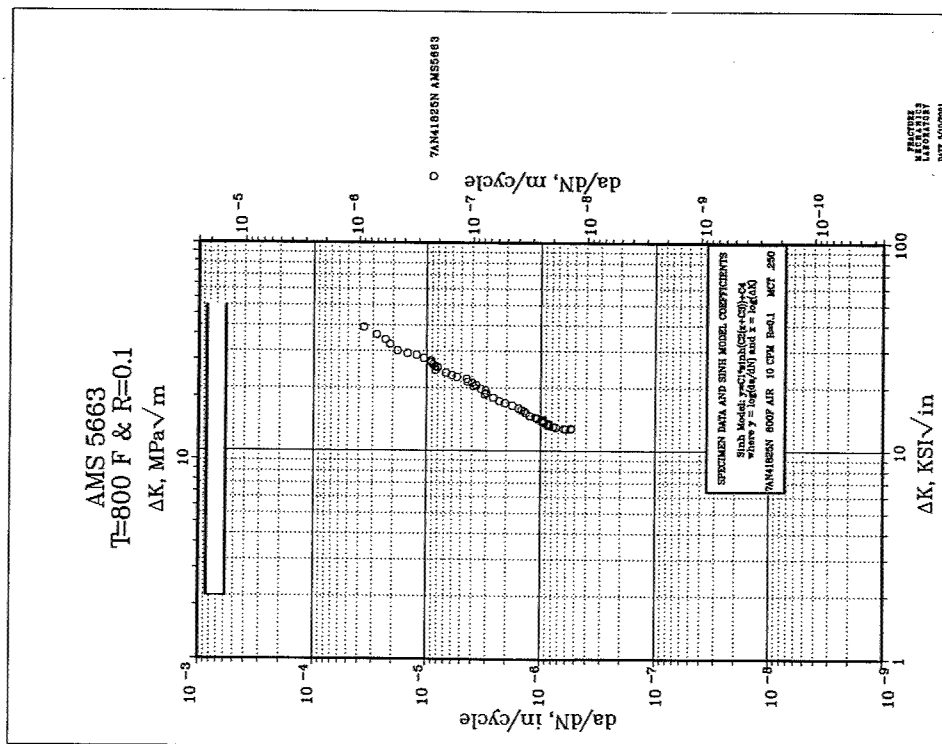


Chart A-107

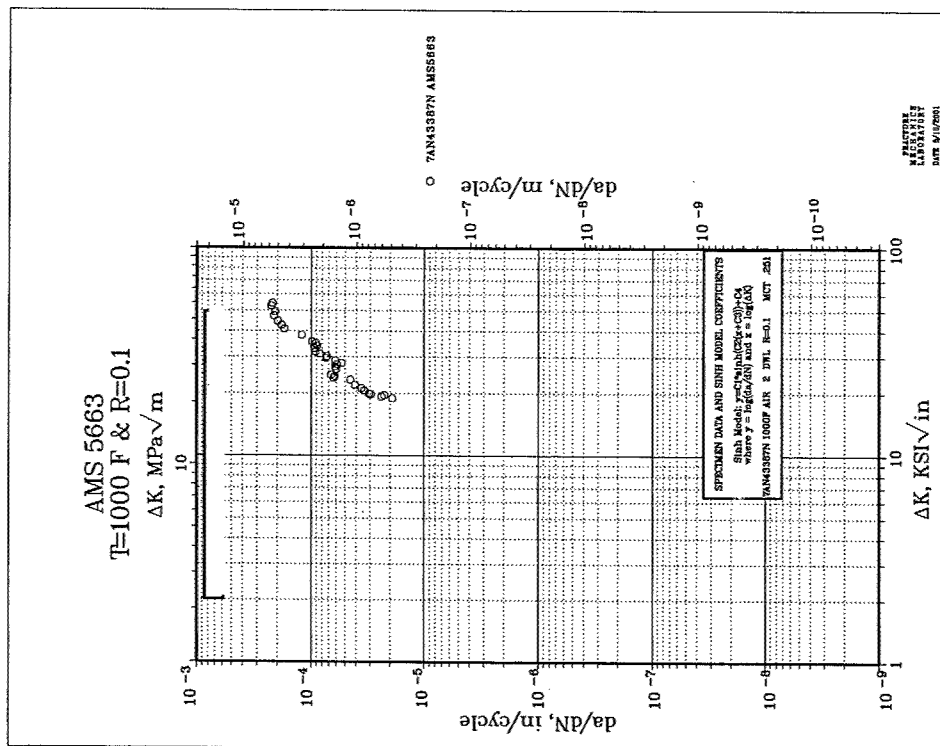


Chart A-108

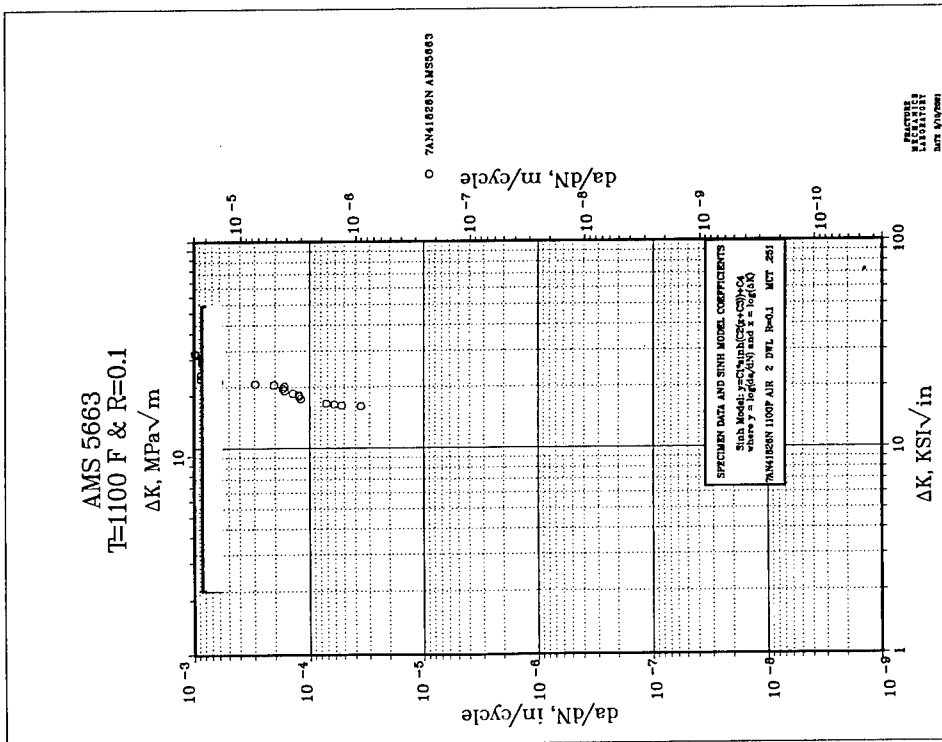


Chart A-109

APPENDIX B—HEAT TREAT STUDY OF INCONEL 718

B.1 COARSE GRAIN AMS 5663.

B.1.1 HEAT TREAT PROCEDURE.

Samples were removed from the fully heat-treated high pressure turbine (HPT) case used to supply coarse-grained Inconel 718 material to the test program. Five soak cycles at 1750°F were used, varying in length from 1 to 30 hours. The material was exposed to 1 to 10 cycles with a maximum exposure of 30 hours at temperature. Conversations with several repair shops suggest that it would be rare for a case in service to be exposed to 30 hours at 1750°F, although this was possible with long-life cases. The cooling rate from a solution was added as a factor. The ideal is to cool at rates greater than or equal to 40°F per minute, but it is common to cool at rates between 10° and 20°F per minute. On rare occasions very slow cooling rates have been used. At the completion of each cycle, the sample was aged per the standard 1325°F (8 hrs) FC to 1150°F (8 hrs). While heat-up rates can vary, established controls should keep the variations small. Heat-up rates were not varied in this evaluation.

B.1.2 EVALUATION PROCEDURE.

A section of each heat-treated sample was mounted in bakelite mounts and examined via light metallography. A qualitative assessment of the amount of needle delta present was then made. With time these assessments were consolidated into four categories. No attempt was made to perform a quantitative assessment of the amount of needle delta phase generated on the material.

B.1.3 RESULTS.

The following table presents a matrix of heat treat conditions and metallographic results. Select examples of the metallographic observations are presented on the following page.

Cycle (hrs at 1750°F)	No. of Cycles	Total Time at 1750°F*	Amount of Needle Delta		
			≥40°F per minute	10° to 20°F per minute	2° to 5°F per minute
1	1	1	Low-Mod.	Low-Mod.	Mod.-High
1	2	2	Low-Mod.	Low-Mod.	Mod.-High
1	5	5	Moderate	High	Very High
1	10	10	High	Very High	Very High
2	2	4	Low-Mod.	High	High
2	5	10	Very High	Very High	High
5	1	5	Moderate	n.d.	Mod.-High
5	2	10	High	n.d.	High
10	1	10	High	n.d.	High
10	3	30	Very High	n.d.	Very High
30	1	30	Very High	n.d.	Very High

*Beyond the initial first hour of fully heat-treated material at start of the evaluation.

n.d. = not done

B.1.4 CONCLUSIONS.

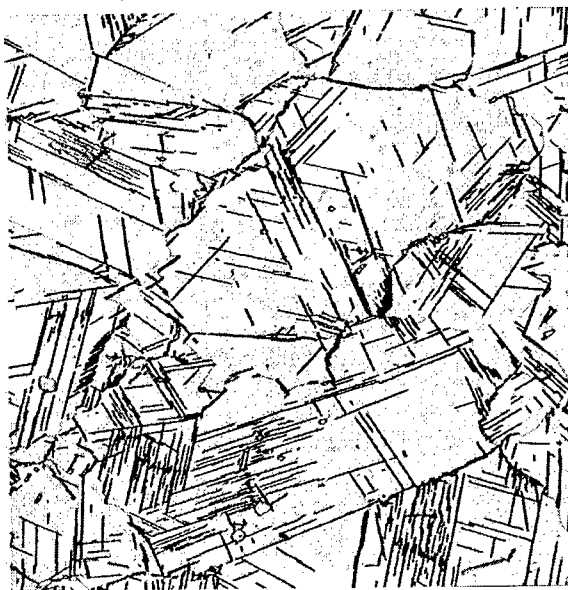
Between the cooling rates more typically experienced when processing cases, a slower cooling rate did result in the precipitation of more needle delta phase. Within any cooling rate the effect of more cycles at shorter times did not seem to be a factor. Total time at temperature was the primary factor with the amount of needle delta phase that was precipitated.



One (1 hr) cycle Fast Cool 200X



One (1 hr) cycle Slow Cool 200X



Five (1 hr) cycles Fast Cool 200X

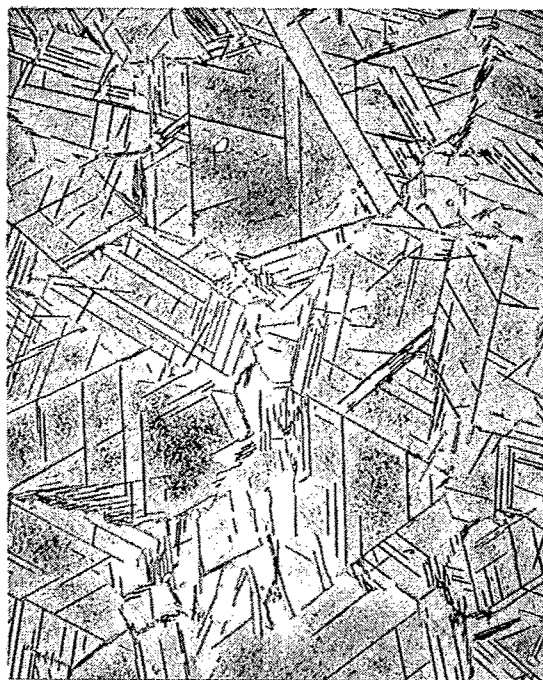


Five (1 hr) cycle Slow Cool 200X

FIGURE B-1. TYPICAL MICROSTRUCTURES ILLUSTRATING DELTA CONCENTRATION IN FULLY HEAT-TREATED COARSE GRAIN AMS 5663 WITH A TOTAL OF 1 (UPPER) AND 5 (LOWER) HOURS AT THE 1750°F SOLUTION TEMPERATURE (Material was both fast cooled (left) and slow cooled (right) from solution prior to precipitation aging.)



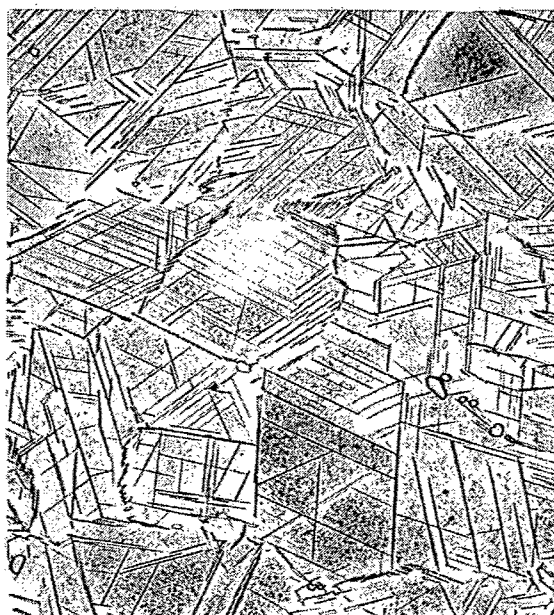
Ten (1 hr) cycles Fast Cool 200X



Five (2 hr) cycles Slow Cool 200X



Three (10 hrs) cycles Fast Cool 200X



One (30 hrs) cycles Slow Cool 200X

FIGURE B-2. TYPICAL MICROSTRUCTURES ILLUSTRATING DELTA CONCENTRATION IN FULLY HEAT-TREATED COARSE GRAIN AMS 5663 WITH A TOTAL OF 10 (UPPER) AND 30 (LOWER) HOURS AT THE 1750°F SOLUTION TEMPERATURE (Material was both fast cooled (left) and slow cooled (right) from solution prior to precipitation aging.)

B.2 FINE GRAIN AMS 5663.

B.2.1 HEAT TREAT PROCEDURE.

Samples were removed from the fully heat-treated barstock case used to supply fine-grained Inconel 718 material to the test program. The heat treat exposure matrix was exactly the same as that used with the coarse grain material described in section B.1. As with the coarse grain material, a maximum exposure of 30 hours at temperature was selected. Again this was guided by conversations with several repair shops that suggested 30 hours of total exposure would more then cover most cases.

B.2.2 EVALUATION PROCEDURE.

A section of each heat-treated sample was mounted in bakelite mounts and examined via light metallography. A qualitative assessment of the amount of needle delta present was then made. With time these assessments were consolidated into four categories. No attempt was made to perform a quantitative assessment of the amount of needle delta phase generated on the material.

B.2.3 RESULTS.

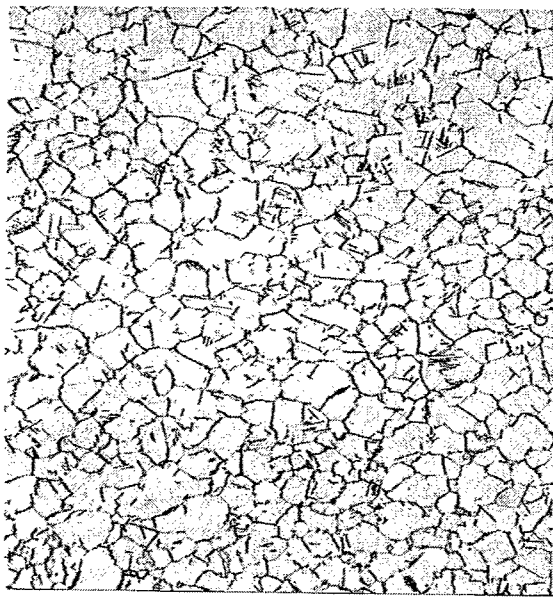
The following table presents a matrix of heat treat conditions and metallographic results. Select examples of the metallographic observations are presented on the following page.

Cycle (hrs at 1750°F)	No. of Cycles	Total Time at 1750°F *	Amount of Needle Delta		
			≥40°F per minute	10° to 20°F per minute	2° to 5°F per minute
1	1	1	Low-Mod.	Low-Mod.	Low-Mod.
1	2	2	Low-Mod.	Low-Mod.	Low-Mod.
1	5	5	Low-Mod.	Low-Mod.	Low-Mod.
1	10	10	Low-Mod.	Low-Mod.	Low-Mod.
2	2	4	Low-Mod.	Low-Mod.	Low-Mod.
2	5	10	Low-Mod.	Low-Mod.	Low-Mod.
5	1	5	Low-Mod.	n.d.	Low-Mod.
5	2	10	Low-Mod.	n.d.	Low-Mod.
10	1	10	Low-Mod.	n.d.	Low-Mod.
10	3	30	Low-Mod.	n.d.	Low-Mod.
30	1	30	Low-Mod.	n.d.	Low-Mod.

*Beyond initial 1hour of fully heat-treated material at start of the evaluation.
n.d. = not done

B.2.4 CONCLUSIONS.

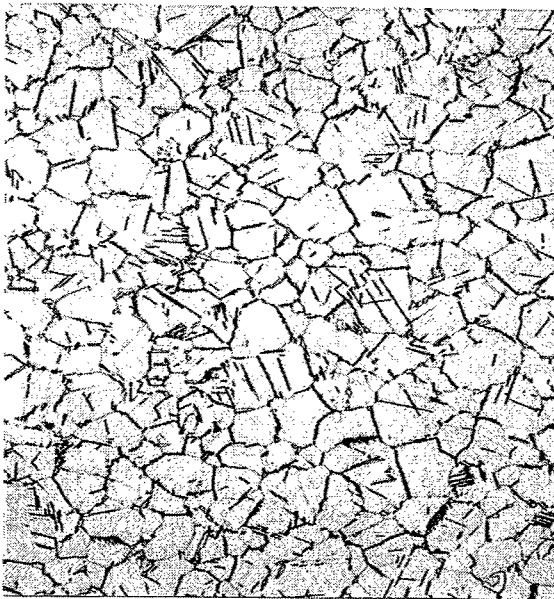
Very little needle delta phase precipitated within the fine grain material. This was true at both the grain boundary and intragranular regions. Further studies would be necessary to determine the reason for this, but it may be related to the fact that the fine grain barstock used in this evaluation had a considerable amount of globular delta phase in its grain boundaries. It is possible this reduced the drive to precipitate additional delta phase.



One (1 hr) cycle Fast Cool 200X



Ten (1 hr) cycles Fast Cool 200X



Three (10 hrs) cycles Fast Cool 200X



Three (10 hrs) cycles Slow Cool 200X

FIGURE B-3. TYPICAL MICROSTRUCTURES OF FULLY HEAT-TREATED FINE GRAIN AMS 5663 WITH 1 (UPPER LEFT), 10 (UPPER RIGHT), AND 30 (LOWER) TOTAL HOURS AT 1750°F (All were fast cooled from solution except that illustrated in the lower right photomicrograph.)

B.3 PWA 1469 AND INCONEL 718 WELDS.

B.3.1 HEAT TREAT PROCEDURE.

Previous in-house studies had shown that the cast form of Inconel 718 responds much slower than the wrought form regarding precipitation of needle delta phase. This is especially true for HIP castings where the homogenized matrix combined with no residual energy results in very slow precipitation of delta phase. Segregated castings, including welds, tend to experience delta precipitation that is concentrated, if not limited, to the interdendritic regions. The solidification process segregates and enriches these areas in niobium. For these reasons the exposure matrix for the cast+HIP Inconel 718 (PWA 1469) and Inconel welds was simplified from that used for the wrought material described in sections A and B of this appendix. Total time of exposure was limited to 40 hours for both Inconel 718 welds and cast+HIP Inconel 718. Cooling rate from solution was 10° to 20°F per minute for all exposures

B.3.2 EVALUATION PROCEDURE.

A section of each heat-treated sample was mounted in bakelite mounts and examined via light metallography. A qualitative assessment of the amount of needle delta present was then made. With time these assessments were consolidated into four categories. No attempt was made to perform a quantitative assessment of the amount of needle delta phase generated on the material.

B.3.3 RESULTS.

The following table presents a matrix of heat treat conditions and metallographic results. Select examples of the metallographic observations are presented on the following page.

Cycle (hrs. at 1750°F)	No. of Cycles	Total Time at 1750°F*	Inconel 718 Weld Fusion Zone	Cast+HIP Inconel 718
1	1	1	Mod. - High	Low-Mod.
1	2	2	n.d.	n.d.
1	5	5	n.d.	Low-Mod.
1	10	10	Mod. - High	Moderate
2	2	4	n.d.	n.d.
2	5	10	Mod. - High	n.d.
5	1	5	n.d.	n.d.
5	2	10	n.d.	n.d.
5	8	40	n.d.	High
10	1	10	n.d.	Moderate
10	3	30	High	n.d.
10	4	40	n.d.	High
30	1	30	High	n.d.
40	1	40	n.d.	High

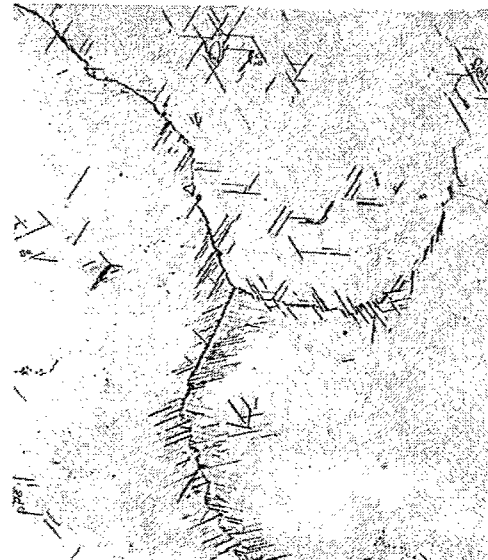
*Actual time for welds; Additional time for fully heat-treated cast+HIP material.
n.d. = not done

B.3.4 CONCLUSIONS.

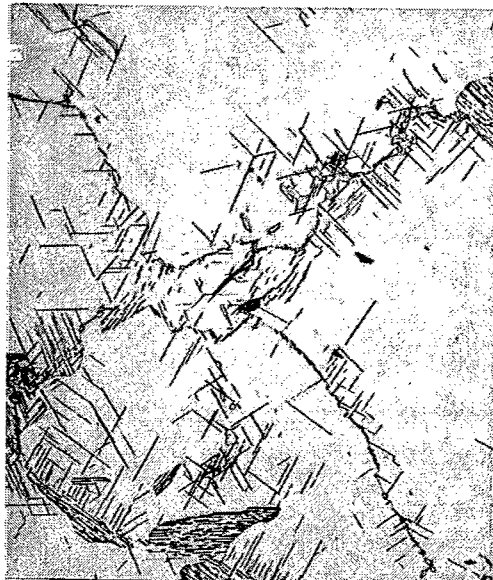
Results confirmed earlier studies regarding the reaction of the cast forms of Inconel 718 with additional exposures to the 1750°F solution temperature. Even where there was a high concentration of needle delta in the weld material, it was restricted to the interdendritic core and grain boundary areas. Most of the delta that precipitated in the cast+HIP material was mainly at the grain boundaries, but there was some intragranular precipitation, especially at the large MC carbides.



One (1 hr) cycles Fast Cool 200X



Five (1 hr) cycles Fast Cool 200X



Ten (1 hr) cycles Fast Cool 200X



Eight (5 hrs) cycles Fast Cool 200X

FIGURE B-4. TYPICAL MICROSTRUCTURE OF FULLY HEAT-TREATED PWA 1469 (CAST+HIP INCONEL 718) WITH 1 (UPPER LEFT), 5 (UPPER RIGHT), 10 (LOWER LEFT), AND 40 (LOWER RIGHT) HOURS AT THE 1750°F SOLUTION TEMPERATURE



Weld Fusion Zone 1 Hour Cycle 200X



Weld Fusion Zone 10 Hour Cycle 200X



Weld Fusion Zone 30 Hour Cycle 200X

FIGURE B-5. TYPICAL MICROSTRUCTURE OF FULLY HEAT-TREATED INCONEL 718 WELD FUSION ZONE WITH 1 (UPPER LEFT), 10 (UPPER RIGHT), AND 30 (LOWER LEFT) HOURS AT THE 1750°F SOLUTION TEMPERATURE

APPENDIX C—DESTRUCTIVE ANALYSIS OF JT9D TURBINE EXHAUST CASE (TEC)

C.1 PLAN.

Two JT9D-7 TECs (Turbine Exhaust Case) were available for this investigation (see section 2.1.4). Case S/N CD8893 was selected for cut up analysis. This case had been operated by Japan Airlines for 63,887 hours and 12,934 cycles. Metallographic samples were removed from the outer ring front flange, rails, mount lugs, and rear flange and from the case walls at the forward, middle, and rearward wall sections. Samples were also removed from one of the struts, the inner ring walls and inner ring flanges. Examples of the assembly welds were also examined. Besides examining general microstructure and possible defects, hardness measurements were made at several of the locations.

C.2. RESULTS.

The inner ring and struts displayed typical martensitic structure with the strut sheet material (AMS 5596) having a measurably finer grain size than the inner ring. Strut-to-case attachment welds were even finer grained. Deep notches were discovered at the strut/case attachment welds within the hollow struts. It is not known if these were present at completion of construction of the case as a new assembly or occurred subsequent to initiation of commercial service. The microstructure of the outer ring displayed a more sensitized like microstructure with grain boundaries that are heavily decorated with carbides. The grain structure of the outer ring was also coarser than the inner ring. No significant difference in microstructure was observed among different areas of the same detail, suggesting that whatever differences in temperature exposure that may have existed during engine operation, they were sufficiently similar as to not create microstructural differences.

Representative photographs of these microstructures are shown in figures C-1 through C-14.

The coarser grain and sensitized microstructure of the outer ring is attributed to its size and the heat treat procedures used with the case. The outer ring is substantially thicker in cross section than the inner ring and sheet metal struts. It would be expected that this hot-rolled ring forging would display a relative coarse grain relative to the thin sheet details and smaller thinner inner ring. Multiple tempers may lead to a sensitized microstructure, but the other case details would also be affected. The more probable cause is that the case experienced a more than typical slower cool from solution than experienced with test material. Most test material, including that used in this program, is hardened by a liquid quench from the solution temperature. However, large structural assemblies such as the TECs cannot be liquid quenched because they would experience severe distortion. Typically the TECs are solution heat treated followed by a forced gas cool, which is not as fast as a liquid quench. The forced gas cool most probably produced the sensitized microstructure. Quantitative metallography was not performed on the case samples, but qualitatively, the outer ring forward areas appeared to be more sensitized than the other case areas. These areas are the hottest operating and the microstructure may reflect this fact. Delta ferrite and other stringers were observed but not to any great degree.

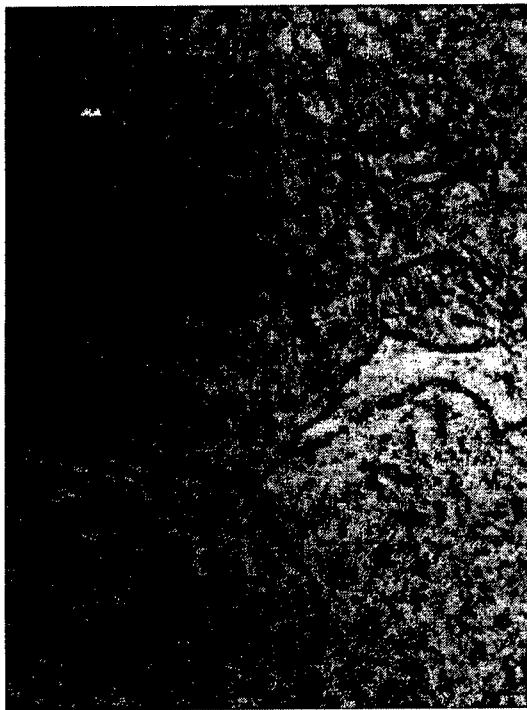


Outer Ring Front Flange 100X

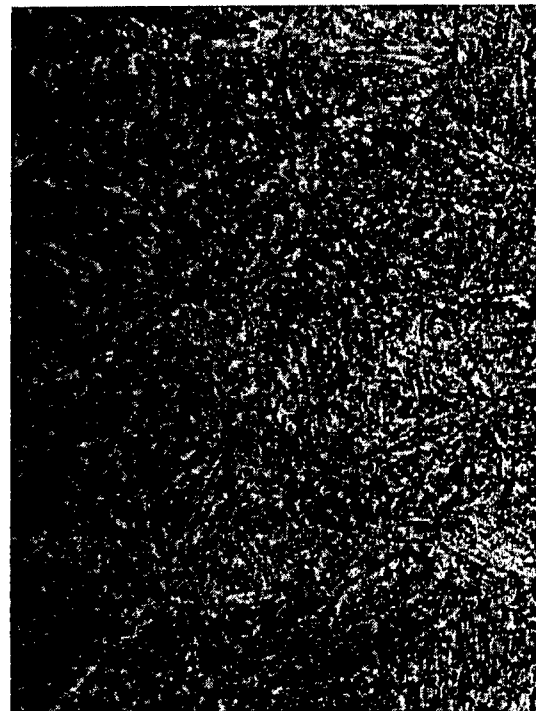


Outer Ring Front Flange 500X

FIGURE C-1. GENERAL MICROSTRUCTURE OF JT9D TURBINE EXHAUST CASE
OUTER FLANGE

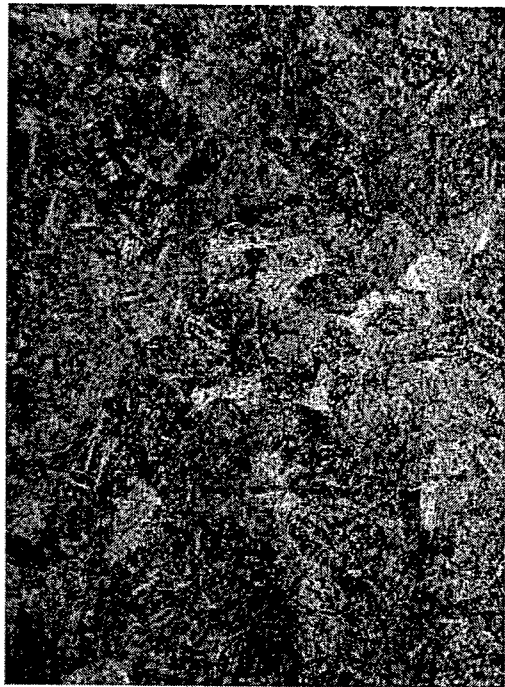


Outer Ring Front Flange 1000X



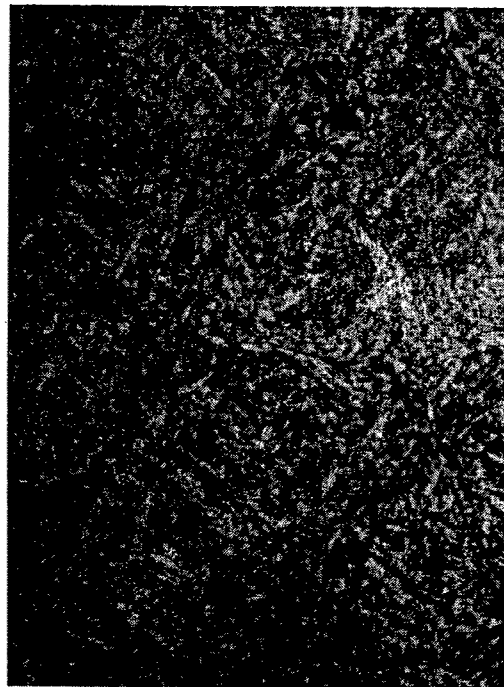
Outer Ring Front Wall 500X

FIGURE C-2. GENERAL MICROSTRUCTURE OF JT9D TURBINE EXHAUST CASE
OUTER RING FRONT FLANGE AND FRONT WALL



Outer Ring Mid-Wall

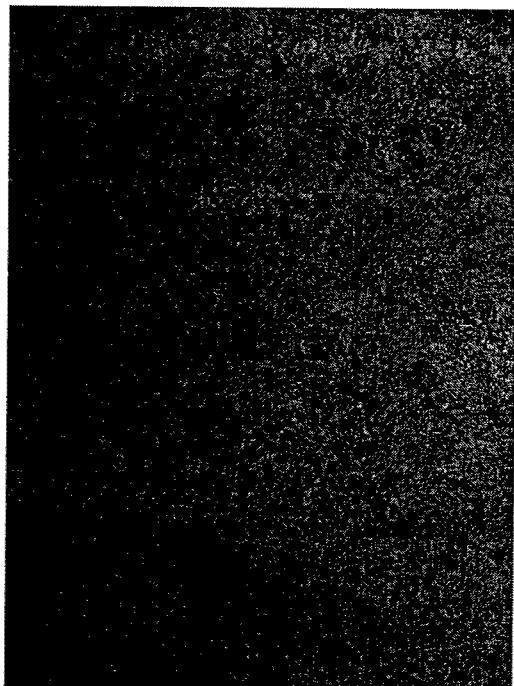
100X



Outer Ring Mid-Wall

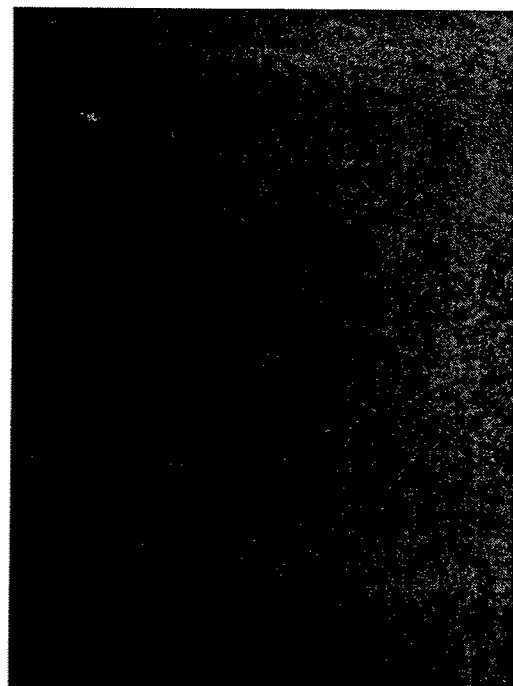
500X

FIGURE C-3. GENERAL MICROSTRUCTURE OF JT9D TURBINE EXHAUST CASE
OUTER RING MID-WALL



Outer Ring Rear Rail

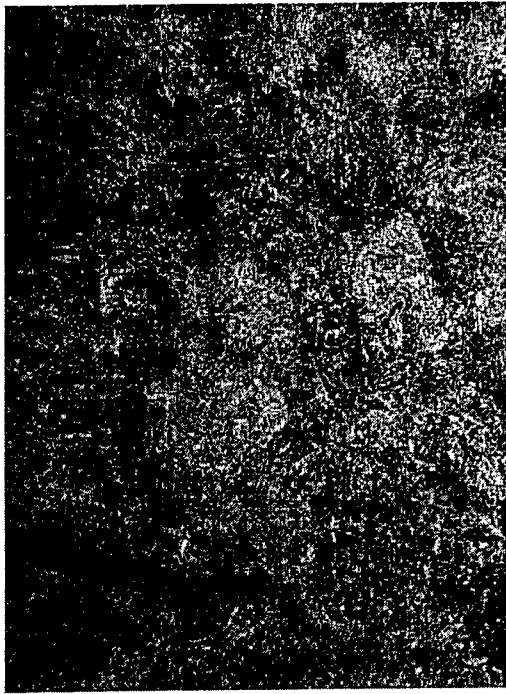
100X



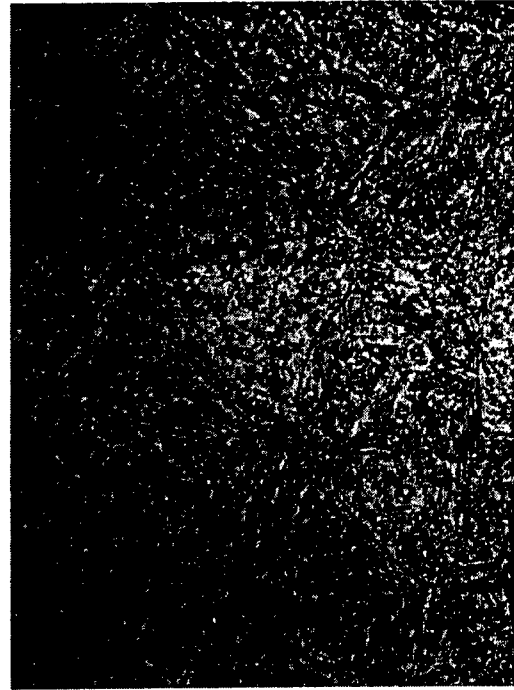
Outer Ring Rear Rail

500X

FIGURE C-4. GENERAL MICROSTRUCTURE OF JT9D TURBINE EXHAUST CASE
OUTER RING REAR RAIL



Outer Ring Mount Lug 100X



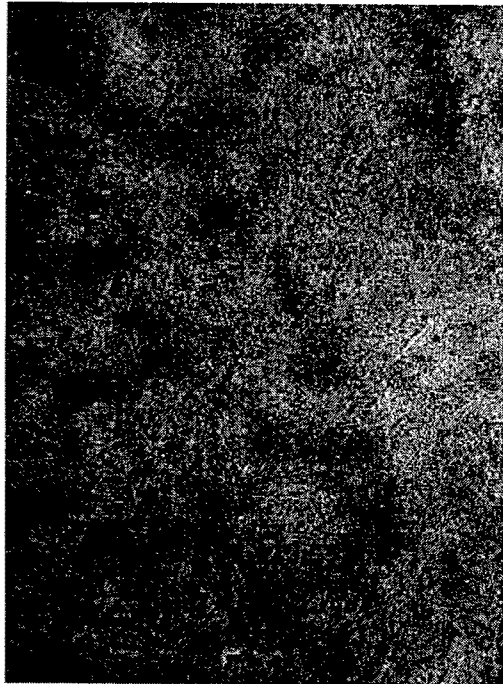
Outer Ring Mount Lug 500X

FIGURE C-5. GENERAL MICROSTRUCTURE OF JT9D TURBINE EXHAUST CASE
OUTER RING MOUNT LUG



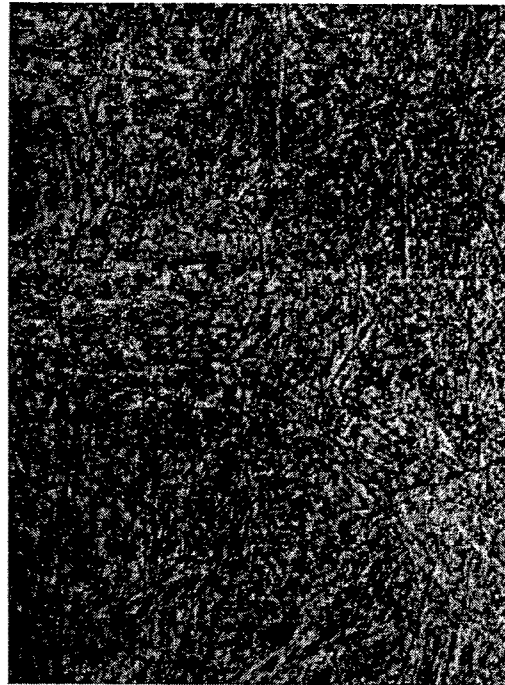
Outer Ring Mount Lug 1000X

FIGURE C-6. GENERAL MICROSTRUCTURE OF JT9D TURBINE EXHAUST CASE
OUTER RING MOUNT LUG



Outer Ring Rear Wall

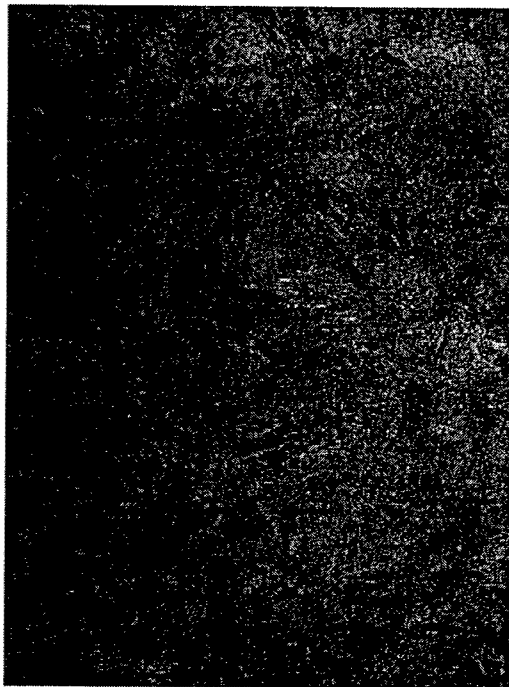
100X



Outer Ring Rear Wall

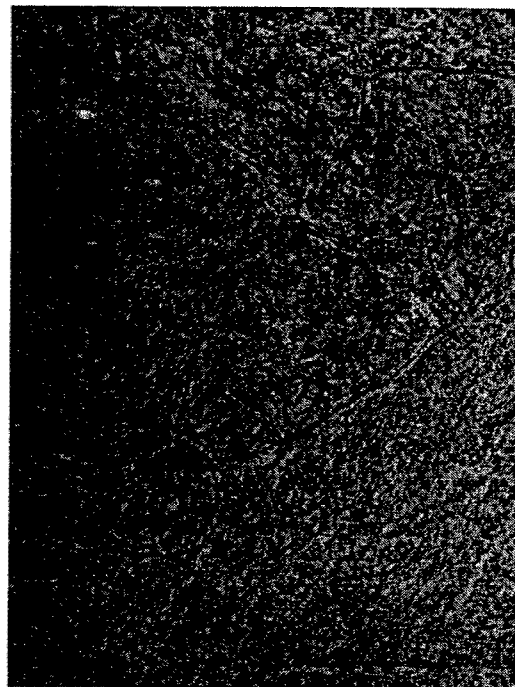
500X

FIGURE C-7. GENERAL MICROSTRUCTURE OF JT9D TURBINE EXHAUST CASE
OUTER RING REAR WALL



Outer Ring Rear Flange

100X



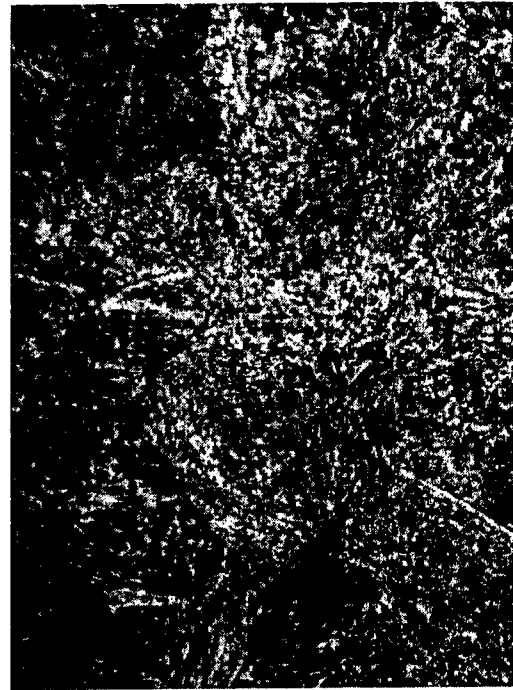
Outer Ring Rear Flange

500X

FIGURE C-8. GENERAL MICROSTRUCTURE OF JT9D TURBINE EXHAUST CASE
OUTER RING REAR FLANGE

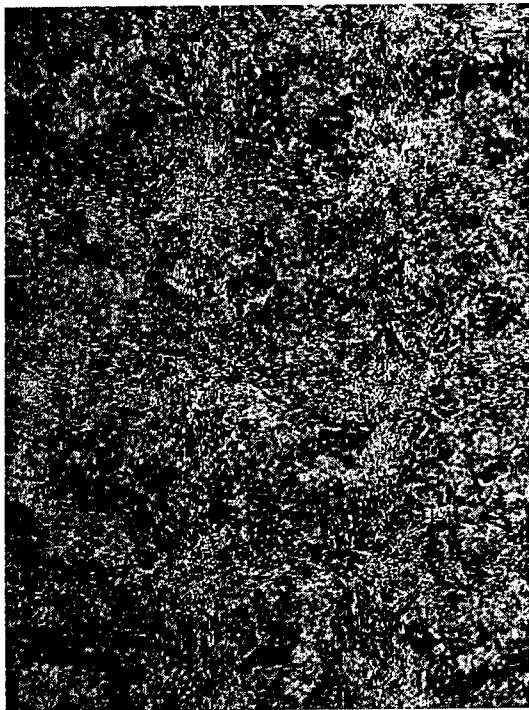


Inner Ring Mid-Wall 100X

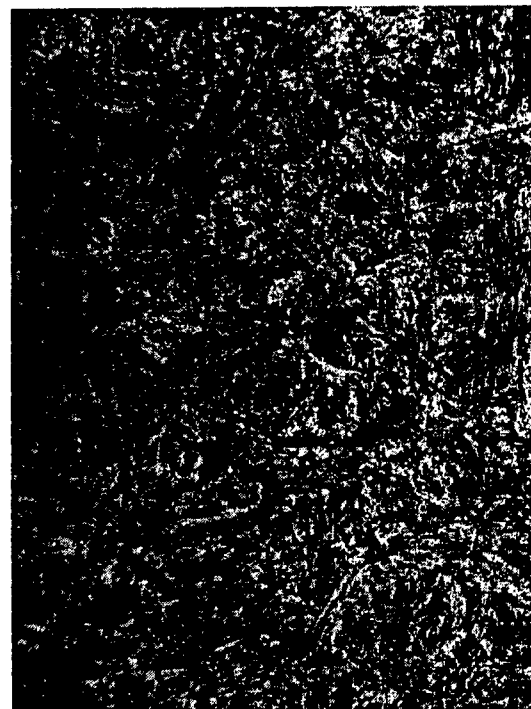


Inner Ring Mid-Wall 500X

FIGURE C-9. GENERAL MICROSTRUCTURE OF JT9D TURBINE EXHAUST CASE
INNER RING MID-WALL



Inner Ring Rear Wall 100X

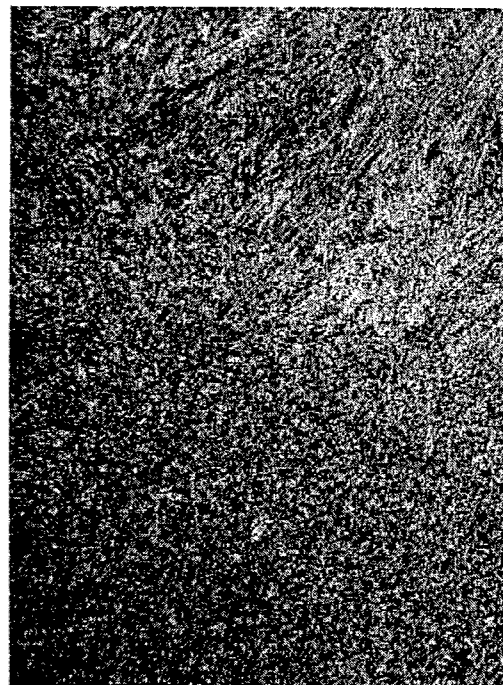


Inner Ring Rear Wall 500X

FIGURE C-10. GENERAL MICROSTRUCTURE OF JT9D TURBINE EXHAUST CASE
OUTER RING REAR WALL

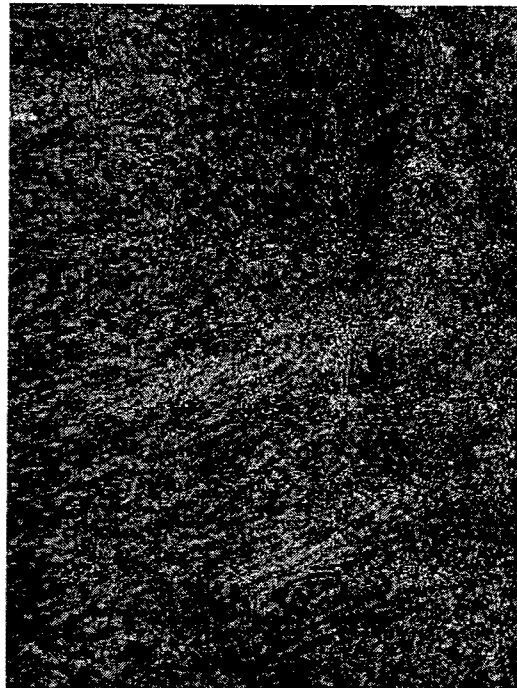


Strut Sidewall 500X

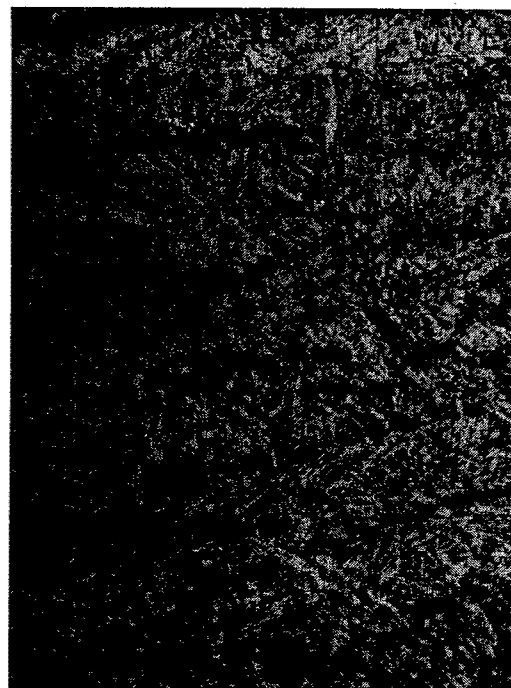


Strut (lower left) Weld 100X

FIGURE C-11. GENERAL MICROSTRUCTURE OF JT9D TURBINE EXHAUST STRUT

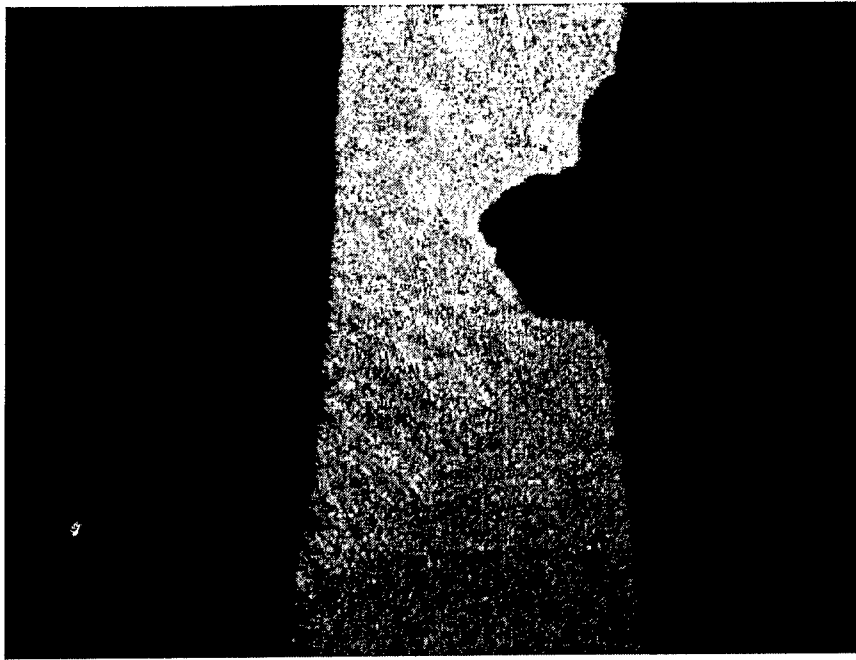


Case (upper right) Weld 100X



Typical Weld 500X

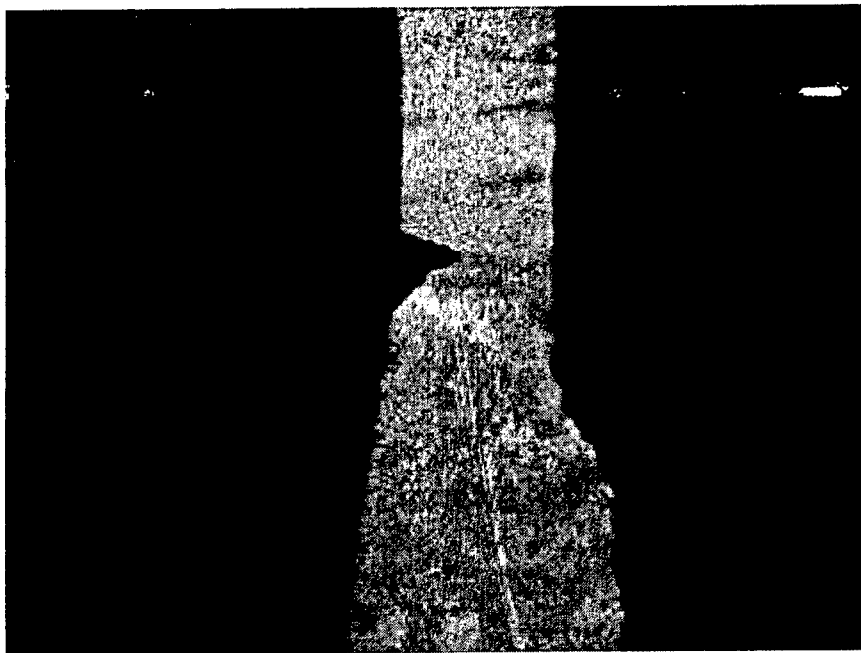
FIGURE C-12. GENERAL MICROSTRUCTURE OF JT9D TURBINE EXHAUST CASE WELD



Strut (lower)/Case Weld

50X

FIGURE C-13. GENERAL MICROSTRUCTURE OF JT9D TURBINE EXHAUST CASE LOWER STRUT/CASE WELD



Strut (Upper)/Case Weld

25X

FIGURE C-14. GENERAL MICROSTRUCTURE OF JT9D TURBINE EXHAUST CASE UPPER STRUT/CASE WELD

APPENDIX D—DESTRUCTIVE ANALYSIS OF JT9D DIFFUSER CASES AFTER EXTENDED SERVICE

D.1 JT9D DIFFUSER SECTIONING PLAN.

Each new JT9D diffuser case is a weld assembly of 17 details. These include:

1. Outer center ring (AMS 5663 forged ring)
2. Outer front skirt with integral front flange (AMS 5663 forged ring)
3. Outer rear skirt with integral rear flange (AMS 5663 forged ring)
4. Sheet metal struts; 10 total (AMS 5596 sheet)
5. Inner front ring with integral front flange (AMS 5663 forged ring)
6. Inner rear ring; rolled sheet with axial weld (AMS 5596 sheet)
7. Inner rear flange (AMS 5663 forging)
8. Inner front flange heat shield and support bracket (AMS 5596 sheet)

Final assembly contains five full-circumferential welds, one axial weld, one set of resistance welds (to attach the support bracket to the heat shield) and twenty manually produced fillet welds that connect each of the ten struts to the inner and outer ring assemblies. Figure D-1 is a photograph of a typical JT9D diffuser case. Once in the field, all but the outer center ring are replaceable either in part or as full details. Thus, each of the outer skirts, inner rings, or struts may be replaced rather than repaired. In addition, any of the four flanges, including the three integral flanges, can be separately replaced at the discretion of the operator. Of course local repairs are always an option. Depending on the size and difficulty of the repair weld, the case may be solution heat-treated prior to welding or welded in the as fully heat-treated condition and then short aged.

During normal engine operation, the greater stresses tend to be on the outer pressure wall rings. The higher temperatures meanwhile tend to be concentrated on the inner ring details. Criteria used in sectioning the cases were to try to include samples from all major case details, each of the assembly welds, and examples of repair welds. Several metallographic samples were made of each detail so at each detail, flanges and walls could be examined and sections along the axial length of the case could be examined to determine if there were microstructural differences from front to rear of the case.

As stated in the main body of the report, three of the available seven cases were selected for metallographic (and mechanical property) evaluation. On average, 40 metallographic samples were made out of each case. Sections of one case, (BW0976) were chemically etched prior to excising metallographic samples so local repairs could be more easily located. The etch however attacked the case surfaces irregularly, which made assessment of surface structure impossible, so the acid etching procedure was eliminated.

The following is a brief discussion of the general microstructure and unique features observed among the three cases followed by an atlas of photomicrographs that illustrate the major features. These represent a small portion of the evaluation and only a sample of the documented microstructures.

D.1.1 CASE AG9961 (JA Operated, 53,487 hrs, 23,869 cycles).

All three AMS 5663 details that comprise the outer pressure wall displayed significant banding. The general microstructure was of moderately coarse grains (ASTM 5 and 6) with areas where there was minimal needle delta structure interspersed with bands of high needle delta phase concentrations. Some areas displayed necklace structure, with coarse grains encircled with fine dynamically recrystallized grains. High magnification examination revealed that most grain boundaries were decorated with globular particles, both delta and carbides. Most surfaces displayed a denuded surface layer beneath which was another layer of concentrated needle delta. The denuded layer varied in depth from 0.0006" to 0.0009", while the layer of concentrated needle delta varied in depth from 0.005" to 0.0075".

Inner pressure wall AMS 5663 details had a similar banded delta structure, surface denuded layer, and concentrated delta layer. Here the denuded layer depth varied from 0.0004" to 0.0005", and the delta layer varied in depth from 0.0044" to 0.006". The rear ring, which is a rolled sheet of AMS 5596, displayed a finer grain structure (ASTM 8) with lighter banding but an overall high concentration of needle delta throughout the microstructure. The separate attached rear flange was coarse (ASTM 3-4) with less overall needle delta but with concentrations of delta in blotches rather than more continuous bands.

Struts and heat shield details also displayed a fine grain (ASTM 8-10) structure with scattered needle delta and lighter delta bands.

No defects were detected at any of the assembly welds but numerous small defects were detected at most of the repair welds. These consisted of gas pores, near HAZ cracks and cracks in "far" HAZ regions. Many, but not all of the repair welds also displayed heavy concentrations of needle delta adjacent to the welds. Cracking at the tip of the resistance weld that attaches the heat shield to its support bracket was discovered. One large crack was found that extended for more than three-quarters of the thickness of a strut attachment weld. It must be noted that when case S/N AG9961 was scrapped, it contained a number of defects that were left without repair, so it should not be implied that the large weld crack at the strut would not have been detected.

Representative photographs of the metallurgical conditions are shown in figures D-2 through D-6.

D.1.2 CASE BW0976 (BA Operated, 63,092 hrs., 13,696 cycles).

The forward skirt and front flange of the outer pressure wall displayed a varied amount of needle delta phase. Grain size varied from moderate (ASTM 6) to coarse (ASTM 4), banding was not prominent, but the heavy concentrations of delta along the grain boundaries extended out to create areas of near solid blocks of high needle concentrations. The outer center ring displayed more delta than did the forward skirt, and the rear skirt in turn displayed even heavier concentrations of needle delta than did the center ring. Almost all areas of the outer rear skirt, including the rear flange, displayed a microstructure marked by very high concentrations of needle delta phase. Surface denuded layers varied in depth from 0.0003" to 0.0009", and layers of concentrated delta extended inward from the surface with depths between 0.0030" and

0.0150". The deepest denuded layers and delta plate layers were on the forward skirt. Concentrations of delta needles were also found associated with the threads on the tapped boltholes located on the inner surface of the forward skirt.

The inner cylinder of case BW0976 presented a myriad of microstructures. The forward flange was a very fine grain (ASTM 10-11) forging that obviously was a replacement for the original integral flange. Microstructure for this piece consisted of globular delta in the grain boundaries and no needle-shaped delta phase. The forward ring was moderately coarse-grained (ASTM 4-6) consisting of generally equiaxed grains with heavy grain boundary needle delta precipitation. Patches of very heavy delta concentrations were observed throughout the material. The rear cylinder (AMS 5596 sheet) was fine grain (ASTM 8-9) with extensive amounts of delta plates scattered somewhat evenly among the microstructure. The separate rear flange was another fine grain (ASTM 11-12) forging with scattered globular delta and no needle delta phase. The heat shield was moderately coarse grain (ASTM 5) while the supporting bracket was much finer (ASTM 6). Both the heat shield and bracket had extensive needle delta phase distributed evenly throughout the microstructure. Surface denuded layers as deep as 0.0009" and surface layers of concentrated needle delta were detected as deep as 0.013". The heat shield also had a shallow oxide layer (0.00015") with oxide spikes or cracks extending into the denuded surface layer. Neither of the very fine-grained flanges displayed any evidence of concentrated needle delta on their respective surfaces but did display a denuded surface layer.

Grain size of the sheet material used to construct the struts was moderate fine grain (ASTM 6-7) but like the other sheet metal details displayed extensive amounts of needle delta phase scattered evenly throughout the microstructure.

Assembly and repair welds on the outer pressure wall were generally sound but several contained large pools of laves phase. Often the adjacent base metal also contained very high concentrations of needle delta phase. Numerous cracks were observed emanating outward from the bracket to heat shield resistance weld and within the fusion zone of the heat shield/bracket assembly weld.

Representative photographs of the metallurgical conditions are shown in figures D-7 through D-12.

D.1.3 CASE CJ3225 (JA Operated, 60,307 hrs., 19,260 cycles).

Within the outer pressure wall, heavy concentrations of needle-shaped delta phase were present throughout the forward skirt (and flange) and in patches and at grain boundaries of the center ring and rear skirt details. The rear skirt displayed the least of the patches but in the thicker sections of the skirt concentrations of needle delta could be extensive. The amount of evenly distributed delta phase in the forward and center rings made it difficult to ascertain if a surface layer of high delta phase concentration existed. However, a surface denuded layer of 0.00078" was observed on the forward skirt regions of the case. Heavy concentrations of delta needles were also observed associated with the tapped lugs on the forward skirt.

The forward ring (and flange) of the inner pressure wall consisted of a duplex microstructure, typically ASTM 4-5, in grain size, but many of the coarse grains were surrounded by a necklace structure of finer grains. The rear ring was finer grain sheet (ASTM 6-7) with heavy delta concentrations of delta phase throughout, while the rear flange was marked by delta phase concentrations in patches.

The sheet metal struts were relatively fine grained with extensive needle delta phase scattered throughout.

This case displayed many repair welds on the outer and inner pressure wall. Many of the welds also displayed subsurface cracks within the weld fusion zone. The numerous layers of weld bead observed suggest that many of the welds are repairs over previous welds. However, there is no way to prove this conclusively. Cracks, lack of fusion, and gas pores were all observed within the fusion zone material of the case. However, in many cases, these regions were actually HAZs to subsequent repairs.

Representative photographs of the metallurgical conditions are shown in figures D-13 through D-17.

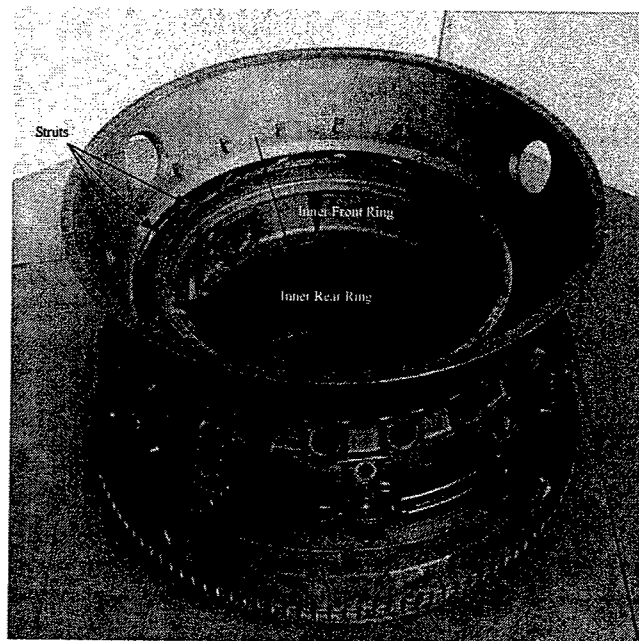
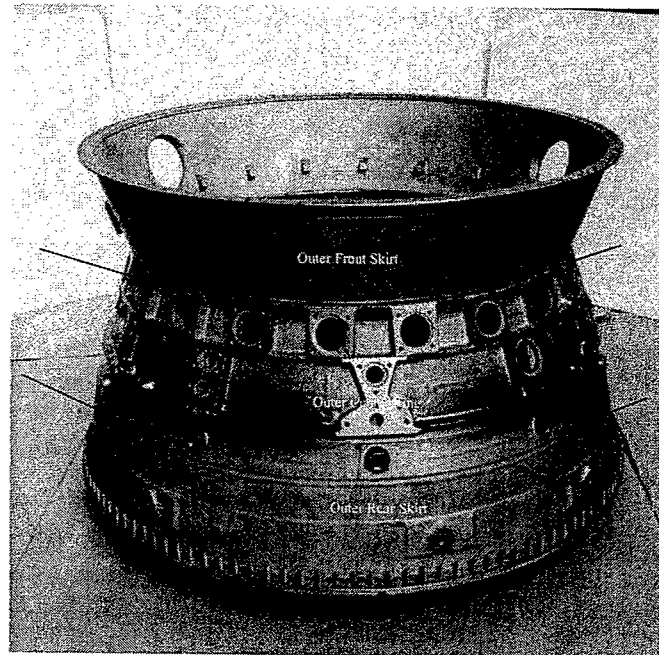
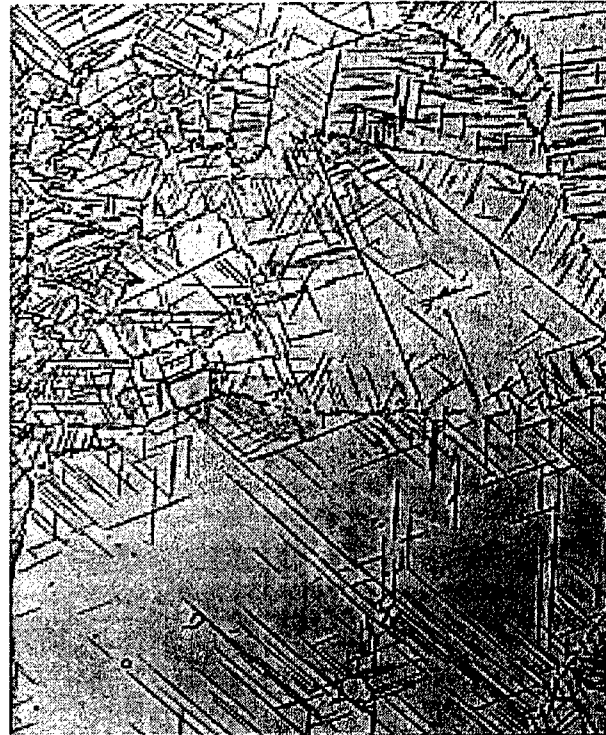


FIGURE D-1. VIEWS OF A JT9D DIFFUSER CASE FROM A SIDE PROFILE POSITION (UPPER) AND FROM A FORWARD POSITION LOOKING AFT (The major details are labeled and the arrows indicate where major circumferential assembly welds are placed.)



Outer Front Flange 400X



Outer Front Skirt 400X



Outer Center Ring 100X



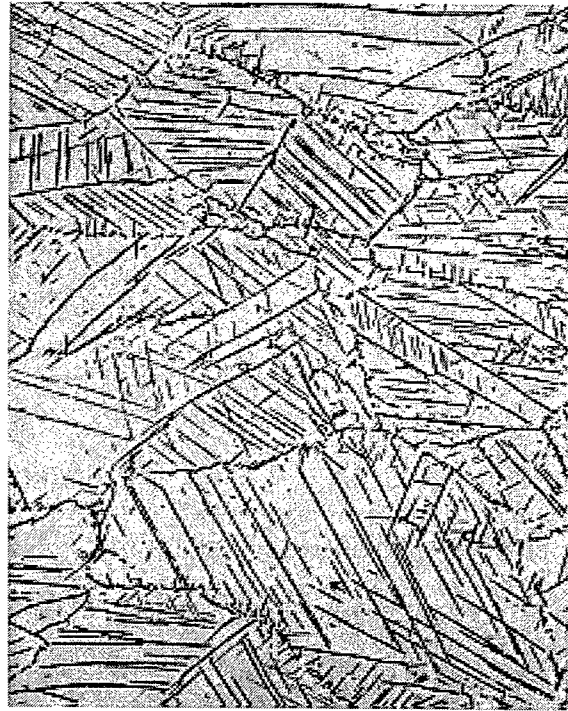
Outer Center Ring 400X

FIGURE D-2. JT9D DIFFUSER S/N AG9961, GENERAL MICROSTRUCTURES OF OUTER PRESSURE WALL DETAILS



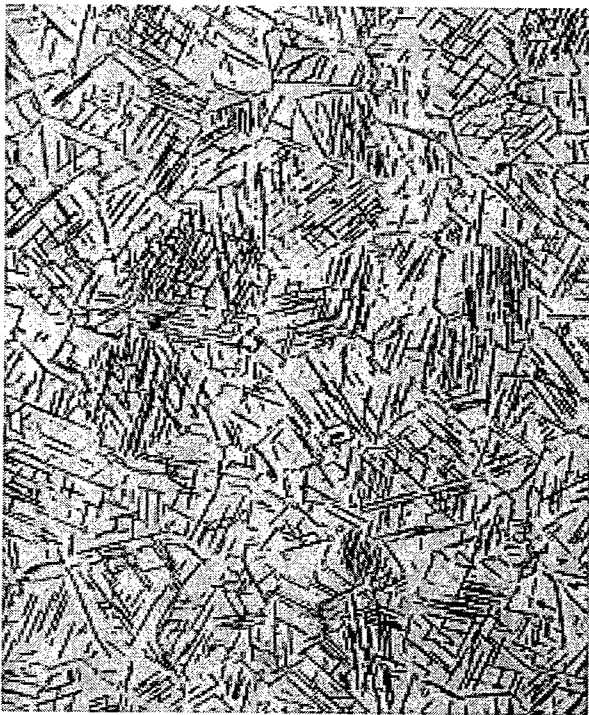
Outer Rear Skirt

400X



Outer Rear Flange

400X



Inner Rear Ring

400X



Inner Rear Flange

400X

FIGURE D-3. JT9D DIFFUSER S/N AG9961, GENERAL MICROSTRUCTURES OF OUTER REAR (UPPER) AND INNER REAR (LOWER) RING DETAILS



Inner Front Flange

100X



Inner Front Flange

400X



Inner Front Ring

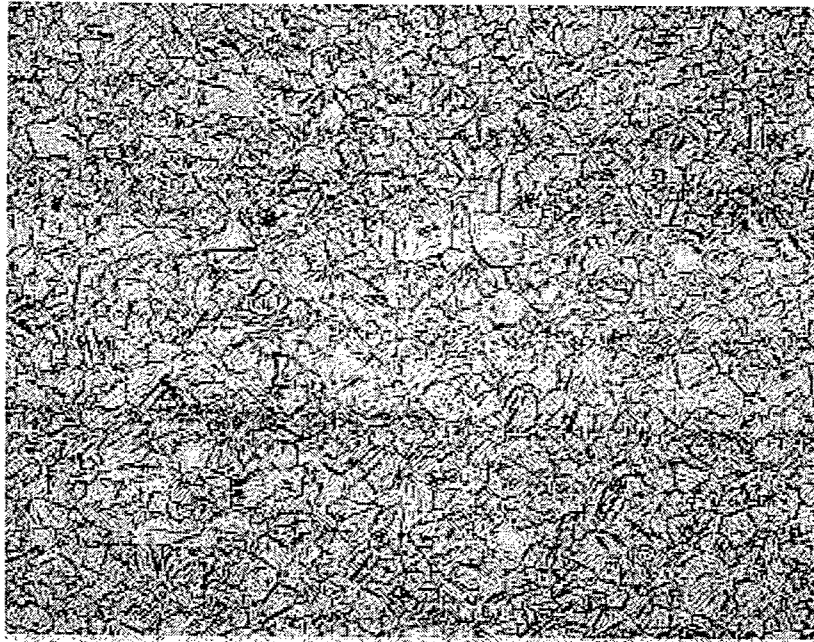
100X



Inner Front Ring

400X

FIGURE D-4. JT9D DIFFUSER S/N AG9961, GENERAL MICROSTRUCTURES OF THE INNER FRONT RING DETAIL



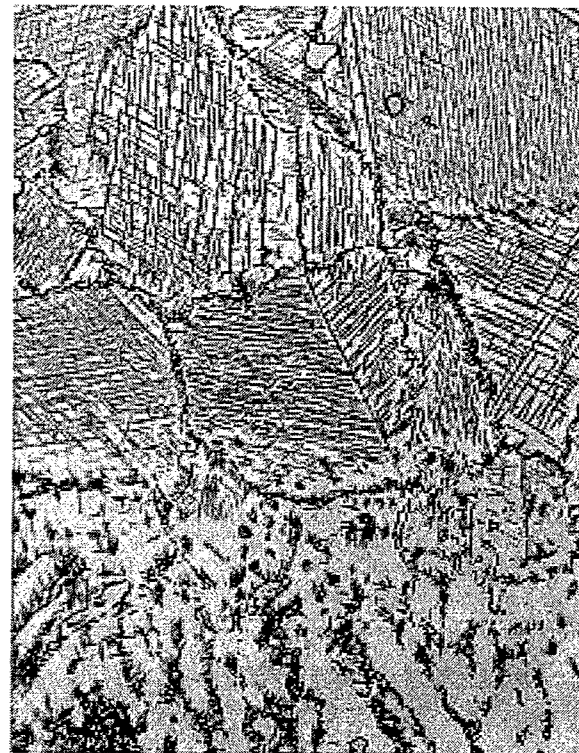
Strut Sidewall

200X



Surface Delta Concentration

400X



Weld HAZ Delta Concentration

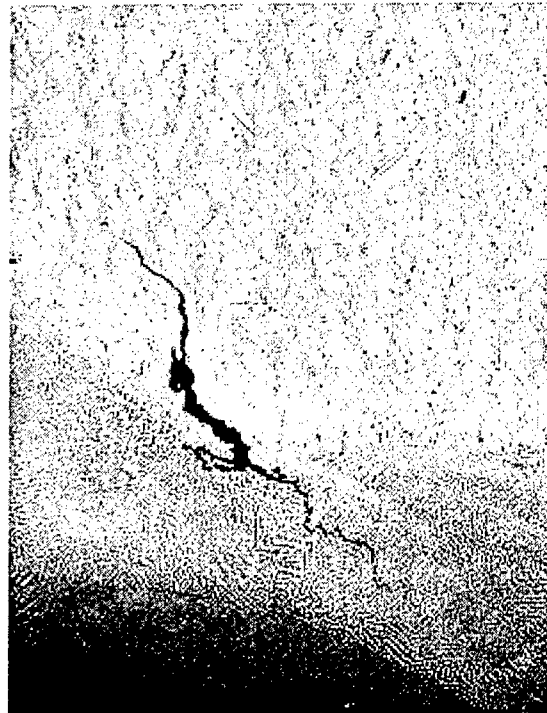
400X

FIGURE D-5. JT9D DIFFUSER S/N AG9961, GENERAL MICROSTRUCTURES OF THE STRUT (UPPER) SHEET MATERIAL AND HEAVY CONCENTRATIONS OF NEEDLE DELTA PHASE ASSOCIATED WITH SOME SURFACES (LOWER LEFT) AND WELD HAZ (LOWER RIGHT)



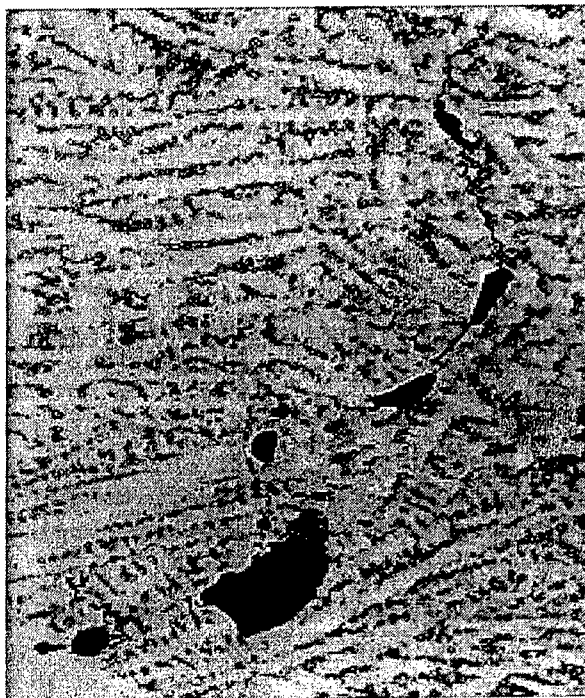
Strut Attachment Weld

20X



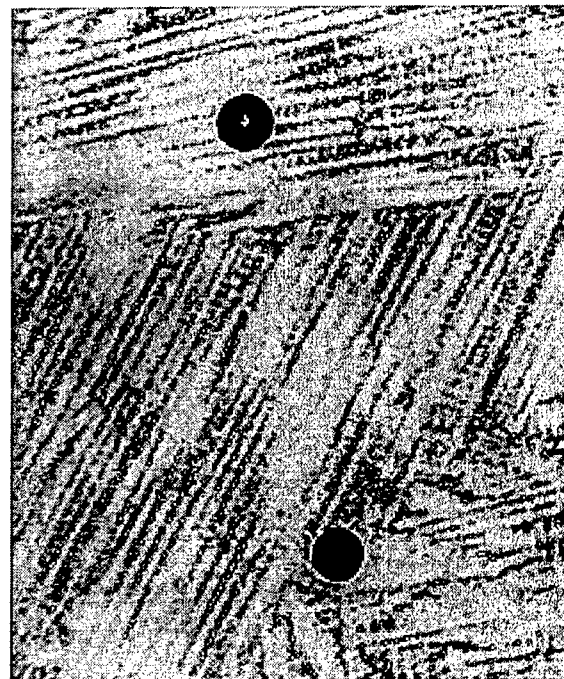
Repair Weld

25X



Repair Weld

200X



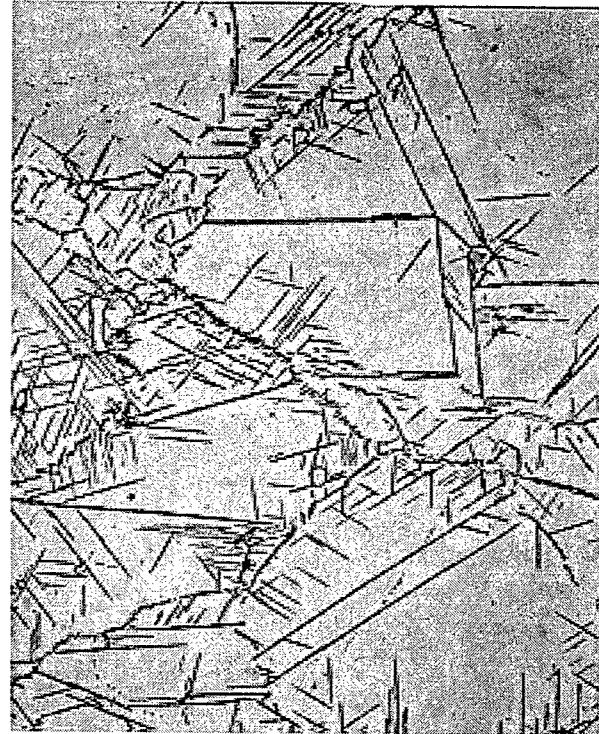
Repair Weld

200X

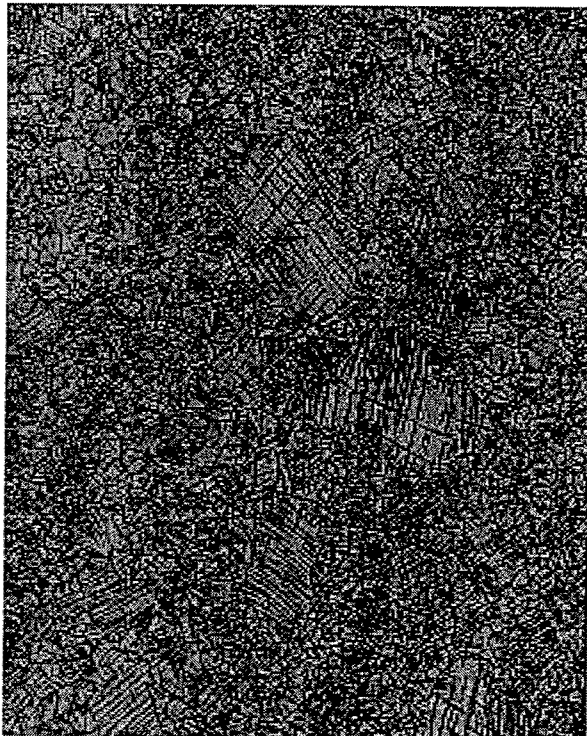
FIGURE D-6. JT9D DIFFUSER S/N AG9961, TYPICAL WELD DEFECTS INCLUDING CRACKS (UPPER), LACK OF FUSION (LOWER LEFT), AND GAS PORES (LOWER RIGHT)



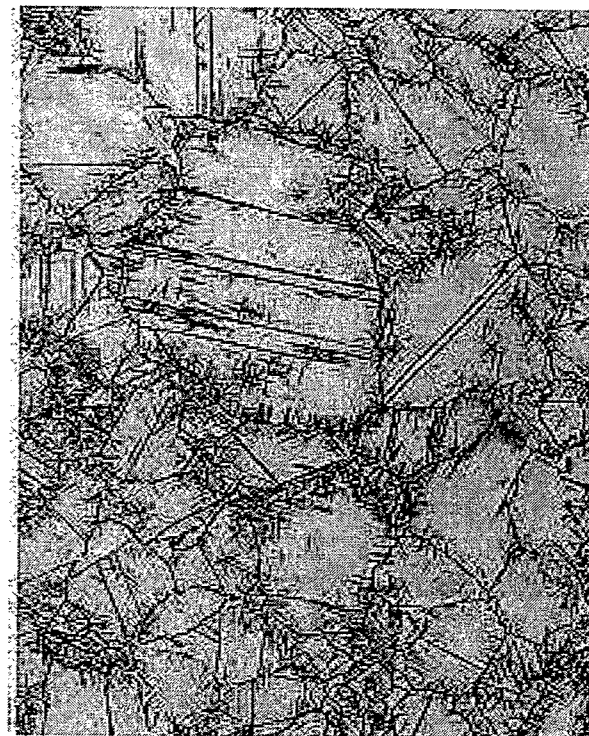
Outer Forward Flange 100X



Outer Forward Flange 400X



Outer Forward Skirt 100X



Outer Forward Skirt 100X

FIGURE D-7. JT9D DIFFUSER S/N BW0976, GENERAL MICROSTRUCTURES OF THE OUTER FRONT SKIRT DETAIL



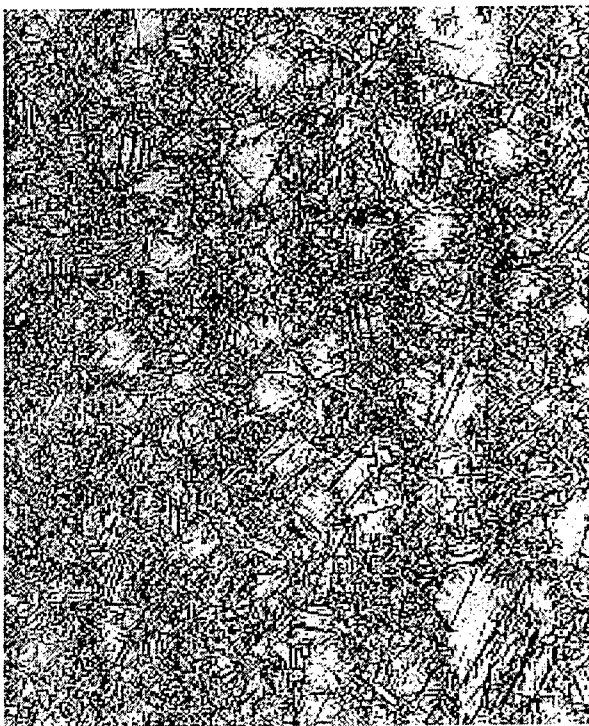
Outer Front Skirt

400X



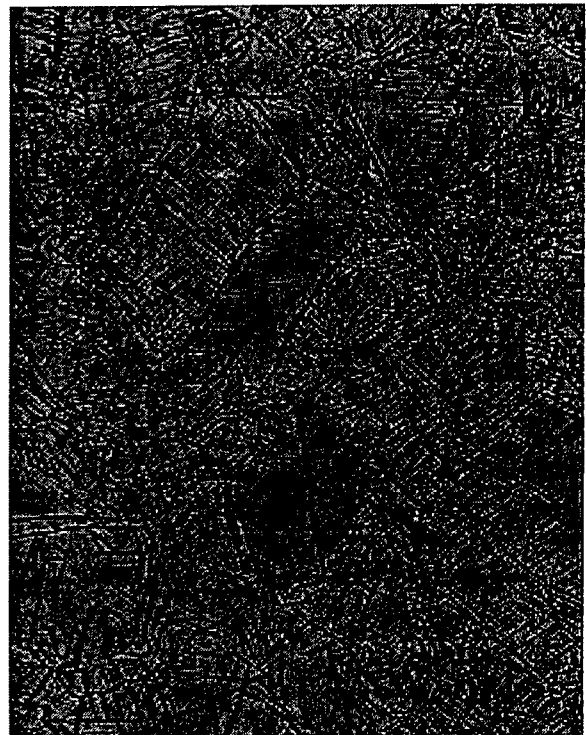
Outer Rear Skirt

400X



Outer Center Ring

100X



Outer Center Ring

400X

FIGURE D-8. JT9D DIFFUSER S/N BW0976, GENERAL MICROSTRUCTURES OF THE OUTER FRONT SKIRT (UPPER LEFT), OUTER REAR SKIRT (UPPER RIGHT), AND OUTER CENTER RING DETAILS



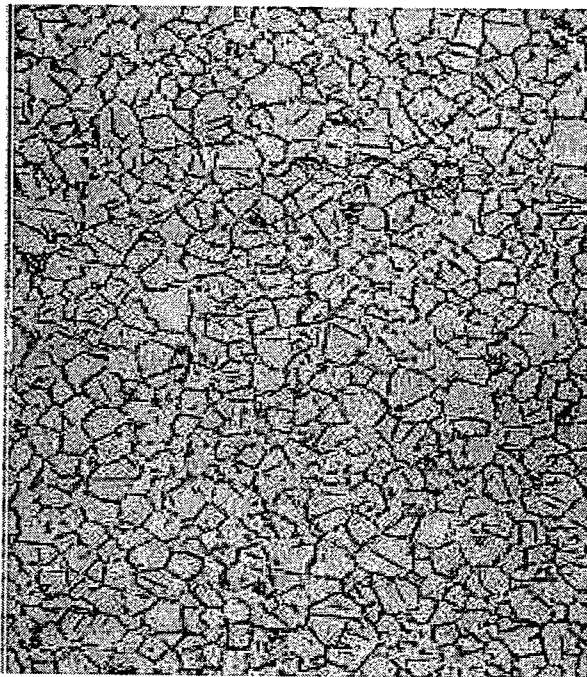
Inner Front Ring

100X



Inner Front Ring

400X



Inner Front Flange

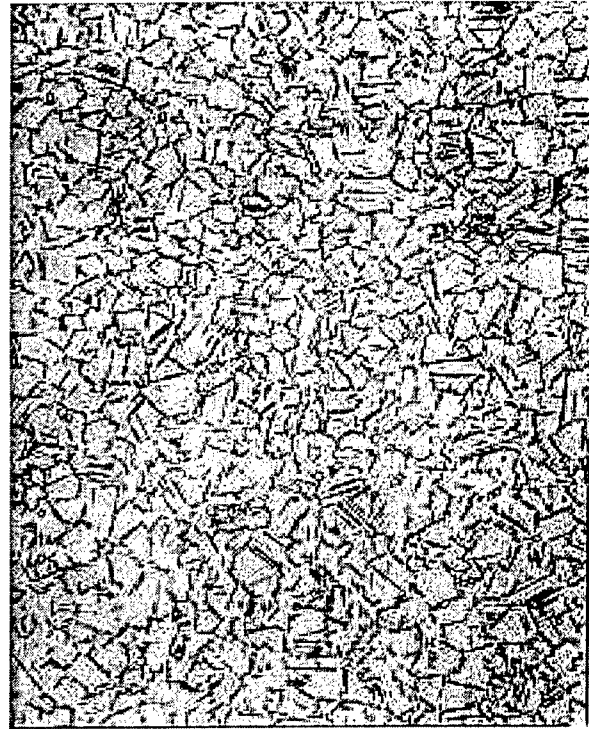
400X

FIGURE D-9. JT9D DIFFUSER S/N BW0976, GENERAL MICROSTRUCTURES OF THE INNER FRONT RING DETAIL (The much finer grain microstructure of the flange (lower) relative to the detail ring wall (upper) illustrates that this front flange is a repair replacement flange attached sometime in the service life of the case.)



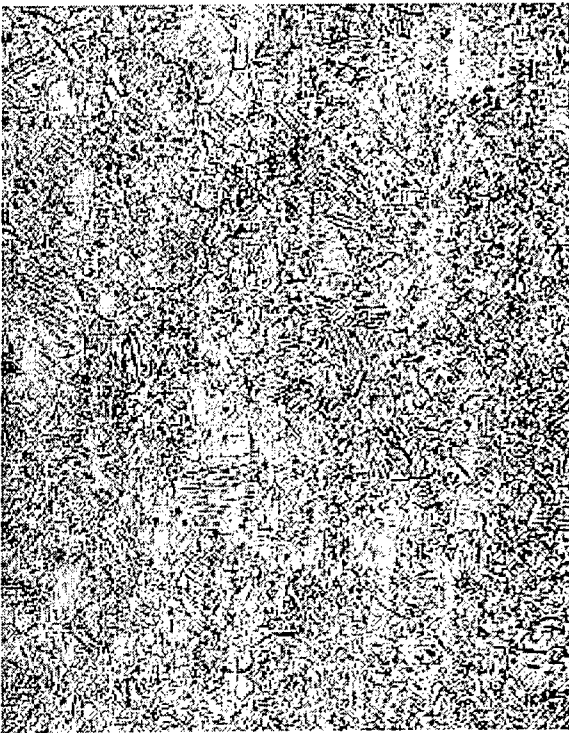
Inner Rear Ring

400X



Inner Rear Flange

400X



Strut Sidewall

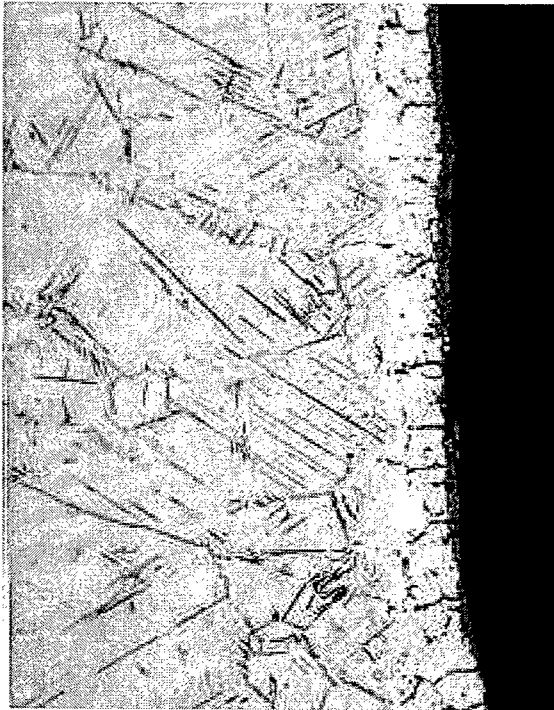
100X



Strut Sidewall

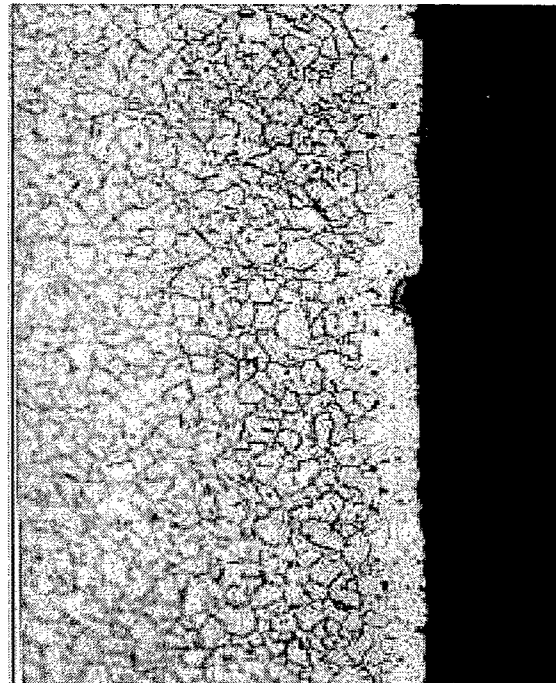
200X

FIGURE D-10. JT9D DIFFUSER S/N BW0976, GENERAL MICROSTRUCTURES OF THE INNER REAR RING (UPPER) AND STRUT (LOWER) DETAILS



Heat Shield

400X



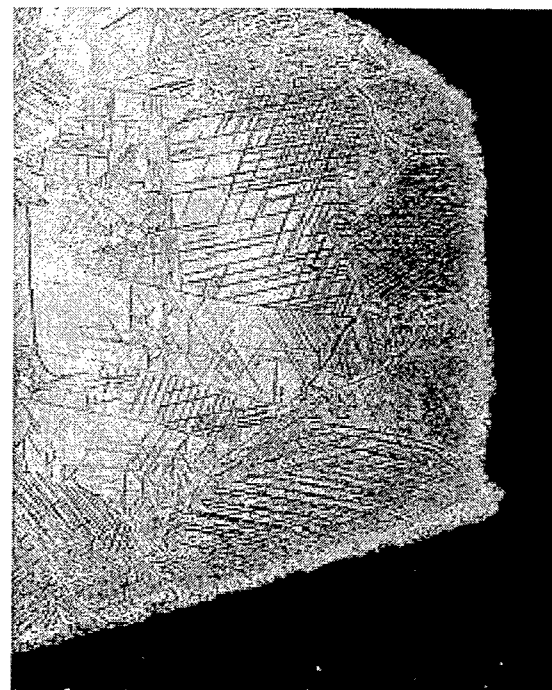
Inner Front Flange

400X



Outer Front Flange

200X



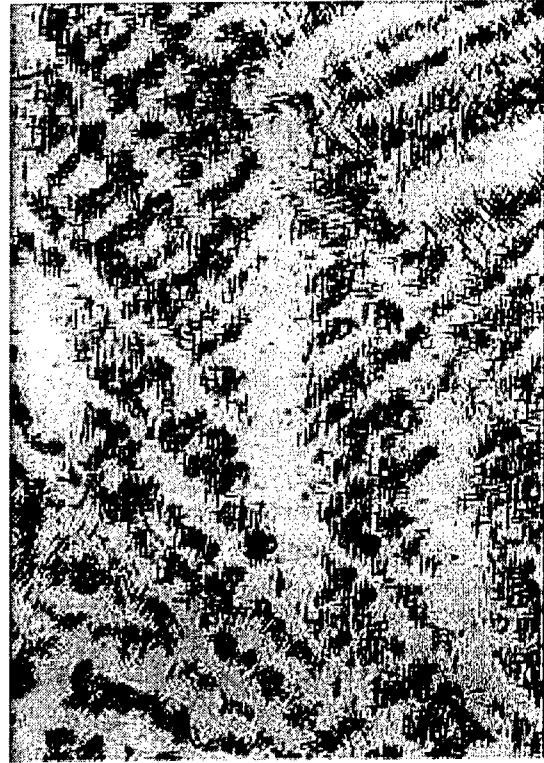
Tapped Hole Thread

200X

FIGURE D-11. JT9D DIFFUSER S/N BW0976, EXAMPLES OF SURFACE DEPLETION ON INNER CASE DETAILS (UPPER) AND CONCENTRATED NEEDLE DELTA ASSOCIATED WITH SOME SURFACES (LOWER LEFT) AND THREADS (LOWER RIGHT)

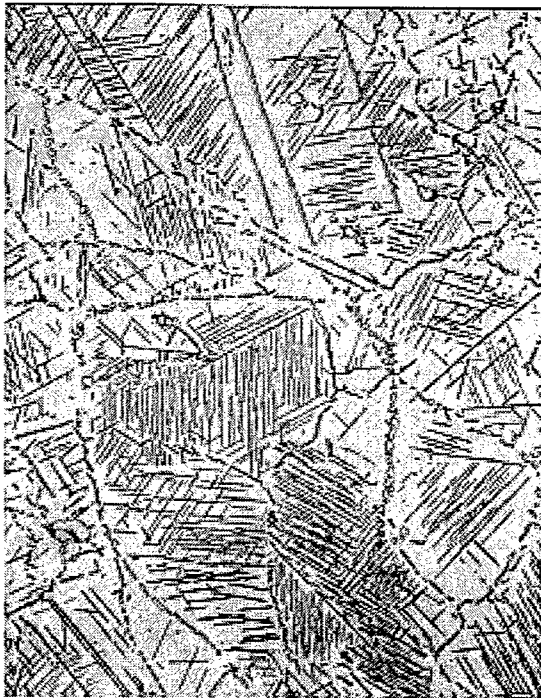


Outer Front Skirt 400X



Outer Center Ring 400X

FIGURE D-12. JT9D DIFFUSER S/N BW0976, REPAIR WELD MICROSTRUCTURES
(The higher (slightly) concentration of needle delta in the weld located on the center ring (left) relative to the front skirt repair (left) suggests that the center ring repair was exposed to more re-solution heat treatments over the service life of the case.)



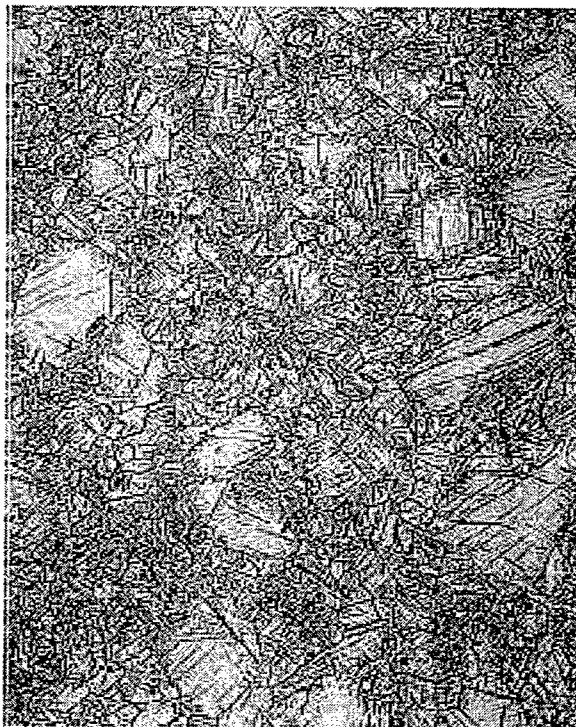
Outer Front Flange

400X



Outer Front Skirt

400X



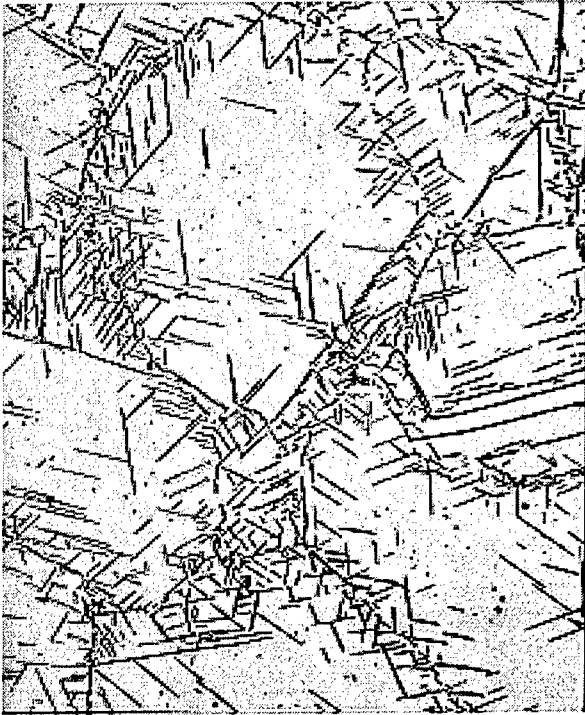
Outer Center Ring 100X



Outer Center Ring

400X

FIGURE D-13. JT9D DIFFUSER S/N CJ3225, GENERAL MICROSTRUCTURES OF THE OUTER FRONT SKIRT (UPPER) AND OUTER CENTER RING (LOWER) DETAILS



Outer Rear Skirt 400X



Outer Rear Flange 400X



Strut Sidewall 200X

FIGURE D-14. JT9D DIFFUSER S/N CJ3225, GENERAL MICROSTRUCTURES OF THE INNER REAR RING (UPPER) AND STRUT (LOWER) DETAILS



Inner Front Ring

100X



Inner Front Ring

100X



Inner Front Ring

400X



Inner Front Flange

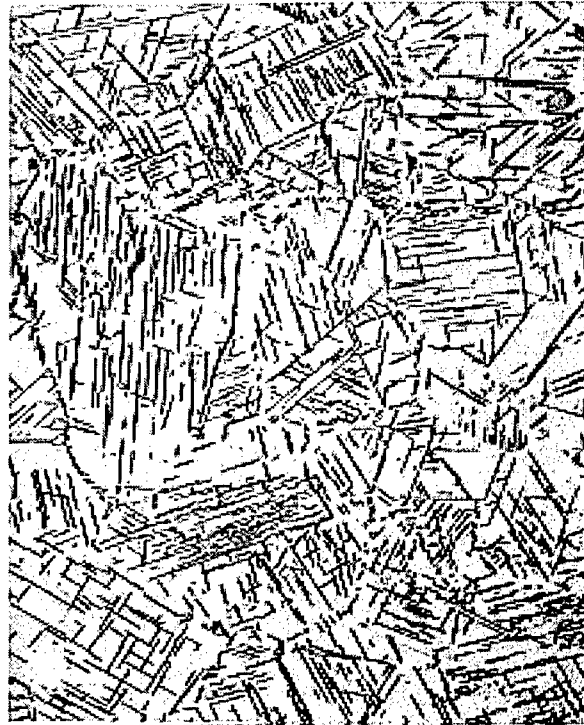
400X

FIGURE D-15. JT9D DIFFUSER S/N CJ3225, GENERAL MICROSTRUCTURES OF THE INNER FRONT RING DETAIL



Inner Rear Ring

200X



Inner Rear Ring

400X



Inner Rear Flange

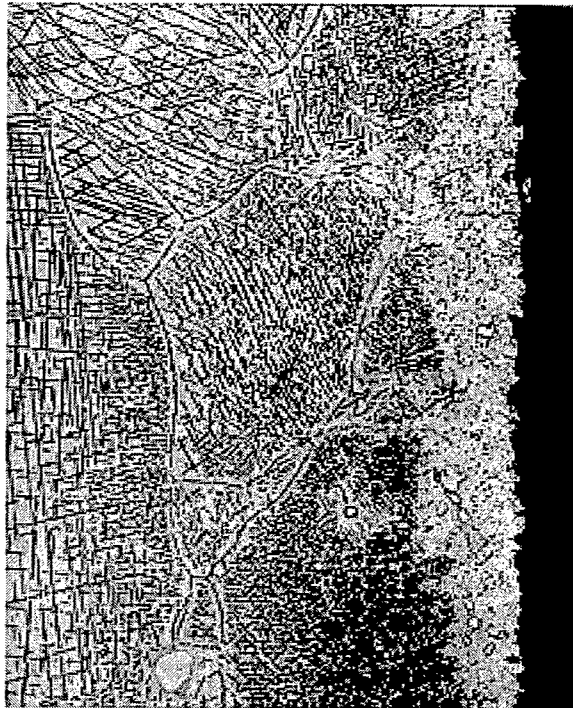
200X



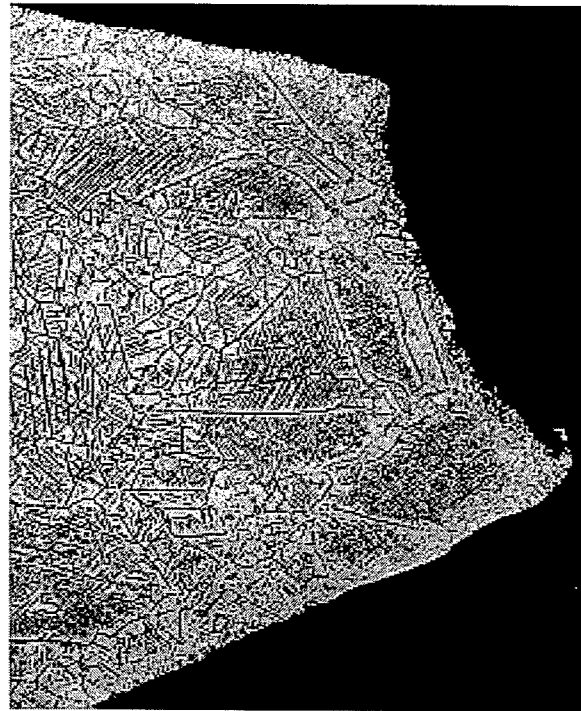
Inner Rear Flange

400X

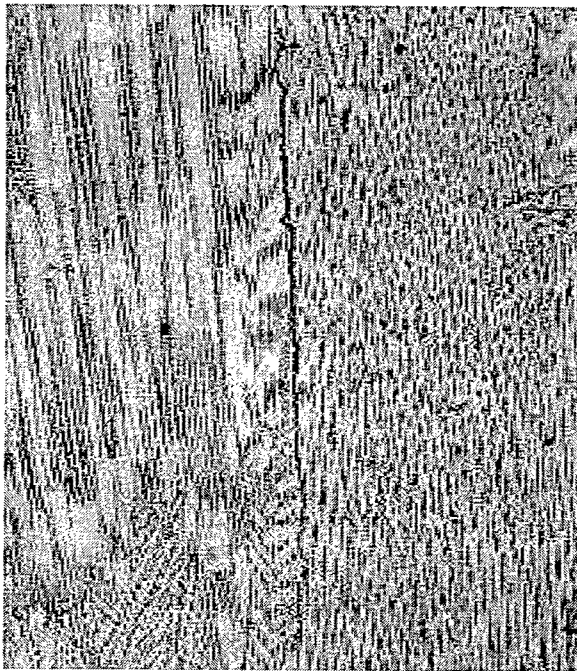
FIGURE D-16. JT9D DIFFUSER S/N CJ3225, GENERAL MICROSTRUCTURES OF THE INNER REAR RING DETAILS



Inner Forward Ring 400X



Outer Pressure Wall Tapped Hole 200X



Outer Center Ring Repair 50X



Outer Center Ring Repair 1000X

FIGURE D-17. JT9D DIFFUSER S/N CJ3225, HEAVY CONCENTRATIONS OF NEEDLE DELTA ASSOCIATED WITH SOME SURFACES (UPPER LEFT) AND TAPPED HOLE THREADS (UPPER RIGHT) AND REPAIR WELD CRACKS (LOWER)
(The crack illustrated in the lower right figure is associated with interdendritic concentrations of laves phase.)